Experimental and numerical study of hydrodynamic oscillations in partially saturated porous media

Yunli Wang

THÈSE

N° d'ordre :

En vue de l'obtention du

DOCTORAT DE L'UNIVERSITÉ DE TOULOUSE

Délivré par : Institut National Polytechnique de Toulouse
Discipline ou spécialité : Sciences de la Terre et des Planètes Solides

---

Présentée et soutenue par **Yunli WANG**
LE 16 SEPTEMBRE 2010

Etude expérimentale et numérique des oscillations hydrodynamiques en milieux poreux partiellement saturés

---

JURY

Mohamed CHAGDALI (rapporteur)	Université Hassan II, laboratoire LCSM, Casablanca
Diane P. HORN (rapporteur)	Birkbeck University, London, School of Geography
Vincent REY (président)	Université du Sud-Toulon-Var, ISITV & LSEET-LEPI
Dominique ASTRUC	Institut National Polytechnique de Toulouse, IMFT
Jérôme BROSSARD	Université du Havre, laboratoire LOMC
David LABAT	Université Paul Sabatier, LMTG, Toulouse
Manuel MARCOUX (co-dir. thèse)	Université Paul Sabatier, IMFT
Rachid ABABOU (dir. thèse)	Institut National Polytechnique de Toulouse, IMFT
Olivier EIFF (invité)	Institut National Polytechnique de Toulouse, IMFT
Michel QUINTARD (invité)	CNRS, laboratoire IMFT, Toulouse

Ecole doctorale : *Sciences de l'univers, de l'environnement et de l'espace (SdU2E)*
Unité de recherche : *Institut de Mécanique des Fluides de Toulouse (IMFT)*
Directeur(s) de Thèse : *Rachid ABABOU et Manuel MARCOUX.*

Title

Experimental and Numerical Study of Hydrodynamic Oscillations in Partially Saturated Porous Media

Résumé

Cette thèse vise à étudier expérimentalement, analytiquement et numériquement, les conséquences de variations et d'oscillations hydrodynamiques à forte variabilité temporelle en milieux poreux partiellement saturés. Les problèmes que nous étudions comportent des surfaces libres tant à l'extérieur qu'à l'intérieur des milieux poreux, celles-ci étant définies comme des isosurfaces de pression d'eau égale à la pression atmosphérique (Pwater = Patm).

Les différentes études expérimentales réalisées en laboratoire sont, respectivement :

- une expérience d'imbibition dans une boite à sable avec effets capillaires importants;
- la transmission d'oscillations de la surface libre à travers un massif sableux intercalaire dans un petit canal à houle (IMFT, Toulouse);
- l'étude de la dynamique et de la propagation des oscillations des niveaux d'eau dans un grand canal à houle (HYDRALAB, Barcelone), partiellement recouvert d'un fond sableux incliné, avec mesures de niveaux d'eau en pleine eau et sous le sable, et mesures du fond sableux (érosion/dépôts).

Pour les études théoriques, nous avons développés des solutions analytiques linéarisées. Un exemple de problème traité analytiquement est: l'équation linéarisée de Dupuit-Boussinesq (D-B) transitoire à surface libre, en hypothèse d'écoulements plans et vidange/remplissage instantané : oscillations forcées, transmission et dissipation d'ondes à travers une boite à sable rectangulaire.

Nous avons aussi développé une solution de l'équation faiblement non linéaire de Dupuit-Boussinesq (D-B) pour étudier le problème d'imbibition avec variation abrupte du niveau d'eau amont (suivi temporel du front de saturation).

Nous avons pu étudier les différents types de problèmes transitoires liés aux expériences citées plus haut par simulation numérique. En particulier, nous avons simulé des écoulements partiellement saturés et insaturés, en coupe verticale, à l'aide d'un code de calcul (BIGFLOW 3D) qui résoud l'équation de Richards généralisée en régime transitoire.

Nous avons ainsi étudié numériquement en régime non saturé, l'expérience d'imbibition dans un sable initialement sec à frontières verticales (*IMFT sandbox*), puis l'expérience de propagation d'ondes dans le grand canal à houle de Barcelone (laboratoire HYDRALAB) comportant une plage de sable inclinée, avec un couplage complètement intégré entre les zones micro-poreuse (sable) et "macro-poreuse" (pleine eau).

Pour analyser les résultats de cette dernière expérience et les comparer aux simulations, nous avons utilisé plusieurs méthodes de traitement et d'analyse des signaux : analyse de Fourier (spectres de fréquences) ; ondelettes discrètes multi-résolution (Daubechies) ; analyses corrélatoires simple et croisée. Ces méthodes sont combinées avec des méthodes de pré-filtrage pour estimer dérives et résidus (moyennes mobiles ; ondelettes multi-résolution). Cette analyse des signaux a permis de comprendre et quantifier la propagation à travers une plage de sable.

Au total, les différentes approches de modélisation mis en œuvre, associé à des procédures de calage en situation de couplage transitoire non linéaire ont permis de reproduire globalement les phénomènes de propagation de teneur en eau et de niveau d'eau dans les différentes configurations étudiées.

Mots-Clé : Eau souterraine; Imbibition ; Propagation d'ondes ; Oscillations et fluctuations; Milieux poreux; Macro-poreux; L'écoulement plan (Dupuit-Boussinesq); Equation de Richards ; Ecoulement partiellement saturé; Plage de sable inclinée; Traitement des signaux ; Ondelettes multirésolution ; Fonction de corrélation croisée; Spectre de fréquences ; Fonction de cohérence ; Canal à houle

Abstract

This thesis aims at investigating experimentally, analytically and numerically, the consequences of hydrodynamic variations and oscillations with high temporal variability in partially saturated porous media. The problems investigated in this work involve “free surfaces” both outside and inside the porous media, the free surface being defined as the “atmospheric” water pressure isosurface (Pwater = Patm).

The laboratory experiments studied in this work are, respectively:

- Lateral imbibition in a dry sand box with significant capillary effects;
- Transmission of oscillations of the free surface through a vertical sand box placed in a small wave canal (IMFT, Toulouse);
- Dynamics of free surface oscillations and wave propagation in a large wave canal (HYDRALAB, Barcelona), partially covered with sand, with measurements of both open water and groundwater levels, and of sand topography (erosion / deposition).

For theoretical studies, we have developed linearized analytical solutions. Here is a sample problem that was treated analytically in this work:

- The linearized equation of Dupuit-Boussinesq (DB) for transient free surface flow, assuming horizontal flow and instantaneous wetting/drainage of the unsaturated zone: forced oscillations, wave transmission and dissipation through a rectangular sandbox.

We also developed a weakly nonlinear solution of the Dupuit-Boussinesq equation to study the sudden imbibition (temporal monitoring of the wetting front).

We have studied the different types of transient flow problems related to the experiments cited above by numerical simulation. In particular, we have simulated unsaturated or partially saturated transient flows in vertical cross-section, using a computer code (BIGFLOW 3D) which solves a generalized version of Richards’ equation.

Thus, using the Richards / BIGFLOW 3D model, we have studied numerically the experiment of unsaturated imbibition in a dry sand (IMFT sandbox), and then, with the same model, we have also studied the partially saturated wave propagation experiment in the large Barcelona wave canal (HYDRALAB laboratory), focusing on the sloping sandy beach, with coupling between the micro-porous zone (sand) and the “macro-porous” zone (open water).

To interpret the results of the latter experiment and compare them to simulations, we use several methods of signal analyzis and signal processing, such as: Fourier analysis, discrete multi-resolution wavelets (Daubechies), auto and cross-correlation functions. These methods are combined with pre-filtering methods to estimate trends and residuals (moving averages; discrete wavelet analyses). This signal analyzis has allowed us to interpret and quantify water propagation phenomena through a sandy beach.

To sum up, different modeling approaches, combined with model calibration procedures, were applied to transient nonlinear coupled flow problems. These approaches have allowed us to reproduce globally the water content distributions and water level propagation in the different configurations studied in this work.

Key-Words: Groundwater; Sand box; Imbibition ; Wave propagation and transmission ; Water level oscillations and fluctuations ; Porous media ; Micro-porous ; Macro-porous ; Numerical simulation ; Plane flow model (Dupuit-Boussinesq) ; Richards nonlinear 3D model ; Partially saturated flow ; Sand Box ; Sloping sand beach ; Signal processing ; Multiresolution wavelets ; Cross-correlation function ; Period ; Frequency spectrum ; Coherency function; Wave canal ; Wave generator.

Remerciements

Ce travail de thèse a été réalisé à l'Institut de Mécanique des Fluides de Toulouse (IMFT), et financé par le gouvernement chinois (CSC scholarship).

Arrivée au bout de ce travail, il m'est agréable de remercier tous ceux qui n'ont pas hésité à me fournir ce qu'ils pouvaient comme aide et assistance.

Je tiens tout d'abord à exprimer ma profonde reconnaissance à mon directeur de thèse le professeur Rachid Ababou, qui a consacré à l'encadrement de ma thèse un temps et une disponibilité d'esprit considérables ; j'y ai été d'autant plus sensible que son emploi du temps est très chargé. J'ai ainsi largement pu profiter de sa grande acuité scientifique et de son enthousiasme indéfectible et communicatif pour le travail de ses étudiants. Je lui suis donc redevable d'avoir pu faire une thèse dans des conditions exceptionnelles.

Je remercie également mon co-directeur de thèse, Dr. Manuel Marcoux, qui m'a accompagnée tout au long de ce travail de thèse. Je souhaite également le remercier en particulier pour le sens qu'il a su donner à mon travail ainsi que pour son aide lors des expériences.

Je tiens à remercier Monsieur Michel Quintard qui m'a présenté au professeur Rachid Ababou m'ayant permis de réaliser ma thèse à IMFT.

Je remercie tous les membres du jury d'avoir accepté l'invitation pour participer à mon jury de thèse : Mohamed Chagdali, Diane P. Horn, Vincent Rey, Dominique Astruc, Jérôme Brossard, David Labat, Olivier Eiff, Michel Quintard.

Je remercie la direction de l'IMFT (directeur Jacques Magnaudet, directeur adjoint Henri-Claude Boisson, assistante de direction Doris Barrau, coordinatrice administrative Sandrine Chupin, agents hygiène et sécurité Bruno Bourret) et tous le personnel (en particulier Suzy Bernard, Lionel Le-Fur, Muriel Sabater, Catherine Thuriot, Jean-Pierre Escafit, Hervé Ayroles, Yannick Exposito) pour leur gentillesse et leur excellent travail. Particulièrement, je tiens à remercier madame Catherine Thuriot qui m'a aidé pour le bon déroulement de l'apéritif de fin de soutenance.

Je remercie les directeurs de l'Université Jiaotong Chongqing qui m'ont donné la chance de faire mes études en France ; également, je remercie la responsable de ma bourse Xiaotao Zhang et tous les employés du Crous qui ont une grande responsabilité dans le déroulement de ce travail, m'ayant permis de réaliser ma thèse dans de bonnes conditions matérielles.

Je remercie tous les doctorants de Groupe GEMP, ceux qui sont toujours là comme ceux qui sont partis : Hassane Fatmi, David Bailly, Khalil Alastal, Clément Louriou, ..., pour leurs amitié et discussions concernant le sujet de thèse mais aussi parcequ'ils ont facilité mon intégration et le bon déroulement de mon séjour en France.

Je remercie tous mes amis, particullierement, Bilal Alhajjar, Faiza Hidri, Long Du, Na Tao, Yua Yang et Thu-Thi-Hoai Le qui m'ont donné beaucoup d'amitié et beaucoup de courage pendant ma thèse, surtout pendand les périodes les plus difficiles.

Je désire enfin remercier mes parents, mes frères et mes soeurs. Je pense à ma mère: ses conseils et ses sacrifices sont gravés dans mon esprit et me guideront pour toute la vie ; à mon père ; sa patience et son soutien moral et matériel au long de mes études ont été pour moi d'un grand réconfort. Je pense aussi, à mes frères et soeurs pour leur compréhension et leur amour qui m'a donné la force de continuer.

Table of contents

List of symbols

Introduction 1

0 Introduction 1

0.1 Objectives of the thesis 1

0.2 Literature review (state of the art) 2

0.2.1 Observations on beach groundwater response to tidal & wave forcing 2

0.2.2 Modeling of beach groundwater response to tidal & wave forcing 7

0.2.3. Other review on topics of interests 11

0.3 Outline of the thesis 14

Part I GOVERNING EQUATIONS AND NUMERICS 17

Chapter 1: Governing equations and constitutive laws for porous media 18

1.1 Introduction 18

1.1.1 Configuration and hypothesis of the problems 18

1.1.2 Navier-Stokes equation and its simplifications 18

1.2 Plane flow equations with a free surface (Dupuit-Boussinesq) 19

1.3 Partially saturated / unsaturated media with capillary effects (3D Richards) 20

1.3.1 Van Genuchten / Mualem model of K(h) and θ(h) 21

1.3.2 Exponential model of θ(h) and K(h) 21

1.3.3 Capacity function C(h) 22

1.3.4 Diffusion function D(h) 22

1.3.5 Interpretation of the parameters (α) in the exponential model 23

1.3.6 Interpretation of the parameters (α) in the VGM model 24

1.4 Partially saturated macro-porous media (3D Richards) 25

Chapter 2: Numerical procedure 26

2.1 General presentation of BigFlow (2D/3D finite volume code) 26

2.2 Flowchart of the numerical iterations in the Bigflow code 27

2.3 Numerical procedure for time-varying Boundary Conditions 27

2.3.1 Boundary conditions for the Boussinesq model and Richards model 27

2.3.2 Compilation of executable file for the time-varying BC's problem 28

2.3.3 Data files for the time-varying BC's problem 30

2.4 Debugging and validation tests for the unsaturated flow 30
2.4.1 Validation tests of macro-porous media: the falling head permeameter 31
Part II MODELING OF NON-OSCILLATORY FLOWS IN POROUS MEDIA 41
Chapter 3: Wetting and discharge problems (non-oscillatory) 42
3.1 Introduction 42
3.2 Wetting problem (variably saturated imbibition in a dry sand) 42
3.2.1 Introduction 42
3.2.2 Laboratory experiment 42
3.2.3 Analytical solution with Boussinesq plane flow (Polubarinova) 43
3.2.4 Numerical simulation and calibration of the wetting problem 46
3.2.5 Conclusion on the wetting problem 54
3.3 Groundwater discharge problem 54
3.3.1 Introduction 54
3.3.2 Analytical solutions of Boussinesq equation 55
3.3.3 Numerical simulations (Boussinesq and Richards) 59
3.3.4 Conclusion on the discharge problem 72
Part III MODELING OF OSCILLATORY FLOWS IN POROUS MEDIA 74
Chapter 4: Wave propagation through a vertical sandbox (small wave canal) 75
4.1 Introduction 75
4.2 Laboratory experiment: vertical sandbox in small wave canal 76
4.2.1 Experiment description and methodology 76
4.2.2 Interpretation of the experimental results 80
4.2.3 Acknowledgment 83
4.3 Linearization and analytical solution of the non-linear Boussinesq equation 83
4.3.1 Linearized Boussinesq analytical solution under oscillatory conditions 83
4.3.2 Physical interpretation 86
4.3.3 Posterior analysis of various effects and limitations (inertial effects, acceleration, erosion) 86
4.4 Numerical simulations of wave propagation in the sandbox 88
4.4.1 Numerical simulation with vertically hydrostatic Boussinesq model 88
4.4.2 Comparisons of the numerical results and analytical solution 90
4.5 Analysis of the maximum error of analytical results 92
4.5.1 Introduction and definition of maximum errors 92
4.5.2 Calculation and analysis of the maximum errors on water levels 93

4.5.3 Applicable range of the analytical solution 97
4.6 Conclusion 97

Chapter 5: Water level measurements in a sandy beach: the Barcelona wave canal experiment 100

5.1 Introduction 100
5.2 Laboratory experiment: sloping sand beach in wave canal (Hydralab Barcelona) 101
5.2.1 Experiment description and methodology 101
5.2.2 Measured water levels $H_i(t)$ of the experiment 108
5.3 Conclusion and outlook 109
5.5 Acknowledgement 110

Chapter 6: Signal analyses and interpretation of water level data H(x,t) in the Barcelona wave canal 111

6.1 Introduction 111
6.2 Analysis of Sensor 1 ($H_1(t)$) used as entry boundary condition 112
6.2.1 Introduction 112
6.2.2 Periodic characteristics of the original signal 112
6.2.3 Fourier spectral analysis of the original signal 112
6.2.4 Multi-resolution wavelet decomposition of the original signal, and Fourier analysis of wavelet components 114
6.2.5 Simplification of the signals 117
6.2.6 Summary 119
6.3 Analysis of Sensor 7 (groundwater) 119
6.3.1 Introduction 119
6.3.2 Analysis of the results 119
6.4 Analysis of the other sensors (between swash zone and deep groundwater) 121
6.5 Cross analysis 121
6.5.1 Introduction 121
6.5.2 Residuals of $H_i(t)$ (i=1, …, 7) with moving average filtering 122
6.5.3 Cross analysis between $H_1(t)$ and $H_i(t)$ (i=2, …, 7) 123
6.5.4 Detailed cross analysis between $H_1(t)$ and $H_3(t)$ 138
6.5.5 Cross analysis between $H_1(t)$ and $H_7(t)$ 144
6.6 Wave propagation velocity 149
6.6.1 Measured wave propagation velocity 149
6.6.2 Theoretical wave propagation velocity 150
6.7 Conclusions 152

Chapter 7: Numerical simulations of wave propagation in the sloping sandy beach of the Barcelona canal 155

7.1 Introduction 155

7.2 Computational domain 155

7.3 Left boundary condition for the numerical simulation of Barcelona experiment 156

7.4 Saturated hydraulic conductivity of the beach sand 157

7.4.1 Kozeny-Carman empirical formula 157

7.4.2 Measured hydraulic conductivity obtained in laboratory experiment 157

7.4.3 Discussion about the saturated hydraulic conductivity 157

7.5 Vertically hydrostatic Boussinesq model (2D) 157

7.5.1 Introduction 157

7.5.2 Numerical simulation with Boussinesq model 158

7.5.3 Comparisons between numerical and experimental results 159

7.5.4 Sensitivity analysis with respect to hydraulic conductivity Ks 161

7.5.5 Conclusion on the Dupuit-Boussinesq model 163

7.6 Simulation with Richards model in vertical cross-section (x,z) 163

7.6.1 Introduction 163

7.6.2 Hydrodynamic behavior of the macro porous medium 163

7.6.3 Coupling of the micro porous medium and macro porous medium 164

7.6.4 Numerical tests with the VGM model for K(h) and θ(h) 164

7.6.5 Numerical simulation with the exponential model for K(h) and θ(h) 179

7.6.6 Comparison of the numerical results with the Exponential and VGM models 182

7.7 Conclusion and outlook 185

Chapter 8 : Conclusions 187

Conclusions et perspectives 188

Conclusions and outlook 194

Part IV APPENDICES 199

Résumé étendu 200

Appendix A 214

Appendix A: Chapter 2 215

AC.2.1 ReadMe_BF2005FORTRAN_Compiling.rtf 215

Appendix B 217

Chapter B9: Signal analysis for oscillatory flows (methodology) 218

9.1 Introduction 218

9.2 Signal filtering methods 218
9.2.1 Introduction ... 218
9.2.2 Moving average filtering (linear integrator filter) ... 218
9.2.3 Differential filtering ... 220
9.2.4 Discrete multi-resolution wavelet filtering ... 220
9.2.5 Comments ... 220
9.3 Signal analysis methods 221
9.3.1 Introduction ... 221
9.3.2 Correlation analysis (single and cross) and temporal transfer function ... 221
9.3.3 Fourier spectral analysis with Fourier transformation of single, cross spectra and frequency gain ... 224
9.3.4 Multi-resolution wavelet analysis ... 235
9.4 Conclusion 241

Chapter B10: Illustrations of the signal processing of the measured water level data $H_1(t)$ and $H_6(t)$ of the experiment in Barcelona ... 244

10.1 Introduction 244
10.2 Preliminary note (Sub-sampling) 244
10.3 Original signal of H_1 (t) and H_6 (t) 245
10.3.1 Introduction ... 245
10.3.2 Original signal of $H_1(t)$ ... 246
10.3.3 Original signal of H_6 (t) ... 247
10.4 Signal processing of H_1 (t) 247
10.4.1 Introduction ... 247
10.4.2 Signal processing of the original signal $H_1(t)$ ... 248
10.4.3 Analysis of the residuals of $H_1(t)$ ... 252
10.4.4 Comparison of the same wavelet dyadic component C_5 ... 261
10.5 Signal processing of $H_6(t)$ 262
10.5.1 Introduction ... 262
10.5.2 Analysis of the original signal $H_6(t)$ ... 262
10.5.3 Analysis of the residual of $H_6(t)$ ... 264
10.5.4 Comparison of the same wavelet dyadic component C_9 ... 273
10.6 Cross analysis between $H_1(t)$ and $H_6(t)$ 274
10.6.1 Introduction ... 274
10.6.2 Cross analysis of the original signal between $H_1(t)$ and $H_6(t)$ ... 274
10.6.3 Cross analysis of the residuals between $H_1(t)$ and $H_6(t)$ ... 276

10.7 Comparison of the wavelet dyadic component C_8 of $H_1(t)$ and $H_6(t)$ 283

10.7.1 Wavelet dyadic component C_8 of the original signal of $H_1(t)$ and $H_6(t)$ 283

10.7.2 Wavelet dyadic component C_8 of the residuals of $H_1(t)$ and $H_6(t)$ with moving average filtering 284

10.7.3 Wavelet dyadic component C_8 of the residuals of $H_1(t)$ and $H_6(t)$ with differential filtering 284

10.7.4 Wavelet dyadic component C_8 of the residuals of $H_1(t)$ and $H_6(t)$ with multi-resolution wavelet filtering 285

10.8 Conclusion 286

Chapter B11: Single harmonic wave numerical experiment for the Barcelona canal (short run) 288

11.1 Introduction 288

11.2 Simulation domain 288

11.3 Boundary and initial conditions 288

11.3 Physical properties of the beach sands and the sea water 289

11.4 Duration of the simulation and numerical parameters 290

11.5 Numerical behaviour of Bigflow during the simulation 290

11.6 Result analysis of the one single harmonic wave test 291

11.6.1 Profiles of the pressure head contour and the flux velocity field 291

11.6.2 Instantaneous water content distribution θ(h) in the vertical section 292

11.6.3 Water levels H(x,t) and pressure head h(x,z=0,t) 293

11.6.4 Evolution of the water level fluctuations in time and space 294

11.7 Analysis on the system energy balance during the numerical simulation 296

11.8 Conclusion on one single harmonic wave test 298

Chapter B12: Single harmonic wave numerical experiment for the Barcelona experiment (long run) 300

12.1 Introduction 300

12.2 Simulation domain 300

12.3 Boundary and initial condition 300

12.3 Physical properties of the sand beach and the sea water 301

12.4 Duration of the simulation and numerical parameters 301

12.5 Numerical behaviour of Bigflow during the simulation 301

12.6 Result analysis of continuous wave test 302

12.6.1 Profiles of the pressure head contour and the flux velocity field 302

12.6.2 Instantaneous water content distribution θ(h) in the vertical section 304

12.6.3 Evolution of the water level fluctuations in time and space 305
12.7 Analysis on the system energy balance during the numerical simulation 309
12.8 Sensitivity analysis of the VGM parameters, soil physical properties, mean free water levels and beach slopes on the groundwater level fluctuations 311
12.9 Conclusions and outlook 314
12.10 Key questions and discussion 315

REFERENCES 316
References 317
List of Figures 326
List of Tables 346

List of symbols

Roman symbols

A Amplutude of the watel level fluctuations, m;

A_X^m Approximation of the dyadic scale ‘m’ (low pass filter) of multi-resolution wavelet, m;

$C_x^j(i)$ Wavelet component of the dyadic scale "j", m;

C_{Phase} Phase velocity of Boussinesq, m/s;

C_{Group} Group velocity of Boussinesq, m/s;

$Coh_{XY}(\omega)$ Fourier frequency coherency function;

C_{XX} Autocovariance function;

C_{XY} Cross covariance function;

$C(h)$ Capacity function with respect to the pressure head h, m^{-1};

$D(h)$ Diffusion function with respect to the pressure head h, m^2/s;

$D_X^j(i)$ Detail of a discrete signal $X(i)$ with the resolution "m" of the multi-resolution wavelet, m;

ENLH3 Convergence criterion of pressure head of no-linear iterations (Picard);

ENORM3 Convergence criterion of pressure head of linear iterations;

f Dimensional frequency;

f^* Dimensionless frequency;

$g_{XY}(\omega)$ Fourier no-reduced gain function (dimensional);

$g^*{}_{XY}(\omega)$ Fourier reduced gain function (dimensionless);

g Gravity acceleration and $g = 9.81m/s^2$;

h_b Bubble pressure head, m;

H Water elevation or water head, m;

h Pressure head in the Richards equation, m;

h Water depth in the Dupuit-Boussinesq equations, m;

$\bar{h}_0$ Mean water depth in the porous media, m;

K_S Saturated hydraulic conductivity, m/s;

K_r Residual hydraulic conductivity, m/s;

$K(h)$ Unsaturated hydraulic conductivity function with respect to the pressure head h, m/s;

$K_R(h)$ Relative hydraulic conductivity function with respect to the pressure head h, m/s;

k Permeability of the porous media, m^2;

K Hydraulic conductivity and $K = \frac{\rho g}{\mu} k = \frac{g}{\nu} k = 0.87310^{+7} k$, m/s;

m Dimensionless exponent of the VGM model and $m = 1 - 1/n$ (Mualem);

n Dimensionless exponent of the VGM model;

$\boldsymbol{q}$ Darcy flux vector, m/s;

Q_{Bound} Total net discharge entering or outgoing through all the faces of the computional domain (instantaneous or local) with Bigflow, m^3/s;

Q_{Mass} Discharge corresponding to the change in volume of water inside the computational domain during the time interval DT (instantaneous or local) with Bigflow, m^3/s;

R_X^m Residual of the dyadic scale 'm' (high pass filter) of multi-resolution wavelet, m;

R_{XX} Autocorrelation function;

R_{XY} Cross correlation function;

S_e Degree of saturation of water content;

$S(h)$ Relative hydraulic conductivity function with respect to the pressure head h;

S_{XX} Dimensional Fourier auto-spectrum, $m^2.s$;

S_{XY} Dimensional Fourier cross spectrum, $m^2.s$;

S^*_{XX} Dimensionless Fourier auto-spectrum;

S^*_{XY} Dimensionless Fourier cross spectrum;

Δt Time step, s;

t Time, s;

T Period, s;

T Hydraulic transmissivity in Dupuit –Boussinesq equation, m^2 /s;

$\boldsymbol{V}$ Velocity vector, m/s;

V_{Bound} Net volume of water entered or exited through all the sides of the field since the beginning of the numeric simulation (accumulative or global) with Bigflow, m^3;

VGM Van Genuchten/Mualem;

V_{Mass} Volume of water formed or disappeared within the area since the beginning of the numerica simulation (accumulative, global) with Bigflow;

W-K Wiener-Khichen;

w_t *half window width of* Moving average filtering, s;

X_F Wetting saturation front toe, m;

$Z_{inf}(x, y)$ Elevation of the impervious substratum

Greek symbols

α Inverse of the capillary length for the VGM model and Exponential model, m^{-1};

β Capillary parameter for the water content function in the Exponential model;

δ Decay length of the wave propagation in the porous media and $\delta = \sqrt{\frac{2K_s\bar{h}_0}{\omega\Phi}}$, m;

η Water depth, m;

$\theta(h)$ Unsaturated water content function with respect to the pressure head h, m^3/m^3;

θ_r Residual water content, m^3/m^3;

θ_s Saturated water content in the Richards equation, m^3/m^3;

$\theta_{XY}(\omega)$ Frequency spectrum of phase density, rad/s;

λ_{CAP} Capillary length and $\lambda_{CAP} = \frac{1}{\alpha}$, m;

μ Dynamic viscosity, $kg/(m \cdot s)$;

ν Cinematic viscosity and $\nu = \mu/\rho, m^2/s$;

ρ Volumic specific density or mass, kg/m^3;

ρ_0 Volumic specific density or mass, kg/m^3;

σ_X^2 Standard deviation function;

τ_{Tuckey} Lag time of Tuckey filter, s;

Φ Unconfined storage coefficient or effective porosity, m^3/m^3;

$\psi_{m,k}(i)$ Wavelet function (mother wavelet);

ω Angular frequency, s^{-1};

Introduction

En hydrologie et l'hydrogéologie, les niveaux d'eau subissent des oscillations ou de brusques changements dans le temps. Cela peut se produire dans les aquifères, réservoirs, lacs, rivières, digues, les estuaires, les ports et les zones côtières. Dans de nombreux cas, les oscillations des surfaces libres ont lieu en eau libre, puis, se propagent dans les milieux poreux adjacents (plages, les aquifères côtiers, les berges, les digues, brise-lames, et ainsi de suite). Dans ce travail, nous étudions la réponse de la nappe phréatique, qui est, à la fois des zones saturées et non saturées (séparés par des surfaces libres) dans des conditions très dynamiques. Nous sommes intéressés à deux cas en particulier: des changements brusques et des oscillations périodiques des niveaux d'eau. Ceux-ci peuvent résulter de conditions environnementales naturelles ou induites par les opérations de l'homme dans le génie civil et hydrologiques applications.

Ainsi, nous nous concentrons sur les effets potentiels des variations des niveaux d'eau dans le voisinage de corps poreux, tels que (**Figures 0-1** et **0-2**):

- Propagation d'ondes dans un environnement cosntitué de milieux poreux (plages, zones côtières et les estuaires) ;
- Transmission / dissipation des marées et des vagues à travers les digues, brise-lames ou (ports) ;
- variations de niveau d'eau de grande amplitude dans les rivières et les réservoirs, par exemple, à cause d'opérations de barrages;
- Interactions crues/eaux souterraines, et inondations/eaux souterraines (interactions sols-nappes-riviere en hydrologie)

Dans cette thèse, nous étudions en particulier la réponse du système de nappe phréatique des milleux poreux avec la surface libre aux variations des niveaux d'eau dans les eaux libres adjacents. Celui-ci peut être traité soit comme une frontière du domaine poreux, ou bien comme une interface interne (cf. plage de sable en pente). Deux types principaux de dynamique sont étudiés: (i) variation brusque du niveau d'eau (cf. problème d'imbibition), et

(ii) des oscillations périodiques dues par exemple à des marées ou vagues (cf. les expériences de canal à houle).

Les analyses développées dans la thèse reposent sur trois approches complémentaires:

- Expériences physique avec des modèles à échelle réduite dans le laboratoire (boites à sable, canaux);
- Solutions analytiques linéarisées ou faiblement non-linéaire en termes des niveaux d'eau (modèle de Dupuit-Boussinesq de l'écoulement plan)
- Solutions numériques complètements non-linéaires de l'équation de Richards en termes de pression interstitielle, teneur en eau et Darcy flux, en 3D ou en coupes verticales, basée sur le code volume finis implicite (BigFlow 3D).

0 Introduction

0.1 Objectives of the thesis

In hydrology and hydrogeology, water levels frequently undergo oscillations or abrupt changes in time. This can occur in aquifers, reservoirs, lakes, rivers, embankments, estuaries, ports, and coastal zones. In many cases, oscillations of free surfaces take place in open water bodies, and then, propagate into adjacent porous media (beaches, coastal aquifers, river banks, dykes, breakwaters, and so on). In this work, we study the response of ground water, that is, both unsaturated and saturated zones (separated by free surfaces) under very dynamic conditions. We are interested in two cases in particular: abrupt changes, and periodic oscillations of water levels. These can arise from natural environmental conditions, or from man induced operations in civil engineering and hydrological applications.

Thus, we focus on the potential effects of variations of water levels in the vicinity of porous bodies, such as (as illustrated in **Figures 0-1** and **0-2**):

- Wave propagation in environmental porous media (beaches, coastal areas and estuaries);
- Transmission/dissipation of tides and swells through dykes, or breakwaters (harbours)
- Large variations of water levels in rivers and reservoirs, e.g. due to dam operations,
- Effect of river floods on groundwater via stream-aquifer interactions (hydrology).

Figure 0-1. Three Gorges Dam Reservoir filled to 135 meters (international PROBE, Mu Lan, June 2003).

Figure 0-2. Sea beach of Rincon, Puerto Rico taken from the Red Door.

In this thesis, we investigate in particular the response of a ‘free surface’ porous medium water system (e.g. a phreatic aquifer with a ‘groundwater table’) to variations of the water levels in adjacent open water bodies. The latter can be treated either as a boundary of the porous domain, or else as an internal interface (cf. sloping sand beach). Two main types of dynamics are investigated: (i) sudden change of water level (cf. ‘imbibition problem’, **Chapter 3**); and (ii) periodic oscillations due for example to tides or swells (cf. wave canal experiments, **Chapter 4, 5, 6, and 7**).

The analyses developed in the thesis rely on three complementary approaches:

- Physical experiments with reduced scale models in the laboratory (sandboxes, canals);
- Linearized or weakly non linear analytical solutions in terms of water levels (Dupuit-Boussinesq plane flow model);
- Fully nonlinear numerical solutions of the Richards flow equation in terms of pore pressure, water contents and Darcy fluxes, in 3D or in vertical cross-sections, based on implicit finite volume code (BIGFLOW 3D).

0.2 Literature review (state of the art)

In this section, we examine the literature on oscillations and wave propagation in groundwater and above the free surface as well (unsaturated zone). We also include the case of sudden variations of water levels, as can occur for instance in dam reservoirs and lakes. However, we do not study two other important topics: the full coupling of porous media and open water hydrodynamics based on Navier-Stokes approaches, and the hydro-mechanical coupling (pressure-stress-strain, erosion, effects on possible terrain failures and slides) that can occur within the porous media under highly variable water levels and water pressures. Rather, we focus mainly on experimental and modeling studies focusing on water level oscillations and wave propagations, e.g., through reservoir dam embankments and through sandy beaches (our review is currently more complete on the latter topic).

0.2.1 Observations on beach groundwater response to tidal & wave forcing

Beach groundwater hydrodynamics are a result of combined forcing from ocean tides (at diurnal of half-diurnal periods) and other shorter waves (swell) generated by wind and by barometric pressure differences, and occurring at a wide range of frequencies or periods (typically around 0.1 Hz or 10 s).

Beach groundwater response to tidal forcing has been studied extensively, and has been reviewed by many authors, including Nielsen et al. (1988)[72], Gourlay (1992)[11], Baird and

Horn (1996)[25], Turner et al. (1997)[59], Turner (1998)[14], Horn (2002)[18] and Horn (2006)[19]. Most early studies concentrated on groundwater in sandy beaches, particularly tide-induced fluctuations of the local beach water table, and generally in the cross-shore direction (perpendicularly to the shoreline).

- **Shape and elevation of the beach water table response to tidal forcing**

A large number of observations describe the shape and elevation of the beach water table in response to tidal forcing at diurnal, semi-diurnal and spring-neap tidal frequencies.

Observations of beach water table behavior show that the water table surface is generally not flat, and that it is asymmetrical (eg: Turner(1993)[12], Raubenheimer et al.(1999)[29], Baird et al.(1998)[26], and Nielsen (1999)[16]).

The propagation of the water table fluctuations is influenced primarily by oscillation frequency, and by vertical flow and capillarity effects. The sloping boundary is responsible for the generation of higher harmonics in the water table oscillations, which have been shown to be stronger in the upper part of the aquifer due to the greater amount of vertical flow in this part of the aquifer (Cartwright et al. (2004b)[64])**.**

The asymmetry and phase lag between the water table and the tide increase in the landward direction, while the amplitude of the water table oscillations decreases in the landward direction (eg. Baird et al. (1998) [26], Raubenheimer et al. (1999) [29], and Robinson et al. (2005) [32]).

Measured watertable elevations are generally higher than the tidal elevation (e.g. Nielsen et al. (1988)[72] [19], and Turner et al. (1997) [59]). This overheight increases as the beachface slope and sediment size decrease and as tidal range and wave infiltration increase (Turner et al. (1997) [59]). In general, the elevation of the beach water table increases as the permeability of the beach decreases.

- **Shape and elevation of the beach water table response to wave forcing**

Wave forcing affects beach groundwater in a number of ways. Time-averaged wave effects contribute to watertable overheight, by two phenomena (e.g: Nielsen and Kang (1995) [67], Kang and Nielsen (1996) [44], and Nielsen (1999) [16] [19]):

- by set-up / raising the mean water surface at the shoreline, and
- by run-up / increasing the mean water surface through infiltration.

Considering a vertical cross-section perpendicular to the shoreline, hydraulic gradients controlled by wave set-up also drive a general groundwater circulation in the beach (e.g: Li and Barry (2000) [53]).

Run-up of individual waves generates high-frequency water table and pore pressure fluctuations, which have been reported in a number of field experiments (e.g. Turner and Nielsen (1997) [47], Horn et al. (1998) [37], Turner and Masselink (1998) [48], Blewett et al. (2001) [31], Baldock et al. (2001) [83], Butt et al. (2001) [81], Cartwright et al. (2005)[61], and Robinson et al. (2005) [32]).

High-frequency water table oscillations exhibit a similar asymmetry to that of tidally induced water table fluctuations, with a faster rate of rise than fall (Hegge and Masselink (1991) [30]).The landward propagation of a swash-induced pore pressure wave has been shown to be similar to that of tidally induced groundwater waves, with the amplitude decaying exponentially and the phase lag increasing linearly in the landward direction (Cartwright et al. (2005) [61]).

Waddell (1973) [38] and Waddell (1976) [5]observed that a wave arriving at the base of the beach face induced an instantaneous rise in the beach water table as a result of a “mass pressure flux” through the saturated sediment. In contrast, Hegge and Masselink (1991) [30]found that the water table elevation increased 4–5 seconds after maximum run-up, attributing this lag to the effects of “frictional retardation” on the input swash water. They suggested that the relative importance of pressure vs. swash infiltration is controlled by the location of the exit point, with pressure forces dominating on the saturated beach face seaward of the exit point and infiltration dominating landward of the exit point. Waddell (1976) [5] made a similar suggestion, and also suggested that sediment size will affect pressure transmission through the beach. Nielsen (1997) [13] noted that neither of these studies measured the actual position of the water table, but rather the pressure at some depth, and argued that such measurements cannot determine how the water table (as opposed to the non-hydrostatic pressure at some depth) behaves under unsaturated conditions landward of the run-up limit.

- **Spatial evolution of the dominant periods of the beach water table fluctuations**

Some field evidence also suggests that wave effects can be observed over long time periods.

For instance, Nielsen (1999) [16] noted that water table oscillations due to relatively slow changes in wave height (say over several days) propagate further inland than higher-

frequency oscillations. Similarly, several authors reported measurements of a beach groundwater pulse which was due to an increase in wave set-up at the shoreline during storms, and which propagated inland into the aquifer (Turner (1998) [14], Cartwright et al. (2004a) [62] , and Cartwright and Nielsen (2004c) [65] [19]).

In the same line of thought, many researchers have noted that the beach acts as a low-pass filter, only allowing the larger or longer period swashes to be transmitted through the beach's porous matrix. It is observed that both the amplitude and the dominant frequency of the groundwater level spectrum decrease in the landward direction. The further landwards the given groundwater spectrum, the narrower its band and the more it is shifted towards lower frequencies (Lewandowski and Zeidler (1978)[22]).

There is indeed some evidence to suggest that some frequencies are less attenuated than others; however, it is not clear what controls the frequency pass band on a particular beach. Waddell (1980) [6] noted that the deeper the well point, the lower the cut-off frequency of the filter function is. Hegge and Masselink (1991) [30] suggested that the cut-off frequencies of the filter will be a function of tidal stage, hydraulic conductivity, beachface slope and the measurement position relative to the shoreline.

Relatively few studies have reported simultaneous measurements of beach groundwater and swash; here are a few such studies and their main conclusions:

- Hegge and Masselink (1991) [30] compared swash zone run-up and groundwater spectra, which showed a considerable reduction in dominant energy and also a shift in dominant energy towards lower frequencies.
- Turner and Nielsen (1997) [47] noted that although the pore water pressures in the beach clearly responded to wave run-up, these fluctuations had a significantly lower frequency than that of the waves. They also noted that rapid water table fluctuations in the swash zone were more evident on the falling tide than on the rising tide, and highlighted the importance of capillary effects.
- Nielsen and Turner (2000) [68] showed measurements of pore water pressure in the beach with a spectral peak at the frequency of the water table exit point, rather than at other forcing frequencies such as surf zone waves or run-up.
- Cartwright et al. (2005) [61] presented shoreline, exit point, and pore pressure spectra. They showed that the transfer of energy from high-frequency swash forcing to low-

frequency groundwater response could be attributed to wave run-up exceedance probabilities relative to the position of the exit point

- **Unsaturated zone and capillary fringe of the beach groundwater**

The presence of a capillary fringe can have a significant effect on the exchange of water between the ocean and the coastal aquifer, particularly in terms of the storage capacity of the coastal / beach aquifer.

Recent studies have demonstrated that due to hysteretic water retention, capillarity affects water table dynamics over a much wider range of frequencies, including the tidal frequency (e.g. Nielsen and Perrochet (2000a) [69], Nielsen and Perrochet (2000b) [70], and Werner and Lockington (2003) [24]). At higher frequencies, the presence of a capillary fringe will have a significant effect on the dispersion of water table waves. Field and laboratory observations have also shown that natural groundwater waves usually propagate faster and decay more slowly in aquifers with a capillary fringe (eg. Nielsen and Turner (2000) [68], Cartwright et al. (2004a) [62], and Cartwright et al. (2004b) [64]).

The height of the capillary fringe can be estimated under quasi-static assumptions (not always stated as such). Thus, Turner and Nielsen (1997) [47] gave an expression for the thickness of the capillary fringe within the beach, *B*, assuming cubic packing of spherical grains of uniform diameter:

$$B = \frac{10\gamma}{\rho g D} \tag{0-1}$$

where γ is the surface tension, ρ is the density of the fluid, and *D* is the mean grain diameter. Atherton et al. (2001) [79] give an expression for the height of capillary rise:

$$H_c = \frac{2\gamma cos\alpha}{\gamma_m \rho g} \tag{0-2}$$

where, γ is the surface tension, ρ the density of the fluid, α the contact angle between water in a pore and the pore side wall (taken to be zero), γ_m the mean pore radius and g is acceleration due to gravity. In terms of macroscopic constitutive relationships, using the Van Genuchten Mualem model, Alastal et al. (2010) [50]point out, from earlier work by Ababou (1991) [10], that the mean static capillary height can be defined and calculated as the point of maximum moisture capacity, i.e., the inflexion point of $\theta(h)$, which leads to an explicit expression:

$$\lambda_{CAP} = \frac{1}{\alpha}\left(1 - \frac{1}{n}\right)^{1/n} \tag{0-3}$$

where "α" is the Van Genuchten pressure scaling parameter (inverse length units), and "n" is the Van Genuchten/Mualem exponent, or shape parameter ("n" is a dimensionless positive real number).

Observations which suggest that horizontal flows may also occur in the capillary zone have been reported (e.g. Atherton et al. (2001) [79], Silliman et al. (2002) [80], Cartwright et al. (2002) [63], Cartwright et al. (2004b) [64]), but the most significant phenomenon is probably the vertical exchanges in that zone under dynamic oscillatory conditions.

- **Effects of infiltration and exfiltration**

The effects of infiltration and exfiltration are generally invoked to explain why beaches with a low water table tend to accrete, and beaches with a high water table tend to erode.

However, the relative importance of processes such as infiltration losses in the swash, changes in the effective weight of the sediment, and modified shear stress due to boundary layer thinning, are not yet clear. Experimental work on the influence of seepage flows within sediment beds provides conflicting results concerning the effect on bed stability (Horn (2006)[19]).

0.2.2 Modeling of beach groundwater response to tidal & wave forcing

There are also a great number of numerical and analytical models for the investigation of the wave propagation in porous media, including the case of a vertical porous boundary (eg. Dominick et al. (1971) [40]) and a sloping porous boundary as occurs for a bach (eg. Nielsen (1990) [9]).

In unconfined aquifers, the dynamics of the water table will be influenced by the capillary fringe for all but the coarsest sands and gravel. Most existing models rely on the Dupuit-Boussinesq equation (**Chapter 1,** for more details) for plane flow, in 1D across the shore (e.g. Nielsen (1990) [9], Baird et al. (1998) [26], Raubenheimer et al. (1999) [29], Song et al., (2007) [92]) and sometimes also in the 2D horizontal plane (e.g. Li et al. (1996) [54], and Li et al. (1997b) [56]). In all these cases, one considers only saturated flow and ignores the unsaturated zone and its capillary effects. Therefore, according to these models, high-frequency forcing does not induce water table fluctuations to any appreciable distance inland, a result which is contradicted by field observations (Li et al. (1997a) [58]).

Many other authors have attempted to capture the effects of the capillary fringe on beach groundwater dynamics based on the Green and Ampt (1911) [86] piston flow approximation,

which assume that the capillary fringe is completely saturated with a constant suction head at the top. Parlange and Brutsaert (1987) [49] added a correction term to the Boussinesq equation to account for the mass transfer of water across the moving watertable due to capillarity. Barry et al. (1996) [25] used this modified Boussinesq equation to investigate the propagation of small amplitude oscillations, and showed that the influence of the capillary fringe increases with oscillation frequency. Li et al. (1997a) [58] derived a dispersion relation including the effects of both finite aquifer depth and capillarity. Their model simulated 2D horizontal saturated flow and included capillary effects through the free-surface boundary condition. They investigated the influence of wave run-up on coastal aquifers and showed that capillary effects are important for high-frequency oscillations and provide the mechanism for high-frequency groundwater waves. Without the capillary correction term, the model was unable to reproduce the propagation of high-frequency watertable waves which has been observed in the field.

Li et al. (2000a) [57] incorporated capillary effects based on the Green and Ampt (1911) [86] piston flow approximation into the intermediate depth groundwater wave equations of Nielsen et al. (1997) [71] to derive a new groundwater wave equation :

$$\frac{\partial h}{\partial t} = \frac{K}{s} tan\left(d\frac{\partial}{\partial x}\right)\frac{\partial h}{\partial x} + \frac{B}{s}\frac{\partial}{\partial t}\left[tan\left(d\frac{\partial}{\partial x}\right)\frac{\partial h}{\partial x}\right] \tag{0-3}$$

where B is the thickness of the capillary fringe, h is the watertable elevation, s is specific yield, d is aquifer depth, K is hydraulic conductivity, t is time and x is horizontal distance. The first term includes the effects of vertical flows. The second term in the right-side of this equation accounts for the apparent water exchange between the capillary fringe and the aquifer that occurs when the water table fluctuates (Li et al. (1997a) [58]). Comparison of their dispersion relation with a capillary term of Nielsen et al. (1997) [71] demonstrated the importance of capillarity for high-frequency oscillations, exhibiting a more realistic representation of high-frequency watertable oscillations as observed in the field by Kang et al. (1994) [52]. Their simulations showed that vertical flow effects reduces as aquifer depth decreases, and that wave damping at high frequencies is sensitive to the thickness of the capillary fringe.

In order to obtain an analytical solution, Li et al. (2000a) [57] assumed a vertical interface with a uniform head fluctuation; however, they noted that their ground water wave equation could be applied to a sloping beach with swash motion, in which case a moving boundary is involved and numerical solutions are required.

Nielsen and Perrochet (2000a) [69], and Nielsen and Perrochet (2000b) [70] incorporated a simplified description of the capillary fringe in the watertable equations, in order to express the change in total moisture (water table and capillary fringe) in terms of derivatives of the water table height only. They introduced the concept of the complex effective porosity, n_e, to account for the observed damping and lag of oscillations in the total moisture compared to those in the watertable alone. They defined the complex effective porosity (n_E) as follows:

$$n\frac{dh_{tot}}{dt} = n_E\frac{dh}{dt} \tag{0-4}$$

where n is the drainable porosity (specific yield), h is water table elevation and h_{tot} is the equivalent saturated height of the total moisture (the sum of the water table height and the thickness of the capillary fringe). This term (n_E) accounts mathematically for damping of fluctuations in the total moisture through its magnitude and for phase lag through its argument. In studies of simple harmonic forcing in a sand column, Nielsen and Perrochet (2000a) [69], and Nielsen and Perrochet (2000b) [70] found that the complex effective porosity (n_E) was a constant for a given sediment at a given compaction. They also showed that the thickness of the capillary fringe varied nearly as much as the water table height.

Nielsen and Turner (2000) [68] extended the work of Nielsen and Perrochet (2000a) [69], and Nielsen and Perrochet (2000b) [70] to consider the case of simple harmonic oscillations and a wider range of sediment sizes, and obtained an empirical expression for the complex effective porosity

$$n_E = \frac{n}{1+C\left(i\frac{\omega H_\psi}{K}\right)^{2/3}} \tag{0-5}$$

where n is the drainable porosity (specific yield), ω is the angular frequency, H_ψ is the height of the capillary fringe obtained from measurements, K is the hydraulic conductivity, and C is an empirical constant (C=2 in Nielsen and Turner (2000) [68], C=2.5 in Cartwright et al. (2002) [63], Cartwright et al. (2004b) [64], and Cartwright et al. (2005) [61]). Eq. (0-5) indicates that the influence of the capillary fringe is reduced for coarse sand and long forcing periods. Nielsen and Turner (2000) [68] noted that Eq. (0-5) is only valid when the capillary fringe is well below the sand surface and suggested when the capillary fringe is close to the sand surface, the flexing of meniscuses may be what determines the effective porosity of the beach.

Cartwright et al. (2004b) [64] considered the effect of a truncated capillary fringe (where the capillary fringe intersects the sand surface) on the dispersion of water table waves. They

investigated the extent to which truncation of the capillary fringe limits moisture exchange under periodic forcing via sand column experiments, and showed that the complex effective porosity was significantly reduced with increasing truncation, by up to a factor of 4. These results showed that truncation effects only became apparent when the distance between the sand surface and the maximum water table elevation was approximately half the height of the capillary fringe. When the sand surface is above the region of saturated moisture, there was no measurable effect of the sand surface on the water table oscillations. However, once the sand surface began to truncate the tension-saturated zone of the capillary fringe, there was a rapid decrease in the magnitude and argument of the complex effective porosity until a point where the sand surface equalled the maximum driving head elevation and the magnitude of the frequency response almost reached unity.

Cartwright et al. (2005) [61] presented simultaneous measurements of shoreline location, exit point location and pore pressure response, which they showed to be influenced by the presence of a capillary fringe. They used the parameter derived by Cartwright et al. (2004b) [64] to represent the reduction in aquifer storage due to both the effects of capillarity and the truncation of the capillary fringe by the sand surface. They compared the predictions of Turner's (1993b) [12] exit point model to their field measurements and showed that the inclusion of capillary effects improved the agreement between measured and predicted exit point location. They concluded that further work is needed to quantify the reduction in aquifer storage in terms of measurable aquifer parameters, and to allow for the dependence of the exit point (and of pore pressure dynamics) on shoreline proximity.

The use of the complex effective porosity does not give any information on the dynamics of the moisture distribution above the water table. It is clear that an improved understanding of processes in the capillary zone is essential for modeling moisture exchange in beaches, particularly in the swash zone. Any model which does not consider capillarity will create a large local hydraulic head gradient during wave run-up, leading to overestimation of infiltration (Li et al. (1999) [55]). Infiltration and/or exfiltration on a beach will be influenced by both the input of water from wave run-up and the ability of the sediment to take in water (hydraulic conductivity, specific yield and moisture content), which will be affected by the presence of a capillary fringe.

Both modeling and experimental work indicates that the hydraulic conductivity of the beach is a critical parameter. However, hydraulic conductivity varies both spatially and temporally on beaches, particularly on gravel and mixed sand and gravel beaches. Another important, but

poorly understood, consideration in beach groundwater studies is the role of air encapsulation during the wetting of beach sand.

Improved predictions of swash zone sediment transport and beach profile evolution cannot be achieved unless the complex fluid and sediment interactions between the surface flow and the beach groundwater are better understood, particularly the sensitivity of sediment transport processes to flow perpendicular to the permeable bed. Important research questions remain to be answered on the role of the capillary fringe in swash /watertable interaction:

- nature of periodic fluctuations in the capillary fringe, both vertical and horizontal; beach groundwater recharge landward of the run-up limit;
- variability of hydraulic conductivity and moisture content/air entrapment, especially on mixed beaches;
- effects of pressure gradients in the swash zone;
- and the effects of infiltration/exfiltration on swash sediment transport, particularly on coarse-grained beaches.

Most of the models require validation against laboratory and field data, particularly those on beach groundwater response to wave forcing and the effects of infiltration/exfiltration. The latter, in particular, are based on theory which needs to be verified. This will require careful laboratory experiments under realistic flow conditions and over a wide range of sediment sizes in order to determine the effect of seepage flows on sediment entrainment and transport. Direct measurements of key parameters such as hydraulic conductivity and moisture content need alos to be carried out in the field and more direct field measurements of infiltration rates are also required (Horn, 2006 [19]).

0.2.3. Other review on topics of interests

Water level dynamics in other porous bodies (other than sand beaches)

We have also reviewed the literature about ground water level variations in other contexts. For instance, in the sloping banks of large dam lakes, we have reviewed several papers focused on the groundwater response to high amplitude variations of water levels due to dam operations (particularly in the Chinese literature, eg. Feng et al. (2006) [87]; Mo et al. (2006)[88]).

Another case of interest is the case of wave propagation and damping through wave breakers (coarse dykes) in harbour engineering. These cases are all relevant to our work. For

instance, concerning the sudden variation of water level, see the imbibition experiment in a dry sandbox (studied in **Chapter 3)**.

Concerning the damping of waves through a porous dyke, see the small wave canal experiment with an inserted vertical sandbox (**Chapter 4)**. In fact, in the literature, problems of reflection and transmission of water waves through porous structures have been studied by the application of the eigenfunction expansion method (e.g., Sollitt and Cross (1972) [51], Dalrymple et al. (1991) [35], Yu and Chwang (1994) [89], Chwang and Chan (1998) [82], Chan and Lee (2001) [27], and Azhar et al. (2008)[28]). To calculate the porous medium flow, either Darcy's law (e.g., Chwang and Chan (1998) [82]) or Forchheimer's law (e.g., Dalrymple et al. (1991) [35], Azhar et al. (2008) [28]) has been used, but without considering the capillary effects that may occur in the unsaturated zone of the porous media.

Oscillations and wave propagation analyses based on the Richards equation

We have reviewed above quite extensively a number of analyses on the effects of oscillatory forcing on free surface groundwater flow based on Dupuit-Boussinesq models with or without an additional capillary fringe submodel (Green and Ampt (1911) [86]).

However, other authors have studied directly unsaturated flow under oscillatory conditions. We only cite here two works that have been developed at IMFT.

The first one (Trégarot (2000) [17], Chap.4) consists in a linearized analyzis of the response of an unsaturated soil column to an oscillatory unsaturated flux imposed at the surface of the column. Damping, phase lag, and wavelength are analyzed mathematically in terms of soil parameters as a function of input frequency (based on earlier unpublished work by Ababou). In addition, the linearized solution is compared to nonlinear simulations of oscillating pressure profiles based on the Richards equation.

The second one is a more recent work by Alastal et al. (2010) [50]. They analyze the response of a partially saturated soil column to a pressure wave input at the bottom of the column. Phase lags due to both saturated and unsaturated zone dynamics are being studied (work in progress).

Coupling Navier-Stokes (or other hydrodynamics) with porous media flow

Coupling Navier-Stokes (or other related hydrodynamics equations) with the Darcy-based porous media flow equations is an important topic to solve the real hydrodynamic problem which occurs in an interface such as sea/beach and river/bank. However, in this work, we will

be using a different approach from a “porous medium perspective”. Indeed, the approach to be implemented in this work (**Chapter 7**) will be based on generalizing the Richards porous media equation in order to include open water zones in the computational domain, rather than using Navier-Stokes based equations.

However, it is recognized that a different approach based on Navier-Stokes might be worthy of consideration, if properly adapted or coupled to porous media hydrodynamics. In order to make progress in this area, research has focused on establishing consistant interface conditions between open water (Navier-Stokes) and porous media (Darcy) domains, such as the Beavers-Joseph interface conditions [91]. This topic will not be pursued further in this work.

Hydro-mechanical coupling and fluid-solid interactions

There are various types of hydro-mecanical coupling and fluid-solid interactions involved in the problems of interest for this thesis work, namely, harbor engineering, beach hydrodynamics (and morphodynamics), and also, estuaries, river banks, and dam lake embankments. In all these cases, fluid-solid interactions take place.

Briefly, two types of cases might be considered, as follows. First, for unconsolidated granular porous media, the changing regime of surface water flow can impact on erosion/deposition processes (beach swash zone); however, subsurface flow also can generate internal erosion and thus, create new flow pathways. Secondly, when porous media are consolidated, pore pressure and/or capillary pressure variations can lead to significant changes in the effective stress, which can have effects on cohesion and on failure mechanisms (rock falls, landslides, collapse of a dyke). This thesis is focused on the hydraulics aspects only, but it is clear that the mechanical consequences of internal pressure fluctuations and water level fluctuations are of great interest for applications and can lead to forgoing work.

Signal analyzis and processing of water levels and pressure time series

In this thesis, we rely on mathematical and statistical methods for analyzing highly variable signals, in particular the water level signals $H(x_i,t)$ obtained from experimental measurements (**Chapter 5** and **Chapter 6**, for more details).

For this sake, multiresolution wavelet analyzis, as well as correlation function and spectral density function have been used. The wavelet concept can be applied to any signal, while the correlation/spectrum concepts are well defined only for statistically stationary random processes. However, note that sometimes the the water level signals have been prefiltered, and

the correlation/spectral analyses have been applied only to their residuals. The soundness of our moving average filter (and the choice of window width) has also been tested by comparing it to the result obtained from wavelet orthogonal decomposition into approximation+residual.

The software tools used in this thesis were originally developed in the form of MATLAB Toolboxes in a previous thesis at IMFT (Fatmi (2009) [21]) for application to the analyzis of pore pressure and atmospheric pressure signals in a hydrogeologic site (Fatmi et al. (2008) [43]). For the present work, they have been adapted and re-interpreted some of these tools for these specific purposes (sometimes in collaboration with H. Fatmi). For completeness, we provide an upgraded version of the corresponding signal analyzis theory in **Appendix B9**.

0.3 Outline of the thesis

After this introductory chapter, the rest of the thesis is structured sequentially into eight chapters regrouped in three main parts, plus appendices, as follows:

First, note that the **APPENDICES** include not only classical appendices for each chapter (Appendices A), but also, additional chapters labeled **Chapter B9** to **Chapter B12** which contain additional results and details on signal analyses and simulations of the Barcelona wave canal (they can be skipped on first reading).

Let us now summarize briefly the contents of each part and each chapter.

PART I (Chapters 1-2): Governing equations & constitutive relations for porous media

Chapter 1 presents the governing equations and the constitutive relations for partially saturated or unsaturated porous media.

Chapter 2 defines the numerical procedures in the plane flow Dupuit-Boussinesq model and in the 3D partially saturated Richards model, taking into account time-varying boundary conditions in both models.

PART II (Chapter 3): Modeling of non-oscillatory flows in porous media

Chapter 3 describes numerical simulations with the Richards unsaturated flow model using the VGM (Van Genuchten / Mualem) model for conductivity and moisture curves versus pressure. The parameters of the VGM model are manually calibrated (fitted) with the results of the imbibition experiment conducted at IMFT (sudden imbibition or wetting of a dry sandbox). On the other hand, the linearized analytical solution of the Dupuit-Boussinesq

equation for the sudden discharge problem is validated by numerical simulations with Dupuit-Boussinesq equations, and these are also compared with the more complete Richards model.

PART III (Chapters 4-7): Modeling of oscillatory flows in porous media

In **Chapter 4**, we describe a lab experiment with a vertical sandbox in a small wave canal (IMFT). We study the transmission of oscillations through the sandbox, experimentally with water level sensors, and numerically with the Dupuit-Boussinesq plane flow model. We also analyze linearized solutions of the Dupuit-Boussinesq equation and use them to interpet the experimental observations (damping). This experiment was also useful to test piezometric water level sensors for the measurements of water level fluctuations in sand (see next experiment in the Barcelona long wave canal).

Chapter 5 describes the experimental set up of the long wave canal (HYDRALAB, Barcelona), including a presentation of the water level measurements in the sloping sandy beach. The water level signals H(x,t) are presented, and their space-time characteristics are simply described (preliminary analyses). This chapter also serves as an introduction to the theories of the signal processing methods that will be used to analyze water level fluctuations.

Note. Theoretical aspects of signal processing are developed in more detail in the appended **Appendix B9**. In addition, more details on the water level signals recorded at different distances from the "coast line" are presented in the appended **Appendix B10**, comparing the entry water level $H_1(t)$ near the "coast line" to the "pure groundwater" level fluctuation $H_6(t)$ further away from the "coast".

In **Chapter 6**, the measured water level fluctuations in the sloping sandy beach of the Barcelona wave canal are analyzed and interpreted via signal processing techniques, based on prefiltering techniques (e.g. moving averages) and three types of methods: Fourier spectra versus frequency; multi-resolution wavelet analyses; and temporal correlation and cross-correlation functions versus lag times. Cross-analyses involve pairs of signals ($H_i(t)$,$H_j(t)$) sampled at two positions in space perpendicular to the shoreline (x_i,x_j).

In **Chapter 7,** the wave propagation process in the sloping sandy beach of the Barcelona wave canal experiment is modeled numerically using the 3D Richards flow model in a vertical cross-section comprising both the "microporous" sand and the supposedly "macroporous" open water zone (swash zone above the sand beach). The partially saturated / unsaturated flow experiments are calibrated using the VGM parameter model, and also the Exponential parameter model, for the unsaturated conductivity and moisture-pressure curves K(h) and θ(h). In addition, the simpler Dupuit-Boussinesq plane flow model is also briefly tested for comparison. This chapter leads not only to a re-interpretation of the observed

experimental groundwater fluctuations, but also, to an evaluation of the numerical approach to coupled open water / porous media hydrodynamics.

Note. In addition, **Appendix B11** and **B12** present simulations of wave propagation in the sloping sandy beach under simpler wave input that those measured, in order to provide some more insights into the process. Thus, a single harmonic wave was forced at the beach entry during one period (**Appendix B11**) and during several wave periods ("continuous wave test" in **Appendix B12**).

Finally, **Chapter 8** summarizes the main conclusions and the outlook for future research.

Note: some parts of this work were published and presented earlier in Wang et al. (2008) [90], Wang et al. (2008) [93], Wang et al. (2010) [94], and some other parts of this work have been submitted more recently for publication.

Part I
GOVERNING EQUATIONS AND NUMERICS

Chapter 1: Governing equations and constitutive laws for porous media

1.1 Introduction

1.1.1 Configuration and hypothesis of the problems

Two types of equation models are used for analyzing transient porous media flows: saturated plane flow equation (Dupuit-Boussinesq), and variably saturated 3D flow (generalized Richards). Both models can treat the case of transient flow in a partially saturated porous medium, under different assumptions. The respective governing equations are detailed below.

1.1.2 Navier-Stokes equation and its simplifications

Note: the interpretation in this section is borrowed from Ababou (2008) [73].

In "open flow" system (non-porous, classical fluid mechanics) the incompressible Navier-Stokes system of equations is given by:

$$div(\vec{V}) = 0 \tag{1-1}$$

$$\rho_0 \frac{\partial V_i}{\partial t} + \rho_0(\vec{V} \cdot \nabla)V_i = -(\nabla p + \rho_0 g \nabla z)_i + \mu(\nabla^2 V) \tag{1-2}$$

Where, $\vec{V}$ is the flow velocity;

ρ_0 is the the fluid density;

μ is is the dynamic viscosity;

g is the gravity acceleration;

z is the elevation head;

∇ is the del operator.

The first equation is the mass conservation PDE (Partial Differential Equations) for an incompressible fluid. It states that the velocity divergence is equal to zero. The second equation is a system of three PDE's enforcing the conservation of momentum, a vector quantity here by taking into account the zero divergence of velocity inferred from mass conservation. In total, the 3D Navier-Stokes equations constitute a system of four equations

(one for mass and three for momentum) with four unknown variables: pressure (p), and velocity components (V_x, V_y, V_z).

In the second equation(1-2), the left two terms are the acceleration terms (eulerian and inertial) and the second term in the right is the viscous dissipation term($\mu\nabla^2 V$). Neglecting the acceleration terms, Darcy's equation is obtained by averaging the N-S equations over many pores:

$\mu\nabla^2 V_i = -\mu\frac{\phi V_i}{k}$ and then $\vec{q} = -\frac{k}{\mu}\left(\vec{\nabla}p + \rho g\vec{\nabla}z\right)$

Where,

$k = permeability \approx c \times r_{PORE}^2$

$\phi V_i = q_i = Flux\ density\left[\frac{\left(m^3/s\right)}{m^2\perp}\right] \Leftrightarrow [m/s]$

$\phi = Porosity$

The viscous dissipation term ($\mu(\nabla^2 V)$) becomes proportional to V upon averaging over many pores. This finally leads to Darcy's linear flux-gradient law, usually expressed in terms of flux density "q" rather than velocity "V".

1.2 Plane flow equations with a free surface (Dupuit-Boussinesq)

The first model is used to analyze wave dissipation and transmission of water table fluctuations in (*x*,*y*,*t*) under plane flow hypotheses (Dupuit-Boussinesq). This model is based on Darcy's linear flux-gradient law. It assumes vertically hydrostatic conditions, and most importantly, it does not take into account unsaturated flow and capillary effects above the moving free surface. This model also neglects the kinetics of retarded flow to/from the unsaturated zone (hypothesis of instantaneous storage/drainage). For more details, see *Ababou (2008 [73], Sec.8.5.4).*

The Dupuit-Boussinesq equations are given by:

2D Conservation equation (vertically integrated): $\Phi\frac{\partial \mathrm{H}}{\partial \mathrm{t}} = -\mathrm{div}(\mathrm{Q})$ (1-3)

2D Darcy equation (vertically integrated): $Q = -T(h)grad(H)$ (1-4)

2D Flow equation in the (x,y) plane: $\Phi\frac{\partial H}{\partial t} = div\left(T(h)grad(H)\right)$ (1-5)

where Φ (m^3/m^3) is the unconfined storage coefficient or effective porosity, h is the water depth, $T(h)$ is the hydraulic transmissivity, and H is the elevation of the free surface, with the relation $h = H - Z_{inf}(x,y)$, where $Z_{inf}(x,y)$ is the elevation of the impervious substratum.

In our work, we focus on a flat substratum, either horizontal or inclined plane. For example, for a bed sloping in the *x*-direction, we have $Z_{inf} = -I_0 x$, therefore: $h = H + I_0 x$, where I_0 is the slope.

1.3 Partially saturated / unsaturated media with capillary effects (3D Richards)

The second model is based on a generalization of the 3D Richards equation for variably saturated heterogeneous porous media, possibly with macro-porous zones (including inertial effects with a quadratic flux-gradient law). This model is fully 3D (not vertically hydrostatic), and it is able to represent multiple free surface dynamics in (*x*,*y*,*z*,*t*). Also, the model accounts for capillary effects in the unsaturated zone.

The equations are given by (Trégarot, 2000 [17]):

3D mass conservation: $\frac{\theta_e(h)}{\partial t} = -div[q]$, (1-6)

3D Darcy-Buckingham (saturated/unsaturated): $q = -K(h)\nabla H$, (1-7)

3D flow equation for pressure head *h*: $\frac{\partial \theta_e(h)}{\partial t} = div[K(h)\nabla h] + div[K(h)\vec{g}_B]$ (1-8)

Where,

$\theta_e(h) = \theta(h) - \theta_r$ is the effective volumetric water content, m^3/m^3;

h is the pressure head, m;

θ_r is the residual water content, m^3/m^3;

$H = h + \vec{g}_B \cdot \vec{x}$ is total hydraulic head, m;

$\vec{x}$ is the point coordinate vector in the (x,y,z);

$\vec{g}_B = -\vec{g}/|\vec{g}|$ is the normalized anti-gravity vector (upwards);

$K(h) = \begin{bmatrix} K_{xx}(h) & 0 & 0 \\ 0 & K_{yy}(h) & 0 \\ 0 & 0 & K_{zz}(h) \end{bmatrix}$ is hydraulic conductivity tensor, m/s.

Note that the hydraulic conductivity tensor is expressed here in the principal system of coordinates. It is assumed that the axes of the computational domain (x, y, z) coincide with the principal system of the permeability tensor. That is, the matrix $K(h)$is assumed diagonal in this work. Nevertheless, it is worth noted that our model allows for the conductivity-pressure relation $K(h)$ to be nonlinearly anisotropic.

Note $K(h)$ and $\theta(h)$ are respectively hydraulic conductivity function and water content function for the unsaturated media. For the unsaturated simulation, the parameter models of the water content $\theta(h)$ and the hydraulic conductivity $K(h)$ are very important. Examples of models that have been often used in the literature are the Brooks and Corey, Brutsaert, Campbell, Van Genuchten / Mualem, and the Exponential model. These models have been often used for hydrological applications in the unsaturated zone, and the Van Genuchten / Mualem, and the Exponential model are most popular. For more details and a literature review, see [1] (Trégarot (2000) [17], Chapter 2). In this thesis, we use two different models:

- Van Genuchten / Mualem model
- Exponential model for both the $\theta(h)$ and the $K(h)$ curve.

1.3.1 Van Genuchten / Mualem model of K(h) and θ(h)

In the unsaturated zone of a porous medium, the model proposed by Van Genuchten (1980)[84] for the water content-pressure relation, $\theta(h)$, is:

$$S(h) = \frac{\theta(h)-\theta_r}{\theta_s-\theta_r} = \left[\frac{1}{1+(-\alpha h)^n}\right]^m \tag{1-9}$$

where,

θ_s is the saturated water content, m^3/m^3;

θ_r is the residual water content, m^3/m^3;

m, n are the dimensionless exponents of the VGN model.

The functional model of Mualem (1976) [4] relates the hydraulic conductivity function $K(h)$ to the $\theta(h)$ function via a functional (integral). When $\theta(h)$ is the Van Genuchten curve of equation (1-9), the resulting $K(h)$ is of the form:

$$K_R(h) = \frac{K(h)-K_r}{K_s-K_r} = \frac{1}{(1+(-\alpha h)^n)^{-m/2}}\left(1-\left[1-\frac{1}{(1+(-\alpha h)^n)}\right]^m\right)^2 \tag{1-10}$$

where,

K_s is the saturated hydraulic conductivity, m/s;

K_r is the residual hydraulic conductivity, m/s;

$m = 1 - 1/n$ (Mualem model).

1.3.2 Exponential model of θ(h) and K(h)

In the exponential model, water content function $\theta(h)$ is defined:

$$\frac{\theta(h)-\theta_r}{\theta_s-\theta_r} = e^{\beta(h-h_b)} \quad \text{if } h \le h_b \tag{1-11}$$

$$\frac{\theta(h)-\theta_r}{\theta_s-\theta_r} = 1 \qquad \text{if } h > h_b$$

And the hydraulic conductivity function $K(h)$ for the unsaturated zone is:

$$\frac{K(h)-K_r}{K_s-K_r} = e^{\alpha(h-h_b)} \qquad \text{if } h \le h_b \tag{1-12}$$

$$\frac{K(h)-K_r}{K_s-K_r} = 1 \qquad \text{if } h > h_b$$

where, $h_b$is the bubbling pressure head, m;

β is the capillary parameter, m^{-1}.

1.3.3 Capacity function C(h)

The capillary capacity of the soil is defined as the slope of the relation $\theta(h)$:

$$C(h) = \frac{d\theta(h)}{dh} \tag{1-13}$$

Let $S_e = \frac{\theta(h)-\theta_r}{\theta_s-\theta_r}$, then $C(h)$ can also be written like:

$$C(h) = \theta_{es}\frac{dS_e}{dh} \text{ and } C(S_e) = C\big(h(S_e)\big) \tag{1-14}$$

where, θ_{es} is the effective saturated water content and $\theta_{es} = \theta_s - \theta_r$.

The capillary capacity of the soil represents the variation of water content per unit change in pressure, and it is a characteristic phenomenon of storage and release of water in the soil.

For the VGM model, $C(h)$ is obtained as follows:

$$C(h) = \frac{mn\alpha\theta_{es}(-\alpha h)^{n-1}}{[1+(-\alpha h)^n]^{m+1}} \tag{1-15}$$

or

$$C(S_e) = mn\alpha\theta_{es}{S_e}^{1+1/m}({S_e}^{-1/m}-1)^{1-1/n} \tag{1-16}$$

For the exponential model, $C(h)$ is obtained as follows:

$$C(h) = \beta\theta_{es}e^{\beta(h-h_b)} \tag{1-17}$$

or

$$C(S_e) = \beta\theta_{es}S_e \tag{1-18}$$

1.3.4 Diffusion function D(h)

The hydraulic diffusivity D (m^2/ s) is introduced by Childs and Collis-George (1950) [39], defined by:

$$D(\theta) = K(\theta)\frac{\partial h(\theta)}{\partial \theta} = \frac{K(\theta)}{C(\theta)} \tag{1-19}$$

or

$$D(h) = \frac{K(h)}{C(h)} \tag{1-20}$$

For the VGM model, the hydraulic diffusivity $D(S_e)$ is obtained as follows:

$$D(S_e) = \frac{(1-m)K_s}{\alpha m \theta_{es}} S_e^{0.5-1/m}\left[\left(1-S_e^{1/m}\right)^{-m} + \left(1-S_e^{1/m}\right)^{m} - 2\right] \tag{1-21}$$

For the exponential model, the hydraulic diffusivity $D(S_e)$ is obtained as follows:

$$D(S_e) = \frac{K_s}{\beta \theta_{es}} S_e^{(\alpha-\beta)/\beta} \tag{1-22}$$

or

$$D(S_e) = D_0 S_e^{(\alpha-\beta)/\beta} \tag{1-23}$$

Where, $D_0 = \frac{K_s}{\beta \theta_{es}}$

If given $\beta = \alpha/3$, $D(S_e) = D_0 S_e^2$, it means that the capillary effect diffuses parabolicaly in an unsaturated zone.

1.3.5 Interpretation of the parameters (α) in the exponential model

In the exponential model, α is the slope of log-conductivity versus pressure, which has a physical meaning, related to pore size distribution:

$$\alpha = \frac{\partial lnK}{\partial h}, \text{ if } h \le h_b \tag{1-24}$$

As a consequence, the exponential conductivity model satisfies several properties (REPORT, Ababou (1991) [10], chapter 4):

$$U(h) = \frac{1}{\alpha}K(h) \tag{1-25}$$

where, $U(h)$ is Kirchhoff Transform and $U(h) = \int_{-\infty}^{h} K(h')\,dh'$

$$\alpha = -\frac{\vec{V}\cdot\vec{\nabla}z}{D\left|\vec{\nabla}z\right|^2} \tag{1-26}$$

where, $\vec{V}$ represents the velocity of moisture disturbances, $\vec{V} = -\frac{\partial K}{\partial \theta}\cdot\vec{\nabla}z$ and $\vec{V_z} = (0,0,1)$ if the chosen coordinate system coincides with the natural system (x,y,z, with z vertical upwards). Equation (1-26) shows α indicates the magnitude of gravity-driven advection relative to diffusion. Advection can also be characterized by a dimensionless Peclet number (a vector), $\vec{P}e = \frac{\vec{V}L}{D} = -\alpha L\vec{\nabla}z$, where L is a characteristic length scale.

From the equation (1-26), it can be seen that the moisture diffusion coefficient D is proportional to "Velocity" times a length scale equal to the inverse of α. By analogy with dispersive transport, this suggests that:

$$\lambda_{CAP} = \frac{1}{\alpha} \tag{1-27}$$

λ_{CAP} is a *capillary dispersivity* length scale. Intuitively, it is the length scale of dispersion of moisture around a moving moisture disturbance traveling at velocity $\vec{V}$. For alternative interpretation of λ_{CAP}, see White and Sully (1987, 1988) [45] [46].

In addition, the 'm' and 'n' parameters are dimensionless exponents or shape factors, which are related to the pore size distribution (Thèse, Trégarot 2000 [17], Chapter 2; REPORT, Ababou (1991) [10], chapter 4).

1.3.6 Interpretation of the parameters (α) in the VGM model

From the equation (1-9), water content $\theta(h)$, and equation (1-10), hydraulic conductivity $K(h)$, we see that the characteristic hydrodynamic parameters of the unsaturated porous medium are:

- α [m^{-1}]
- n [dimensionless]
- θ_s, θ_r [m^3/m^3]
- K_s, K_r [m/s]

All these parameters will have an influence on numerical model results – but some parameters more than others. Here is a brief physical interpretation of these parameters.

The α can be interpreted as an inverse capillary length scale (mean capillary length):

$\lambda_{CAP} = \alpha^{-1}$ [m].

The curve of the function $C(h)$ (equation (1-15)) of VGM model exhibits a maximum C_{max} for a pressure head $h_{max} \neq 0$, where the curve of $S_e(h)$ marks a inflection point ($S_e(h_{max}) = S_{e\,max}$). Therefore, we have:

$$h_{max} = -\frac{1}{\alpha}\left(1 - \frac{1}{n}\right)^{1/n} \tag{1-28}$$

$$C_{max} = \alpha m n \theta_{es} \frac{(m)^m}{(m+1)^{m+1}} \tag{1-29}$$

$$S_{e\,max} = \left(\frac{1}{m+1}\right)^m \tag{1-30}$$

with $m = 1 - 1/n$ (Mualem)

In the equation (1-28) of h_{max} function, $n \to \infty$, $h_{max} = -\frac{1}{\alpha} = -\lambda_{CAP}$.

1.4 Partially saturated macro-porous media (3D Richards)

The macro porous media is an extremely course media. The effective water content model $\theta_e(h)$ of the ideal macro porous media is the step function as seen in **Fig. 1-1**. The hydraulic conductivity model $K(h)$ is defined in the same way with the model $\theta_e(h)$, shown in **Fig. 1-2** (Thèse, Trégarot 2000 [17]).

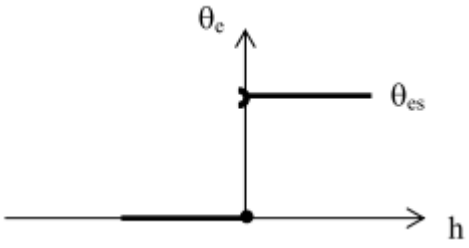

Fig. 1-1 Effective water content model $\theta_e(h)$ of the macro porous media

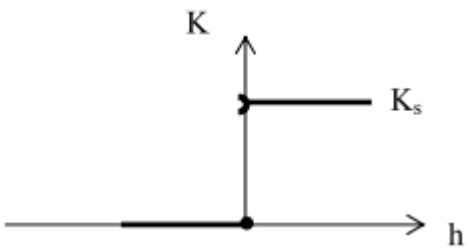

Fig. 1-2 Hydraulic conductivity model $K(h)$ of the macro porous media

The Richards equation with the macro-porous media parameters of $\theta_e(h)$ and $K(h)$ can be used to simulate the flow in the macro-porous media.

Chapter 2: Numerical procedure

2.1 General presentation of BigFlow (2D/3D finite volume code)

We use the numerical code BigFlow (Ababou and Bagtzoglou 1993 [74]; Ababou 2008 [73]) to investigate the highly transient flow problems described previously. Vertically hydrostatic plane flow is modelled with the "2D" plane flow model of **BigFlow** (Ababou and Al-Bitar 2007 [75]). On the other hand, variably saturated flow is handled with the 3D model of **BigFlow**, taking into account vertical velocities as well as unsaturated capillary effects (the 3D model is also used to simulate vertical cross-sections as a special case).

The Bigflow code is based on the implicit finite volume, with sparse Preconditioned Conjugate Gradient matrix solver, and modified Picard iterations for nonlinear problem. The code was developed for high resolution simulation of 3D groundwater and unsaturated flow in heterogeneous media, and was tested for high-performance computations.

The equation model being solved is a generalized Darcy-type equation, with a mixed formulation of mass conservation, capable of simulating various types of flows within the same domain. Bigflow's generic equation, for 3D as well as 2D plane flow, is of the form:

$$\frac{\partial \Theta(h,\vec{x})}{\partial t} = -\vec{\nabla} \cdot \vec{q} \tag{2-1}$$

$$\vec{q} = -\overleftrightarrow{K}\left(h, \vec{\nabla}H, \vec{x}\right)\vec{\nabla}H \tag{2-2}$$

$$H = h + \vec{g}(\vec{x}) \cdot \vec{x} \tag{2-3}$$

where only the first equation is actually solved, once the second and third equation have been inserted. The first equation expresses mass conservation in a partially saturated medium with known water retention or storage law $\Theta(h)$; the second question is generalized nonlinear flux-gradient head loss law with tensorial hydraulic conductivity/transmisivity "K"; and the third equation is the relation between total head or elevation (H) and pressure head or water depth (h) via a normalized gravitational vector (g).

2.2 Flowchart of the numerical iterations in the Bigflow code

In the numerical simulation, the numerical iterations include linear iteration (inter iteration) and non-linear iteration (outer iteration). In general, the numerical calculation begins from the linear iteration, then the non-linear iteration, and finally finishes a time step. The relationship of the time step, linear iteration, and non-linear iteration are illustrated in **Fig. 2-1**.

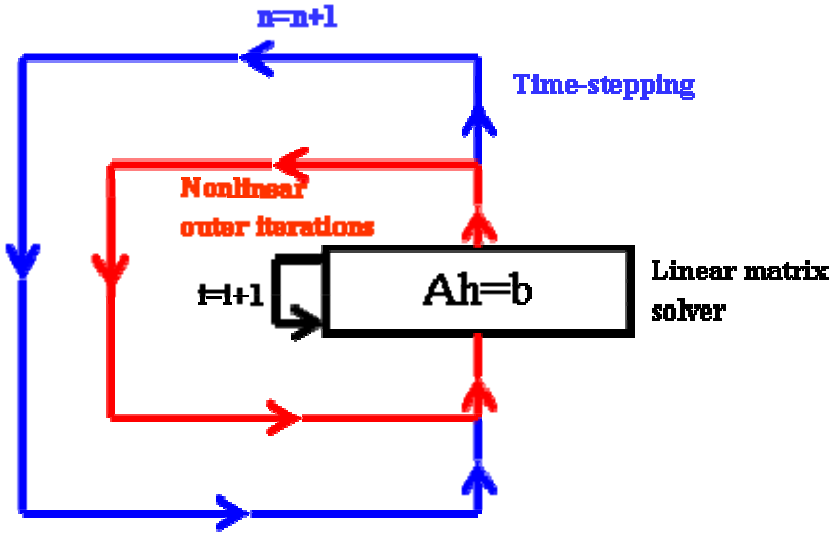

Fig. 2-1 Schematic of the numerical iterations in the Bigflow code

Note:

- **Linear matrix solver: Preconditioned Conjugate Gradients**
- **Nonlinear iterations: modified Picard scheme (fixed point)**
- **Time stepping (implicit finite differences – Euler backwards)**

2.3 Numerical procedure for time-varying Boundary Conditions

2.3.1 Boundary conditions for the Boussinesq model and Richards model

There are two types of the time-varying boundaries to be used in this thesis: (1) time-varying water level $H(x_0, y, t)$ boundary condition for the 2D Boussinesq model; (2) time-varying pressure head $h(x_0, y, t)$ boundary condition for the 3D Richards model. The corresponding schemas are respectively shown in **Fig. 2-2** and **Fig. 2-3**. In each of the two figures, the figure (a) shows the time-varying BC's problem, and figure (b) shows how to impose the different boundary condition.

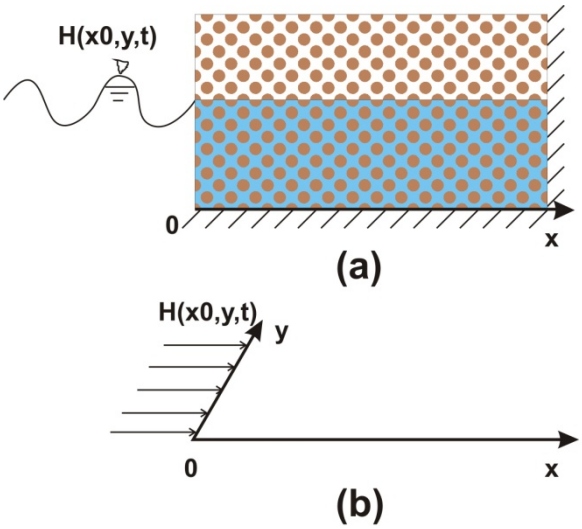

Fig. 2-2 Schematic of the time-varying water level $H\left(x_0, y, t\right)$ boundary condition in time and space for the Boussinesq model

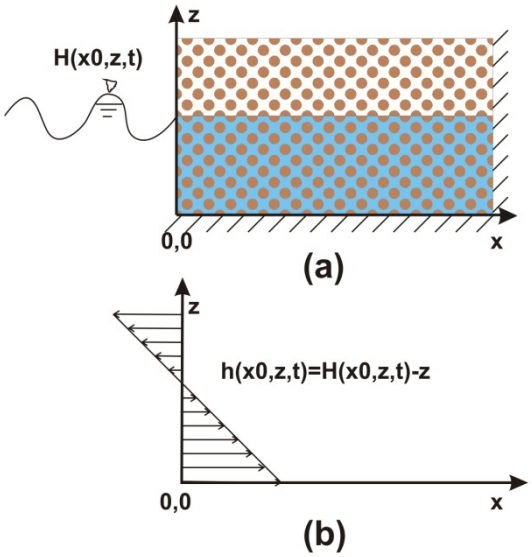

Fig. 2-3 Schematic of the time-varying pressure head $h(x_0, z, t)$ boundary condition in time and space for the Richards model

2.3.2 Compilation of executable file for the time-varying BC's problem

In Bigflow, each problem has a model, for instance, the plane flow 2D Boussinesq model, the partially saturated flow 3D Richards model. Furthermore, according to the different parameter model, each model has different sub-model, such as exponential sub-model and VGN sub-model for the 3D Richards model. As a result, the running of each sub-model needs an executable file (Bftest.exe) and at the same time, the compilation of the executable file for each sub-model needs a common file Combig and five source files: mainflow.f , ftime.f, fbqvt_chezy.f, fcond_*.f and ftheta_*.f.

Note that the mainflow.f is the main programme of Bigflow, ftime.f originally programmed by G. Tregarot is the file especially to treat the time-varying boundary condition, fbqvt_chezy.f has been programmed by G. Tregarot to calculate the transmissivity of the isotropic Boussinesq equation and St Venant equation, and fcond_*.f and ftheta_*.f are two parameter model files for the hydraulic conductivity function $K(h)$ and the water content function $\theta(h)$.

In Version Bigflow2.0 (07-04-2007), the time-varying boundary condition which can be expressed as a formula, can be directly programmed in the ftime.f for two types of boundary conditions: time-varying water level (Boussinesq model) and time-varying pressure head (Richards model). Its advantage is that it doesn't need a extra data file for the time-varying boundary condition, while its disadvantage is that for any modification of the time-varying boundary condition, it needs to recompile the executable file, and the most inconvenient is

that it can not treat the random time-varying boundary condition such as the measured data from the experiments.

In the Version Bigflow2.0 (09-2007), A. MALLET modified the mainflow.f and ftime.f in order to treat the random time-varying boundary condition. Then this version of Bigflow can treat the time-varying boundary condition by adding the extra data files such as BoundA1.txt , and BoundB1.txt outside of the executable file. However, the modification of A. MALLET can just treat the random time-varying water level boundary condition for the Boussinesq model and saturated flow 3D Richards model.

In order to treat the random time-varying pressure head boundary condition for the partially saturated 3D Richards model, R. Ababou, Y. Wang et K. Alastal did the second modification in the mainflow4.3.f from the April through September of 2009. At this time, the parameter of the time dependence parameter (LTRA(j),LTRB(j),j=1,2,3) in the INPUT1 (Trégarot 2000[17]) is set to 2 for the random time-varying pressure head boundary condition of the variably saturated 3D Richards model, instead of 1 for the random time-varying water level boundary condition of the 2D Boussinesq model, see **Table 2-1**. In addition, if 2 is chosen for the parameter of the time dependence, this version of Bigflow4.3 (25 September 2009) is forced to treat the time-varying linear distribution of the pressure head in the z direction without consideration of the other types of time-varying boundary condition such as the spatial flux distribution.

Table 2-1 Time-varying boundary condition in the INPUT1 of Bigflow

2D Plane flow Boussinesq model	3D partially saturated flow Richards model
TYPE OF B.Cs: LTYPA(j),LTYPB(j),j=1,2,3: 1 2 2 2 2 2 VALUE OF B.Cs:(FIXAj,FIXBj)j=1,2,3: 2.47 0.0 0.0 0.0 0.0 0.0 TIME DEPENDANCE OF B.Cs: LTRA(j),LTRB(j),j=1,2,3: 1 0 0 0 0 0	TYPE OF B.Cs: LTYPA(j),LTYPB(j),j=1,2,3: 11 2 2 2 2 2 VALUE OF B.Cs:(FIXAj,FIXBj)j=1,2,3: 2.47 0.0 0.0 0.0 0.0 0.0 TIME DEPENDANCE OF B.Cs: LTRA(j),LTRB(j),j=1,2,3: 2 0 0 0 0 0

At the same time, it is worth noted that in Bigflow4.3, for the partially saturated flow Richards model, in the outside data file of BoundAi.txt or BoundBi.txt, it is still given the water level condition $H(x_0, t)$, as in Version Bigflow2.0 (09-2007).

To compile the executable file for each model of Bigflow, it needs to follow the steps written in the '*README FILE ReadMe_BF2005FORTRAN_Compiling.rtf*' by R.Ababou and A.Al-Bitar (6 Feb.2006), listed in the appendix AC2-1. The settings of the project options in the *ABSOFT 9.0 Developer Tool Interface* play very important role in the compilation of the executable file, and especially the CPU of the computer. Accordingly, it's better to make the compilation in a fixed computer, instead of a mobile computer. The model types and the needed source files for the compilation of the corresponding executable file are listed in **Table 2-2**.

Table 2-2 Model types and corresponding source files for the executable files of Bigflow

Model & Corresponding executable file	2D Boussinesq unconfined plane flow	3D Richards exponential parameters	3DRichards VGN parameters
	BF_2D_unconf.exe	BF_3D_U_exp.exe	BF_3D_U_vgn.exe
Source files for generating the executable files	mainflow_v4-3.f, ftime_v3-0.f, Combig		
	fbqvt_chezy.f	fbqvt_chezy.f	fbqvt_chezy.f
	fcond_bq_unconf.f	fcond_exp5	fcond_vgn5
	ftheta_bq_unconf.f	ftheta_exp5	ftheta_vgn5

2.3.3 Data files for the time-varying BC's problem

For the time-varying BC's problem, whether the plane flow Boussinesq model or partially saturated flow Richards model, both need the water level fluctuation data file as the entry boundary condition. According to the time-varying boundary, the data files are named as BoundAi.txt and BoundBi.txt($i = 1,2,3$). The format of the data file is given by [t H] two columns, as listed in the following example:

```
t                    H
0.0000000e+000 2.0200000e-001
1.0000000e-002 2.0190211e-001
2.0000000e-002 2.0161803e-001
3.0000000e-002 2.0117557e-001
4.0000000e-002 2.0061803e-001
5.0000000e-002 2.0000000e-001
6.0000000e-002 1.9938197e-001
7.0000000e-002 1.9882443e-001
8.0000000e-002 1.9838197e-001
```

2.4 Debugging and validation tests for the unsaturated flow

For unsaturated flow modelling, the shapes and parameters of the water content $\theta(h)$ and the hydraulic conductivity $K(h)$ curves are very important. In this section, we also use these curves to distinguish between:

- actual porous media (such as sand or any other “microporous” medium), and
- very coarse media, or even open cavities and free water bodies (“macroporous media”).

2.4.1 Validation tests of macro-porous media: the falling head permeameter

The falling head permeameter is used here as a first test and validation of the concept of “macroporous medium”. Indeed, the falling head permeameter is a vertical column made up of two parts (cf. **Fig. 2-4**):

- The upper part is a cylindrical tube containing free falling water (this part is modelled as a “macroporous medium with 100% porosity and very large permeability…)
- The bottom part is a cylindrical tube with same diameter, containing the porous medium (such as sand)

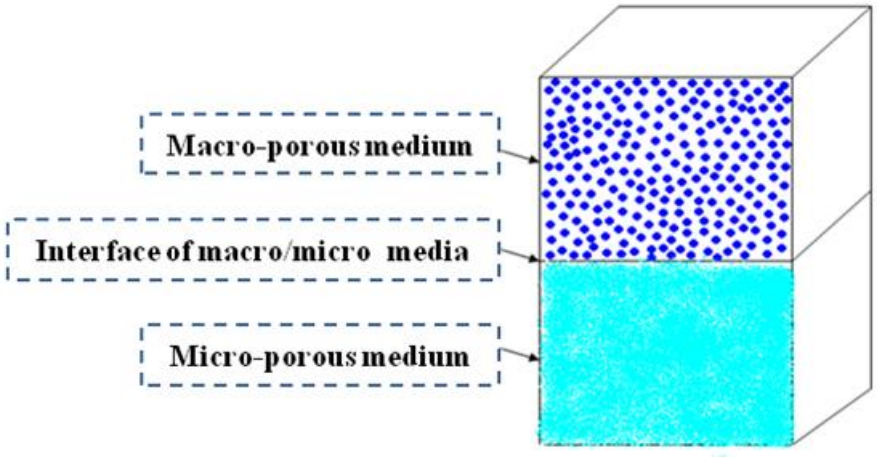

Fig. 2-4 Simplified schema of the permeameter made up of the macro/micro porous media

In fact, as shown in **Fig. 2-5**, the water in the permeameter flows from the reservoir section *s* to a sample section *S* with vertical length *L*. We identify the level of liquid in the tank by the side h_2 and hence we obtain a curve of water depth *h* in terms of observed time that we use to determine the hydraulic conductivity.

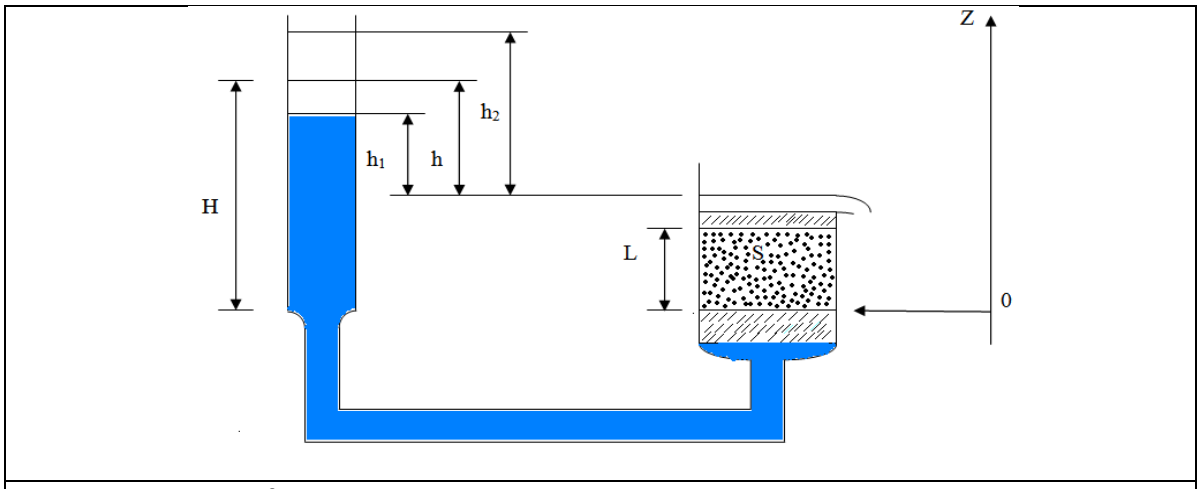

Fig. 2-5 Schema of the variable head permeameter

The analytical expression of the hydraulic conductivity is obtained from the following assumptions:

- Vertical monodimensional water flow
- Darcy flow
- Instantaneous draining / refilling of the column
- Incompressible porous media

Considering the permeameter as a column containing two layers: macro /micro porous media (as shown in **Fig. 2-4**), we simulate this problem with two unsaturated Richards model (Exponential and VGM models for the water content curve $\theta(h)$ and the hydraulic conductivity curve $K(h)$) of BIGFLOW, and we will study the behavior of this column after a sudden discharge of water. We are interested in analyzing the variation of flow and especially, the hydraulic head over time that help us determine the saturated hydraulic conductivity of the micro porous medium and compare it with theoretical value (put directly in the numerical model).

2.4.4.1 Analytical solution of the saturated hydraulic conductivity of the micro porous media

From **Fig. 2-5**, by applying Darcy's Law in the section of length L and surface S, we obtain that:

$$q = K_s \frac{h}{L} S \tag{2-4}$$

Where,

K_s is the saturated hydraulic conductivity (m/s);

h is the water depth (m).

The law of conservation of mass gives:

$$q\ dt = -s\ dh \tag{2-5}$$

Substituting the equation (2-4) in (2-5), we have:

$$\frac{K_S}{L} S\ dt = -s\ \frac{dh}{h} \tag{2-6}$$

where, s is the reservoir section. By integrating (2-6) we obtain the expression of the hydraulic conductivity as follows:

$$K_s = \frac{s}{S} * \frac{L}{(t_2 - t_1)} * Ln(\frac{h_1}{h_2}) \tag{2-7}$$

2.4.4.2 Numerical simulation conditions

- **Simulation domain**

L_x=2m, L_y=2.0m, L_z=1m;

Dx=1m, Dy=1, Dz=0.01m;

The schema of the simulation domain is shown in **Fig. 2-4**

- **Boundary condition**

The boundary conditions on six faces of the calculated column are shown in **Table 2-3**.

Table 2-3 Boundary conditions on six faces of the calculated column

Faces	Faces « 1 » ⊥ X1	Faces « 2 » ⊥ X2	Faces « 3 » ⊥ X3
Faces « A » (Xj=0)	Flux ⊥ nul : q_1=0	Flux ⊥ nul : q_2=0	Unform head: h = 0m
Faces « B » (Xj=Lj)	Flux ⊥ nul : q_1=0	Flux ⊥ nul : q_2=0	Flux ⊥ nul : q_3=0

- **Initial condition**

The linear distributed initial pressure head in the column of two porous media:

$h(x, y, z)$=0.95 –z (m)

- **Hydraulic properties and numerical parameters of the micro and macro porous media**

The main hydraulic properties and numerical model parameters (Exponential model and VGM model) of the two porous media are listed in **Table 2-4**.

Table 2-4 Hydraulic properties and numerical parameters of the micro and macro porous media

Parameters		Micro porous medium	Macro porous medium
Saturated hydraulic conductivity K_s		10e-3 m/s	1 m/s
Saturated water content θ_s		0.3 m^3 /m^3	1 m^3 /m^3
Exponential model for *k(h), θ(h)*	α	9 m^{-1}	27 m^{-1}
	β	3 m^{-1}	9 m^{-1}
	$\lambda_{Cap} = \frac{1}{\alpha}$	0.111 m	0.037 m
VGM model for *k(h), θ(h)*	α	9 m^{-1}	27 m^{-1}
	n	2.0	2.0
	$\lambda_{Cap} = \frac{1}{\alpha}$	0.111 m	0.037 m

- **Duration of the simulation and numerical parameters**

Two numerical simulations both simulate the free water falling process of 2000s.

The numerical calculation time parameters and the numerical criteria are listed in **Table 2-5**.

Table 2-5 Numerical parameters (INPUT1) for the calculation of time step, non-linear/outer (Picard) and linear/inner iterations

Time step	Intial time step	DTIN=0.0001s
	Minimum time step	DTMIN=0.0001s
	Maximum time step	DTMAX=0.01
	Time step multifier	DTMUL=1.2
No-linear iterations (Picard)	Convergence criterion of pressure head	ENLH3=1.0E-4
	Maximum number of no-linear iteration	INLMAX=15
Linear iterations	Convergence criterion of pressure head	ENORM3=1.0E-6
	Maximum number of linear iterations	ITEND=100
Method to caculate the middle nodal conductivities		Geometric mean

2.4.4.2 Numerical behaviour of Bigflow during the simulation

- **Exponential model**

The standarlized linear and nonlinear iteration process curves of the pressure head are shown in **Fig. 2-6** and **Fig. 2-7**.

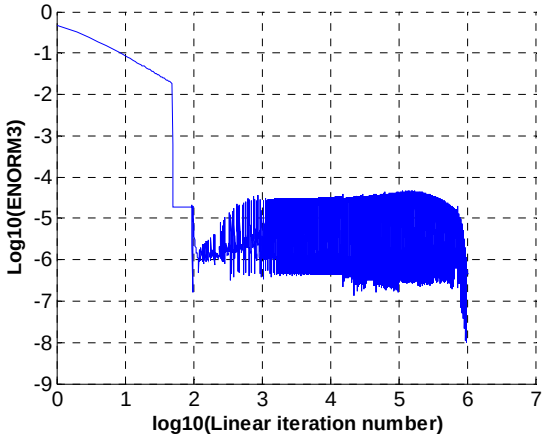

Fig. 2-6 Standardized linear iteration process curve of the pressure head in log10

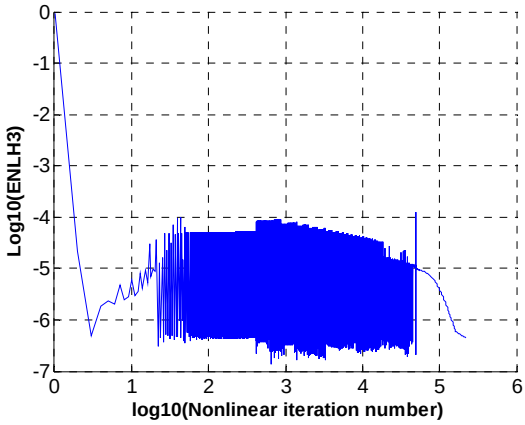

Fig. 2-7 Standardized nonlinear iteration process curve of the pressure head in log10

Although there is a bigger beginning value about 1.0, the linear and noliear errors decrease with respect to the iteration number and at last each of two satisfies its own convergence criteria .

Fig. 2-8 shows that the curve of the evolution of Q_{Mass} almost superposes on the curve of the evolution of Q_{Bound}f, except that there is a certain fluctuation of the Q_{Mass} in the first part of the simulation. In contrast, the V_{Bound} curve surperposes totally on V_{Mass}, as shown in **Fig. 2-9**. In addition, the turning point in the Q_{Bound} curve indicates that the transition of the water surface from the macro porous medium to the micro porous medium.

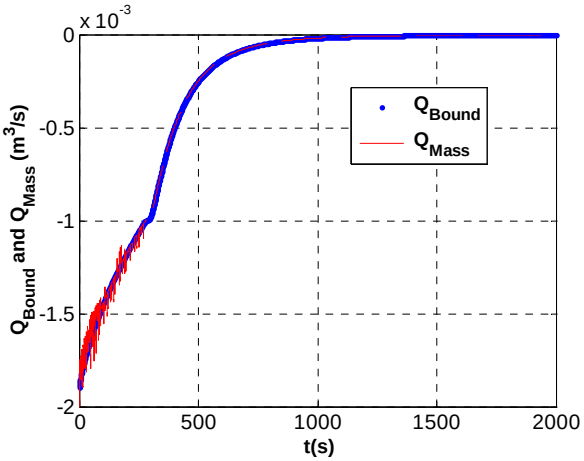

Fig. 2-8 Evolution of Q_{Bound} and Q_{Mass} (local mass balance)

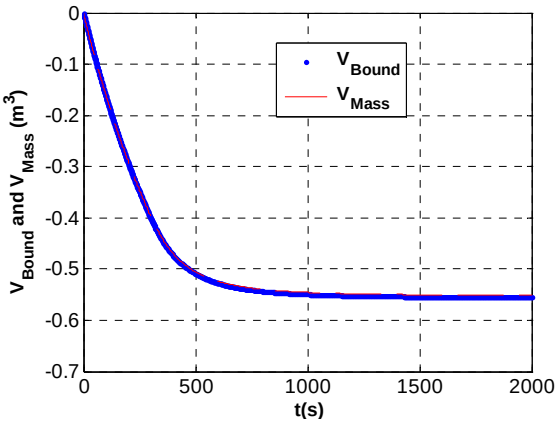

Fig. 2-9 Evolution of V_{Bound} and V_{Mass} (global volume balance)

- **Van Genuchten / Mualem model**

The numercial simulation with VGM model has the similar standarlized linear and nonlinear iteration process curves of the pressure head to Exponential model, as shown in **Fig. 2-10** and **Fig. 2-11**.

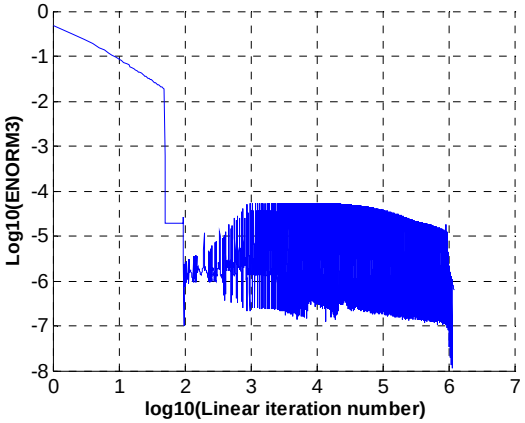

Fig. 2-10 Standarlized linear iteration process curve of the pressure head in log10

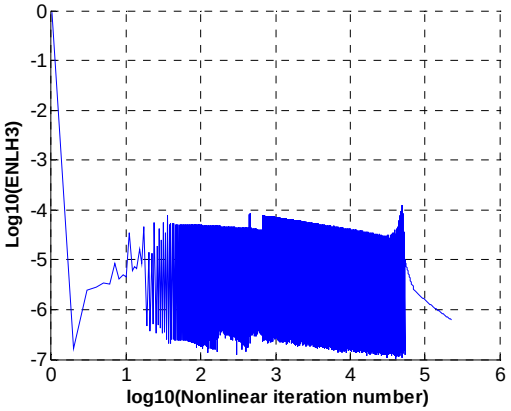

Fig. 2-11 Standarlized nonlinear iteration process curve of the pressure head in log10

Similar to Expenential model, **Fig. 2-12** also indicates that the Q_{Mass} curve has the same trend as the V_{Bound} curve. Here it is noted that the VGM parameter 'n' has great influence on the nonlinear iteration convergence. In addition, the V_{Mass} curve superpose almost on the V_{Bound} curve, as shown in **Fig. 2-13**.

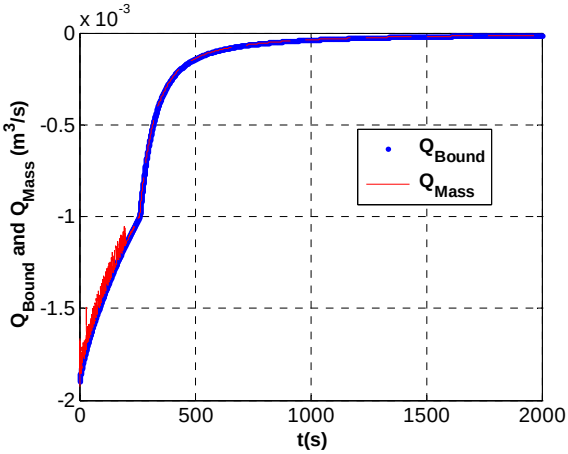

Fig. 2-12 Evolution of Q_{Bound} and Q_{Mass} (local mass balance)

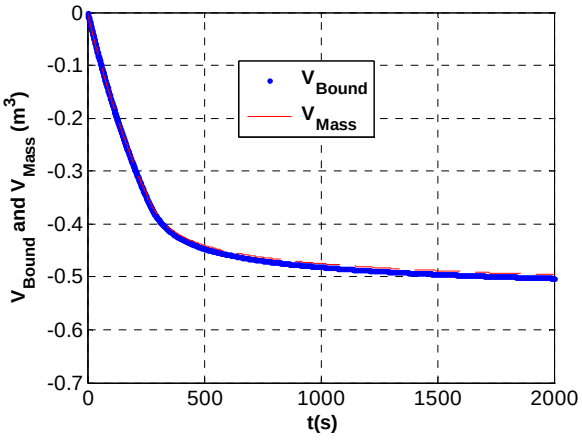

Fig. 2-13 Evolution of V_{Bound} and V_{Mass} (global volume balance)

2.4.4.3 Calculation of the saturated hydraulic conductivity of the micro porous medium

The above expression (2-7) of the theoretical hydraulic conductivity indicates that the water depth curve *h(t)* above the micro porous medium column, or more precisely, the positive pressure head *h(t)* curve at the boundary between the macro and micro porous media is the exponential function with the form $\exp\left(-\frac{t}{\tau}\right)$, and $\tau = -\frac{L*\varphi}{K_s}$.

Where,

K_s is the saturated hydraulic conductivity of the micro porous column (m/s);

L is the vertical length of the micro porous medium column (m);

φ is the saturated water content θ_{sat}(m^3/m^3) of the micro porous medium column.

Then, we can write the logarithmic expression of *h(t)* in the following form:

$$Ln(h) = at + b \qquad \text{avec } a = -\frac{1}{\tau} \tag{2-8}$$

As a result, the saturated hydraulic conductivity of the micro porous column can be obtained by doing the linear curve fitting on the logarithmic expression of the calculated pressure head *h(t)* at the boundary between the macro and micro porous media with Exponential model and VGM model.

- **Exponential model**

Fig. 2-14 shows the vertical profiles of the calculated pressure head for different time at t=0s, 90s, 180s, 280s, 500s, 1000s, and 2000s with Exponential model.

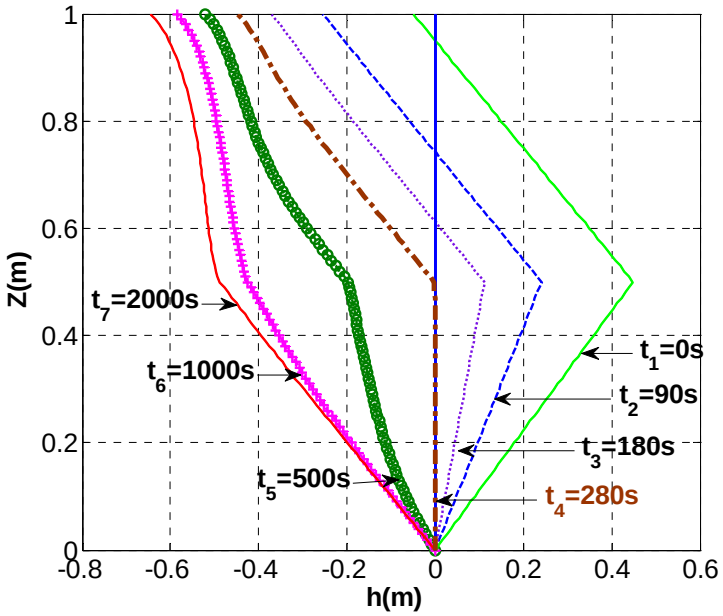

Fig. 2-14 Vertical profiles of the calculated pressure head for different time (t=0s, 90s, 180s, 280s, 500s, 1000s, and 2000s) with Exponential model

From this figure, it can be seen, on the one hand, the evolution of the pressure head of the column, and on the another head, the evolution of the water table (*h=0*) during the desaturation process. Thus, from this figure, it can be also seen that when t≈280s, the water table descends at the boundary between the macro and micro porous media from the macro porous medium.

In addition, **Fig. 2-15** shows the evolution of the pressure head *h(t)* at the boundary (z=0.5m) between the macro porous medium (water) and the micro porous medium (sand).

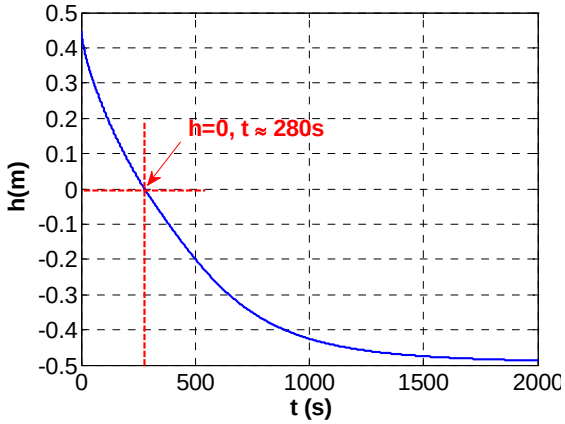

Fig. 2-15 Evolution of the pressure head h(t) at the boundary (z=0.5m) between the macro (water) and micro (sand) porous media at t=0-2000s

From this figure, it can be seen that the pressure head decreases progressively and become zero at about t=280s, which comfirms the result shown in **Fig. 2-14**. Therefore, the time t=280s can be regarded as a transition time from the unsaturated to saturated porous media, or more precisely, it is the maximum time for which the regression equations can be applied to to determine the hydraulic conductivity K_s for the micro porous medium.

Considering the influence of the boundary transition from unsaturated to saturated porous media, the pressure head curve *h(t)* from t=0-180s is just taken to do the linear curve fitting and the result is shown in **Fig. 2-16**.

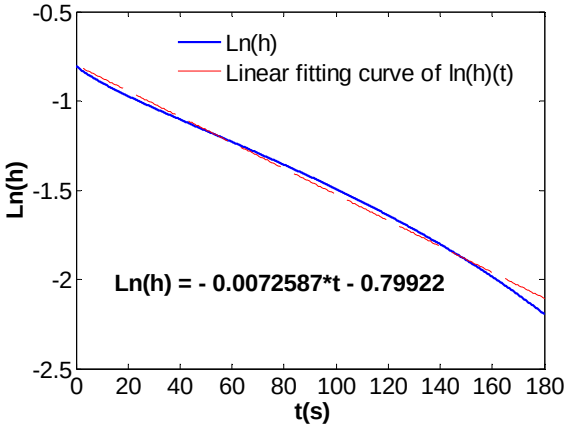

Fig. 2-16 Ln(h) (t, z=0.5m) and the corresponding linear fitting curve at t=0-180s

From this figure, we obtain that, in the equation (2-8), a=-0.0072587. Therefore, we obtain that:

$$K_s = 0.0011 m/s$$

This means that the calculated saturated hydraulic conductivity (adjusted numerically) with Exponential model is very approximate to the theoretical value 0.001m/s (put directly in the numerical model). As a result, the coupling Exponential model between micro and macro porous media has been effectively validated by the falling head permeameter test.

- **Van Genuchten / Mualem model**

Fig. 2-17 illustrates the vertical profiles of the calculated pressure head for different time at t=0s, 90s, 180s, 260s, 500s, 1000s, and 2000s with VGM model.

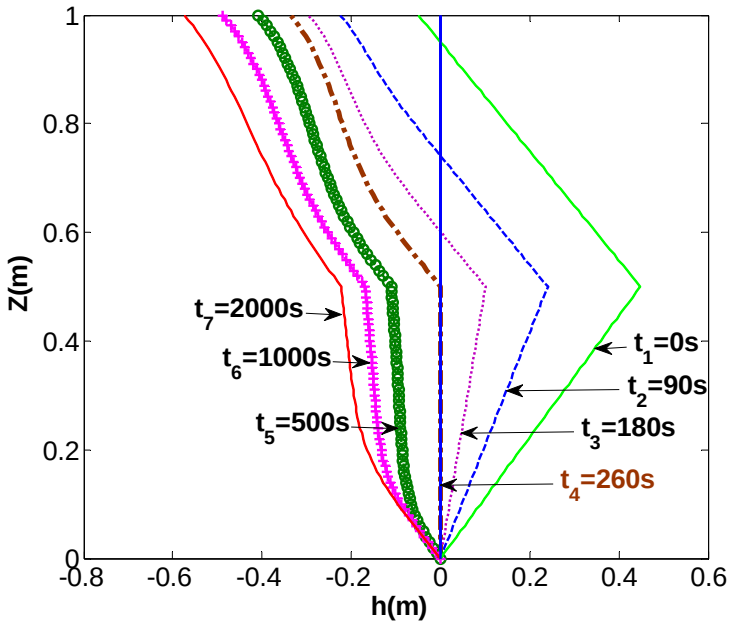

Fig. 2-17 Vertical profiles of the calculated pressure head for different time (t=0s, 90s, 180s, 260s, 500s, 1000s, and 2000s) with VGM model

From this figure, we know that it needs about 260s for the water table to descend to the boundary between the macro and micro porous media from the macro porous medium. This means that the calculated water table with VGM model descends more quickly than the calculated one with Exponential model.

Similarily, the evolution curve of the pressure head h(t) at the boundary (z=0.5m) between the macro (water) and micro (sand) porous media (**Fig. 2-18**) further confirm the result shown in the vertical profile of the calculated pressure head (**Fig. 2-17**): the transition time from the unsaturated to saturated porous media is about 260s which is also the maximum time to be used to do linear curve fitting to determine the hydraulic conductivity K_s for the micro porous medium.

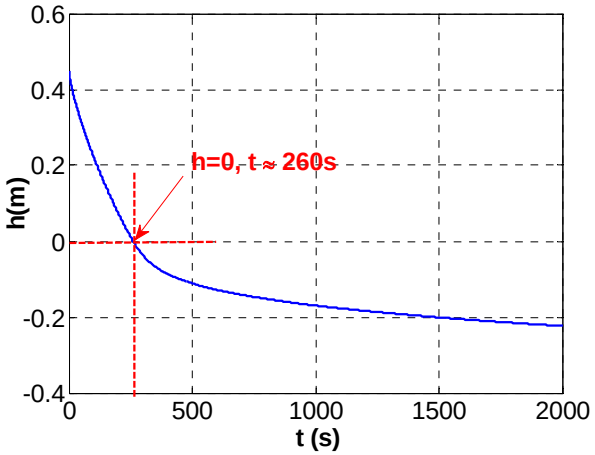

Fig. 2-18 Evolution of the pressure head h(t) at the boundary (z=0.5m) between the macro (water) and micro (sand) porous media at t=0-2000s

The same time of the pressure head curve *h(t)* from t=0-180s as the result with Exponential model is taken to do the linear curve fitting and the result is shown in **Fig. 2-19**.

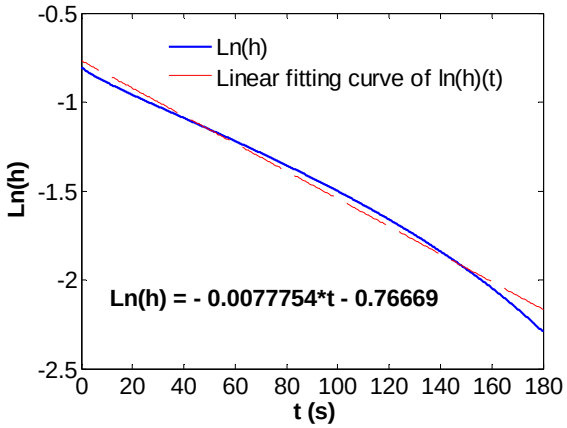

Fig. 2-19 Ln(h) (t, z=0.5m) and the corresponding linear fitting curve at t=0-180s

From this figure, we also obtain that, in equation (2-8), a=-0.0077754. Finally, we obtain that:

$$K_s = 0.0012m/s$$

This also means that the calculated saturated hydraulic conductivity with VGM model is very approximate to the theoretical value, even though it is a little bigger than the one with Exponential model. Therefore, the coupling VGM model between micro and macro porous media has been also effectively validated by the falling head permeameter test.

Part II
MODELING OF NON-OSCILLATORY FLOWS IN POROUS MEDIA

Chapter 3: Wetting and discharge problems (non-oscillatory)

3.1 Introduction

Wetting and discharge problems exist everywhere in the nature and they are two good examples to investigate the capillary effect of the porous media. The capillary effect will be well understood with comparing the results with different methods: experiment, numerical simulations and analytical solution, which will be helpful to investigate the most complete problem: oscillations in a large wave canal (Barcelona) with a sloping sandy beach.

3.2 Wetting problem (variably saturated imbibition in a dry sand)

3.2.1 Introduction

In this section, a wetting experiment in a vertical sandbox is conducted in order to investigate the capillary effect, and at the same time, the numerical simulation of highly nonlinear unsaturated /partially saturated flow (3D Richards model) using a finite volume code Biglflow is done to model the wetting problem in a dry porous bank. In addition, the analytical solution with Boussinesq plane flow (Polubarinova) will be used to be compared with the experimental and numerical results.

3.2.2 Laboratory experiment

3.2.2.1 Physical properties of the fine sand

The diameter measured by sieve analysis of the sand varies from about 0.02 through 0.32mm, and the weighted average diameter is 0.16mm, as seen in **Fig. 3-1**.

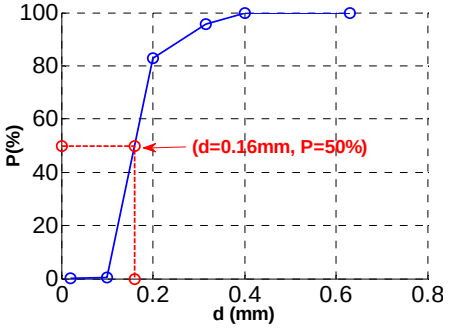

Fig. 3-1 Sand size distribution curve

The measured water content at saturation θ_s and saturated hydraulic conductivity K_s are respectively equal to 0.38m^3/m^3 and 2.0E-4m/s.

3.2.2.2 Experiment conditions and methodology

The experimental device is a thick vertical slab of sand (or sand tank) containing initially dry sand, which is suddenly connected at right to a fixed water level reservoir (3.7 cm high). This emulates the lateral imbibition process in a dry porous bank from an open water reservoir or a canal in vertical cross-section. The internal dimensions of the porous domain are: 16 cm high × 40 cm long for the vertical slice (as in the numerical model) and 20 cm thick in the third direction (orthogonal to mean flow).

The experimental results are shown (optically) as the evolution of the wetted zone seen via photographs taken at different times. The vertical profile of the wetted zone at T=14 minutes is shown in **Fig. 3-2**.

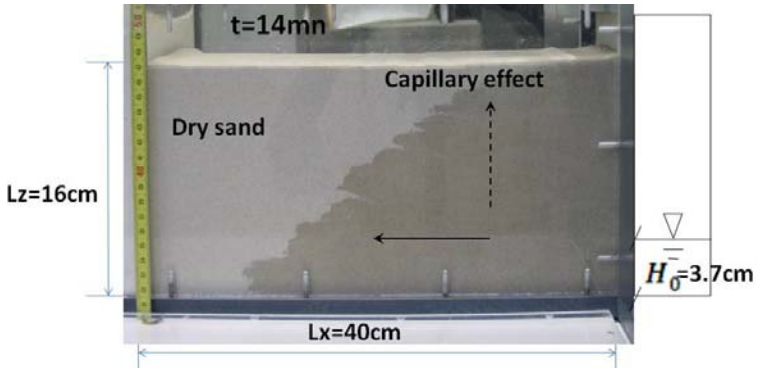

Fig. 3-2 Sand box-imbibition in a dry river bank: imbibition profile at t=14minutes

3.2.3 Analytical solution with Boussinesq plane flow (Polubarinova)

It is noted that the following section is inspired (or directly taken) from Tregarot's thesis (Tregarot 2000 [17]).

For the wetting problem, Polubarinova-Kochina proposed an analytical solution giving the position $\eta(x,t)$ of the free surface in the bank. Using her solution, with our notation, we derive the expressions of the downstream position of the wetting front on the impermeable floor, $x_F\ (t)$ and the specific flow entering the interface channel / bank $Q_S(t)$.

In view of the wetting problem, the Boussinesq equation is rewritten as follows:

$$\phi_e \frac{\partial \eta}{\partial t} = K_s \frac{\partial}{\partial X}\left(\eta \frac{\partial \eta}{\partial X}\right) \tag{3-1}$$

where, η is the water depth. Here, since the porous medium constituting the bank is initially very dry and its instantaneous imbibition, we can assume that ϕ_e, its effective porosity, is defined by $\phi_e \approx \theta_S - \theta_d$.

To find an analytical solution of this equation, Polubarinova-Kochina makes, like for the equation of heat conduction, the following variable, $\chi = \frac{X}{a\sqrt{t}}$, where a is a constant to be determined. This change of variables applied in the equation (3-1) gives us:

$$\frac{d^2\eta^2}{d\chi^2} + \frac{\phi_e a^2}{K_s}\chi\frac{d\eta}{d\chi} \tag{3-2}$$

Now let:

$$u = \eta/\eta_0,\ \chi = \frac{X\sqrt{\phi_e}}{2\sqrt{K_s\eta_0 t}} \text{ and } a = 2\sqrt{\frac{K_s\eta_0}{\phi_e}}$$

where, η_0 is the limit water depth at the entry of the bank.

Then the equation (3-2) becomes :

$$\frac{d^2u^2}{d\chi^2} + 4\chi\frac{du}{d\chi} \tag{3-3}$$

Finally, we introduce the variable $\xi = \chi\sqrt{2} = \frac{X\sqrt{\phi_e}}{\sqrt{2K_s\eta_0 t}}$ in the equation (3-3):

$$\frac{d^2u^2}{d\xi^2} + 2\xi\frac{du}{d\xi} = 0 \tag{3-4}$$

The expansion of the equation (3-4) can be written as:

$$uu'' + u'^2 + \xi u' = 0 \tag{3-5}$$

Taking $u = 0$ in equation (3-5), since $u'' \neq \infty$, we have:

$$u'(u' + \xi) = 0$$

where, if $u' \neq 0$, then $u' = -\xi$

Consider the point of intersection of the graph of u (ξ) with the x-axis. To the point where $\xi = c$, we have $u = 0$ and $u' = -\xi = -c$. A series expansion of the difference $\xi - c$ applied to the function $u(\xi)$ gives us:

$$u(\xi) = u(c) + \frac{(\xi - c)}{1!}u^{(1)}(c) + \frac{(\xi - c)^2}{2!}u^{(2)}(c) + \frac{(\xi - c)^3}{3!}u^{(3)}(c) + \frac{(\xi - c)^4}{4!}u^{(4)}(c) + \frac{(\xi - c)^5}{5!}u^{(5)}(c) + 0(\xi)^6$$

The equation (3-5) is differentiated as follows:

$$uu^{(2)} + \left(u^{(1)}\right)^2 + \xi u^{(1)} = 0$$
$$uu^{(3)} + 3u^{(1)}u^{(2)} + \xi u^{(2)} + u^{(1)} = 0$$

$$uu^{(4)} + 4u^{(1)}u^{(3)} + \xi u^{(3)} + 3\left(u^{(2)}\right)^2 + 2u^{(2)} = 0$$

$$uu^{(5)} + 5u^{(1)}u^{(4)} + \xi u^{(4)} + 10u^{(2)}u^{(3)} + 3u^{(3)} = 0$$

$$uu^{(6)} + 6u^{(1)}u^{(5)} + \xi u^{(5)} + 15u^{(2)}u^{(4)} + 4u^{(4)} + 10\left(u^{(3)}\right)^2 = 0$$

Knowing that $u(c) = 0$ and $u'(c) = -c$, we get the coefficients:

$$u^{(2)}(c) = -\frac{1}{2} \qquad u^{(3)}(c) = -\frac{1}{12c}$$

$$u^{(4)}(c) = +\frac{1}{24c^2} \qquad u^{(5)}(c) = -\frac{11}{720c^3}$$

The series expansion is then written at the fifth order:

$$u(\xi) =$$

$$-c\left(\frac{X\sqrt{\phi_e}}{\sqrt{2K_s\eta_0 t}} - c\right) - \frac{1}{4}\left(\frac{X\sqrt{\phi_e}}{\sqrt{2K_s\eta_0 t}} - c\right)^2 - \frac{1}{72c}\left(\frac{X\sqrt{\phi_e}}{\sqrt{2K_s\eta_0 t}} - c\right)^3 + \frac{1}{576c^2}\left(\frac{X\sqrt{\phi_e}}{\sqrt{2K_s\eta_0 t}} - c\right)^4 + 0(\xi)^5$$

Or :

$$u = \frac{\eta}{\eta_0} \approx -c\left(\frac{X\sqrt{\phi_e}}{\sqrt{2K_s\eta_0 t}} - c\right) - \frac{1}{4}\left(\frac{X\sqrt{\phi_e}}{\sqrt{2K_s\eta_0 t}} - c\right)^2 - \frac{1}{72c}\left(\frac{X\sqrt{\phi_e}}{\sqrt{2K_s\eta_0 t}} - c\right)^3 + \frac{1}{576c^2}\left(\frac{X\sqrt{\phi_e}}{\sqrt{2K_s\eta_0 t}} - c\right)^4 \qquad (3\text{-}6)$$

The constant c is obtained by making $\xi = 0$ in the expansion equation. For example, the 5th order is taken:

$$u(0) = 1 \approx c^2\left(1 - \frac{1}{4} + \frac{1}{72} + \frac{1}{576} + \frac{11}{86400}\right)$$

where, $c = 1.142762$

From the solution (3-6) found by Polubarinova-Kochina, we seek x_F position at the intersection of the wetting front with impermeable floor of the aquifer, for which $u = \frac{\eta}{\eta_0} = 0$:

$$X_F = c\sqrt{\frac{2K_s\eta_0}{\phi_e}}\sqrt{t} \qquad (3\text{-}7)$$

Finally, we can find the expression of the specific flow entering the interface channel / bank. Knowing that the flow is uniform across the interface (pseudo-horizontal and vertically equipotential water flow), according to Darcy's law, integrated over the interface:

$$Q_s = K_s\eta_0\left(\frac{d\eta}{dX}\right)_{X=0} = K_s\eta_0^2\left(\frac{du}{dX}\right)_{X=0}$$

$$\left(\frac{du}{dX}\right) = \frac{\sqrt{\phi_e}}{\sqrt{2K_s\eta_0 t}}\left[-c - \frac{1}{2}\left(\frac{X\sqrt{\phi_e}}{\sqrt{2K_s\eta_0 t}} - c\right) - \frac{1}{24c}\left(\frac{X\sqrt{\phi_e}}{\sqrt{2K_s\eta_0 t}} - c\right)^2 + \frac{1}{144c^2}\left(\frac{X\sqrt{\phi_e}}{\sqrt{2K_s\eta_0 t}} - c\right)^3\right]$$

$$\left(\frac{du}{dX}\right)_{X=0} = \frac{\sqrt{\phi_e}}{\sqrt{2K_s\eta_0 t}}\left[-c + \frac{1}{2}c - \frac{1}{24}c - \frac{1}{144}c\right] = \frac{-79c}{144}\frac{\sqrt{\phi_e}}{\sqrt{2K_s\eta_0}}\frac{1}{\sqrt{t}}$$

It is then obtained the specific discharge of the outflow (m^2/s):

$$Q_s = \frac{79c}{144}\eta_0\sqrt{\frac{K_s\eta_0\phi_e}{2}}\frac{1}{\sqrt{t}} \tag{3-8}$$

3.2.4 Numerical simulation and calibration of the wetting problem

3.2.4.1 Introduction

For the wetting problem in a dry sand box, the numerical simulation has the characteristics of the highly nonlinear unsaturated / partially saturated flow. The finite volume code Bigflow 3D unsaturated model is used to simulate this problem.

In the unsaturated flow simulation, the Van Genuchten/ Mualem parameter model is chosen to calculate the hydraulic conductivity $K(h)$ and the water content $\theta(h)$. In order to calibrate the experiment results, a large number of numerical simulations have been done. In this section, the best numerical simulation will be introduced in detail and its results will be compared with the experimental result. In addition, its result will be compared with the ones of the other two numerical simulations with different α *and* n, for analyzing the influence of the two parameters (α and n) on the evolution of the wetting front on the impermeable floor, $x_F\ (t)$.

3.2.4.2 Numerical simulations

- **Simulation domain**

Vertical 2D: L_x=0.40m; L_z=0.16m;

dx=0.0005m; dz=0.0005m

As a result, there are up to ¼ million nodes in a 2D vertical cross-section (40cm×16cm) as shown in **Fig. 3-2**.

- **Boundary condition**

Left boundary, top boundary and bottom boundary are the same: Flux=0.0;

Right boundary: h(L,t)=0.037-z (linear distribution head).

- **Initial condition**

$h_0 = -1.35 - z$ (linear distribution pressure head)

It means that the initial sand is very dry, and the initial water content $\theta_{In} \approx 0.00067\, m^3/m^3$

- **Physical properties**

The saturated hydraulic conductivity K_s of the sand is taken as 2.0e-4m/s, which is obtained by the experiment; the saturated water content θ_s is also taken to the measured value of 0.38 m^3/m^3. On contrast, the residual hydraulic conductivity K_r is taken as 2.0e-7m/s, and the residual water content θ_r is 0.0m^3/m^3.

For the Van Genuchten Mualem parameter model, α is taken as $4.6m^{-1}$ (the capillary length is about 21.74cm) and n is taken as 5 (power of the parameter function); the water content function curve $\theta(h)$, the hydraulic conductivity function curve $K(h)$, the capillary diffusion function curve $D(h)$ and the capillary capacity function curve $C(h)$ are respectively shown in **Fig. 3-3**, **Fig. 3-4**, **Fig. 3-5** and **Fig. 3-6**.

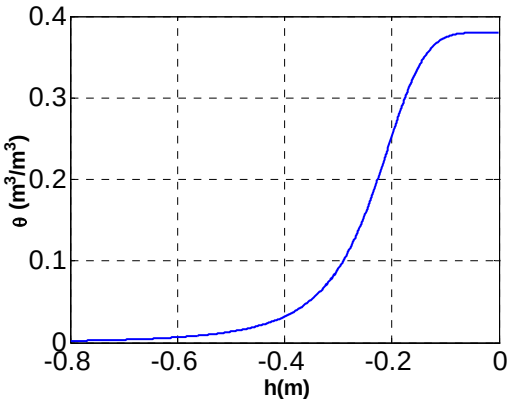

Fig. 3-3 Water content curve $\theta(h)$ of the sand with $\alpha = 4.6m^{-1}$ and n=5.

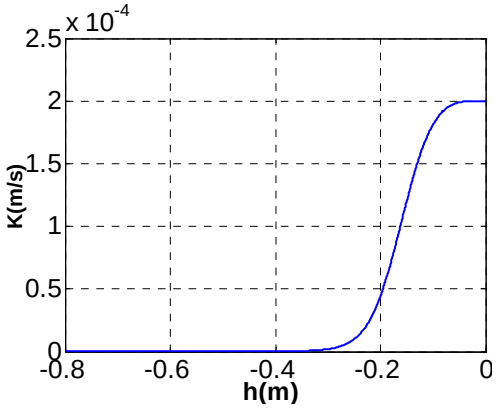

Fig. 3-4 Hydraulic conductivity curve K(h) of the sand with $\alpha = 4.6m^{-1}$ and n=5.

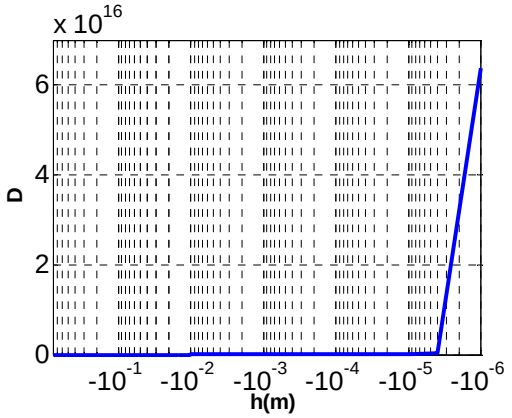

Fig. 3-5 Capillary diffusion $D(h)$ of the sand with $\alpha = 4.6m^{-1}$ and n=5.

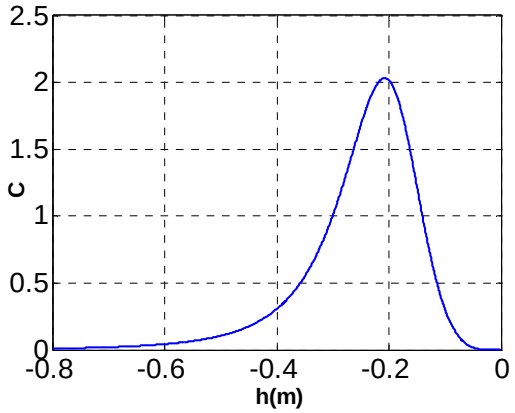

Fig. 3-6 Capillary capacity $C(h)$ of the sand with $\alpha = 4.6m^{-1}$ and n=5.

▪ **Duration of the simulation and numerical parameters**

The numerical simulation models the imbibition process of 30 minutes .

The numerical calculation time parameters and the numerical criteria are listed in **Table 3-1**.

Table 3-1 Numerical parameters (INPUT1) for the calculation of time step, non-linear/outer (Picard) and linear/inner iterations

Time step	Intial time step	DTIN=0.02s
	Minimum time step	DTMIN=0.02s
	Maximum time step	DTMAX=1.0
	Time step multifier	DTMUL=1.2
No-linear iterations (Picard)	Convergence criterion of pressure head	ENLH3=1.0E-4
	Maximum number of no-linear iteration	INLMAX=2
Linear iterations	Convergence criterion	ENORM3=1.0E-6
	Maximum number of linear iterations	ITEND=50
Method to caculate the middle nodal conductivities		Arithmetic mean

▪ **Numerical behaviour of Bigflow during the simulation**

Although there are bigger beginning values about 1.0, the linear and nolinear errors decrease with respect to the iteration number and at last each of two satisfies the convergence criteria , as shown in **Fig. 3-7** and **Fig. 3-8**.

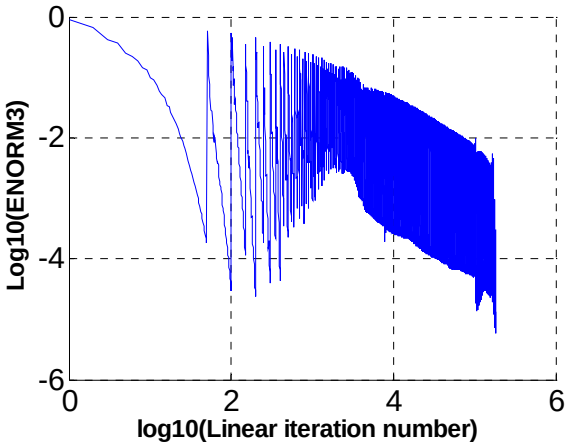

Fig. 3-7 Standarlized linear iteration process curve of the pressure head in log10

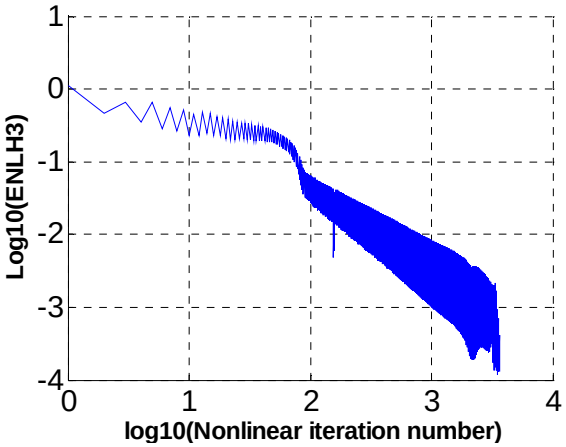

Fig. 3-8 Standarlized nonlinear iteration process curve of the pressure head in log10

Fig. 3-9 shows that the curve of the evolution of Q_{Bound} almost superposes on the curve of the evolution of Q_{Mass}, except that there is a small difference at the beginning and the end of the simulation. The similar situation occurs to V_{Bound} and V_{Mass}, as shown in **Fig. 3-10** .

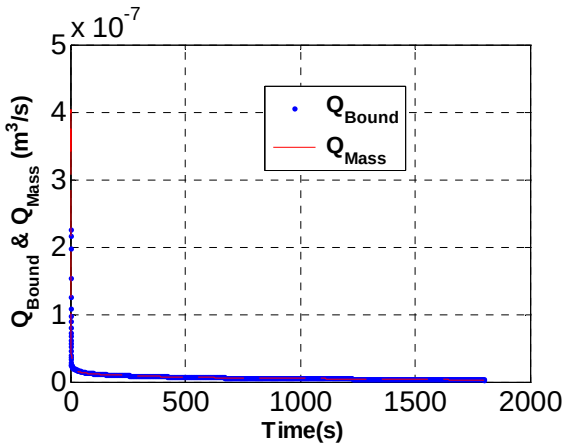

Fig. 3-9 Evolution of Q_{Bound} and Q_{Mass} (local mass balance)

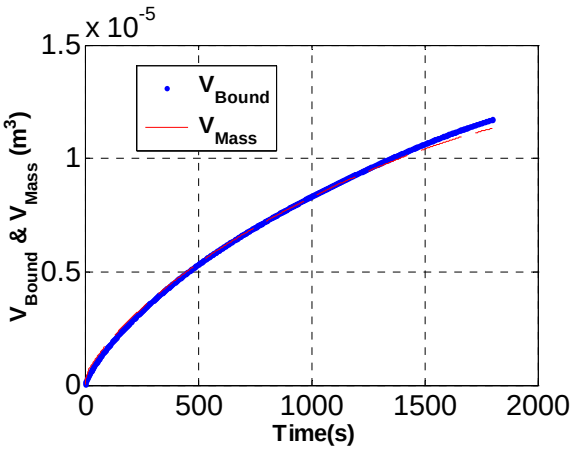

Fig. 3-10 Evolution of V_{Bound} and V_{Mass} (global volume balance)

3.2.4.3 Comparisons of the numerical and experimental results

In order to compare the two results, the numerically computed pressure head isovalues are superimposed on the photos of the imbibitions profile of the experiment. Furthermore the numerical flux field is also plotted on the photos of the experiment to understand the imbibitions procedure. Comparison results indicate that, in spite of a small difference at the beginning (t<6minutes), the numerical imbibitions procedures agree very well with the experimental one. The difference at the beginning may be caused by the experiment operation.

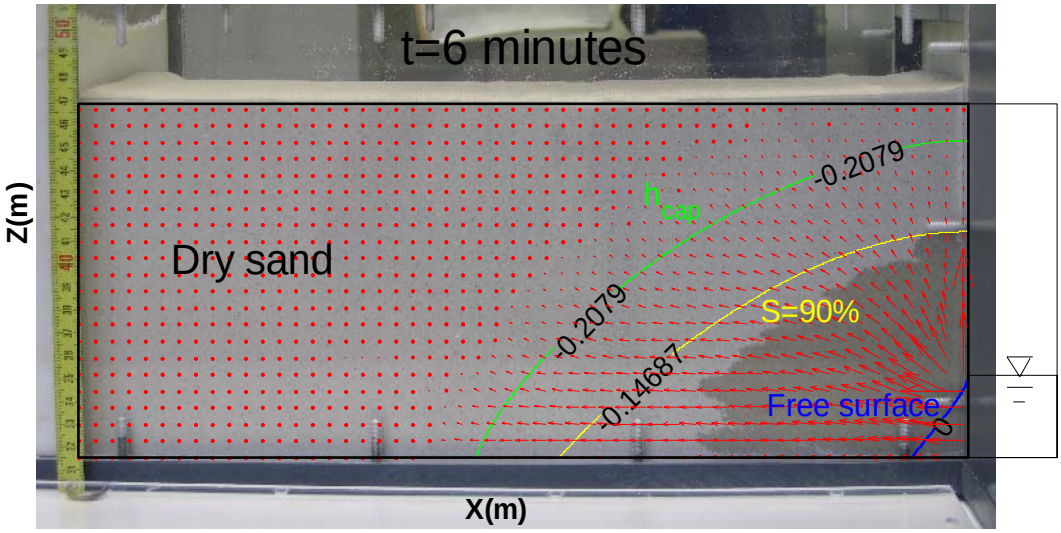

Fig. 3-11 The flux field at t=6 minutes. The green curve (h=-0.20m) corresponds to S=0.62, and it also corresponds to the isovalue $h = h_{cap} = -\alpha^{-1} m^{1/n}$ (chapter.4, R. Ababou, 1991 [10]).

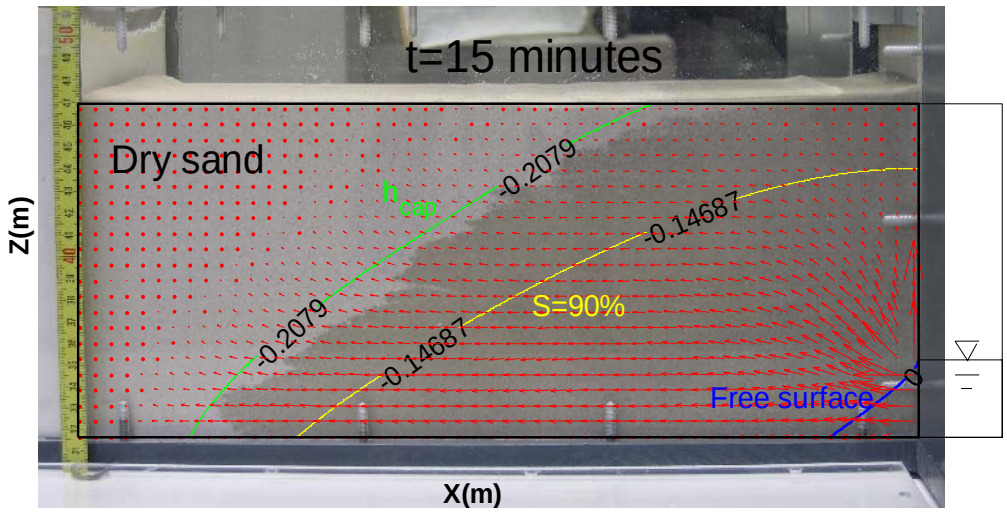

Fig. 3-12 The flux field at t=15 minutes. The green curve (h=-0.20m) corresponds to S=0.62, and it also corresponds to the isovalue $h = h_{cap} = -\alpha^{-1}m^{1/n}$ (chapter.4, R. Aababou, 1991 [10]).

The two instantaneous profiles of the comparisons at t=6minutes and t=15minutes are respectively shown in **Fig. 3-11** and **Fig. 3-12**. In the figures, the green curve (h=-0.20m) corresponds to S=0.62 (degree of saturation), and it also corresponds to the isovalue $h = h_{cap} = -\alpha^{-1}m^{1/n}$ (chapter.4, R. Ababou, 1991); the yellow curve (h=-0.15m) corresponds to S=0.90 and blue curve is the free surface. In addition, it is noted that the initial pressure condition at the bottom H_{In}=-1.35m (the initial saturation is: θ_{In}=0.00067) for the numerical simulation.

3.2.4.4 Sensitivity analysis of "α" and "n" on the numerical results

For the numerical simulation of the unsaturated flow with VGM model, the parameter α is interpreted as the inverse of the capillary length of the sand and the 'n' parameter is a dimensionless exponent, which is related to the pore size distribution (Tregarot's thesis [17], Chapter 2, page 110) or shape factors (Ababou, 1991 [10], Chapter4, page 24). More exactly, during the numerical simulations of the wetting experiment, n plays the dominant role on the slope of the pressure head contours in the vertical profile of the imbibitions. Therefore, it is necessary to do the sensitivity analysis of $\boldsymbol{\alpha}$ and n on the numerical results.

In order to do the sensitivity analysis, the other two numerical simulations (Num.2 and Num.3) are added to be done. In the Num.2, α has been kept same as the best simulation (Num.1 and α =4.6m^{-1}), n has been increased to 6 to study the role of n. On contrast, in the Num.3, n has been kept equal to 5 (same with Num.1), and α has been increased to 6.6 m^{-1} to investigate the influence of α.

The comparison results of the evolution of the toe of saturation front X_F with respect to $\sqrt{t}$ are shown in **Fig. 3-13**. From the figure, it can be seen that, in contrast with n, α has bigger influence on the evolution of the saturation front toe in the sandbox bottom, the bigger α is, the faster the saturation front toe moves in the x direction. However, according to the numerical results, there is the inverse situation which occurs to the saturation front toe in the y direction. This implies that the sand is not totally homogeneous and the hydraulic conductivity in the x direction is a little bigger than the one in the y direction.

Fig. 3-14 indicates that, in spite of the difference at the beginning, n has smaller influence on the evolution of inflow discharge at the interface of bank-river; on contrast, when $t > 2.7s$, due to the increased α, the difference of the inflow discharge between Num.1 and Num.3 become bigger and bigger, and then keeps constant for a longer time. It is also noticed that the maximum differences appearing at the beginning and in the last part of the simulation are in the same order. Furthermore, from **Fig. 3-14**, it can also be seen that the natural logarithm of the inflow discharge has almost linear relationship with the natural logarithm of the time.

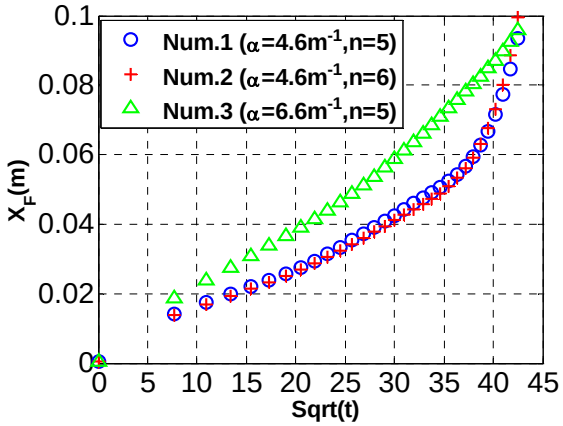

Fig. 3-13 Sensitivity analysis: evolution of the saturation front toe $X_F(\sqrt{t})$ for the 3 group of parameters:
Num.1: $\alpha = 4.6m^{(-1)}, n = 5$
Num.2: $\alpha = 4.6m^{(-1)}, n = 6$
Num.3: $\alpha = 6.6m^{(-1)}, n = 5$.

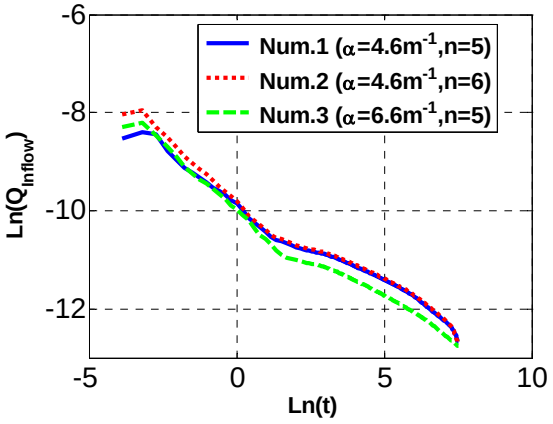

Fig. 3-14 Sensitivity analysis: inflow discharge at bank-river interface with respect to the time $Q_{\inf low}(t)$ in log-log for the 3 group of parameters:
Num.1: $\alpha = 4.6m^{(-1)}, n = 5$
Num.2: $\alpha = 4.6m^{(-1)}, n = 6$
Num.3: $\alpha = 6.6m^{(-1)}, n = 5$.

In addition, considering that the initial condition (pressure head or degree of saturation) has very important role for succeeding in modeling the wetting problem, the sensitivity analysis has been done to investigate the influence of the initial pressure head at the sandbox bottom on the toe of the saturation front in the x direction and the inflow discharge. The results

indicate that when $h_{in} < -1.0m$(the initial sand is very dry) , the initial head has no influence on the toe of the saturation front in the x direction, and it just has very little influence on the inflow discharge at the very beginning of the imbibitions ($t < 0.36s$)

3.2.4.5 Comparisons of the numerical results and the analytical solution of Polubarinova

Since the analytical solution of Polubarinova with Boussesq saturated plane flow equation has not considered the capillary effect of the sand, it doesn't suit really the wetting problem with very fine sand (with about 20cm capillary length). **Fig. 3-15 (a)** and **(b)** shows that, for the saturation front toe X_F at the sandbox bottom (x direction), the analytical solution has a linear relationship with the square root of the time; on contrast, the numerical one behaves differently with the time; the two types of results have bigger and bigger difference with the time increasing . At the same time, from **Fig. 3-16**, it can be seen although the analytical and numerical inflow discharges both are power functions of the time and both have the same power, however, there is a big difference between the analytical and the numerical value.

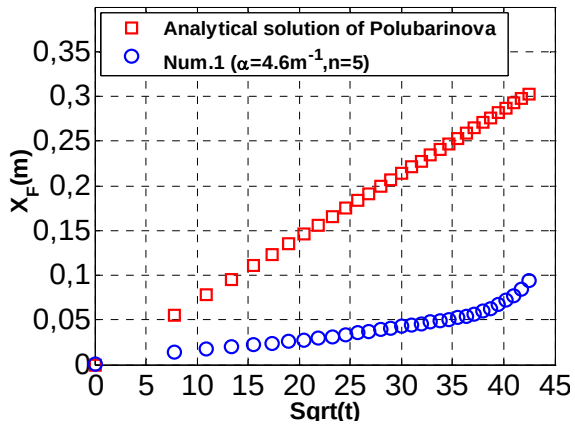

(a) : $X_F\left(\sqrt{t}\right)$

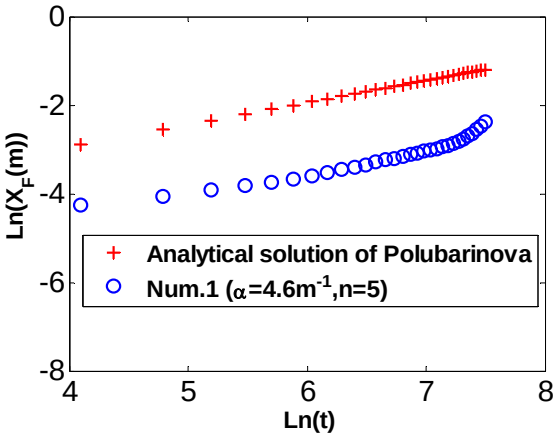

(b) : $Ln(X_F)(\ln(t))$

Fig. 3-15 (a) (b) Evolution of the saturation front toe. Comparison between the analytical solution of Polubarinova (without any capillary effect) and the numerical Richards model (Num.1) which includes capillary effects in the unsaturated zone.

Note: Parameters of simulation "Num.1":

$\alpha = 4.6m^{-1}, n = 5$ (Num.1, Bigflow);

$h_{in} = -1.35m$ (Num.1, Bigflow);

$\theta_s = 0.38\text{m}^3/\text{m}^3$, $\theta_r = 0.0$;

$K_s = 2.0E-4\text{m/s}$, $K_r = 2.0E-7\text{m/s}$.

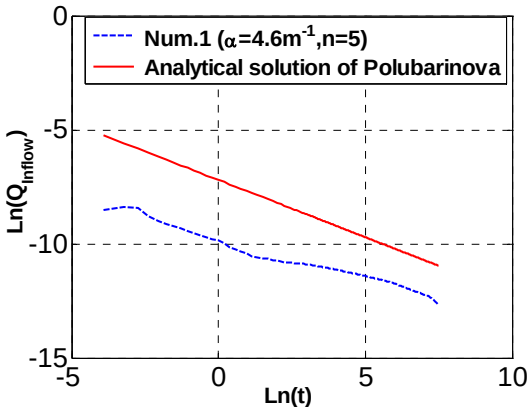

Fig. 3-16 Inflow discharge at bank-river interface with respect to the time $Q_{\inf low}(t)$ in log-log. Comparison between the analytical solution of Polubarinova without any capillary effect and the numerical Richards model (Num.1).

Considering that the sand for the wetting experiment has large capillary effect (small α), decreasing the capillary effect by increasing α to 100 m^{-1} (capillary length is equal to 1 cm), the other parameters remaining unchanged (same as in "Num.1"). Simulation "Num.4" has been conducted to watch the evolution of the saturation front toes and the inflow discharge obtained with Richards model and with the analytical solution of Polubarinova.

Fig. 3-17 shows that the relationship curve of the computed $X_F(\sqrt{t})$ becomes linear and it is very approximate to the analytical one. However, due to the small saturated hydraulic conductivity $K_S = 2.0E-4\,\text{m/s}$ for the case with a very small capillary effect (capillary length is equal to 1cm), the difference of the inflow discharge has not diminished, as shown in **Fig. 3-18**.

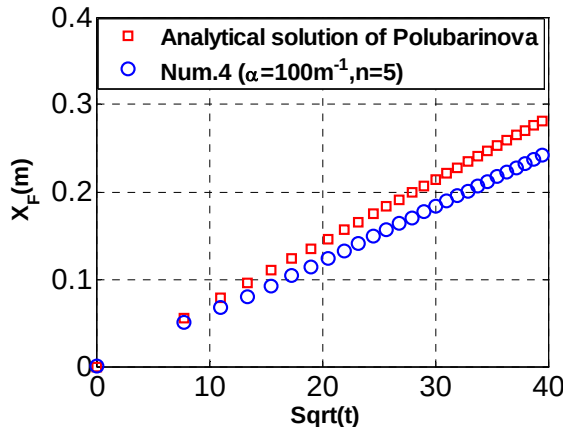

Fig. 3-17 Evolution of the saturation front toe $X_F(\sqrt{t})$: simulation "Num.4". Comparison between the analytical solution of Polubarinova without any capillary effects and the numerical Richards model (Num.4).

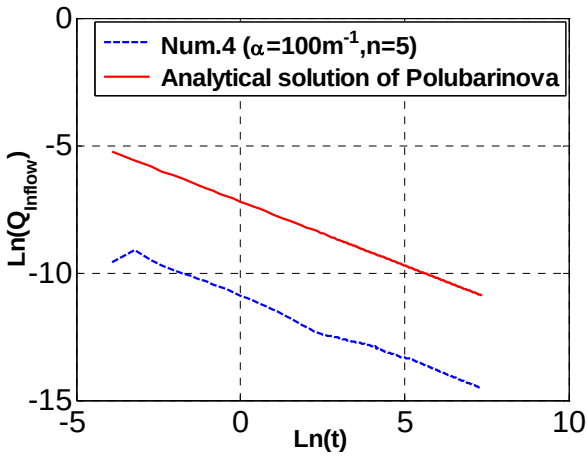

Fig. 3-18 Inflow discharge $Q_{\inf low}(t)$ at the bank-river interface in log-log (simulation "Num.4"). Comparison between Polubarinova's solution and the numerical Richards model (Num.4).

Note: Parameters of simulation "Num.4":
$\alpha = 100\ m^{-1}, n = 5;$
$h_{in} = -1.35m;$
$\theta_s = 0.38\text{m}^3/\text{m}^3$, $\theta_r = 0.0;$
$K_s = 2.0E-4\text{m/s}$, $K_r = 2.0E-7\text{m/s}.$

3.2.5 Conclusion on the wetting problem

At first, the wetting process of a dry porous medium with a right boundary condition of a sudden increasing water level which then keeps constant has been studied by a laboratory experiment. The experimental results are shown (optically) as the evolution of the wetted zone seen via photographs taken at different times.

Secondly, 3D Richards model with the Van Genuchten/ Mualem parameter for the hydraulic conductivity $K(h)$ and the water content $\theta(h)$ is chosen to simulate wetting experiment. A good calibration result (α=4.6m^{-1}, n=5) has been obtained through the fine grids (up to ¼ million nodes in a 2D vertical cross-section), manually repeating the simulation tests with different unsaturated parameters, and comparing the simulation results of the unsaturated curves with the measured humility of the sand in the optical photos. Furthermore, sensitivity analysis result indicates that in contrast with n, α has bigger influence on the evolution of the saturation front toe $x_F\ (t)$ in the sandbox bottom, the bigger α is, the faster the saturation front toe moves in the x direction. However, according to the numerical results, the inverse situation occurs to the saturation front toe in the y direction. This implies that the sand is not totally homogeneous and the hydraulic conductivity in the x direction is a little bigger than the one in the y direction.

Finally**,** the comparison between the numerical and the analytical results of the wetting problem furthermore demonstrates that the analytical resolution of Polubarinova with Boussinesq saturated plane flow equation doesn't suit the wetting problem with very fine sand (with about 20cm capillary length). However, if the capillary effect is diminished, for example, α is increased, the agreement of the results between the numerical simulation and the analytical solution is improved, which means that it can be found a type of course sand to suit the analytical solution of Polubarinova.

3.3 Groundwater discharge problem

3.3.1 Introduction

The linearized solution developed by Prof. Ababou (Ababou, 2007 [20]) for the discharge problem in the river bank after the infiltration of rain until a steady state will be used to

validate the VGM parametric model and the exponential parametric model of the 3D partially saturated Richard model of Bigflow and further to investigate the influence of the two parametric models on the capillary effect and the free surface of the river bank aquifer during the discharge process.

An example of the discharge problem of the river bank will be solved with analytical solution and the numerical simulations with Boussinesq plane flow model and two partial saturated Richards models. As a result, 5 numerical simulations will be conducted to investigate the discharge problem of the river bank: one with Boussinesq model (Num.1), two with VGM model (Num.2 and Num.3) and the other two with exponential model (Num.4 and Num.5). Furthermore, the two with VGM model have different a values (different capillary length) and have the same n value (same distribution of the characteristic curves such as the degree of saturation of the water content $S(h)$); the other two with exponential model have different a values and β=a/3, which means that the two diffusion functions $D(\theta)$ both are the square curve with respect to the water content θ (equation (1-23)). In addition, the same a values have been taken for the two with different parameter model, namely, Num.2 with VGM model has the same smaller a (bigger capillary length) as Num.4; Num.5 with VGM model has the same bigger a (smaller capillary length) as Num.5.

3.3.2 Analytical solutions of Boussinesq equation

3.3.2.1 Problem

Consider an aquifer with free surface water feeding a river. After recharging the aquifer until a steady state by direct infiltration of rain, the flows into the soil surface is equal to the flows out of the bank-water interface, and as a result, the surface feeding of the soil is removed. Begins at t = 0, for the discharge of the aquifer, we will attempt to find an analytical expression giving the position of any point on the free surface in the aquifer with respect to time: $H(x,t)$. In addition, an evolution law of the flow $Q(t)$ into the river from the aquifer will also be sought (depletion law). The schema of the discharge problem is illustrated in **Fig. 3-19**.

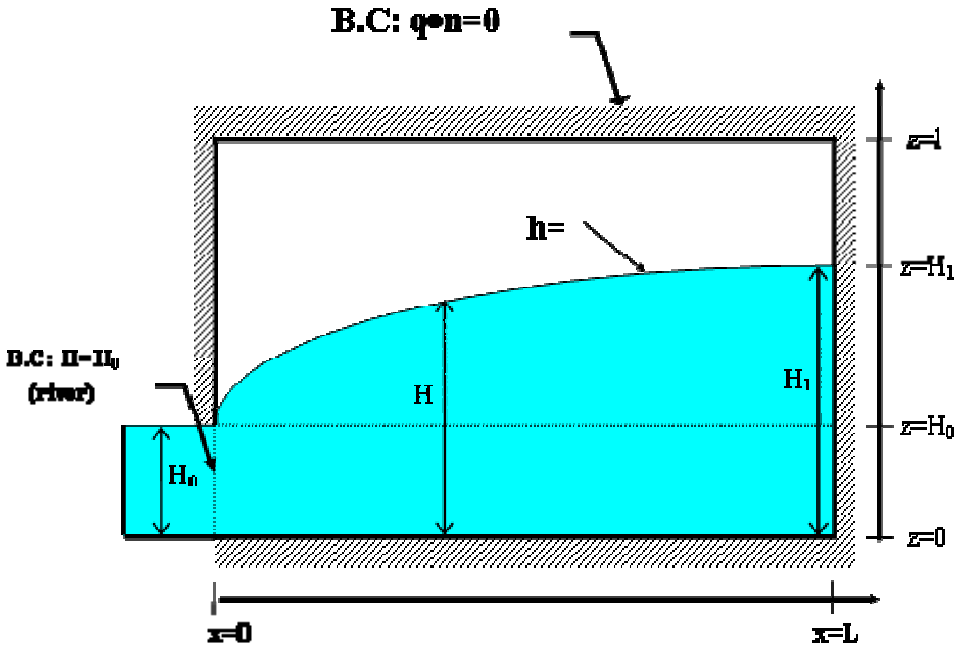

Fig. 3-19 The schema of the discharge problem

3.3.2.2 Assumptions

- The flow occurring in the saturated zone are almost horizontal and verify the Boussinesq equations;
- The emptying of the water in the rivers is instantaneous and the flow in the unsaturated zone is neglected;
- The medium is incompressible;
- The initial profile of the aquifer is approximated by:

$$H(x,0) = H_0 + (H_1 - H_0)\sin\left(\frac{\pi x}{2L}\right)$$

3.3.2.3 Boussinesq equation applied to the saturated zone

The equation of mass conservation and Darcy's equation are integrated over the height of the water assuming quasi-horizontal flow (Dupuit assumptions), where the equations of 2D (x, y):

$$S\frac{\partial H}{\partial t} = -div[q] \text{ and then } q = -KHgrad(H)$$

where,

- H is the hydraulic head averaged over the height of the saturated zone based on a horizontal basis. In fact, considering the pseudo-horizontal flow in the groundwater, the head H = h + z is constant on any section perpendicular to the plane (x, z) and it is equal to the height of the water.
- S is a dimensionless storage coefficient defined by $S = \phi + S_S$ where is the effective

porosity of the porous medium (m^3/m^3), and S_S is the specific storativity reflecting the compressibility effects. For a free surface, we can neglect the compressibility to the storage capacity of the pores (take $S = \phi$).

- K is the hydraulic conductivity of the medium at saturation (m/s).
- KH is hydraulic transmissivity T (m^2/s) for a horizontal aquifer.
- q is specific discharge, or flow per unit length transverse to the flow (m^2/s). Combining the two previous equations, and given the above remarks, we have:

$$\phi \frac{\partial H}{\partial t} = \left[\frac{\partial}{\partial x}\left(T \frac{\partial H}{\partial x}\right) + \frac{\partial}{\partial y}\left(T \frac{\partial H}{\partial y}\right)\right]$$

Finally, by plane symmetry in the y direction, assuming a straight section of river-basin in the y direction, we get:

$$\phi \frac{\partial H}{\partial t} = \frac{\partial}{\partial x}\left(T \frac{\partial H}{\partial x}\right) \tag{3-9}$$

This equation is nonlinear because of the term $T = KH$. To solve it, we make the approximation $T^* = T \approx KH^*$ to make equation (3-9) linearized, where H^* is a fixed height of the water to be determined. We then obtain the linearized equation:

$$\phi \frac{\partial H}{\partial t} = T * \frac{\partial^2 H}{\partial x^2} \tag{3-10}$$

With initial and boundary conditions:

I-C : t = 0 : $H(x,0) = H_0 + (H_1 - H_0) sin\left(\frac{\pi x}{2L}\right)$

B-C : x = 0 : $H(0,t) = H_0$ B-C: x = L : $\left(\frac{\partial H}{\partial x}\right)_{x=L} = 0$

We solve this problem with the method of separation of variables applied to the transformed variable:

$$h(x,t) = H(x,t) - H_0$$

Let:

$$h(x,t) = X(x)T(t)$$

Finally, it is obtained that:

$$H(x,t) = H_0 + (H_1 - H_0) sin\left(\frac{\pi x}{2L}\right) exp\left(-\frac{\pi^2}{4L^2}\frac{T^*}{\phi} t\right) \tag{3-11}$$

We deduce the specific discharge (in m^2/s) exiting at the interface bank-river and obtain:

$$Q(0,t) = -K \cdot H(0,t) \cdot \left(\frac{\partial H}{\partial x}\right)_{x=0}$$

Or:

$$Q(0,t) = -KH_0 \frac{\pi}{2L}(H_1 - H_0) exp\left(-\frac{\pi^2}{4L^2}\frac{T^*}{\Phi}t\right) \quad (3\text{-}12)$$

The equations (3-11) can be written as:

$$Q(0,t) = -Q_0 exp\left(-\frac{t}{\tau}\right), \text{ with } \tau = \frac{4L^2}{\pi^2}\frac{\Phi}{KH^*} \text{ and } Q_0 = KH_0\frac{\pi}{2L}(H_1 - H_0)$$

and we see that the discharge is dwindling exponentially with a characteristic time τ given above. It only remains to give an appropriate value for H^* to justify the linearization of equation (3-8). We see that this hypothesis is valid only if the ratio $(H_1 - H_0) \,/\, H_0$ is much less than 1, in which case we may take for example: $H^* \approx (H_0 + H_1)/2$.

3.3.2.4 Analytical solution of the linearized Boussinesq equation (discharge)

- **Calculation domain**

L=100m, dx=1.0.

- **Boundary condition**

x=0 (left): $H(0,t) = H_0$; x=L (right) **:** $\left(\frac{\partial H}{\partial x}\right)_{x=L} = 0$

- **Initial condition**

t=0: $H(x,0) = H_0 + (H_1 - H_0) sin\left(\frac{\pi x}{2L}\right)$

with H_0=10.0m, H_1=10.8m, $H^* = (H_0 + H_1)/2.0$.

The profile of the initial surface in the river bank is shown in **Fig. 3-20**.

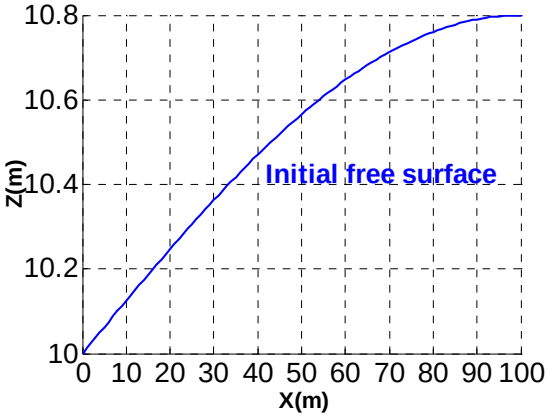

Fig. 3-20 Profile of the initial surface in the river bank

- **Physical properties of the soil of the river bank**

θ_s=0.2m^3/m^3, K_s=1.0E-3m/s

- **Analytical results of the free surface in the aquifer**

Free surface: $H(x,t) = H_0 + (H_1 - H_0)sin\left(\frac{\pi x}{2L}\right)exp\left(-\frac{\pi^2}{4L^2}\frac{T^*}{\phi}t\right)$

The discharge process of the free surface in the river bank is illustrated in **Fig. 3-21**.

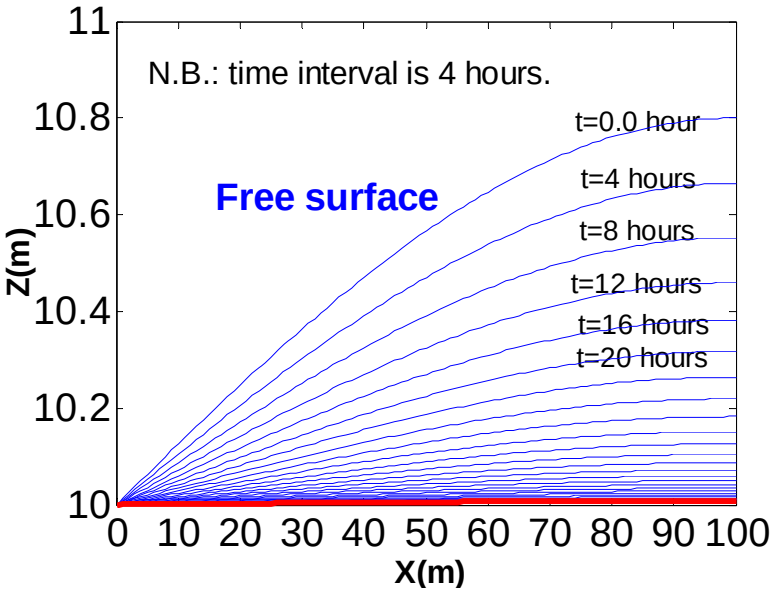

Fig. 3-21 The discharge process of the free surface in the river bank (aquifer)

From this figure, it can be seen that it needs about100 hours for the water in the saturated aquifer to totally discharge into the river for this example.

3.3.3 Numerical simulations (Boussinesq and Richards)

3.3.3.1 2D Dupuit-Boussinesq's equation model (vertically integrated)

- **Simulation domain**

L=100m, dx=1.0.

The computed domain and time parameters are same with the analytical example above.

- **Boundary condition**

Left boundary: $H(0,t)$=10m (uniform water head=constant)

Right boundary: flux=0

- **Initial condition**

Free surface: $H(x,0) = H_0 + (H_1 - H_0)sin\left(\frac{\pi x}{2*100}\right)$ with H_0=10.0m and H_1=10.8m.

- **Hydrodynamic propperties of the aquifer**

θ_s=0.2m^3/m^3, K_s=1.0E-3m/s

- **Duration of the simulation and numerical parameters**

The numerical simulation models a discharge process of 100hours as the analytical example.

The numerical caculation time parameters and the numerical criteria are listed in **Table 3-2**.

Table 3-2 Numerical parameters (INPUT1) for the calculation of time step, non-linear/outer (Picard) and linear/inner iterations

Time step	Intial time step	DTIN=0.1s
	Minimum time step	DTMIN=0.1s
	Maximum time step	DTMAX=100.0
	Time step multifier	DTMUL=1.05
No-linear iterations (Picard)	Convergence criterion of pressure head	ENLH3=1.0E-4
	Maximum number of no-linear iteration	INLMAX=10
Linear iterations	Convergence criterion of pressure head	ENORM3=1.0E-6
	Maximum number of linear iterations	ITEND=800
Method to caculate the middle nodal conductivities		Geometric mean

- **Numerical behaviour of Bigflow during the simulation**

Although the maximmum errors of the presure head are about 0.001 for the linear or nonlinear iterations, finally each of the both satisfies the convergence criteria , as shown in **Fig. 3-22** and **Fig. 3-23**.

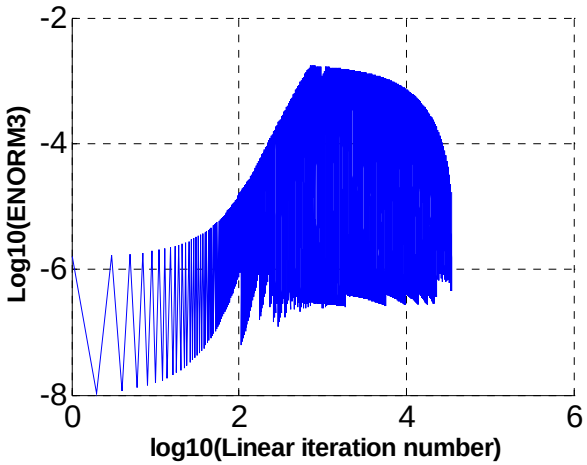

Fig. 3-22 Standarlized linear iteration process curve of the pressure head in log10

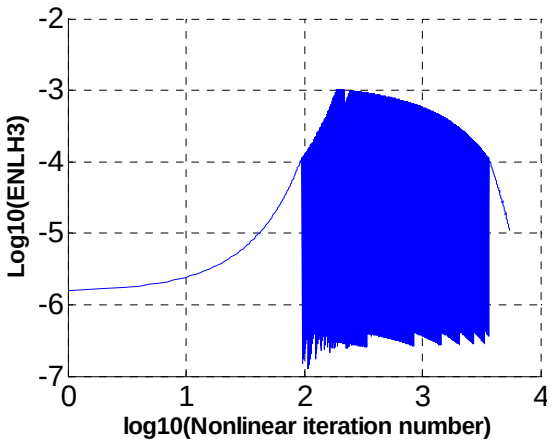

Fig. 3-23 Standarlized nonlinear iteration process curve of the pressure head in log10

Fig. 3-24 shows that the curve of the evolution of Q_{Bound} completely superposes on the curve of the evolution of Q_{Mass}. The similar situation occurs to V_{Bound} and V_{Mass}, as shown in the **Fig. 3-25**.

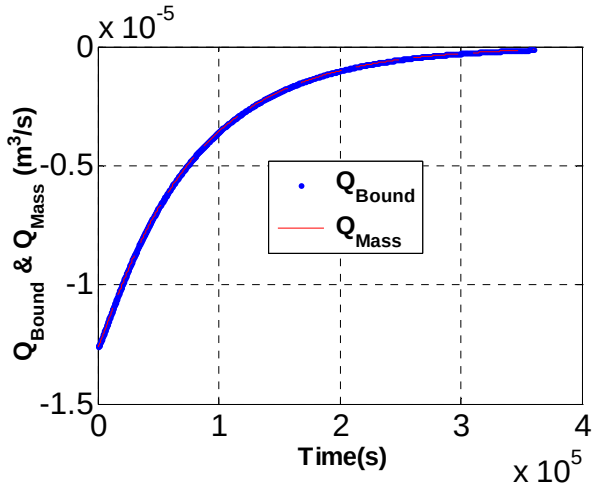

Fig. 3-24 Evolution of Q_{Bound} and Q_{Mass} (local mass balance)

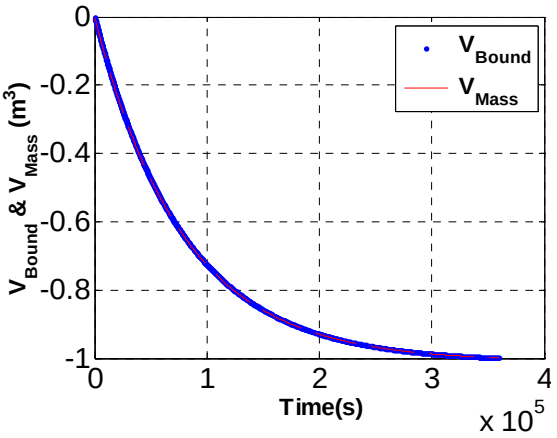

Fig. 3-25 Evolution of V_{Bound} and V_{Mass} (global volume balance)

- **Analysis of the numerical results (comparison with the analytical result)**

The instantaneous profiles of the free surface during the discharge in the river bank at t=3 hours (**Fig. 3-26**) and t=10hours (**Fig. 3-27**) have been plotted to be compared to the corresponding analytical results (linearized Boussinesq equation:(3-11)).

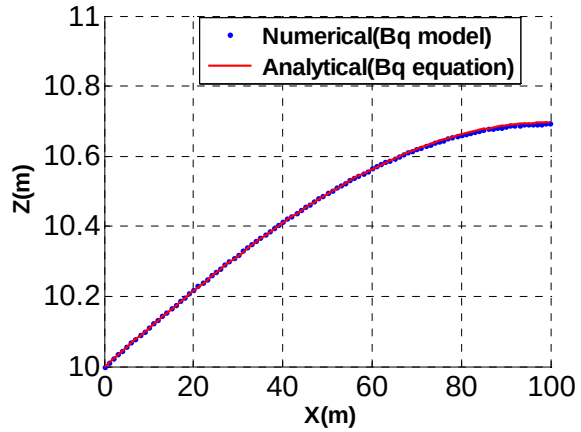

Fig. 3-26 Comparison: instantaneous profile of the free surface in the river bank ($h(x,z,t_0)=0.0$) at t=3 hours

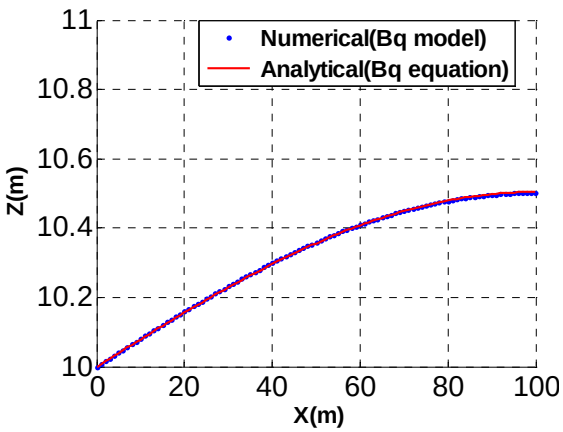

Fig. 3-27 Comparison: instantaneous profile of the free surface in the river bank ($h(x,z,t_0)=0.0$) at t=10 hours

From these two figures, it can be seen that the free surfaces computed numerically with Boussinesq model agree very well with the linearized analytical solution of the Boussinesq equation.

In addition, the computed outflow discharge $Q(0,t)$ at the bank/ river interface has also been compared (**Fig. 3-28**). It can be seen that the outflow rate decreases exponentially with the numerical solution as in the analytical solution. There is only a small difference of about 0.6E-5m^3/s between the two results at the beginning of the discharge.

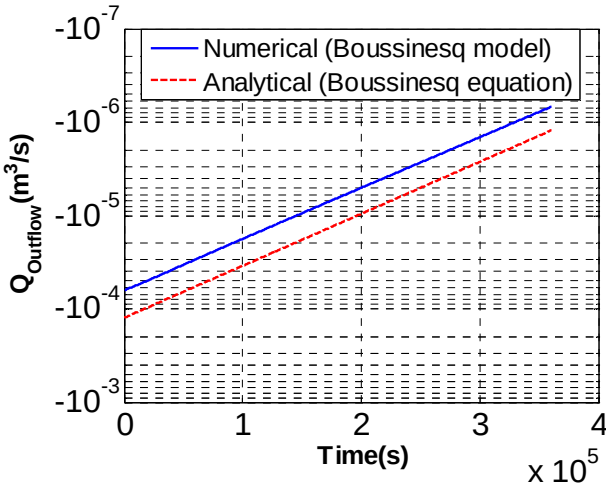

Fig. 3-28 Evolution of the outflow discharge $Q(0,t)$ at the left boundary (river/bank inter face) in semi-log scale, and comparison with the linearized analytical solution.

3.3.3.2 Richards' equation model for the discharge problem (VGM model)

- **Simulation domain**

Vertical 2D: L_x=100m, L_z=11m;

dx=1.0m, dz=0.02m

- **Boundary condition**

The boundary conditions are imposed as the same shown in **Fig. 3-19**:

On the right boundary, top boundary and bottom boundary: Flux=0.0;

On the left boundary: $h(0,t) = H_0 - z$ (linear distribution head), if $z \le H_0 = 10m$;

flux=0.0, if $0 \le z \le L_z = 11m$

- **Initial condition**

Initial water level:

$H(x,z,0) = H_0 + (H_1 - H_0)sin\left(\frac{\pi x}{2*100}\right)$ with H_0=10.0m and H_1=10.8m.

Initial pressure head:

$h(x,z,0) = H(x,z,0) - z$ (linear distribution pressure head)

- **Physical properties**

θ_s=0.2m^3/m^3, K_s=1.0E-3m/s; θ_r=0.0m^3/m^3, K_r=1.0E-7m/s

Two numerical simulations with Van Genuchten Mualem parameter model have been done: (1) α=6m^{-1}, n=3; (2) α=20m^{-1}, n=3. The water content function curve $\theta(h)$, the hydraulic conductivity function curve $K(h)$, the capillary diffusion function curve $D(h)$ and the capillary capacity function curve $C(h)$ are respectively shown in **Fig. 3-29**, **Fig. 3-30**, **Fig. 3-31** and **Fig. 3-32**.

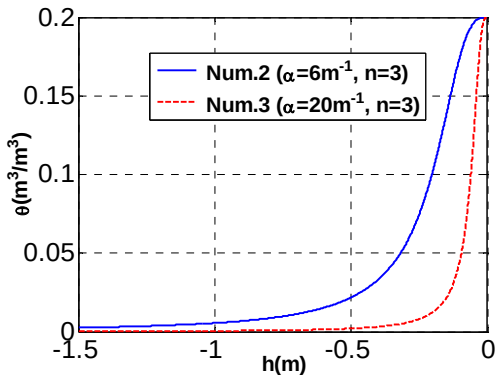

Fig. 3-29 Water content curve $\theta(h)$ of the river bank soil.

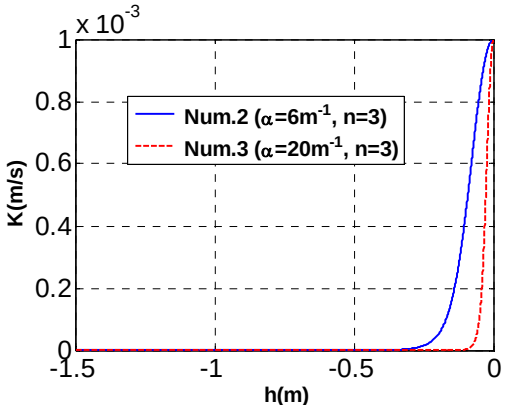

Fig. 3-30 Hydraulic conductivity curve $K(h)$ of the river bank soil.

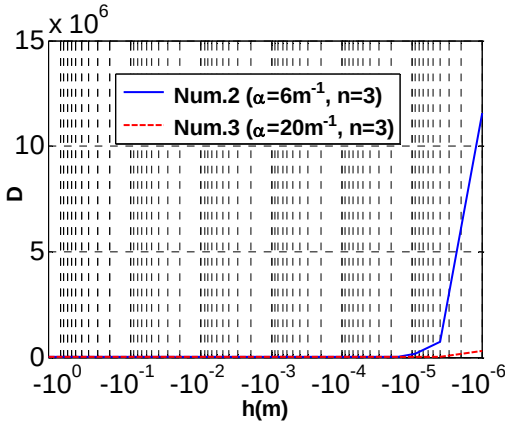

Fig. 3-31 Capillary diffusion $D(h)$ of the river bank soil.

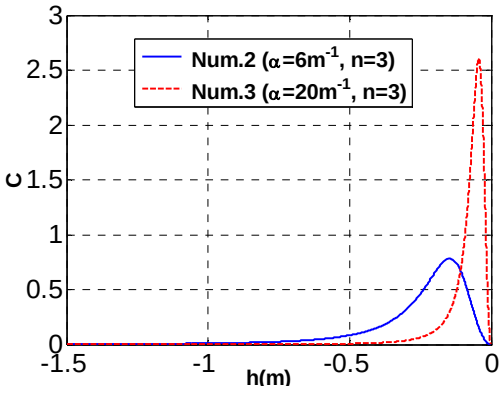

Fig. 3-32 Capillary capacity $C(h)$ of the river bank soil.

- **Duration of the simulation and numerical parameters**

The numerical simulations models a discharge process of 100 hours as the analytical example and the numerical simulation with Boussinesq model.

The numerical caculation time parameters and the numerical criteria are also same as the numerical simulation with Boussinesq model, as shown above in **Table 3-2**.

- **Numerical behaviour of Bigflow during the simulation**

Same as the simulation with Boussinesq model, the maximmum errors of the presure head of the linear or nonlinear literation both satisfy the convergence criteria , as shown in **Fig. 3-33** and **Fig. 3-34**.

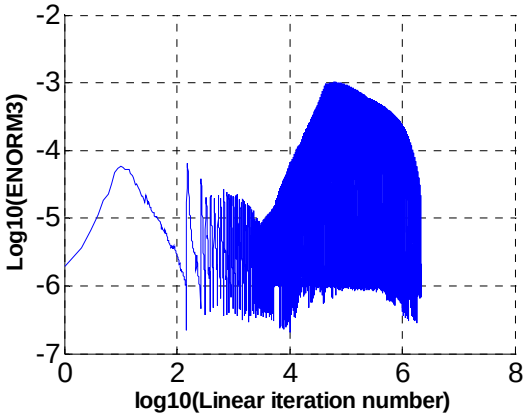

Fig. 3-33 Standarlized linear iteration process curve of the pressure head in log10 for the case: α=20 $m^{(-1)}$, n=3 (VGM)

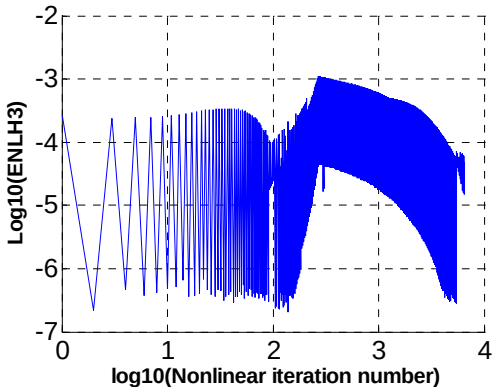

Fig. 3-34 Standarlized nonlinear iteration process curve of the pressure head in log10 for the case: α=20 $m^{(-1)}$, n=3 (VGM)

Fig. 3-35 shows that the curve of the evolution of Q_{Bound} almost superposes on the curve of the evolution of Q_{Mass}, except that there is small difference at the beginning. At the same time, the curve V_{Bound} coincides very well with the curve V_{Mass}, as shown in **Fig. 3-36**.

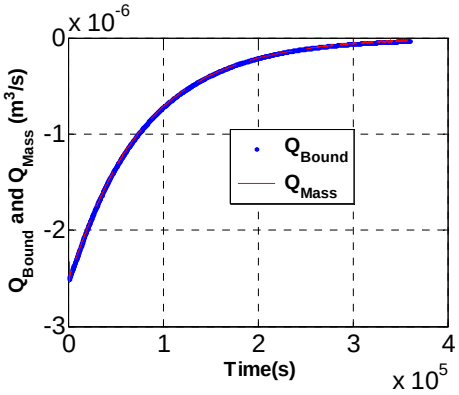

Fig. 3-35 Evolution of Q_{Bound} and Q_{Mass} (local mass balance) for the case: α=20 $m^{(-1)}$, n=3 (VGM)

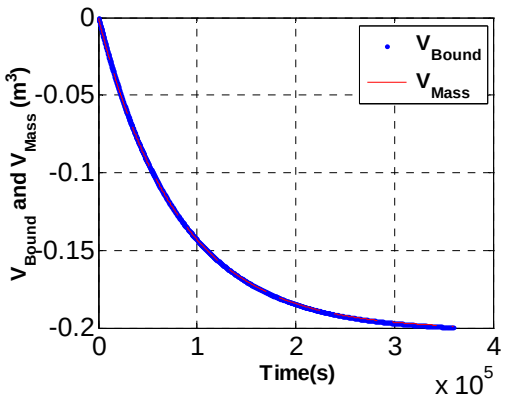

Fig. 3-36 Evolution of V_{Bound} and V_{Mass} (global volume balance) for the case: α=20 $m^{(-1)}$, n=3 (VGM)

3.3.3.3 Richards' equation model for the discharge problem (Exponential model)

The same simulation conditions (simulation domain, boundary condition, initial condition, etc.) as the two above numerical simulations with VGM model have been used for the other two numerical simulations with the exponential parameter model.

- **Physical properties (parameters for exponential model)**

Two groups of the parameters are respectively: (1) α =6m^{-1}, β =2m^{-1}, Hb=0.0; (2) α=20m^{-1}, β=6.667m^{-1}, Hb=0.0.The water content function curve $\theta(h)$, the hydraulic conductivity function curve $K(h)$, the capillary diffusion function curve $D(h)$ and the

capillary capacity function curve $C(h)$ are respectively illustrated in **Fig. 3-37**, **Fig. 3-38**, **Fig. 3-39** and **Fig. 3-40**.

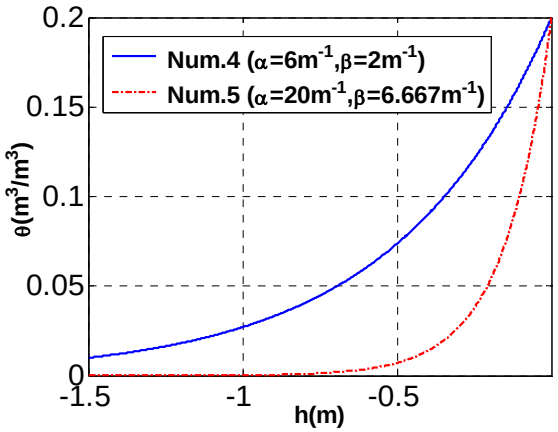

Fig. 3-37 Water content curve $\theta(h)$ of the river bank soil (Exp.).

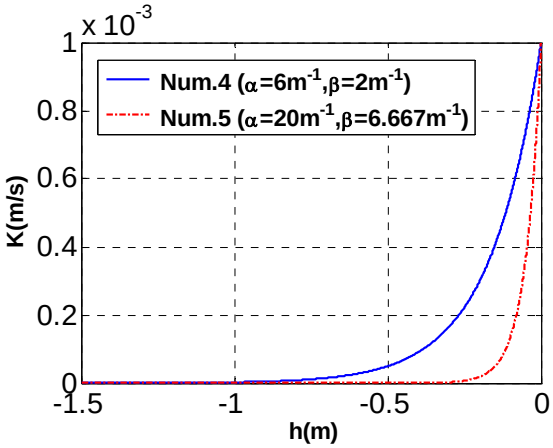

Fig. 3-38 Hydraulic conductivity curve $K(h)$ of the river bank soil (Exp.).

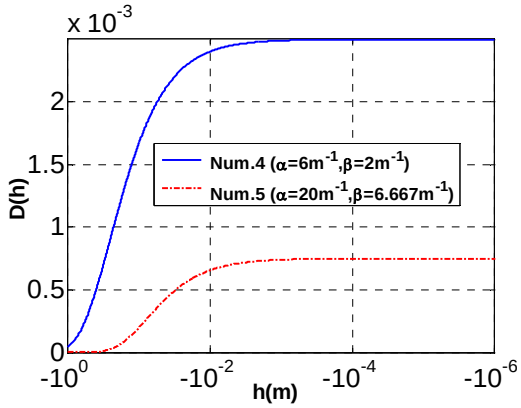

Fig. 3-39 Capillary diffusion $D(h)$ of the river bank soil (Exp.).

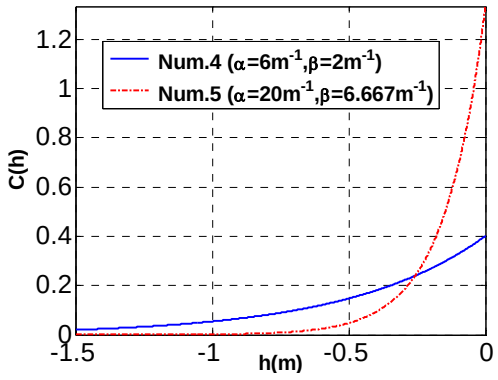

Fig. 3-40 Capillary capacity $C(h)$ of the river bank soil (Exp.).

- **Numerical behaviour of Bigflow during the simulation**

The numerical behaviours of Bigflow during the simulation are very similar to the ones of the Num.3 with the VGM model, as seen in **Fig. 3-41**, **Fig. 3-42**, **Fig. 3-43**, and **Fig. 3-44**.

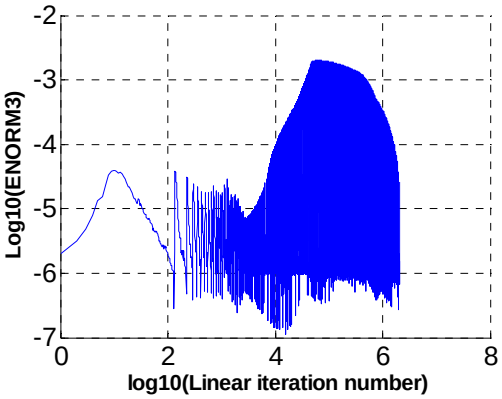

Fig. 3-41 Standarlized linear iteration process curve of the pressure head in log10

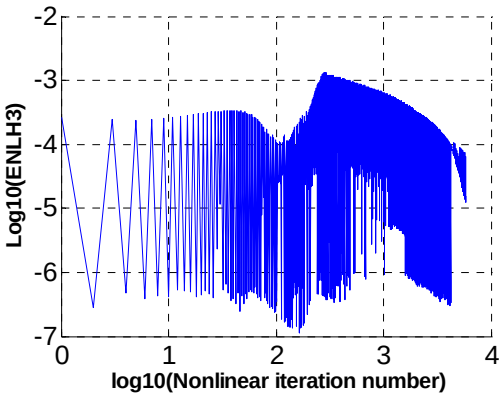

Fig. 3-42 Standarlized nonlinear iteration process curve of the pressure head in log10

for the case: α =20m^{-1}, β =6.667m^{-1}, Hb=0.0 (Exp.)

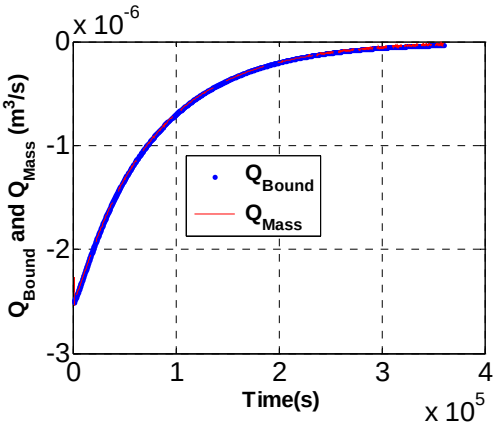

Fig. 3-43 Evolution of Q_{Bound} and Q_{Mass} (local mass balance) for the case: α =20m^{-1}, β =6.667m^{-1}, Hb=0.0 (Exp.)

for the case: α =20m^{-1}, β =6.667m^{-1}, Hb=0.0 (Exp.)

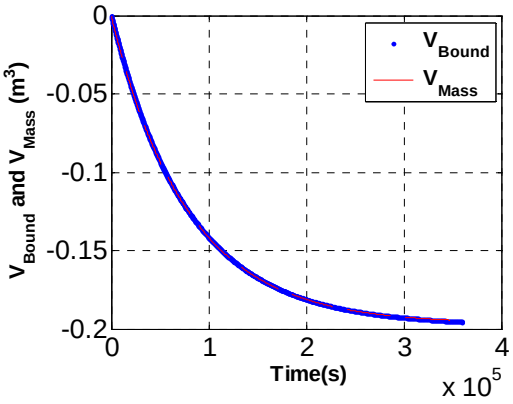

Fig. 3-44 Evolution of V_{Bound} and V_{Mass} (global volume balance) for the case: α =20m^{-1}, β =6.667m^{-1}, Hb=0.0 (Exp.)

3.3.3.4 Analysis of the numerical results of VGM model and exponential model

- **Analysis of the vertical distribution of the computed dynamic degree of saturation**

At the position of a horizontal distance of X_0=50m from the river (left boundary), two vertical profiles of the instantaneous static curve and dynamic curve of the degree of saturation with VGM model at t=10 hours for the two cases ((a) α=6m^{-1}, n=3, m=1-1/n; (b) α=20m^{-1}, n=3, m=1-1/n) are shown in **Fig. 3-45**.

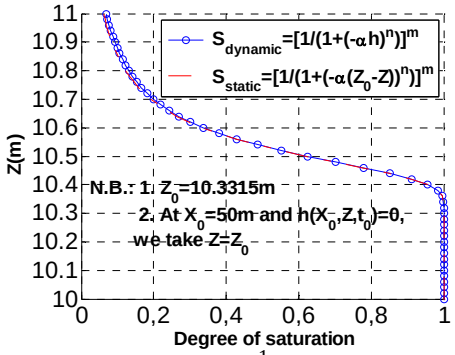

(a) VGM: α=6m^{-1}, n=3, m=1-1/n

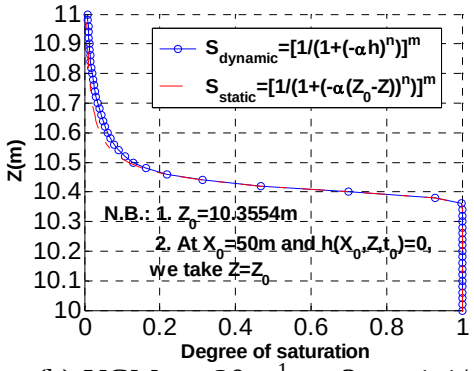

(b) VGM: α=20m^{-1}, n=3, m=1-1/n

Fig. 3-45 Comparison of the vertical profile of the instantaneous static curve and the VGM dynamic curve of the degree of saturation at t=10 hours at X_0=50m with partially saturated Richards model in the case of VGM parameters: (a) α=6m^{-1}, n=3, m=1-1/n; (b) α=20m^{-1}, n=3, m=1-1/n.

The above figure indicates that, during the transient simulation with Richards model, the profile of the water content above the free surface is nearly hydrostatic for all the time, which can explain the hydrostatic initial condition: $h(x,z,0) = z - H(x,z,0)$, where, $H(x,z,0)$ is the initial profile of the free surface of the aquifer (river bank).

Fig. 3-46 demonstrates the above same results with the exponential model for the other 2 simulations.

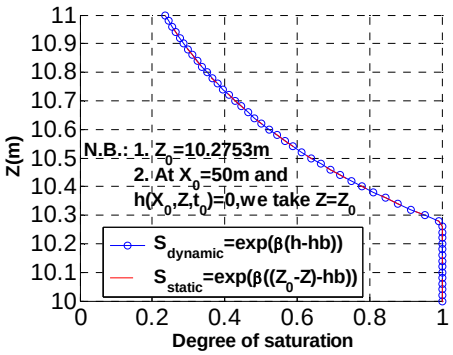

(a) Exp: α=6m^{-1}, β=2m^{-1}, Hb=0.0

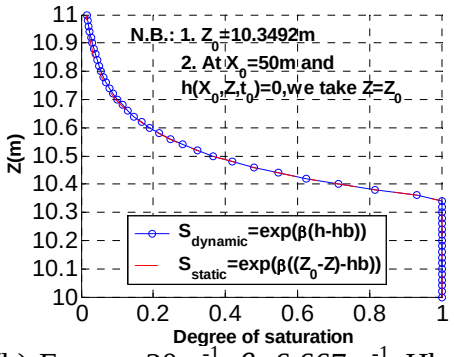

(b) Exp: α=20m^{-1}, β=6.667m^{-1}, Hb=0.0

Fig. 3-46 Comparison of the instantaneous static curve and the computed dynamic curve of the degree of saturation at t=10 hours at X_0=50m with partially saturated Richards model in the case of the exponential model parameters: (a) α=6m^{-1}, β =2m^{-1}, Hb=0.0; (b) α =20m^{-1}, β =6.667m^{-1}, Hb=0.0.

- **Analysis of the instantaneous vertical profile of the degree of saturation with the pressure head isovalues**

The Num.2 has a different value of α with the Num.3. This means that the two numerical simulations with VGM model have different capillary length: $\lambda_{Cap(Num.2)}$ =0.17m; $\lambda_{Cap(Num.3)}$=0.05m, which is clearly shown in **Fig. 3-47** (a) and (b).

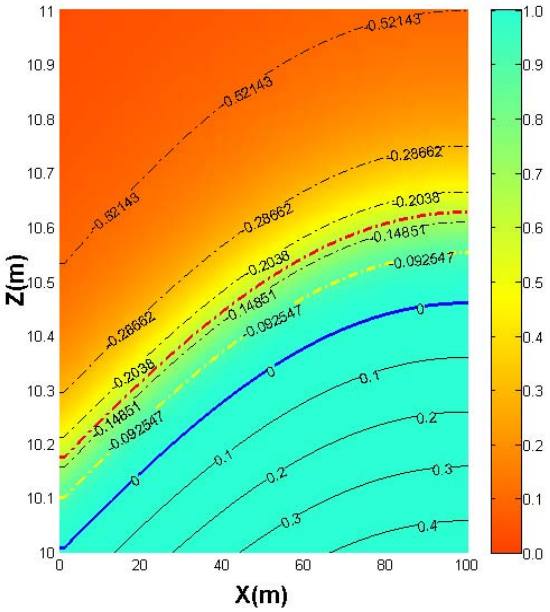

(a) VGM: α=6m^{-1}, n=3, m=1-1/n

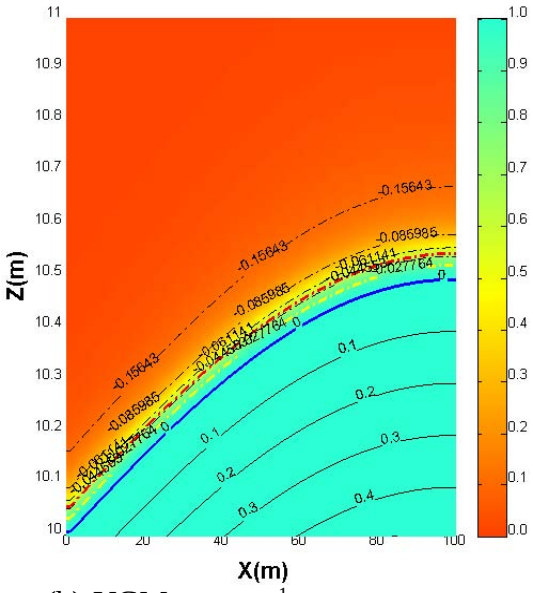

(b) VGM: α=20m^{-1}, n=3, m=1-1/n

Fig. 3-47 Vertical profile of the instantaneous distributions of the pressure head $h(x,z,t_0)$ and the degree of saturation $S(x,z,t_0)$ at t=10 hours with partial saturated Richards model in the case of VGM parameters: (a) α=6m^{-1}, n=3, m=1-1/n; (b) α=20m^{-1}, n=3, m=1-1/n
Note: 1. in the figure (a)**,** the red curve (h=-0.17m) corresponds to S=0.63 and the yellow curve (h=-0.09m) corresponds to S=0.9; **2.** in the figure (b), the red curve (h=-0.05m)

corresponds to S=0.63 and the yellow curve (h=-0.03m) corresponds to S=0.9.

In the figure, two red curves correspond to the degree of saturation S=0.63, their pressure head values are respectively -0.17m and -0.05m, and it can be seen that the capillary domain of the Num.3 is much narrower than that of the Num.2.

The similar situation occurs to the Num.4 and Num.5 with exponential model, as shown in **Fig. 3-48** (a) and (b).

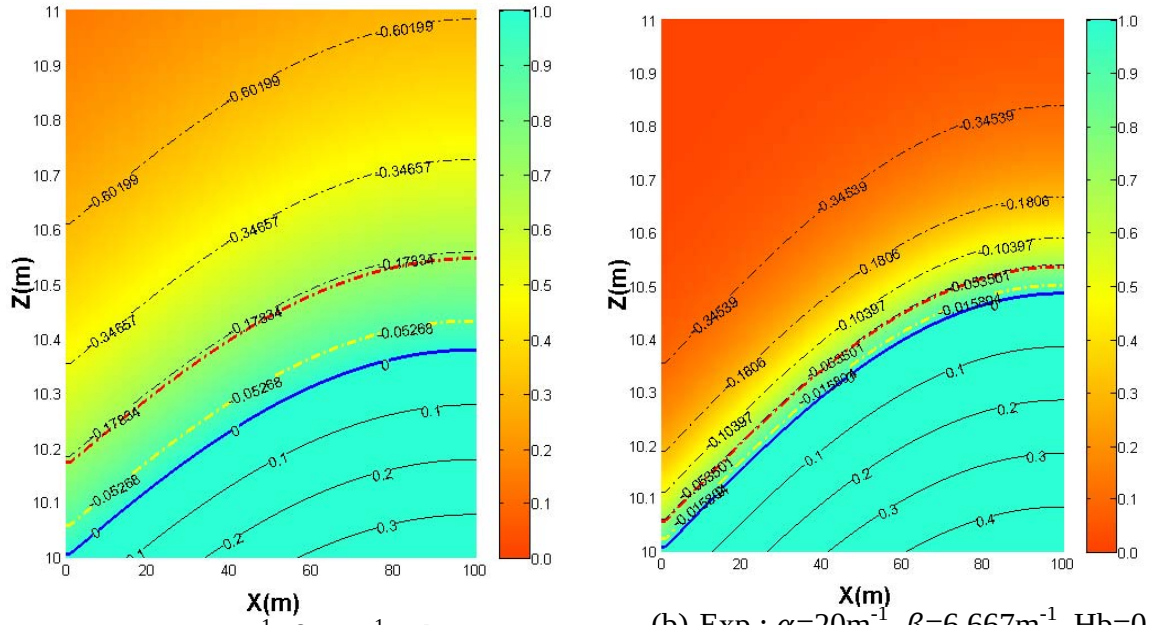

(a) Exp.: α=6m^{-1}, β=2m^{-1}, Hb=0.0 (b) Exp.: α=20m^{-1}, β=6.667m^{-1}, Hb=0.0

Fig. 3-48 Vertical profile of the instantaneous distributions of the pressure head $h(x,z,t_0)$ and the degree of saturation $S(x,z,t_0)$ at t=10 hours with 3D Richards unsaturated model in the case of the exponential model parameters: (a) α=6m^{-1}, β=2m^{-1}, Hb=0.0; (b) α=20m^{-1}, β=6.667m^{-1}, Hb=0.0**.** Note: 1. in the figure (a), the red curve (h=-0.17m) corresponds to S=0.72 and the yellow curve (h=-0.05m) corresponds to S=0.9; **2.** in the figure (a), the red curve (h=-0.05m) corresponds to S=0.72 and the yellow curve (h=-0.02m) corresponds to S=0.9.

However, for the numerical simulations with VGM model and exponential model which have the same α value, the degree of saturation corresponding to the capillary pressure head are different, and they are respectively 0.63 for the numerical simulations with VGM model and 0.72 for the ones with exponential model. In addition, from **Fig. 3-47** and **Fig. 3-48**, it can be seen that the suction values corresponding to the degree of saturation S=0.90 have been decreased from 0.09m to 0.05 for Num.2 to Num.4 and from 0.03m to 0.02m for Num.3 to Num.5, and the distribution of the degree of saturation is different: the band width between the two pressure head contours with the same increment of the degree of saturation from the free surface to the unsaturated zone become more and more larger with the exponential model, while it is the narrowest around the capillary pressure head contour with the VGM

model. The different distribution of the degree of saturation can be explained due to the different diffusion curve $C(h)$, as seen in **Fig. 3-31** (VGM model) and **Fig. 3-39** (Exponential model).

- **Analysis of the instantaneous vertical profile of the flux field with the pressure head contours**

The vertical profiles of the instantaneous flux field $q(x,z,t_0)$ and pressure head $h(x,z,t_0)$contours at t=10 hours for the 4 numerical simulations with Richards model are illustrated in **Fig. 3-49** and **Fig. 3-50**.

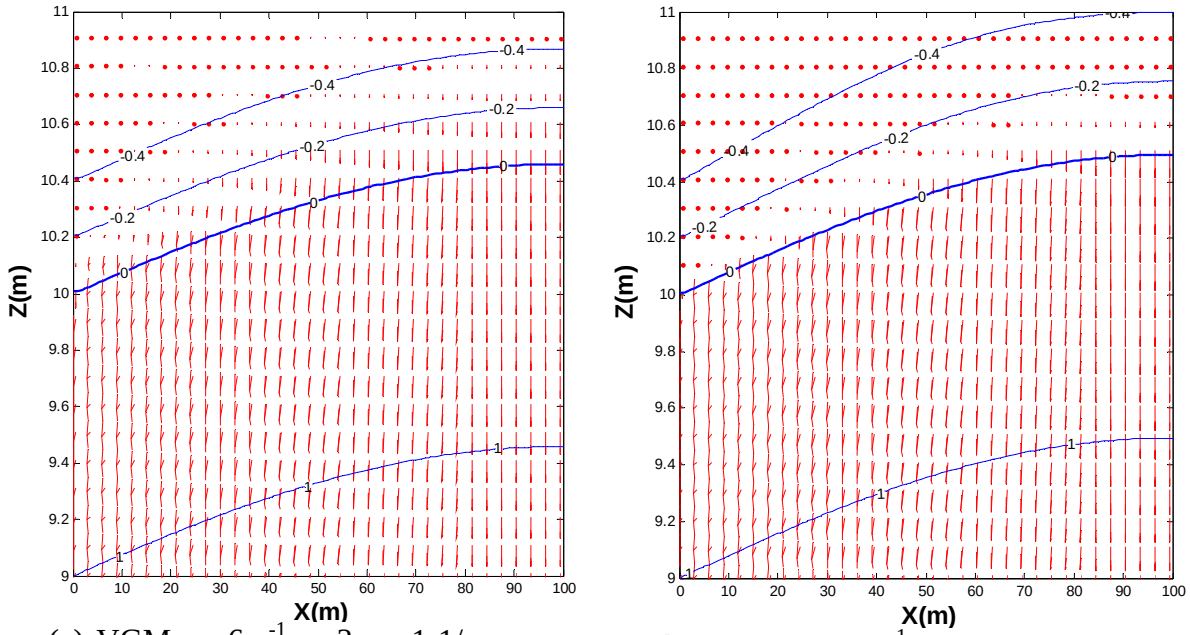

(a) VGM: α=6m^{-1}, n=3, m=1-1/n (b) VGM: α=20m^{-1}, n=3, m=1-1/n

Fig. 3-49 Vertical profile of the instantaneous flux field $q(x,z,t_0)$ and pressure head $h(x,z,t_0)$contours at t=10 hours with partial saturated Richards model in the case of VGM parameters: (a) α=6m^{-1}, n=3, m=1-1/n; (b) α=20m^{-1}, n=3, m=1-1/n. Note: Scale$_{flux}$=0.7.

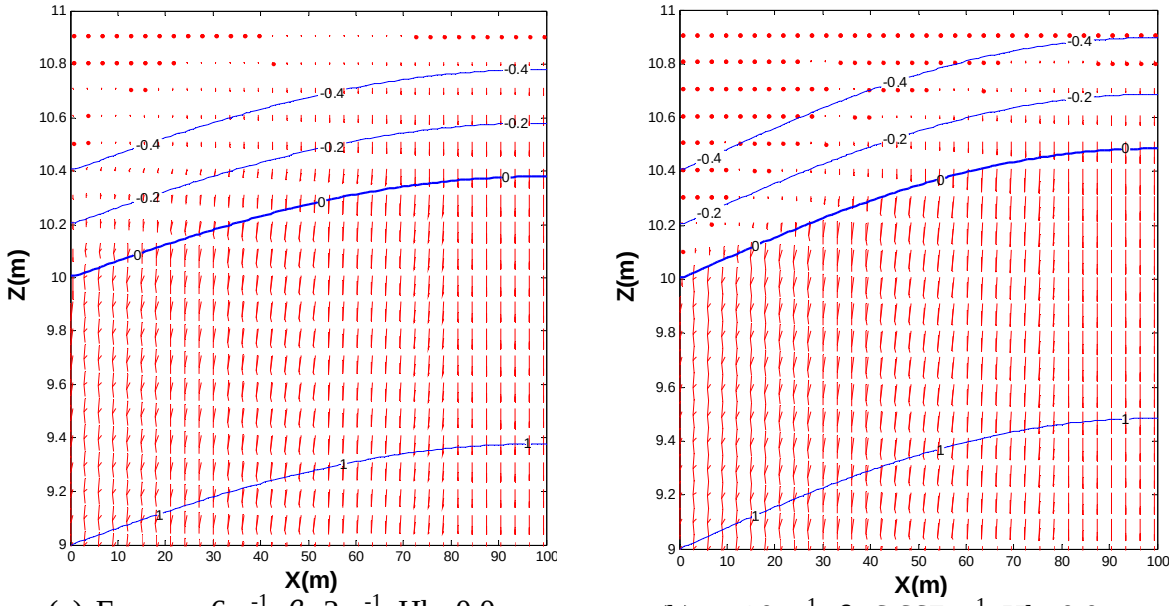

(a) Exp.: α=6m^{-1}, β=2m^{-1}, Hb=0.0 (b) α=20m^{-1}, β=6.667m^{-1}, Hb=0.0

Fig. 3-50 Vertical profile of the instantaneous flux field $q(x,z,t_0)$ and pressure head $h(x,z,t_0)$ contours at t=10 hours with partial saturated Richards model in the case of exponential model parameters: (a) α=6m^{-1}, β=2m^{-1}, Hb=0.0; (b) α=20m^{-1}, β=6.667m^{-1}, Hb=0.0. Note: $\beta = \alpha / 3$ and Scale$_{flux}$=0.7.

From these figures, it can be seen that the flux field in the saturated zone has no difference and however, the flux field in the unsaturated zone is different for the 4 numerical simulations: the flux begins to decrease from the free surface and drastically diminish to zero after the capillary length pressure head contour. Relatively, the flux with exponential model diminishes slower than the one with VGM model.

- **Analysis of the profile of the instantaneous free surfaces ($h(x,z,t_0)$ =0) in the river bank and the outflow discharge at the bank/river interface**

The free surfaces of numerical simulations with same α value have been plotted in the same figure to be compared with the analytical result. As a result, **Fig. 3-51** shows the instantaneous free surfaces ($h(x,z,t_0)$ =0) at t=10 hours of the analytical solution, the Num.2 and Num.4 with α = 6m^{-1}, and it can be seen that the free surface at the right boundary of the Num.2 with VGM model is about 0.05m lower than that of the analytical and the one of Num.4 with exponential model is about 0.12m lower than the analytical. This can be further explained by the fact that the analytical solution of the plane flow equation of Boussinesq doesn't suit the problem with big capillary effect. In addition, the role of α in the VGM model is not totally the same as the one in the exponential model due to the different definition of the water content function $\theta(h)$ and the hydraulic conductivity function $K(h)$. However, for the problem with very small capillary effect, the results obtained with all the models should be

the same. This result can be obtained from **Fig. 3-52**. In the figure, instantaneous free surfaces at=10 hours in the river bank of Num.3 and Num.5 agree very well with the linearized analytical one.

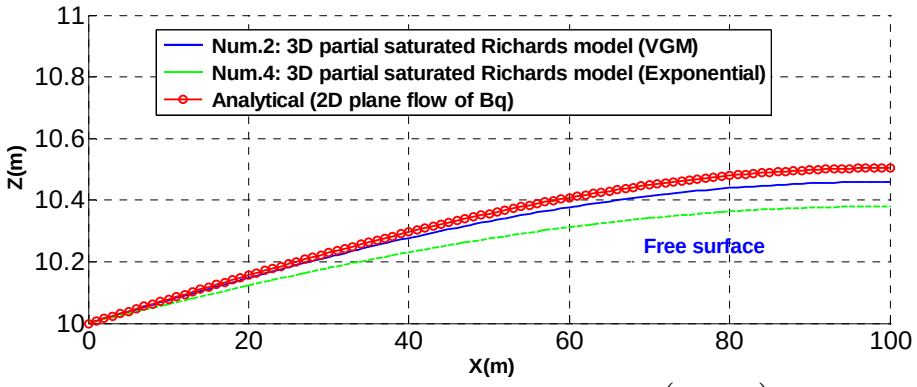

Fig. 3-51 Comparison of the instantaneous free surfaces ($h(x,z,t_0)$ =0) at t=10 hours in the river bank of the linearized analytical solution of the plane flow Boussinesq equation and the numerical simulations with 2 partially saturated Richards models in the case of the parameters of VGM model (Num.2): α =6m^{-1}, n=3, m=1-1/n and parameters of exponential model (Num.4): α=6m^{-1}, β=2m^{-1}, Hb=0.0.

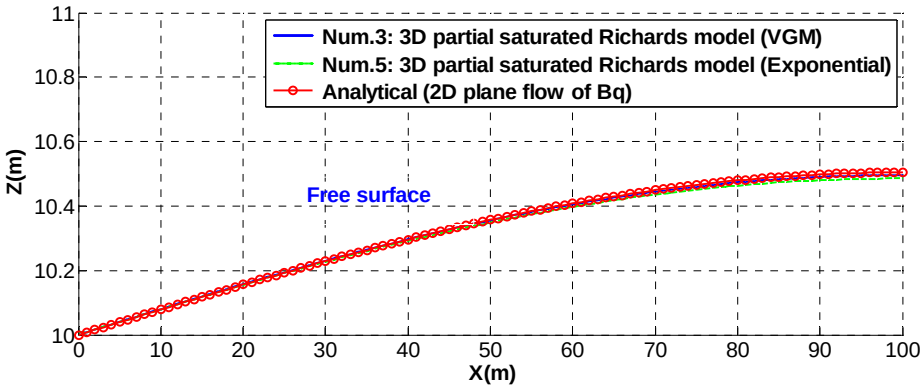

Fig. 3-52 Comparison of the instantaneous free surfaces ($h(x,z,t_0)$=0) t=10 hours in the river bank of the linearized analytical solution of the plane flow Boussinesq equation and the numerical simulations with 2 partially saturated Richards models in the case of the parameters of VGM model (Num.3): α =20m^{-1}, n=3, m=1-1/n, and the parameters of exponential model (Num.5): α=20m^{-1}, β=6.667m^{-1}, Hb=0.0.

At the same time, the evolution of the outflow discharge $Q(0,y,z,t)$ at the bank/river interface has been compared among Num.1 (Boussinesq model), Num.3 (Richards equation with VGM parameter mode), Num.5 (Richards equation with exponential parameter mode) and the linearized analytical solution of Boussinesq equation, as shown in **Fig. 3-53**. From the figure, it can be seen that in spite of a tiny difference between the result with numerical Boussinesq model and the ones with Richards model at the end of the discharge of the aquifer, all the computed outflow discharges are in a very good agreement, and however,

there is still a very small difference between the numerical results and the analytical one, which may be due to the linearization of the analytical solution.

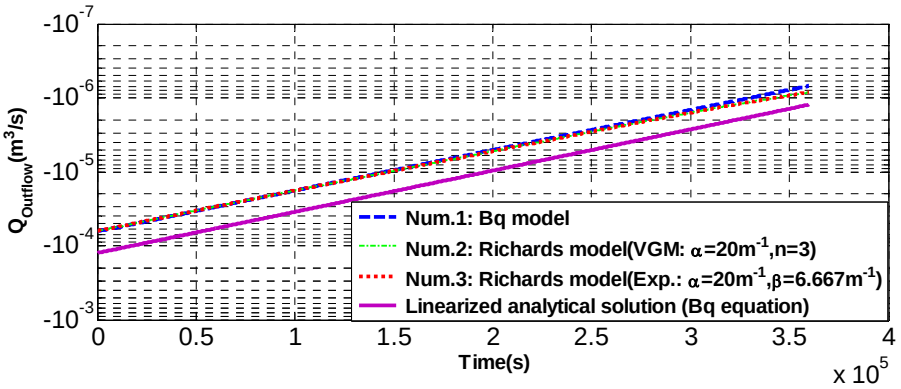

Fig. 3-53 Comparison of the outflow discharge $Q(0,z,t)$ at the bank/river interface: (1) linearized analytical solution of Boussinesq equation; (2) numerical simulation of the Boussinesq equation (Num.1); (3) simulation with Richards model for 2 sets of parameters:

- VGM model (Num.3): α=20m^{-1}, n=3, m=1-1/n;
- Exponential model (Num.5): α=20m-1, β=6.667m-1, Hb=0.0.

3.3.4 Conclusion on the discharge problem

Through the approximation of the hydraulic transmissivity $T^* = T \approx KH^*$ in the Boussinesq equation, the linearized analytical solution has been obtained for the discharge process of the water level in the river bank with the initial free surface of the sinusoidal curve, and accordingly, the outflow discharge at the bank/river has been calculated with Darcy law.

An example of the discharge problem of the river bank has been solved with analytical solution and the numerical simulations with Boussinesq plane flow model and two partial saturated Richards models. The results indicate that:

(1) The discharge process of the free surface obtained with Boussinesq model has a very good agreement with the analytical solution, and at the same time, there is a small difference of the outflow discharge of about 0.6e-5m^3/s at the bank/ river interface between the two results at the beginning of the river bank discharge;

(2) The analytical solution of the plane flow equation of Boussinesq doesn't suit the problem with big capillary effect. Similarly, for the problem with big capillary effect, due to the different definition of the water content function $\theta(h)$ and the hydraulic conductivity function $K(h)$, the role of α in the VGM model is not totally the same as the one in the exponential model. For instance, Num.2 (VGM) and Num.4 (Exp.) with the same smaller $\alpha = 6$ m^{-1}(the same bigger capillary length of 0.17m) have given the different instantaneous free surfaces.

(3) For the porous mede with very small capillary effect, the results obtained with all the numerical models are the same. For example, Num.3 (VGM) and Num.5 (Exp.) with the same bigger $\alpha = 20$ and therefore the same smaller capillary length of about 0.05m, have given the same instantaneous free surface for the discharge process of the river bank, and their results are also in a very good agreement with the one with Boussinesq model as well as the analytical solution.The biggest difference of the outflow discharge at the bank/river interface between the analytical and the numerical can be explained as the consequence of the linearization of the nonlinear Boussinesq equation.

Part III
MODELING OF OSCILLATORY FLOWS IN POROUS MEDIA

Chapter 4: Wave propagation through a vertical sandbox (small wave canal)

4.1 Introduction

In this chapter, three complementary approaches (laboratory experiment, analytical solution, and numerical simulation) are used to investigate the wave propagation in a sandbox with vertical boundary, which may represent a river bank, a breakwater, or a sandy beach.

Firstly, in order to validate a sensor to be used to measure the water level fluctuations in the porous media under the oscillatory entry water level condition (high frequency wave forcing), and, furthermore, to investigate the propagation of the water level fluctuation in the porous media with very small periods such as T_{min}=0.5s, a small "Darcy-scale" experiment is conducted in a water wave canal at IMFT laboratory. In this experiment, two types of pressure sensors and one capacitive sensor will be tested and finally only one type of sensor is going to make the measurement. Furthermore, the measured water level fluctuations in the vertical sandbox will be interpreted to obtain the saturated hydraulic conductivity of the sand under the high frequency foring oscillatory hydrodynamic entry water levels. As a result, this estimated hydraulic conductivity value will be compared with the ones obtained by the empirical formulas of Kozeny-Carman [20].

Secondly, the linearized analytical solutions of the 1D nonlinear equation of Dupuit-Boussinesq for the saturated plane flow with a free surface will be developed for a vertical sandbox. 4 cases of boundary conditions which will be considered in the linearized analytical solutions: on the left entry boundary, the water level fluctuations of the periodical sine wave and the periodical cosine wave are respectively imposed; on the right boundary, two types of boundary conditions are respectively imposed: a flux is equal to zero and a water level constant. As a result, the linearized analytical solution for the same boundary case with the vertical sandbox experiment will be used to analyze the inertial effects on wave oscillations in order to find out the criterion for the erosion at the oscillatory entry interaction boundary: porous media/open water.

Thirdly, an example of the analytical case 2 of boundary condition will be simulated with vertically hydrostatic Boussinesq model. In this example, the fluctuation characteristic parameter of the entry water level fluctuations, the ratio of the fluctuation amplitude to the water depth is taken as 0.5. As a result, the simulated water heads will be compared with the corresponding analytical values.

At last, two relative error formulas for the analytical water heads to the simulated ones are built up to estimate the precision of the analytical solution. Furthermore, the maximum errors of the analytical results for the boundary condition case 3 will be investigated in detail and as a result, the relationship curve of the maximum error and the ratio of the fluctuation amplitude to the mean water depth will be obtained.

4.2 Laboratory experiment: vertical sandbox in small wave canal

4.2.1 Experiment description and methodology

4.2.1.1 Infrastructure of wave canal with sandbox

The canal is about 4.7 m long, 0.14 m wide and 0.25 m high. At the right end of the canal, a mechanical wave generator with adjustable period and amplitude has been designed. A sandbox is immersed in the canal and it is 0.70 m long, 0.137 m wide and 0.50 m high. The transverse faces of the box are made of a metallic grid, and the other two faces are made of plexiglas. The upstream face of the sandbox is about 1.93 m from the wave generator. The profile of the whole wave canal is shown in **Fig. 4-1**.

Fig. 4-1 “Darcy-scale” experiment in a small wave canal at IMFT laboratory.

4.2.1.2 Sediment characteristics

Two types of sands have been used to test this experiment: fine sand used to do the wetting experiment in chapter 3 and coarse sand. For the fine sand, the grain diameter ranges from 0.02mm through 0.32mm and d_{50} is 0.16mm; for the coarse sand, the grain diameter ranges from 0.8mm through 2.5mm and the corresponding d_{50} is about 1.8mm.

Finally, the coarse sand is chosen for this experiment.

4.2.1.3 Wave conditions

The wave generator can make waves with periods ranging from T = 0.57 s to 1.95 s. In contrast, the forced amplitude of the water level fluctuations depends on the period of the wave generator and the still water level H_0 in the canal. Considering that the height of the wave canal is 25cm, the still water level is set equal to 7.6cm and the height of the sand layer in the sandbox is 12.1cm, which is set about half smaller than the height of the wave canal. As a result, the amplitudes of the water level fluctuations at the entry vary from A_0 = 0.11 cm to 0.61 cm for all the wave generator periods in all the tests.

4.2.1.4 Tested water level sensors

In total, three types of sensor have been tested in this experiment.

The first tested sensor is a CP5230 transmitter (a model of pressure sensors made by HITEC), as shown in **Fig. 4-2** (a). Its general features are water level measurement on free fluids for sewage, waste water, river and canal. The water level measurement is performed through the differential pressure measurement between liquid surface and the submersible sensor.

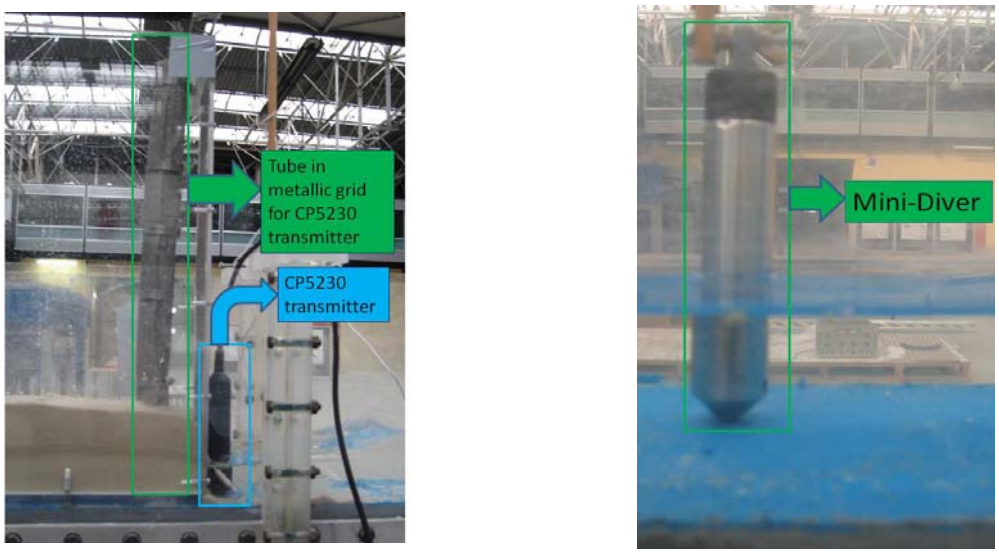

(a) CP5230 transmitter (b) Mini-Diver

Fig. 4-2 Tested sensors: CP5230 transmitter and Mini-Diver

This CP5230 transmitter can follow the water level fluctuations with very short period (high frequency) such as T=0.5s. However, in comparison with the sandbox, its volume is too big, its diameter is 3cm and it needs also a tube in metallic grid to separate the sand to measure the

water level fluctuations, as seen in **Fig. 4-2** (a).

The second tested sensor is a Mini-Diver (a model of sensors made by Schlumberger Water Services) shown in **Fig. 4-2** (b), which is another type of pressure sensor. Mini-Diver determines the height of a water column by measuring the water pressure with the built-in pressure sensor. When the Diver is above water, the atmospheric pressure is measured. Below the water surface the pressure of the water is added: the higher the water column is, the higher the pressure is. Based on the measured pressure, the height of the water column above the Diver's pressure sensor can be determined.

Compared with CP5230 transmitter, although the diameter of Mini-Diver is a little smaller (22mm), it is not able to follow the water level fluctuations with short periods such as T=1.95s for the sandbox experiment in the small wave canal in IMFT.

The third tested and finally chosen sensor is a capacitive sensor developed specially by the electronic specialist H. Ayroles of IMFT lab, as illustrated **Fig. 4-3**. The principal is to measure the water level by measuring the capacitance between the conductive water and a conductive metal rod surrounded by an insulating sheath made by a particular material (non-conductor). The metal rod is installed in the tube with holes in order to avoid sand enterance into the tube connectted with the insulating sheath. The black fine line is used to provide ground connection.

Fig. 4-3 Tested sensors: capacitve sensor used to measure the water level fluctuations in the sandbox

In general, the capacitance has a linear relationship with the measured water level:

$$C = a.H + b,$$

where, C is the capacitance, H is the measured water level, a is the slope of the linear variation and b is the intercept. As a result, the capacitance is converted into electrical signal by a transformation box to provide electric voltage output signal with a maximum electric voltage of 4 volts. Therefore, the electric voltage almost has a linear relationship with the measured water level, namely, $U = a.H + b$, where, U is the electric voltage. This relationship is finally used to calibrate the capacitive senor to measure the water level fluctuations in the sand.

Compared with CP5230 transmitter and Mini-Diver, the capacitive sensor made by H. Ayroles has two advantages: (1) the volume is very small, the diameter of the tube used is 0.5mm, and it suits very much the small sandbox; (2) its sample time interval is 0.01s (sample frequency of 100Hz), which satisfes the needs for the experiment whose minimum period is about 0.5s.

Therefore, the capacitive sensor is finally chosen to measure the water level fluctuations in the sand for the small sandbox experiment in the wave canal of IMFT and for the experiment in the Barcelona wave canal (Chapter 5).

4.2.1.5 The measured instrument arrangement and the test boundary conditions

One capacitive sensor has been placed in the front of the upstream face of the sandbox in order to measure the entry water level fluctuations at the porous boundary.

In the sandbox, the water level fluctuations at 3 different positions have been measured and the positions are respectively x_1=3cm, x_2=6cm, x_3=8.2cm from the right (upstream) face of the sandbox. **Fig. 4-4** (a) shows the measurement of the water level fluctuations at x_1=3cm with the capacitive sensor. In this experiment, on the left boundary of the sandbox is imposed a constant water level equal to the still water level in the right wave canal; the periodically oscillatory water level generated by the wave generator at the right end of the canal is imposed on the right boundary of the sandbox, as seen in **Fig. 4-4** (a).

In addition, the voltage transformation box and the computer are installed on a table near the sandbox, as shown in **Fig. 4-4** (b).

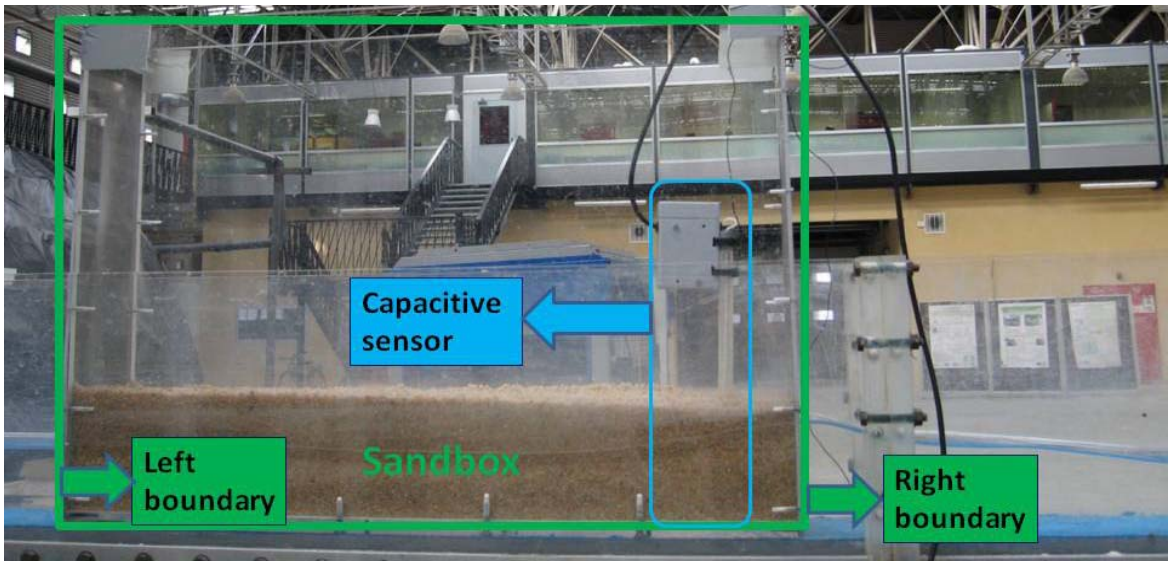

(a) Arrangement of the capacitive sensor

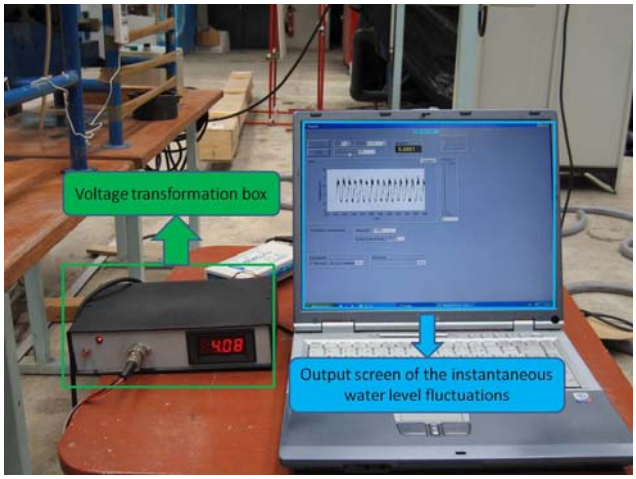

(b) Arrangement of the voltage transformation box and the computer

Fig. 4-4 Instrumentation of the sandbox experiment in a small wave canal of IMFT laboratory: (a) capacitive sensor; (b) voltage transformation box and the computer.

4.2.2 Interpretation of the experimental results

4.2.2.1 Empirical formulas of Kozeny-Carman for the estimation of the hydraulic conductivity

From Ababou (2007), three empirical formulas of Kozeny-Carman about the relationship between the intrinsic permeability k and the mean diameter d_m as well as the porosity ϕ are as follows:

Formula 1:

$$k = \frac{d_m^2}{180}\frac{\phi^3}{(1-\phi)^2} \tag{4-1}$$

Formula 2:

$$k = \frac{d_m^2}{36h_K}\frac{\phi^3}{(1-\phi)^2} \quad (4\text{-}2)$$

$$h_K = 4.5 \pm 1.5(\phi < 0.7\, m^3/m^3)$$

Formula 3:

$$k = \frac{1}{72}\frac{\phi^3 d_m^2}{(1-\phi)^2} \quad (4\text{-}3)$$

At the same time, the hydraulic conductivity K has the following relationship with the intrinsic permeability k :

$$K = \frac{\rho g}{\mu}k \text{ or } K = \frac{g}{\vartheta}k$$

Note that:

k is the intrinsic permeability (m^2);

$K$is hydraulic conductivity (m/s);

d_m is the mean diameter d_m (equivalent sphere) of grains (m);

ϕ is the porosity (m^3/m^3);

μ is the dynamic viscosity (kg/(m.s));

ϑ is the cinematic viscosity (m^2/s);

ρ is the density or volumic mass (kg/m^3);

g is the gravity acceleration and g=9.81 m/s^2.

4.2.2.2 Evolution of water levels versus space (x) and time (t) (decay)

In the below, **Fig. 4-5** shows the evolution of the measured water levels and the corresponding theoretical values at the positions in the sandbox: $x_0 = 0.0$, $x_1 = 3.0$, $x_2 = 6.0$, and $x_3 = 8.2$cm for the period T=0.6896s and the entry amplitude $A_0 = 0.2521$ cm.

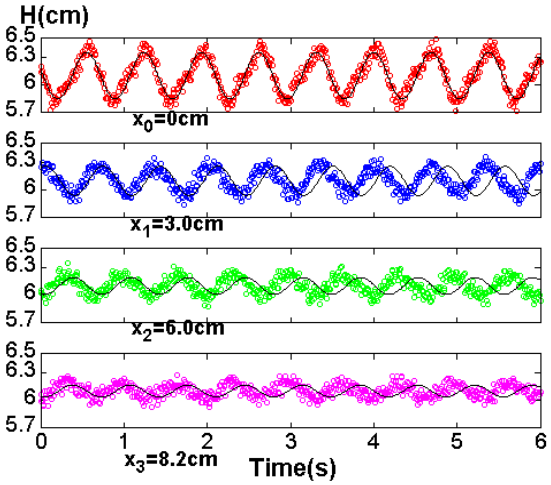

Fig. 4-5 Time evolution of measured water levels H(x,t) (symbols) and the corresponding theoretical values (solid curves) at different locations in the sandbox: x_0=0.0, x_1=3.0, x_2=6.0cm, x_3=8.2cm (period T=0.6896s, amplitude A_0 = 0.2521 cm).

From the figure, it can be seen that the amplitude of the water level fluctuations in the sand decay with respect to the distance from the entry boundary.

4.2.2.3 Identification of hydraulic conductivity Ks and comparisons with Kozeny-Carman

Based on the measured results and the analytical study of the plane flow problem (see further below, section **4.3.2**), it is assumed that the amplitude of fluctuations decays exponentially with distance:

$$A(x) = A_0 e^{-\frac{x}{L_D}} \tag{4-4}$$

where, A_0 is the amplitude of the entry water level fluctuations, $A(x)$ is the amplitude of the water level fluctuations in the sand at the position of x, and L_D is the decay length.

It can be therefore obtained, from the measurements, the characteristic decay length L_D of water level fluctuations in the porous medium for the given period and amplitude (**Fig. 4-6**).

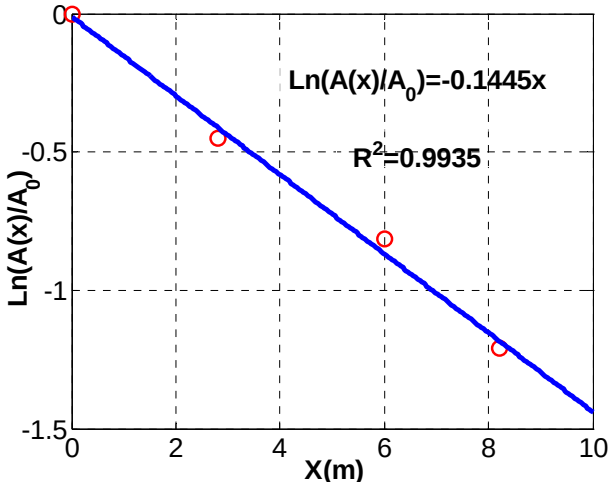

Fig. 4-6 Plot of ln(A(x)/Ao) versus distance x from the right boundary of the sandbox (inlet): measured values (symbols) and straight line fit, in the case: T = 0.6896 s, A_0 = 0.2521 cm.

From this figure, it can be seen that the semi-log linear fit is quite good. Now, according to the analytical theory, the following relationship between the decay length L_D (m), the hydraulic diffusion coefficient D (m^2/s), and the angular frequency ω (rad/s) of the incoming wave can be achieved:

$$L_D = \sqrt{\frac{D}{\omega}} \text{ with } D = \frac{K_s \times h_0}{\theta_s} \tag{4-5}$$

where θ_s is the effective porosity of the sand ($\theta_s = 0.36\, m^3/m^3$ in this experiment), K_s is the saturated conductivity and h_0 is the initial water depth in the sand . Therefore, it the apparent hydraulic conductivity K_s can also be identified from the water level fluctuation measurements in the sand, and it is obtained $K_s = 1.918 \times 10^{-1}$ m/s.

The estimated hydraulic conductivities by the measured water fluctuations and the formulas of Kozeny-Carman are shown in the **Table 4-1**.

Table 4-1 Estimated saturated hydraulic conductivity

Method		Saturated water content θ_S(m^3/m^3)	Estimated saturated hydraulic conductivity $\widehat{K_S}$ (m/s)		
Experiment (Sand diameter: d=0.8-2.5mm)		0.36	1.918E-1		
Empirical formula of Kozeny-Carman	Formulas		Sand diameter		
			d=0.8mm	d=1.8mm	d=2.5mm
	Formula1		3.536E-3	1.790E-2	3.453E-2
	Formula2 (h_k=3)		3.893E-3	2.983E-2	5.755E-2
	Formula3		8.839E-3	4.475E-2	8.632E-2

From the table, it can be seen that the estimated saturated hydraulic conductivity value $K_s = 1.918 \times 10^{-1} m/s$ is 5-10 times larger than the ones obtained by the formulas of Kozeny-Carman for the mean diameter d=1.8mm, which may be due to hydro-mechanical interactions or to other neglected effects (vertical velocities, capillary effects).

4.2.3 Acknowledgment

During the test of the sensors, the electronic specialist of the IMFT lab H. Ayroles was very helpful. In addition, L. Le Fur, the technician of GEMP, here strongly contributed to the installation of the sandbox.

4.3 Linearization and analytical solution of the non-linear Boussinesq equation

4.3.1 Linearized Boussinesq analytical solution under oscillatory conditions

The analytical solutions of Boussinesq's plane flow equation submitted to the periodic water levels by linearization methods have been developed. The simplest approximation consists in linearizing hydraulic transmissivity $T = K_s.H(x,t)$ in the form $T \approx K_s.H^*$, where, K_s is the saturated hydraulic conductivity and H^* is the mean water depth.

Two cases of boundary condition are treated, the first one (Case 1) in a finite domain with reflective boundary at right, the second (Case 2) in a semi-infinite domain with fixed water level at right:

Case 1: Left boundary condition (x=0): $H(0,t) = H_0 + A_0 cos(\omega t)$

Right boundary condition (x=L): $\boldsymbol{q} \cdot \boldsymbol{n} = 0$

Case 2: Left boundary condition (x=0): $H(0,t) = H_0 + A_0 cos(\omega t)$

Right boundary condition (semi-infinite domain: x→∞): $H(\infty, t) = H_0$

Here, H is the water level in the porous media, H_0 is the mean water level or the still water level, A_0 is the amplitude of the fluctuation or oscillation, and ω is angular frequency.

The equation (3) (Depuit-Boussinesq, in chapter 2) of one dimension in the x direction is rewritten as follows:

$$\Phi \frac{\partial H}{\partial t} = \frac{\partial}{\partial x}\left(T \frac{\partial H}{\partial x}\right) \tag{4-6}$$

where, $T = K.H$ and Φ is the effective porosity.

The equation (4-6) is non-linear. We linearize it by making the approximation that $T \approx T^* = KH^*$ and H^* is supposed fixed to obtain:

$$\Phi \frac{\partial H}{\partial t} = T^* \frac{\partial^2 H}{\partial x} \tag{4-7}$$

Supposing that $h(x,t) = H(x,t) - H_0$, we apply the method of the variable separation to solve this problem.

For **Case 1**, we put that

$$h(x,t) = a(x)e^{i\omega t} \tag{4-8}$$

So the equation (4-7) becomes $\frac{\partial h}{\partial t} - \frac{T^*}{\Phi}\frac{\partial^2 h}{\partial x^2} = 0$, or namely, $a''(x) - i\omega \frac{\Phi}{T^*} a(x) = 0$. Then the corresponding characteristic equation of this 2nd order linear diffusion equation is:

$$r^2 - i\omega \frac{\Phi}{T^*} = 0$$

and hereof $r = \pm e^{i\pi/4}\sqrt{\omega \frac{\Phi}{T^*}} = \pm \frac{1+i}{\sqrt{2}}\sqrt{\omega \frac{\Phi}{T^*}} = \pm \frac{1+i}{\delta}$ with $\delta = \sqrt{\frac{2T^*}{\omega\Phi}}$

where, $a(x) = Ae^{-\frac{1+i}{\delta}x} + Be^{\frac{1+i}{\delta}x}$

At the right boundary, we put that the flux $q = 0.0$. According to the Darcy's law, we have that $q = -KHgrad(H)$. Then, $q = -KHgrad(H) = 0.0$. Since $h(x,t) = H(x,t) - H_0$, then $\frac{\partial h(x,t)}{\partial x}|_{x=L} = 0.0$. And according to equation (4-8), there is $a'(x)|_{x=L} = 0.0$, while $a'(x) = -Ae^{-\left(\frac{1+i}{\delta}\right)x} + Be^{\left(\frac{1+i}{\delta}\right)x}$, then

$$\frac{A}{B} = \left(e^{\left(\frac{1+i}{\delta}\right)L}\right)^2 \tag{4-9}$$

At the left boundary, we have $H(0,t) = H_0 + A_0 cos(\omega t)$, so $h(0,t) = A_0 cos(\omega t)$. Then,

$h(0,t) = a(0)e^{i\omega t}$ and $a(0) = A_0$. Or just as $a(x) = Ae^{-\left(\frac{1+i}{\delta}\right)x} + Be^{\left(\frac{1+i}{\delta}\right)x}$, and then

$$a(0) = A + B = A_0 \tag{4-10}$$

From equations (4-9) and (4-10), we obtain that

$$A = \frac{A_0 e^{2\left(\frac{1+i}{\delta}\right)L}}{e^{2\left(\frac{1+i}{\delta}\right)L}+1} \tag{4-11}$$

$$B = \frac{A_0}{e^{2\left(\frac{1+i}{\delta}\right)L}+1} \tag{4-12}$$

So $a(x) = \frac{A_0 e^{2\left(\frac{1+i}{\delta}\right)L}}{e^{2\left(\frac{1+i}{\delta}\right)L}+1} e^{-\left(\frac{1+i}{\delta}\right)x} + \frac{A_0}{e^{2\left(\frac{1+i}{\delta}\right)L}+1} e^{-\left(\frac{1+i}{\delta}\right)x}$ and then

$$h(x,t) = \left(\frac{A_0 e^{2\left(\frac{1+i}{\delta}\right)L}}{e^{2\left(\frac{1+i}{\delta}\right)L}+1} e^{-\left(\frac{1+i}{\delta}\right)x} + \frac{A_0}{e^{2\left(\frac{1+i}{\delta}\right)L}+1} e^{-\left(\frac{1+i}{\delta}\right)x}\right) e^{i\omega t}$$

Generally, $h(x,t)$ is written as follows:

$$h(x,t) = \frac{A_0}{e^{2\frac{L}{\delta}}\cos\left(\frac{2L}{\delta}\right)+1}\left[e^{\frac{2L-x}{\delta}}\cos\left(\frac{2L}{\delta}\right)\cos\left(\omega t - \frac{x}{\delta}\right) + e^{\frac{x}{\delta}}\cos\left(\omega t + \frac{x}{\delta}\right)\right] \tag{4-13}$$

According to the initial condition $h(x,0) = 0.0$, then $a(L) = 0.0$, namely,

$$\frac{A}{B} = -\left(e^{\left(\frac{1+i}{\delta}\right)L}\right)^2 \tag{4-14}$$

From equations (4-8) and (4-13), $\left(e^{\left(\frac{1+i}{\delta}\right)L}\right)^2 = 0.0$, namely, $\cos\left(\frac{L}{\delta}\right) = 0.0$, and then the supplementary constraint is obtained as follows:

$$L = L_n = \left(\frac{1}{2} + n\right)\pi \times \delta, (n = 0, 1, 2, \dots) \tag{4-15}$$

Finally, the linearized analytical hydraulic head for the oscillatory boundary condition case 1 is written as follows:

$$H(x,t) = H_0 + \frac{A_0}{e^{2\frac{L}{\delta}}\cos\left(\frac{2L}{\delta}\right)+1}\left[e^{\frac{2L-x}{\delta}}\cos\left(\frac{2L}{\delta}\right)\cos\left(\omega t - \frac{x}{\delta}\right) + e^{\frac{x}{\delta}}\cos\left(\omega t + \frac{x}{\delta}\right)\right] \tag{4-16}$$

where, $\delta = \sqrt{\frac{2T^*}{\omega\Phi}}$ $L = L_n = \left(\frac{1}{2} + n\right)\pi \times \delta, (n = 0, 1, 2, \dots)$, and L is the length of the domain.

As a result, for a periodic stationary regime as $t \rightarrow \infty$, the result equation (4-16) works with the constraint on the parameter of the problem L, the length of the domain.

For **Case 2** (semi-infinite domain with fixed water level at infinity) the mathematical procedure is similar to that of Case 1, and the corresponding result is obtained as follows:

Case 2: $H(x,t) = H_0 + A_0 e^{-\frac{x}{\delta}} cos\left(\omega t - \frac{x}{\delta}\right)$ (4-17)

4.3.2 Physical interpretation

For **Case 1** (finite domain with reflective boundary at one end) the basic form of the equation (4-13) can also be written as follows

$$h(x,t) = Ae^{-\frac{x}{\delta}} cos\left(\frac{x}{\delta} - \omega t\right) + Be^{+\frac{x}{\delta}} cos\left(\frac{x}{\delta} + \omega t\right) \quad (4\text{-}18)$$

The equation (4-16) indicates that in its propagation domain, the wave is the combination of a forward wave (right wave) and a backward wave (left wave); at the same time, the forward wave amplitude decays and the backward wave amplitude amplifies with on exponential law with respect to the horizontal distance from the fluctuation boundary.

All the terms are explained in detail as follows:

- ➢ $Ae^{-\frac{x}{\delta}} cos\left(\frac{x}{\delta} - \omega t\right)$: forward wave (right wave)
- ➢ $Be^{+\frac{x}{\delta}} cos\left(\frac{x}{\delta} + \omega t\right)$: backward wave (left wave)
- ➢ Phase velocity: $V_\phi = \frac{\omega}{\frac{1}{\delta}} = \omega\delta$
- ➢ Decay length: $\delta = \sqrt{\frac{2T^*}{\omega\Phi}}$
- ➢ Wave length: $\lambda = 2\pi\delta$.

Similarly, when the left boundary condition is given as sinusoidal water level fluctuation and the right condition is given a flux equal to zero, the wave in the propagation domain is also the combination of a forward wave (right wave) and a backward wave (left wave). Meanwhile, for the case that the right boundary condition corresponds to constant water level, the wave in the propagation domain just consists of one progressive wave.

As a result, for the various types of boundary conditions, the forward wave amplitude decays and the backward wave amplitude amplifies exponentially with respect to the horizontal distance from the fluctuation boundary.

4.3.3 Posterior analysis of various effects and limitations (inertial effects, acceleration, erosion)

4.3.3.1 Horizontal maximum acceleration terms and max Reynolds number

According to equation (4-17), Darcy's equation is written as follows:

$$Q_s = -K_s H(x,t) \frac{\partial H(x,t)}{\partial x}$$

Then the Darcy flux density is:

$$q_x = \frac{Q_s}{H(x,t)} = -K_s \frac{\partial H(x,t)}{\partial x} \tag{4-19}$$

And the water flow velocity in the porous media is:

$$V_x = \frac{q_x}{\theta_s} = -\frac{K_s}{\theta s}\frac{\partial H(x,t)}{\partial x} \tag{4-20}$$

According to the equation (4-17), for the boundary conditions of **Case 2**:

$$\frac{\partial H(x,t)}{\partial x} = -\frac{A_0}{\delta} e^{-\frac{x}{\delta}}\left(\cos\left(\omega t - \frac{x}{\delta}\right) + \sin\left(\omega t - \frac{x}{\delta}\right)\right)$$

As $\cos\left(\omega t - \frac{x}{\delta}\right) + \sin\left(\omega t - \frac{x}{\delta}\right) = \sqrt{2}\cos\left(\omega t - \frac{x}{\delta} - \frac{1}{\sqrt{2}}\right)$, then

$$\frac{\partial H(x,t)}{\partial x} = -\frac{A_0}{\delta} e^{-\frac{x}{\delta}}\sqrt{2}\cos\left(\omega t - \frac{x}{\delta} - \frac{1}{\sqrt{2}}\right) \tag{4-21}$$

And accordingly, at the entry boundary ($x = 0$), the maximum horizontal water level gradient is obtained as follows:

$$\left(\frac{\partial H(x,t)}{\partial x}\right)_{max}(0,t) = -\sqrt{2}\frac{A_0}{\delta} \tag{4-22}$$

and then

$$q_{xmax}(0,t) = \sqrt{2}K_s\frac{A_0}{\delta} \tag{4-23}$$

According to the equation (4-20), $V_x(x,t) = -\frac{K_s}{\theta s}\frac{\partial H(x,t)}{\partial x} = \sqrt{2}\frac{K_s}{\theta s}\frac{A_0}{\delta} e^{-\frac{x}{\delta}}\cos\left(\omega t - \frac{x}{\delta} - \frac{1}{\sqrt{2}}\right)$, and so the maximum water flow velocity in the porous media is obtained as follows:

$$V_{xmax}(0,t) = \pm\sqrt{2}\frac{K_s}{\theta s}\frac{A_0}{\delta} \tag{4-24}$$

As a result, the horizontal acceleration is $\gamma = \frac{dv_x(x,t)}{dt} = -\sqrt{2}\omega\frac{K_s}{\theta s}\frac{A_0}{\delta} e^{-\frac{x}{\delta}}\sin\left(\omega t - \frac{x}{\delta} - \frac{1}{\sqrt{2}}\right)$, and so

$$\gamma_{max}(0,t) = \pm\sqrt{2}\frac{K_s}{\theta s}\frac{A_0}{\delta}\omega = \frac{2\pi}{T}V_{xmax} \tag{4-25}$$

4.3.3.2 Analysis and discussion

For the experiment in the small wave canal in the IMFT, the conditions are: physical properties of the sand: $K_s = 1.918e-1\,m/s$, $\theta_s = 0.36\,m^3/m^3$, the oscillatory water level characteristics: $T = 1.95s$, $A_0 = 0.23cm$, and the mean water level $H_0 = water\ depth = 6.1cm$, and then, the following characteristic parameter values can be computed:

$$\delta = \sqrt{\frac{2K_sH_0}{\theta_s}\frac{T}{2\pi}} = 0.142m$$

$$\left(\frac{\partial H(x,t)}{\partial x}\right)_{max} = -\sqrt{2}\frac{A_0}{\delta} = -0.0229$$

$q_{xmax} = \sqrt{2}K_s\frac{A_0}{\delta} = 4.393e-3$ (m^2/s)

$\mathrm{V_{xmax}}(0,\mathrm{t}) = \sqrt{2} \times \frac{1.918\mathrm{e}-1}{0.36} \times \frac{0.0023}{0.142} = \pm 0.0122$(m/s)

$\gamma_{\max}(0,\mathrm{t}) = \frac{2\pi}{\mathrm{T}}\mathrm{v_{xmax}} = \pm\frac{2\pi}{1.95} * 0.0122 = \pm 0.0393$ms^{-2}

$Re_1 = \frac{V_{xmax}d_{sand}}{\nu} = \frac{0.0122\times 2.5e-3}{1.005e-6} = 30.348$ (d=2.5mm)

$Re_1 = \frac{V_{xmax}d_{sand}}{\nu} = \frac{0.0122\times 1.8e-3}{1.005e-6} = 21.851$ (d=1.8mm)

$Re_1 = \frac{V_{xmax}d_{sand}}{\nu} = \frac{0.0122\times 1.8e-3}{1.005e-6} = 9.711$ (d=0.8mm)

$Re_2 = \frac{q_{xmax}\sqrt{k_{Darcy}}}{\nu} = \frac{4.393e-3\times\sqrt{19.649e-9}}{1.005e-6} = 0.613$

$(1-\theta_s)\frac{\rho_s-\rho_w}{\rho_w} = (1-0.36)\frac{2.65-1.0}{1.0} = 1.056$

Analysis and discussion of the above results:

(1) The horizontal maximum acceleration $\gamma_{\max} = 0.0393$ms^{-2} is much smaller than the gravity acceleration g=9.81ms^{-2};

(2) Since the mean diameter of the sand is about 2.5mm, the mean Reynolds number of the oscillatory flow in the open water at the entry boundary is much bigger than 10, while the Reynolds number of the oscillatory flow in the porous media at the entry boundary is equal to 0.613, much smaller than 10.

(3) The key question remains: what is the criteron for the initial erosion?

4.4 Numerical simulations of wave propagation in the sandbox

4.4.1 Numerical simulation with vertically hydrostatic Boussinesq model

- **Simulation domain**

Simulated length: Lx=0.05m;

Grid size: dx=0.0001m, dy=0.0001m.

- **Initial condition**

Initial water head: $H_{In} = 0.2m$

- **Boundary condition**

Left boundary: $H(0,t) = H_0 + a_0 sin(\omega t)$ with $a_0 = 0.1m = H_0 \times 50\%$ and $T = 0.2s$

Right boundary: $H(L,t) = H_0$ (water level=constant)

- **Physical properties of the porous media**

$\theta_s = 0.2\, m^3/m^3$, K_s =1.0E-3(m/s)

- **Duration of the simulation and numerical parameters**

We have modeled 3 periods: t=3T=0.6s. The numerical caculation time parameters and the numerical criteria are shown in **Table 4-2.**

Table 4-2 Numerical parameters (INPUT1) for the calculation of time step, non-linear/outer (Picard) and linear/inner iterations

Time step	Intial time step	DTIN=0.0001s
	Minimum time step	DTMIN=0.0001s
	Maximum time step	DTMAX=0.001s
	Time step multifier	DTMUL=1.2
No-linear iterations (Picard)	Convergence criterion of pressure head	ENLH3=1.0E-4
	Maximum number of no-linear iteration	INLMAX=10
Linear iterations	Convergence criterion of pressure head	ENORM3=1.0E-6
	Maximum number of linear iterations	ITEND=800

- **Numerical behaviour of Bigflow during the simulation**

The evolution of the total net discharge entering or outgoing by all the faces of the domain Q_{Bound} and the evolution of the discharge corresponding to the change in volume of water inside the domain during the time interval DT Q_{Mass} have been watched, as seen in the **Fig. 4-7**. The evolution of the net volume of water entered or exited through all the sides of the field since the beginning of the simulation V_{Bound} (accumulative), and the evolution of the volume of water that has formed or that disappeared within the area since the beginning of the simulation V_{MASS} (accumulative) have also been watched, as seen in the **Fig. 4-8** . In the **Fig. 4-7**, the evolution of Q_{Mass} completely superimposes on the evolution of Q_{Mass}. In the **Fig. 4-8**, the evolution of V_{Bound} coincides very well with the evolution of V_{Mass}.

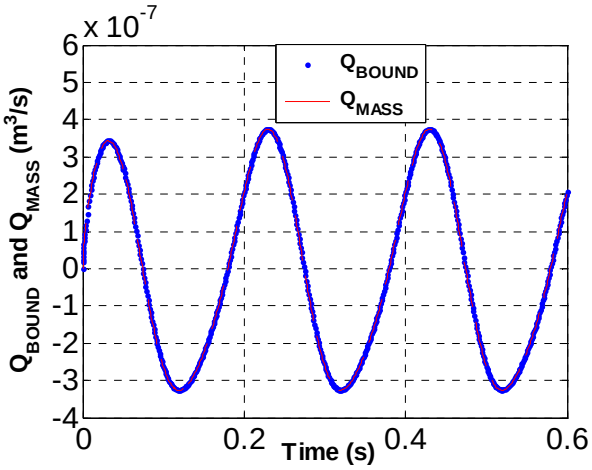

Fig. 4-7 Evolution of Q_{Bound} and Q_{Mass}

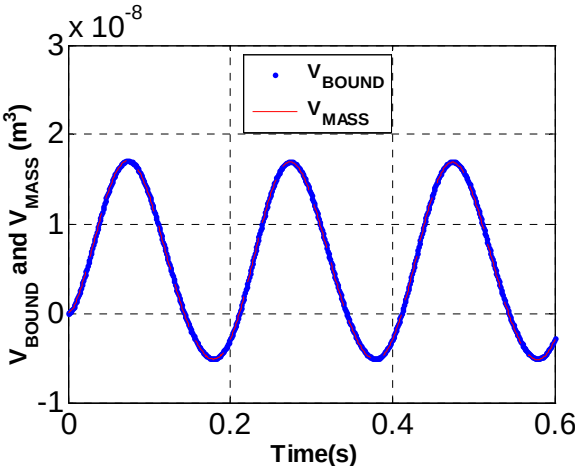

Fig. 4-8 Evolution of V_{Bound} and V_{Mass}

It is clearly observed that the evolution of Q_{Mass} and Q_{Bound} and the one of V_{Bound} and V_{Mass} has the same period with that of the left entry water level fluctuation.

4.4.2 Comparisons of the numerical results and analytical solution

The numerical and the corresponding analytical transient profiles of water height $H(x,t)$at time t = T/4, T/2, 3T/4 and T are shown in the **Fig. 4-9** ((a): analytical; (b) numerical) and **Fig. 4-10**. In spite of a few differences, the main features are the same for the linear/nonlinear solutions; in particular, it can be seen that the decay length of the progressive wave (progressing to the right) is on the same order or even smaller than its wavelength.

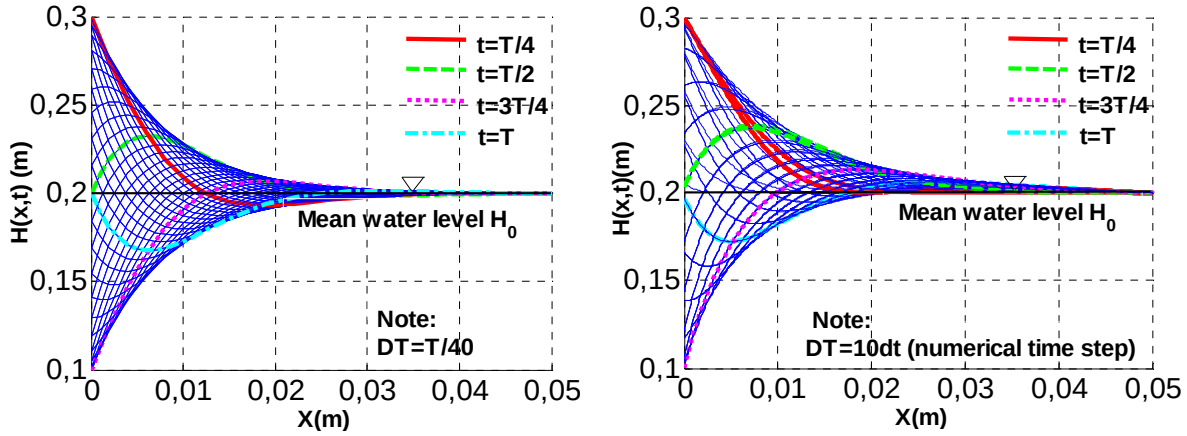

(a) Analytical (b) Numerical (Bq model)

Fig. 4-9 Transient profiles of water height $H(x,t)$ at time t = T/4, T/2, 3T/4 and T, where T (0.2s) is the period of the water level imposed at the left boundary. Note: the amplitude of boundary oscillations is 50% of the mean water depth H_0 and H_0=0.2m.

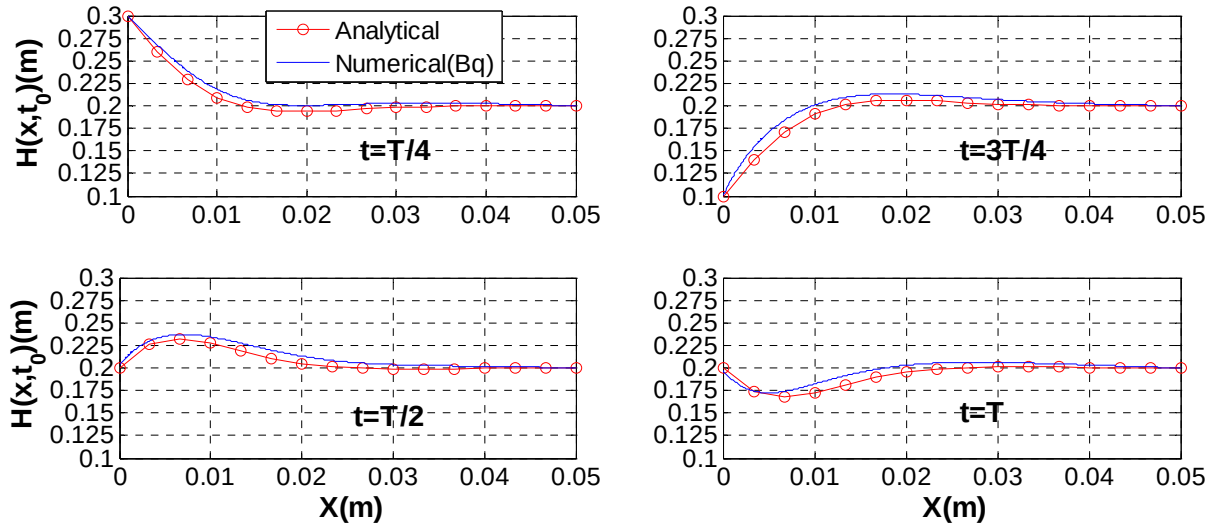

Fig. 4-10 Water level profile $H(x,t_0)$ at t_0=T/4, T, 3T/4 and T: response to oscillations at left in the case: H_0=0.2m, A_0/H_0=0.5, K_s=1.0E-3m/s, θ_s =0.2m^3/m^3 and $T=0.2s$.

In addition, from the evolution of the water level $H(x_0,t)$ at $x_0=\delta/2$=0.004m shown in **Fig. 4-11**, it can be seen that the numerical water level agrees very well with the analytical one, and the biggest differences always appear at the minimum values of the analytical water level.

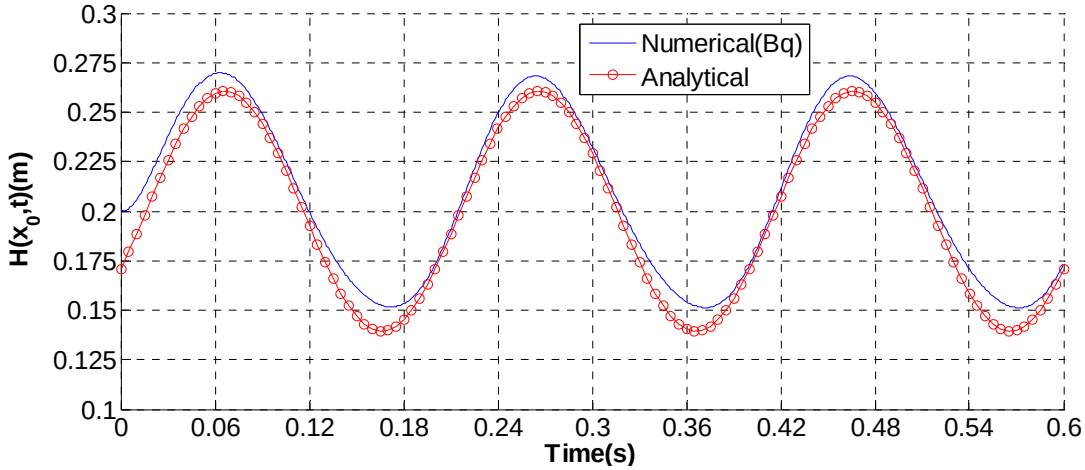

Fig. 4-11 Evolution of water level $H\left(x_0,t\right)$: response to oscillations at $x_0=\delta/2$=0.004m, where δ is the wave decay length.

4.5 Analysis of the maximum error of analytical results

4.5.1 Introduction and definition of maximum errors

The linear equation can be solved by a simple algebraic operation, while the non-linear equation cannot be solved by algebraic operations and only can be solved by a complicated numerical method with a great number of iterations. Therefore, lots of non-linear problems are usually linearized and applied widely to solve the real problems. However, due to the linearization of the equation, the analytical only well agrees with the numeric within a certain range. Therefore, the establishment of an error criterion and the study of the applicable range are very important.

In this section, the maximum relative error equation is built up. The maximum errors of the analytical results for the boundary condition case 3 will be investigated by comparing the corresponding numerical results with 2D Boussinesq model.

Two error formulas are proposed to analyser the errors of the analytical water head: one is the absolute value of the difference of the numerical hydraulic head and the corresponding analytical hydraulic head relative to the average water depth, namely,

$$\varepsilon_{Max1}=\max_{t\in[t,tmax]}\frac{\left|H_{Numerical}(t)-H_{analytical}(t)\right|}{H_0} \tag{4-26}$$

and the other one is the absolute value of the difference of the numerical hydraulic head and the corresponding analytical hydraulic head relative to the amplitude of the fluctuation, namely,

$$\varepsilon_{Max2}=\max_{t\in[t,tmax]}\frac{\left|H_{Numerical}(t)-H_{analytical}(t)\right|}{A_0} \tag{4-27}$$

4.5.2 Calculation and analysis of the maximum errors on water levels

4.5.2.1 Numerical simulations for assessing the maximum errors

In total, 12 cases of numerical simulations have been modelled to calculate the analytical maximum errors. It is noted that in each case, according to the ratio A_0/H_0, 9 sub-cases have been all modelled . In each case, the limit condition of the periodic fluctuation of the cosine on the left boundary is identically imposed, except changing the average hydraulic head H_0, or the amplitude $A_0$of the fluctuation, or the period T. That is to say, on the left boundary, the imposed entry water level fluctuation is $H(0,t) = H_0 + a_0 cos\left(\frac{2\pi}{T}t\right)$. In addition, on the right boundary, uniform head is imposed to be equal to H_0 and the initial condition is also a uniform head equal to H_0.

During the simulations, the instantaneous spatial distributions of the water level $H(x,t_0)$ in the x direction indicate that the wave decay length δ has an important influence on the propagation distance of the fluctuation put on the left boundary. At the position with the distance of about 6δ from the fluctuation boundary, the total flux of the right boundary is about 1.0E-7m/s. Therefore, in the each simulation case, the simulated length is taken to be equal to 6δ, which means that the calculated domain varies with respect to the wave decay length δ.

According to the analytical equation (4-17) for the analytical case 3, the amplitude of the propagation of the fluctuation in the porous media decays with the coefficient of the exponential negative index, namely $a_0 e^{-\frac{x}{\delta}}$, and therefore $dx < \delta/10$ for each simulation.

The maximum time step is taken as $DT_{Max} = T/200 \ll T$, the initial time step $DT_{In} = T/2000$ and the minimum time step $DT_{Min} = DT_{In} = T/2000$.

Here, it is worthy noted that the calculation maximum time interval have not only a very important influence on the numerical calculation precision, but also on the visualisation of the propagation of the fluctuation. The distance interval mainly plays a great role in the visualisation of the fluctuation propagation.

In addition, it has been set that the convergence criteria of the non-linear iteration S=1.0E-4 and the max number of non-linear iterations=15, while the convergence criteria of linear iterations=1.0E-6, and the max number of linear iterations=500.

The main parameters of the simulated cases are listed in the **Table 4-3**.

Table 4-3 Main parameters for the cases of the numerical simulations

Cases	T (s)	K (m/s)	H_0 (m)	Φ (m^3/m^3)	δ (m)	$L = 6\delta$ (m)
1	0.2	1.00E-03	0.2	0.20	0.0080	0.0479
2	10	1.00E-03	0.2	0.20	0.0564	0.3385
3	0.2	1.00E-03	0.5	0.20	0.0126	0.0757
4	0.2	1.00E-03	10	0.20	0.0564	0.3385
5	10	1.00E-03	10	0.20	0.3989	2.3937
6	3600	1.00E-03	10	0.20	7.5694	45.4163
7	3600	1.00E-05	10	0.20	0.7569	4.5416
8	3600	1.00E-03	10	0.20	5.3524	32.1142
9	3600	1.00E-03	1	0.40	2.3937	14.3619
10	43200	1.00E-03	3	0.20	14.3619	86.1714
11	43200	1.00E-03	5	0.20	18.5411	111.2468
12	43200	1.00E-03	10	0.20	26.2211	157.3268
N.B.	Each case includes the 9 sub-cases: A_0/H_0=0.1,0.2,0.3,0.4,0.5,0.6,0.7,0.8 and 0.9.					

4.5.2.2 Time of occurrence of the maximum errors

From the above, we know that the maximum errors between the analytical and the numerical results always appear at the moment when the analytical hydraulic head reaches the minimum. Therefore, the time of the appearance of the maximum errors can be obtained by taking the derivative of the analytical equation with respect to the time t. The result of the derivative indicates that the time is a function of the position x, that is to say, the maximum error at the different position x occurs at the different time. As a result, the time of the maximum error is

$$t_{\varepsilon_{max}} = \frac{x}{\delta\omega} + \frac{T}{2} + T \times i (i = 1, 2, \dots) \tag{4-28}$$

4.5.2.3 Maximum errors of analytical versus numerical water levels (results)

After the minimum analytical hydraulic head are calculated with the analytical equation (4-17) , and at the same time, the numerical hydraulic head at the corresponding time of the minimum analytical water head are found, the maximum relative errors can be obtained with the error formula (4-26) and the error formula (4-27) .

The profiles of the distribution of the maximum relative errors of the analytical water heads to the corresponding numerical values with the horizontal distance and the ratio of the amplitude to the mean water depth A_0/H_0 for all the simulated cases are plotted to observe the results.

The distribution of the maximum relative error with the x and the ratio A_0/H_0 for the numerical case 1 with the error formula (4-26) and the one with the error formula (4-27) are respectively illustrated in **Fig. 4-12** (a) and **Fig. 4-13** (a).

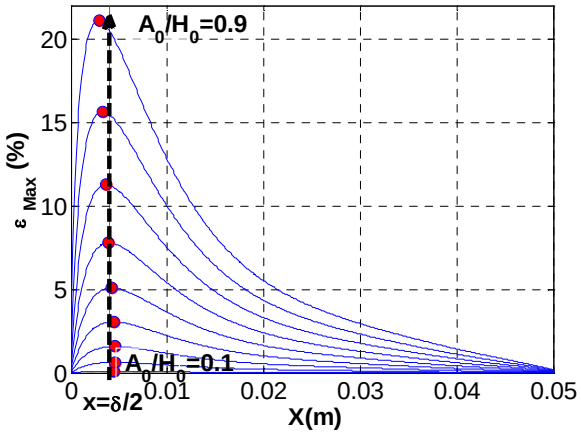

(a) $\varepsilon_{Max}(A_0/H_0, x)$

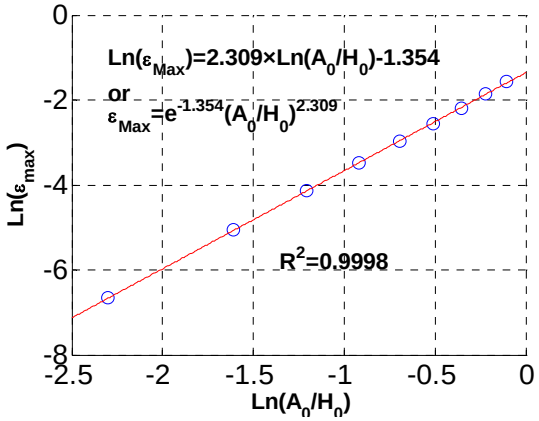

(b) $\varepsilon_{Max}(A_0/H_0)$

Fig. 4-12 Profile of the distribution of the maximum relative error $\varepsilon_{Max}(A_0/H_0, x)$ and the relationship curve of the ε_{Max} with respect to dimensionless parameter A_0/H_0 with the formula 1 for the numerical case 1:
$H_0 = 0.2m$, $T = 0.2s$, $\Phi = 0.2\,\mathrm{m}^3/\mathrm{m}^3$, $K = 1.0E-3m/s$, $\delta = 0.008m$, $L_x = 0.05m \approx 6\delta$, $t_{Max} = 3T$
A_0/H_0=0.1, 0.2, 0.3, 0.4, 0.5, 0.6, 0.7, 0.8, 0.9.

N.B.: $\varepsilon_{Max1} = \max_{t\in[t,tmax]} \dfrac{\left|H_{Numerical}(t) - H_{analytical}(t)\right|}{H_0}$

The corresponding relationship curve of the maximum error ε_{Max} with respect to dimensionless parameter A_0/H_0 for the numerical case 1 with the formula 1 and the one with the formula 2 are respectively shown in **Fig. 4-12** (b) and **Fig. 4-13** (b).

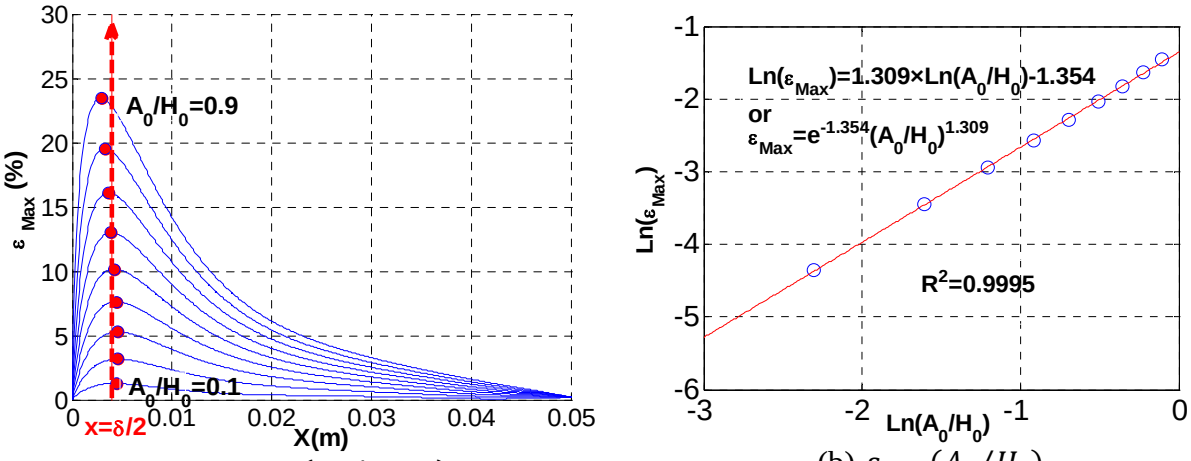

(a) $\varepsilon_{Max}(A_0/H_0, x)$ (b) $\varepsilon_{Max}(A_0/H_0)$

Fig. 4-13 Profile of the distribution of the maximum relative error $\varepsilon_{Max}(A_0/H_0, x)$ and the relationship curve of the ε_{Max} with respect to dimensionless parameter A_0/H_0 with the formula **2** for the numerical case 1:

$H_0 = 0.2m$, $T = 0.2s$, $\Phi = 0.2\mathrm{m}^3/\mathrm{m}^3$, $K = 1.0E-3m/s$, $\delta = 0.008m$, $L_x = 0.05m \approx 6\delta$, $t_{Max} = 3T$

A_0/H_0=0.1, 0.2, 0.3, 0.4, 0.5, 0.6, 0.7, 0.8, 0.9.

N.B.: $\varepsilon_{Max2} = \max_{t\in[t,tmax]} \dfrac{\left|H_{Numerical}(t) - H_{analytical}(t)\right|}{A_0}$

It is found that: (1) the maximum errors always appear at around the position of $x = \delta/2$; (2) the maximum errors have no relationship with the decay length δ and they stay constant with the increasing of δ; (3) the maximum errors have a good relationship with the ratio of the amplitude to the mean water depth A_0/H_0.

Therefore, we suppose that:

$$\varepsilon_{Max} = \beta\left(\frac{A_0}{H_0}\right)^{\alpha} \tag{4-29}$$

Then the coefficients α and β are obtained with the Basic Fitting of Matlab tool. They are respectively: $\alpha_1 = 2.309$ and $\beta_1 = e^{-1.354}$ for the maximum errors with the error formula (4-26) and $\alpha_2 = 1.309$ and $\beta_2 = e^{-1.354}$ for the error formula (4-27).

As a result, we obtain:

$$\varepsilon_{Max1} = e^{-1.354}\left(\frac{A_0}{H_0}\right)^{2.309} \tag{4-30}$$

And

$$\varepsilon_{Max2} = e^{-1.354}\left(\frac{A_0}{H_0}\right)^{1.309} \tag{4-31}$$

It can be seen that equations (4-30) and (4-31) have the same coefficient β.

4.5.3 Applicable range of the analytical solution

If the maximum relative error of the analytical and the numerical water head can't be greater than 10%, the corresponding ratios of the amplitude to the mean water depth A_0/H_0 can be obtained with the equation (4-30) and (4-31) for the two error formulas:

$$0.0 \leq \frac{A_0}{H_0} \leq 0.66 \text{ if } \varepsilon_{Max1} \leq 10\% \quad (4\text{-}32)$$

$$0.0 \leq \frac{A_0}{H_0} \leq 0.48 \text{ if } \varepsilon_{Max2} \leq 10\% \quad (4\text{-}33)$$

It can be seen that the error formula (4-26) is more strict than the error formula (4-27).

4.6 Conclusion

In this chapter, three approaches: a laboratory experiment, an analytical solution, and numerical simulations have respectively been used to investigate the wave propagation in a sandbox with vertical boundary.

A small "Darcy-scale" experiment has been conducted in a water wave canal at IMFT. In this experiment, two pressure sensors and one capacitive sensor have been tested. The capacitive sensor developed by the IMFT laboratory was chosen to measure the water level fluctuations in the vertical sandbox, considering two important factors: the size of the sandbox, and the sensitivity of the sensor with respect to short period fluctuations.

Based on the analytical study of the plane flow problem (see further below), the assumption is made that the amplitude of fluctuations decays exponentially with distance, which has been well verified by the measured water level fluctuations, and accordingly, the saturated hydraulic conductivity of the sand in the sandbox in the wave canal of IMFT has been obtained. The estimated value $K_s = 1.918 \times 10^{-1} m/s$ is 5-10 times larger than the ones obtained by the formulas of Kozeny-Carman for the mean diameter d=1.8mm, which may be due to hydro-mechanical interactions or to other neglected effects (vertical velocities, capillary effects).

The linearized solutions of the one dimensional nonlinear equation of Dupuit-Boussinesq for the saturated plane flow with a free surface has been obtained for 2 cases of boundary conditions: on the left boundary, it is respectively imposed the periodic water level fluctuations of the sine wave and cosine wave; on the right boundary, it is respectively imposed zero flux and the constant water level.The linearized solutions indicate that:

- for the case with the right boundary of zero flux, the wave in its propagation domain in the porous media is the combination of a forward wave (right wave) and a backward wave (left wave), while for the case with right boundary of constant water level, the wave in the propagation domain is just consisted of one progressive wave (forward wave);
- for 2 cases of boundary condition, the amplitude of the forward wave decays and the one of the backward wave amplifies by the exponential law with respect to the horizontal distance from the fluctuation boundary.

In addition, the criterion for the erosion at the interaction boundary: porous media/ open water with the forced entry water level fluctuation is always an open question to be discussed.

An example of the analytical case 2 (boundary condition case 2) has been simulated with vertically hydrostatic Boussinesq model. In this example, the fluctuation characteristics parameter: the ratio of the fluctuation amplitude to the water depth is taken as 0.5. The compared results of the simulated water heads and the corresponding analytical values demonstrate that:

- in spite of a few differences, the main features are the same for the linear/nonlinear solutions, and in particular, the decay length of the progressive wave (progressing to the right) is on the same order or even smaller than its wavelength;
- the evolution of the simulated water level agrees very well with that of the analytical one, and the biggest differences of the water heads always appear at the minimum values of the analytical water levels.

Two error formulas have been built up to analyze the errors of the analytical water head: one is the absolute value of the difference of the numerical hydraulic head and the corresponding analytical hydraulic head relative to the average water depth, and the other one is the absolute value of the difference of the numerical hydraulic head and the corresponding analytical hydraulic head relative to the amplitude of the fluctuation. Through the comparisons of the analytical solutions with the boundary case 2 and the corresponding simulated water heads for 12 numerical cases, it has been obtained:

- The maximum errors of the analytical water head always appear at the time when the analytical hydraulic head arrives at the minimum and the corresponding time is the function of the position x;

- The maximum errors of the analytical water head always appear at around the position of $x = \delta/2$ and they have nothing related with the decay length δ;
- The maximum errors of the analytical water head are the power functions with respect to the ratio of the amplitude to the mean water depth A_0/H_0, with a same coefficient for the two maximum errors formulas, and they are:

$$\varepsilon_{Max1} = \max_{t\in[t,tmax]} \frac{|H_{Numerical}(t) - H_{analytical}(t)|}{H_0} = e^{-1.354}\left(\frac{A_0}{H_0}\right)^{2.309}$$

$$\varepsilon_{Max2} = \max_{t\in[t,tmax]} \frac{|H_{Numerical}(t) - H_{analytical}(t)|}{A_0} = e^{-1.354}\left(\frac{A_0}{H_0}\right)^{1.309}$$

- For maximum errors lower than 10%, A_0/H_0 must be less smaller than 0.66 with the maximum error formula 1 (ε_{Max1}), and while the maximum ratio of A_0/H_0 is 0.48 with the maximum error formula 2 (ε_{Max2}). This means that the error of formula 2 is more strict than the error of formula 1. The analytical hydraulic head is in a very good agreement with the numerical result when $A_0/H_0 \leq 0.48$.

For the numerical simulation, the decay length δ has an important influence on the propagation length of the fluctuation on the limit boundary. The simulation length should be greater than or equal to 6δ, and otherwise, due to the influence of the fixed hydraulic head on the opposite boundary, the distribution of the space and the value of the maximum error will both change.

The existing problems for the analytical solution are the following:

- the initial error of all results are always very big;
- when $A_0/H_0 > 0.5$, the maximum errors are greater than 10%.

In general, the non-linear analytical solution will be better than the linear analytical solution for the non-linear problem, and maybe it will be able to solve the existing problem. In fact, the asymptotic method of Polubarinova has been tried, but the results have not been completely analyzed and so they are not used here. Other non-linear methods should be investigated in order to improve on the analyses of the nonlinear Boussinesq equation in the presence of fluctuations (other effects like bottom slope).

Chapter 5: Water level measurements in a sandy beach: the Barcelona wave canal experiment

5.1 Introduction

Beach groundwater interacting with tides, waves and swash is a complex and dynamic system. Groundwater fluctuations driven by oceanic oscillations enhance water exchange between the ocean and coastal aquifer. Interaction between swash dynamics and groundwater may also be important with regard to onshore sediment transport and beach profile evolution. There is currently limited understanding of how the beach groundwater system responds to oceanic forcing at various frequencies. Especially, models of water table response to wave forcing are less developed and require verification, and relatively few studies have reported simultaneous measurements of beach groundwater and swash. Improved predictions of swash zone sediment transport and beach profile evolution cannot be achieved unless the beach groundwater are better understood (Horn, 2006 [19]).

A “wave-beach” experiment was conducted in a large water wave canal equipped with a wave generator (CIEM flume in Barcelona). The experiment was part of a European project, HYDRALAB-SANDS, undertaken in collaboration between the HYDRALAB laboratory in Barcelona (Spain) and the OTE group of IMFT laboratory (Toulouse, France). The experiment was initially designed to measure the erosion of the swash zone in a sandy beach, with periodic water level oscillations.

This work focuses on a related problem, namely, the effect of surface water waves and swash zone phenomena on subsurface oscillations in the sandy porous medium, and the possible interactions between surface and subsurface oscillations. In this experiment, water level fluctuations H(t) in the sloping sandy beach were measured by 7 capacitive sensors ($H_i(t)$ indicates the water level fluctuations measured by the i-th sensor).

5.2 Laboratory experiment: sloping sand beach in wave canal (Hydralab Barcelona)

5.2.1 Experiment description and methodology

5.2.1.1 Infrastructure

The wave canal is 100m long, 3m wide and 5m high. At the back end of the canal, we have designed a mechanical wave generator ("batteur") with adjustable period and amplitude. The schema of the infrastructure of the wave canal is showed in **Fig. 5-1**.

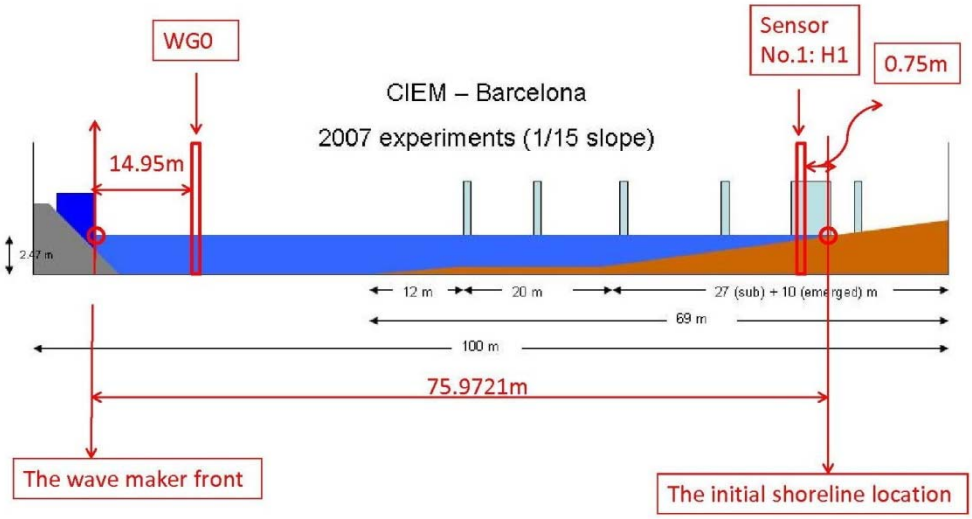

Fig. 5-1 Schema of the infrastructure of the wave canal

5.2.1.2 Sediment characteristics

In this experiment, we have considered the erosion of the sand-bed (beach). The mean diameter d_{50} of the sand is about 0.20 mm. The grain size distribution is shown in **Fig. 5-2** and in **Table 5-1**. The sample statistics of the sand are listed in **Table 5-2**. The grain size distribution and the sample statistics of the sand have been provided by Spanish group. In addition, the beach has a slope of 1/15.

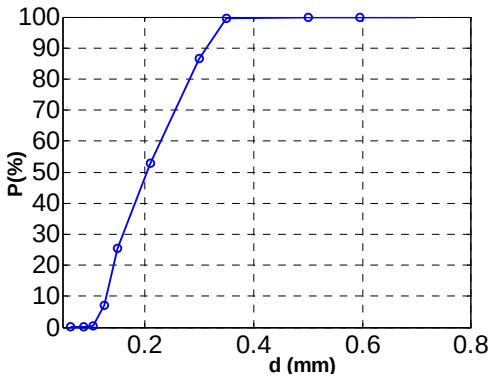

Fig. 5-2 Sand size distribution of the sediments

Table 5-1 Grain size distribution

50-60			
Total Weight	199,192		
Sieve (mm)	**Weight**	**%**	
0.710	0.020	0.010%	0.010%
0.595	0.027	0.014%	0.024%
0.500	0.668	0.336%	0.360%
0.350	26.006	13.093%	13.453%
0.300	66.983	33.723%	**47.175%**
0.210	54.242	27.308%	**74.484%**
0.149	36.515	18.384%	92.867%
0.125	13.070	6.580%	99.447%
0.105	0.738	0.372%	99.819%
0.088	0.240	0.121%	99.940%
0.063	0.050	0.025%	99.965%
Remainder	0.070	0.035%	100.000%
	198.629		

Table 5-2 Sample statistics

SIEVING ERROR: 0,0% **SAMPLE STATISTICS**

SAMPLE IDENTITY: **50-60** ANALYST & DATE: ,

SAMPLE TYPE: Trimodal, Moderately Well Sorted TEXTURAL GROUP: Sand

SEDIMENT NAME: Moderately Well Sorted Fine Sand

	µm	ϕ
MODE 1:	327,5	1,616
MODE 2:	231,0	2,119
MODE 3:	165,0	2,605
D_{10}:	154,4	1,426
MEDIAN or D_{50}:	245,8	2,024
D_{90}:	372,3	2,695
(D_{90} / D_{10}):	2,411	1,891
(D_{90} - D_{10}):	217,9	1,270
(D_{75} / D_{25}):	1,871	1,573
(D_{75} - D_{25}):	156,0	0,904

GRAIN SIZE DISTRIBUTION

GRAVEL: 0,0%	COARSE SAND: 0,4%
SAND: 100,0%	MEDIUM SAND: 46,8%
MUD: 0,0%	FINE SAND: 52,3%
	V FINE SAND: 0,5%
V COARSE GRAVEL: 0,0%	V COARSE SILT: 0,0%
COARSE GRAVEL: 0,0%	COARSE SILT: 0,0%
MEDIUM GRAVEL: 0,0%	MEDIUM SILT: 0,0%
FINE GRAVEL: 0,0%	FINE SILT: 0,0%
V FINE GRAVEL: 0,0%	V FINE SILT: 0,0%
V COARSE SAND: 0,0%	CLAY: 0,0%

	METHOD OF MOMENTS			FOLK & WARD METHOD		
	Arithmetic	Geometric	Logarithmic	Geometric	Logarithmic	Description
	µm	µm	ϕ	µm	ϕ	
MEAN ($\bar{x}$):	266,6	251,7	1,990	241,7	2,049	Fine Sand
SORTING (σ):	83,87	1,401	0,486	1,415	0,501	Moderately Well Sorted
SKEWNESS (Sk):	0,089	-0,372	0,372	-0,066	0,066	Symmetrical
KURTOSIS (K):	2,191	2,011	2,011	0,678	0,678	Platykurtic

5.2.1.3 Instrumentation

Before the experiment, the 7 capacitive sensors had been calibrated in the IMFT laboratory, as shown in **Fig. 5-3**.

Fig. 5-3 Calibration of the capacitive sensors of the groundwater level for the Barcelona experiment

As mentioned in Chapter 4, electric voltage output signal corresponding to the capacitance of the sensor has a linear relationship with the measured water level:

$$U(volt) = A \times H + B \tag{5-1}$$

Where, U is the electric voltage output signal, H is the measured water level, A is the slope of the linear line and B is its intercept.

After measuring a series of water levels and the corresponding electric voltage output signals, by the linear line fitting, the coffficients A and B can be obtained. The coefficients A and B obtained in the static clear water at IMFT are showed in **Table 5-3**.

Table 5-3 Coefficient values of the linear relationship between the voltage output signal and the measured water level in the static clear water for seven capacitive sensors

Coefficients	Capacitive sensors						
	No.1	No.2	No.3	No.4	No.5	No.6	No.7
A	0.0643	0.0579	0.0609	0.0661	0.068	0.0689	0.0783
B	-0.2429	0.0042	-0.132	-0.3199	-0.3551	-0.4078	-0.5078

In the Barcelona experiment, the reference water level or base water level is different from the one in IMFT, and the static water level or initial water level 2.47m has been chosen as the base water level. Due to this, the coefficients B for all the sensors had changed, and the new coefficients B for the experiment are showed in **Table 5-4**. Considering about the sensitivity of the capacitive sensor, the coefficients B were recalibrated for all the sensors before the test of each day, even though the initial water level of each day was always kept the same 2.47m

Table 5-4 Coefficient values of the linear relationship between the voltage output signal and the measured water level in Barcelona wave canal for seven capacitive sensors

Test date	Coefficients	Capacitive sensors						
		No.1	No.2	No.3	No.4	No.5	No.6	No.7
12/03/2008	B	1.4440	1.4140	0.9120	1.5430	1.2070	1.2070	1.3140
13/03/2008	B	1.4320	1.4140	0.9120	1.5430	1.2070	1.2070	1.3140
14/03/2008	B	1.4130	1.4180	0.9268	1.5700	1.2320	1.2320	1.3225
17/03/2008	B	1.3940	1.3940	0.9130	1.5210	0.8931	0.6477	0.4700
18/03/2008	B	1.3940	1.3840	0.9225	1.5310	0.8931	0.6477	0.4700
19/03/2008	B	1.3940		1.6290	1.4740	0.8833	0.6281	0.4700
20/03/2008	B	1.3940		1.6290	1.4740	0.8833	0.6281	0.4700
All the tests	A	0.0643	0.0579	0.0609	0.0661	0.068	0.0689	0.0783

Note:
Sensor No.2 had fallen down in the wave canal since the local serial 8 test carried on the 18 March 2009.

As shown in **Fig. 5-4** and **Fig. 5-5 Fig. 5-5**, 7 capacitive sensors were installed at regular intervals of about 1.5 m in the beach in order to measure groundwater level fluctuations. In particular, one sensor (No.1) was placed near the still water / beach boundary to measure the water level fluctuations corresponding to the entry condition of the model.

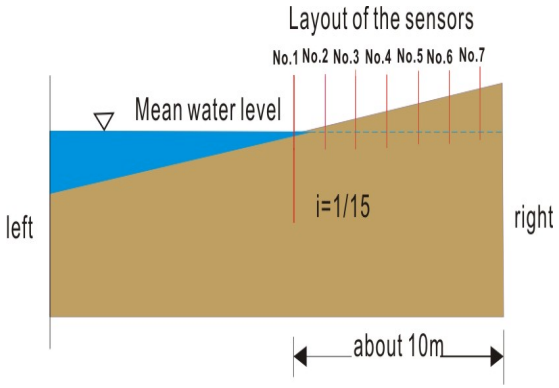

Fig. 5-4 Schematic of the layout of the capacitive sensors in the swash zone (vertical axial section). Sensor N°1 is closest to the free water.

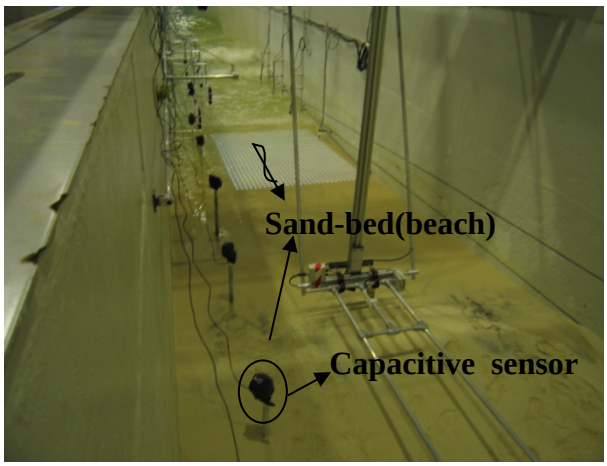

Fig. 5-5 Sand beach with capacitive sensors / micro-piezometers at the HYDRALAB-SANDS wave canal (CIEM flume) in Barcelona. Incoming water waves are visible in the rear.

In addition to these 7 piezometers, there were 14 other pressure sensors installed in the canal by the Barcelona group (I. Caceres, J. Alsina, et al.). These 14 sensors measure the free water level fluctuations in the canal's open water system (upstream of the swash zone). The horizontal distances are listed in **Table 5-5** (as provided by the Barcelona group). The reference point is the wave maker front, located at the left end of canal. The relative

horizontal distance of sensor No.1 " H_1 " (the "entry" point at the still water / beach boundary) is 75.222 m with respect to the wave maker position.

Table 5-5 Position of the 14 sensors for the free water level fluctuations from the wave generator front to the swash zone

Sensor	WG0	WG1	WG2	WG3	WG4	WG5	WG6
X (m)	14.95	15.71	16.66	17.39	24.91	37.91	43.41
Y (m)	0.65	0.65	0.65	0.65	0.65	0.65	0.65
Sensor	WG7	WG8	WG9	WG10	WG11	WG12	WG13
X (m)	49.19	55.08	58.04	61	63.93	66.86	68.61
Y (m)	0.65	0.65	0.65	0.65	0.65	0.65	0.65
Note: The zero point of X is the wave maker front, as seen in Fig. 1.							

5.2.1.4 Wave condition of the wave generator

The larger amplitude of all wave time series is around 0.9 m for erosive conditions of the swash zone of the sloping beach. The period of the wave generator is about 4 seconds.

The wave generator produces a non-harmonic wave of the "JONSWAP" type. **Fig. 5-6** (**a)** and **(b)** shows the water level signal at sensor WG_0 (15m from the wave maker front as shown in **Fig. 5-1**. The Fourier spectrum of this signal is shown in **Fig. 5-7**.

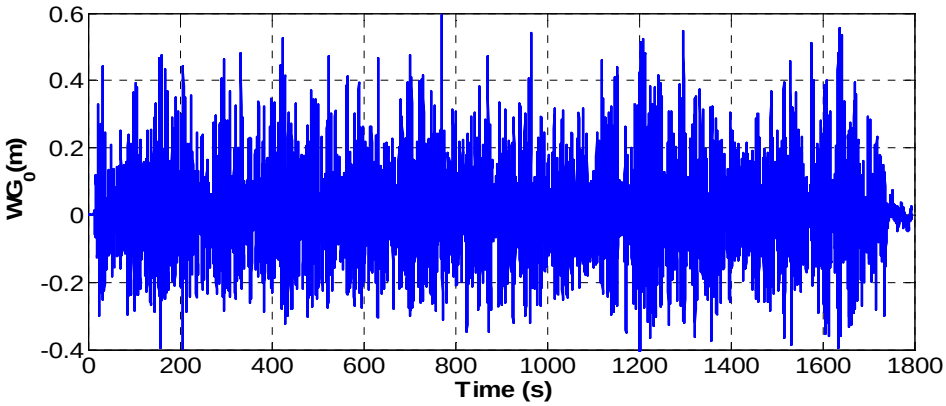

(a): t=0-1800s

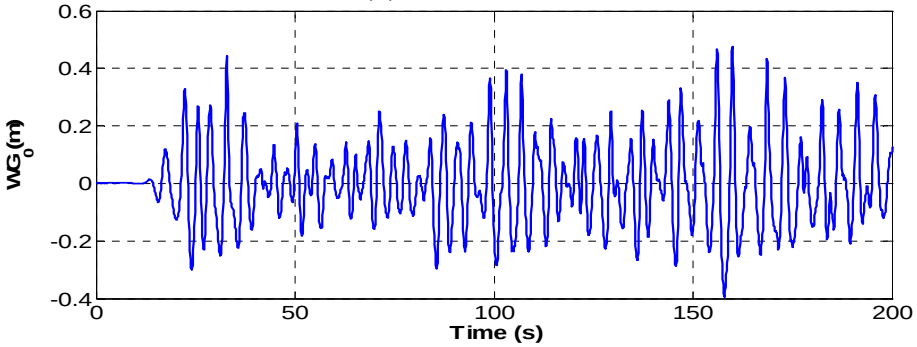

(b): t=0-200s

Fig. 5-6 (a) (b) Evolution of the free water level fluctuation $WG_0(t)$ (15m right from the wave maker front).

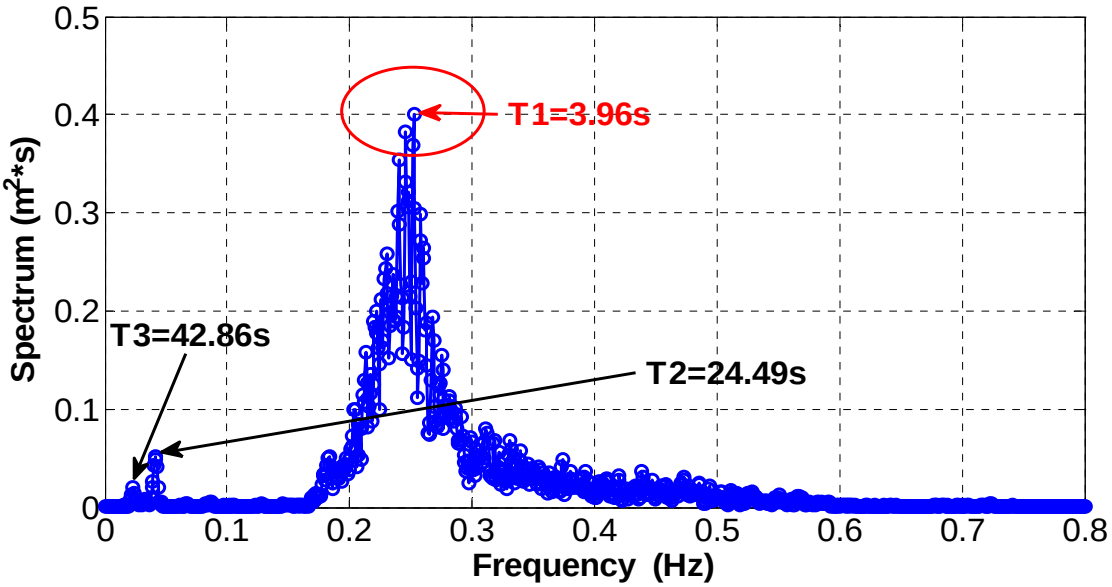

Fig. 5-7 Fourier spectrum of *WG0(t)* (t = 0-1800 s, $\tau_{Tuckey} = 600s$).

It can be observed from both figures that the wave maker signal WG_0 has one most dominant period, which is about 4 s (T1 = 3.96 s) and close to the originally designed period (4 s) of the wave maker. The temporal zoom in **Fig. 5-6 (b)** exhibits the appearance of low frequency "beats", similar to acoustic beats due to the interference of two very close frequencies. Looking at the spectrum of **Fig. 5-7** seems to confirm indeed that there are two dominant frequencies that are close enough to interfere (around period T1 = 3.96 s).

The spectral characteristics of water levels along the canal (and also in the beach) can be seen in **Fig. 6-18**, which will be discussed later in section **6.5.3.3.**

5.2.1.5 Carried tests

The time required to reproduce the wave time series is around 30 minutes for erosive conditions. We began to measure the groundwater levels before the wave time series and finished measuring after the wave time series for each test. In all, we have done 39 tests to measure the groundwater level fluctuations in the sloping sandy beach.

All the carried tests and the corresponding test time are shown in **Table 5-6**.

Table 5-6 All the carried tests in the Barcelona wave canal

Test date	Test name	Number of the test series		Start time of the series(time of the PC)
		local	total	
12/03/2008	Ht-SIGN6-TotalSerial1-LocalSerial1-120308.dat	1	1	20:04:54.84
13/03/2008	Ht-SIGN6-TotalSerial2-LocalSerial1-130308.dat	1	2	16:43:40
	Ht-SIGN6-TotalSerial3-LocalSerial2-130308.dat	2	3	17:30:43
14/03/2008	Ht-SIGN6-TotalSerial4-LocalSerial1-140308.dat	1	4	12:44:46
	Ht-SIGN6-TotalSerial5-LocalSerial2-140308.dat	2	5	13:50:47
	Ht-SIGN6-TotalSerial6-LocalSerial3-140308.dat	3	6	14:46:20
	Ht-SIGN6-TotalSerial5-LocalSerial4-140308.dat	4	7	16:42:45
	Ht-SIGN6-TotalSerial6-LocalSerial5-140308.dat	5	8	17:36:51
17/03/2008	Ht-SIGN6-TotalSerial7-LocalSerial1-170308.dat	1	9	10:45:23
	Ht-SIGN6-TotalSerial10-LocalSerial2-170308.dat	2	10	11:42:38
	Ht-SIGN6-TotalSerial11-LocalSerial3-170308.dat	3	11	12:28:11
	Ht-SIGN6-TotalSerial12-LocalSerial4-170308.dat	4	12	13:11:59
	Ht-SIGN6-TotalSerial13-LocalSerial5-170308.dat	5	13	14:23:27
18/03/2008	Ht-SIGN6-TotalSerial14-LocalSerial1-180308.dat	**1**	14	10:13:57
	Ht-SIGN6-TotalSerial15-LocalSerial2-180308.dat	2	15	10:57:38
	Ht-SIGN6-TotalSerial16-LocalSerial3-180308.dat	3	16	11:50:12
	Ht-SIGN6-TotalSerial15-LocalSerial4-180308.dat	4	17	12:27:59
	Ht-SIGN6-TotalSerial16-LocalSerial5-180308.dat	5	18	13:07:47
	Ht-SIGN6-TotalSerial17-LocalSerial6-180308.dat	6	19	13:59:00
	Ht-SIGN6-TotalSerial20-LocalSerial5-180308.dat	7	20	14:39:55
	Ht-SIGN6-TotalSerial21-LocalSerial6-180308.dat	8	21	15:24:11
	Ht-SIGN6-TotalSerial22-LocalSerial7-180308.dat	9	22	16:14:28
	Ht-SIGN6-TotalSerial23-LocalSerial10-180308.dat	10	23	16:56:59
	Ht-SIGN6-TotalSerial24-LocalSerial11-180308.dat	11	24	17:36:56
	Ht-SIGN6-TotalSerial25-LocalSerial12-180308.dat	12	25	18:15:06
19/03/2008	Ht-SIGN6-TotalSerial26-LocalSerial1-190308.dat	1	26	11:03:54
	Ht-SIGN6-TotalSerial25-LocalSerial2-190308.dat	2	27	10:37:47
	Ht-SIGN6-TotalSerial26-LocalSerial3-190308.dat	3	28	12:03:44
	Ht-SIGN6-TotalSerial27-LocalSerial4-190308.dat	4	29	12:43:08
	Ht-SIGN6-TotalSerial30-LocalSerial5-190308.dat	5	30	13:37:20
	Ht-SIGN6-TotalSerial31-LocalSerial6-190308.dat	6	31	14:17:34
	Ht-SIGN6-TotalSerial32-LocalSerial5-190308.dat	7	32	14:56:17
	Ht-SIGN6-TotalSerial33-LocalSerial6-190308.dat	8	33	15:54:18.5
	Ht-SIGN6-TotalSerial34-LocalSerial7-190308.dat	9	34	16:38:09
	Ht-SIGN6-TotalSerial35-LocalSerial10-190308.dat	10	35	17:12:22
20/03/2008	Ht-SIGN6-TotalSerial36-LocalSerial1-200308.dat	1	36	10:05:57
	Ht-SIGN6-TotalSerial35-LocalSerial2-200308.dat	2	37	10:40:39
	Ht-SIGN6-TotalSerial36-LocalSerial3-200308.dat	3	38	
	Ht-SIGN6-TotalSerial37-LocalSerial4-200308.dat	4	39	11:50:33

Note:

- The expression of the test date such as 120308 means that the test date is on 12th March 2008.
- TotalSerial means that we rank the test serial numbers from the first day to the last day. LocalSerial means that we rank the test serial numbers by each day. For example, we had done 39 total test series from the 12th March 2008 to the 20th March 2008. The TotalSerial number is 3 for the second test serial (Local Serial) on the 13th March 2008 and Local Serial number is 2.

5.2.2 Measured water levels $H_i(t)$ of the experiment

The water level measurements at the capacitive sensors began from the static initial water level (step (1) in **Fig. 5-8** t=…-30s), then lasted about 30 minutes corresponding to water level fluctuations forced by the wave generator (step (2) in **Fig. 5-8**, t=30-1800s), and finally ended during the draining phase (step (3) in **Fig. 5-8** t=1800s-…). The measured water levels $H(t)$ shown in **Fig. 5-8** correspond to just one "test" (the "first test", conducted the 18th of March 2008).

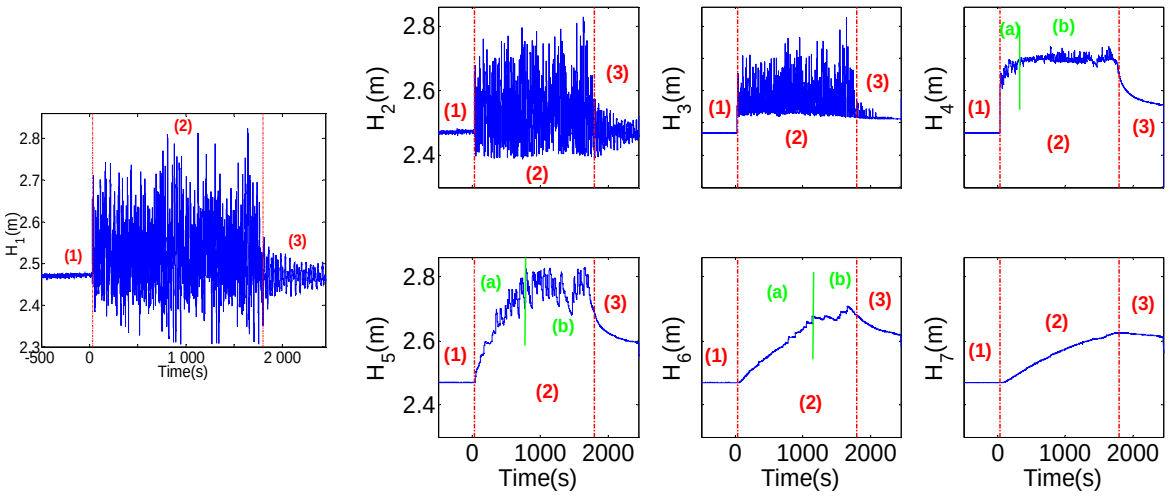

Fig. 5-8 Water levels $H_i(t)$ versus time at the 7 sensors (Test 1: 18 March 2008).

The measurement results show clearly two effects: the spatial decaying of the amplitudes away from the shore, and the filtering out of the shortest periods. Furthermore, the signals away from the shore ($H_5(t)$, H_6(t), H_7(t)) exhibit a very different behavior from those closer to the shore (see **Fig. 5-8**). In fact, during the experiment, according to the eye observation, the water level fluctuations measured by the sensors No.2, No.3, No.4 and No.5 are the mixed

water levels composed of the surface water and the groundwater, and on contrast, the ones measured by the sensors No.6 and No.7 are pure groundwater levels**.**

From **Fig. 5-8**, we can see that the action of tides and waves results in a net super-elevation of the mean groundwater surface above the elevation of mean sea level. The net super-elevation of the mean groundwater in these sensors may be caused by three principal factors: (1) the sloping beach face favoring vertical infiltration relative to horizontal outflow, (2) a 'decoupling' between the ocean and water table around low tide, and (3) wave setup and runup further elevating the region of ocean infiltration above the elevation of the tide. (Turner 1997 [59])

The measured water level fluctuations of the other 38 tests are very similar to the ones of the first test conducted on the 18th of March 2008. Thus, we just choose the measured results of this test to analyze in the thesis.

5.3 Conclusion and outlook

The measured water level fluctuations exhibit extremely irregular characteristics in time and space. Several signal processing techniques have been used to analyze these measured results. The preliminary illustrations of the signal processing of the $H_1(t)$ and $H_6(t)$ are described in a detail in the **Appendix B**: **Chapter B10**. The results obtained show that , spectral frequency methods, time correlations, and multi-resolution wavelet analyses can be used to analyze the original signal, the residuals and the components of $H_1(t)$, $H_2(t)$,$H_3(t)$, $H_4(t)$ and $H_5(t)$, and at the same time, the dominant fluctuation periods of $H_6(t)$,$H_7(t)$ can be indirectly obtained by analyzing the residuals of the original signal with Fourier spectrum analysis and temporal analysis. $H_1(t)$ has very low coherency with $H_6(t)$

The further detailed analysis and the corresponding interpretation on the measured water levels in the sloping sandy beach will be described in the next chapter (**Chapter 6**)

This experiment has been initially designed to measure the erosion of the swash zone with the periodic oscillations of the free water levels. For our focused problem, it existed two deficiencies: (1) The initial condition could not been exactly (precisely) verified; (2) Each test time is not enough long. For the future, if there is possibility to run a more specific exprement for investigating the similar problem, several remarks should be taken into account:

(1) The number of the tests should be reduced and each test time will be prolonged until 3 times or 4 times of the current test time, 2 or 3 tests are enough, and test time depends on the results of the sensor No.7, until the curve trend of the groundwater level is clear.

(2) Initial water level should be more precisely observed. The time for observing the initial water level will be prolonged to one week or even 2 weeks, which depends on the sand seepage velocity of the groundwater, until the initial water level is clearly observed constant in the sandy beach.

(3)The wave period of the wave generator should be much longer than T=4s, for instance, T=20 or 30s which will cause less erosion in the swash zone. Less erosion in the swash zone will make complex problem easier to analyze.

Therefore, numerical simulations have been implemented in order to complement the experimental water level signal analyses and to compare them with various water flow models (a preliminary version of modeling results was presented in *Wang et al. 2008*). The numerical models being used for these comparisons include:

(1) A 2D plane flow model based on the vertically averaged Dupuit-Boussinesq equation for unconfined groundwater flow (with fluctuating boundary conditions);

(2) A 3D variably saturated flow model based on a generalized Richards' equation.

The detailed numerical simulations and the corresponding comparisons with experimental results will be described in the **Chapter 7**.

5.5 Acknowledgement

This part of the research has been conducted through a collaborative effort on a long wave canal experiment (I. Caceres, J. Alsina, et al., SANDS/HYDRALAB, Barcelona, Spain) and in collaboration with the OTE group at IMFT Toulouse (D. Astruc, O. Eiff, et al., IMFT, Toulouse, France). In addition, in the sensor designing and testing, the electronic specialist H. Ayroles was of a great help, we are very grateful to him. At the same time, Technician L. Le Fur was very helpful to install the sensors in the Barcelona canal, we appreciate his help.

Chapter 6: Signal analyses and interpretation of water level data H(x,t) in the Barcelona wave canal

6.1 Introduction

The Fourier spectral analysis reflects the structure of the signal by decomposing a signal in periodic functions. Its advantage is to clearly manifest the distribution of the Fourier spectral functions with respect to the frequency (period). Accordingly, it can be used to study the fluctuation characteristics with respect to the frequency (period). For example, for a single analysis, it can be used to study the dominant periods of the measured water level fluctuations, and the propagation of the fluctuation energy of certain periods in the slopping sandy beach; for a cross analysis, it can be used to determine the coherency with the frequency between two water level fluctuations.

The wavelet transform makes the time-scale phenomena localized temporally or transient extend over a range of scales. The multi-resolution wavelet analysis makes a dyadic signal decomposed into a succession of approximations corresponding to increasing scales. It can especially be used to study the detail (one component) of any dyadic scale "m" of the measured data. This makes possible to study the fluctuation characteristics of one component signal corresponding to time scale $2^m \times \Delta t$ such as the Fourier dominant period, the standard deviation, and so on. This also makes possible to make the correlation between the components with the same dyadic time scale of the two different signals. Especially, for the non-stationary water level fluctuations, it gives more satisfactory results than the ones obtained with Fourier spectral analysis.

The measured water level fluctuations exhibit extremely irregular characteristics in time and space in the sloping sandy beach of the Barcelona big wave canal. For this reason, single processing method such as direct Fourier analysis appears ineffective or not enough effective to analyze this kind of irregular water level fluctuations.

This paper presents an analysis of these measured water level fluctuations $H_i(t)$ in the sloping sandy beach in a single and cross way with Fourier spectrum, multi-resolution

wavelet methods and correlation analysis, together with the moving average and multi-resolution wavelet filtering methods, by using signal analysis tools previously developed in the IMFT laboratory (*Fatmi et al. 2008 [43]*; *Fatmi 2009 [21]*).

6.2 Analysis of Sensor 1 ($H_1(t)$) used as entry boundary condition

6.2.1 Introduction

As described in **Chapter 5**, the sensor No.1 was placed near the still water / beach boundary to measure the water level fluctuations $\boldsymbol{H_1(t)}$ corresponding to the entry condition of the model. This sensor lied in the centre of the swash zone, and as result, the water level fluctuations $\boldsymbol{H_1(t)}$ are very irregularly periodic.

6.2.2 Periodic characteristics of the original signal

In order to analyze the periodic characteristics of the original signal of the water level fluctuations at sensor No.1 ($H_1(t)$), $H_1(t)$ is respectively zoomed with the time period t_1=200s (**Fig. 6-1**) and the time period t_2=50s (**Fig. 6-2**). From **Fig. 6-1** and **Fig. 6-2,** it can be seen that there are mainly two range of periods which play a dominant role in the original signal of H_1(t): T_1=23-53s (**Fig. 6-1**)and T_2=4.2-7.2s (**Fig. 6-2**).

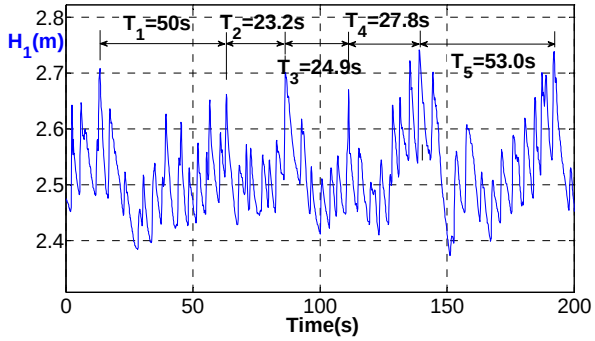

Fig. 6-1 Zoom of the evolution of water level H_1(m) (Original signals, t=30-230s)

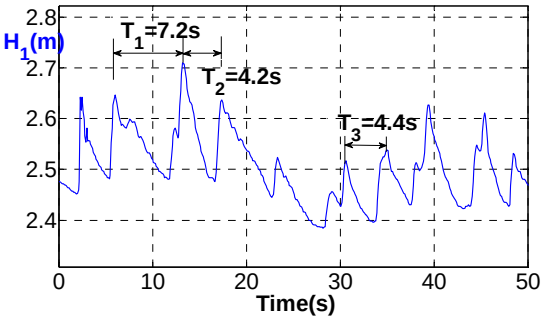

Fig. 6-2 Zoom of the evolution of water level H_1(m) (Original signals, t=30-80s)

6.2.3 Fourier spectral analysis of the original signal

In order to evaluate and interpret the dominant fluctuation periods affecting the beach water table, Fourier spectral analysis (**Appendix B9**, more details about the concerned theory) is applied to the water level signal at the beach "entry" point, namely, $H_1(t)$. This "entry" signal is analyzed as follows, using three versions (or pieces) of the signal:

- **i.** Water levels measured from the beginning of the wave generator motion, until the end of the measurements (t=30-2459s);
- **ii.** Water levels measured during the motion of the wave generator (t=30-1800s);

iii. Water levels measured after the stop of the wave generator (t=2000-2459s).

The resulting spectra are respectively shown in **Fig. 6-3, Fig. 6-4 a** and **b.**

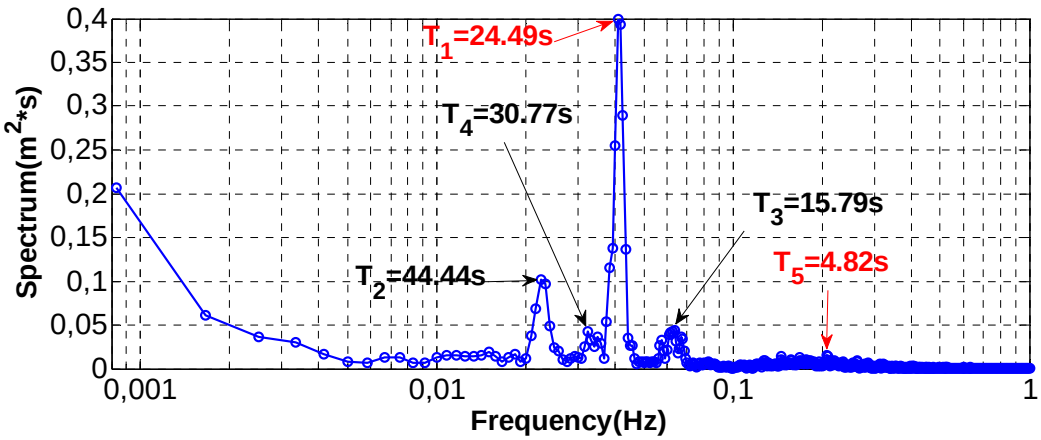

Fig. 6-3 Fourier frequency spectrum of the water level fluctuations $H_1(t)$ (t=30-2459s). Tuckey filter: τ_{Tuckey} =600s

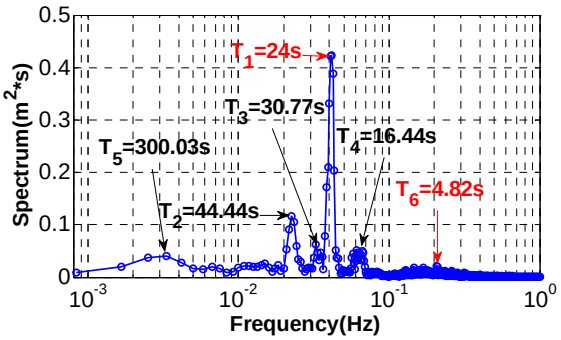

a: t=30-1800s (during wave generation)
τ_{Tuckey}=600s

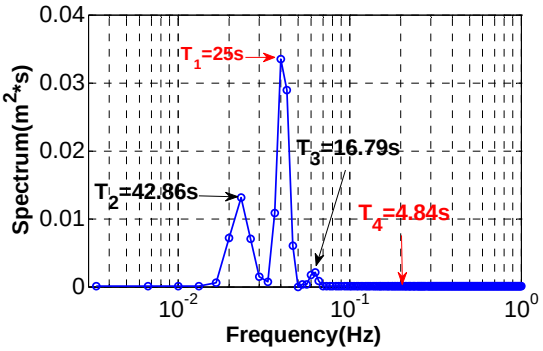

b: t=2000-2459s, τ_{Tuckey}=150s

Fig. 6-4 Fourier frequency spectrum of the water level fluctuations $H_1(t)$ for two different time windows (during and after wave generation).

From these 3 figures, it can be seen that there are 3 periods which always prevail in the beach entry signal $H_1(t)$. Among them, $T_1 \approx 24$s plays the most important role, then $T_2 \approx 43$s, and finally T_3=16s.

The period T_1 = 24s is considered, at this stage of the analyzis, as the result of the run-up and rundown flow influenced by the size and shape of the wave canal and, more importantly, also by the existence of a sloping sandy beach at one end of the canal.

On the other hand, period T_4 = 4.83 s is obviously close to the wave generator period (T_0 = 4 s). It can be seen that this period $T_4 \approx 4.83$s, plays a much small role in the $H_1(t)$ signal than the other 3 periods. Period T_4 has spectral energy S=2.09E-2m^2.s (obtained from **Fig. 6-4 a**) during the working of the wave generator. In the frequency spectrum of the signal

analyzed after wave generation as stopped (**Fig. 6-4 b**), the wave generator period $T_4 \approx 4.83$s almost totally disappears (very small spectral energy S=8.203E-7m^2.s).

6.2.4 Multi-resolution wavelet decomposition of the original signal, and Fourier analysis of wavelet components

In contrast with Fourier analysis, multi-resolution wavelet decomposition intuitively demonstrates the evolving (non stationary) temporal variability of the water level fluctuation $H_1(t)$ for each dyadic wavelet time scale (analogous to a period or an inverse frequency). Therefore, to validate and further interpret the dominant periods of $H_1(t)$ obtained with Fourier spectral analysis, a multi-resolution wavelet analysis is used to decompose the complete original signal at the beach entry ($H_1(t)$, t=30-2459s).

Considering that the data number analyzed by multi-resolution wavelet must be $N=2^L$ (L is the wavelet time scale, and more details about the theory are explained in **Appendix B9**), in order to analyze all the data, especially the third part data, $H_1(t)$ (the time step dt=0.1s, $2^{14}<N_1=24291<2^{15}$) needs to be completed in the end with the mean water level of $H_1(t)$. As a result, the number of data is artificially extended from to N_1 to $N_2=2^{L+1}+1=32769$, and the time window is extended from t_1=2459s to t_2=3306.8s. In this way, the signal becomes dyadic and suitable for multi-resolution wavelet analyzis.

Fig. 6-5 illustrates the evolution of the main wavelet components C_4, C_5, C_6, C_7, C_8, C_9, C_{10} and C_{11} of the completed dyadic signal**.** It can be seen that the wavelet components $\mathbf{C_7}$ (time scale 12.8s) and $\mathbf{C_8}$ (time scale 25.6s) prevail from t=30s through t=2459s, and the other components totally disappear after about t=1800s (the time of the stop of the wave generator).

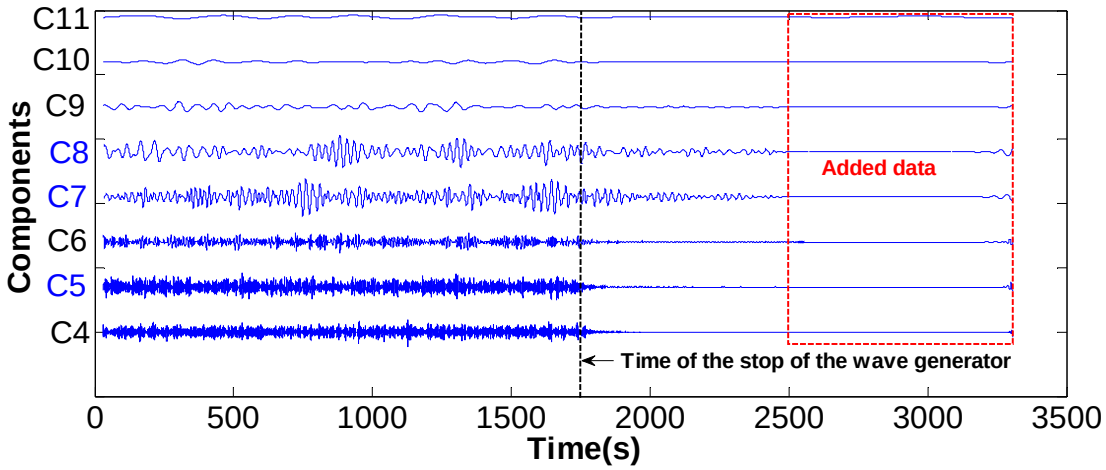

Fig. 6-5 Evolution of the main components C_4, C_5, C_6, C_7, C_8 , C_9 , C_{10} and C_{11} of the completed signal $H_1(t)$ by adding the mean water level (t = 30- 3306.8s, the number of the data is $N=2^L+1$, and L=15 is the dyadic scale).

The results of the wavelet decomposition of $H_1(t)$ suggest that the dominant components C_7 and C_8 (12.8s and 25.6s, compared to wave maker period 4s) are due to the effects of wave run-up and run-down flow due to the sloping sandy beach. In addition, it can be seen that the "amplitude" of component $\mathbf{C_5}$ (3.2s) is indeed a bit less than $\mathbf{C_7}$ and $\mathbf{C_8}$ during the working of the wave generator.

Since the wavelet dyadic time scales of the components C_7, C_8 and C_5 are respectively 12.8s, 25.6 and 3.2s, which are a bit different from the dominant periods of the Fourier spectrum, we decided to patch up the two types of analyses (Wavelet and Fourier) by examining also the dominant periods in the Fourier spectrum of the selected wavelet components.

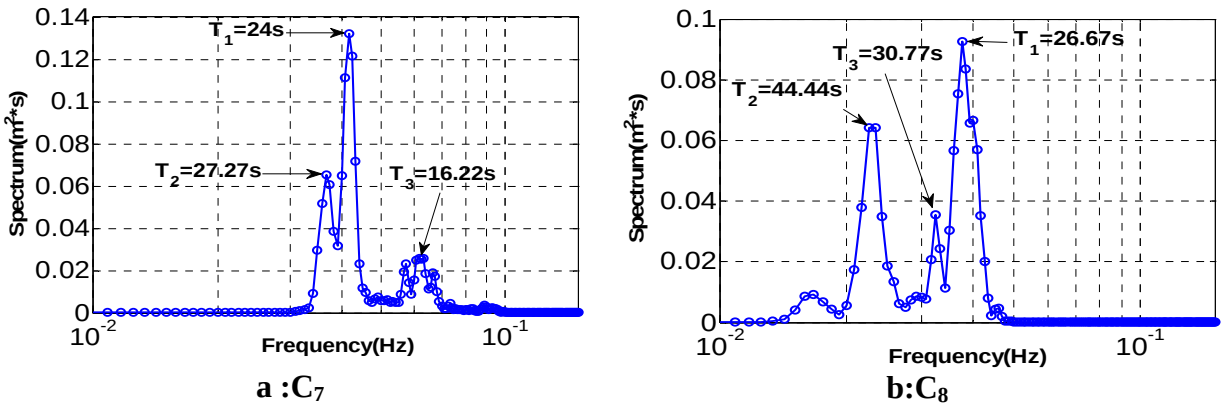

Fig. 6-6 Fourier frequency spectrum S(f) of the component C_5 and C_7 of $H_1(t)$ with τ_{Tuckey} =600s.

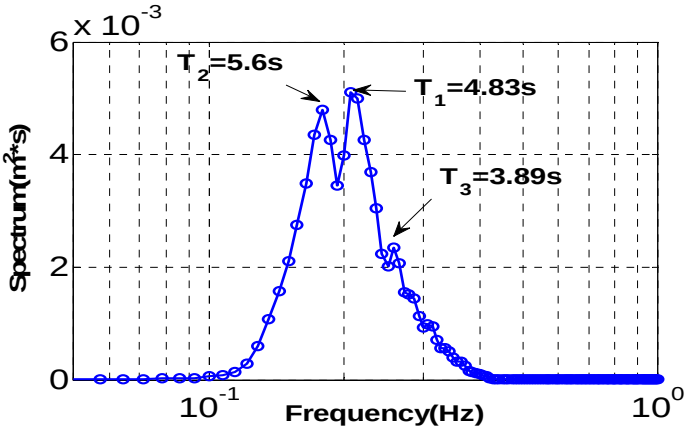

Fig. 6-7 Fourier frequency spectrum S(f) of the component C_5 of $H_1(t)$ (τ_{Tuckey}=70s).

The results indicate that the dominant Fourier periods of C_7, C_8 and C_5 are respectively 23.33s (**Fig. 6-6 a**), 28s (**Fig. 6-6 b**) and 4.83s (**Fig. 6-7**). At the same time, when the dyadic time scale n≤7, the dominant Fourier period of the wavelet dyadic component of $H_1(t)$ (a non-harmonic wave) falls between the corresponding wavelet dyadic time scale (n) and the next dyadic time scale (n+1), and in contrast, when n>7, the wavelet time scale periods are greater than the corresponding Fourier periods, and the difference between the both becomes greater and greater with increasing wavelet dyadic time scale n, as shown in **Table 6-1**.

Table 6-1 Wavelet component dyadic time scale and corresponding Fourier period of $H_1(t)$

Component C_i	C_1	C_2	C_3	C_4	C_5	C_6	C_7
Dyadic time scale T_i (s)	0.2	0.4	0.8	1.6	3.2	6.4	12.8
Fourier period TF_i (s)	0.349	0.651	1.513	2.469	4.82	6.859	23.529
C_i	C_8	C_9	C_{10}	C_{11}	C_{12}	C_{13}	C_{14}
Dyadic time scale T_i (s)	51.2	102.4	204.8	409.6	819.2	1638.4	3276.8
Fourier period TF_i (s)	26.089	54.555	133.33	300.03	400.0	599.88	1200.0

Note :
1. Wavelet component dyadic time scale: $T_i=2^i \times dt$ and dt=0.1s.
2. Fourier period TF_i is obtained from the corresponding component C_i with Fourier analysis.

As a result, we conclude that the most dominant period T_1=24s of $H_1(t)$ obtained with the Fourier spectrum is close to dominant periods (T_2=23.33s and T_3=28s) obtained with multi-resolution wavelet analyzis.

Therefore, the dominant period T≈24s is further validated. It can be interpreted as the effect of the geometry of the wave canal or more precisely, the effect of the run-up and run-down flow due to the sloping sandy beach.

On the other hand, we observe that the short period component of $H_1(t)$ (T ≈ 4.83s, close to the wave generator period) appears stronger with multi-resolution wavelet than with Fourier spectrum analyzis.

6.2.5 Simplification of the signals

Water level fluctuations at sensor No.1 ($H_1(t)$) reflect surface water levels and can be considered as the entry boundary condition with respect to all the other 'subsurface' sensors. The regular periodic wave with period T = 4 seconds produced at the wave generator, seems much less regular when it arrives at Sensor No.1, in the swash zone (**Fig. 6-1** and **Fig. 6-2**). To simplify such complex signals, we want to find the dominant periods of *$H_1(t)$*. Accordingly, we choose the following bimodal Fourier approximation for water level signal *$H_1(t)$*:

$$H_1(t) = H_0 + A_1 \sin(\omega_1 t + \varphi_1) + A_2 \sin(\omega_2 t + \varphi_2) \qquad (6\text{-}1)$$

From the results obtained with Fourier spectral analysis (**Fig. 6-3** and **Fig. 6-4**) as well as the results obtained with wavelet decomposition in **Fig. 6-5**, we can see clearly that period T_1 = 23.33 s prevails among the *$H_1(t)$* signals. So far, we consider that period T_1 = 23.33 s is the result of the geometry of the wave canal or more precisely, it is the dominant period of the run-up flow induced by the effect of the sloping sandy beach. On the other hand, period T_4 = 4.83 s is obviously close to the wave generator period (T_0 = 4 s).

We then used orthogonal multi-resolution wavelet analysis to verify the results of Fourier analysis and to obtain the corresponding amplitudes and phases for the dominant periodic waves. In **Fig. 6-8**, we can see that the sum of the dyadic wavelet component C_7 and the dyadic wavelet component C_5 agree well with the original signal. After that, we obtain the amplitudes (defined as the 90% confidence band) of the wavelet components C_7 and C_5: $A_{C7} = 1.64 \times \sigma_{C7} = 0.0672m$ and $A_{C5} = 1.64 \times \sigma_{C5} = 0.0524$ (C_5 and C_7 are shown in **Fig. 6-9**). Concerning the phases, we can directly measure them from **Fig. 6-9**. A simple method was used at first, namely: $\varphi = 2\pi(t_n^* - 0)/T$, where t_n^* is the first 0-crossing of the signal (this method will be revised with a statistical identification of the positive phase). We obtain here: $\varphi_{C7} = 0.238 rad$, and $\varphi_{C5} = 0.982 rad$.

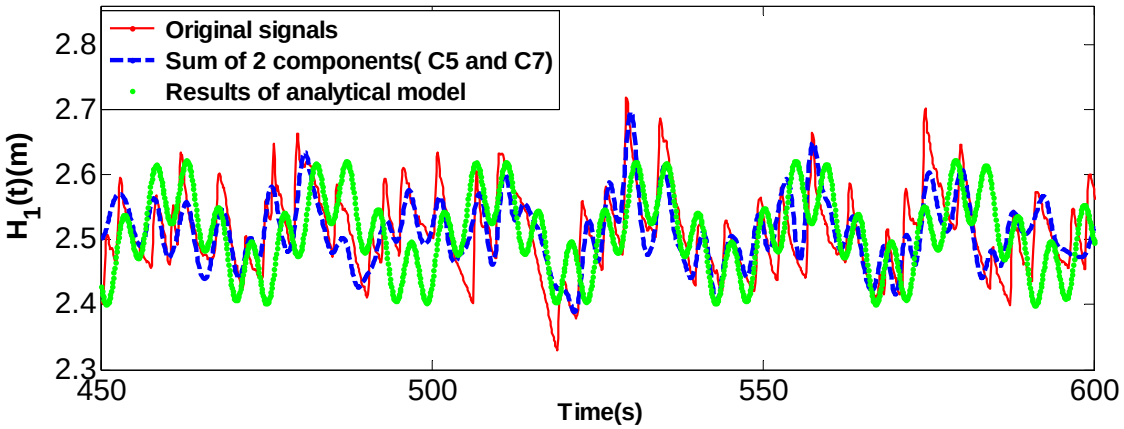

Fig. 6-8 Wavelet analysis of signal $H_1(t)$: comparison of original signal, bimodal Fourier signal, and 2-component wavelet.

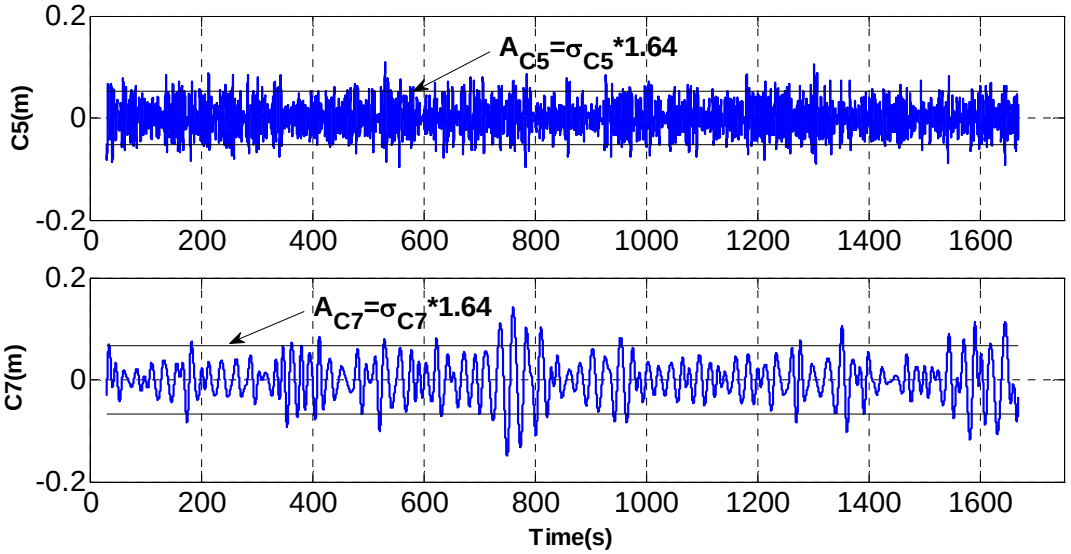

Fig. 6-9 Wavelet analysis of signal $H_1(t)$: the dyadic components C_7 & C_5

We have now obtained all the coefficients for the analytical bimodal Fourier model of equation (6-1), as shown in **Table 6-2**. From **Fig. 6-8**, it can be seen that this 'analytical model' is a good approximation of the original signal, and is confirmed with wavelet analysis. Note that the amplitude of period T2 (5 s) is almost the same as T1 (24s), whereas the spectrum of (**Fig. 6-7**) shows a much weaker spectral peak for T2 (5 s) compared to T1 (24s). This could be due to the folding of the energy of other fluctuation periods onto period T2 in the bi-modal approximation (this issue remains open).

Table 6-2 Coefficients of the 'analytical' bimodal approximation

Coefficients	H_0(m)	T_1(s)	A_1(m)	φ_1(rad)
Values	2.5112	24	0.0672	0.238
Coefficients		T_2(s)	A_2(m)	φ_2(rad)
Values		4.83	0.0524	0.982
Methods	Mean signal	Fourier	Wavelet	Wavelet

6.2.6 Summary

The spectrum curve with respect to the frequency can be obtained with Fourier spectrum analysis. The roles of all periods in the signal can be observed immediately and intuitively from the Fourier spectrum curve, however, the evolution of roles of all periods with respect to the time cannot be obtained with Fourier spectrum analysis.

In contrast, the evolution of the components can be obtained with Multi-resolution wavelet.

The evolution of the roles of all dyadic components can be observed with Multi-resolution wavelet, and at the same time, the corresponding amplitude and the phase can also be obtained.

Accordingly, combined the two methods, the complex irregular signal can be simplified by a bimodal Fourier model, which is a good approximation of the original signal and therefore, which can be used as the entry water level for the numerical simulations in order to eventually make the complex sea/beach hydrodynamic partial saturated sloping sandy beach system easy understood. In addition, evolution of the roles of all components will be helpful to interpreter the dominant period T≈24s, which is different from the one of the wave generator of the canal.

6.3 Analysis of Sensor 7 (groundwater)

6.3.1 Introduction

The micro-piezometric tube i =7 is the farthest sensor away from the swash zone. In fact, it is located about one meter or so from the impervious wall located at the end of the canal (in hydrogeologic terms, this boundary can be thought of as a groundwater divide).

6.3.2 Analysis of the results

From **Fig. 6-10,** it can be seen that signal $H_7(t)$ is totally different from $H_1(t)$. Indeed, signal $H_7(t)$ clearly exhibits a slowly increasing stage (water filling) and a descending stage (water draining). Contrary to $H_1(t)$, which measures surface water phenomena, piezometer $H_7(t)$ is thought to provide a direct measurement of groundwater variations.

The Fourier method is not directly suited for analyzing this type of strongly non periodic and non stationary signal (*Conway and Frame, 2000* [66]). Instead, a moving average filter is first used to remove the nonlinear trend, and then, the residual of the original signal is

analyzed. In other words, it is the spectrum of the residual of $H_7(t)$ that is analyzed, not the original non stationary signal.

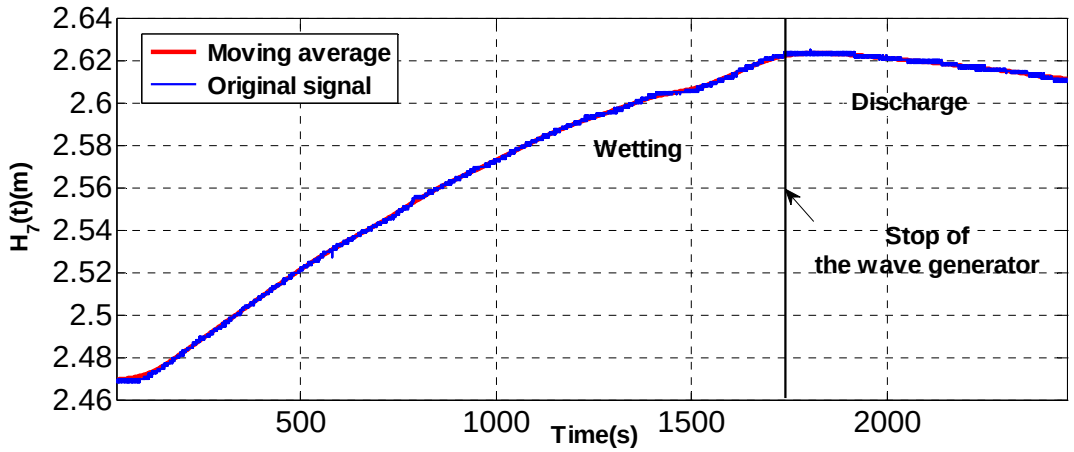

Fig. 6-10 Original signals $H_7(t)$ (t=30-2459s) and its moving average with window halfwidth w_t=70s.

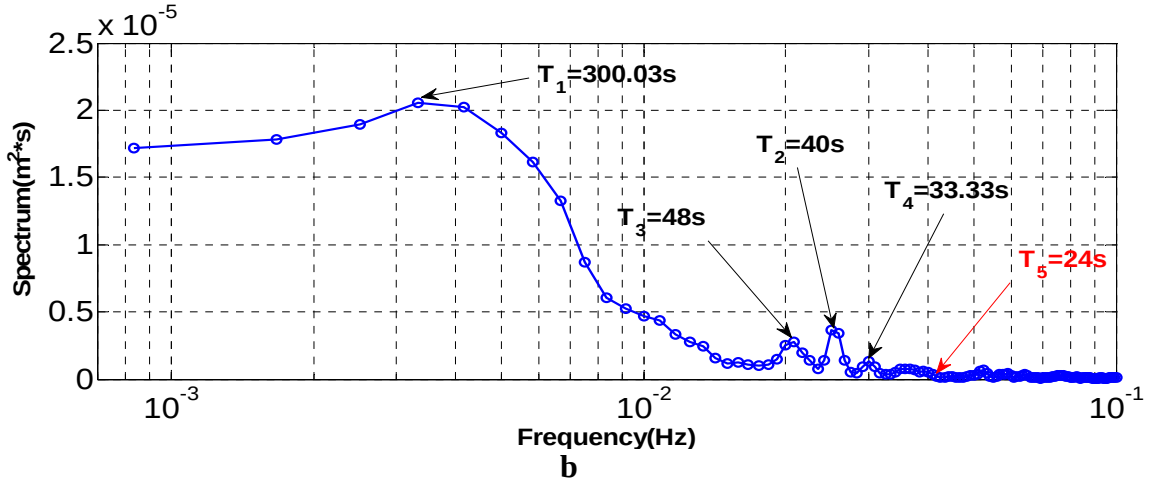

b

Fig. 6-11 Fourier frequency spectrum of the residual of $H_7(t)$ with moving average filtering (w_t=70s and τ_{Tuckey}=600s)

The Fourier frequency spectrum of the detrended $H_7(t)$ is shown in **Fig. 6-11.** In comparison with the entry spectrum at sensor i=1, it can be seen here that all the high frequency waves have disappeared. The remaining dominant period is T_1 = 300 s, a rather long period, about 12 times longer than the dominant period of the $H_1(t)$ signal (T_1 = 24 s). Wave periods about 6 to 12 times shorter than T_1 = 300 s are still visible in the residual $H_7(t)$ spectrum, but they are sub-dominant and have much less energy.

In addition, its dominant Fourier spectrum energy is about 2.0e-5 m^2.s and it is 2.0E-7 times smaller than that of $H_1(t)$ (0.4 m^2.s)

6.4 Analysis of the other sensors (between swash zone and deep groundwater)

We analyze in this section the water levels at the intermediate sensors 2,3,4,5,6 (between the open water sensor No.1 located before the swash zone, and the groundwater sensor No.7 located nearest to the end wall of the canal).

Due to complex wave hydrodynamics and to strong erosion in the swash zone, the shorewise position of the "static" free water boundary evolved during the wave generation tests. It finally reached the position of sensor No.3 at the end of the series of wave generation tests (9 days). Thus, during part of the wave tests, sensor No.2 also could be considered as measuring surface water rather than groundwater fluctuations.

The original water level signals of sensors No.2, 3, and 4, were analyzed directly via Fourier spectra, without detrending (same as sensor No.1). The resulting spectra (not shown here) are similar to those of sensor No.1.

On the other hand, given the structure of the signals obtained at sensors No.5 and No.6, further away from the shoreline, we chose to perform Fourier spectral analysis of the 'detrended' signals (i.e., of the residuals obtained by moving averages). The resulting residual spectra (see **Fig. 6-15** further below) are similar to those of sensor No.7.

We now focus on cross-analyses of these water level signals and/or their residuals.

6.5 Cross analysis

6.5.1 Introduction

We try here to interpret and to quantify the propagation of water level fluctuations in space, through the sloping sandy beach, using as an "input" the complex multimodal water level signal observed at the entry position (sensor No.1). In particular, we aim at characterizing:

- the spatial evolution of dominant frequency modes in the cross-shore direction;
- the spatial propagation of fluctuation energy (i.e., intensity of the spectrum);
- the maximum cross-correlation between pairs of signals (No.1, No.i), and the corresponding lag time, leading also to an estimation of wave velocity;
- the cross-spectral coherency functions between $H_1(t)$ and $H_i(t)(i=2,\ldots,7)$.

It was emphasized earlier that the original water level signals ($H_5(t), H_6(t), H_7(t)$) are strongly non-stationary. They are also, for this reason, very different from ($H_1(t), H_2(t)$,

$H_3(t)$) in terms of time structure and frequency content. Keeping this in mind, we conducted the cross analyses between $H_1(t)$ and $H_i(t)$ (i=2,…,7) based on the residuals rather than the original signals (this for all sensors i=1 to 7).

6.5.2 Residuals of $H_i(t)$ (i=1, …, 7) with moving average filtering

6.5.2.1 Introduction

Considering that the water level fluctuations $H_5(t)$, $H_6(t)$ and $H_7(t)$ are extremely non-stationary and are different from $H_1(t)$, $H_2(t)$ and $H_3(t)$, in order to do the cross analysis between $H_1(t)$ and $H_i(t)$ (i=2,…,7) , the original signals are filtered with moving average filtering (**Appendix B9**). Then, the corresponding residuals after taking away the moving average from the original signals will be used to be analyzed.

6.5.2.2 Residuals of $H_i(t)$ (i=1, …, 7) with moving average filtering

The residuals of $H_i(t)$ (i=1, …, 7) are obtained by taking away the moving average from the original signals. The moving averages of $H_i(t)$ (i=1,…,7) (**Fig. 6-12** and **Fig. 6-13**) are obtained with moving average filtering with the half window width of the filter W_t=300s for $H_i(t)$ (i=1,…,6) , and W_t=70s for $H_7(t)$. The corresponding residuals of $H_i(t)$ (i=1,…,7) are shown in the **Fig. 6-14**.

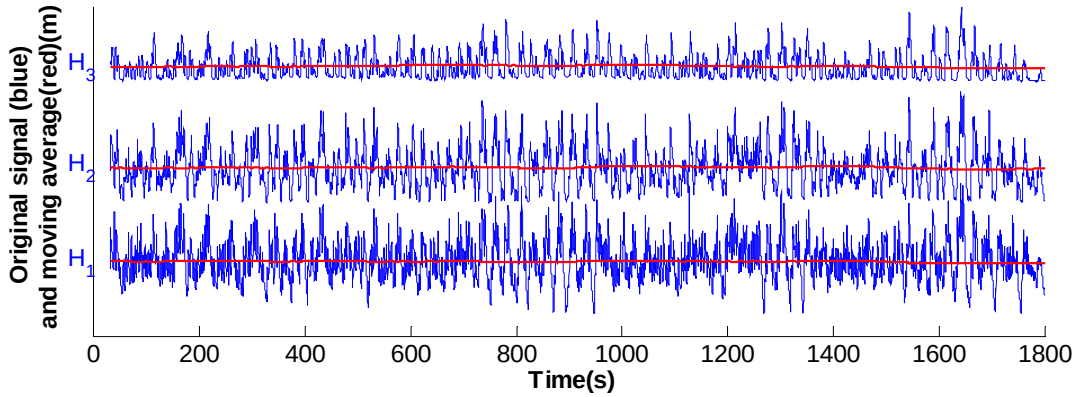

Fig. 6-12 Original signals and the moving averages of $H_i(t)$ (i=1, …, 3) with moving average filtering

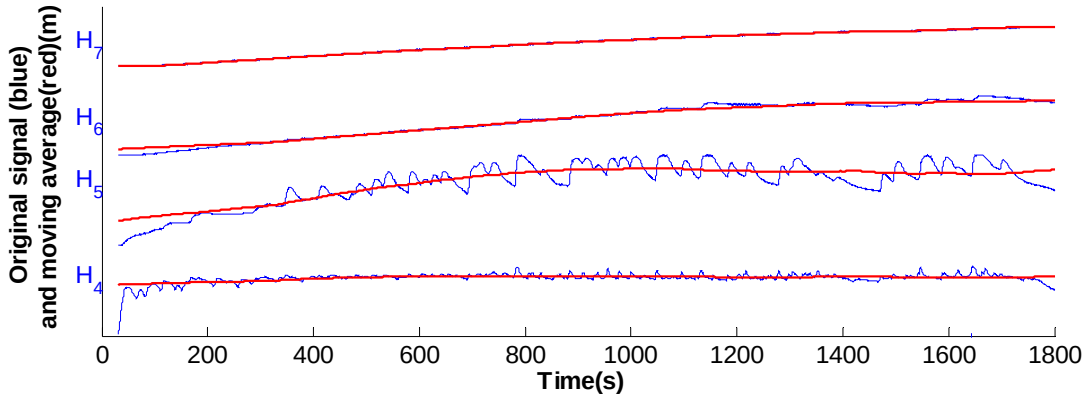

Fig. 6-13 Original signals and moving averages of $H_i(t)$ (i=4, …, 7) with moving average filtering

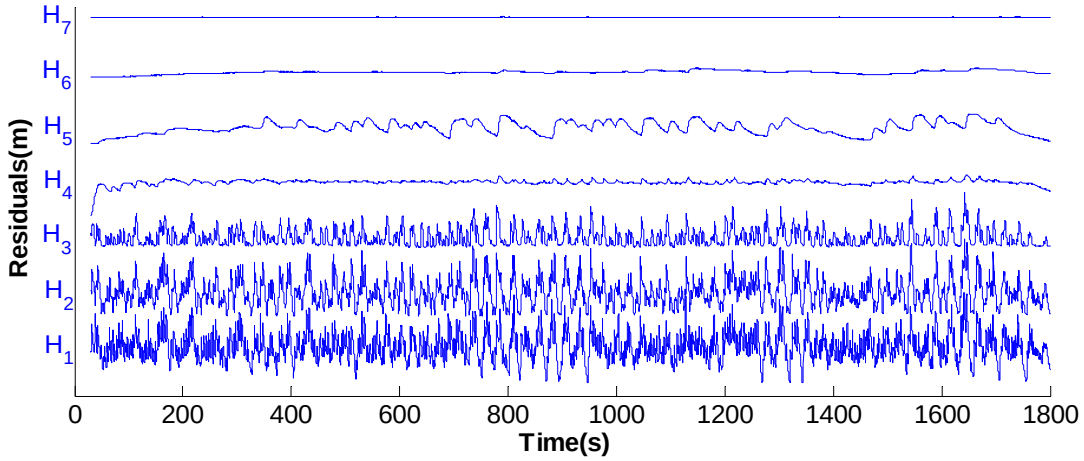

Fig. 6-14 Residuals of $H_i(t)$ (i=1, …, 7) with moving average filtering

Note: The residuals of $H_i(t)$ (i=1,…,7) are obtained with the half window width of the filter W_t=300s for $H_i(t)$ (i=1,…,6) , and W_t=70s for $H_7(t)$.

6.5.2.3 Criterion for the half window width W_t of $H_i(t)$ with moving average filtering

We have aso attempted to derive a more general criterion for selecting the best *Wt* in a moving average filter; however this particular work is not completed at this time (ongoing research).

Note: a compatibility criterion between the choice of the Tukey filter width (max lag) (**Appendix B9**) and the moving average window width (half-width W_t) is developed further, in Section **6.5.3.6**.

6.5.3 Cross analysis between $H_1(t)$ and $H_i(t)$ (i=2, …, 7)

6.5.3.1 Introduction

The spacial variation of the water level fluctuation characteristics such as the dominant periods, Fourier spectrum energy, cross correlation, coherency, and wave propagation

velocity in the sloping sandy beach will be investigated in this section with 3 signal processing methods.

During the analysis, according to the analysis methods, the original signals or the residuals of the original signals with moving average obtained in the section **6.5.2.2** are chosen. For instance, Fourier spectral analysis is used to analyze the spectral functions of the residuals and the multi-resolution wavelet is used to decompose the original signal.

6.5.3.2 Spatial evolution of dominant periods in the sloping sandy beach (cross-shore)

The cross-shore spatial evolution of the dominant periods in the sloping sandy beach is shown in **Fig. 6-15**. This figure was obtained by spectral (Fourier) analyzis of the residuals of $H_i(t)$ $(i=1,\ldots,7)$ as explained earlier. There are 11 dominant periods marked out on the spectra of $H_i(t)$ $(i=1,\ldots,7)$ in the figure.

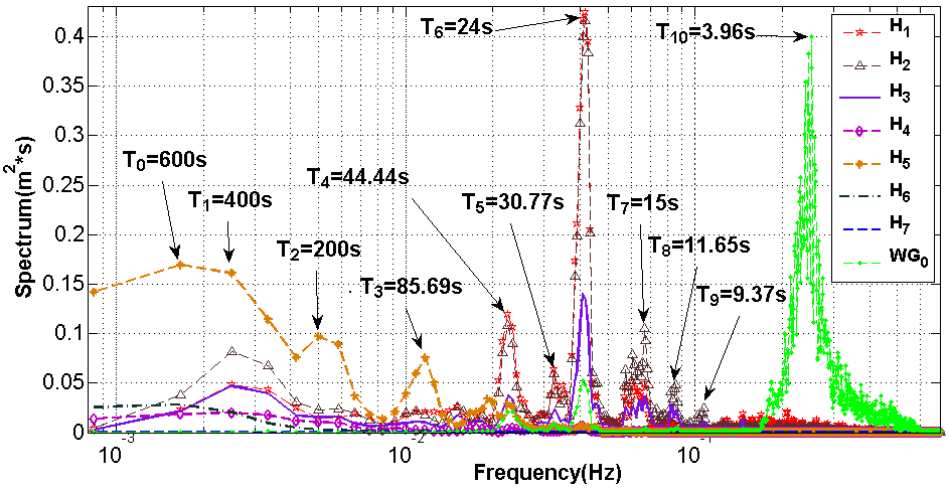

a: the Fourier spectrum plotted in semi-log form

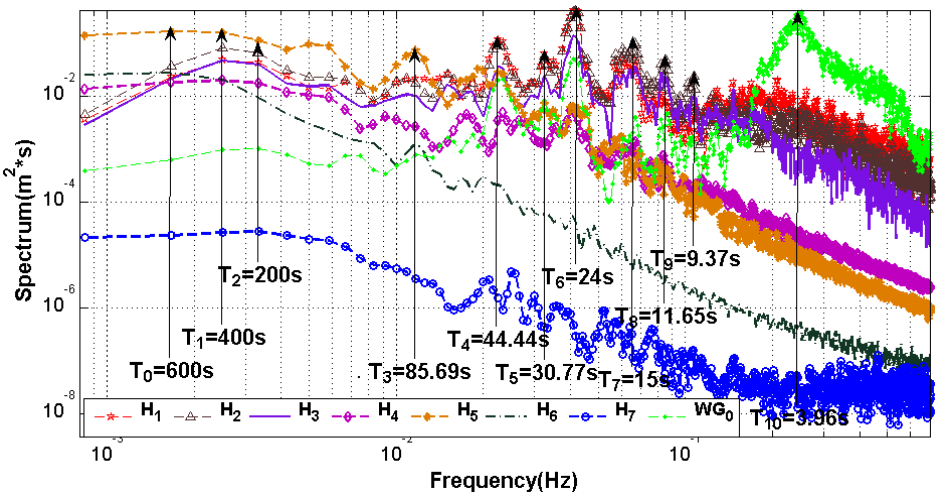

b: the same Fourier spectrum plotted in log-log form

Fig. 6-15 Fourier frequency spectrum of the residuals of $H_i(t)$ (i=1,…,7) and of $WG_0(t)$, the "free water level" measured in the vicinity of the wave maker (free water level).

Note: Moving average filtering was performed with a *half window width* $W_t = 300s$ for signals $H_i(t)(i = 1,\ldots,6)$, and $W_t = 70s$ for signal $H_7(t)$. All Fourier spectra were estimated with a Tuckey filter using a maximum lag cut-off τ_{Tuckey} =600s.

The period $T_6 = 24s$ plays the most dominant role in $H_1(t)$ (spectral energy S_1 (T=24s) ≈ 0.42 m^2.s), as well as in $H_2(t)$ and $H_3(t)$. Then, its energy decays rapidly at $H_4(t)$, and becomes very weak in the spectra of $H_5(t)$, $H_6(t)$ and $H_7(t)$ (spectral energy S_7 (T=24s) ≈ 1.0E-6 m^2.s) (**Fig. 6-15**, **Fig. 6-16** and **Fig. 6-17**).

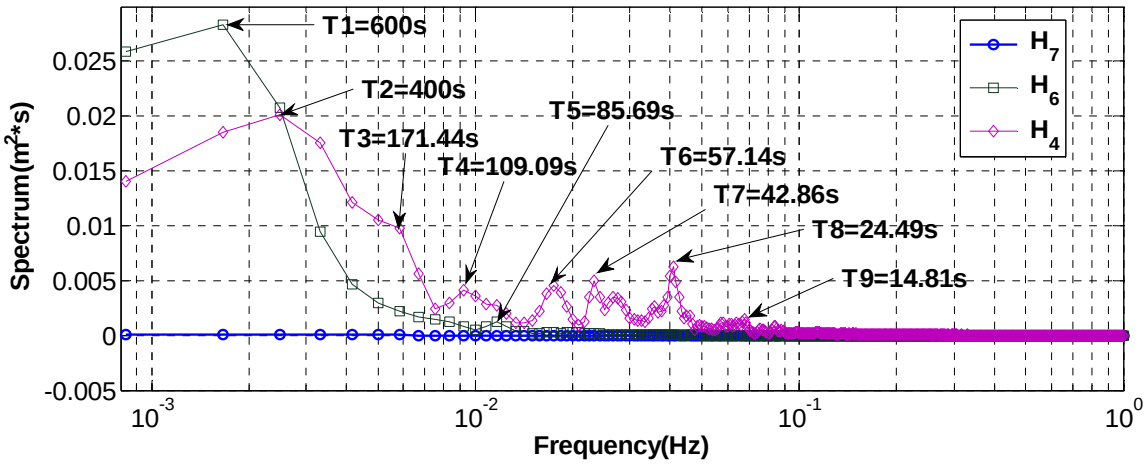

Fig. 6-16 Fourier spectrum function with respect to the frequency of the residuals of $H_i(t)$ (i=4,6,7).

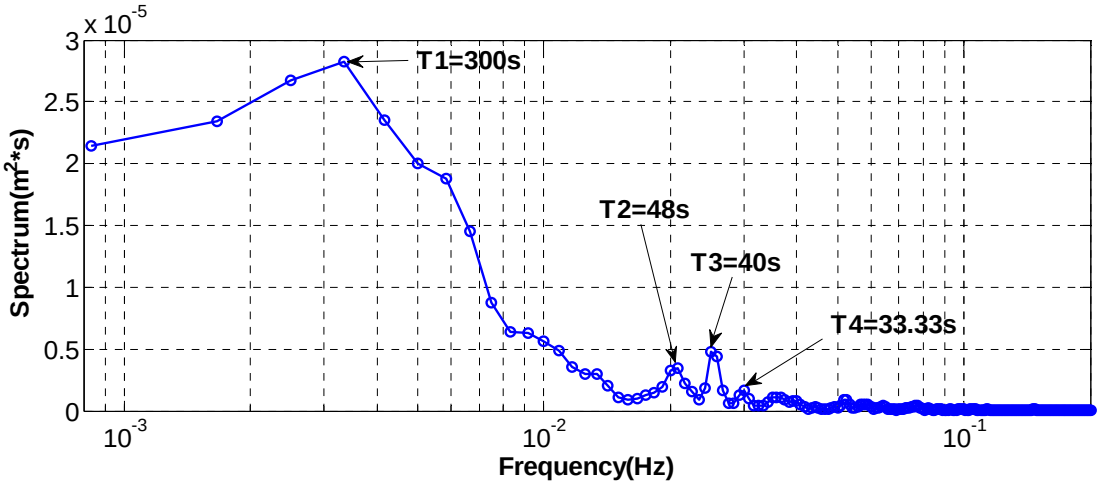

Fig. 6-17 Fourier spectrum function with respect to the frequency of the residual of $H_7(t)$.

The period $T_5 = 44.44s$ is the 2nd most dominant period in the entry signal $H_1(t)$ (spectral energy S_1 (T44s) ≈ 0.12 m^2.s), as well as in $H_2(t)$ and $H_3(t)$. Its energy decays then rapidly

at $H_4(t)$, $H_5(t)$, $H_6(t)$ and $H_7(t)$. However, this period is still weakly subdominant at $H_7(t)$, although its energy is very small there (6.0E-6m^2.s), see also **Fig. 6-17.**

Furthermore, the most dominant periods at piezometers $H_4(t)$, $H_5(t)$, $H_6(t)$ and $H_7(t)$ are much longer periods than the dominant periods of $H_1(t)$, $H_2(t)$, $H_3(t)$. Indeed, the most dominant periods of $H_4(t)$, $H_5(t)$, $H_6(t)$ and $H_7(t)$ are respectively 400s, 600s, 600s and 300s.

In addition, it is noticed that $H_5(t)$ is most "dynamic", not only for the long period T_0=600s (which is dominant at H_5), but also for all periods $T \geq 85.69s$; in particular T_3=85.69s and T_2=200s are also very dominant in $H_5(t)$ and their energies are much greater that the energy of the dominant period T_1=400s of $H_4(t)$ (as can be seen from **Fig. 6-15**). This is due to the particular location of piezometer No.5, which lies near the exit point of the groundwater table in the sloping sandy beach, where the sloping boundary is responsible for the generation of higher harmonics of water table oscillations (*Horn, 2006 [19]; Cartwright et al., 2004b [64]*).

Note. To better comprehend the latter remarks, it should be kept in mind that sensors No.1-No.2 are basically in the swash zone, with sensor No.1 being frequently or almost permanently flooded. Sensor No.3 is beyond the swash zone (marginally so). In fact, it should also be noted that, due to beach erosion, the free water level moves progressively downstream (or landward) from sensors No1-No2 towards sensor No.3, during the wave generation test.

6.5.3.3 Energy propagation of water levels from the "sea" (wave generator) towards the "shore" and through the beach

In order to better interpret the spatial evolution of the dominant periods observed at $H_1(t)$ (T_1=24s, T_2=44.44s, T_3=400s and $T_0 \approx 4s \approx$ period of the wave maker), we also examined the spectrum of water level fluctuations measured at all available sensors along the Barcelona wave canal, from the "open sea" (wave generator position) to the shoreline (WG_i (i=0, …, 13), provided by Barcelona Group) and beyond the shoreline (beach, $H_i(t)$ (i=1, …, 7)). In other words, we now combine spectral analyses from all water level sensors, including both open water sensors (in the canal) and piezometric sensors (through the sandy beach).

The cross-shore spatial distribution of the dominant periods in the canal is depicted in **Fig. 6-18**. For each dominant period, the Fourier spectral energy "S" (m2.s) is displayed on a log-scale and plotted versus sensor position "x" along the canal (both open water and beach).

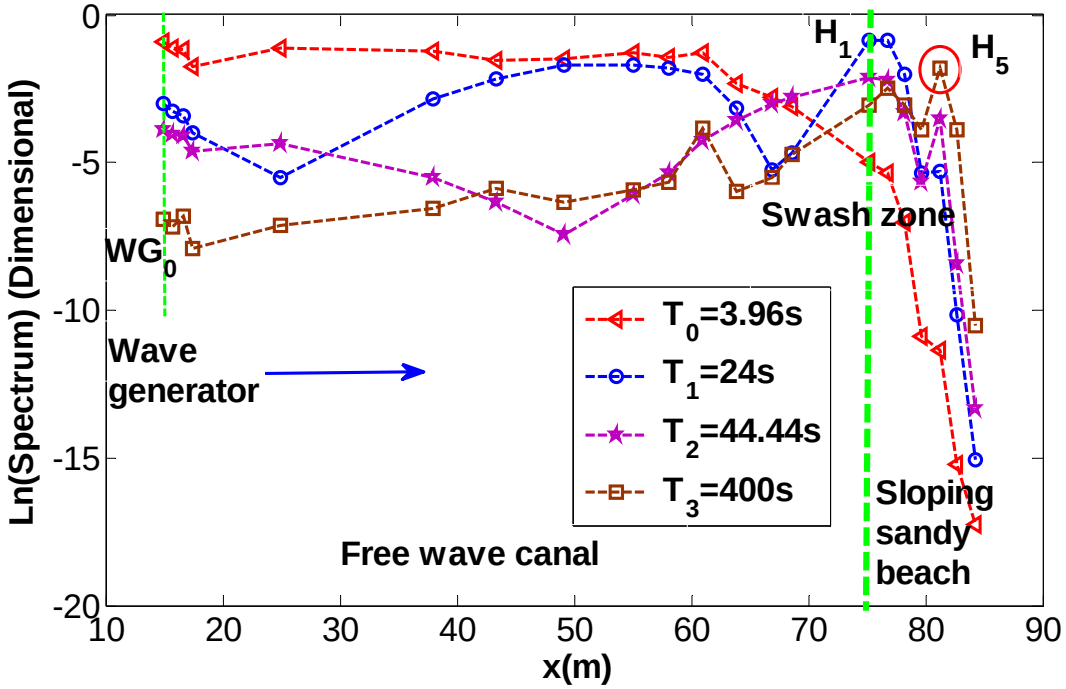

Fig. 6-18 Fourier frequency spectrum (energy spectrum) of water levels in the canal as a function of position (x), for different selected frequencies f_i f_i or periods $T_i = 1/\ f_i T_i = 1/f_i$.
Note: the spectra are estimated using a Tuckey filter, with a lag window $\tau_{Tuckey} = 600s$

Let us examine **Fig. 6-18** in terms of the propagation of the spectral energy of the 3 dominant periods T_1=24s, T_2=44.44s, T_3=400s, and of the period of the wave generator T_0=4s. We focus on the evolution of the water level spectra from the position of the wave maker (or the "open sea", at left) towards the beach and then inland (at right). The following remarks can be made:

- The wave maker period $T_0 \approx 4$s is dominant in the "open sea" (that is, in the canal, before reaching the swash zone). However, its spectral energy begins to decrease rapidly from a position ahead of the swash zone (WG_{10}) where its Fourier spectrum is about 0.4 m^2.s, to less than 0.01 m^2.s at Sensor No.1 in the swash zone, and then less than 1.0E-5m^2.s at sensor $H_7(t)$ inland.
- The energy of period T_1=24s is somewhat less dominant but on the same order as T_0=4s before the swash zone. In the middle of the swash zone, its energy appears to decrease sharply and then rises again, and becomes dominant further inland, at piezometers $H_1(t)$, $H_2(t)$, and a bit beyond (we are still in the swash zone area).

- Similarly, the spectral energy of period T_2=44.44s gradually increases throughout the swash zone, reaches a global maximum (with less energy than period T_1=24s) at piezometers $H_1(t)$ and $H_2(t)$ in the swash zone, and then another relative maximum at piezometer $H_5(t)$ further inland.
- Finally, concerning the longest period (T_4=400s), its spectral energy, very low in the open sea, increases gradually from the wave maker (S≈1.004E-3m^2.s) to the beach's zone where it peaks (there is however also a small intermediate peak of energy at the very beginning of the swash zone, WG_{10}). The global maximum of energy of T_4 is observed further inland, at piezometer $H_5(t)$. Note that T_4=400s is a rather long period, namely, 100 times longer than the wave maker period.

Before concluding this part, recall that the four harmonics (T_1, T_2, T_3, T_4) analyzed here were selected because they appeared dominant with respect to other frequencies, throughout various spatial positions along the canal and beach.

Now, as a follow up from the previous remarks, it can be seen from **Fig. 6-18** that the energies of the four harmonics (T_1, T_2, T_3, T_4) all decrease drastically in the sloping sandy beach ($H_1(t)$ through $H_7(t)$), although a local peak of energy can be observed at piezometer $H_5(t)$. It can also be seen that the longest period T_3=400s is the most dominant in the far beach region ($H_5(t)$, $H_6(t)$ and $H_7(t)$). This suggests that the energy of the longer period has decayed less, or propagated farther through the beach, than the energy of the shorter periods. At the same time, the relative peak of spectral energy observed at $H_5(t)$ for several periods (T_1,T_2,T_3) seems to be consistent with observation by Nielsen and Turner (2000) [68], and Cartwright et al. (2004b) [64], concerning the measured amplitude or energy of water table fluctuations in actual sloping beaches. In the case of our wave canal, the spectral peak observed at the longer periods (T_2 and/or T_3) is probably due to the indirect effects of wave run up flow on the subsurface water table fluctuations.

In real systems, a large amplitude (peak of energy) can be observed in relation with the return period of storm events, which cause wave set up at the shoreline at relatively low frequencies. These long periods then induce water table fluctuations that propagate further inland. Finally, another possible "effect" which can enhance the energy of lower frequencies is capillarity. Indeed, both measurements and simulations (eg. **Chapter 5**, **Chapter 6**, **Chapter 7** and Horn 2006 [19]) indicate that the fluctuating water table beneath the sloping beach surface drops off more slowly than it rises, as a result of capillary effects. Incidentally, the slower drawdown of the water table due to unsaturated drainage can be taken into account

by the Richards equation, but not by the Dupuit-Boussinesq model of groundwater flow (**Chapter 8**).

6.5.3.4 Cross correlation, lag time and wave propagation velocity between $H_1(t)$ and $H_i(t)$ (i=2, …, 7)

The cross correlation between $H_i(t)$ and $H_{i+1}(t)$ $(i = 1, \ldots, 6)$ are obtained with temporal analysis by analyzing the residuals (t=400s-1700s) shown in the above with moving average filtering.

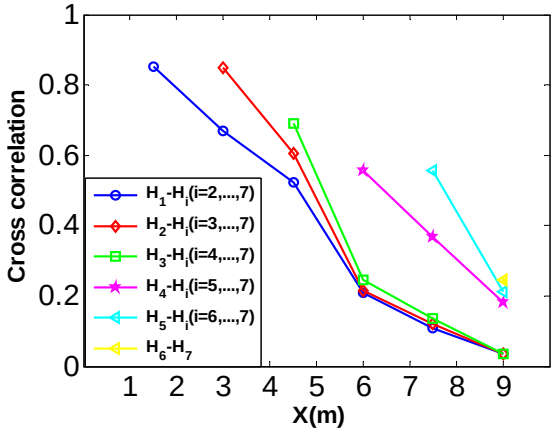

(a) Cross correlation

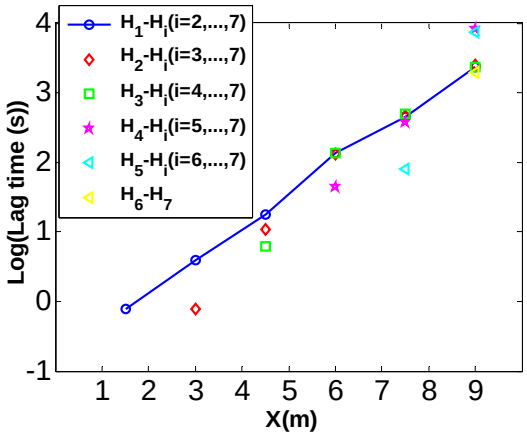

(b) Lag time

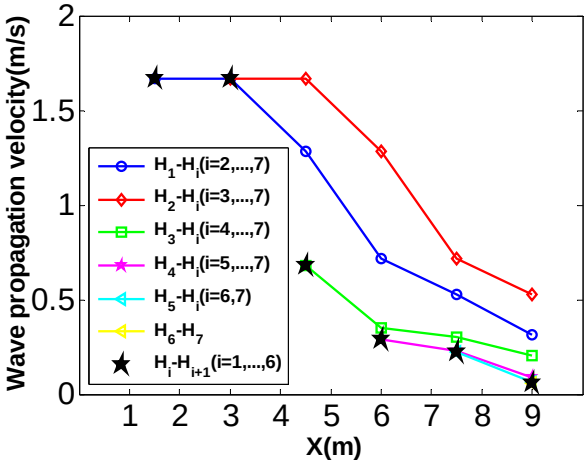

(c) Wave propagation velocity

Fig. 6-19 Maximum cross correlation coefficient, lag time and wave propagation velocity of the residuals between $H_i(t)$ and $H_{i+1}(t)$ $(i = 1,\ldots,6)$ (spatial distribution).

Notes:

(1) moving average filtering, *half window width* $w_t = 300s$ for $H_i(t)(i = 1,\ldots,6)$, and $w_t = 70$s for $H_7(t)$;

(2) Cross correlation function $R_{XY} = \frac{C_{XY}}{\sigma_X \sigma_Y}$ (unbiased estimate), and the first positive maximum value in the positive lag time; (3) lag time corresponding to the maximum correlation coefficient;

(3) Wave propagation velocity = the horizontal distance between $H_i(t)$ and $H_{i+1}(t)$ divides the corresponding lag time.

First, from the figure of maximum cross correlation coefficient of the future first wave with respect to the horizontal distance from $H_1(t)$ to $H_7(t)$ (**Fig. 6-19** (a)), it can be seen that the

correlation coefficient almost decreases linearly with the distance from more than 0.8 (between $H_1(t)$ and $H_2(t)$, and between $H_2(t)$ and $H_3(t)$) to less than 0.05 (between $H_1(t)$ and $H_7(t)$), except that there is a turning point at $H_4(t)$). This means that $H_1(t)$ has a very good cross correlation with $H_2(t)$ and $H_3(t)$) , and it has very bad cross correlation with $H_6(t)$ and $H_7(t)$), because of the fluctuation decay in the sloping sandy beach. Even though the cross correlation between the adjacent sensors of $H_6(t)$ and $H_7(t)$) is still very bad, and the cross correlation coefficient is less than 0.25.

Secondly, the lag time corresponding to the cross correlation between $H_i(t)$ and $H_{i+1}(t)$ $i = 1, \dots, 6$) exponentially increases with the horizontal distance from $H_1(t)$ to $H_7(t)$ (**Fig. 6-19** (b)).

Finally, the spacial wave propagation velocities in the sloping sandy beach are obtained by the flowing equation:

$$v_{i,i+1} = \frac{Dx_{i,i+1}}{\tau_{i,i+1}} \tag{6-2}$$

Where,

$v_{i,i+1}$ is the wave propagation velocity between H_i and $H_{i+1}(i = 1, \dots, 6)$;

$Dx_{i,i+1}$ is the horizontal distance between H_i and $H_{i+1}(i = 1, \dots, 6)$;

$\tau_{i,i+1}$ is the lag time between H_i and $H_{i+1}(i = 1, \dots, 6)$.

The spacial distribution of the wave propagation velocities with the horizontal distance is shown in **Fig. 6-19** (c). From this figure, it can be seen that the mean wave propagation velocity almost decreases gradually with horizontal distance from H_4 to H_7, v_{67} is less than 0.1m/s, while $v_{12} = v_{13} = v_{23} = v_{24} = 1.67 m/s$, the free wave propagation velocity in the swash zone.

The spatial migration of this point of maximum cross-correlation indicates a statistical phase lag, analogous to that obtained for a pure progressive wave (for a similar analyzis of wave like processes in a vertical unsaturated column, see Alastal et al. 2010 [50]).

6.5.3.5 Cross correlation and lag time of the wavelet components between $H_1(t)$ and $H_i(t)$ (i=2,…,7)

Multi-resolution wavelet analysis can be used to decompose the whole signal in dyadic number of components, which makes possible the cross correlation between the same components of two different signals. Accordingly, the cross correlations between the

components of the original signal with respect to the dyadic time scale (**Fig. 6-20** (a)) are analyzed and the results can be compared with the ones of the residuals in **6.5.4.4**.

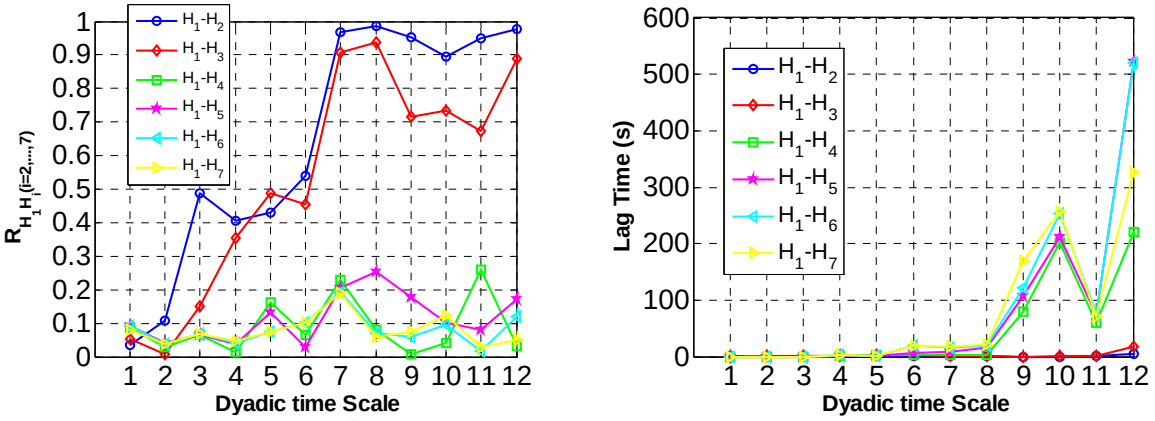

(a) Cross correlation (b) Lag time

Fig. 6-20 The maximum cross-correlation coefficient of the future first wave and the corresponding lag time of the components of the original signal between $H_1(t)$ and $H_i(t)$ (i=2,…,7) with respect to the dyadic time scale.

From **Fig. 6-20** (a), it can be seen that the same components of $H_1(t)$ and $H_2(t)$ have the best cross correlation, as for $H_1(t)$ and $H_3(t)$, while the same components of $H_1(t)$ have very bad cross correlation with the ones of $H_i(t)$(i=4,…,7). The cross correlation of C_7 and C_8 between $H_1(t)$ and $H_2(t)$ is the best among all, then it is the ones between $H_1(t)$ and $H_3(t)$, and their correlation coefficients are all greater than 0.90; meanwhile the maximum cross correlation coefficient of the components between $H_1(t)$ and $H_i(t)$(i=4,…,7) is less than 0.3. This result is consistent with the one of the residuals between $H_1(t)$ and $H_i(t)$(i=2,…,7).

The corresponding lag time with the dyadic time scale is shown in **Fig. 6-20** (b). From this figure, it can be seen that the lag time is very small (about zero) from C_1 to C_5; then from C_5 to C_8, it is a little bigger, and it almost keeps constant and the maximum lag time is 20.8s (C_8, between $H_1(t)$ and $H_7(t)$); then from C_8 to C_{10}, it linearly increases.

Furthermore, the spacial distribution of the cross correlation coefficient of the dominant components C_7, C_8, C_9 and C_{10} between $H_1(t)$ and $H_i(t)$(i=2,…,7) and the responding lag time with respect to the horizontal distance are respectively illustrated in **Fig. 6-21** (a) and (b).

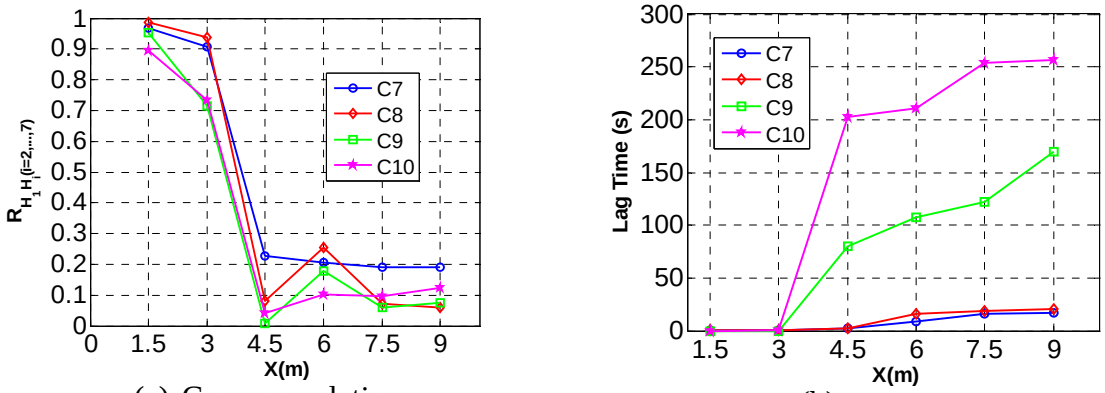

(a) Cross correlation (b) Lag time

Fig. 6-21 The maximum cross-correlation coefficient of the future first wave and the corresponding lag time of the components C_7, C_8, C_9 and C_{10} of the original signal between $H_1(t)$ and $H_i(t)$ (i=2,…,7) with respect to the horizontal distance.

Note: the wavelet dyadic time scales of C_7, C_8, C_9 and C_{10} are respectively equal to 12.8s, 25.6s, 512s, and 102.4s.

It is again shown that the components of $H_1(t)$ have a good cross correlation with the ones of $H_2(t)$ and $H_3(t)$, while they have very bad cross correlation with the ones of $H_4(t)$, $H_5(t)$, $H_6(t)$, and $H_7(t)$. It can be further explained that the dominant components (C_7 and C_8) of $H_1(t)$, $H_2(t)$ and $H_3(t)$ are totally different from the ones of $H_4(t)$, $H_5(t)$, $H_6(t)$, and $H_7(t)$. In addition, the lag time of the C_7 and C_8 is much smaller than the one of C_9 and C_{10} from $H_3(t)$ to $H_7(t)$, and the lag time of C_{10} is bigger than the one of C_9. It seems that there is a transient zone in which the lag time has a bigger slope than in the sea (macro porous media) and in the sloping sandy beach. The transient zones for C_7, C_8, C_9 and C_{10} are respectively from $H_4(t)$ to $H_6(t)$, from $H_5(t)$ to $H_6(t)$, from $H_3(t)$ to $H_4(t)$ and $H_3(t)$ to $H_4(t)$.

Finally, it is worthy noted that the wavelet component dyadic time scale of $H_1(t)$ is not equal to the dominant period obtained with Fourier spectrum analysis for the measured water level fluctuations in Barcelona wave canal (**Table 6-1**). However, the original signal and the residual of $H_1(t)$, the same component has the same dominant period with Fourier spectrum analysis.

6.5.3.6 Spectral coherency function between $H_1(t)$ and $H_i(t)$

The spectral coherency between the residuals of $H_1(t)$ and $H_i(t)$ (i=2,…,7) were computed at different frequencies in the frequency range f = 0-0.2 Hz (or: $T \geq 5s$). These coherency functions are plotted in:

- **Fig. 6-22**. ($H_1(t)$ and $H_i(t)$ (i=2,3,4), with τ_{Tuckey} =300s (moderate smoothing);

- **Fig. 6-23**. ($H_1(t)$ and $H_i(t)$ (i=5,6,7), with τ_{Tuckey} =300s (moderate smoothing);
- **Fig. 6-24**. ($H_1(t)$ and $H_i(t)(i=2,\ldots,7)$, with τ_{Tuckey} =30s (more smoothing).

where the term "smoothing" refers to spectral smoothing induced by the Tuckey filter, as defined for instance in Yevjevich (1972) [3], Priestley (1981) [60], Papoulis and Pillai (2002) [23], and others (see also : Blackman and Tuckey 1958 [78]).

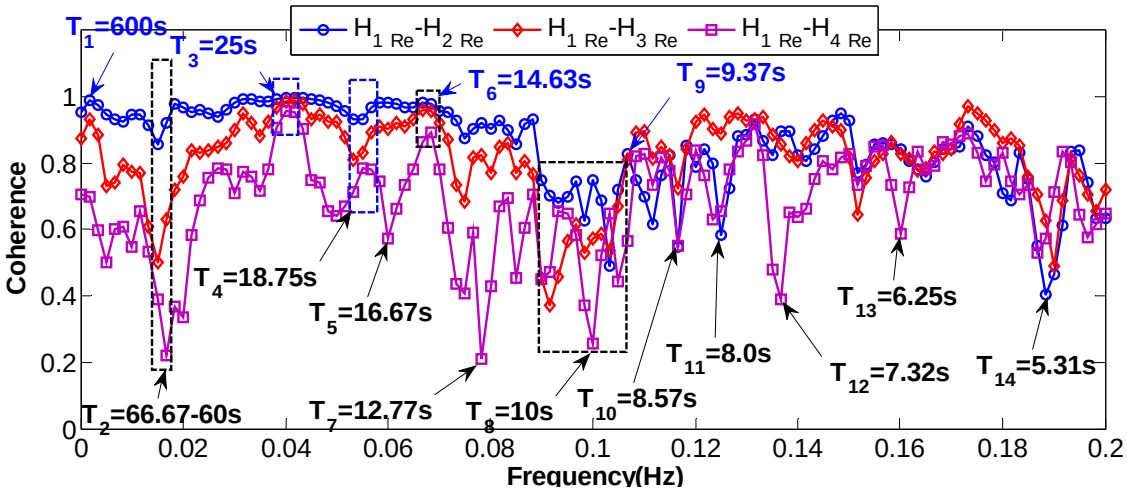

Fig. 6-22 Fourier cross analysis: spectral coherency between the residuals of $H_1(t)$ and $H_i(t)(i=2,3,4)$ at t=400-1700s for a frequency range f = 0-0.2 Hz (or $T \geq 5s$). Spectral estimation with τ_{Tuckey} =300s.

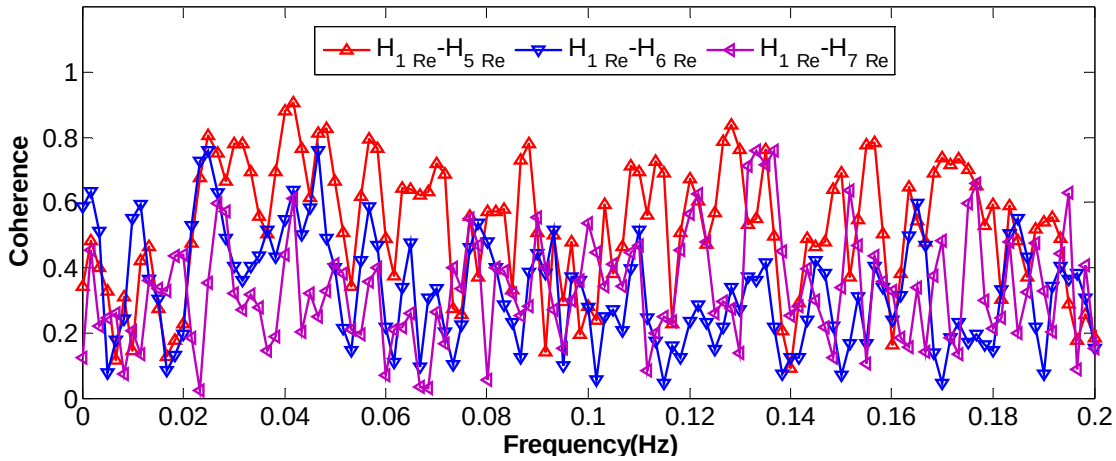

Fig. 6-23 Fourier cross analysis: spectral coherency between the residuals of $H_1(t)$ and $H_i(t)(i=4,\ldots,7)$ for a frequency range f = 0-0.2 Hz (or $T \geq 5s$). Spectral estimation with τ_{Tuckey} =300s.

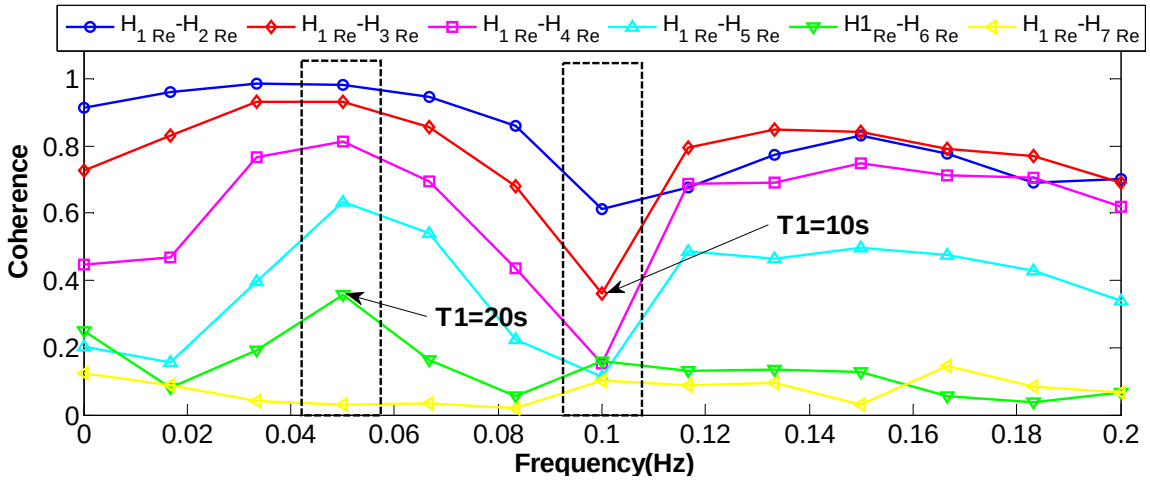

Fig. 6-24 Fourier cross analysis: spectral coherency between the residuals of $H_1(t)$ and $H_i(t)(i=2,\ldots,7)$ for a frequency range f = 0-0.2 Hz (or $T \geq 5s$). Spectral estimation with τ_{Tuckey} =30s instead of 300s.

Here, it is worth noting that:

- the residuals used to calculate the coherency are obtained with moving average filtering, choosing a window half-width $w_t = 300s$ for $H_i(t)(i=1,\ldots,6)$ and $w_t = 70s$ for $H_7(t)$;
- in the Fourier spectral analysis, the spectra are estimated by Fourier transform of the covariance functions using a Tuckey filter, with a maximum lag window τ_{Tuckey} =300s for **Fig. 6-22** and **Fig. 6-23**, and $\tau_{Tuckey} = 30s$ for **Fig. 6-24** (the smaller the lag window τ_{Tuckey}, the more smoothing there is);
- in order to estimate the coherency function of moving average residuals in a consistent way, we used the following criterion : $\tau_{Tuckey}^{max} = w_t$;

The spectral coherency functions obtained with $\tau_{Tuckey} = 300s$ and shown in **Fig. 6-22** and **Fig. 6-23** are very noisy. In order to show more clearly the spatial trend of the frequency coherency function, we also recalculated the spectra and the coherencies with more "Tuckey smoothing" ($\tau_{Tuckey} = 30s$): the result is shown in **Fig. 6-24**.

Furthermore, we can notice that the spectral resolution is inversely proportional to the max size of the Tuckey window τ_{Tuckey}^{max} :

$$\Delta f = \frac{1}{2 \times \tau_{Tuckey}^{max}}$$

Since $f = \frac{1}{T}(Hz)$, we can deduce the expression of the spectral resolution in terms of a time increment (or period increment):

$$\Delta T = \Delta f / f^2 \text{ or } \Delta T = T^2 \Delta f$$

For example, in **Fig. 6-22**, and **Fig. 6-23**, we have:

$$\Delta f = \frac{1}{2 \times 300} = 0.001667 Hz,$$

$$\text{T=24s} \Rightarrow \Delta T = T^2 \Delta f = 24^2 \times 0.001667 = 0.96 s;$$

Similarly, in **Fig. 6-24**, we have:

$$\Delta f = \frac{1}{2 \times 30} = 0.01667 Hz$$

$$\text{T=24s} \Rightarrow \Delta T = 24^2 \times 0.01667 = 9.6 s.$$

In **Fig. 6-22**, the spectral coherency functions between signal $H_1(t)$ and signals $H_2(t)$,…, $H_4(t)$ are noisy, but nevertheless, a few common features can be observed (coherency troughs and peaks). For instance, there are 3 common coherency troughs at T_2=66s, T_8=10s, and T_{14}=5.31s (serious incoherency), and there are 3 common coherency peaks at T_3=25s, T_6=14.63s and T_9=9.37s (good coherency). For $T \geq 15s$, the residual of $H_1(t)$ has the best coherency with the one of $H_2(t)$ among all the signals. For $T_9 = 9.37s \geq T \geq 2s$, compared with the coherency of the residual between $H_1(t)$ and $H_2(t)$, the coherencies of the residual between $H_1(t)$ and $H_3(t)$ as well as $H_4(t)$ have been improved a little, as seen in **Fig. 6-22** and **Fig. 6-24**.

From **Fig. 6-23**, it can be seen that the spectral coherencies between the residuals of $H_1(t)$ and $H_i(t)(i = 5,\ldots,7)$ are totally noisy. This indicates in another way that the signal $H_1(t)$ is different from the signals of $H_i(t)(i = 5,\ldots,7)$. However, in **Fig. 6-24**, the spectral coherency functions have been smoothed out indirectly (via the spectra themselves, with a more severe Tuckey filter). A single coherency peak (good coherency) and a single coherency trough (bad coherency) emerges, for all the pairs of signals (H_1,H_i). The peak occurs for period T=20s and the trough occurs of period T=10s. The spatial evolution of coherency is also very clear.

In fact, except the period of the wave generator T≈4s, all the dominant periods of $H_1(t)$ or its residual can be interpreted as the effect of the geometry of the wave canal. For example, for T=25s $T = 25s$ and T=15s, there is a strong coherency between $H_1(t)$ and $H_i(t)(i = 2,3,4)$: this can be explained by the fact that the run-up and down flow with these two periods periodically arrives at $H_4(t)$ in the beach. For T=66s, 10s and 5.31s, there are only weak coherencies between $H_1(t)$ and $H_i(t)(i = 2,3,4)$: the canal waves with these 3 periods just barely arrive at $H_1(t)$ and then return into the canal. For T=12.77s, 7.32s and 6.25s, there are strong coherencies between $H_1(t)$ and $H_i(t)(i = 2,3)$, while there are incoherencies between $H_1(t)$ and $H_4(t)$ this may indicate that the run-up flow with these 3 periods just barely arrives at $H_4(t)$, or between $H_3(t)$ and $H_4(t)$. Here, it should be noted that the observed principal run-up limits lie between piezometers $H_4(t)$ and $H_5(t)$; in fact, the run-up limits appear to be a little lower than $H_4(t)$ and rarely higher than $H_4(t)$ (or even $H_5(t)$ sometimes). Finally, the coherencies between $H_1(t)$ and $H_i(t)(i = 5,6,7)$ are weak at all frequencies or periods. This $H_i(t)(i = 5,6,7)$is probably due to the gradual decay of all the dominant periods of $H_1(t)$ as they propagate through the sandy beach towards those 3 sensors, while at the same time, there emerges new dominant periods (lower frequencies) at $H_4(t)$, $H_5(t)$, $H_6(t)$ and $H_7(t)$.

In **Fig. 6-24**, the coherency obtained with $\tau_{Tuckey} = 30s$ can be regarded as the mean coherency. The coherency peak at $T \approx 20s$ can be explained by the fact that this period has a great influence on all the water level fluctuations in the sloping sandy beach, except $H_7(t)$, because the fluctuation has almost decayed when it arrived at $H_7(t)$. The coherency trough at $T \approx 10s$ indicates that there is a periodic backflow wave limit at $H_1(t)$, or between $H_1(t)$ and $H_2(t)$, and it only has a local influence on $H_1(t)$.

The result obtained above can be further explained in **Fig. 6-25** (spatial distribution of the coherency for the five dominant periods with respect to the horizontal distance, $\tau_{Tuckey} = 30s$).

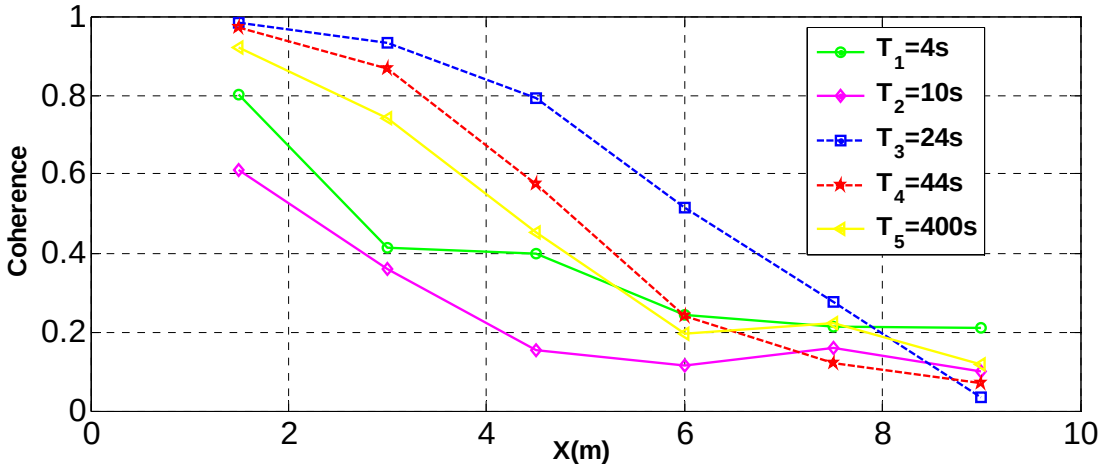

Fig. 6-25 Coherencies of the residuals, plotted with respect to horizontal distance, for several particular harmonics (periods T_j). Note: τ_{Tuckey} =30s (strong spectral smoothing).

From the figure, it can be seen that T=24s has a great influence on all the water level fluctuations except $H_7(t)$, while T=10s has little, or no influence, on any of water level fluctuations.

In addition, according to Menke et al. (1991) [85], we have tried to find if the coherency loss can be fitted by an exponential "law", that is:

$$Coherency = exp\{-k\, f\, \Delta\tau\}$$

Where, k is the decay rate;

f is the dimensional frequency (in Hz);

$\Delta\tau$ is the lag time increment between $H_1(t)$ and $H_i(t)(i=2,\ldots,7)$.

Note that $\Delta\tau$ could be seen also as a spatial lag distance Δx between sensors, via a relation of the form $\Delta x = c.\,\Delta\tau$ with some characteristic velocity "c".

The corresponding coherency loss curves are shown in **Fig. 6-26**.

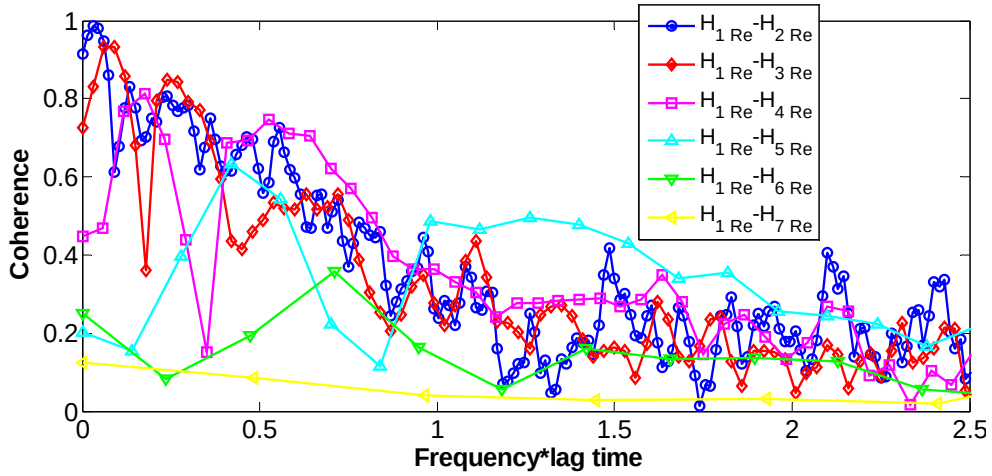

Fig. 6-26 Coherency function versus normalized frequency (frequency × lag time increment $\Delta\tau$, as explained in the text).

From this figure, it can be seen that the "law" of exponential decay of coherency with frequency×lag is not totally verified, especially concerning the coherencies between sensor $H_1(t)$ and sensors $H_i(t)(i=5,\ldots,7)$. However, it seems that the coherencies between sensor $H_1(t)$ and sensors $H_i(t)(i=2,3,4)$ approximately follow the exponential decay law, in spite of significant spectral fluctuations.

6.5.4 Detailed cross analysis between $H_1(t)$ and $H_3(t)$

6.5.4.1 Introduction

Sensor No.3 ($H_3(t)$) is installed in the sloping sandy beach at about right, 3 meters horizontal from Sensor No.1. The characteristics of $H_3(t)$ are very similar to the ones of $H_1(t)$. The cross analysis can be investigated by analyzing the original signals and the residuals with Fourier cross analysis, temporal analysis and Multi-resolution wavelet methods.

6.5.4.2 Measured wave propagation velocity

The wave propagation velocity between the sensor No.1 and No.3 can be directly observed from the zoom figure (t=0-200s) of the evolution of the water level fluctuation of $H_1(t)$ and $H_3(t)$ (**Fig. 6-27**).

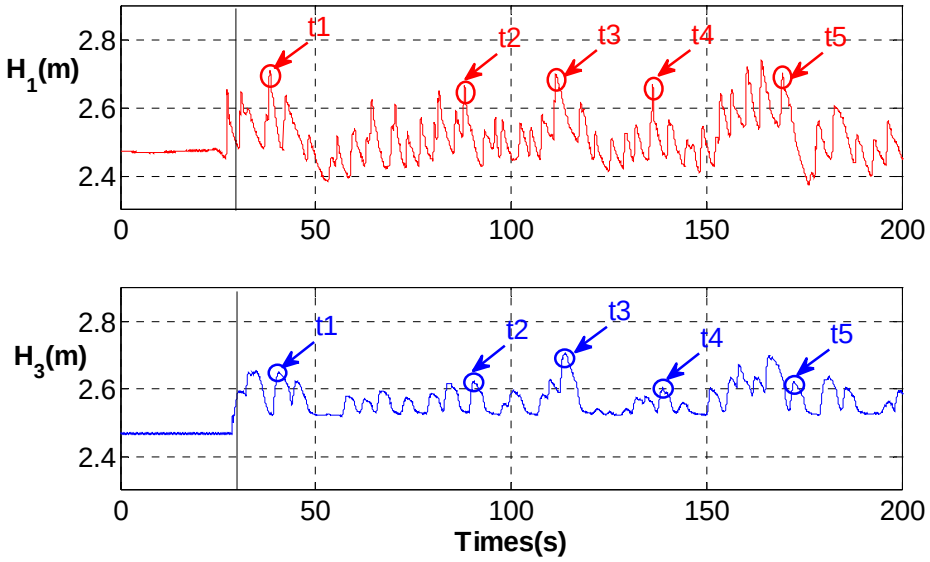

Fig. 6-27 Evolution of $H_1(t)$ and $H_3(t)$ at t=0-200s

The corresponding results are listed in the **Table 6-3**. From this table, the average of wave propagation velocity between $H_1(t)$ and $H_3(t)$ is about 1.17m/s.

Table 6-3 The wave propagation velocity between Sensor No.1 and Sensor No.3

Termes	Peak wave time **(s)**				
	t1	t2	t3	t4	t5
H_1	38.21	88.17	111.6	136.3	169.5
H_3	40.69	90.5	114.1	138.9	172.4
Lag time (s)	-2.48	-2.33	-2.50	-2.60	-2.90
Propagation velocity (m/s)	1.21	1.29	1.20	1.15	1.03
Average of Propagation velocity (m/s)	1.17				

In addition, from another zoom (t=1700-1900s, before and after the wave generator working) of the evolution of the water level fluctuation of $H_1(t)$ and $H_3(t)$ (**Fig. 6-28**), we can see that the propagation velocity of the wave peaks after the stop of the wave generator is slower than the ones during the work of the wave generator.

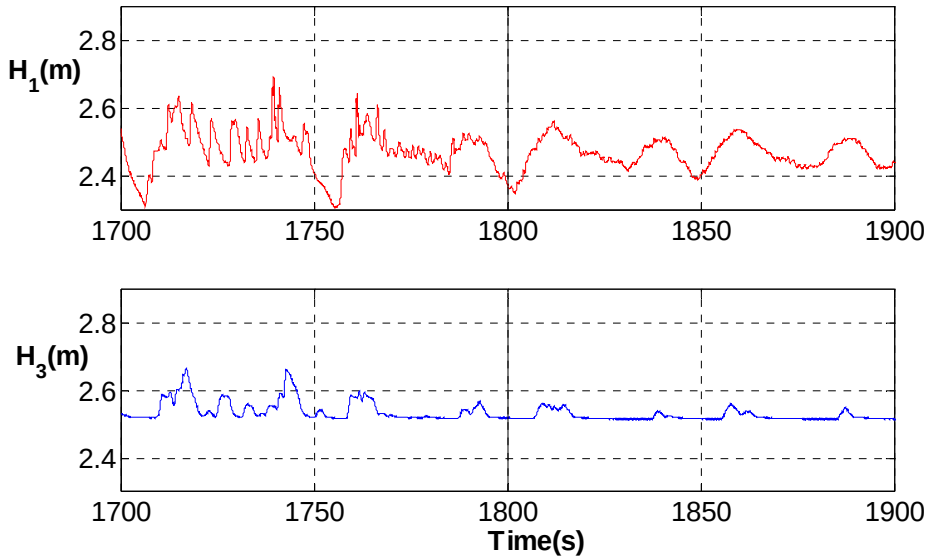

Fig. 6-28 Evolution of $H_1(t)$ and $H_3(t)$ at t=1700-1900s

6.5.4.3 Cross-spectral analysis between $H_1(t)$ and $H_3(t)$ residuals

The $H_1(t)$ and $H_3(t)$ residuals have been obtained with moving average filtering and the *half window width* w_t *=300s.* In general, the criterion between the *half window width of* moving average filtering and the maximum time lag of Turkey filter should be $\tau_{Tuckey}^{max} = w_t$

The coherencies with $\tau_{Tuckey} = 30s$ and $\tau_{Tuckey} = 300s$ are shown in **Fig. 6-29**.

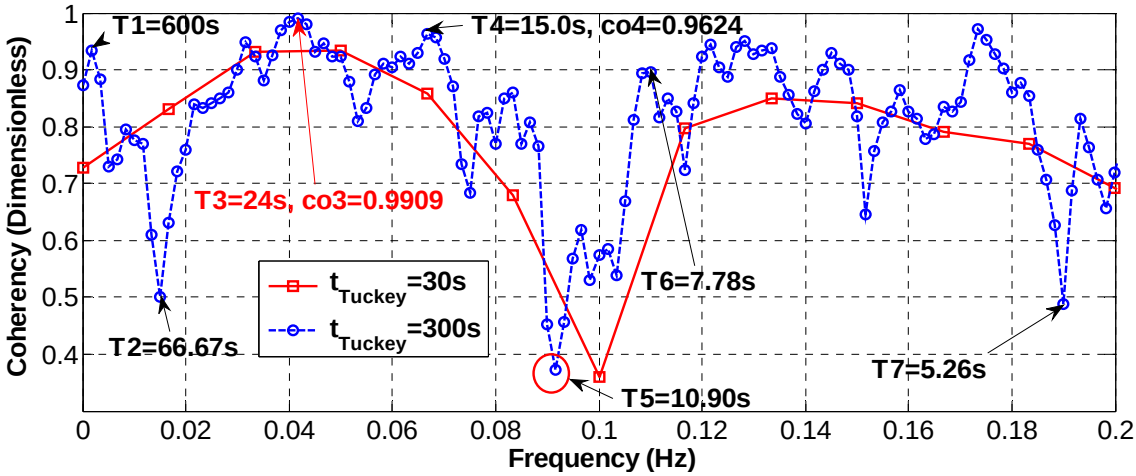

Fig. 6-29 Coherency between the residuals of $H_1(t)$ and $H_3(t)$ with respect to dimensional frequency

The result is consistent with the one obtained above. Here, the coherencys with $\tau_{Tuckey} = 30s$ and $\tau_{Tuckey} = 300s$ are put together in one figure to observe if the coherency $\tau_{Tuckey} = 30s$ can be regarded as the mean coherency of the one with $\tau_{Tuckey} = 300s$. From **Fig. 6-29**, the answer is positive.

The reduced gains of the residuals of $H_1(t)$ and $H_3(t)$ $\tau_{Tuckey} = 30s$ and $\tau_{Tuckey} = 300s$ are shown in **Fig. 6-30**.

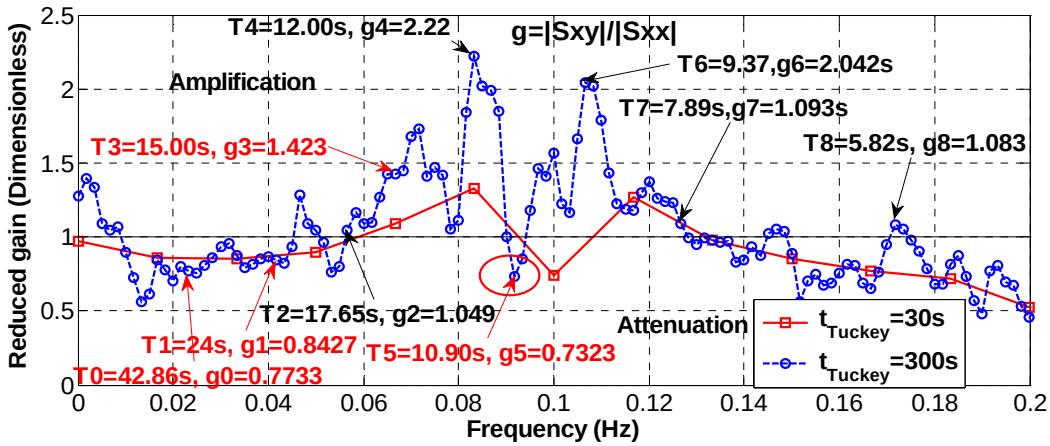

Fig. 6-30 Reduced gain between the residuals of $H_1(t)$ and $H_3(t)$ with respect to dimensional frequency

From this figure, it can be seen that compared with $H_1(t)$, the energies of the periods between 17.65s and 7.89s are all amplified at $H_3(t)$, except a gain dip at T=10.90s, in which the fluctuation energy is attenuated by about 27%. In addition, the energies of the dominant periods T_1=24s and T_2=42.86s are respectively slightly attenuated by about 16% and 23% , while the one of T_3=15s is amplified by about 42% at $H_3(t)$.

The phases of the residuals of $H_1(t)$ and $H_3(t)$ $\tau_{Tuckey} = 30s$ and $\tau_{Tuckey} = 300s$ are shown in **Fig. 6-31**.

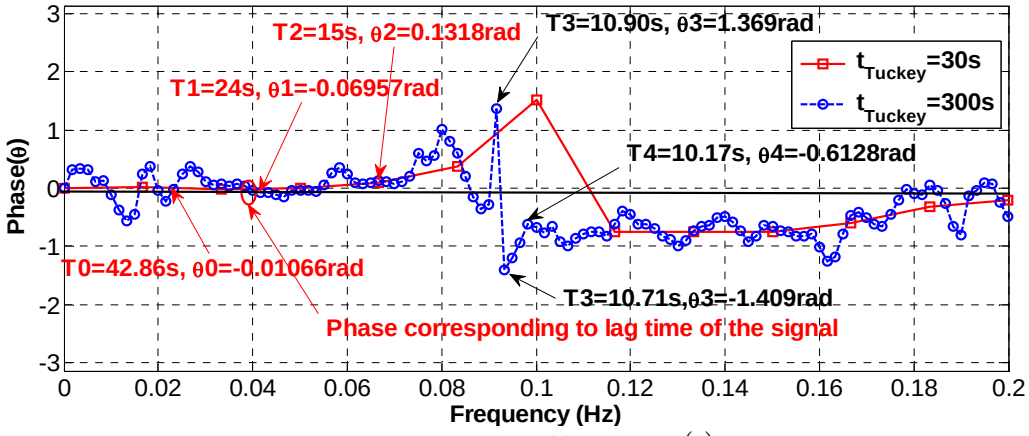

Fig. 6-31 Phase between the residuals of $H_1(t)$ and $H_3(t)$ with respect to dimensional frequency

From this figure, it can be seen that there are respectively a positive big phase peak at T=10.9s and a negative big trough at T=10.71s, and this further explains the existence of a big backward flow fluctuation with about T=10s at $H_1(t)$ or between $H_1(t)$ and $H_2(t)$.

In addition, phase function can be used to verify the lag time obtained with the temporal analysis. Since for the analogy with harmonic wave: $cos(\omega + \varphi_{12}) = cos(\omega(t + \tau_{12}))$, where, $\tau_{12} = \frac{\varphi_{12}}{\omega} = \frac{\varphi_{12}}{f} \times 2\pi$, and then at a given '$f_0$', we have: $\tau_{12}(f_0) = \frac{\varphi_{12}(f_0)}{f} \times 2\pi$. In theory, the lag time of the most dominant period of the signal is approximate to the one of the signal. In **Fig. 6-31**, for the most dominant period T=24s, it can be obtained that

$$\bar{\tau}_{H_1H_3}\left(\frac{1}{24}\right) = \frac{\varphi_{12}\left(\frac{1}{24}\right)}{\frac{1}{24}} \times 2\pi = \frac{0.06957}{0.04164} \times 2\pi = 10.49s > 1.8s = \tau_{H_1H_3}$$

(obtained with correlation analysis Matlab function xcov, unbiased estimate). This error can be explained as a consequence of the τ_{Tuckey} value for the phase function.

6.5.4.4 Temporal cross correlation between the residuals of $H_1(t)$ and $H_3(t)$

The cross-correlation function (unbiased estimate) between the residuals of $H_1(t)$ and $H_3(t)$ with respect to the lag time is shown in the **Fig. 6-32**.

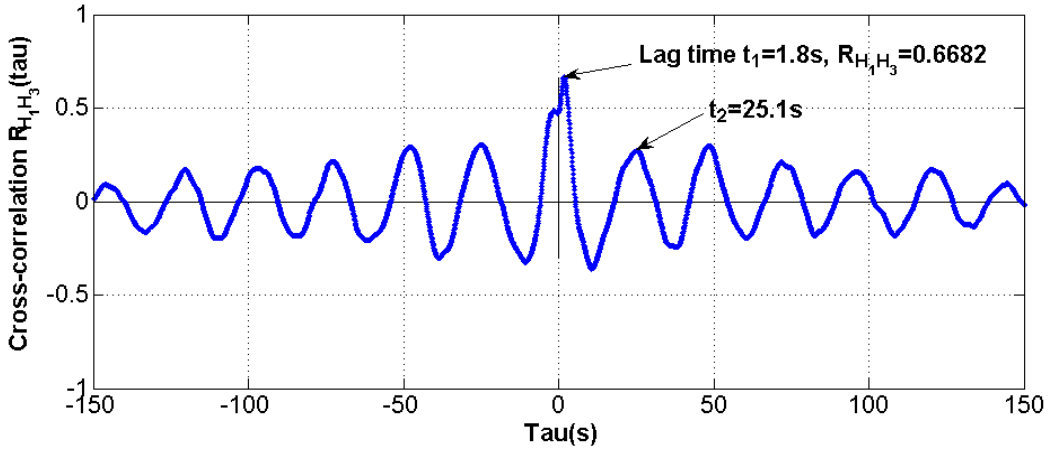

Fig. 6-32 Cross-correlation function of the residuals of $H_1(t)$ and $H_3(t)$ (t=400s-1700s) with respect to lag time (Matlab function xcov, *unbiased* estimate)

From this figure, it can be seen that there is a lag time of 1.8s from $H_1(t)$ to $H_3(t)$. In addition, $H_1(t)$ and $H_3(t)$ have a middle and upper cross correlation and the maximum correlation coefficient is 0.6682. The main period of the cross correlation function 23.5s is approximate to the most dominant period of $H_1(t)$ and $H_3(t)$, which is obtained with Fourier single spectral analysis.

6.5.4.5 Cross analysis with multi-resolution wavelet and temporal analysis

The multi-resolution wavelet analysis is used to decompose the original signals of $H_1(t)$ and $H_3(t)$ into components in 13 dyadic scales and then the temporal analysis is used to do the cross correlation between the same component at all dyadic scales. The maximum cross correlation function with respect to the dyadic scale and the corresponding lag time are shown in **Fig. 6-33**.

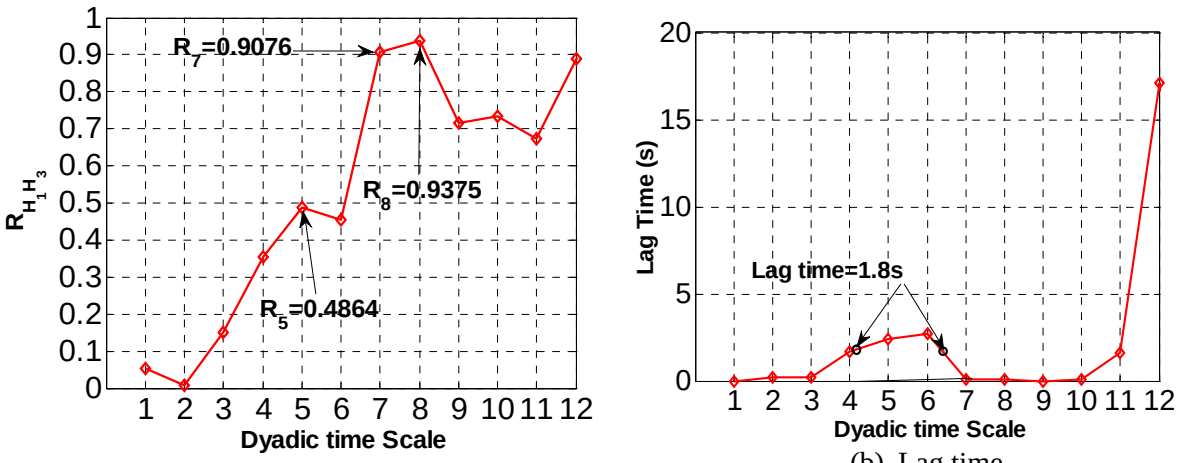

(a) Cross correlation (b) Lag time

Fig. 6-33 The maximum positive cross-correlation coefficient of the positive lag time, and the corresponding lag time of the components of the original signal between $H_1(t)$ and $H_3(t)$

From this figure, it can be seen that the component C_8 has the largest cross correlation between $H_1(t)$ and $H_3(t)$, and then it is C_7. The two cross correlation are greater than 0.9. There is a cross correlation peak at C_5, but its cross correlation coefficient is about 0.5. It means that the wave generator period has a very low influence between $H_1(t)$ and $H_3(t)$. **Fig. 6-33** (b) indicates that the lag time of the whole signal 1.8s appears between C_3 and C_7, rather than in the principal components C_7 and C_8. This is not totally consistent with the result with Fourier gain function presented above.

In addition, the cross correlation of the components C_5, C_7 and C_8 are illustrated in **Fig. 6-34**.

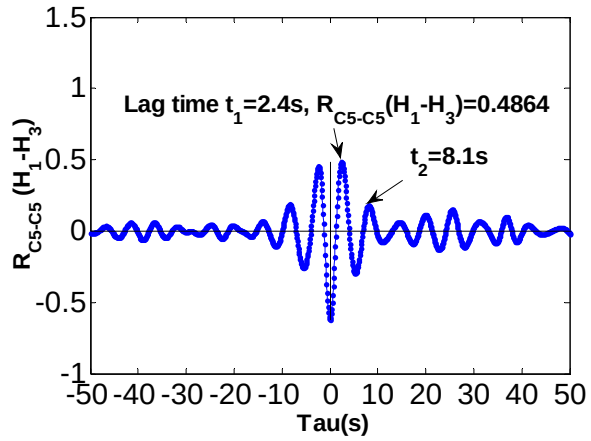

(a) C_5

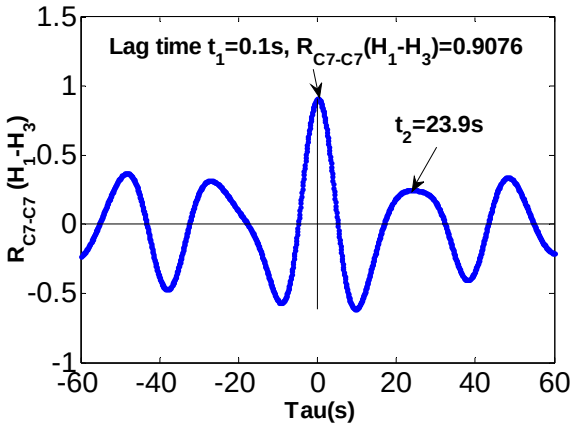

(b) C_7

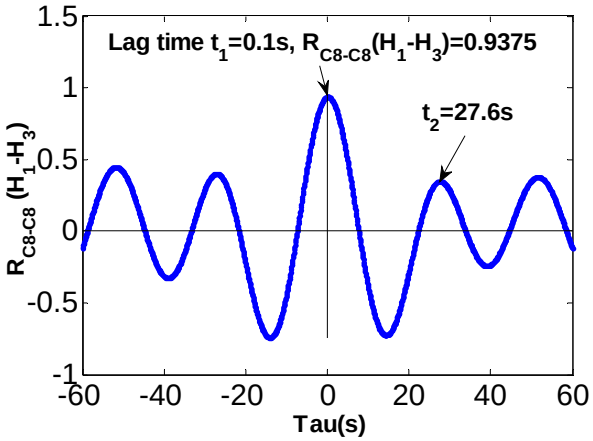

(c) C_8

Fig. 6-34 Cross correlation function of the wavelet dyadic components C_5, C_7 and C_8 between $H_1(t)$ and $H_3(t)$.

Note:
The dyadic time scales of C_5, C_7 and C_8 are respectively equal to 3.2s, 12.8s and 25.6s.

From this figure, it can be seen that the period of the cross correlation function is approximate to the dyadic wavelet time scale or more exactly Fourier period of the component.

6.5.5 Cross analysis between $H_1(t)$ and $H_7(t)$

6.5.5.1 Introduction

Sensor No.7 is installed in the slopping sandy beach at the right end of the canal, and it is about 1 m from the right vertical impermeable wall. $H_7(t)$ is very 'no-stationary' and it is total different from $H_1(t)$. The residuals of $H_1(t)$ and $H_7(t)$ by moving average filtering method is used to investigate the cross analysis of the whole signal with Fourier analysis, while the original signals are used to realize the component cross analysis with multi-resolution wavelet.

6.5.5.2 Residuals of $H_1(t)$ and $H_7(t)$ by moving average filtering

The residuals of $H_1(t)$ and $H_7(t)$ (**Fig. 6-36**) are obtained with moving average filtering by taking away the moving average from the original signal (**Fig. 6-35**).The half window width for the moving average of $H_1(t)$ is 300s and the one for $H_7(t)$ is 70s.

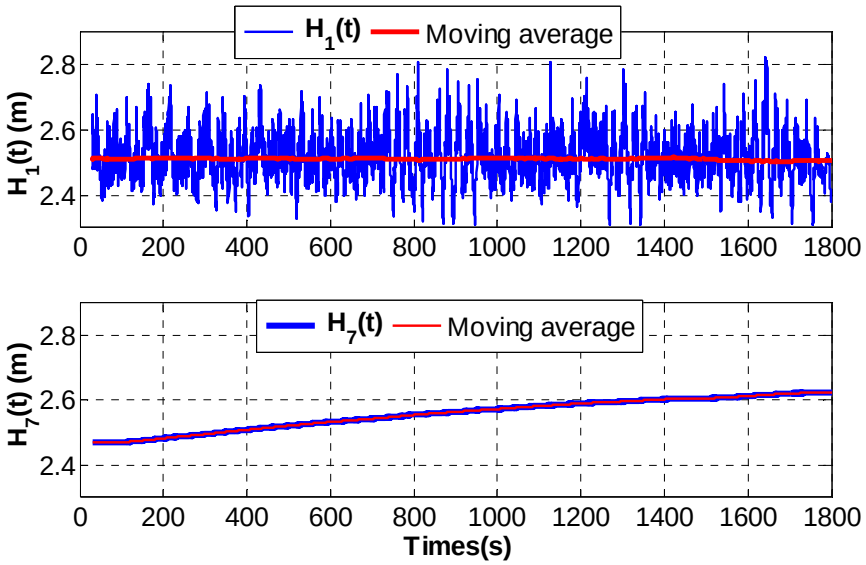

Fig. 6-35 Evolution of $H_1(t)$ and $H_7(t)$ & the corresponding moving average

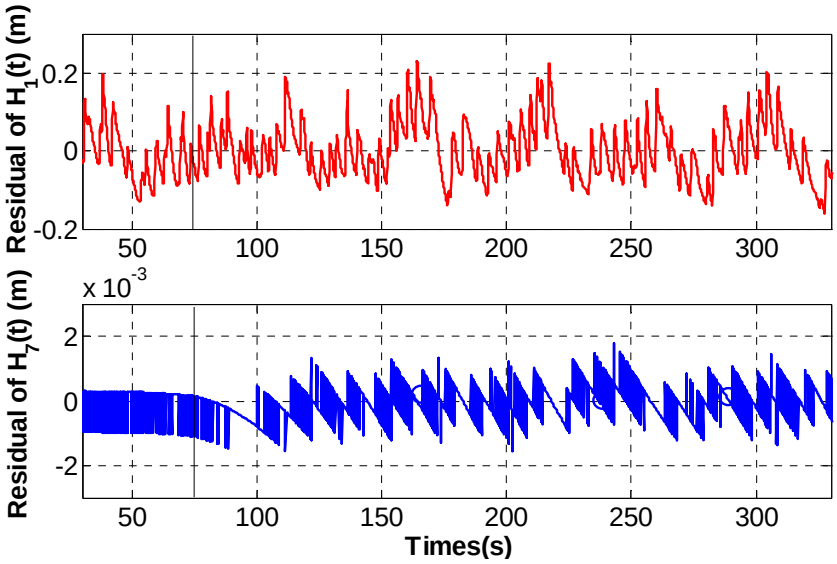

Fig. 6-36 Evolution of the residual of $H_1(t)$ and $H_7(t)$

From **Fig. 6-36**, it can be clearly seen the fluctuation decaying, and the amplitude of $H_7(t)$ is about 1/1000 of the one of $H_1(t)$.

6.5.5.3 Cross-spectral analysis of the residuals of $H_1(t)$ and $H_7(t)$

The coherency functions obtained with $\tau_{Tuckey} = 30s$ and $\tau_{Tuckey} = 300s$ are presented in **Fig. 6-37**.

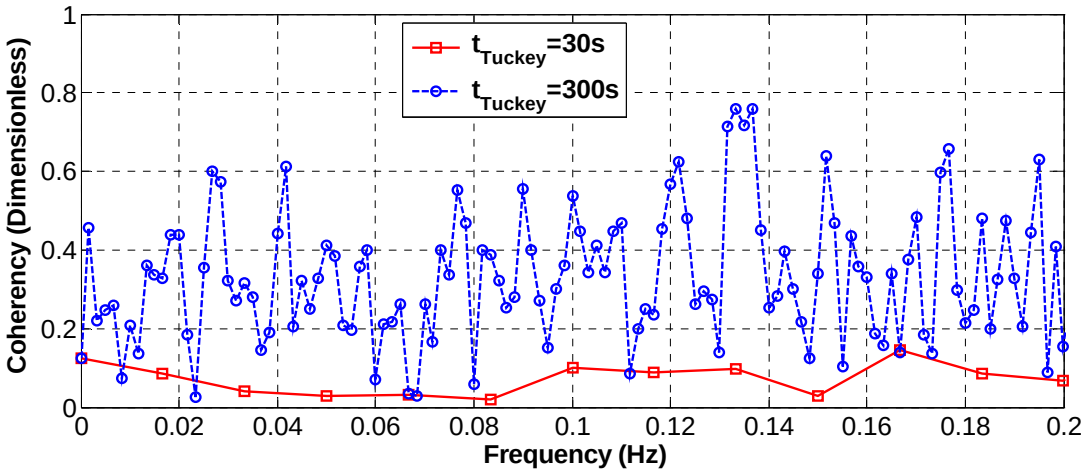

Fig. 6-37 Coherency functions of the residuals of $H_1(t)$ and $H_7(t)$ with respect to the frequency at $\tau_{\mathbf{Tuckey}}$ =30s and $\tau_{\mathbf{Tuckey}}$ =300s

This figure shows that the coherency between the residuals of $H_1(t)$ and $H_7(t)$ is very low, and the average coherency coefficient with $\tau_{Tuckey} = 300s$ is about 0.3 and the maximum obtained $\tau_{Tuckey} = 30s$ is less than 0.2. Therefore, for the two signals, the coherency functions with $\tau_{Tuckey} = 30s$ cannot be regarded as the mean value of the coherency function

with $\tau_{Tuckey} = 300s$. It indicates that the dominant periods of $H_1(t)$ has almost totally decayed at $H_7(t)$.

The reduced gain function (**Fig. 6-38**) indicates that the fluctuation energy gradually decay from $H_1(t)$ and $H_7(t)$ at all frequencies. At the same time, it can be seen that T=200s, g=1.005. This means the longer period can be easily propagated in the sloping sandy beach. What's more, for T=50, 37.5, 13.04, and 10s, the energy is attenuated by less than 50%.

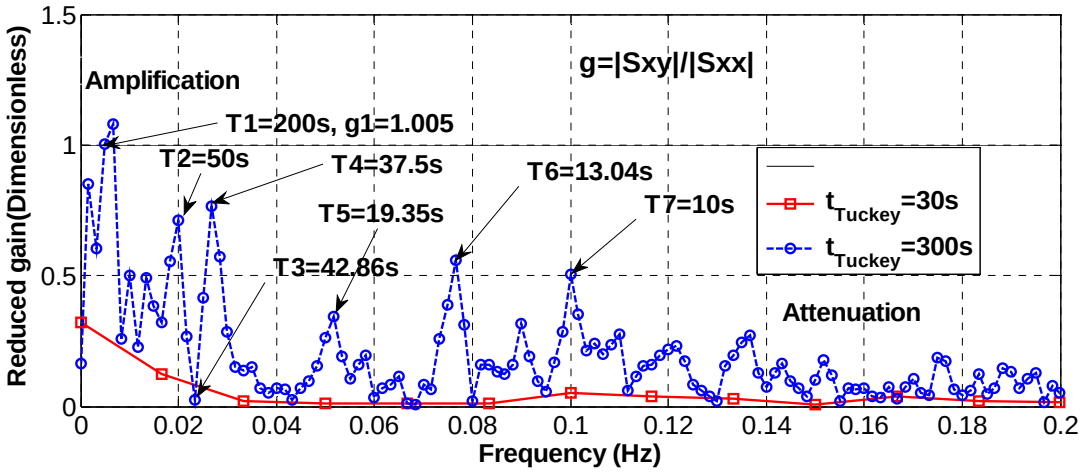

Fig. 6-38 Reduced gain function of the residuals of $H_1(t)$ and $H_7(t)$ with respect to the frequency at $\tau_{\mathbf{Tuckey}}$ =30s and $\tau_{\mathbf{Tuckey}}$ =300s

In addition, the approximate lag time of the whole signal can be found around the period T=40s in the phase function (**Fig. 6-39**), although phase function is very noisy when $T < 40s$.

$$\bar{\tau}_{H_1H_7}\left(\frac{1}{40}\right) = \frac{\varphi_{12}\left(\frac{1}{40}\right)}{\frac{1}{40}} \times 2\pi = \frac{0.05234}{0.025} \times 2\pi = 13.15s < 28.9s = \tau_{H_1H_7}$$

(obtained with correlation analysis Matlab function xcov, unbiased estimate)

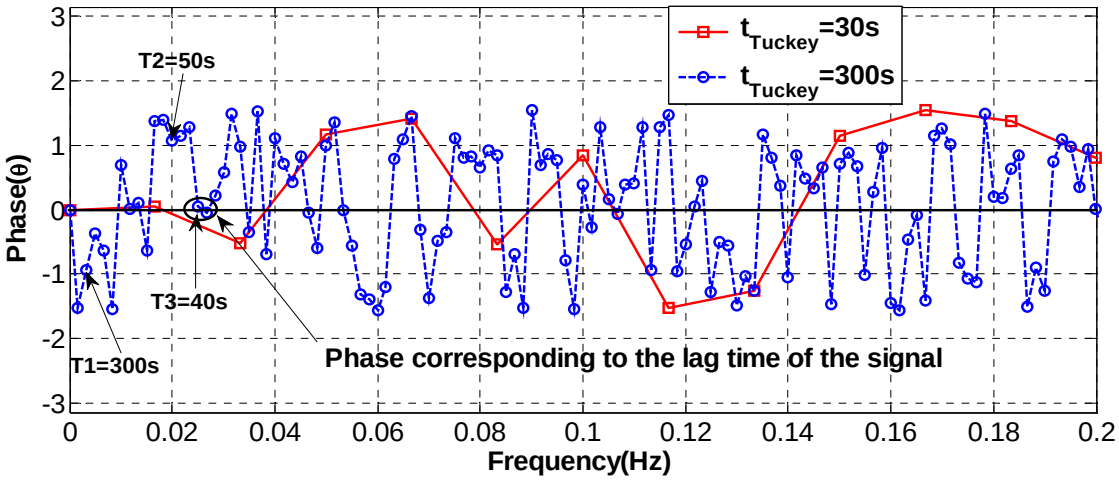

Fig. 6-39 Phase function of the residuals of $H_1(t)$ and $H_7(t)$ with respect to the frequency at $\tau_{\mathbf{Tuckey}}$ =30s and $\tau_{\mathbf{Tuckey}}$ =300s

6.5.5.4 Temporal cross-correlation between $H_1(t)$ and $H_7(t)$ residuals

The water level fluctuations $H_7(t)$ has a very bad cross correlation with the beach entry water level fluctuation $H_1(t)$. From the cross correlation function between the residuals of $H_1(t)$ and $H_7(t)$ (**Fig. 6-40**), it can be seen that the maximum cross-correlation coefficient of the first wave in the positive lag time is 0.03576. In addition, the lag time from $H_1(t)$ to $H_7(t)$ is 28.9s. This means that the mean wave propagation velocity from $H_1(t)$ to $H_7(t)$ is $V_7 = \frac{9}{28.9} = 0.311(m/s)$

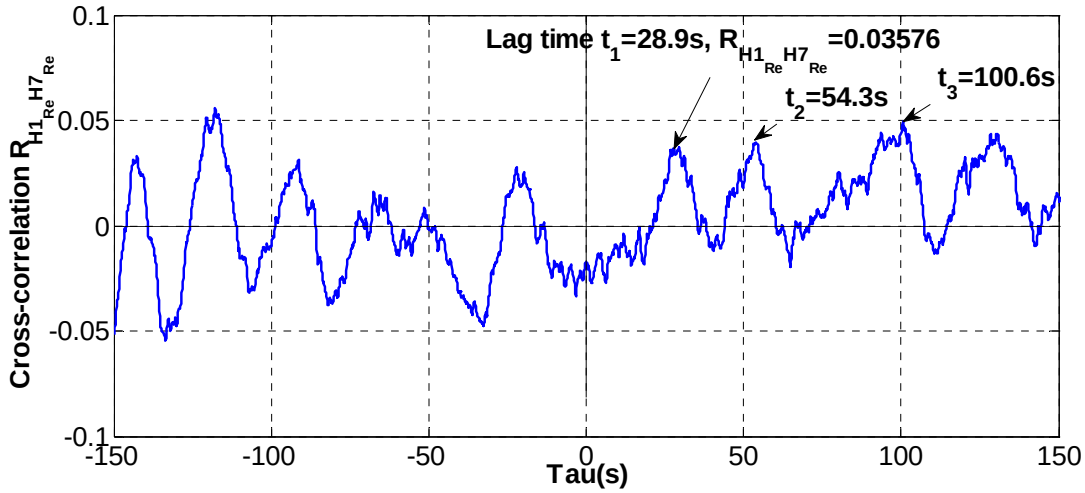

Fig. 6-40 Cross-correlation function of the residuals of $H_1(t)$ and $H_7(t)$ with respect to the past and the future lag time (Matlab function xcov, *unbiased estimate*)

6.5.5.5 Cross correlation analysis of multi-resolution wavelet components

The maximum cross correlation and the corresponding lag time of the original signal between $H_1(t)$ and $H_7(t)$ with respect to the dyadic time scale are shown in **Fig. 6-41**.

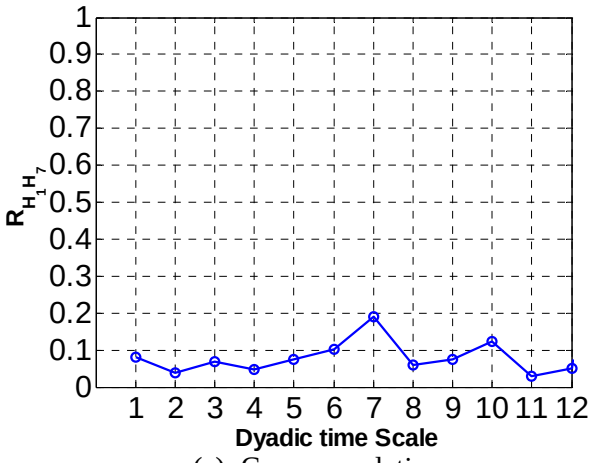

(c) Cross correlation

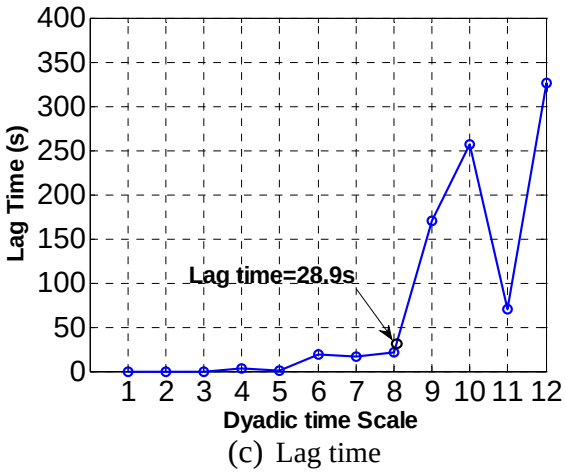

(c) Lag time

Fig. 6-41 The maximum cross-correlation coefficient of the first wave in the positive lag time and the corresponding lag time of the components of the original signals between $H_1(t)$ and $H_7(t)$

In this figure, there are two cross correlation peaks at components C_7 and C_{10}. The cross correlation for C_7 is a little better than C_{10}, but the two cross correlation coefficients are less than 0.2. The lag time $\tau_{H_1H_7} = 28.9s$ is found around C_8.

In addition, the cross correlation functions with unbiased estimate of C_7, C_8 and C_{10} are illustrated in **Fig. 6-42**.

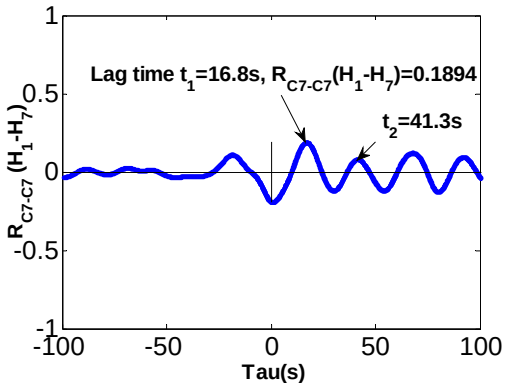

(a) C_7

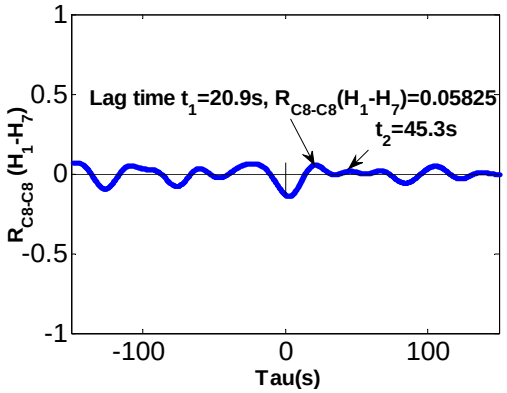

(b) C_8

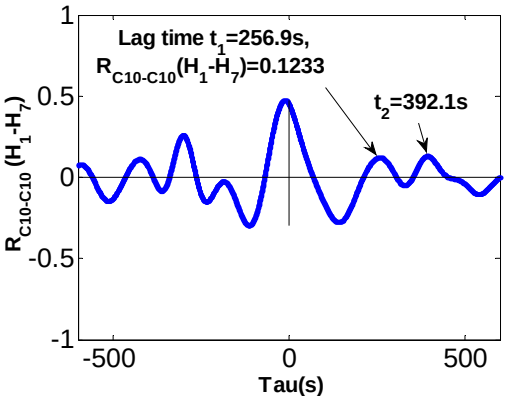

(c) C_{10}

Fig. 6-42 Cross correlation function of the wavelet dyadic components C_5, C_7 and C_8 between $H_1(t)$ and $H_7(t)$.

Note:
The dyadic time scales of C_7, C_8 and C_9 are respectively equal to 12.8s, 25.6s and 102.4s

From these three figures, it can be seen that the period of the cross correlation function is approximate to the dyadic wavelet time scale or more exactly Fourier period of the component.

In summary, the results of the cross-correlation between wavelet components of the original signal $H_1(t)$s and $H_7(t)$further validate that $H_1(t)$ has a very different fluctuation with $H_7(t)$.

6.6 Wave propagation velocity

6.6.1 Measured wave propagation velocity

In this section, we analyze wave propagation velocities in the Barcelona wave canal, via analyses of water levels $H_i(t)$ at different positions, both in surface water and ground water (sandy beach).

From the section **6.5.3.4,** the mean wave propagation velocity between H_i and H_{i+1} in the sloping sandy beach between has been obtained (see **Fig. 6-19** (c)). Similarly, the mean wave propagation velocity between open water sensors WG_i and $WG_{i+1}$is calculated in this section.

The mean wave propagation velocities in both open and ground water are shown together in **Fig. 6-43**.

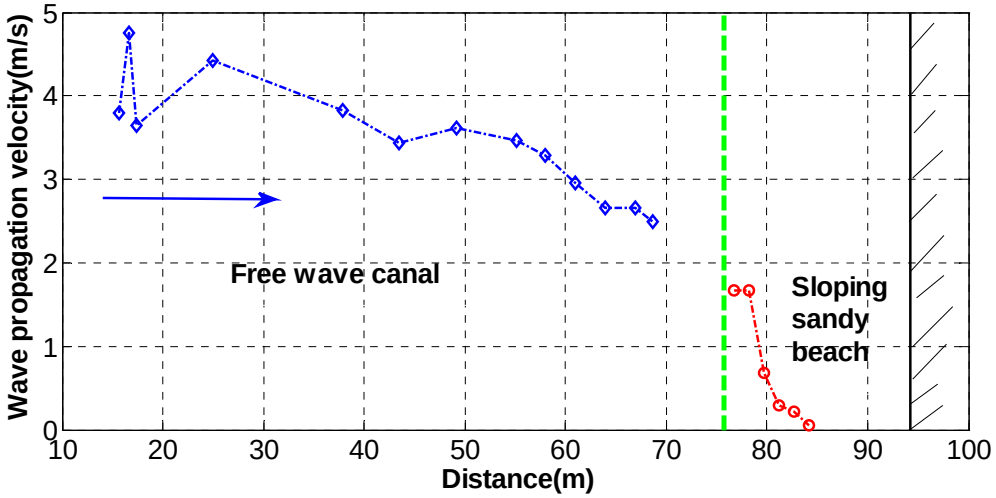

Fig. 6-43 Wave phase velocity between water level sensors $H_i(t)$ and H_{i+1} (groundwater micro-piezometers) and the one between WG_i and WG_{i+1}(open water pressure sensor) with respect to the horizontal x(i+1), in the Barcelona wave canal.

It is noted that the wave phase velocity was obtained here based on temporal cross-correlation analyses, programmed as a MATLAB script using MATLAB's XCOV function with the '*unbiased*' approach (R.Ababou); see also Alastal et al. (2010) [50]. More precisely, in the open water canal, the cross-analysis was conducted on the original signals, while in the sandy beach, the cross-analysis was conducted on the residual water levels obtained after removing the moving average.

From the **Fig. 6-43**, it can be seen that the average wave propagation velocity decreases with respect to the horizontal distance from the front of the wave generator towards the sloping sandy beach. The maximum value is equal to about 4.8m/s in the open water in front of the wave generator and the minimum value is about 0.056m/s in the sloping sandy beach

near the impermeable wall. It is also noticed that the wave propagation velocity between H_1 and H_2 is equal to the one between H_1 and H_3 in the sloping sandy beach.

6.6.2 Theoretical wave propagation velocity

6.6.2.1 Average wave propagation velocity of the open water with open wave equation

The average wave propagation velocity of the open water can be calculated with the equation: $\bar{C} = \sqrt{g.\bar{h}}$, where, g is the gravity acceleration, $\bar{h}$ is the mean water depth of the Barcelona wave canal and $\bar{h}$=2.47m for the Barcelona wave canal experiment. Therefore, it can be obtained

$$\bar{C} = \sqrt{9.81 \times 2.47} = 4.92 m/s \quad (6\text{-}3)$$

It means that the theoretical average wave propagation velocity $4.92 m/s$ in the open water is approximate to the maximum measured value about $4.8 m/s$ in front of the wave generator at the left end of the wave canal.

6.6.2.2 Average wave propagation velocity in the sloping sandy beach with Bousinesq equation

There are phase velocity and group velocity for the wave propagation in the porous media (Dean and et Dalrymple (2000) [41] ; Vichnevetsky and Bowles (1982) [77])**.**

(1) Phase velocity of Boussinesq:

$C_{Phase} = C_{Phase}(\omega) = \delta \times \omega$ (Wang, 2008 [90]) (6-4)

where,

δ is the wave decay length, and $\delta = \sqrt{\frac{2K_s\bar{h}}{\omega\Phi}}$

K_s is the saturated hydraulic conductivity of the porous media;

ω is the angular frequency;

Φ is the saturated water content.

So the phase velocity C_{Phase} of Boussinesq depends on the angular frequency ω and accordingly, the Boussinesq wave is dispersive.

For the application, the phase velocity of Boussinesq can be directly expressed with respect to the period T:

$$C_{Phase} = C_{Phase}(T) = \sqrt{\frac{4\pi K_s\bar{h}}{\Phi}}\left(\frac{1}{T}\right)^{(1/2)} \quad (6\text{-}5)$$

Now, given K_s =0.005m/s (saturated hydraulic conductivity obtained by calibrated numerical simulations of beach groundwater hydrodynamics with the Richards model in Chapter 7), Φ =0.38m^3/m^3, and $\bar{h}$ =2.47m, the period T is the only unknown parameter that remains in the above Boussinesq phase velocity equation (6-5). Then, the phase velocity of the beach groundwater can be plotted with respect to the period T in the range T=0-40s, as illustrated in **Fig. 6-44**. These results of the phase wave velocity will be helpful to obain the group wave velocity and will be analyzed with the group wave velocity.

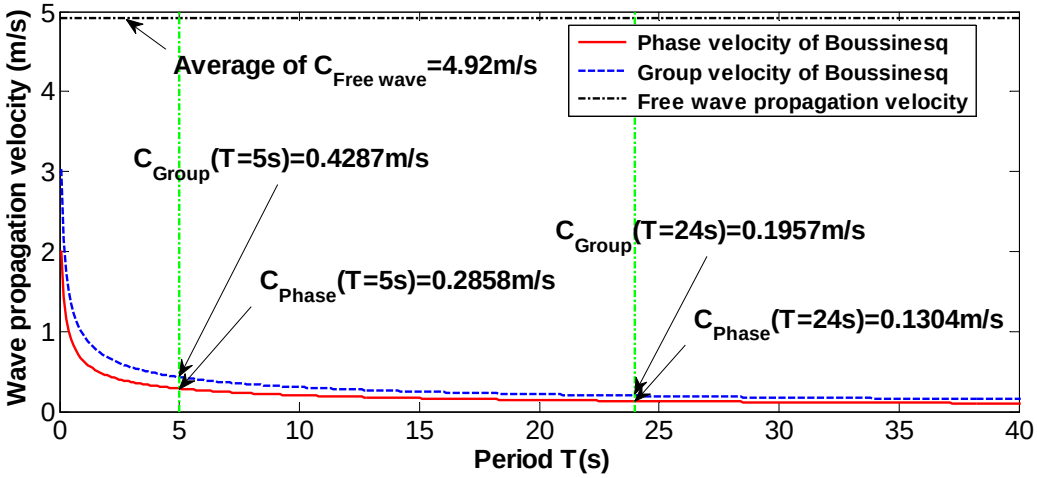

Fig. 6-44 Wave phase velocity in the sandy beach from the Dupuit-Boussinesq model, plotted with respect to the period T (range T=0-40s).

(2) Group velocity of Boussinesq:

Referencing to the books of *Dean R. G. and R. A. Dalrymple* [41] , and *Vichnevetsky R. and J. B. Bowles* [77], and an internal work on wave packets, modulated waves, and envelopes -- in either deterministic (harmonic) or statistical (random process) frameworks, the group velocity can be written as follows:

$$C_{Group} = \frac{d}{d\omega}\left(\omega . Cphase(\omega)\right) \tag{6-6}$$

Applying the phase velocity of Boussinesq equation (6-5) into the equation (6-6), the relationship equation between the phase velocity and group velocity is:

$$C_{Group} = \frac{3}{2} C_{Phase} \tag{6-7}$$

Finally, the group velocity with respect to the period is also illustrated together with the phase velocity in **Fig. 6-44**.

As a result, for the most dominant period of H_1, T=24s, we obtain:

$C_{Phase}(T = 24s) = 0.1304m$ and C_{Croup}(T=24s)=0.1957m/s;

For the wave maker period T≈5s, we obtain:

C_{Phase}(T=5s)=0.2858m/s, and C_{Croup}(T=5s)=0.4287m/s.

Here, it is noted that in the sloping sandy beach, the position H_5 is the demarcation point between the mixed zone and the pure groundwater zone. From **Fig. 6-43**, the average wave propagation velocity from H_5 to H_7, is in the range 0.2239m/s to 0.0556m/s. It is quite close to the theoretical group wave velocity (or the theoretical phase wave velocity) at T=24s, and it is about 50% smaller than the one at T=5s. In spite of this indetermination, we emphasize that the theoretical values for the two periods are on the same order with the corresponding measured values, that is, somewhat less than 0.5m/s from H_4 to H_7 (see **Fig. 6-43**).

6.7 Conclusions

In order to better understand the propagation or spatial variation characteristics of the complex entry water level fluctuations in the sloping sandy beach, we have used several methods of signal analyzis and signal processing, such as auto and cross-correlation functions, Fourier spectra and cross-spectra, and discrete multi-resolution wavelets. These methods are combined with pre-filtering methods to estimate trends and residuals (moving averages; discrete wavelet decomposition) of the measured water level fluctuations. These methods were exploited to interpret and quantify water propagation phenomena along the canal and, particularly, through the sandy beach. The main results obtained can be summarized as follows:

- A bimodal Fourier model has been obtained to simplify the complex irregular signal $H_1(t)$, which is a good approximation of the original signal and therefore, which can be used as the entry water level for numerical simulations in order to eventually make the complex sea/beach hydrodynamic partial saturated sloping sandy beach system easy understood;
- Two dominant periods (T_1=24s and T_4 = 4.83) at the entry boundary were identified with spectral analysis and multi-resolution wavelets. Period T_1=24s is interpreted as the result of the run-up and rundown flow influenced by the size and shape of the wave canal and, more importantly, also by the existence of a sloping sandy beach at one end of the canal. On the other hand, period T_4 = 4.83 s is obviously close to the wave generator period (T_0 = 4 s). Furthermore, when the dyadic time scale n≤7, it is found that the dominant Fourier period of the wavelet dyadic component of $H_1(t)$

(a non-harmonic wave) falls between the corresponding wavelet dyadic time scale (n) and the next dyadic time scale (n+1);

- The most dominant period at piezometers $H_i(t)$ $(i=1,2,3)$ is about 24 seconds, while the most dominant periods for piezometers $H_i(t)$ $(i=4,5,6,7)$ are over 10 times longer (400s, 600s, 600s again, and 300s, respectively, at i=4,5,6,7). The spectral energy of these long periods decays in the landward direction, but they are still identifiable as dominant periods when reaching groundwater piezometers $H_i(t)(i=4,5,6,7)$. These "long periods" can be interpreted as the consequence of the geometry of the wave canal and (especially) of the sloping sandy beach;
- All the fluctuation energies of the dominant periods drastically decrease along the sloping sandy beach away from the shore. The fluctuation energy of the longer periods propagates farther away from the shore (landward) compared to the shorter dominant periods;
- At the exit point of the sloping sandy beach ($H_5(t)$), the spectral peaks observed at the longer periods (T_2 =200s and/or T_3=85.69s which are shorter than the dominant period T_1=400s of $H_4(t)$) are probably due to the indirect effects of wave run up flow on the subsurface water table fluctuations or due to the vertical flow caused by the capillary effect of the sloping sandy beach. This phenomenon is consistent with the observations of Nielsen and Turner (2000), and Cartwright et al. (2004);
- Maximum cross-correlation almost decreases linearly away from the wave generator, and the corresponding lag time increases exponentially with respect to the horizontal distance in the landward direction;
- The measured average wave propagation velocity decreases with respect to horizontal distance from the wave maker towards the sandy beach. The minimum measured value 0.056m/s is fairly close to (about twice smaller than) the group velocity of period T=24s in the far beach near the impervious end wall of the canal (period T=24s is the dominant period at the beach's entry point No.1);
- Coherency functions have been used to investigate the spatial propagation of the particular periods (frequencies). For example, the peak of spectral coherency observed at $T \approx 24s$ indicates that this period has a great influence on water level fluctuations all along the sloping sandy beach, except at the farthest piezometer $H_7(t)$ near the canal right end wall. The spectral coherency trough at $T \approx 10s$ indicates that there is a

periodic backflow wave limit at $H_1(t)$ or between $H_1(t)$ and $H_2(t)$, as could be expected at the entry of the swash zone;

- The decay of the spectral coherency function with respect to normalized frequency×lag time does not really follow the exponential law suggested by Menke et al. (1991), especially between $H_1(t)$ and $H_i(t)(i=5,\ldots,7)$. The exponential decay law seems better satisfied between $H_1(t)$ and $H_i(t)(i=2,3,4)$, i.e., not too far away from the swash zone (landward).

In addition, besides these signal analyses and interpretations, numerical simulations have also been implemented in order to complement the experimental water level signal analyses and to compare them with various flow models. A preliminary version of modeling results was presented in *Wang et al. 2008*, and a more complete set of simulations have been developed in the next chapter (**Chapter 7)**.

Chapter 7: Numerical simulations of wave propagation in the sloping sandy beach of the Barcelona canal

7.1 Introduction

In order to complement the experimental water level signal analyses and to compare the measured results with various water flow models, several numerical models have been used.

The numerical models used for these comparisons include:

- A 2D plane flow model based on the vertically averaged Dupuit-Boussinesq equation for unconfined groundwater flow (with fluctuating boundary conditions);
- A 3D variably saturated flow model based on a generalized Richards' equation with two different unsaturated parameter models: VGM model and Exponential model.

7.2 Computational domain

Boussinesq model and Richards model are two types of numerical models. Accordingly, each model has its own computational domain:

(1) Boussinesq model is, in fact, a 1D numerical simulation in the x direction, and its computational length L_x will be 10m;

(2) Richards model is generalized with a fictitious macro porous medium and its computational domain is shown in **Fig. 7-1**.

Similar to the canal wave experiment in Barcelona, the length of the computational domain of Richard model is 10m and the beach slope is $1/15$.

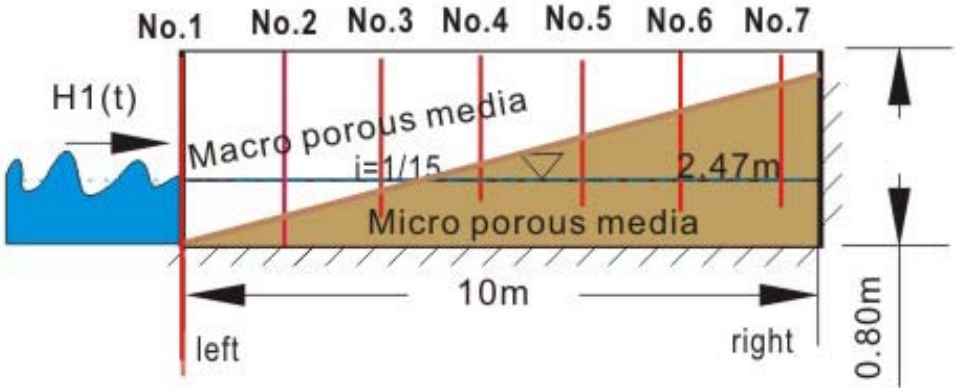

Fig. 7-1 vertical cross section of the numerical simulations of Richards model

In the numerical simulations, 7 probes (sensors) with same x position as the ones of the experiment are placed in the porous medium to measure the numerical water level fluctuation $H_i(t)$ in order to compare them with the corresponding experimental results. Their positions in the computation domain are listed in **Table 7-1**.

Table 7-1 Horizontal distance of the sensors from the left boundary

Sensor	**No.1**	**No.2**	**No.3**	**No.4**	**No.5**	**No.6**	**No.7**
Distance L_x(m)	0	1.5	3.0	4.5	6.0	7.5	9.0

7.3 Left boundary condition for the numerical simulation of Barcelona experiment

The measured water level $H_1(t)$ in the Barcelona experiment is used as the left boundary condition for the numerical simulation (see **Fig. 7-2**).

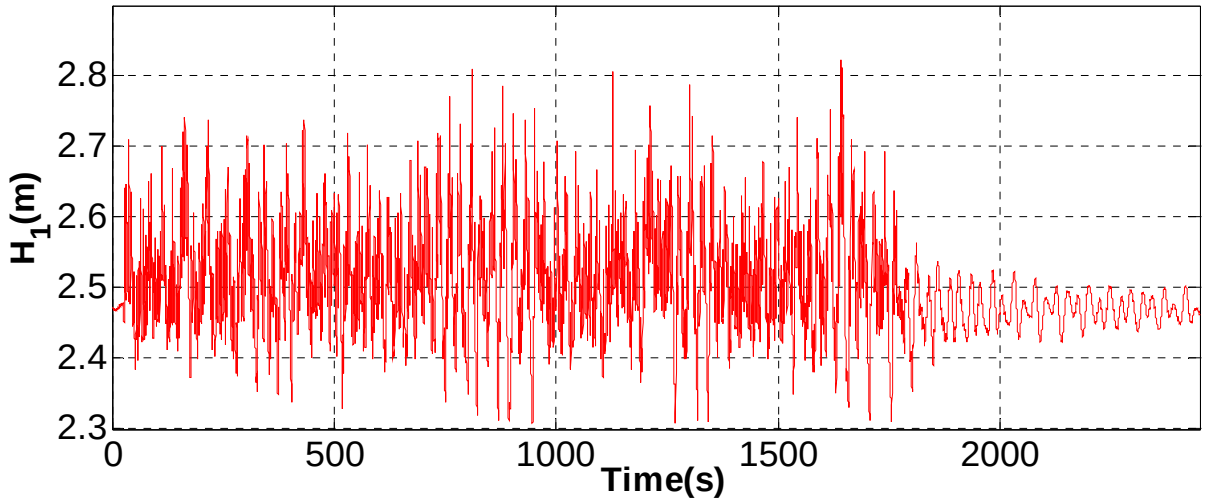

Fig. 7-2 Boundary water level condition $H_1(t)$ (experimental results)

7.4 Saturated hydraulic conductivity of the beach sand

7.4.1 Kozeny-Carman empirical formula

According to Kozeny-Carman empirical formla 1(equation (4-1), **Chapter 4**), the calculated saturated hydraulic conductivities which corresponds respectively to the minimum, mean and maximum diameters of the beach sands are listed in **Table 7-2**.

Table 7-2 Calculated saturated hydraulic conductivity by Kozeny-Carman formula 1

θ_s (m^3/m^3)	d_{50} (mm)	K_s(m/s) (Kozeny-Carman)	d_{min} (mm)	K_s(m/s) (Kozeny-Carman)	d_{max} (mm)	K_s(m/s) (Kozeny-Carman)
0.38	0.20	2.77E-4	0.063	2.75E-5	0.71	3.49E-3

7.4.2 Measured hydraulic conductivity obtained in laboratory experiment

Constant-head test (Braja 2008 [36], Bear 1972 [2]) has been used to measure the coefficient of permeability of sand.

As a result, the saturated hydraulic conductivity measured at IMFT is K_s= 1.7e-4m/s and it is of the same order with the empiric value (2.77e-4) of d_{50} with Kozneny-Carman formula.

7.4.3 Discussion about the saturated hydraulic conductivity

The Kozeny–Carman equation works well for describing coarse-grained soils such as sand and some silts (Braja 2008 [36], Bear 1972[2]). The measured saturated hydraulic conductivity is enough precise. However, the two results are obtained from cases in which the flow is laminar and in the Barcelona experiment, the entry water flow is very turbulent. It is reasonable to expect that the real saturated hydraulic conductivity will be bigger than the empiric value or the lab experimental result. The real saturated hydraulic conductivity value for the slopping sandy beach will be validated by the numerical simulations and the measured results.

7.5 Vertically hydrostatic Boussinesq model (2D)

7.5.1 Introduction

The objective of the numerical simulations in this section is to compare the results between the Boussinesq model and the experimental in the Barcelona wave canal.

This comparison will be completed in the next section with the use of the unsaturated / partially saturated Richards flow model in the (x,z) plane, without assuming vertically hydrostatic plane flow.

7.5.2 Numerical simulation with Boussinesq model

- **Simulation domain**

1D: Lx=10m; dx=0.01m.

- **Boundary condition**

Left boundary: $H(0,t)=H_1(t)$ (The experimental result, t=0-2450s)

Right boundary: flux=0.0 (Impermeable wall)

- **Initial condition**

$$H_0 = 2.47m$$

- **Physical properties of the beach**

$\theta_s = 0.38\, m^3/m^3$, K_s =2.8E-2(m/s)

- **Duration of the simulation and numerical parameters**

We have modeled one complete test of t=2450s: 30s static phase (step (1)), 1770s movements of the wave generator (step (2)), and 650s draining phase (step (3)). The numerical caculation time parameters and the numerical criteria are shown in **Table 7-3.**

Table 7-3 Numerical parameters (INPUT1) for the calculation of time step, non-linear/outer (Picard) and linear/inner iterations

Time step	Intial time step	DTIN=0.1s
	Minimum time step	DTMIN=0.1s
	Maximum time step	DTMAX=0.1s
	Time step multifier	DTMUL=1
No-linear iterations (Picard)	Convergence criterion of pressure head	ENLH3=1.0E-4
	Maximum number of no-linear iteration	INLMAX=10
Linear iterations	Convergence criterion of pressure head	ENORM3=1.0E-6
	Maximum number of linear iterations	ITEND=800

- **Numerical behaviour of Bigflow during the simulation**

Concerning the convergence of the numerical behaviour, it is difficult to find an appropriate criterion for this kind of simulations with very dynamic boundary condition. The evolution of the total net discharge entering or outgoing through all the faces of the domain Q_{Bound}(instantaneous or local) and the evolution of the discharge corresponding to the change in volume of water inside the domain during the time interval DT Q_{Mass}(instantaneous or local) have been observed, as seen in **Fig. 7-3**. The evolution of the net volume of water

entered or exited through all the sides of the field since the beginning of the simulation V_{Bound} (accumulative or global), and the evolution of the volume of water that has formed or disappeared within the area since the beginning of the simulation V_{Mass} (accumulative, global) have also been watched, as seen in **Fig. 7-4** . In **Fig. 7-3**, the evolution of Q_{Bound} completely superimposes on the evolution of Q_{Mass}. In **Fig. 7-4**, the evolution of V_{Bound} coincides very well with the evolution of V_{Mass}.

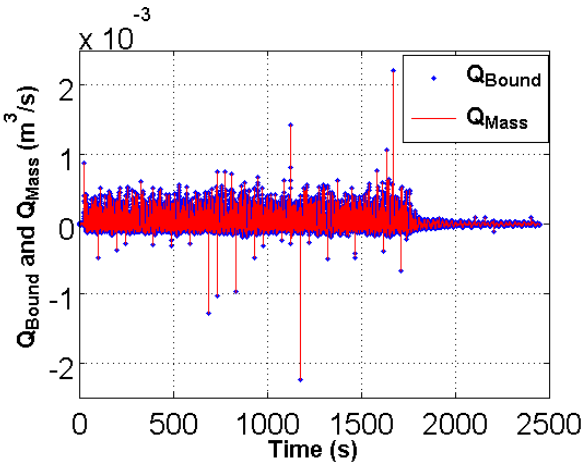

Fig. 7-3 Evolution of Q_{Bound} and Q_{Mass}

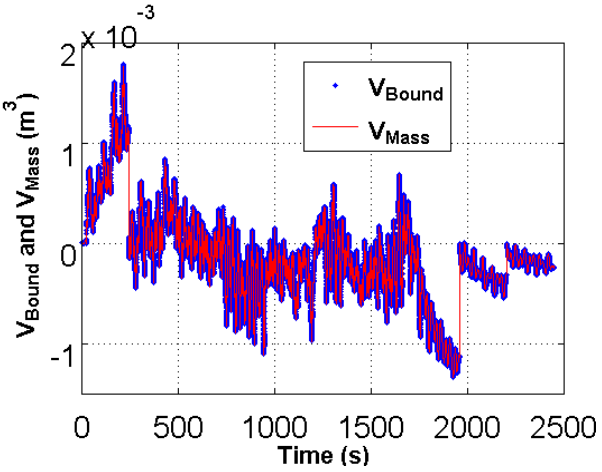

Fig. 7-4 Evolution of V_{Bound} and V_{Mass}

7.5.3 Comparisons between numerical and experimental results

The experimental and the numerical results about the evolution of the water level fluctuations at the positions Sensors No.2, No.3, No.4 , No.5, No.6, and No.7 are shown in **Fig. 7-5**.

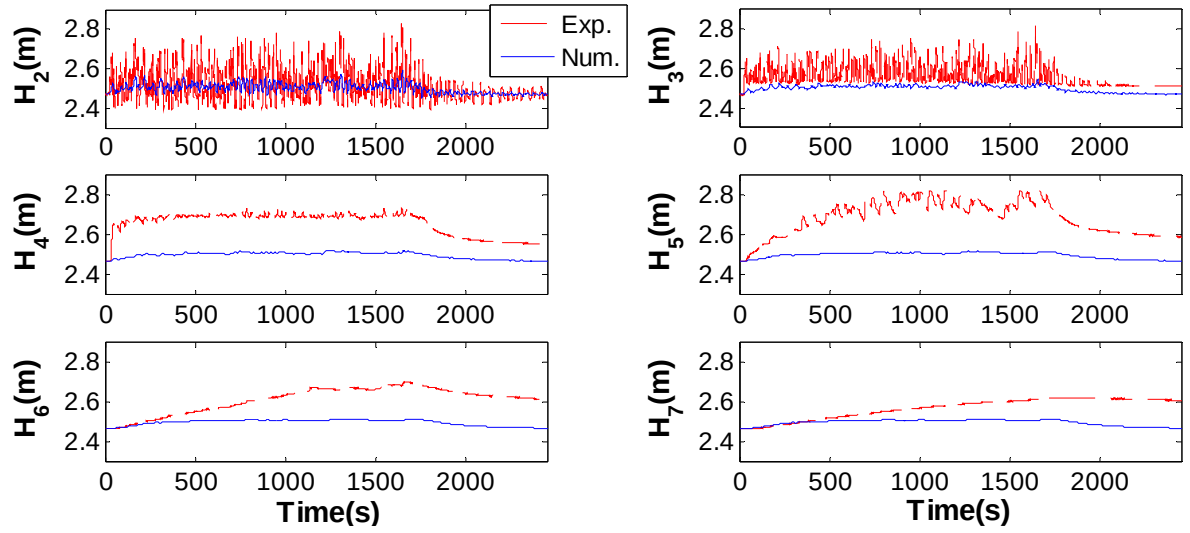

Fig. 7-5 (a) Comparisons of the measured water levels and the numerical results for the Boussinesq flow model with Ks=2.8E-2m/s: evolution of the water level at different positions : Sensors No.2, No.3, No.4, No.5, No.6 and No.7.(t=0-2450s)

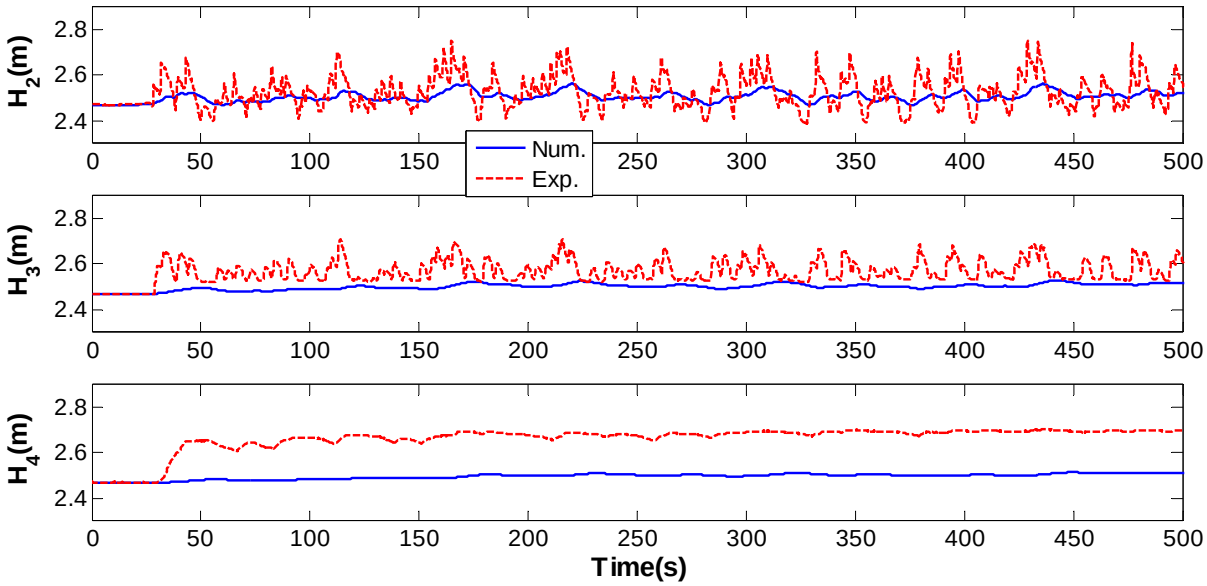

Fig. 7-5 (b) Zoom of the comparisons of the measured water levels and the numerical results for the Boussinesq flow model with Ks=2.8E-2m/s: evolution of the water level at different positions : Sensors No.2, No.3, and No.4.(t=0-500s)

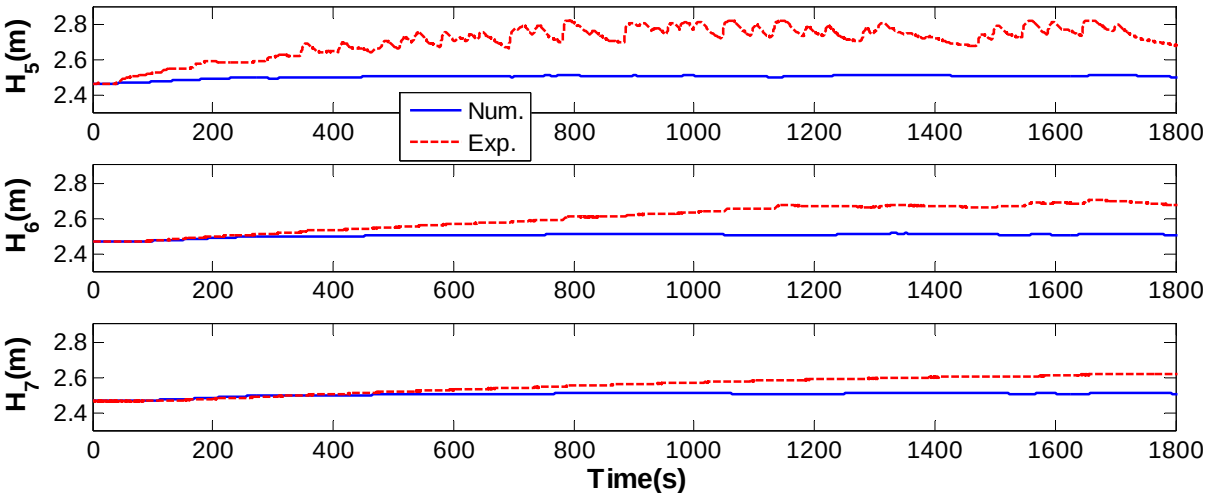

Fig. 7-5 (c) Zoom of the comparisons of the measured water levels and the numerical results for the Boussinesq flow model with Ks=2.8E-2m/s: evolution of the water level at different positions : Sensors No.5, No.6, and No.7.(t=0-1800s)

From this figure, it can be seen that the numerical results have the same evolution trend as the experimental: first, the water level fluctuations increase, then they fluctuate around a mean water level, and after the stop of the wave generator, they decrease with an exponential law. However, at the same time, it can be seen clearly that the measured water levels are still much higher than the ones of the numerical simulation in the case of $K_s = 2.8$E-2m/s. The amplitudes of the measured data are also much bigger than those of the numerical simulation for the sensors No.2 to No.5.

For these reasons, it's necessary to conduct a sensibility analysis on the soil physical properties, boundary conditions and initial conditions, in order to improve the numerical results of Boussinesq model.

7.5.4 Sensitivity analysis with respect to hydraulic conductivity Ks

In the Boussinesq model, there are mainly two dominant physical parameters: the saturated water content θ_s and the saturated hydraulic conductivity K_s of the porous media. In the experiment in Barcelona, one kind of sand was used, so the saturated water content θ_s of the sand was constant and only the single saturated hydraulic conductivity could be changed. All the conditions are kept the same as the above numerical simulation whose results are shown in the **Fig. 7-5** in the case of K_s=2.8E-2m/s, except increasing the hydraulic conductivity value by 10 times and decreasing it by 10 times. The results of the evolution of the water level fluctuations of the numerical simulations with three different saturated hydraulic conductivities: K_s=2.8E-1m/s, 2.8E-2m/s and 2.8E-3m/s are shown in **Fig. 7-6.**

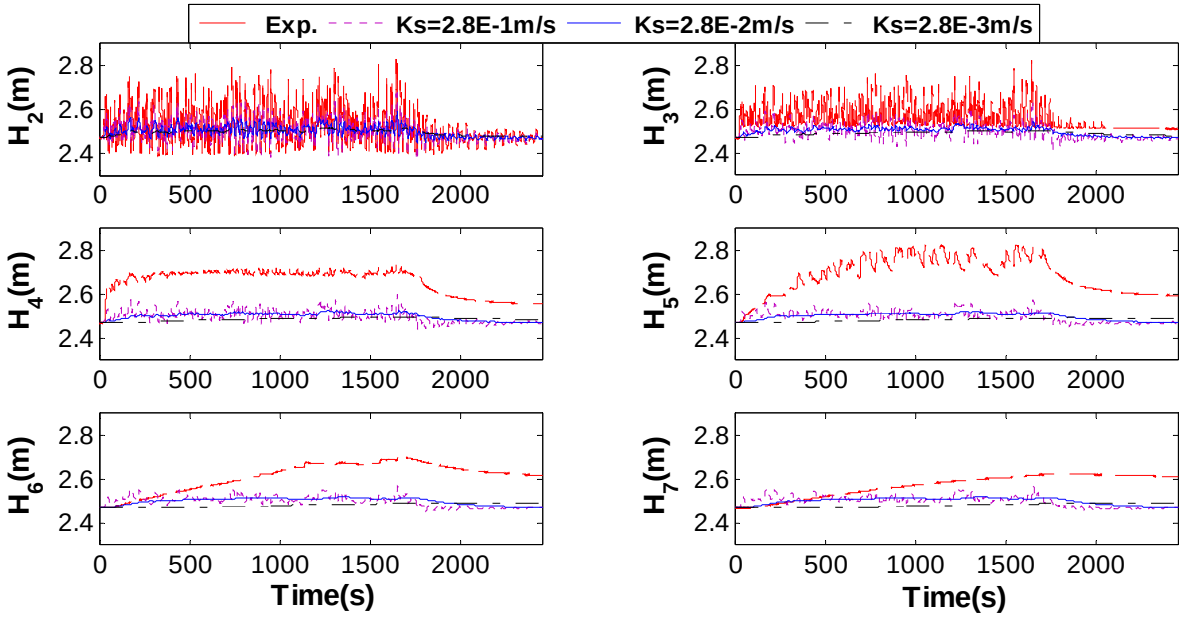

Fig. 7-6 (a) Sensitivity analysis of simulated water level evolution at different positions : Sensors No.2, No.3, No.4, No.5, No.6 and No.7.(t=0-2450s) in the cases: Ks=2.8E-1, 2.8E-2, and 2.8E-3m/s.

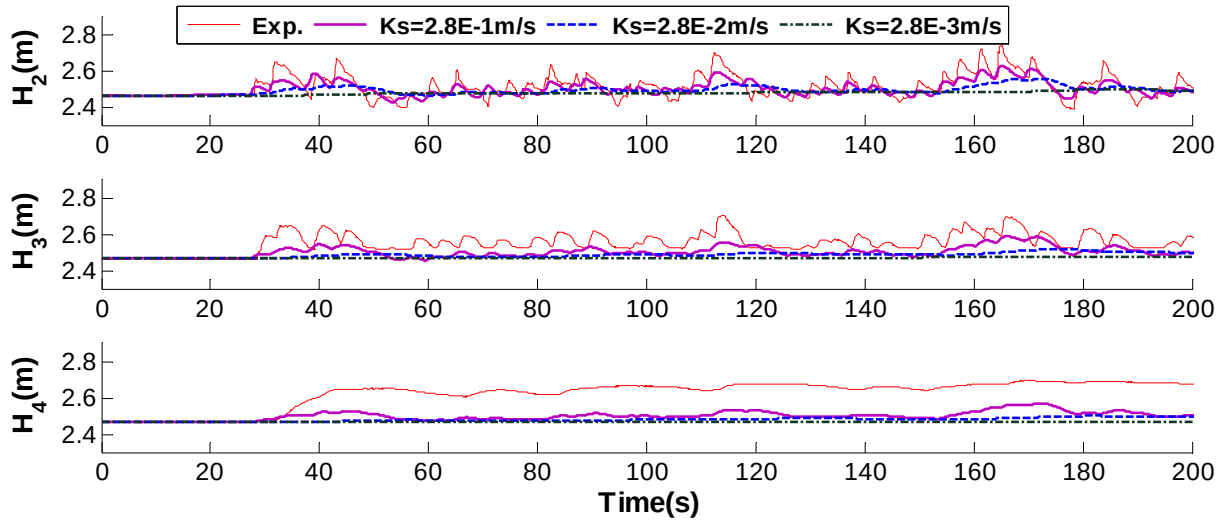

Fig. 7-6 (b) Zoom of the sensitivity analysis of simulated water level evolution at different positions : Sensors No.2, No.3, and No.4. (t=0-200s) in the cases: Ks=2.8E-1, 2.8E-2, and 2.8E-3m/s.

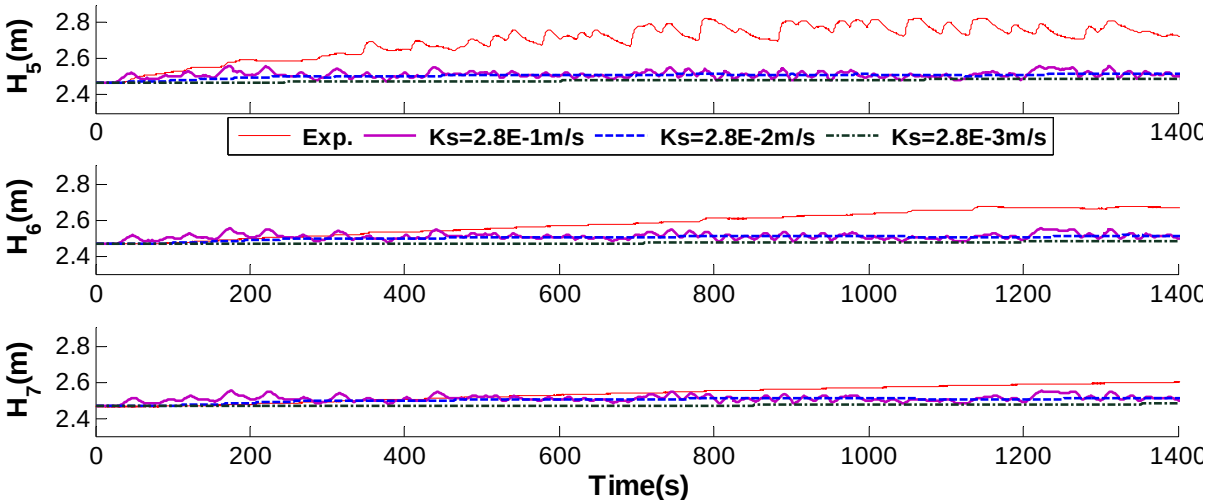

Fig. 7-6 (c) Zoom of the sensitivity analysis of simulated water level evolution at different positions: Sensors No.5, No.6, and No.7. (t=0-1400s) in the cases: Ks=2.8E-1, 2.8E-2, and 2.8E-3m/s.

From this figure, it can be seen that the bigger the hydraulic conductivity is, the bigger the amplitudes of the water level fluctuations. The mobile average water levels of the cases : K_s=2.8E-1m/s and 2.8E-2m/s are bigger than those of the case : K_s=2.8E-3m/s during the working of the wave generator, while for the two cases: K_s=2.8E-1m/s and 2.8E-2m/s ,its mobile average water levels are almost the same. Compared with the experimental results, the case of : K_s=2.8E-1m/s gives the bigger amplitudes of the water level fluctuations for the sensors from No.2 to No.5, but for the sensors No.6 and No.7, the amplitudes are much bigger than the ones of the experimental measurements.

The important thing is that the mobile average water levels of the three numerical simulations are all much smaller than those of the experimental. All other Boussinesq numerical simulations with positive height of the substratum, higher initial water level, and shorter simulated length in the x direction can't increase more the mobile average water levels.

7.5.5 Conclusion on the Dupuit-Boussinesq model

The simulated water levels $H_i(t)$ obtained with the Boussinesq plane flow model do not agree exactly with the measured water levels: the simulated water level fluctuations seem to be less important than the measured ones, and/or, the moving average water level is underestimated by the simulations (see for instance H_3, H_4, and H_5). The moving average water levels remained smaller than the observed ones for a broad range of parameters, as shown by sensitivity analysis with respect to K_s (shown in **Fig. 7-6**) -- and also with respect to substratum height, initial water levels, and domain length (not shown here). Analysis and interpretation of these discrepancies:

- The Boussinesq model does not allow vertical velocities
- The sloping beach boundary is not represented in the Boussinesq plane flow model.

Therefore, the 3D Richards flow model will next be used to simulate the oscillatory hydrodynamics in the partial saturated beach with a sloping surface, in a vertical cross-section (x,z).

7.6 Simulation with Richards model in vertical cross-section (x,z)

7.6.1 Introduction

Richards model is used to model the variably partial saturated flow. In the Richards model, the VGM model and the exponential model are used to model the unsaturated water content function $\theta(h)$ and the unsaturated hydraulic conductivity function $K(h)$.

In this Chapter, the VGM model is mainly used to validate Barcelona experiment and model this kind of problem: hydrodynamics in a sloping sand beach.

7.6.2 Hydrodynamic behavior of the macro porous medium

The effective water content model $\theta_e(h)$ and the hydraulic conductivity function $K(h)$ of the ideal macro porous media are the step functions and respectively shown in **Fig. 1-1** and **Fig. 1-2** in **Chapter 1**. In this chapter, for the numerical simulations with Richards model, the

totally saturated macro porous media is the sea water and the residual macro porous media is the air.

7.6.3 Coupling of the micro porous medium and macro porous medium

In the Barcelona experiment, the left entry water flow conditions are very complex. The entry water flow interact with the slopping sand beach by three ways: directly enter into the beach, going up and going down along the beach. It is very difficult to directly measure the real entry water flow condition. In order to simplify it, the sensor No.1 is installed near the still water / beach boundary to correspond to the entry water level fluctuations condition of the numerical simulation.

Actually, in the numerical model (domain shown in **Fig. 7-1**), there are three kinds of media: the sea water, the air and the beach sand. Therefore, the Richards model used in this Chapter is a coupling model between the macro porous media (sea water and the air) and the micro porous media (beach sand).

In the numerical Richards coupling model, the oscillatory entry water level fluctuations are directly put on the slopping beach. That is to say, the saturated hydraulic conductivity should be enough big in order to model the extremely high porous flow. As a result, there is almost no water head loss for the entry water level fluctuations during the propagation in the macro porous media and they will be put directly on the slopping beach.

In order to realize the above idea, the ratio of the saturated hydraulic conductivity of the macro porous and the micro porous media plays a dominant role in the numerical coupling. In general, this ratio should be greater than or at least equal to 10000. However, this will bring some difficulty for the iteration convergence.

7.6.4 Numerical tests with the VGM model for K(h) and θ(h)

7.6.4.1 Introduction

In the VGM model, the two principal parameters of α and n are together related to the hydraulic conductivity function $K(h)$ and the water content function $\theta(h)$.

Due to the complexity of the problem of the hydrodynamic groundwater with the sloping beach, the numerical simulations have been done by three principal steps:

Firstly, a single harmonic wave numerical experiment with one period (short run) has been done to test the ratio of the saturated hydraulic conductivity between the macro porous media (sea water) and the micro porous media (beach sands) and to make the hydrodynamic

groundwater easy understood. The detailed description of this numerical test is shown in the Appendix B: **Chapter 11**.

Secondly, a serial of one single harmonic wave numerical experiment with several periods (long run) have been done to analyze the parameters sensitivity on the groundwater level amplitudes, and the steady mean ground water levels. The detailed presentation is described in the Appendix B: **Chapter 12**.

Finally, the measured water level fluctuation of $H_1(t)$ has been used as the left entry boundary condition for the numerical simulations with VGM parameter model. The computed results will be compared with the experimental ones.

In addition, the sensitivity analysis of the main 4 parameters: K_s, θ_s, α and n, on the water level fluctuations in the slopping sandy beach has been done in order to well understand the role of each parameter and eventually, try to improve the consistency of the numerical and the experimental results.

7.6.4.2 Numerical simulation with entry water level of the experimental results $H_1(t)$

- **Simulation domain**

Vertical 2D: L_x=10m; L_z=0.8m;

dx=0.02m; dz=0.02m

The beach slope is 1/15. The schema of the simulation domain is same as the single harmonic numerical experiments, shown in **Fig. 7-1**.

- **Boundary condition**

Left boundary: $H(0,t)=H_1(t)-2.30$; (The experimental result)

Right boundary: flux=0.0. (Impermeable wall)

- **Initial condition**

$H_0 = 0.17m$, $h_0 = H_0 - z$ (linear distribution)

- **Physical properties**

The saturated hydraulic conductivity K_s for the micro porous media is taken as 0.005m/s and the one for the macro porous media is taken as 50m/s, by keeping the same ratio with one wave test. All the other physical properties for the micro porous medium and the macro medium are same as the single harmonic numerical experiment (short run). The main physical parameters are listed in **Table 7-4.**

Table 7-4 Physical properties of the micro and macro porous media

Porous media	Physical properties							
	Hydraulic conductivity			Water content		VGN model		Capillary length
	K_S (m/s)	$\frac{K_{s\,Macro}}{K_{s\,Micro}}$	K_r (m/s)	θ_s (m^3/m^3)	θ_r (m^3/m^3)	α (m^{-1})	n	λ_{cap} (cm)
Micro porous medium	0.005	1E+04	1.0E-7	0.38	0.0	5.0	1.5	20.00
Macro porous medium	50.0		1.0E-7	1	0.0	100.0	3.0	1.00

The water content curve $\theta(h)$ in log-log and the hydraulic conductivity curve $K(h)$ in log-log, the capillary diffusion coefficient $D(h)$ and the capillary capacity $C(h)$ of the two media are respectively shown in **Fig. 7-7, Fig. 7-8, Fig. 7-9** and **Fig. 7-10.**

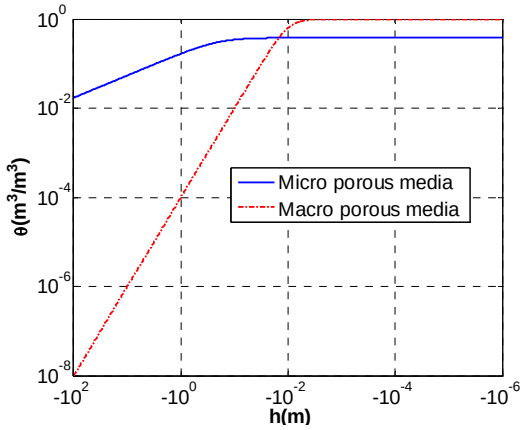

Fig. 7-7 Water content curve $\theta(h)$ in log-log of the micro porous media and the macro porous media

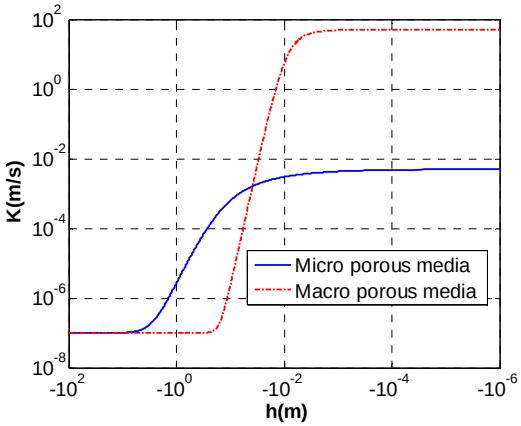

Fig. 7-8 Hydraulic conductivity curve $K(h)$ in log-log of the micro porous media and the macro porous media

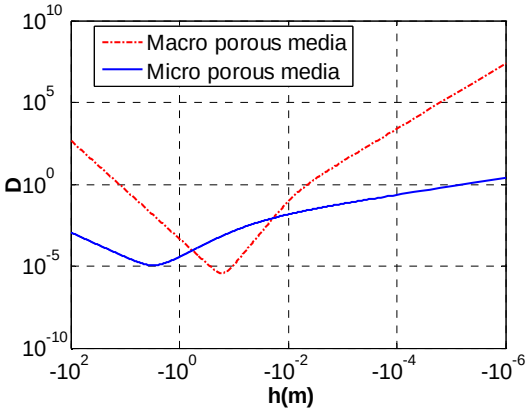

Fig. 7-9 Capillary diffusion $D(h)$ in log-log of the micro porous media and the macro porous media

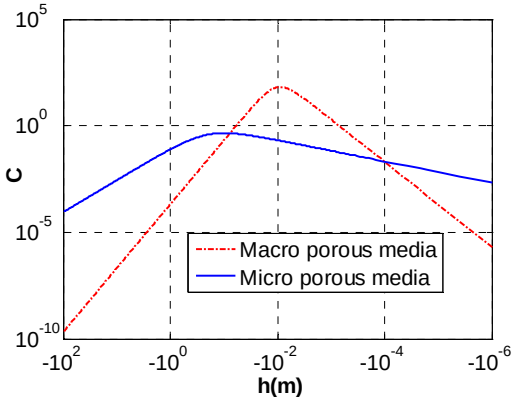

Fig. 7-10 Capillary capacity $C(h)$ in log-log of the micro porous media and the macro porous media

From these 4 figures, it can be seen that all the slopes of the curves of the properties of the macro porous media are more rapid than the ones of the micro porous media.

- **Duration of the simulation and numerical parameters**

The validation test simulates the same time as the one of the experiment (serial 14), t=2450s.

The numerical caculation time parameters and the numerical criteria are same as those of the single harmonic numerical experiments and that of the numerical simulation with Boussinesq model, shown in **Table 7-3**.

- **Numerical behaviour of Bigflow during the simulation**

The maximum errors of the linear and nonliear iterations of the pressure head are smaller than 0.1, as seen in **Fig. 7-11** and **Fig. 7-12**.

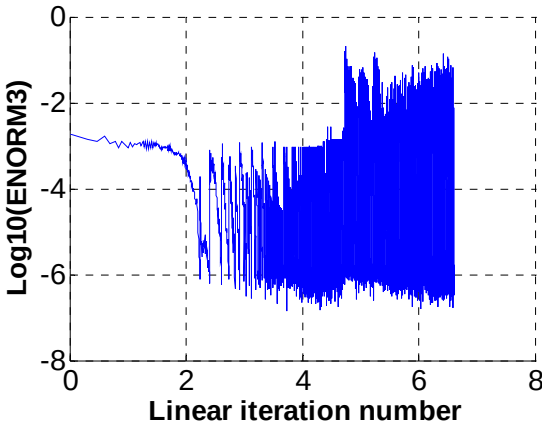

Fig. 7-11 Standardized linear iteration process of the pressure head in log10

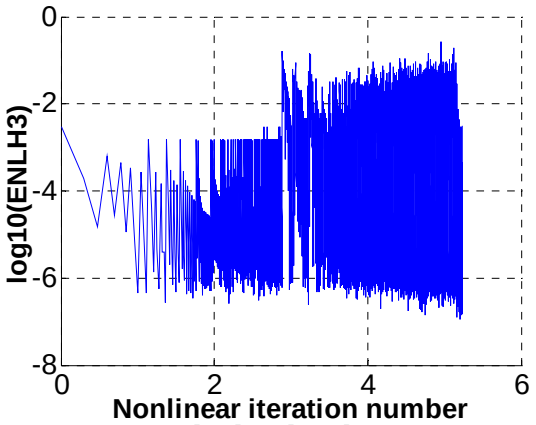

Fig. 7-12 Standardized nolinear iteration process of the pressure head in log10

From **Fig. 7-13**, it can be seen that the curve of the evolution of Q_{Bound} totally superposes on the curve of the evolution of Q_{Mass}. At the same time, it can be clearly seen the effect of the difference of the entry water level fluctuations $H_1(t)$ on Q_{Bound} and Q_{Mass} from **Fig. 7-13** and **Fig. 7-14**, especially, at t=27.3s,1127s and 1635s, the three water level differences cause the three extremely biggest values for Q_{Bound} and Q_{Mass}.

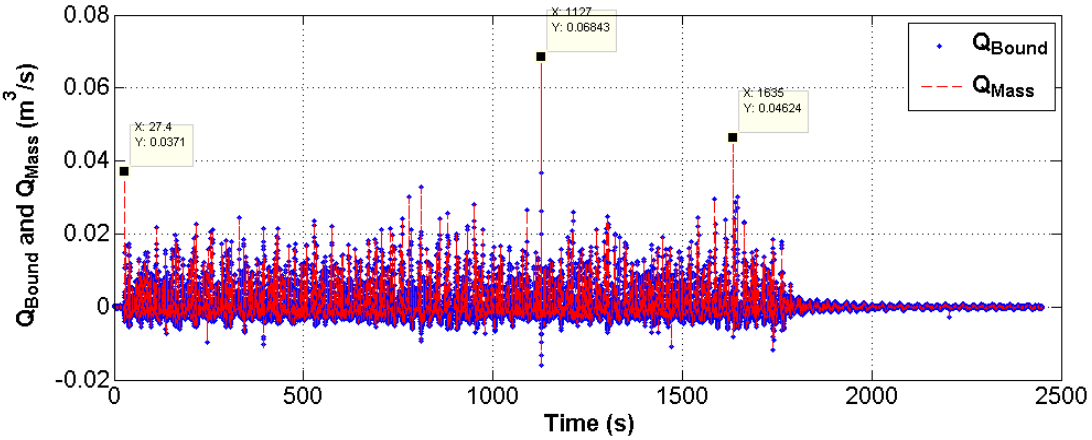

Fig. 7-13 Evolution of Q_{Bound} and Q_{Mass}

Note: The print time of the Head_Tx file has the influence on the evolution of Q_{Bound} and Q_{Mass}. This plot is the results of the simulation without the output file Head_Tx.

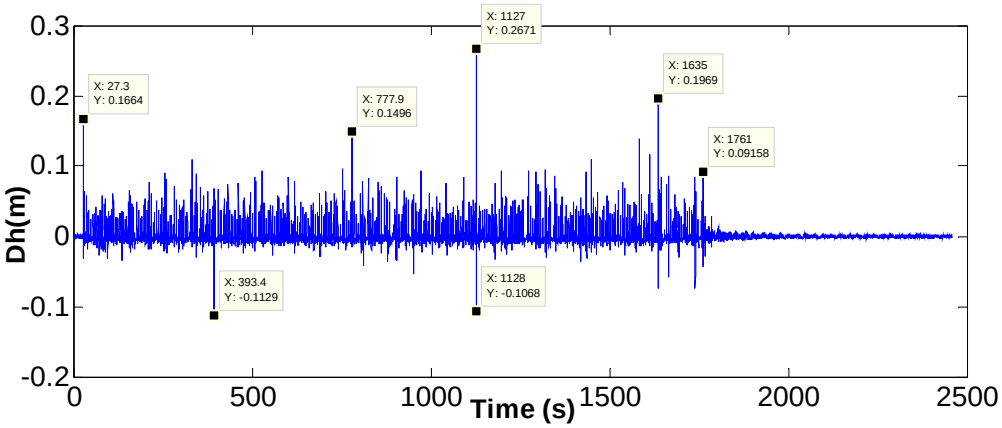

Fig. 7-14 Evolution of the difference of the entry water level fluctuations
Note: the difference of the water level $Dh(t_i)=H_1(t_{i+1})- H_1(t_i)$

7.6.4.3 Analysis and comparisons between the numerical and experimental results

The numerical results will be compared with the experimental results from the 5 following aspects:

- **Comparisons of the profiles of the water level fluctuations $H(x,t)$ and $H(x,t_0)$ (qualitative appearance)**

From the two profiles (**Fig. 7-15** and **Fig. 7-16**) of the instantaneous water level fluctuations *H*in the vertical section, it can be seen that the overall appearance of the numerical profile is very similar to the experimental one, except that there are no waves on the numerical results in the sea.

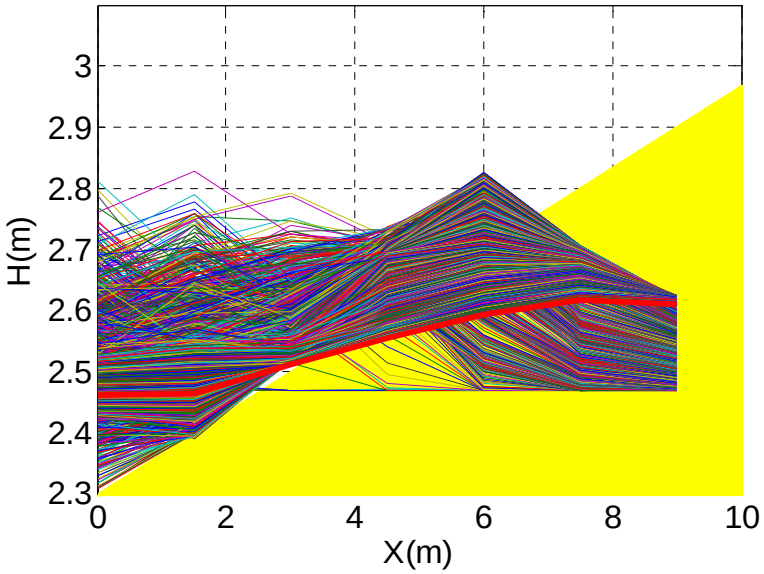

Fig. 7-15 Experimental profile of the instantaneous water level fluctuations in the vertical section (7 sensors) per 1s. Note the red course line is the free surface of the last time.

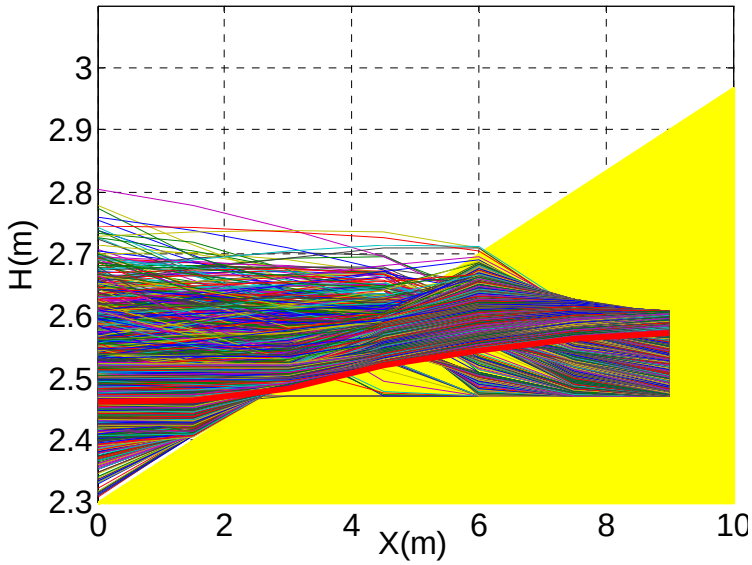

Fig. 7-16 Numerical profile of the instantaneous water level fluctuations in the vertical section (7 sensors) per 1s. Note the red course line is the free surface of the last time.

In addition, **Fig. 7-17** shows the instantaneous water level profiles of the vertical section at t=0.1s, t=38s, t=290s, t=800s, t=1300s, t=1650s, t=1800s, and t=2450s. This figure indicates that the numerical water levels near the sea and near the right wall of the canal are very approximate to the experimental results.

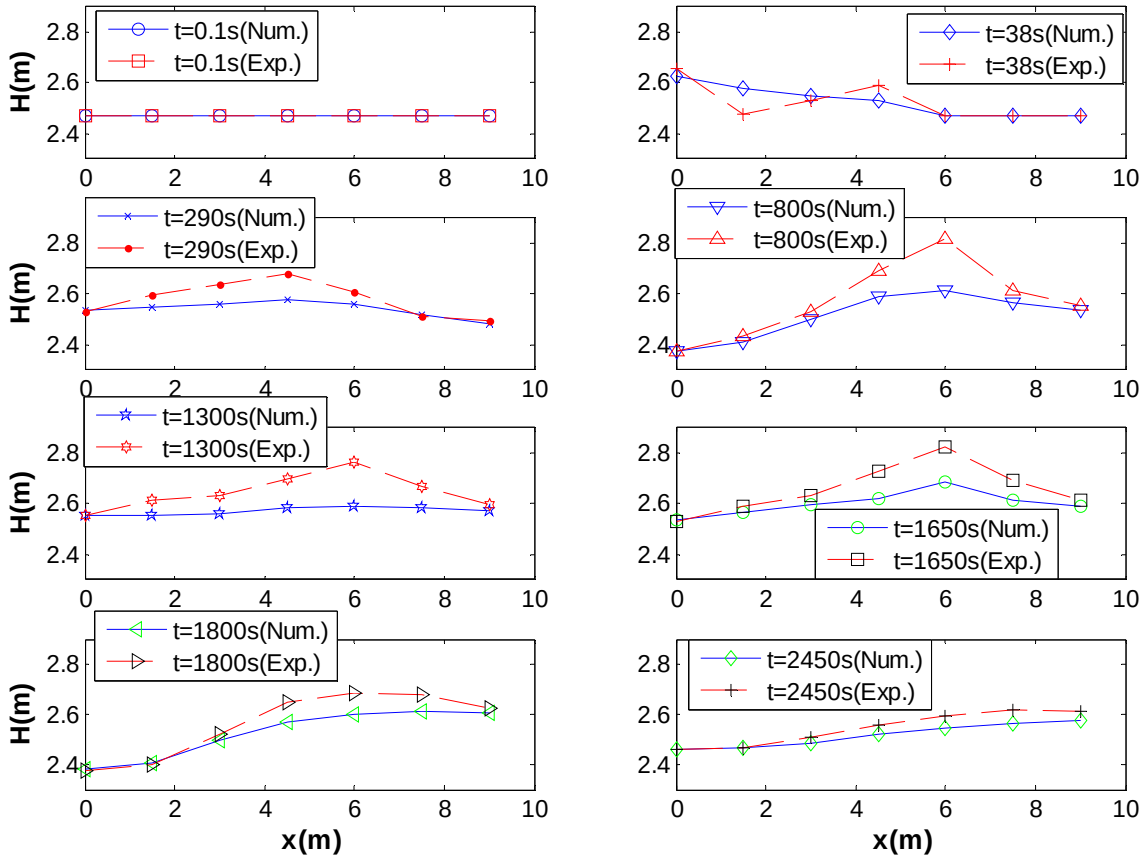

Fig. 7-17 Profiles of the instantaneous water level fluctuations in the vertical section: comparison between the numerical results (Richards model) and the experimental results.

- **Comparisons of the evolution of the water level fluctuations $H(x_0, t)$ (moving average)**

From **Fig. 7-18** and **Fig. 7-19**, it can be seen that the computed fluctuation characteristics of the water levels, and especially the computed curve trend are very similar to the experimental ones. In particular, the curve of $H_2(t)$ almost superposes with the the experimental one.

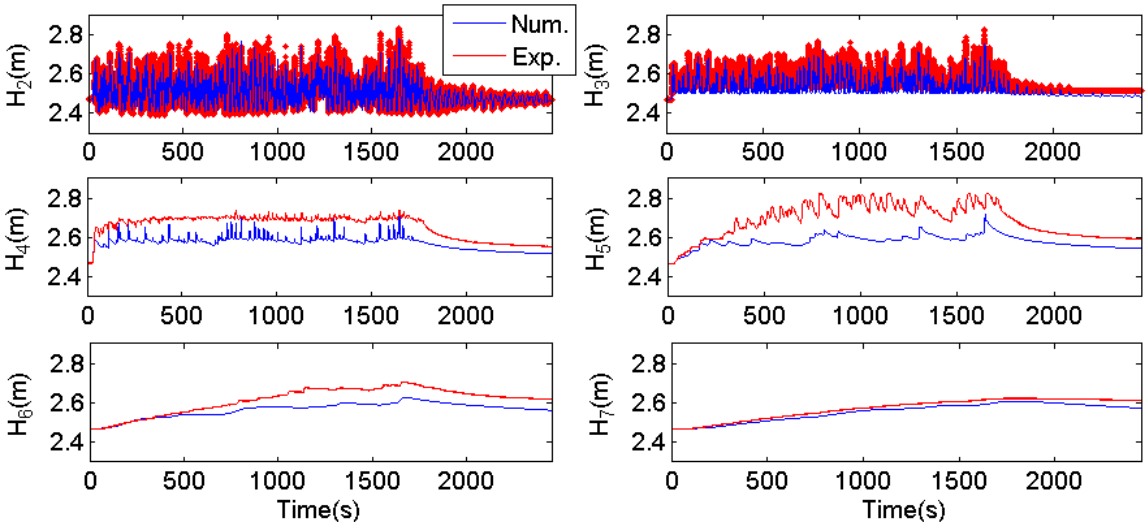

Fig. 7-18 Evolution of the water levels of 6 sensors (comparison with the experimental results)

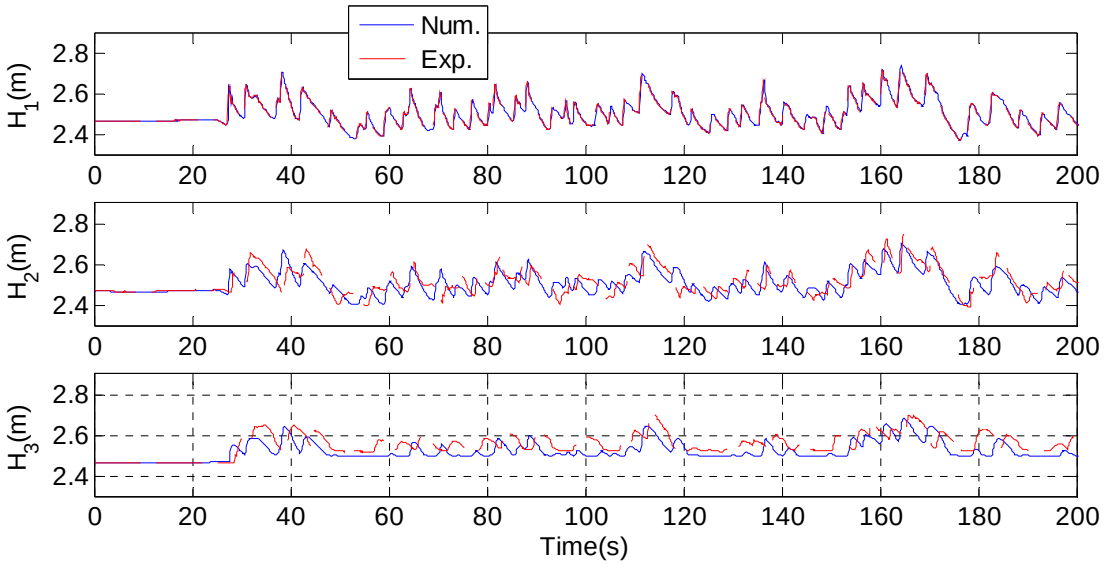

Fig. 7-19 Zoom of evolution of the water levels of 3 sensors at t=0-200s (comparison with the experimental results)

- **Comparisons of the Fourier spectrum (dominant period)**

From the results of the signal processing of the water level fluctuations $H_3(t)$ with Fourier spectrum analysis (**Fig. 7-20**), it can be seen that the computed water level fluctuations $H_3(t)$ has the same dominant periods as the experimental ones such as the most dominant period T_1=23.33s, and the Fourier spectrum energy almost has same distribution curve with respect to the period for the both results.

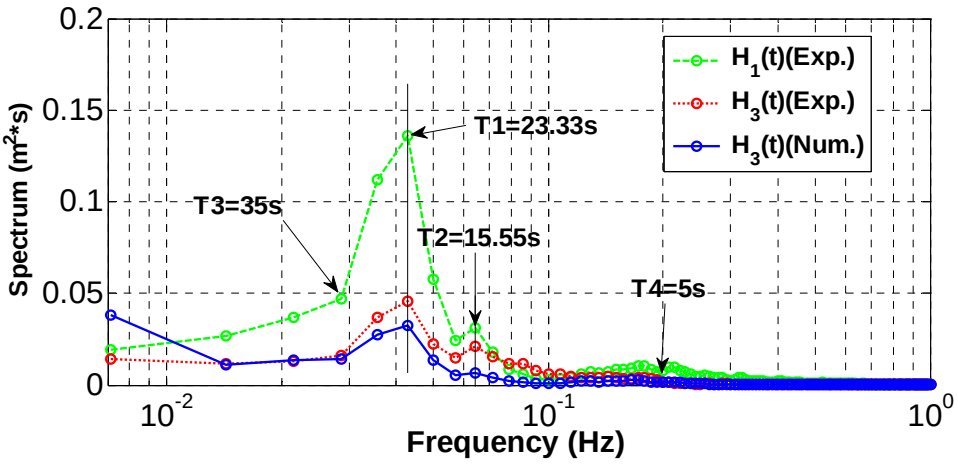

Fig. 7-20 Fourier spectrum function with respect to the frequency (m=700, dt=0.1s)

In addition, the residual of the simulated $H_6(t)$ has the same most dominant period T=600s as the experiment. From **Fig. 7-21** and **Fig. 7-22**, it can be seen that the residual of the computed $H_6(t)$ with moving average (*window halfwidth=300s*) has a similar fluctuation curve and accordingly, the similar Fourier spectrum curve to the experiment.

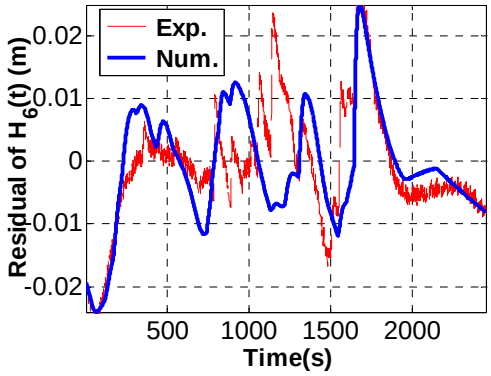

Fig. 7-21 Evolution of the residual of $H_6(t)$ (window halfwidth=300s, k=1,dt=0.1s)

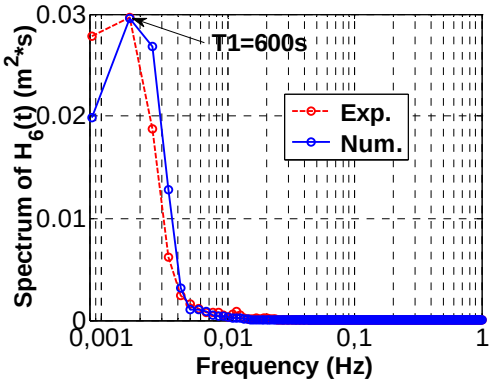

Fig. 7-22 Fourier spectrum function with respect to the frequency (m=6000, dt=0.1s)

- **Comparisons of the autocorrelation function (structure of the signal)**

The auto-correlation function $R_{H_3H_3}(\tau)$ of $H_3(t)$ and the one of the residual of $H_6(t)$ are respectively shown in **Fig. 7-23** and **Fig. 7-24**.

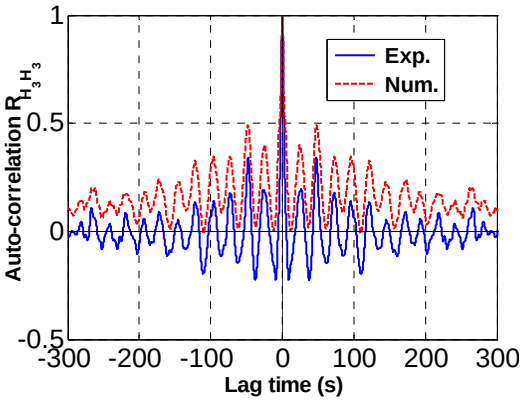

Fig. 7-23 Auto-correlation function $R_{H_3H_3}(\tau)$ of $H_3(t)$ with respect to the lag time

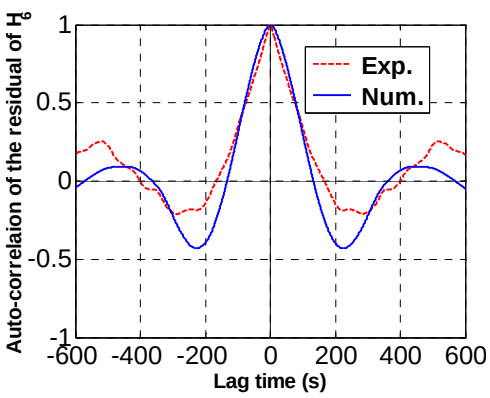

Fig. 7-24 Auto-correlation function of the residual of $H_6(t)$ $R_{H_{6\,Re}H_{6\,Re}}(\tau)$ with respect to the lag time
Note: the residual of $H_6(t)$ obtained with moving average filtering and the window halfwidth w_t =300s

From these two figures, it can be seen that the signal structure of the computed $H_3(t)$ (in the mixed zone) is very similar to the experimental, and the similar situation occurs with the residual of the computed $H_6(t)$ and the experimental results.

- **Comparisons of the cross analysis between $\mathbf{H_1(t)}$ and $\mathbf{H_3(t)}$**

The computed Fourier coherency curve for the longer periods (T>7.78s) and the shorter periods (T<0.5s) almost superposes on the experimental curves (**Fig. 7-25**).

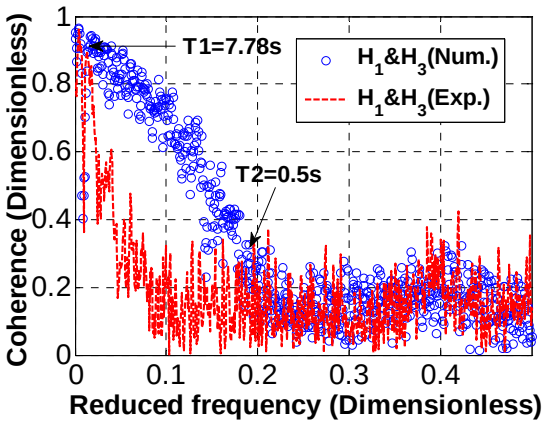

Fig. 7-25 Coherency function with respect to the reduced frequency
(Fourier analysis: m=700, dt=0.1s)

At the same time, for the middle periods (0.5<T<7.8s), the simulated Fourier coherency has been improved, because there is no further broken wave in the simulated sea.

There is nearly no amplification of the Fourier spectrum energy for the computed $H_3(t)$ (**Fig. 7-26**).

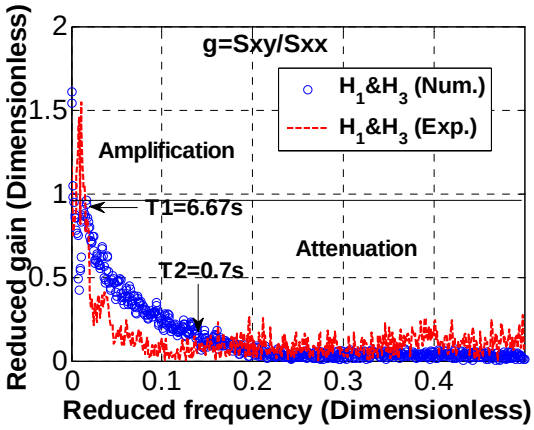

Fig. 7-26 Reduced gain function ($H_1(t)$ & $H_3(t)$) with respect to the reduced frequency (Fourier analysis: m=700, dt=0.1s)

Fourier spectrum energy of the computed $H_3(t)$ almost has been no-linearly attenuated with decreasing period, which can also be seen in **Fig. 7-20** (Fourier spectrum function) . This is because the run-up and run-down sea flow are ignored along the beach slope in the numerical simulation.

The computed water level fluctuations $H_3(t)$ are more regular than the experimental ones. From the Fourier phase function (**Fig. 7-27**), it can be seen that there are gradually increasing positive phases for the periods T>1.63s and there are gradually decreasing negative waves for 0.52<T<1.21s with decreasing period. On contrast, the experimental phase between $H_1(t)$ and $H_3(t)$ fluctuates frequently for the 2 corresponding time.

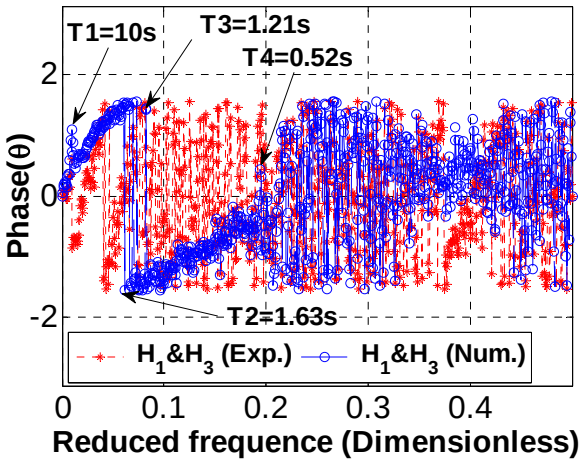

Fig. 7-27 Phase function ($H_1(t)$ & $H_3(t)$) with respect to the reduced frequency (Fourier analysis: m=700, dt=0.1s)

Numerical results of $H_1(t)$ and $H_3(t)$ have cross-correlation curve very similar to the experimental one (**Fig. 7-28**).

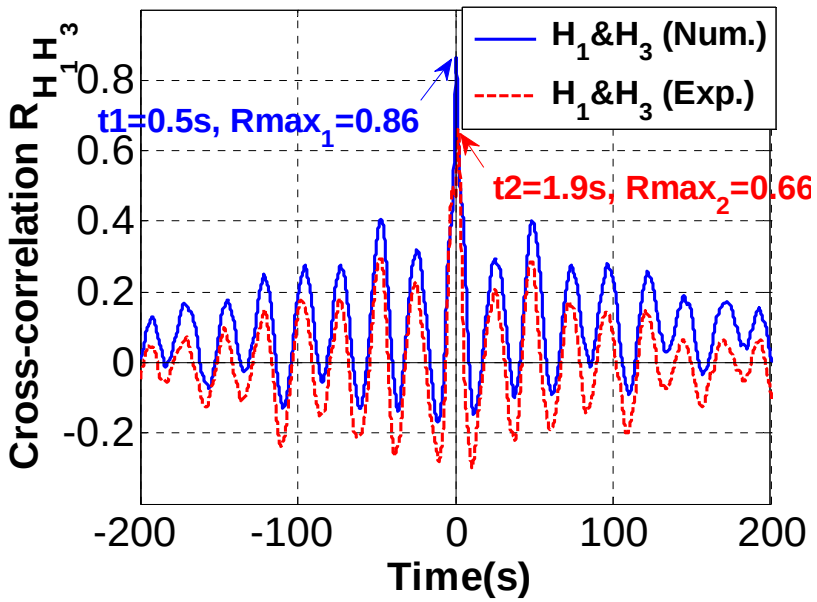

Fig. 7-28 Cross-correlation ($H_1(t)$ & $H_3(t)$) with respect to the lag time

What's more, the simulated maximum cross-correlation is better than the experimental one and the simulated lag time (0.5s) corresponding to the maximum cross-correlation is shorter than the experimental one (1.9s). This is caused by the 'great velocity' (10000m/s) of the macro porous media between $H_1(t)$ and $H_3(t)$ in the numerical simulation.

Through the decomposition with multi-resolution wavelet and the inter-correlation of the components between $H_1(t)$ and $H_3(t)$ with temporal analysis, from **Fig. 7-29** , it can be seen that there are very similar maximum inter-correlation curves with respect to the dyadic time scale for the experimental and numerical results, and the best maximum inter-correlation component C8 of $H_3(t)$ has very similar fluctuation curves for the both results (**Fig. 7-30**).

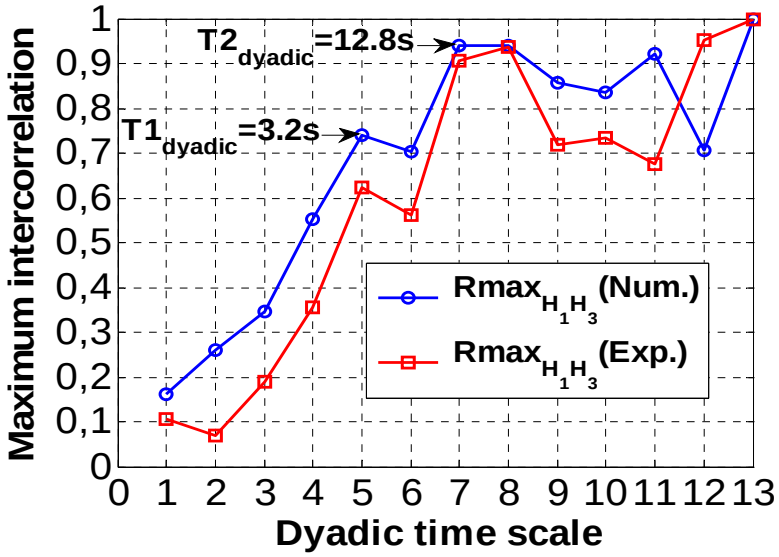

Fig. 7-29 Relationship of the maximum inter-correlation and the dyadic time scale between $H_1(t)$ and $H_3(t)$ with multi-resolution wavelet and temporal analysis methods.

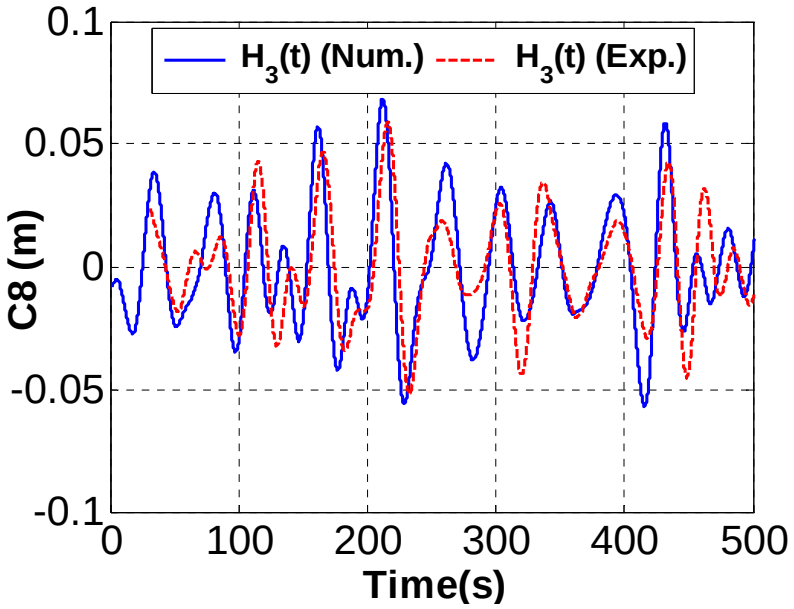

Fig. 7-30 Evolution of the wavelet dyadic component C8 of $H_3(t)$.

7.6.4.4 Sensitivity analysis of hydrodynamic parameters (Ks, θs, α, n)

The objective of the sensitivity analysis is to understand the influence of the beach soil main physical properties (K_s and θ_s) and the unsaturated VGM model parameters (α and n) on the water level fluctuations in a slopping sandy beach, and further to attempt to look for the method to improve the results of the numerical simulation by adjusting the parameters.

The parameter values used to do the sensitivity analysis for the numerical results are listed in **Table 7-5**.

Table 7-5 Pamameter values for the sensitivity analysis on the numerical results

Physical parameters	K_s(m/s)	5.0e-3	2.8e-3	5.0e-2
	θ_s(m^3/m^3)	0.38	0.36	0.34
VGM model parameters	α(m^{-1})	5.0	10.0	2.5
	n	1.5	3.0	5.0

The influence of the numerical model parameter on the water level fluctuations in the slopping sandy beach includes two aspects: the raised mean water levels and the fluctuation amplitudes. The evolution of the water level fluctuations of the 6 probed sensors has been observed. In fact, the influence of the parameters on the water level fluctuations of $H_2(t)$, $H_3(t)$, $H_4(t)$, and $H_5(t)$ is very weak and it can nearly be not observed. At the same time, the influence on $H_6(t)$ and $H_7(t)$ is obvious and similar. The influence of the 4 parameters on $H_7(t)$ is shown in **Fig. 7-31**.

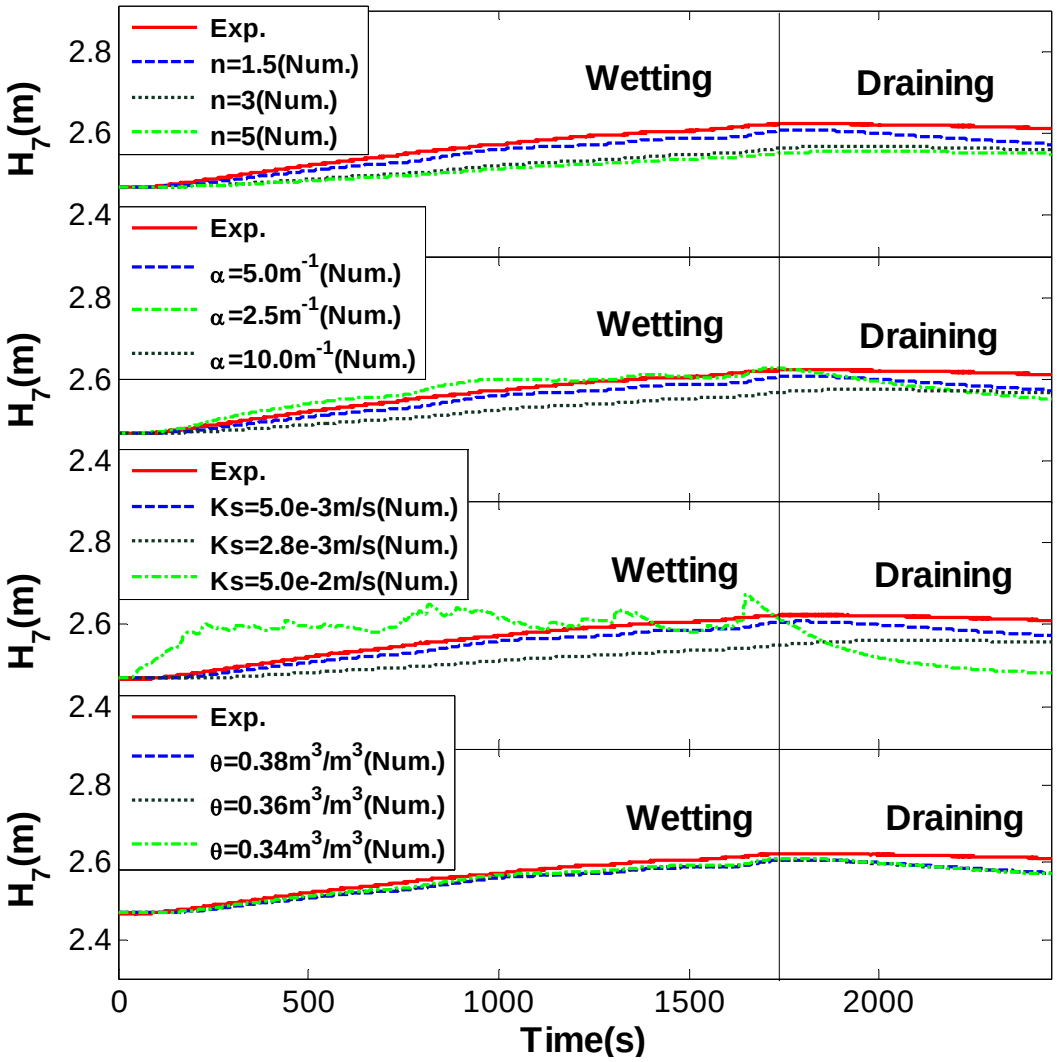

Fig. 7-31 Sensitivity analysis: evolution of the water levels of sensor No.7 $H_7(t)$ (comparison with the experimental results)

The simulated results show the hydraulic conductivity K_s plays the most dominant role whether in the raised mean water level or the fluctuation amplitudes of the water level fluctuations in the slopping sandy beach. The bigger K_s is, the bigger the amplitude is, the higher the raised mean water level is and the rapider the rising curve slope is in the wetting period, and the rapider the draining curve slope is also in the draining period, especially for $H_6(t)$ and $H_7(t)$. On contrast, α plays the second dominant role, and in detail, the smaller α (longer capillary length) is, the higher the raised mean water level is and the more rapid the rising curve slope in the wetting period, and the more rapid draining curve slope in the draining period. At the same time, n plays the third dominant role, and its influence is similar to the one of α. At last, the saturated water content θ_s has very weak influence and even the influence can even not be observed.

In addition, the influence of K_s on the profiles of the instantaneous water level fluctuations in the vertical section for several particular time have been observed, shown in the **Fig. 7-32**. From this figure, it can be seen that, firstly, the differences of the water levels in the mixed zone are smaller than the ones in the groundwater zone; secondly, during the work period of the wave generator (t<1800s), the difference of the measured water level and the simulated water levels are biggest at the sensor No5, the separated point of the mixed zone and the groundwater zone; finally, during the draining period (t>1800s), the bigger K_s makes the bigger descending velocity of the water level, for instance, the water levels of the 6 sensors of the numerical simulation with the biggest K_s firstly arrive at the initial mean water level than the ones of the other 2 smaller K_s at t=2450s.

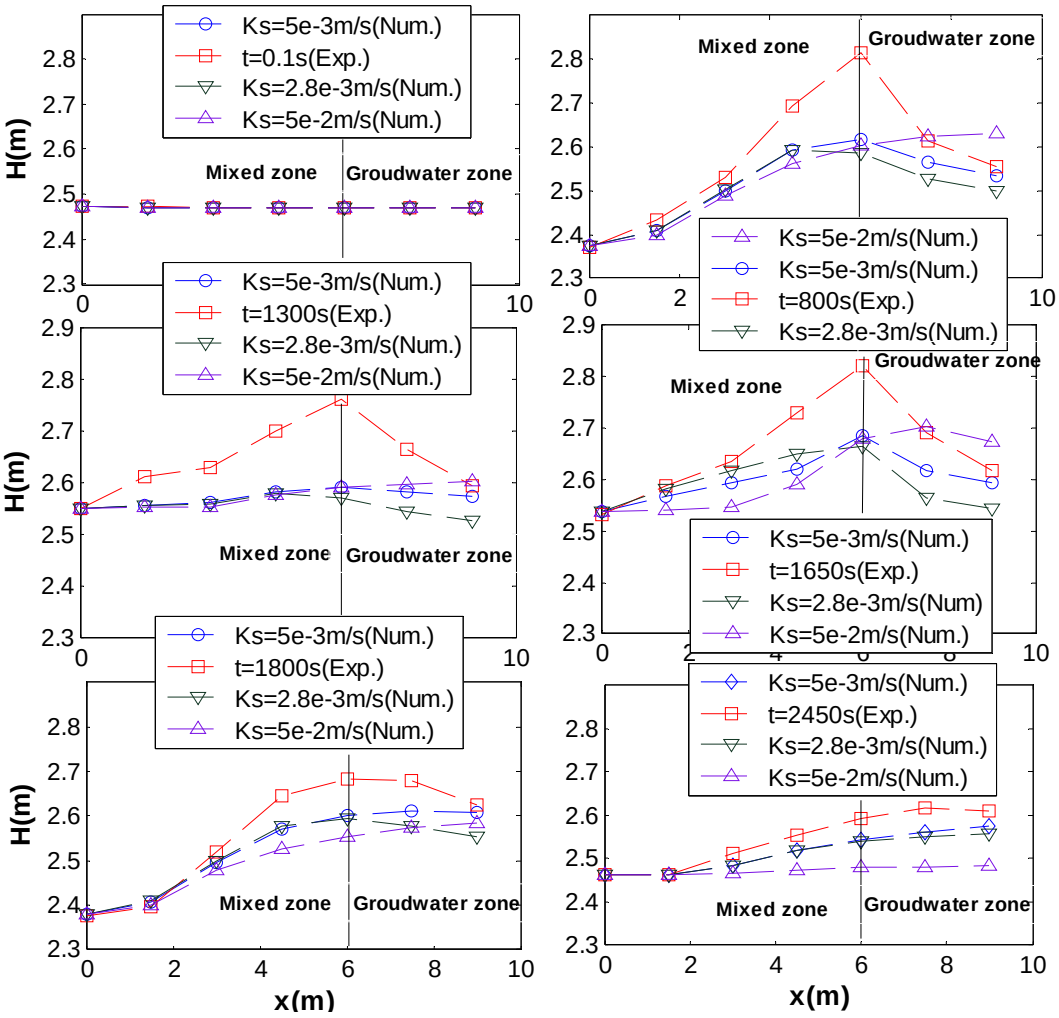

Fig. 7-32 Sensitivity analysis: Profiles of the instantaneous water level fluctuations in the vertical section (comparison with the experimental results)

7.6.5 Numerical simulation with the exponential model for K(h) and θ(h)

7.6.5.1 Introduction

Compared with VGM model, the numerical iteration is more easier for the exponential model to converge.

Since the different parameter functions, α in the VGM model is not the total same as the one in the exponential model, although they are both defined as the inverse of the capillary length. If the same α value used in the above presented VGM model is taken in the exponential model, and $\alpha = 3\beta$ for the macro porous media and micro porous media, what will happen for the coupling model between the sea and the slopping sandy beach? This will be analyzed in the last part.

7.6.5.2 Numerical simulation with an entry water level of the experimental results $H_1(t)$

The simulation domain, boundary condition, initial condition, duration of the simulation and numerical parameters are same as the numerical simulation VGM model for the Barcelona experiment.

- **Physical properties of the beach and the sea (micro and macro porous media)**

The main physical properties of the beach and the sea with expenential model are listed in **Table 7-6**

Table 7-6 Physical properties of the beach and the sea of the numerical simulation with exponential model

Physical parameters	$K_{s\,Micro}$	0.005m/s	$\theta_{s\,Micro}$	0.38m^3/m^3
	$K_{s\,Macro}$	50m/s	$\theta_{s\,Macro}$	1.0m^3/m^3
VGM model parameters	α_{Micro}	5m^{-1}	$\beta_{Micro}(\alpha_{Micro}/3)$	$1.6667m^{-1}$
	α_{Macro}	100m^{-1}	$\beta_{Macro}(\alpha_{Macro}/3)$	$33.33m^{-1}$;

All other parameters are the same as the above numerical simulation with VGM model for the Barcelona experiment.

The curves of the water content $\theta(h)$, hydraulic conductivity $K(h)$, capillary diffusion $D(S_e)$ and capillary capacity $C(S_e)$ for the micro porous media (the beach) and the macro porous media (the sea) have been respectively illustrated in **Fig. 7-33**, **Fig. 7-34**, **Fig. 7-35** and **Fig. 7-36**.

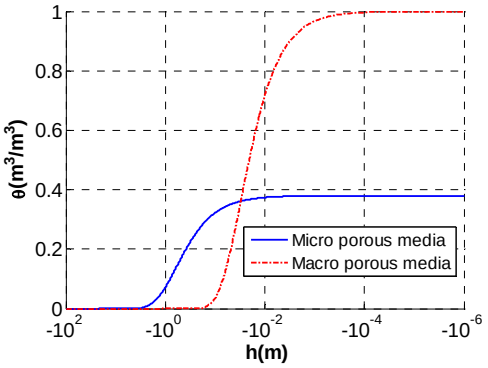

Fig. 7-33 Water content curve $\theta(h)$ in semi-log x axis of the micro porous media and the macro porous media (*Exp. model*)

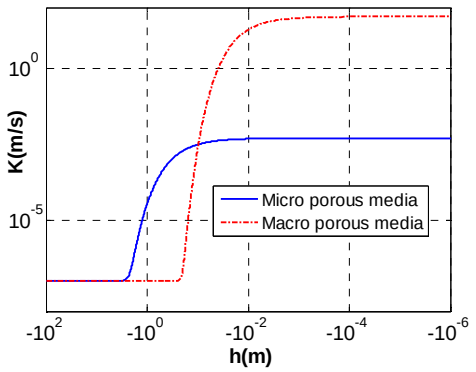

Fig. 7-34 Hydraulic conductivity curve $K(h)$ in log-log of the micro porous media and the macro porous media (*Exp. model*)

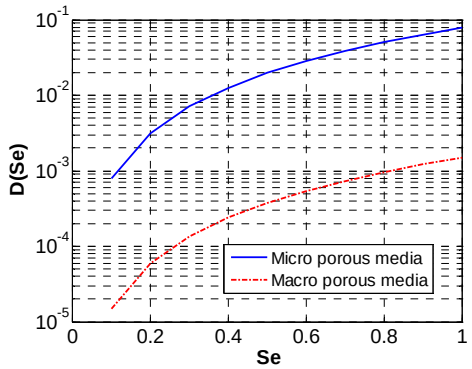

Fig. 7-35 Capillary diffusion $D(S_e)$ in semi-log y axis of the micro porous media and the macro porous media

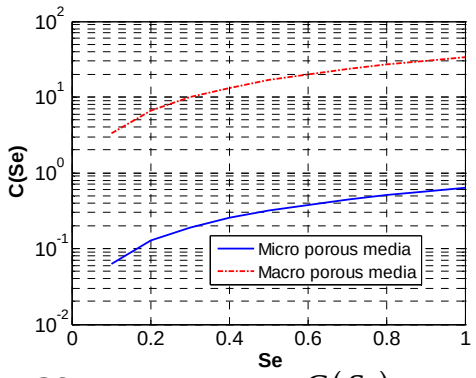

Fig. 7-36 capillary capacity $C(S_e)$ in semi-log y axis of the micro porous media and the macro porous media

- **Numerical behaviour of Bigflow during the simulation**

The minimum errors of the linear and nonliear iterations of the pressure head are smaller than 1.0E-6, which is similar to the VGM model, as seen in **Fig. 7-37** and **Fig. 7-38**.

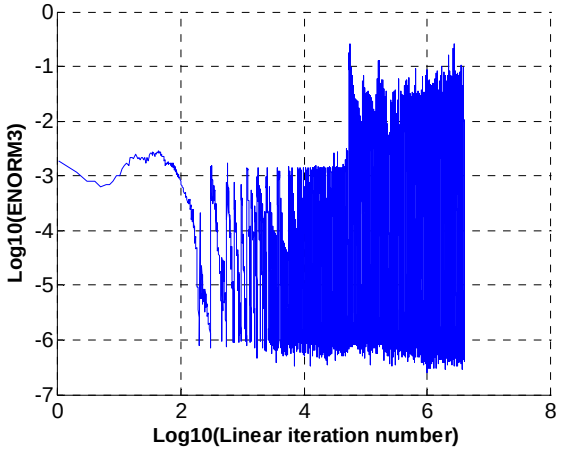

Fig. 7-37 Standarlized linear iteration process of the pressure head in log10 (*Exp. model*)

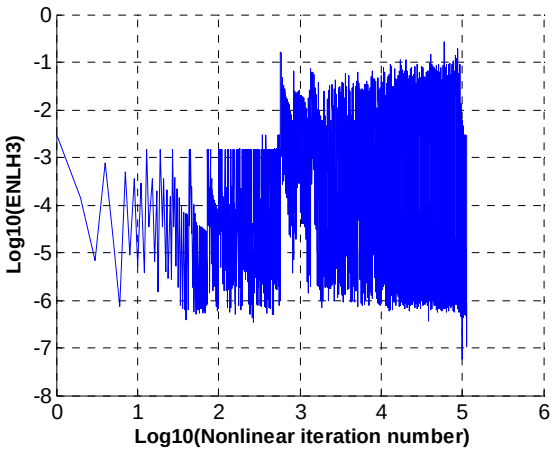

Fig. 7-38 Standarlized nolinear iteration process of the pressure head in log10 (*Exp. model*)

The curve of the evolution of Q_{Bound} totally superposes on the curve of the evolution of Q_{Mass}, as seen in **Fig. 7-39**. Similarly to the VGM model, it can be clearly seen the effect of the difference of the entry water level fluctuations on Q_{Bound} and Q_{Mass} from **Fig. 7-39** and **Fig. 7-14**.

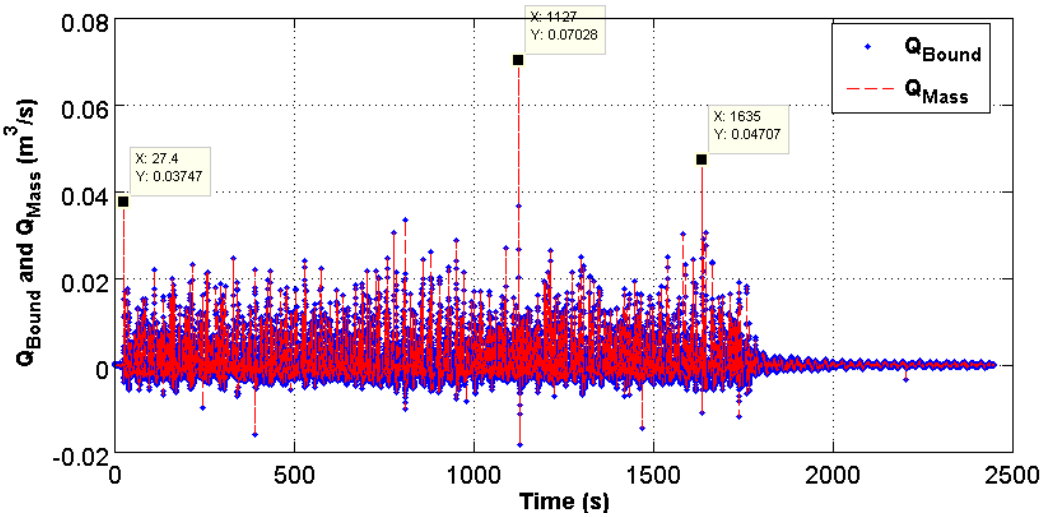

Fig. 7-39 Evolution of Q_{Bound} and Q_{Mass} (*Exp. model*)

- **Comparisons with the experimental results**

Compared with the VGM model (**Fig. 7-18**), a similar result has been obtained through the comparison of the evolution of the water level fluctuations of the 6 probed sensors: the computed water level fluctuations have the same curve trend and similar fluctuation characteristics with the experimental results, and accordingly, the computed results agree very well as the experimental results, as seen in **Fig. 7-40**.

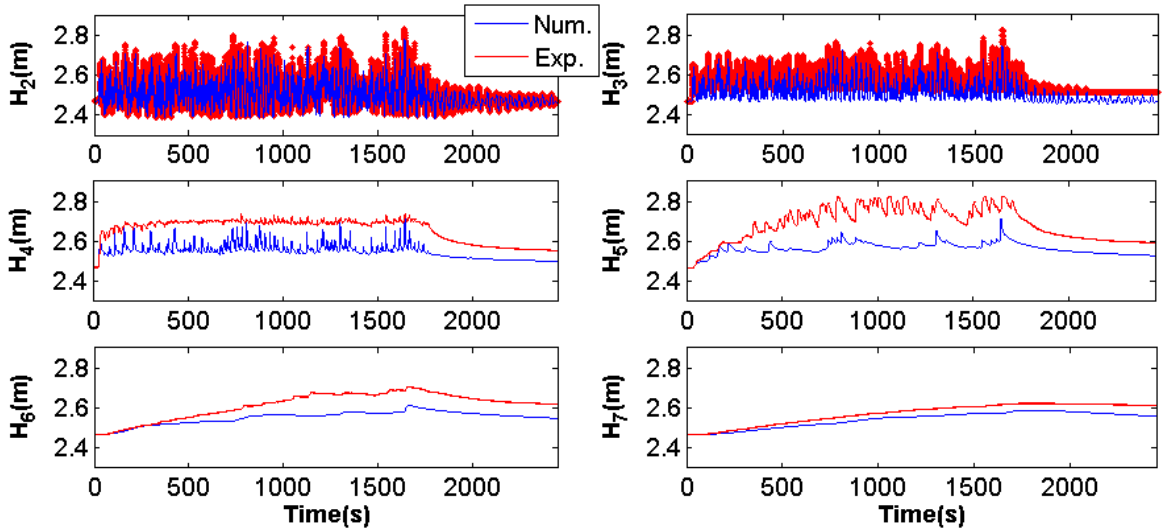

Fig. 7-40 Evolution of the water levels of 6 sensors (comparison with the experimental results) (*Exp. model*)

7.6.6 Comparison of the numerical results with the Exponential and VGM models

7.6.6.1 Introduction

Exponential model and VGM model are two different parameter models for the unsaturated soil physical properties: hydraulic conductivity $K(h)$ and water content $\theta(h)$.

For the exponential model, the functions $K(h)$ and $\theta(h)$(equation $(1-11)$ and $(1-12)$, Chapter 1) are independent with their each own parameter α (the inverse of the capillary length due to the hydraulic conductivity) and β (the inverse of the capillary length due to the water content). In spite of this, they can be linked together by supposing a relationship with the diffusion coefficient function $D(S_e)$ (equation (1-22), Chapter 1). Therefore, in the above numerical simulation test for Barcelona experiment, $D(S_e) \sim D_0 {S_e}^2$, and so $\alpha = 3\beta$.

For the VGM model, the functions $K(h)$ and $\theta(h)$ are linked by parameter α, the inverse of the capillary length, and the power n (equation (1-9) and (1-10), Chapter 2).

In general, the α in the exponential model and in the VGM model do not mean the same capillary length, due to the different definition of the parameter function. However, in the above presented exponential model and in the VGM model, the same α value is used and very similar results are obtained. As a result, it is very interesting to compare the corresponding pressure head contour distribution, water content distribution and flux field in vertical section for the two models.

7.6.6.2 Comparison of the numerical results with the Exponential and VGM models

The difference of the results between the two models appears in the unsaturated zone of the macro porous media and the micro porous media. The distribution of the pressure head contours with the same serial values and the corresponding water content distribution in the vertical section for the two models at t=735s and t=980s are chosen and respectively shown in **Fig. 7-41** to **Fig. 7-48**.

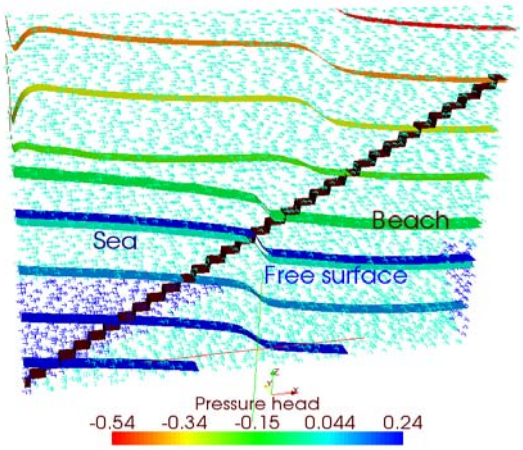

Fig. 7-41 Profile of the pressure head contours, the flux velocity and the beach slope at t=735s (length scale in z and in y are 10) (*Exp. model*)

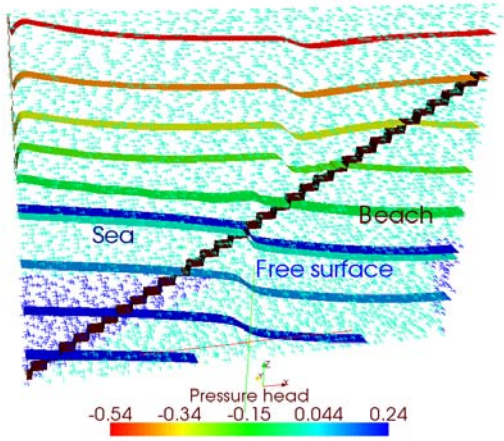

Fig. 7-42 Profile of the pressure head contours, the flux velocity and the beach slope at t=735s (length scale in z and in y are 10) (*VGM model*)

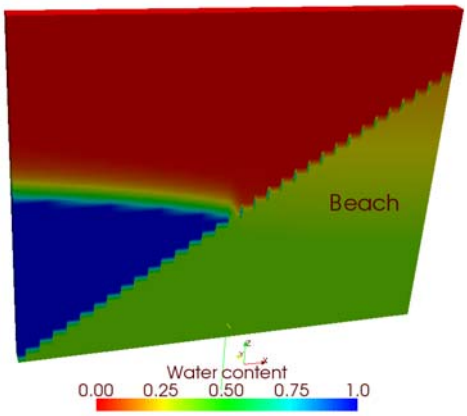

Fig. 7-43 Profile of the water content $\theta(h)$ at t=735s in the xz plane (length scale in z and in y are respectively 10) (*Exp. model*)

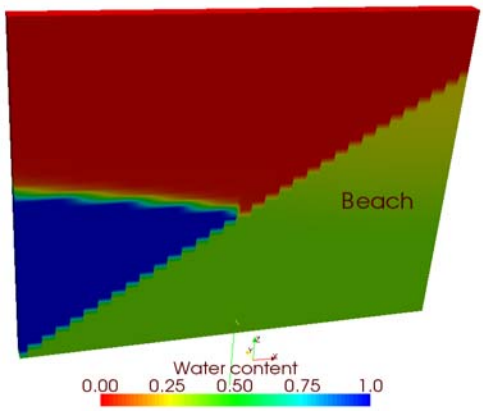

Fig. 7-44 Profile of the water content $\theta(h)$ at t=735s in the xz plane (length scale in z and in y are respectively 10) (*VGM model*)

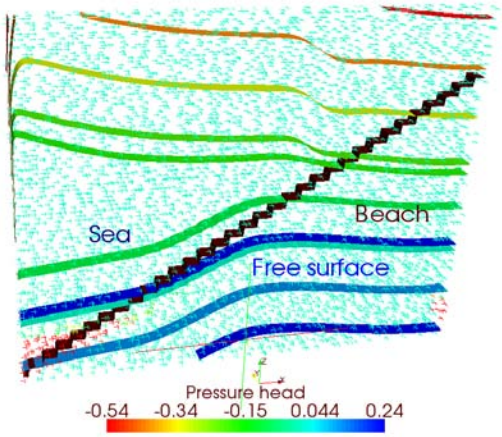

Fig. 7-45 Profile of the instantaneous pressure head contours, the flux velocity and the beach slope at t=980s (length scales in z and in y are respectively 10) (*Exp. model*)

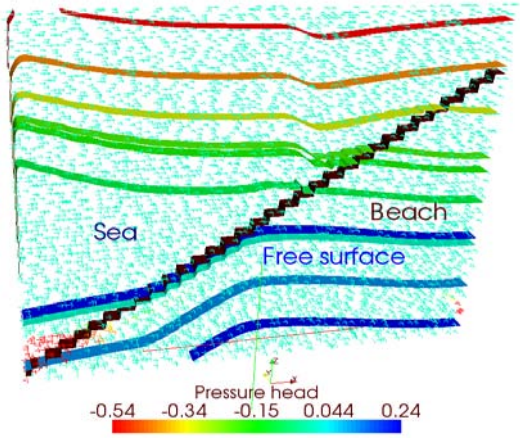

Fig. 7-46 Profile of the instantaneous pressure head contours ,the flux velocity and the beach slope at t=980s (length scales in z and in y are respectively 10) (*VGM model*)

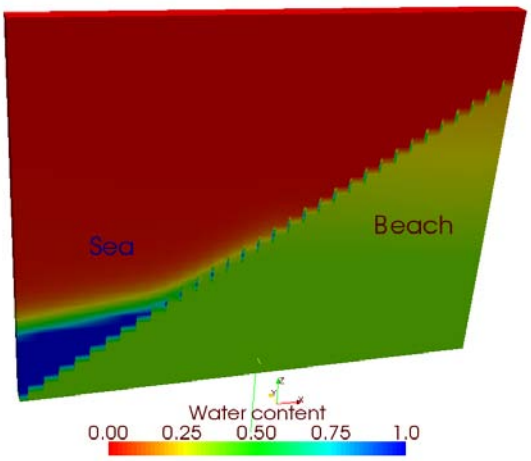

Fig. 7-47 Profile of the instantaneous water content $\theta(h)$ at t=980s in the xz plane (length scales in z and in y are respectively 10) (*Exp. model*)

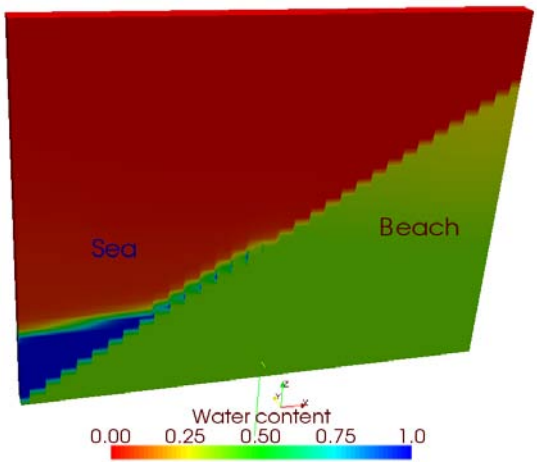

Fig. 7-48 Profile of the instantaneous water content $\theta(h)$ at t=980s in the xz plane (length scales in z and in y are respectively 10) (*VGM model*)

From the distribution of the pressure contours, it can be seen that the distribution density of the pressure head contours of the macro porous media of the exponential model is very different from the one of the VGM model. Especially, for the first 3 pressure contours, the distribution density is totally different and it varies very much. On contrast, in the unsaturated zone of the micro porous media, the distribution density of the pressure head contours of the two models is so small that it needs to be observed in detail. At the same time, from the water content distribution figures, it is obvious to observe that the capillary length obtained with the exponential model is longer than the one obtained with VGM model for the two times, and however, the difference is not big. At last, the flux is almost uniform in the all vertical sections and it doesn't change very much for the different time with the two models.

In addition, the wetting and the draining phenomena are clearly observed from the instantaneous pressure head contours profile at t=735s and t=980s for the two models. From a zoom of the evolution of $H_1(t)$ (**Fig. 7-49**), it can be seen that when t=735s, the left entry water level just began to descend from a peak value and when t=980s, the left entry water level will go up from the bottom value. Accordingly, it is clearly observed that the free surface levels in the macro porous media (sea water levels) are higher than the ones in the micro media (beach water levels) for the two models (**Fig. 7-41** and **Fig. 7-42**) at t=735s (wetting phenomenon). At the same time, the free surface levels in the macro porous media (sea water levels) are lower than the ones in the micro porous media (beach water levels) for the two models (**Fig. 7-45** and **Fig. 7-46**) at t=980s (draining phenomenon)

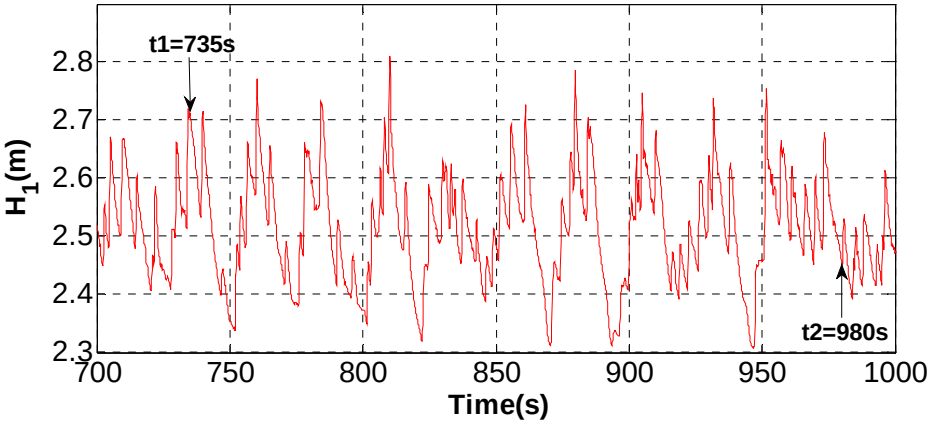

Fig. 7-49 Zoom of the evolution of $H_1(t)$ at t=700s-1000s

7.7 Conclusion and outlook

A 2D plane flow Boussinesq model, and a 3D variably unsaturated flow Richard model with two different unsaturated parameter models (VGM model and exponential model) have been used to simulate the Barcelona wave canal experiment.

Although the computed water levels obtained with Boussinesq plane flow model have the same evolution trend with the one of the experiment, they do not agree exactly with the measured water levels: the simulated water level fluctuations seem to be less important than the measured ones, and the moving average water level is underestimated with the simulations.

Compared with the simulated results with Boussinesq plane flow model, the ones obtained with VGM model (Richard models) agree much better with the measured water levels in 3 aspects: (1) the qualitative appearance of the profiles of the water level fluctuations $H(x,t)$, and the signal structure of the evolution of the water level fluctuation $H_i(t)$ by the comparisons of the auto-correlation function $R_{H_i(t)H_i(t)}$; (2) the trend of the evolution of the average water level confirmed by the comparisons of $H_i(t)$; (3) the same dominant periods by the comparisons of Fourier spectrum of $H_i(t)$.

Furthermore, the exponential model with about the same capillary length (same α) with VGM model gives the very similar water level fluctuations as the ones with VGM model. The results of the sensivtivity analysis indicate that the saturated hydraulic conductivity K_s has the most important imfluence on the ground water level fluctuations.

In fact, Richards model used to model the Barcelona wave canal experiment is a simplified coupling model. In the numerical simulations, the oscillatory entry water level fluctuations

$H_1(t)$ are supposed to directly put (or act) on the slopping beach, and this is not consistent with the actual situation. The moving average level is still underestimated with the simulations, and especially for the one of $H_5(t)$, however the parameters are changed, the simulated moving average level does not improved enough.

In addition, in all the numerical simulations, it could be necessary to consider the erosion problem (in surface and intern) and some other couplings like hydro-mechanics (pore pressures, Terzaghi, rupture criteria, landslides).

Chapter 8 : Conclusions

Conclusions et perspectives

Les conséquences de variations et d'oscillations hydrodynamiques à forte variabilité temporelle en milieux poreux partiellement saturés et comportant des surfaces libres tant à l'extérieur qu'à l'intérieur des milieux poreux ont été étudiés expérimentalement, analytiquement et numériquement.

Concernant le problème d'imbibition, un bon résultat de calibration a été obtenu avec le modèle de Richards en coupe verticale (les paramètres les plus adaptées pour le modèle VGM étant: $\alpha = 4{,}6\ m^{-1}$, n = 5). L'évolution de la position aval du front de saturation $x_F\ (t)$ est très sensible à α qui est lié à la longueur capillaire inverse du milieu poreux (environ 20 cm ici). En changeant la valeur de α, nous trouvons que plus grand est α (plus petite est la longueur capillaire), plus rapides sont les mouvements du front de saturation se déplaçant dans la direction *x*. En outre, la solution analytique de Polubarinova (Polubarinova-Kochina (1962)[1], Trégarot(2000)[17]) ne correspond pas du tout au processus d'imbibition expérimental. Ceci était prévisible, car la solution de Polubarinova est basée sur l'équation saturée de Dupuit-Boussinesq avec l'hypothèse de drainage/ imbibition instantanée de la zone non saturée à la surface libre. Ces hypothèses ne sont valables que pour les milieux poreux grossiers ayant une petite longueur capillaire. Au contraire, dans ce sable très fin, les effets capillaires sont importants (longueur capillaire de 20 cm).

Nous avons également étudié séparément le problème hypothétique de drainage brusque d'une nappe phréatique dans une rivière, en utilisant des hypothèses d'écoulement plan et en négligeant les effets capillaires (Dupuit-Boussinesq). Nous avons utilisé une solution linéarisée *H(x,t)* (développée par Ababou (2007)[20]), et nous avons obtenu un très bon accord avec une solution numérique de l'équation de Dupuit-Boussinesq en écoulement plan (avec transmissivité non linéaire). Nous avons également comparé les résultats de Dupuit-Boussinesq avec l'équation de Richards plus complète, permettant le drainage de la nappe phréatique (simulé comme un problème d'écoulement partiellement saturé/non saturé). Similairement au problème d'imbibition, il est vérifié à nouveau ici que l'équation de Boussinesq n'est bonne que lorsque la longueur capillaire est négligeable. Enfin, nous avons

également utilisé ce problème pour comparer deux différentes paramétrisations des courbes ($K(h)$, $\theta(h)$) dans le modèle de Richards. Il a été constaté que, en mettant une même échelle de longueur capillaire ($1/\alpha$) dans le modèle de VGM et dans le modèle exponentiel, bien que les courbes ($K(h)$, $\theta(h)$) dans ces modèles soient différentes formes, le même débit de décharge $Q(t)$ est obtenu à l'interface nappe-rivière.

La propagation des ondes dans une boite à sable rectangulaire placée dans un petit canal à houle a ensuite été étudiée expérimentalement, numériquement et analytiquement. Les solutions analytiques obtenues avec le modèle Dupuit-Boussinesq de l'écoulement plan indiquent que, en supposant une condition limite à sortie de niveau d'eau constant, l'onde dans le domaine poreux est constituée d'un seule vague progressive $H(x,t)$ qui décroit exponentiellement. Cette décroissance exponentielle est confirmée par comparaison de l'approximation analytique avec les niveaux d'eau mesurés, bien que la perméabilité calculée obtenue par cette approximation semble trop élevée, peut-être en raison de l'érosion interne ou des effets lies à l'écoulement vertical. Enfin, il est intéressant de noter que, dans l'hypothèse d'une frontière fermée (ce qui n'était pas le cas pour notre boite à sable immergée), le niveau d'eau résultant $H(x,t)$ est une combinaison d'une onde progressive avant et d'une onde progressive arrière, avec décroissance exponentielle d'amplitude par rapport à la distance à la frontière d'entrée (pour les ondes avant) -- ou à la frontière réflective (pour les ondes arrière).

Par la suite, dans le grand canal à houle (Hydralab à Barcelone), nous avons installé 7 micro-piézomètres équipés de capteurs capacitifs, permettant de mesurer les fluctuations des niveaux d'eau de la nappe souterraine en des positions différentes dans la plage de sable inclinée. Nous avons aussi également mesuré d'autres fluctuations de niveaux d'eau dans l'eau libre (écoulement externe). Les résultats expérimentaux montrent une décroissance spatiale des fluctuations de niveau de la nappe souterraine, et aussi un « filtrage » (par la plage de sable) des périodes les plus courtes losque l'on s'éloigne du rivage. En outre, les mesures des niveaux d'eau loin de la rive ($H_6(t)$, $H_7(t)$) présentent un comportement très différent de ceux plus près du rivage (comme $H_2(t)$). En effet, étant donné les multiples fréquences du spectre des ondes qui arrivent à la rive (périodes de 5 s jusqu'à 600 s environ), le résultat est apparemment une surélévation de la surface libre moyenne (à distance du rivage) par rapport au "niveau d'eau moyen de la mer".

En fait, il a été observé que les fluctuations des niveaux d'eau mesurés présentent des caractéristiques inhomogènes dans le temps et l'espace. Dans ce cas, les méthodes de traitement simples comme l'analyse de Fourier directe de chaque signal $H_i(t)$ apparaît

inefficace ou ne fournit que des informations incomplètes. Pour cette raison, nous avons appliqué une série de tests et d'analyses sur les fluctuations de niveau d'eau mesurése, incluant à la fois les analyses croisées et univariées, la fréquence spectrale ainsi que des analyses de corrélation temporaire, analyses des ondelettes orthogonales multi-résolution, et les méthodes du pré-filtrage basées sur des moyennes mobiles ou de décomposition en ondelettes. Les principaux résultats obtenus avec les analyses du signal de ces méthodes sont les suivantes:

- Étant donné que la période de géneration des ondes pas le batteur est d'environ 4-5 secondes, la période dominante T_1 = 24s de l'onde incidente sur la rive (piézomètre $H_1(t)$) est interprétée comme l'effet de la géométrie du grand canal à houle, ou plus précisément, comme la période dominante issue du ‘run-up and run-down flow’ qui lié à la topographie et la nature de la plage inclinée de sable fin.
- Pour les trois piézomètres proches de la rive et dans la zone de swash $H_i(t)(i=1,2,3)$, les périodes dominantes sont la même, environ 24 secondes ; les périodes dominantes sont un ordre de magnitude plus longue pour les piézomètres situés plus loin du rivage $H_i(t)(i=4,5,6,7)$: leur périodes dominantes sont respectivement 400s, 600s, 600s et 300s.
- Les énergies de fluctuation des périodes dominantes diminuent considérablement avec la distance du rivage dans la plage de sable fin en pente. L'énergie de fluctuation de la période la plus longue se propage plus loin dans la plage que l'énergie des périodes plus courtes.
- La corrélation maximale diminue presque linéairement, et le délai correspondant augmente de façon exponentielle par rapport à la distance horizontale dans la direction vers la terre (loin de la rive).
- Les vitesses de propagation des ondes ont été toutes estimées le long du canal (en eau libre, et en eau souterraine) en utilisant des délais temporels (déphasages) mis en évidence par les corrélations croisées. La moyenne de la vitesse de propagation des ondes mesurées diminue avec la distance horizontale vers la plage de sable fin (en partant du générateur de houle). La valeur minimale mesurée (c=0.056m/s) est proche de la vitesse de groupe d’onde en poreux (2 fois plus petite), celle-ci étant calculée par Dupuit-Boussinesq pour T=24s, la période dominante du point d’entrée $H_1(t)$.
- On obtient un pic de cohérence spectrale à $T \approx 24s$ entre le signal $H_1(t)$ et les signaux $H_2(t)$, $H_3(t)$, etc. Ceci indique que cette période a une grande influence sur toutes les fluctuations de niveaux d’eau souterraine dans la plage inclinée de sable fin, à

l'exception du piézomètre $H_7(t)$ le plus éloigné de la rive et le plus proche de la paroi du fond imperméable du canal. D'autre part, on observe un creux de cohérence à $T \approx 10s$. Ceci peut indiquer qu'il y a une vague de reflux périodique dont la limite est située quelque part entre $H_1(t)$ et $H_2(t)$, et qui n'influence pas directement les piézomètres plus éloignés $H_3(t)$, $H_4(t)$, etc.

Nous avons finalement développé un outil numérique pour modéliser l'expérience du grand canal à houle de Barcelone. L'utilisation du modèle 2D de Dupuit-Boussinesq de l'écoulement plan, comme on s'y attendait, n'a pas été vraiment concluante. Bien que les niveaux d'eau calculés aient la même évolution générale que les données expérimentales, ils ne sont pas vraiment en accord avec les niveaux d'eau mesurés: les fluctuations du niveau d'eau simulé semblent être moins importantes que celles mesurées, et la variation de niveau d'eau moyenne est très sous-estimée par les simulations. A noter que la plage en pente ne peut pas être représentée explicitement dans un tel modèle d'écoulement plan simplifié.

Nous avons ensuite porté notre attention sur un modèle d'écoulement partiellement saturé / non saturé, basé sur l'équation généralisée de Richards, avec un milieu macroporeux pour représenter le domaine au-dessus de la surface du sable en pente. Plus précisément, deux types de modèles ont été utilisés pour les courbes non saturées ($K(h)$, $\theta(h)$) dans le modèle de Richards : le modèle de Van Genuchten/Mualem (VGM) et le modèle exponentiel.

Les niveaux d'eau obtenus par la simulation numérique avec le modèle de Richards (en utilisant des courbes de VGM et un sous-domaine macroporeux pour l'eau libre) correspondent beaucoup mieux avec les niveaux d'eau mesurés que les simulations de Dupuit-Boussinesq.

Les résultats numériques ont été bien validés par comparison avec ceux de l'expérience sur trois aspects:

(1) Les courbes $H(x_i, t)$ de fluctuation du niveau d'eau, qui sont quantitativement confirmées par la comparaison des structures d'auto-corrélation des signaux $H(x_i, t)$ expérimentaux et modélisés;

(2) La tendance de l'évolution du niveau d'eau moyen;

(3) Les périodes dominantes, par comparaison des spectres de Fourier simulés et expérimentaux des signaux $H(x_i, t)$.

De plus, on obtient un ensemble très similaires de fluctuations du niveau d'eau $H(x_i, t)$, en utilisant la même longueur capillaire (1/α) dans le modèle exponentiel et dans le modèle VGM.

En perspective, pour étudier les interactions entre l'hydrodynamique de la plage et des eaux souterraines, il sera intéressant et nécessaire de tenir compte également des processus d'érosion/dépôt de surface, ainsi que de l'érosion interne et d'autres couplages fluide/solide. Parmi ces derniers, citons les couplages hydro-mécaniques impliquant une loi contrainte/déformation, un couplage avec la pression interstitielle (contrainte effective de Terzaghi), effet de succion capillaire sur la cohésion et les critères de rupture, etc.

Le groupe OTE de l'IMFT (avec qui nous avons collaboré pour récupérer et analyser les données du canal à houle) est actuellement en train d'effectuer des analyses sur le processus d'érosion/dépôt basées sur des mesures de surface de sable réalisées par imagerie laser pour le même ensemble de génération de tests d'onde. Il sera intéressant par la suite d'étudier l'influence des fluctuations des niveaux d'eau de la nappe souterraine et de la dynamique de la zone non saturée sur ces phénomènes d'érosion/ dépôt.

Enfin, nous terminons avec trois illustrations des applications potentielles des fluctuations des niveaux d'eau en présence d'interactions surface/subsurface (ouvert/poreux):

a) Les berges des rivières, estuaires, et lacs des barrages limités par des fondations imperméables et une couche verticale de noyau d'argile;

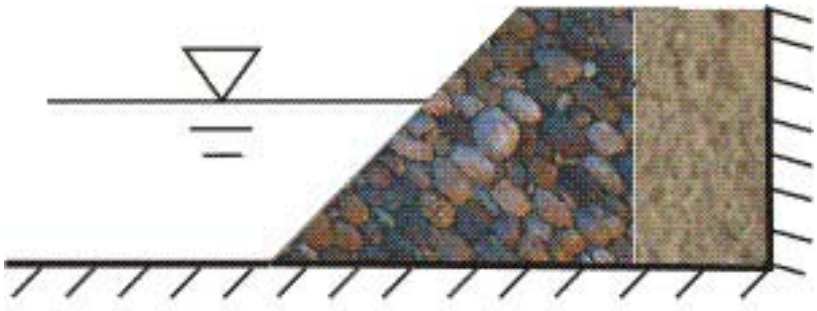

b) Les berges des rivières, estuaires, et lacs des barrages limités par des fondations imperméables et une couche oblique de noyau d'argile;

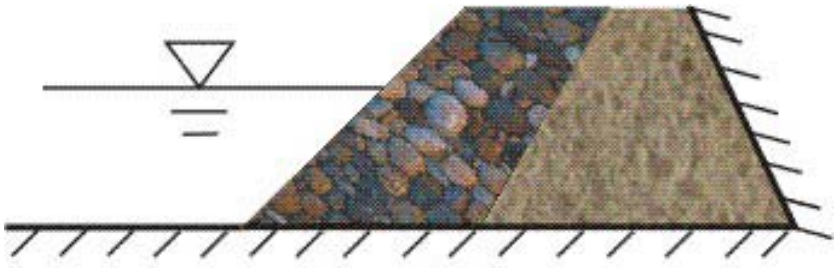

c) Les lits des rivières, et les digues limités par des fondations imperméables :

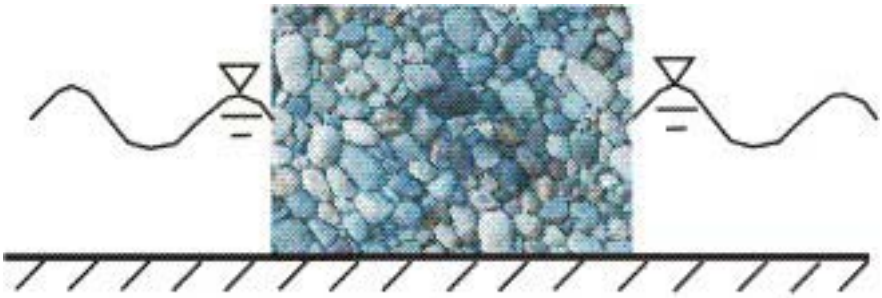

Ces applications correspondent à des problèmes réalistes, qui peuvent être traités comme des extensions du travail présenté dans cette thèse.

Conclusions and outlook

The consequences of hydrodynamic variations and oscillations with high temporal variability in partially saturated porous media with free surfaces both outside and inside the porous media have been investigated experimentally, analytically and numerically.

For the wetting problem in a sandbox, a good calibration result was obtained with the Richards model in vertical cross-section (best fitted parameters for the Van Genuchten/Mualem (VGM) model: α=4.6m^{-1}, n=5). The evolution of the saturation front toe $x_F\ (t)$ on the sandbox bottom is quite sensitive to parameter α which is related to the inverse capillary length of the medium (about 20cm here). By changing the value of α, we find that the larger α is (the smaller the capillary length is), the faster the saturation front toe moves in the *x* direction. Also, the Polubarinova analytical solution (Polubarinova-Kochina (1962)[1], Trégarot (2000)[17]) does not fit at all the experimental wetting process. This is to be expected, because Polubarinova's solution is based on the Dupuit-Boussinesq plane flow equation, with supposedly instantaneous drainage/wetting of the unsaturated zone at the free surface. The latter assumption would hold only for coarse media with small capillary length. On the contrary, in this very fine sand (d_{50}=0.16mm), capillary effects are important (20 cm capillary length).

We also studied, separately, the hypothetical problem of sudden discharge of a phreatic aquifer in a river bank, using plane flow assumptions and neglecting capillary effects (Dupuit-Boussinesq). We used a linearized solution of the transient water table *H(x,t)* (developed by Ababou (2007) [20]), and we obtained a very good agreement with the numerical solution of the Dupuit-Boussinesq plane flow model (whith non linear transmissivity). We also compared the Dupuit-Boussinesq results with the more complete Richards equation, whereby water table discharge is simulated as a partially saturated / unsaturated flow problem. Similar to the wetting problem, it is verified again here that the Boussinesq equation is good only when capillary length is negligible. Finally, we also used this test problem to compare two different

parametrizations of the curves ($K(h),\theta(h)$) in the Richards model. Using the same capillary length scale ($1/\alpha$) in both the VGM and Exponential models, and in spite of the different shapes of ($K(h),\theta(h)$) curves in these models, the same water table discharge rate $Q(t)$ was obtained at the river bank.

Wave propagation through a rectangular sandbox in a small wave canal was then investigated experimentally, numerically and analytically. The analytical solutions obtained with the Dupuit-Boussinesq plane flow model indicate that, assuming an exit boundary of constant water level, the wave in the porous domain consists of a single exponentially damped progressive wave $H(x,t)$. This exponential damping is confirmed by fitting the analytical wave with measured water levels, although the calculated permeability obtained by this fitting seems too high, due perhaps to internal erosion or to vertical flow dynamics. Finally, it is interesting to note that, in the hypothetical case of a closed boundary (which was not the case for our immersed sandbox), the resulting water level $H(x,t)$ is a combination of a forward (and a backward) progressive wave, with exponentially decaying (increasing) amplitude with respect to horizontal distance "x" from the fluctuating water level boundary.

Next, we studied water level fluctuations in a long (100 m) wave canal at HYDRALAB in Barcelona, Spain. We have placed 7 micro-piezometers equipped with capacitive sensors, to measure groundwater level fluctuations at different positions in the sloping sandy beach. We have also analyzed other water level fluctuations measured in the open water along the canal. The experimental results show the spatial decay of groundwater level fluctuations, and also, the filtering out of the shortest periods as one moves away from the shore ("landward"). Furthermore, the water level signals away from the shore ($H_6(t), H_7(t)$) exhibit a very different behavior from those closer to the shore (such as $H_2(t)$). Indeed, given the multiple Fourier frequencies of the waves that arrive at the shore, the result is apparently a net super-elevation of the mean groundwater table (at a distance from the shore) compared to "mean sea level".

In fact, it was observed that the measured water level fluctuations exhibit inhomogeneous characteristics in time and space. For this reason, simple processing methods such as direct Fourier analysis of each signal $H_i(t)$ appears ineffective or provides only incomplete information. Therefore, we have applied a series of tests and analyses to the measured water level fluctuations $H_i(t)$, including both single and cross-signal analyses, spectral frequency as well as correlation time lag analyses, orthogonal multi-resolution wavelet analyses, and pre-

filtering methods based on moving averages or wavelet decompositions. The main results obtained with these signal analyses methods are the following:

- Given that the wave generator period is about 4-5seconds, the dominant period T_1=24s of the incoming wave at the entry point of the shore (piezometer $H_1(t)$) is interpreted as the effect of the "geometry" of the wave canal, or more precisely, it is the dominant period of the run-up and run-down flow due to the topography and the nature of the sloping sandy beach.
- The most dominant period is the same, about 24 seconds, for the 3 piezometers closest to the shore and located in the swash zone $H_i(t)$ $(i=1,2,3)$; in comparison, the dominant periods are one order of magnitude longer for the piezometers located further away from the shoreline, after the swash zone $H_i(t)$ $(i=4,5,6,7)$: their dominant periods are respectively 400s, 600s, 600s and 300s.
- The fluctuation energies of the dominant periods drastically decrease with distance from the shore in the sloping sandy beach. The fluctuation energy of the longer period is propagated farther in the sloping sandy beach than the energy of the shorter periods.
- The maximum correlation almost decreases linearly, and the corresponding lag time increases exponentially with respect to the horizontal distance in the landward direction (i.e., away from the shoreline).
- The wave propagation velocities have been estimated all along the canal (open water as well as groundwater) using cross-correlation lag times (and phase lags). The measured average wave propagation velocity decreases with horizontal distance from the wave generator towards the sandy beach. The minimum measured value c = 0.056m/s is close to (but twice smaller than) the wave group velocity calculated from the Dupuit-Boussinesq model for the dominant period T = 24s of the entry point signal $H_1(t)$ located near the shoreline.
- We analyzed the spectral coherency between $H_1(t)$ and all the other beach groundwater signals ($H_2(t)$, $H_3(t)$, …). The spectral coherency peak obtained at $T \approx 24s$ indicates that this period has a great influence on all the groundwater level fluctuations in the sloping sandy beach, except for piezometer $H_7(t)$ furthest from the shore and closest to the impervious end wall of the canal. On the other hand, the coherency trough at $T \approx 10s$ may indicate that there is a periodic backflow wave

whose upper limit (landward) is located somewhere between $H_1(t)$ and $H_2(t)$, and therefore, this backflow does not directly influence piezometers $H_3(t)$, $H_4(t)$, etc.

We have finally developed a numerical model of the Barcelona wave canal experiment. The 2D plane flow Dupuit-Boussinesq model, as expected, was not really conclusive. Although the computed water levels have the same general evolution as the experimental ones, they do not really agree with the measured water levels: the simulated water level fluctuations seem to be less important than the measured ones, and the moving average water level is much underestimated by the simulations. Indeed, note that the sloping beach could not be represented explicitly in such a simplified plane flow model.

We then focused on a vertical cross-section model of partially saturated / unsaturated flow based on the generalized Richards equation, with a macroporous medium to represent the open air/water domain above the sloping sand surface. Specifically, two different types of models were used for the unsaturated curves ($K(h), \theta(h)$): the Van Genuchten / Mualem (VGM) model, and the Exponential model.

The simulated water levels obtained with the Richards model (using VGM curves and a macroporous subdomain for open water) agree much better with the measured water levels, compared with the Dupuit-Boussinesq simulations. The agreement is clear in three respects:

(1) the qualitative appearance of water level signals $H(x_i, t)$, which are quantitatively confirmed by comparing the auto-correlation structures of experimental versus simulated $H(x_i, t)$ signals;

(2) the trend of the average water level evolution;

(3) the dominant periods are also found to be in agreement, based on comparisons of the simulated and experimental Fourier spectra of $H(x_i, t)$.

Furthermore, using the same capillary length ($1/\alpha$) in the Exponential model and in the VGM model, yields a very similar set of water level fluctuations $H(x_i, t)$.

Finally, as an outlook for the study of beach hydrodynamics and groundwater interactions, it will be interesting and useful to consider, in a future work, surface processes of erosion/deposition, as well as internal erosion, and other solid-fluid and hydro-mechanical couplings. The latter should involve a stress/strain law, coupling with pore pressure (Terzaghi effective stress), capillary suction effects on cohesion, yield strength criteria, etc.

The OTE group at IMFT (with whom we have collaborated to retrieve and analyze wave canal data) is currently carrying out analyses of the erosion/deposition process based on sand surface measurements performed by laser imagery, for the same set of wave generation tests in the Barcelona canal. Then, it will be interesting to study the influence of groundwater fluctuations and the dynamics of the unsaturated zone on the erosion/deposition processes.

At last, we finish with three illustrations of potential applications of coupled surface/subsurface water level fluctuations:

a) Banks of rivers, estuaries and dam lakes limited by impermeable foundations and a vertical layer of clay core;

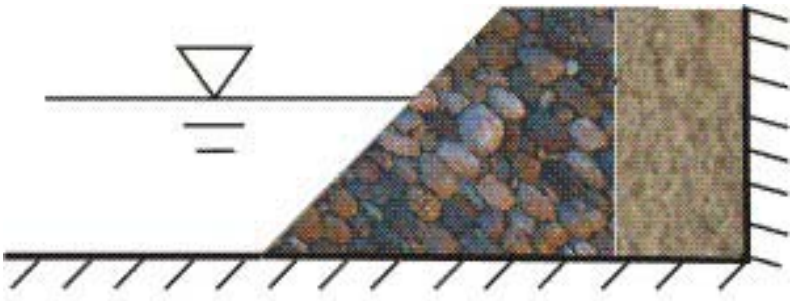

b) River banks, estuaries and dam lakes limited by impermeable foundations and an oblique layer of clay core;

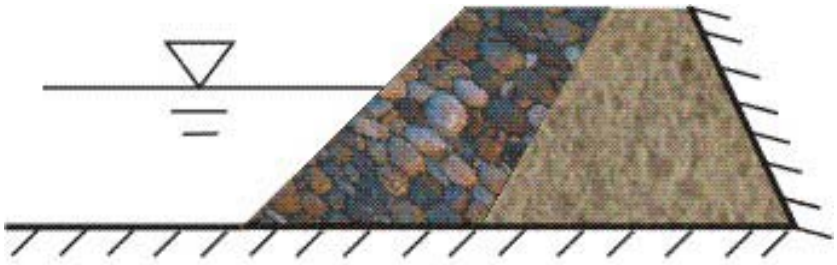

c) River banks, and dykes limited by impermeable foundations.

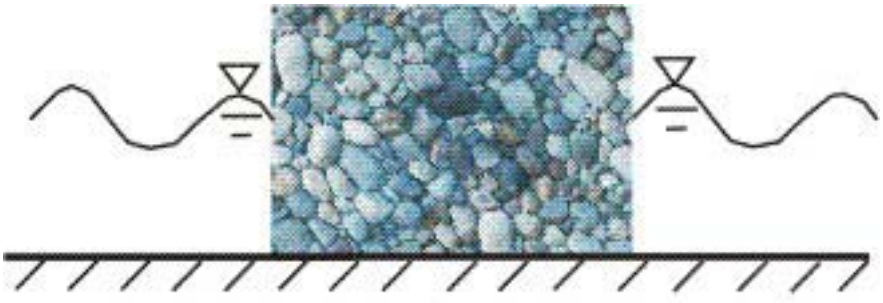

These applications correspond to realistic problems, which can be treated as extensions of this doctoral thesis work.

Part IV
APPENDICES

Résumé étendu

Cette thèse vise à étudier expérimentalement, analytiquement et numériquement, les conséquences de variations et d'oscillations hydrodynamiques à forte variabilité temporelle en milieux poreux partiellement saturés et comportant des surfaces libres tant à l'extérieur qu'à l'intérieur de milieux poreux.

Ce type de problème survient lorsque le massif poreux (digue, remblai, berge, sol, ...) est soumis à des oscillations dues aux marées et à la houle (littoral et portuaire), au passage de crues (rivières), et aux variations de niveaux de lacs et de réservoirs.

1. Introduction et objectifs

En hydrologie et hydrogéologie, les niveaux d'eau subissent des oscillations ou de brusques changements dans le temps. Cela peut se produire dans les aquifères, réservoirs, lacs, rivières, digues, les estuaires, les ports et les zones côtières. Dans de nombreux cas, les oscillations des surfaces libres ont lieu en eau libre, puis, se propagent dans les milieux poreux adjacents (plages, aquifères côtiers, berges, digues, brise-lames, …). Dans ce travail, nous étudions la réponse de la nappe phréatique, qui est à la fois dans des zones saturées et non saturées (séparés par des surfaces libres) dans des conditions très dynamiques. Nous nous sommes intéressés à deux cas en particulier: des changements brusques et des oscillations périodiques des niveaux d'eau. Ceux-ci peuvent résulter de conditions environnementales naturelles ou induites par des opérations de l'homme dans le génie civil et les applications hydrologiques.

Ainsi, nous nous concentrons sur les effets potentiels des variations des niveaux d'eau dans le voisinage de corps poreux, tels que:

- propagation d'ondes dans un environnement constitué de milieux poreux (plages, zones côtières et les estuaires) (**Figure 1**);
- transmission / dissipation des marées et des vagues à travers un milieu poreux (digues, brise-lames ou ports) ;
- variations de niveau d'eau de grande amplitude dans les rivières et les réservoirs, par exemple à cause d'opérations de barrages (**Figure 2**);

- interactions crues/eaux souterraines, et inondations/eaux souterraines (interactions sols-nappes-riviere en hydrologie)

Figure 1. Sea beach of Rincon, Puerto Rico taken from the Red Door.

Figure 2. Three Gorges Dam Reservoir filled to 135 meters (international PROBE, Mu Lan, June 2003).

Dans cette thèse, nous étudions en particulier la réponse du système de nappe phréatique des milieux poreux avec la surface libre aux variations de niveaux d'eau dans les eaux libres adjacentes. Ce milieu peut être traité soit comme une frontière du domaine poreux, ou bien comme une interface interne (cf. plage de sable en pente). Deux types principaux de dynamique sont étudiés: (i) variation brusque du niveau d'eau (cf. problème d'imbibition), et (ii) oscillations périodiques dues par exemple à des marées ou à des vagues (cf. les expériences de canal à houle).

Les analyses développées dans la thèse reposent sur trois approches complémentaires:

- Expériences physique avec des modèles à échelle réduite dans le laboratoire (*boites à sable*, *canaux*);
- Solutions analytiques linéarisées ou faiblement non-linéaire en termes des niveaux d'eau (modèle de Dupuit-Boussinesq de l'écoulement plan)
- Solutions numériques complètements non-linéaires de l'équation de Richards en termes de pression interstitielle, teneur en eau et flux de Darcy, en 3D ou en coupes verticales, basée sur un code volume finis implicite (BigFlow 3D).

2. Equations régissant nos problèmes

Les équations régissant nos problèmes sont basées sur la loi de Darcy et diverses généralisations :

- Equations des écoulements plans de nappes libres (Dupuit-Boussinesq),
- Equations des écoulements 3D en milieu variablement saturé avec capillarité (Richards)

De plus, dans les équations de Richards, nous utilisons la fonction de Van Genucheten/

Mualem (VGM) et la function exponentielle pour calculer la teneur en eau $\theta(h)$ et la conductivité hydraulique $K(h)$ dans la zone non-saturé du milieux poreux.

3. Méthodes numériques

Nous utilisons le code numérique BIGFLOW version 2007 (Ababou et Bagtzoglou 1993 [74]; Ababou et Al-Bitar 2007 [75]) basé sur la méthode des volumes finis afin d'étudier les problèmes décrits dans l'introduction. Nous avons, en particulier, développés des conditions limites permettant de traiter les problèmse avec des conditons limites variables dans le temps and l'espace. L'écoulement variablement saturé/non saturé est simulé avec le module 3D de BIGFLOW, et l'écoulement saturé quasi-plan est simulé avec le module plan "2D" de BIGFLOW.

4. Expériences de laboratoire

Pour étudier nos problèmes, nous avons réalisés trois expériences de laboratoire :

- Expérience d'imbibition dans une boite à sable (avec grande capillarité, **Figures 3** et **4**) ;

Figure 3 : Expérience d'imbibition (IMFT)

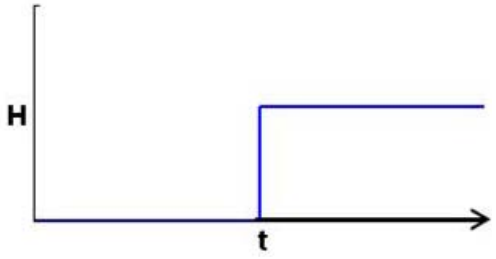

Figure 4 : Schéma de niveau d'eau de l'entrée H(t)

- Transmission de niveau d'eau dans un canal à travers un massif sableux intercalé (écoulement oscillatoire, **Figure 5** et **6**) ;

Figure 5 : Petit canal à houle (IMFT)

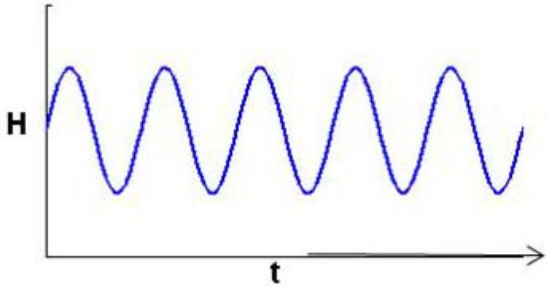

Figure 6 : Schéma de niveau d'eau de l'entrée H(t)

- Transmission de niveau d'eau dans un grand canal avec fond sableux incliné (expérience Hydralab-Sands à Barcelone, **Figure 7** et **8**) avec prise en compte de l'érosion.

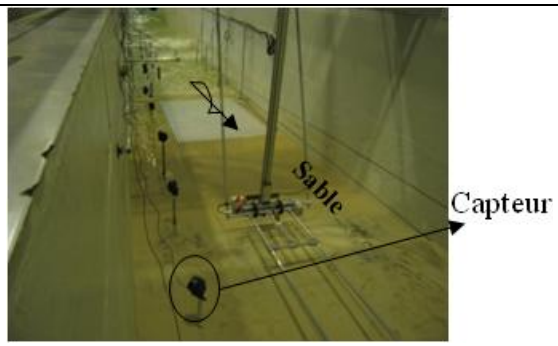

Figure 7 : Grand canal à houle à Barcelone (Hydralab)

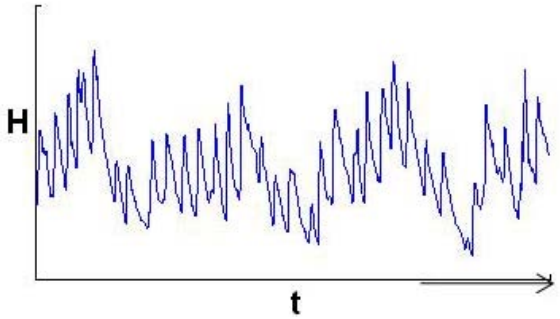

Figure 8 : Schéma de niveu d'eau d'entrée H(t)

Dans l'éxpérience d'imbibition, le niveau d'eau statique dans le réservoir s'infiltre brusquement dans une boite à sable sec et très fin (longueur capillaire d'envron 20cm). Nous avons étudié optiquement les évolutions des effets capillaires dans le milleu poreux.

En revanche, dans le petit canal à houle de l'IMFT, le massif sableux est beaucoup plus grossier ($d_{50} \approx 1.8mm$, sable grossier) et l'effet capillaire est négliseable. D'une part, nous avons utilisé cette expérience d'étudier la transmission de fluctuations de niveau d'eau à travers le massif sableux avec une condition de fontière d'écoulement oscillatoire forcé. D'autre part, nous l'avons aussi utilisé pour developer un capteur permettent de mesurer les fluctuations de niveaux d'eau dans les milleux poreux et qui a servi pour mesurer les fluctuations de niveaux d'eau dans une plage de sable fin en pente (grand canal à houle à Barcelone).

One peut ici noter que par la suite :

(1) pour l'éxpérience d'imbibition, la frontière d'entrée est verticale, il n'y a pas de condition limite oscillatoire forcé et le mileu poreux est très fin avec un grand effet capilaire;

(2) pour l'expérience dans le petit canal à houle de l'IMFT, la condition d'entrée est un écoulement oscillatoire forcement, la frontière d'entrée est verticale, et les effects capillaires sont négligeables.

Afin d'étudier le problème le plus complet de transmission de niveau d'eau dans le milieu massif poreux avec grand effet capillaire et avec la frontière d'entrée inclinée, nous avons réalisé une expérience dans un grand canal à houle (Hydralab). Dans cette expérience, nous avons installé 7 capteurs capacitifs (piézometriques) dans la plage pour mesurer les fluctuations de niveaux d'eau libre (dans le zone de swash) et souterraine. Le Capteur No.1 a été installé à la frontière entre l'eau libre et la plage pour mesurer les conditions d'entrée de niveaux d'eau dans la plage.

De plus, cette expérience de "vague/plage" a été menée dans un canal d'eau de grande dimension équipé d'un générateur d'ondes (canal CIEM à Barcelone). L'expérience a été menée dans le cadre d'un projet européen, Hydralab-Sands, entrepris en collaboration entre le laboratoire Hydralab à Barcelone (Espagne) et le groupe OTE du laboratoire IMFT (Toulouse, France). L'expérience était initialement conçue pour mesurer l'érosion de la zone de swash dans une plage de sable fin, avec des oscillations périodiques du niveau d'eau.

5. Problème d'imbibiton et problème de drainage

5.1 Problème d'imbibiton

Pour étudier le prolème d'imbibition avec variation abrupte du niveau d'eau amont (par suivi temporel du front de saturation), une solution de l'équation faiblement non linéaire de Dupuit-Boussinesq (D-B) et la simulation numérique dans la section verticale avec le module Richards '3D' (VGM) ont été utilisés et comparés avec les résultats expérimentaux.

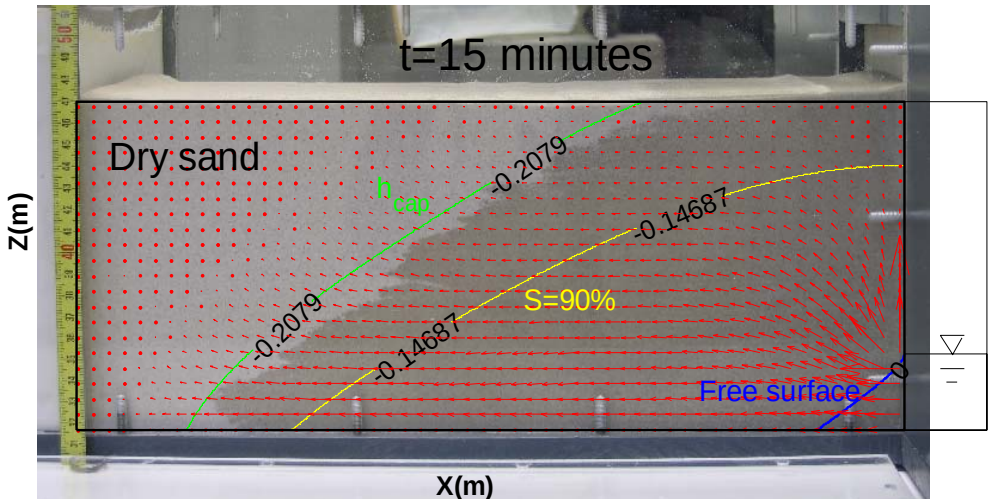

Figure 9: Photo et simulation numérique (Richards) de l'expérience d'imbibition, montrant les isovaleurs de saturation calculés (S=90%, S=62% (S_{CAP}) et S=1 (surface libre).
Les flèches rouges représentent le flux. L'échelle de longueur capillaire est de 22 cm.

Un bon résultat de calibration (**Figure 9**) a été obtenu avec le modèle de Richards en coupe verticale (les paramètres les plus adaptées pour le modèle VGM étont: $\alpha = 4{,}6\ m^{-1}$ et n = 5). L'évolution de la position aval du front de saturation x_F (t) est très sensible à α qui est liée à la longueur capillaire inverse de milieu poreux (environ 20cm ici). En changeant la valeur de α, nous trouvons que plus grand est α (plus petite est la longueur capillaire), plus rapide sont les mouvements du front de saturation se déplaçant dans la direction x. En outre, la solution analytique de Polubarinova (Polubarinova-Kochina (1962)[1],Trégarot(2000)[17]) ne correspond pas du tout avec le processus d'imbibition expérimental. Ceci était prévisible, car la solution de Polubarinova est basée sur l'équation saturée de Dupuit-Boussinesq avec

l'hypothèse de drainage/ imbibition instantanée de la zone non saturée vers la surface libre. Cela n'est valable que pour des milleux poreux avec une longueur capillaire petite. Au contraire, dans ce sable très fin, les effets capillaires sont ici importants (longueur capillaire de 20 cm).

5.2 Problème de drainage

Nous avons également étudié séparément le problème hypothétique de drainage brusque d'un aquifère phréatique dans une rivière en utilisant des hypothèses d'écoulement plan et en négligeant les effets capillaires (Dupuit-Boussinesq). Nous avons utilisé une solution linéarisée de surface libre transitoire *H(x,t)* (développé par Ababou (2007)[20]), et nous avons obtenu un très bon accord avec une solution numérique du modèle Dupuit-Boussinesq de l'écoulement plan (avec transmissivité non linéaire). Nous avons également comparé les résultats de Dupuit-Boussinesq avec l'équation de Richards plus complète, permettant le drainage de la nappe phréatique simulé comme un problème d'écoulement partiellement saturé/non saturé. Similairement au problème d'imbibition, il est vérifié à nouveau ici que l'équation de Boussinesq n'est bonne que lorsque la longueur capillaire est négligeable. Enfin, nous avons également utilisé ce problème pour comparer deux différentes paramétrisations des courbes (K(h), θ(h)) dans le modèle de Richards. Il a été constaté que, en mettant une même échelle de longueur capillaire (1/α) dans le modèle de VGM et le modèle exponentiel, bien que les courbes (K(h), θ(h)) dans ces modèles soient de formes différentes, le même débit de drainage Q(t) est obtenue au bord de la rivière.

6. Transmission et dissipation d'ondes à travers une boite à sable rectangulaire

Pour les études théoriques, nous avons développé des solutions analytiques linéarisées.

Un exemple de problème traité analytiquement est: l'équation linéarisée de Dupuit-Boussinesq (D-B) transitoire à surface libre, avec l'hypothèse d'écoulements plans et vidange/remplissage instantanés: oscillations forcées, transmission et dissipation d'ondes à travers une boite à sable rectangulaire.

Cette solution analytique de surface libre (*H(x,t)* a été comparée avec celle issue de simulations numériques ave le module plan "2D" de l'équation non-linéaire de Dupuit-Boussinesq. Les comparaisons montrent deux types de résultats:

- les profils de fluctuations de niveaux d'eau *H(x,t)* des deux types de résultats

(solutions lineaires/nonlineaires) sont très ressemblants, et en particulier les longueurs de décroissance des vagues progressives sont du meme ordre de magnitude ;

- les fluctuations de niveaux d'eau *H(x₀,t)* analytiques linéarisées sont en bon accord avec celles des simulations numériques de l'équation non-linéaire de Dupuit-Boussinesq, sauf certaines erreurs périodiques.

De plus, concernant les erreurs $\varepsilon(x,t) = \frac{|\mathrm{H_{Numérique}(x,t) - H_{analytique}(x,t)}|}{\mathrm{H_0}}$ ou $\varepsilon(x,t) = \frac{|\mathrm{H_{Numérique}(x,t) - H_{analytique}(x,t)}|}{\mathrm{A_0}}$ ($\mathrm{A_0}$ est l'amplitude de fluctuation d'entrée) entre les niveaux d'eau analytiques linéarisés et numériques nonlinéaires, on a trouvé que:

- Les erreurs $\varepsilon(x_0,t)$ atteingnent des maximums lorsque les niveaux d'eau sont minimums, les erreurs $\varepsilon(x,t_0)$ atteingnent les maximums à la position $x = \delta/2$, où δ est la longueur de décroissance de vague dans le milieu poreux;
- L'erreur maximale est une fonction puissance vis à vis du rapport de l'amplitude avec le tirant d'eau moyen, et pour les deux formules d'erreurs, on a :

$$\varepsilon_{Max1} = \max_{\mathrm{t\in[t,tmax]}} \frac{|\mathrm{H_{Numérique}(t) - H_{analytique}(t)}|}{\mathrm{H_0}} = e^{-1.354}\left(\frac{A_0}{H_0}\right)^{2.309}$$

$$\varepsilon_{Max2} = \max_{\mathrm{t\in[t,tmax]}} \frac{|\mathrm{H_{Numérique}(t) - H_{analytique}(t)}|}{\mathrm{A_0}} = e^{-1.354}\left(\frac{A_0}{H_0}\right)^{1.309}$$

Concernant la simulation numérique, la longueur de décroissance δ joue un role dominant influant sur la longueur de propagation de la fluctuation dans le milieu poreux. La longueur simulée devrait être supérieure ou égale à 6δ, sinon, en raison de l'influence de frontière de sortie, la distribution de l'erreur va complètement changer spatialement.

En général, la solution analytique faiblement non linéairisé sera meilleure que la solution analytique linéarisée pour le problème non-linéaire, et sera peut-être en mesure de résoudre le problème existant. D'autres méthodes non-linéairisées devraient être examinées afin d'améliorer les analyses de l'équation de Boussinesq non linéaire en présence de fluctuations (avec d'autres effets comme un fond en pente).

La propagation des ondes dans une boite à sable rectangulaire placé dans un petit canal à houle a été étudiée expérimentalement, numériquement et analytiquement. Les solutions analytiques obtenues avec le modèle Dupuit-Boussinesq de l'écoulement plan indiquent que, en supposant une condition limite en sortie à niveau d'eau constant, l'onde dans le domaine poreux est constituée d'un seule vague progressive *H(x,t)* qui décroit exponentiellement. Cette

décroissance exponentielle est confirmée par l'approximation analytique avec les niveaux d'eau mesurés, bien que la perméabilité calculée obtenus par cette approximation semble trop élevée, peut-être en raison de l'érosion interne ou des effets de l'écoulement vertical. Enfin, il est intéressant de noter que, dans l'hypothèse d'une frontière fermée (ce qui n'était pas le cas pour la boite à sable immergée), le niveau de l'eau résultant *H(x,t)* est une combinaison d'une onde avant (et arrière) progressive, avec décroissance (et croissance) exponentielle d'amplitude par rapport à la distance horizontale "x" de la frontière du niveau d'eau variable.

7. Traitement des signaux de l'expérience de Barcelone

Afin d'étudier la transmission des fluctuations de niveau d'eau dans les mileux micros-poreux avec pente inclinée dans le grand canal à houle de Hydralab à Barcelone, nous avons installé 7 micro-piézomètres (capteurs capacitifs) permettent de mesurer les fluctuations des niveaux des eaux souterraines à des positions différentes dans la plage de sable fin en pente (**Figure 10**). Nous avons aussi également mesuré d'autres fluctuations du niveau d'eaux dans l'eau libre.

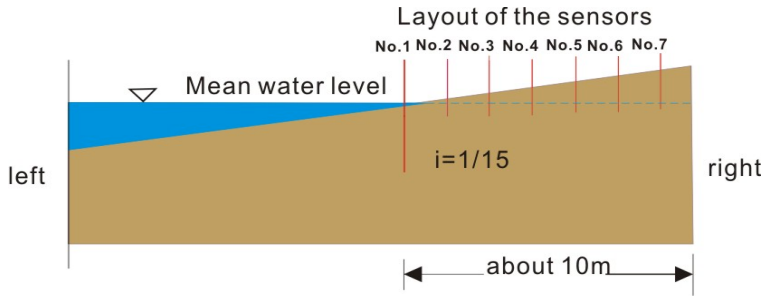

Figure 10 : Schéma de l'arrangement des capteurs capacitifs dans la zone de swash en coupe vertical. Le Capteur N°1 est le plus proche de l'eau libre.

Les résultats expérimentaux (**Figure 11**) montrent la décroissance spatiale des fluctuations de niveau des eaux souterraines, et aussi le filtrage des périodes les plus courtes losque l'on s'éloigne du rivage. En outre, les signaux des niveaux d'eaux loin de la rive ($H_6(t)$, $H_7(t)$) présentent un comportement très différent de ceux plus près du rivage (comme $H_2(t)$). En effet, étant donné les multiples fréquences du spectre des ondes qui arrive à la rive (semblable à une combinaison de marées et d'ondes courtes), le résultat est apparemment une surélévation de la surface libre moyenne (à distance du rivage) par rapport au 'niveau d'eau moyen de la mer'.

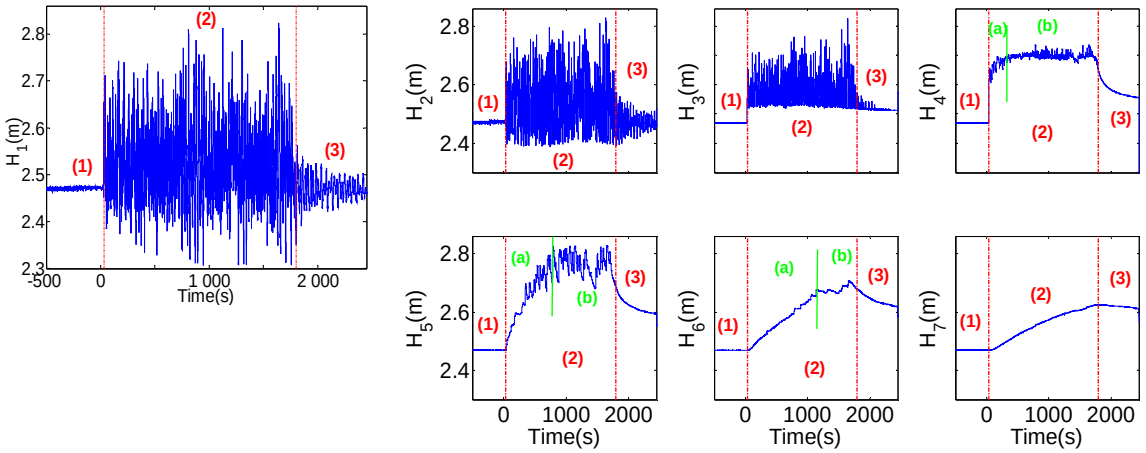

Figure 11 : Evolution des niveaux d'eau *H(x,t)* pour le serie-1 le 18 mars, 2008 (Barcelone)

En fait, il a été observé que les fluctuations des niveaux d'eau mesurés présentent des caractéristiques inhomogènes dans le temps et l'espace. Dans ce cas, les méthodes de traitement simples comme l'analyse de Fourier directe de chaque signal $H_i(t)$ apparaît inefficace ou ne fournit que des informations incomplètes. Pour cette raison, nous avons appliqué une série de tests et d'analyses sur les fluctuations de niveau d'eau mesurés, incluant à la fois les analyses croisées et univariées, la fréquence spectrale ainsi que des analyses de corrélation temporaire, l'analyse des ondelettes orthogonales multi-résolution, et les méthodes de pré-filtrage basées sur des moyennes mobiles ou des décompositions en ondelettes. Les principaux résultats obtenus avec les analyses du signal de ces méthodes sont les suivants:

- Étant donné que la période de géneration d'onde est d'environ 4-5 secondes, la période dominante T_1 = 24s de l'onde incidente sur la rive (piézomètre $H_1(t)$) est interprétée comme l'effet de la géométrie du grand canal à houle, ou plus précisément comme la période dominante de l'écoulement de 'run-up and run-down' lié à la topographie de la plage de sable fin en pente (**Figure 12**).
- Pour les trois piézomètres proches de la rive et dans la zone de swash $H_i(t)(i=1,2,3)$, les périodes dominantes sont les mêmes, environ 24 secondes ; les périodes dominantes sont d'un ordre de magnitude plus longue pour les piézomètres situés plus loin du rivage $H_i(t)(i=4,5,6,7)$: leur périodes dominante sont respectivement 400s, 600s, 600s et 300s (**Figure 13**).
- Les énergies de fluctuation des périodes dominantes diminuent considérablement avec l'éloigement du rivage dans la plage de sable. L'énergie de fluctuation de la période la plus longue se propage plus loin dans la plage que l'énergie des périodes plus courtes.

- La corrélation maximale diminue presque linéairement, et le délai correspondant augmente de façon exponentielle par rapport à la distance horizontale dans la direction de l'intérieur de la terre (loin de la rive).
- Les vitesses de propagation des ondes ont été toutes estimées le long du canal (eau libre, ainsi que les eaux souterraines) en utilisant des temps de délai de corrélation croisée. La moyenne de la vitesse de propagation des ondes mesurée diminue avec la distance horizontale à partir du générateur d'ondes vers la plage de sable fin. La valeur minimale mesurée c = 0.056m / s est proche de la vitesse de groupe d'onde calculé pour la période dominante T = 24s de $H_1(t)$ près de la rive, bien que environ 2 fois plus petite.
- Le pic de cohérence spectrale obtenu à $T \approx 24s$ indique que cette période a une grande influence sur toutes les fluctuations de niveau des eaux souterraines dans la plage, à l'exception du piézomètre $H_7(t)$, le plus éloigné de la rive et le plus proche de la paroi du fond imperméable du canal. D'autre part, le creux de la cohérence à $T \approx 10s$ indique qu'il y a une vague de refoulement périodique limite située quelque part entre $H_1(t)$ et $H_2(t)$ (**Figure 14**).

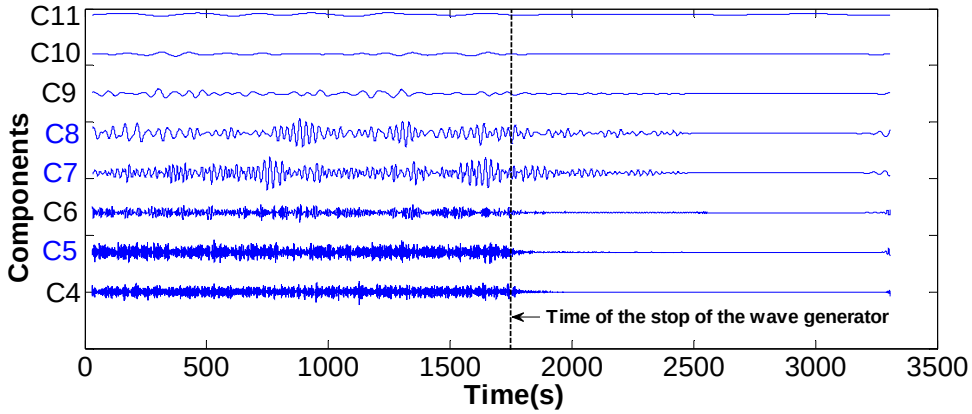

Figure 12 : Evolution de composantes principales du signal $H_1(t)$ (analyse par ondelette discrète multi-résolution)

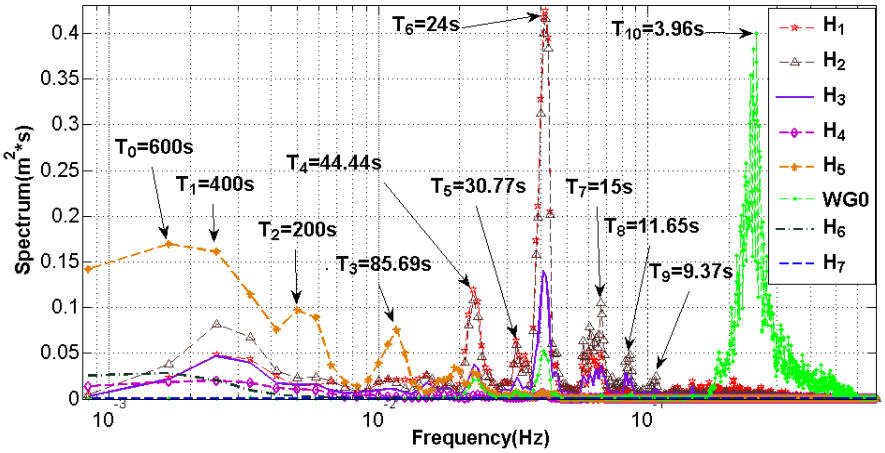

Figure 13 : Fonctions spectrales de Fourier de Hi(t)(i=1,..., 7) (analyse simple de Fourier)

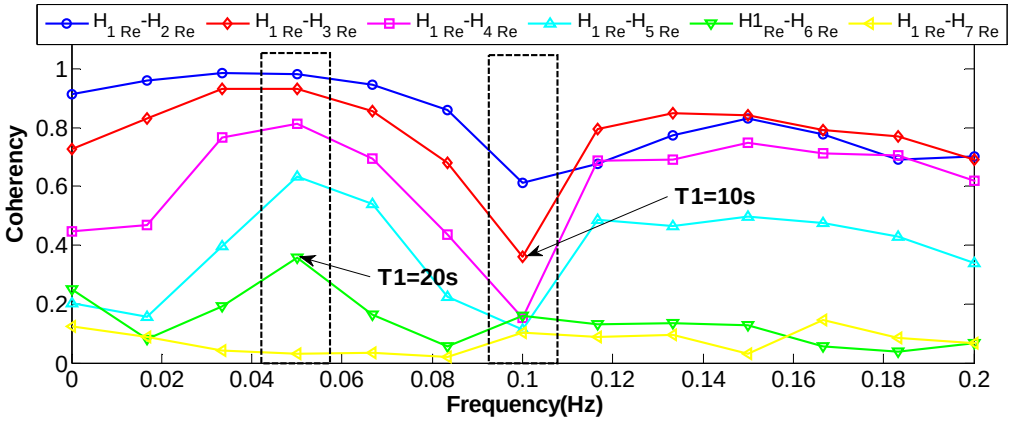

Figure 14 : Fonctions de cohérences en fonction à la fréquence dimensionale entre les résidus de $H_1(t)$ et $H_i(t)$ (i = 2, ..., 7) (T ≥ 5s) (analyse croisée de Fourier)

8. Simulations numériques de l'expérience de Barcelone

Nous avons développé un modèle numérique pour modéliser l'expérience du grand canal à houle de Barcelone. L'utilisation du modèle 2D de Dupuit-Boussinesq de l'écoulement plan, comme on s'y attendait, n'a pas été vraiment concluante. Bien que les niveaux d'eau calculés aient la même évolution générale que les données expérimentales, ils ne sont pas vraiment en accord avec les niveaux d'eau mesurés: les fluctuations de niveau d'eau simulées semblent être moins importantes que celles mesurées, et la variation de niveau d'eau moyenne est très sous-estimée par les simulations. A noter que la plage en pente ne peut pas être représentée explicitement dans un tel modèle d'écoulement plan simplifié.

Nous avons ensuite porté notre attention sur un modèle d'écoulement partiellement saturé /non saturé basé sur l'équation généralisée de Richards, avec un milieu macroporeux pour représenter le domaine de l'air /l'eau libre au-dessus de la surface du sable en pente. Plus précisément, deux types de modèles ont été utilisés pour les courbes caractéristiques des

milieux non saturés (K(h), θ(h)): le modèle de Van Genuchten/Mualem (VGM) et le modèle exponentiel dans le modèle de Richards.

Les niveaux d'eau obtenus par la simulation numerique avec le modèle de Richards (en utilisant des courbes de VGM et un sous-domaine macroporeux en eau libre) conviennent beaucoup mieux avec les niveaux d'eau mesurés (**Figure 15**), en comparants avec les simulations de Dupuit-Boussinesq.

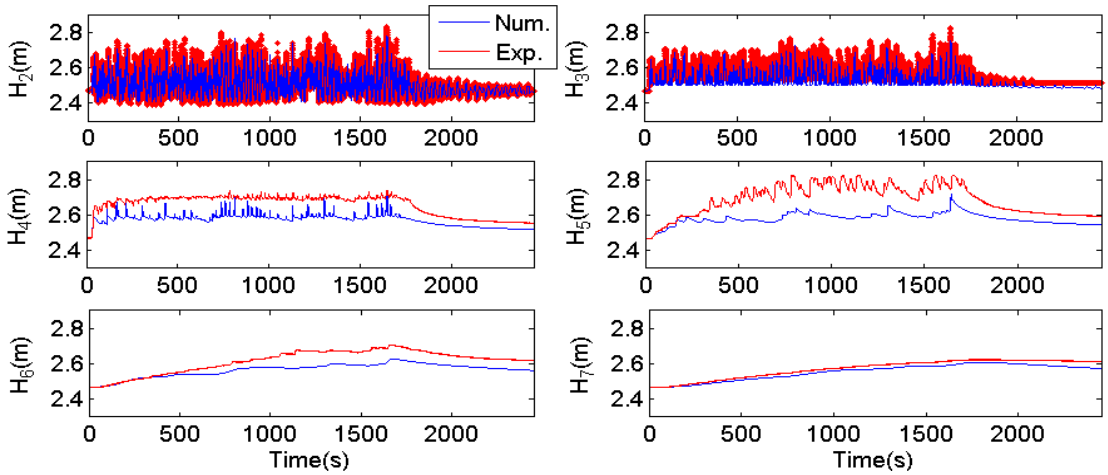

Figure 15 : Comparaison des signaux $H_i(t)$ numériques / expérimentaux : evolution des fluctuations de niveaux d'eau $H(x_i,t)$ dans la plage de sable pour différents capteurs (x_i)

Les résultats numériques ont été bien validés avec ceux de l'expérience sur trois aspects:

(1) Les courbes $H(x_i, t)$ de fluctuation du niveau d'eau, quantitativement confirmées par la comparaison des structures d'auto-corrélation de signaux $H(t)$ experimentaux et modélisés;

(2) La tendance de l'évolution du niveau d'eau moyen, par comparaison de $H(x_0, t)$

(3) Les périodes dominantes, par la comparaison des spectres de Fourier simulés et expérimentaux de $H(x_0, t)$.

De plus, on obtient un ensemble très similaire de fluctuations de niveau d'eau $H(x_i, t)$ en utilisant la même longueur capillaire (1 / α) dans le modèle exponetiel et dans le modèle VGM.

9. Conclusions et perspectives

Dans cette thèse, en partant du problème simple d'imbibtion (avec frontière poreuse et sans oscillations forcés) pour aller jusqu'au cas plus complet de transmission de niveau d'eau dans une plage de sable fin en pente avec un signal d'entrée oscillatoire, nous avons étudié expérimentalement, analytiquement et numériquement, les conséquences de variations et

d'oscillations hydrodynamiques à forte variabilité temporelle en milieux poreux partiellement saturés et comportant des surfaces libres tant à l'extérieur qu'à l'intérieur de milieux poreux.

L'étude théorique et numérique d'oscillations hydrodynamiques dans les milieux poreux partiellement saturé ont conduit aux résultats suivants:

- L'équation de Dupuit-Boussinesq de l'écoulement plan n'est valable que pour les milleux poreux avec une longueur capillaire petite, car elle ne comporte pas de termes permettent de décrire l'écoulement vertical et l'effet capillaire;
- Les equations (modèle VGM et modèle exponentiel) des écoulements 3D en milieu variablement saturé de Richards permettent d'obtenir de bons résultats pour les milieux poreux avec grands effets capillaires;
- Les equations pour les milieux partiellement saturés de Richards peuvent être utilisés pour le couplage numérique entre écoulements de surface et souterrain dans le modèle 3D, en imposant le rapport de conductivité hydraulique en saturation entre le milleu macro-poreux et le milieu micro poreux suffisamment grand.

L'analyse et le traitement de signaux appliqués aux fluctuations des niveaux d'eau mesurés avec des caractéristiques inhomogènes dans le temps et l'espace obtenus lors de l'expérience dans le grand canal à houle de Barcelone, ont donné les résultats suivants:

- La période dominante d'onde incidente sur la rive est identifiée par analyse de Fourier ou plus précisement, par la décomposition d'ondelette multi-résolution discrete;
- L'énergie de fluctuation de la période la plus longue se propage plus loin dans la plage que l'énergie des périodes plus courtes.
- La corrélation maximale diminue presque linéairement, et le délai correspondant augmente de façon exponentielle par rapport à la distance horizontale dans la direction vers la terre (loin de la rive).
- Les vitesses de propagation des ondes dans la plage sont estimées en utilisant l'analyse de corrélation croisée ('time lag') ou les vitesses de groupe de propagation d'ondes de périodes dominantes près de la rive avec l'équation théorique de Boussinesq.
- Les fonctions de cohérence spectrale de Fourier sont utilisées pour detecter la variabilité spatiale de la propagation des fluctuations de niveaux d'eau dans les milieux poreux.

Pour terminer, les fluctuations de niveaux d'eau ont été reproduites par des résultats numériques, et validées par trois aspects avec les résultats expérimentaux :

- Les structures d'auto-corrélation de signaux;
- La tendance de l'évolution du niveau d'eau moyen ;
- Les périodes dominantes (spectres de Fourier).

En perspective, pour étudier les interactions entre l'hydrodynamique de la plage et les eaux souterraines, il sera nécessaire de tenir compte également des processus d'érosion/dépôt de surface, ainsi que de l'érosion interne et d'autres couplages de fluide/solide (couplages hydro-mécaniques impliquant une loi de contrainte /tension, la pression interstitielle, la contrainte effective de Terzaghi, les effets de succion capillaire sur la cohésion, les critères de rupture, etc.). Le groupe OTE à l'IMFT (avec qui nous avons collaboré pour récupérer et analyser les données du canal à houle) est actuellement en train d'effectuer des analyses du processus d'érosion/dépôt basées sur des mesures de surface de sable réalisée par imagerie laser pour le même ensemble de génération de tests d'onde que celui étudie. Il sera intéressant par la suite d'étudier l'influence des fluctuations de niveaux d'eaux souterraines sur ces phénomène d'érosion/ dépôt.

Appendix A

Appendix A: Chapter 2

AC.2.1 ReadMe_BF2005FORTRAN_Compiling.rtf

README FILE "ReadMe_BF2005FORTRAN_Compiling.rtf" by R.Ababou and A.Al-Bitar (6 Feb.2006)

==========

1. **Topic** : Compiling "BIGFLOW" & its FUNCTIONS using "ABSOFT 9.0" FORTRAN compiler.

2. **Fortran version of BigFlow** : BigFlow2000, Ver.1.0, Dec.2005/Jan.2006

3. **Source files :**
   1.1. BigFlow_main_source.f ...under various names, such as : <<mainflow_3DSWIM_3.f>>
   1.2. COMBIG (fortran file invoked by INCLUDE in the main source) and its back-up (COMBIG*.f)
   Functions *(possibly located in a subdirectory "func"):*
   2.1. FBQVT*.f (Transmissivity model for 2D planar flows: Boussinesq, Diffusive Wave, SWIM2D)
   2.2. FCOND*.f (Conductivity - pressure curve model for 3D flows...)
   2.3. FTHETA*.f (Water content - pressure curve model for 3D flows...)
   2.4. FTIME.f (Time evolution of forcing functions : boundary fluxes, and/or interior source term)

4. ABSOFT 9.0 Developer Tool Interface*:*

STEPS: 1. Set project options; 2. Add/remove files (add main&functions); 3. Build (compile&link)

1. Set project options (details) : *special options that may have to differ from default values*

Console Appli. : CPU : Pentium 4 (e.g., case of laptop computer Fujitsu LifeBook Series E)
Options Subset ==> FPU (Floating Point Unit) : Round Up (do not choose "Round to Nearest"!)
F77 : no warning
F77 compatibilty ==> do not choose "static storage" ! (static storage should be turned off)
==> choose "Promote REAL and COMPLEX" (-N113) :
this turns on "real double-precision" (advisable!)
Link options :

	Reserve	Commit
Stack size	Reserve less than the max available RAM size (in number of bytes). *Example with 1 Gbyte RAM:* **536870912** *which is a half Gbyte: 0.5*(1024)**3 bytes.*	**0x8000** *Note: T*his is the default (in hexadecimal).
Heap size	**0x10000** *Note:* This is the default (in hexadecimal).	**0x1000** *Note:*This is the default (in hexadecimal).

2. Add/remove files (add main source.f and functions.f);
See list of fortran files above...

3. Build (compile and link)
Compile and link should be successfull : a single executable file *****.exe** will be produced.
This executable can be renamed and moved in another directory to be used by BF-Python.

5. **Assumed name and location of the BigFlow executable file in the BF-Python package** : **"...../...../.....".**

Appendix B

Chapter B9: Signal analysis for oscillatory flows (methodology)

9.1 Introduction

The measured water level fluctuations in the slopping sandy beach of the Barcelona wave canal are very irregular and non-stationary. In order to analyze their fluctuation characteristics, to study the propagation of the water level fluctuation in the partially unsaturated porous media with a inclined entry boundary, and eventually to understand the beach hydrodynamic response in the sea/beach system, the Fourier spectrum, multi-resolution wavelet, and temporal analysis signal processing methods are used together with the moving average, differential, and multi-resolution filtering methods in this thesis.

In this chapter, the theories of the three filtering methods and the three signal processing methods will be respectively introduced.

9.2 Signal filtering methods

9.2.1 Introduction

In order to analyze the oscillatory characteristics of the measured non-stationary water level fluctuations in Barcelona wave canal experiment such as $H_6(t)$ and $H_7(t)$, the moving average, differential, and multi-wavelet filtering methods are used to filter the original signal.

The used theories about the three filtering methods will be introduced in this section.

9.2.2 Moving average filtering (linear integrator filter)

For any random time serial with a variable time step $\Delta t(i)$, the moving average is calculated by a sliding window $\Delta t_w(i)$ through the values of chronic. The schema explaining in detail the simplified algorithm of the program is shown in **Fig. 9-1**.

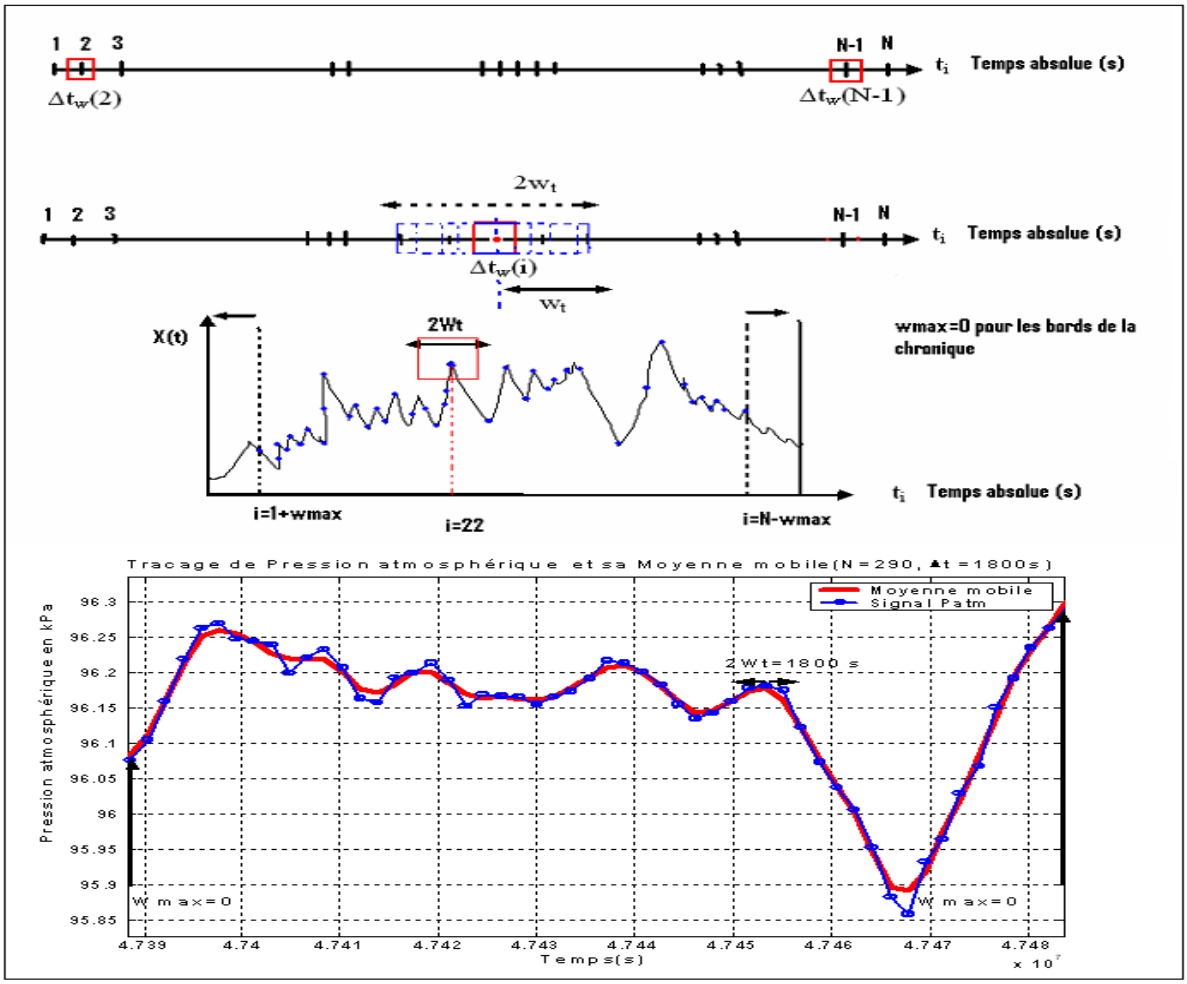

Fig. 9-1 Calculation of the moving average for a random time serial of the atmospheric pressure with time $\Delta t\ (i)$

The values of W_t and W_{max} are selected by the user based on variable time step $\Delta t(i)$, which is written according to the index i as flows:

$$\Delta t_w(i) = \frac{(t(i+1)-t(i-1))}{2} \tag{9-1}$$

Where,

$\Delta t_w(i)$ is time step weighted centered around the time t_i.

Note:

w_t is the size of half window in seconds;

W_{max} is the estimation of the maximum size of the half-window in number of time;

$\Delta t(i)$ is the variable time step in seconds;

$t(i)$ is the absolute time in seconds and $w_t \geq \Delta t(i)$.

Based on linear interpolation and extrapolation, this moving average uses a fixed window--half window width w_t in time units with a constant or variable time step. Compared with the

one in Matlab by putting the data point number of the span which must be odd, the advantage of this moving average is that we can put directly the filter time w_t.

9.2.3 Differential filtering

This filtering removes the trend of the signal by calculating the one-time increase in the chronicle.

If $X(t)$ is a time serial, the differentiated $\Delta Y(t)$ is given by the following equation (9-2) for the case of $\Delta t = costant$:

$$\Delta Y(t) = X(n+1) - X(n) \tag{9-2}$$

For the case of Δt is variable, the derivative of the function X (t) is written as:

$$\Delta \boldsymbol{Y(t)} = \frac{\boldsymbol{X(n+1)-X(n)}}{\boldsymbol{t(n+1)-t(n)}} \tag{9-3}$$

This method preserves the structure and magnitude of the phenomena while eliminating the tendency. Thus, the use of this second mode of filtering is entirely consistent with the theory of random functions which relate the correlation and spectral analysis (Mangin, 1984) [7].

9.2.4 Discrete multi-resolution wavelet filtering

The multi-resolution wavelet analysis can also be used to filter the signal. The multi-resolution wavelet analysis makes a dyadic signal decomposed into a succession of approximations corresponding to increasing scales. The difference between the measured signal and its approximation to the order 'm' is called "residual". Therefore, a measured discrete signal $X(i)$ can be expressed by the sum of the approximation A_X^m and the residual R_X^m in the multi-resolution wavelet function as flows:

$$X(i) = A_X^m(i) + R_X^m(i) \tag{9-4}$$

where,

i can be replaced by $t_i = i\Delta t$;

A_X^m is the approximation of the dyadic scale 'm' (low pass filter);

R_X^m is the residual of the approximation of the dyadic scale 'm' (high pass filter);

The detailed multi-resolution wavelet analysis will be introduced in the latter of this Chapter.

9.2.5 Comments

If the same filter time is chosen, the moving average and the multi-resolution wavelet filtering methods can obtain the same filtered and residual signals. However, compared with

the moving average filtering, it is more complicated to determine the exact filter time for the multi-resolution wavelet filtering.

Differential filtering is different from the moving average and the multi-resolution wavelet filtering. For the case that $\Delta t = costant$, the fluctuation characteristics of the difference of the original signal can be obtained by studying the filtered signal.

As a result, the three filtering methods will be tested and eventually used to filter the extremely non-stationary water level fluctuations in the Barcelona wave canal experiment.

9.3 Signal analysis methods

9.3.1 Introduction

The Fourier spectrum, multi-resolution wavelet and temporal analysis (correlation analysis) signal processing methods are used together to analyze the measured water level fluctuations in the slopping sandy beach in the Barcelona wave canal.

The analysis on the measured water level fluctuations includes the single and cross analysis. The corresponding theories about the above three signal processing methods are introduced in this section.

9.3.2 Correlation analysis (single and cross) and temporal transfer function

Correlation function analysis is used to study the temporal structure of the beach water level fluctuations $H_i(t)\left(i=1,2,\ldots,7\right)$ (or their residuals) in the time domain, using either auto-correlation functions versus time lag (τ), or cross-correlation functions for the joint analyzis of two signals such as H1(t) and H2(t+τ). *Note on terminology*: correlation functions are defined in this text as the normalized versions of the covariance functions (the two become identical for unit standard deviations). For background on correlation functions for (supposedly) stationary random processes, see Papoulis and Pillai (2002) [23], Bras et al. (1985) [76], Labat et al. (2000a) [33]. These references also describe methods to estimate the frequency spectrum of a stationary random process by Fourier transform of the correlation function (see further below).

Correlation analysis is used to study the evolution of events in the time domain in a single or cross way. The temporal structure of the signal $X(t)$, or both signals $X(t)$ and $Y(t)$ together, is captured by functions of time structure at two points $(t, t+\tau)$, which depends only on the lag (τ) in the case of statistically stationary process.

For the correlation analysis functions, there are biased and unbiased two estimations.

Biased estimation:

- Cross covariance functions:

$$C_{XX}(j) = \frac{1}{N}\sum_{i=1}^{i=N-j}(X(t_i) - \bar{X})\left(X\left(t_{i+j}\right) - \bar{X}\right) \quad (9\text{-}5)$$

$$C_{XY}(j) = \frac{1}{N}\sum_{i=1}^{i=N-j}(X(t_i) - \bar{X})\left(Y\left(t_{i+j}\right) - \bar{Y}\right) \quad (9\text{-}6)$$

- Cross correlation functions:

$$R_{XY}(j) = \frac{C_{XY}(j)}{\sigma_X.\sigma_Y} \quad (9\text{-}7)$$

Where**,**

$$\sigma_X^2 = C_{XX}(0) \quad (9\text{-}8)$$

$$\sigma_Y^2 = C_{YY}(0) \quad (9\text{-}9)$$

Unbiased estimation:

- Cross covariance functions:

$$C_{XX}(j) = \frac{1}{N-j}\sum_{i=1}^{i=N-j}(X(t_i) - \bar{X})\left(X\left(t_{i+j}\right) - \bar{X}\right) \quad (9\text{-}10)$$

$$C_{XY}(j) = \frac{1}{N-j}\sum_{i=1}^{i=N-j}(X(t_i) - \bar{X})\left(Y\left(t_{i+j}\right) - \bar{Y}\right) \quad (9\text{-}11)$$

- Cross correlation functions:

$$R_{XY}(j) = \frac{C_{XY}(j)}{\sigma_X.\sigma_Y} \quad (9\text{-}12)$$

$$R_{YX}(j) = \frac{C_{YX}(j)}{\sigma_Y.\sigma_X} \quad (9\text{-}13)$$

Where,

$$\sigma_X^2 = C_{XX}(0) \quad (9\text{-}14)$$

$$\sigma_Y^2 = C_{YY}(0) \quad (9\text{-}15)$$

For the biased and unbiased cases, the inter-correlation function is not symmetric for values of -j and + j. The standard deviation functions are also the same for the two cases and they are written as follows:

$$\sigma_X^2 = \frac{1}{N}\sum_{i=1}^{i=N}(X(t_i) - \bar{X})^2 = C_{XX}(0) \quad (9\text{-}16)$$

$$\sigma_Y^2 = \frac{1}{N}\sum_{i=1}^{i=N}(Y(t_i) - \bar{Y})^2 = C_{YY}(0) \quad (9\text{-}17)$$

In particular, it is worth noted that, according to the different authors, there are several definitions of the cross covariance:

$$C_{XY}(\tau_m) = E\left\{(X_t - \bar{X})\left(Y_{t+\tau_m} - \bar{Y}\right)\right\} \quad \text{(cf. Vanmarcke)} \quad (9\text{-}18)$$

$$C_{XY}(\tau_m) = E\left\{(X_t - \bar{X})\left(Y_{t+\tau_m} - \bar{Y}\right)\right\} \quad \text{(cf. Ababou)} \quad (9\text{-}19)$$

$$C_{XY}(\tau_m) = E\left\{\left(X_{t+\tau_m} - \bar{X}\right)(Y_t - \bar{Y})\right\} \quad \text{(cf. Papoulis)} \quad (9\text{-}20)$$

$$C_{XY}(\tau_m) = E\{(X_{t+\tau_m} - \bar{X})(Y_t - \bar{Y})\} \quad \text{(cf. Matlab)} \tag{9-21}$$

From the above equations (9-18), (9-19), (9-20) and (9-21), it can be seen that the definition of Ababou is the same as the one of Vanmarcke, and the definition of Papoulis is same as the one of Matlab. The two kinds of definition have the flowing relationship:

$$C_{XY}(\tau_m)(Matlab) = C_{XY}(-\tau_m)(Vanmarcke) = C_{YX}(\tau_m)(Vanmarcke) \tag{9-22}$$

Note:

- $R_{XY}(j)$ is the cross correlation function with respect to discrete lag j;
- $C_{XY}(j)$ is the cross covariance function with respect to discrete lag j;
- τ_j is the lag time (if $k_0 = 1$) and $\tau_j = j\Delta t$ [time unit, eg. s];
- τ_j is the general lag time and $\tau_j = j \times k_0 \Delta t$ [time unit, eg. s];
- k_0 is the sampling step and $k_0 = 1, or, 2, ou\ 3, ou, \dots, M$;
- N is the total number of the measured data;
- j is the discrete lag (dimensionless). If $k_0 = 1$, j =0, 1, 2, ..., M;
- M is the truncation number;
- Δt is the time step.

For our case, the smallest sampling step number ($k_0 = 1$) is chosen to scan all the time serial. Otherwise, for a very long chronic with small time step, it is possible to make a sub-sampling (k0 ≥ 2).

In the case of a simple single analysis, let $Y(t) = X(t)$, then the auto-covariance function defined above of the signal $X(t)$ (with respect to the lag time τ) can be obtained. In the case of a cross-analysis, the concept of cross-covariance is generally used to obtain the temporal transfer function $X(t) \rightarrow Y(t)$, causal or non-causal described in the thesis of Fatmi (2009).

In practice, the biased estimation is used to calculate the Fourier spectrum, and at the same time, the unbiased estimation is used to do the direct single or cross analysis such as cross covariance function with respect to the lag to show the cross correlation of the signals between $Y(t)$ and $X(t)$. Because unbiased estimation will intuitively show the hidden periodicity of the two signals, while the 'biased' cannot show this characteristic.

9.3.3 Fourier spectral analysis with Fourier transformation of single, cross spectra and frequency gain

9.3.3.1 Introduction

The Fourier spectral analysis reflects the structure of the signal by decomposing a signal in periodic functions. Its advantage is to clearly manifest the distribution of the Fourier spectral density (or fluctuation energy) with respect to the frequency (period).

Fourier single and cross spectral analysis in discrete time will be used to analyze the measured and simulated water level fluctuations. The single spectral analysis allows to study the frequency spectrum of a single column (auto-spectrum S_{XX}), while the cross spectral analysis allows to simultaneously treat two signals to study the cross spectrum S_{XY}.

The direct Fourier transformation and the inverse of the Fourier transformation of a real signal, the Fourier transformation of autocorrelation of Wiener-Khichen (W-K), and Tuckey filter for the Fourier spectral function, will be introduced in this section. Considering the consistence of the theory, corresponding Fourier transformations will be introduced from the continuous time to the discrete time for the single and cross analysis. Concerning the theory of spectral estimation, see Priestley (1981) [60], or Yevjevich (1972) [3]. For more details on specific procedures, see Fatmi et al. (2008) [43], and Fatmi (2009) [21].

9.3.3.2 Fourier single spectral analysis (estimation of the spectrum with Tuckey filter)

The auto-spectrum signal $X(t)$ can be defined in several ways. For example, there are Fourier spectral functions in continuous time and in discrete time, and there are also reduced (dimensionless) and unreduced spectral functions. The reduced spectrum of $X(t)$ in discrete time, which is mainly used in this thesis, will be defined later in this section

In order to clearly explain the Fourier spectral theory, the Fourier transformation in continuous time is firstly introduced.

- **Direct Fourier transformation complex of the real signal in continuous time**

The direct Fourier transformation complex of the real signal in continuous time can be written as follows:

$$\hat{X}(\omega) = \frac{1}{2\pi}\int_{-\infty}^{\infty} e^{-i\omega t} X(t)\, dt,\ X(t) \in \Re \tag{9-23}$$

where,

$$e^{-i\omega t} = cos(\omega t) - isin(\omega t)$$

or

$$\hat{X}(\omega) = \frac{1}{2\pi}\int_{-\infty}^{\infty} [cos(\omega t) - isin(\omega t)] X(t)\, dt \tag{9-24}$$

or

$$\hat{X}(\omega) = X_{Re}(\omega) + iX_{Im}(\omega)\ ,\ \hat{X}(\omega) \in C \tag{9-25}$$

where,

$$X_{Re}(\omega) = \frac{1}{2\pi}\int_{-\infty}^{\infty} cos(\omega t)\, X(t)dt \tag{9-26}$$

$$X_{Im}(\omega) = \frac{1}{2\pi}\int_{-\infty}^{\infty} sin(\omega t)\, X(t)dt \tag{9-27}$$

- **Inverse of Fourier transformation of the real signal in continuous time**

The signal can be reconstructed (the inverse of the Fourier transformation) in the following:

$$X(t) = \int_{-\infty}^{\infty} e^{i\omega t}\, \hat{X}(\omega)d\omega \tag{9-28}$$

$$X(t) = \int_{-\infty}^{\infty} [cos(\omega t) + isin(\omega t)]\, \hat{X}(\omega)d\omega \tag{9-29}$$

where,

$$\hat{X}(\omega) = X_{Re}(\omega) + iX_{Im}(\omega) \tag{9-30}$$

So we find $X(t)$ as follows:

$$X(t) = \int_{-\infty}^{\infty} [cos(\omega t) + isin(\omega t)]\, \big(X_{Re}(\omega) + iX_{Im}(\omega)\big)d\omega \tag{9-31}$$

or

$$X(t) = \int_{-\infty}^{\infty} [X_R(\omega)cos(\omega t) - X_{Im}sin(\omega t)]\, d\omega + i\int_{-\infty}^{+\infty} [X_R(\omega)sin(\omega t) + X_{Im}(\omega)cos(\omega t)]\, d\omega \tag{9-32}$$

We can the write $X\ (t)\ =\ A\ +\ iB$ as follows:

$$A = \int_{-\infty}^{\infty} [X_{Re}(\omega)cos(\omega t) - X_{Im}(\omega)sin(\omega t)]\, d\omega \tag{9-33}$$

$$B = \int_{-\infty}^{\infty} [X_{Re}(\omega)cos(\omega t) + X_{Im}(\omega)sin(\omega t)]\, d\omega \tag{9-34}$$

$X(t)$ is therefore decomposed into real and imaginary parts. According to the assumption of direct Fourier transform in the above, $X(t)$ is real number which implies two conditions:

(1) $B = 0$, then

$$\begin{cases} X_R(\omega)sin(\omega t) = 0 \\ X_{Im}(\omega)cos(\omega t) = 0 \end{cases} \rightarrow \begin{cases} X_R(\omega) = X_R(-\omega) \\ X_{Im}(\omega) = -X_{Im}(-\omega) \end{cases}$$

(2) Synthesis:

For a real signal $X(t)$, its Fourier transform complex $\hat{X}(\omega)$ has:

$$\begin{cases} X_R(\omega) = X_R(-\omega) \\ X_{Im}(\omega) = -X_{Im}(-\omega) \end{cases} \quad \forall\omega \in [-\infty, +\infty]$$

It means that $Re\left(\hat{X}(\omega)\right)$ is pair (even) function, and $Re\left(\hat{X}(\omega)\right)$is unpaired (odd) function.

- **Fourier transformation of the autocorrelation of W-K in continuous time**

According to the theorem of Wiener-Khichen, the Fourier transform of the autocorrelation function is written as follows:

$$S_{XX}(\omega) = \frac{1}{2\pi}\int_{-\infty}^{\infty} R_{XX}(\tau)e^{-i\omega\tau}d\tau \tag{9-35}$$

$$\int_{-\infty}^{\infty} S_{XX}(\omega)d\omega = \begin{cases}\sigma_X^2 \\ 1\end{cases} \tag{9-36}$$

where,

R_{XX} is the autocorrelation function related to the auto-covariance function by the relation:

$$R_{XX}(\tau) = \frac{C_{XX}(\tau)}{\sigma_X^2} = \frac{C_{XX}(\tau)}{Var(X)} \tag{9-37}$$

where, σ_X is standard deviation of $X(t)$;

The autocorrelation is a pair (even) function and $R_{XX}(-\tau) = R_{XX}(\tau)$;

The auto-covariance is also a pair (even) function and $C_{XX}(\tau) = C_{XX}(-\tau)$;

The spectral density is symmetric (pair) and $S_{XX}(-\omega) = S_{XX}(\omega)$;

The spectral density $S_{XX}(\omega)$ of the signal $X(t)$ is always real and $S_{XX} \in \Re$. The imaginary part of $S_{XX}(\omega)$ is equal to zero:

$$Im\big(S_{XX}(\omega)\big) = -\frac{i}{2\pi}\int_{-\infty}^{+\infty} R_{XX}(\tau)sin(\omega t)d\tau = 0 \tag{9-38}$$

Direct estimation of $S_{XX}(\omega)$:

$$\hat{S}_{XX} = \left|\hat{X}(\omega)\right|^2 = X_{Re}^2(\omega) + X_{Im}^2(\omega) \tag{9-39}$$

- **Fourier transformation of the autocorrelation of W-K in discrete time**

From the above, we know that the continuous Fourier transformations of the signal for the spectrum and the auto-covariance are defined as follows:

$$\begin{cases} S_{XX}^{(2)}(\omega) = \frac{1}{2\pi}\int_{-\infty}^{+\infty} exp^{(-i\omega\tau)}C_{XX}(\tau)d\tau \\ C_{XX}(\tau) = \int_{-\infty}^{+\infty} exp^{(+i\omega\tau)}S_{XX}^{(2)}(\omega)d\omega \end{cases} \tag{9-40}$$

where,

C_{XX} –auto-covariance function;

$S_{XX}^{(2)}$ --bilateral continuous spectral density (2-sided);

For the continuous case, the maximum time is $t_{max} = \infty$.

According to the continuous Fourier transformations (equation(9-40)), the discrete Fourier transformations for the spectrum and the auto-covariance are defined as follows:

$$\begin{cases} S_{XX}^{(2)}(\omega_k) = \sum_{j=-N}^{j=+N} exp^{(-i(k\Delta\omega j\Delta t))}C_{XX}(\tau_j)\,\Delta t \\ C_{XX}(\tau_j) = \frac{1}{N}\sum_{j=-N}^{j=+N} exp^{(+i(k\Delta\omega j\Delta t))}S_{XX}^{(2)}(\omega_k)\,\Delta\omega \end{cases} \tag{9-41}$$

where,

$\substack{\omega_k=k\Delta\omega \\ \tau_j=j\Delta t}$ and conveniently, we can write that: $C_{XX}(\tau_j) = C_{XX}(j)$

For the discrete case, the maximum time is $t_{max} = N\Delta t$.

The dimensional bilateral (2-sided) discrete spectrum is defined by the following equation:

$$S_{XX}^{(2)}(\omega_k) = \sum_{j=-N}^{j=+N} exp^{\left(-i(\omega_k\tau_j)\right)} C_{XX}(j)\,\Delta t \tag{9-42}$$

where,

$$exp^{\left(-i(\omega_k\tau_j)\right)} = cos(\omega_k\tau_j) - isin(\omega_k\tau_j) \tag{(9-43}$$

Substituting (9-43) in equation (9-42), we find:

$$S_{XX}^{(2)}(\omega_k) = \sum_{j=-N}^{j=+N}\left[cos(\omega_k\tau_j) - isin(\omega_k\tau_j)\right] C_{XX}(j)\,\Delta t = \sum_{j=-N}^{j=+N}\left[cos(\omega_k\tau_j)\right] C_{XX}(j)\,\Delta t \tag{9-44}$$

The function $sin(x)$ is asymmetric and the function $cos(x)$ is symmetric, so:

$$S_{XX}^{(2)}(\omega_k) = \left[\left(\sum_{j=-N}^{j=-1}\left[cos(\omega_k\tau_j)\right] + \sum_{j=1}^{j=N}\left[cos(\omega_k\tau_j)\right]\right) C_{XX}(j) + C_{XX}(0)\right]\Delta t \tag{9-45}$$

$$S_{XX}^{(2)}(\omega_k) = \left[\left(2\sum_{j=1}^{j=N}\left[cos(\omega_k\tau_j)\right]\right) C_{XX}(j) + C_{XX}(0)\right]\Delta t \tag{9-46}$$

Then the relationship between the auto-covariance and the autocorrelation is given by:

$$R_{XX}(\tau_j) = \frac{C_{XX}(\tau_j)}{\sigma_X^2} = \frac{C_{XX}(\tau_j)}{Var(X)} \tag{9-47}$$

We obtain:

$$S_{XX}^{(2)}(\omega_k) = \left[\left(2\sum_{j=1}^{j=N}\left[R_{XX}(\tau_j)cos(\omega_k\tau_j)\right]\right) + R_{XX}(0)\right]\Delta t \times \sigma_X^2 \tag{((9-48}$$

The dimensional bilateral (2-sided) discrete spectrum is written:

$$S_{XX}^{(2)}(\omega_k) = \left(1 + 2\sum_{j=1}^{j=N}\left[R_{XX}(j)cos(\omega_k\tau_j)\right]\right)\Delta t \times \sigma_X^2 \tag{9-49}$$

where,

$S_{XX}^{(2)}(\omega_k)$ –dimensional bilateral (2-sided) spectrum;

$\omega_k = 2\pi f_k$;

$\tau_j = j\Delta t$;

The reduced bilateral (2-sided) discrete spectrum compared with the variance of $X(t)$ with respect to the dimensionless frequency f^* is written as follows:

$$S^{*(2)}_{XX}\left(f^*_k\right) = \left(1 + 2\sum_{j=1}^{j=N}\left[R_{XX}(j)cos\left(2\pi f^*_k j\right)\right]\right) \tag{9-50}$$

where, $f^*_k = f_k \times \Delta t$

Conventionally, the relationship between the unilateral (1-sided) spectrum $S_{XX}^{(1)}(\omega)$ and the bilateral (2-sided) spectrum $S_{XX}^{(2)}(\omega)$ is written:

$$\sigma_X^2 = \int_0^{+\infty} S_{XX}^{(1)}(\omega)d\omega = \int_{-\infty}^{+\infty} S_{XX}^{(2)}(\omega)d\omega \tag{9-51}$$

$$S_{XX}^{(1)}(\omega) = 2 \times S_{XX}^{(2)}(\omega) \tag{9-52}$$

The reduced unilateral (1-sided) discrete spectrum is written:

$$S^{*(1)}_{XX}(\hat{f}_k) = 2S^{*(2)}_{XX}(f^*_k) = 2\left(1 + 2\sum_{j=1}^{j=N}\left[R_{XX}(j)cos\left(2\pi f^*_k j\right)\right]\right) \tag{9-53}$$

Finally, the dimensional unilateral (1-sided) discrete spectrum is written:

$$S_{XX}^{(1)}(\omega_k) = 2S_{XX}^{(2)}(\omega_k) = \sigma_X^2 \Delta t \times 2\left(1 + 2\sum_{j=1}^{j=N}\left[R_{XX}(j)cos\left(\omega_k \tau_j\right)\right]\right) \tag{9-54}$$

- **Fourier transformation of the autocorrelation in the case of a finite duration (discrete frequency)**

The bilateral (2-sided) spectrum must meet:

$$\sigma_X^2 = \int_{-\infty}^{+\infty} S_{XX}^{(2)}(\omega)\, d\omega \tag{9-55}$$

By discretizing ($\omega \to \omega_i$), we find:

$$\sigma_X^2 = \left(2\sum_{i=1}^{i=N}\left[S_{XX}^{(2)}(\omega_i)\right] + 1 \times S_{XX}^{(2)}(0)\right) \times \Delta\omega \tag{9-56}$$

where,

$$\Delta\omega = 2\pi\Delta f = \frac{\pi}{N\Delta t} \text{ and } \Delta f = f_{min} = \frac{1}{T_{max}}$$

For the unilateral (1-sided) spectrum $S_{XX}^{(1)}(\omega)$, we have:

$$\sigma_X^2 = \left(\sum_{i=1}^{i=N}\left[S_{XX}^{(1)}(\omega_i)\right] + \frac{1}{2} \times S_{XX}^{(1)}(0)\right) \times \Delta\omega \tag{9-57}$$

The reduced unilateral (1-sided) discrete spectral density can be written:

$$S^{*(1)}_{XX}(\omega_i) = \frac{S_{XX}^{(1)}(\omega_i)}{\sigma_X^2} \times \Delta\omega = \frac{S_{XX}^{(1)}(\omega_i)}{\sigma_X^2} \times \frac{\pi}{N\Delta t} \tag{9-58}$$

$$S^{*(1)}_{XX}(\omega) = 2 \times S^{*(2)}_{XX}(\omega)$$

$$1 = 2 \times \left(2\sum_{i=1}^{i=N}\left[S^{*(2)}_{XX}(\omega_i)\right] + S^{*(2)}_{XX}(0)\right) \tag{9-59}$$

Note:

The Fourier transform we use is discrete both in time and frequency, which is explained as follows:

- The time is discrete ($t_i = i \times \Delta t$) because the observations are discrete. The consequence of Δt is the existence of a maximum frequency f_{max} (frequency of Nyquist, theorem of Shannon)
- The frequency is discrete because the size of the temporal window of the observation is finite. Therefore, there is a lower frequency f_{min} which gives the discrete frequency increment: $\Delta f = f_{min}$.

- **Temporal filter for estimating the Fourier spectrum (Tuckey filter)**

The bilateral spectrum (2-sided) will not be used in this thesis. The unilateral spectrum (1-sided) reduced temporarily (equation 9-58), which is defined in the frequency range of Shannon by applying Shannon's theorem and introducing the Tuckey filter, is used in this work.

In fact, in order to obtain the autocorrelation function, the time serial is discretized by step j in respecting the sampling theorem of Shannon.

The truncation M (maximum value to be taken) must meet the following inequality: ($M \leq N/3$), where N denotes the total number of observation.

If j is the number of discrete steps in terms of lag, the information is usable between 2j and M. This interval is called the observation window. The Fourier transformation is from - ∞ to + ∞ and in our problem, the autocorrelation function is bounded between 0 and M (truncation). Hence, it is necessary to smooth this function when the autocorrelation is discrete and the Fourier transformation is not discrete.

Several temporal filters have been considered in the literature. The rectangular could solve the problem mentioned above (the noise problem of the estimated spectrum). However, it is advisable to use temporal filters less steep than the rectangular window (coincidence effects). The Parzen (2) (in the below) filter eliminates too much information, while the Tuckey (2) (in the below) filter appears to retain the maximum information with maintaining its function of the smoothing of the estimated spectrum in a optimal way [Blackman and Tukey (1958) [78], Papoulis and Pillai (2002) [23], Priestley (1981) [60] and Yevjevich (1972) [3]]. The variance of the estimated errors on $R_{XX}(\tau)$ increases with increasing lag (τ) (Fatmi et al., 2008, [43]). For all these reasons, Tukey filter is chosen and used later in this work. It can be noted that this type of filter is necessary to obtain a good spectral estimation from a signal of the finite duration in discrete time.

If $D(j)$ is the temporal filter function of Tuckey by the Fourier transform for the finite size of the domain [0, M], then

Filtre (D_j) :

The Fourier transform applies:

- to a continuous function
- and infinite support.

Hence there is the necessity to:

- do the smoothing due to the discretization

- and to nullify the values beyond the truncation *M*.

Two possibilities are:

- the pre-filtering of $R_{XX}\ (j)$ corresponding to $D(j)$
- and the post-filtering of the obtained spectrum.

In our case, several filter methods are referred for the pre-filtering $D(j)$ and they respectively are:

- Bartlett: $D_j = 1 - \frac{j}{m}$ (9-60)
- Parzen (1): $D_j = 1 - \frac{j^2}{M^2}$ (9-61)
- Parzen (2): $D_j = 1 - \frac{6j^2}{M^2\left(1-\frac{j}{M}\right)},\ 0 \le j \le \frac{M}{2}$ (9-62)
- Parzen (3): $D_j = 1 - \frac{6j^2}{M^2\left(1-\frac{j}{M}\right)},\ \frac{M}{2} \le j \le M$ ((9-63)
- Tukey (1): $D_j = 1 - 0.46 + 0.46cos\left(\frac{\pi j}{M}\right)$ (9-64)
- Tukey (2): $D_j = \frac{\left(1+cos(\pi j/M)\right)}{2}$ or (9-65)
- Tukey (3): $D_j = \frac{\left(1+cos(2\pi j\Delta t/2M\Delta t)\right)}{2}$ or (9-66)

Note:

Opposed to the moving average, Tukey filter applies to the autocorrelation function, instead of the data itself.

Spectral estimation with Tuckey filter:

Finally, the reduced spectrum used in this thesis is written as follows:

$$S^*\left(f^*_i\right) = 2\left[1 + 2\sum_{j=1}^{j=M} D_j.R_{XX}(j)\,.\,cos\left(2\pi f^*_i.j\right)\right] \quad (9\text{-}67)$$

Where,

$$f^*_i = \frac{i}{2\times M\times k_0}$$

$$i = 0, 1, 2, \dots, M;$$

$$C_{XX}(j) = \frac{1}{N}\sum_{i=1}^{i=N-j}(X(t_i) - \bar{X})\left(X\left(t_{i+j}\right) - \bar{X}\right) \quad (9\text{-}68)$$

$$R_{XX}(j) = \frac{C_{XX}(j)}{\sigma_X^2} \quad (9\text{-}69)$$

Equation (9-67) is the dimensionless reduced spectrum normalized by the variance of the signal $X(t)$ with respect to the dimensionless frequency f^* defined later.

The dimensional frequency is defined as :

f_i : the "hertzienne" frequency (1 Hz=1 s^{-1})➔ $f_i = \frac{1}{T_i}[Hz]$

Fig. 9-2 shows some notions of the signal sampling.

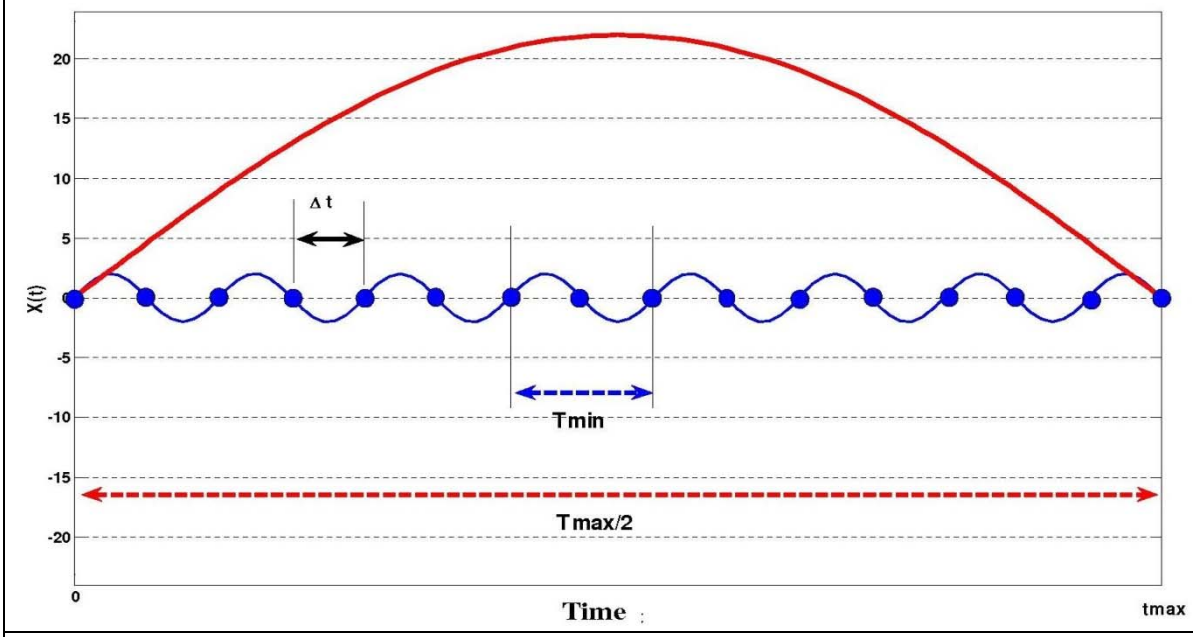

Fig. 9-2 Schema of the sampling of a discrete-time signal on a temporal observation window with the finite size.

Note:

T_{min} is the minimum period likely to be sampled ;

T_{max} is the maximum period likely to be sampled;

Δt is the time step (s);

N is the number of discrete observations;

t_{max} is the maximum possible lag time (s), and $t_{max} = M\Delta t$;

M is the truncation lag that can be chosen for convenience with a cutoff $M \leq N$, eg. $M \approx N/3$.

Using the definitions of this figure, by the sampling theorem of Shannon, we have:

$$f_{max} = \frac{1}{T_{min}}[Hz] \Rightarrow f_{max} = \frac{1}{2\Delta t}[Hz] \text{ and } f_{min} = \frac{1}{T_{max}} = \frac{1}{2t_{max}}[Hz]$$

Then: $t_{max} = M\Delta t \Rightarrow f_{min} = \frac{1}{2M\Delta t}[Hz] \Rightarrow (T_{max} \geq 2T_{min})$

Then we can derive a dimensionless frequency f^* defined by:

$$f^*{}_i = f_i \times \Delta t \Rightarrow f^*{}_i = \frac{i}{2 \times M \times k_0} \quad (9\text{-}70)$$

Note:

Here, we take $k_0 = 1$ (more generally, $k_0 \geq 1$ represents the temporal sampling step used in the Fourier transform).

And the dimensional spectrum used in the thesis is written as follows:

$$S(f_i) = S(f^*{}_i).\sigma_X^2.dt \quad (9\text{-}71)$$

The reduced frequency belongs to the interval: $0 \leq f^*_i \leq 0.5$ (dimensionless).

Note:

The truncation lag M can be replaced by the total duration of the time serial N, which corresponds to the application of Shannon's theorem in the absence of filtering. Our approach here (with M instead of N) amounts to reduce the number of discrete frequency and to increase the frequency increment Δf.

Example: $\Delta t = 1000s$, $N = 500$, $M = 50$.

- With N we obtain $\Delta f = 1/(1000000s) = 10^{-6} Hz$;
- With M we obtain $\Delta f = 1/(100000s) = 10^{-5} Hz$.

For $k_0 = 1$, we have :$\hat{f}_0 = 0$ and $f^*_N = 0.5$.

Finally, the term D_j is a temporal filter and Tukey filter (2) is used:

$$D_j = \frac{\left(1+cos\left(\frac{\pi j}{M}\right)\right)}{2} \quad (9\text{-}72)$$

where,

j is the number of time steps and $j = 1,2, \ldots, M \leq N/3$ (or, at most, $= N$);

M is the window size of the truncation in number of the time step Δt;
N is the total number of the sequential data;

Δt is the time step of the measurement.

Used in the W-K theorem for estimating the spectrum of a signal, the weighting function $D(j)$ is a filter of $R_{XX}(j)$. In fact, for various reasons, to apply the Fourier transform, it is necessary to carry out smoothing. Tuckey filter is used in this thesis, because it makes better filtering of the long periods (low frequencies). The experience shows that Tuckey filter skews less the value of the variance and it overestimates the total variance of 8% (Mangin, 1984). The bandwidth of the filter must be greater than the one of the signal so that the sampling does not interfere in the reconstruction of the signal and let pass any information it contains.

9.3.3.3 Cross spectral analysis

- **Fourier transformation of the cross correlation function of W-K in continuous time**

The cross spectral density of $X(t)$ and $Y(t)$ is decomposed in the frequency domain by Fourier transform with a complex number of the cross correlation function:

$$S_{XY}(\omega) = \frac{1}{2\pi}\int_{-\infty}^{+\infty} R_{XY}(\tau) e^{-i\omega\tau} d\tau \quad (9\text{-}73)$$

$$\int_{-\infty}^{+\infty} S_{XY}(\omega)d\omega = \begin{cases} C_{XY}(0) \\ R_{XY}(0) \end{cases} \quad (9\text{-}74)$$

Note:

The cross correlation function R_{XY} is asymmetrical:

$$R_{XY}(-\tau) \neq R_{XY}(\tau) \text{ or } R_{XY}(-\tau) \neq R_{YX}(\tau)$$

It automatically deducts the cross spectral density is complex: $S_{XY}(\omega) \in C$, then

$$S_{XY}(\omega) = S_{Re}(\omega) - iS_{Im}(\omega) \text{ or } S_{XY}(\omega) = |S_{XY}(\omega)|e^{(-i\theta_{XY}(\omega))} \quad (9\text{-}75)$$

Where,

$S_{Re}(\omega)$— co-spectrum;

$S_{Im}(\omega)$-- quadrature spectrum;

Amplitude density spectrum:

$$|S_{XY}(\omega)| = \sqrt{S_{Re}^2(\omega) + S_{Im}^2(\omega)} \quad (9\text{-}76)$$

Phase density spectrum:

$$\theta_{XY}(\omega) = arctan\left(\frac{S_{Im}(\omega)}{S_{Re}(\omega)}\right) \quad (9\text{-}77)$$

- **Fourier transformation of the cross correlation function of W-K in discrete time**

The function of inter-covariance in discrete time is written as:

$$C_{XY}(j) = \frac{1}{N}\sum_{i=1}^{i=N-j}(X(t_i) - \bar{X})\left(Y\left(t_{i+j}\right) - \bar{Y}\right), j > 0 \quad (9\text{-}78)$$

$$R_{XY}(j) = \frac{C_{XY}(j)}{\sigma_X.\sigma_Y}$$

$$C_{YX}(j) = \frac{1}{N}\sum_{i=1}^{i=N-j}(Y(t_i) - \bar{Y})\left(X\left(t_{i+j}\right) - \bar{X}\right), j < 0 \quad (9\text{-}79)$$

$$R_{YX}(j) = \frac{C_{YX}(j)}{\sigma_Y.\sigma_X}$$

$$\sigma_X^2 = \frac{1}{N}\sum_{i=1}^{i=N-j}(X(t_i) - \bar{X})^2 \quad (9\text{-}80)$$

$$\sigma_Y^2 = \frac{1}{N}\sum_{i=1}^{i=N-j}(Y(t_i) - \bar{Y})^2 \quad (9\text{-}81)$$

The inter-correlation function is not symmetric from -j to + j, and the spectrum function is expressed by a complex number. Here the two expressions represented by the imaginary and real part are:

- General expression of Fourier cross spectrum complex:

$$S_{XY}(\omega) = S_{Re}(\omega) - iS_{Im} \quad (9\text{-}82)$$

The real part (co-spectrum):

$$S_R(\omega) = 2\left\{R_{XY}(0) + \sum_{j=1}^{j=M}\left(R_{XY}(j) + R_{YX}(j)\right)D(j)\,cos\left(2\pi f^*_i j\right)\right\} \quad (9\text{-}83)$$

The imaginary part (quadrature spectrum):

$$S_{Im}(\omega) = 2\sum_{j=1}^{j=M}\left(R_{XY}(j) - R_{YX}(j)\right) D(j) sin\left(2\pi \hat{f}_i j\right) \quad (9\text{-}84)$$

- Exponential expression of Fourier cross spectrum complex:

$$S_{XY}(\omega) = |S_{XY}(\omega)| e^{\left(-i\theta_{XY}(\omega)\right)} \quad (9\text{-}85)$$

where, spectrum density of amplitude:

$$|S_{XY}(\omega)| = \sqrt{S_{Re}^2(\omega) + S_{Im}^2};$$

Spectrum of phase density:

$$\theta_{XY}(\omega) = arctan\left(\frac{S_{Im}(\omega)}{S_{Re}(\omega)}\right).$$

- Combination of simple and cross spectrum:

The coherency function is written as follows:

$$Coh_{XY}(\omega) = \frac{|S_{XY}(\omega)|}{\sqrt{S_{XX}(\omega).S_{YY}(\omega)}} = Coh(\omega) exp\left(i\theta_{XY}(\omega)\right) \quad (9\text{-}86)$$

The phase function (rad/s) is written as follows:

$$\theta_{XY}(\omega) = arctan\left(\frac{S_{Im}(\omega)}{S_R(\omega)}\right) \quad (9\text{-}87)$$

The reduced gain function (dimensionless) is written as follows:

$$g^*_{XY}(\omega) = \frac{|S^*_{XY}(\omega)|}{S^*_{XX}(\omega)} \quad (9\text{-}88)$$

where, $S^*_{XY}(\omega)$ is the dimensionless cross spectrum;

$S^*_{XX}(\omega)$ is the dimensionless single spectrum.

The relationship between the no-reduced and reduced gain functions is written as follows:

$$g_{XY}(\omega) = \frac{|S_{XY}(\omega)|}{S_{XX}(\omega)} = \frac{\sigma_Y}{\sigma_X} . g^*_{XY}(\omega)$$

Where, $S_{XY}(\omega)$ is the dimensional cross spectrum;

$S_{XX}(\omega)$ is the dimensional single spectrum.

It is worth noted that the reduced gain $g^*_{XY}(\omega)$ is the ratio of the absolute value of the dimensionless cross-spectrum $S^*_{XY}(\omega)$ to the dimensionless auto-spectrum $S^*_{XX}(\omega)$, while the no-reduced gain $g_{XY}(\omega)$ is the ratio of the absolute value of the dimensional cross-spectrum $S_{XY}(\omega)$ to the dimensional auto-spectrum $S_{XX}(\omega)$. For the same type of signals such as two signals are the water level fluctuations, the no-reduced gain $g_{XY}(\omega)$ is also dimensionless.

9.3.4 Multi-resolution wavelet analysis

9.3.4.1 Introduction

The main objective of the wavelet transform is to analyze and decompose time-scale phenomena without losing information on time localization (transients, jumps, trends). From this point of view, the discrete multi-resolution wavelet framework, with its orthogonal basis, gives a more satisfactory decomposition than the time-frequency Fourier transform (which globalizes all times into a single frequency parameter). It is also more satisfactory than the sliding window Fourier analyzis of Gabor type. Concerning mathematical and computational aspects of multiresoultion wavelets, see Mallat (1989)[8], Strang & Nguyen (1996) [42], Mallat (1999) [15], and other references therein.

Here, the orthogonal basis of discrete multi-resolution wavelets (Daubechies basis, more precisely, Daubechies wavelets of order N=20) is chosen to analyze the measured water level fluctuations. The programs used for this analysis were put together into a custom-made Matlab Toolbox, including the wavelet functions proposed and published online by Stanford University (WaveLab: (http://www-stat.stanford.edu/ ~ wavelab/.), as well as the Matlab's Wavelet Toolbox which itself contains also its own toolkit and its own analysis functions. Previous publications along these lines, using similar wavelet tools, are those of Labat et al. (2000.b) [34]and Fatmi et al. (2008) [43].

The corresponding theory about the multi-resolution wavelet will be introduced in this section. It includes the decomposition, construction and the detail (component) of a signal as well as the application with the multi-resolution wavelet analysis.

9.3.4.2 Decomposition of a signal

The signal $X(t)$ in continuous time is represented in the coefficients ($C_{j,k}^{X}$) as follows:

$$X(t) = \int_{k=-\infty}^{k=+\infty} C_{j,k}^{X}(t)\,\psi_{j,k}(t)dt \tag{9-89}$$

In this equation, the coefficients of the discrete orthogonal wavelet transform $C_{j,k}^{X}$ are given by the convolution:

$$C_{j,k}^{X}(t) = \int_{-\infty}^{+\infty} X(t)\,\psi_{j,k}dt \tag{9-90}$$

where,

$$\psi_{j,k}(t) = 2^{j/2}\psi\left(2^{j}.t - k\right)\ (j > 0\text{: compression, } j < 0\text{: dilation}) \tag{9-91}$$

or

$$\psi_{j,k}(t) = \frac{1}{2^{-j/2}}\psi\left(\frac{t-2^{-j}.k}{2^{-j}}\right)\ (j > 0\text{: compression, } j < 0\text{: dilation}) \tag{9-92}$$

In such an orthonormal basis, the wavelets of the basis $\psi_{j,k}(t)$ are ortho-normal to their images obtained by translations and dilations. Therefore, we have:

$$\int_{-\infty}^{+\infty} \psi_{m,n}(t)\, \psi_{m',n'} dt = \delta_{m,m'}\delta_{n,n'} \tag{9-93}$$

where, δ is the Kronecker symbol defined as follows:

$$\delta_{i,j} = \begin{cases} 1, & \text{if i = j} \\ 0, & \text{if i} \neq \text{j} \end{cases}$$

It is possible to construct a complete orthogonal basis in order that the signal at discrete time of the finite energy $X(i)$ can be decomposed into a linear combination of translations and dilations of the basis functions with appropriate coefficients:

$$X(i) = \sum_{j=0}^{j=+\infty} \sum_{k=-\infty}^{k=+\infty} C_{j,k}^{X}(i)\psi_{j,k}(i) \tag{9-94}$$

where, i can be replaced by $t_i = i\Delta t$.

The relation (9-94) corresponds to the discretization of continuous time equation corresponding to the synthesis of a signal based on these wavelet coefficients. This can also be interpreted as a succession of approximations of the discrete signal $X(i)$ (in the sense of least squares) by a sequence $(X_n(i), n = 1, \ldots, N)$ defined by the following equation:

$$X_n(i) = \sum_{j=0}^{j=n-1} \sum_{k=-\infty}^{k=+\infty} C_{j,k}^{X}(i)\, \psi_{j,k}(i) \tag{9-95}$$

The above equations constitute the conceptual basis of the multi-resolution analysis. For more details on this theory, see Mallat (1989).

9.3.4.3 Approximation and detail of a signal

As mentioned above, the multi-resolution wavelet analysis makes a dyadic signal decomposed into a succession of approximations corresponding to increasing scales "j". The difference between the measured signal and its approximation to the order (n) is called "residual". The difference between the approximations of order (n +1) and (n) is called "detail" of order (n). Intuitively, the approximation thus corresponds to a large-scale time phenomena, while the detail accounts for the phenomena more specifically at a smaller scale than the order of the approximation. Or in another way, the approximation corresponds to a smoothed image signal, while the detail highlights the irregularities of the signal at a certain scale.

The approximation A_m and the detail D_m of a discrete signal $X(i)$ with the resolution "m", are given by:

$$A_X^m(i) = \sum_{k=-\infty}^{k=+\infty} \langle X, \varphi_{m,k} \rangle . \varphi_{m,k}(i) \tag{9-96}$$

$$D_X^m(i) = \sum_{k=-\infty}^{k=\infty} \langle X, \psi_{m,k} \rangle \psi_{m,k}(i) \tag{9-97}$$

Here, $\varphi_{m,k}$ is called scaling function, and $\psi_{m,k}$ is called wavelet function (mother wavelet).

However, basically, the approximation $A_m(t_i)$ is a sum of the successive wavelet components $X_m(t_i)$ from the long scale $k = M$ to the cutoff scale m, and the detail $D_m(t_i)$ is just the next component $X_{m+1}(t_i)$ of the one scale $k = m + 1$.

Remark:

- Several different conventions are used in the literature and the dyadic scales may be increasing or decreasing with the index "m" (here "m" decreases from long scale to short scale)
- Some authors choose to draw 1/scale or -log (scale) on the scale axis (ordinate). With this choice, the shorter scales (residuals) are placed at the top of the graph, and the longer scales (approximations) are below the graph.
- A wavelet component of the dyadic scale "j" is often noted as $C_x^j(i)$, and sometimes it is noted like with the wavelet coefficients.

$$C_x^j(t_i) = \sum_{k=-\infty}^{k=+\infty} \langle x, \psi_{m,k} \rangle \cdot \psi_{m,k}(i) \tag{9-98}$$

$$X(i) = A_X^m(i) + \sum_{j=m+1}^{j=M} D_X^j(i) = A_X^m(i) + R_X^m(i) \tag{9-99}$$

where,

$N_{dyadic} = 2^M \leq N_{total}$;

A_X^m is the approximation of the dyadic scale ‘m’ (low pass filter);

R_X^m is the residual of the approximation of the dyadic scale ‘m’ (high pass filter);

The main equations of the orthogonal multi-resolution wavelet analysis are summarized in **Table 9- 1**.

Table 9- 1 Main equations of the orthogonal multi-resolution wavelet analysis

$$X(i) = \sum_{j=0}^{j=+\infty} \sum_{k=-\infty}^{k=+\infty} C_{j,k}^X(i) \psi_{j,k} = A_X^m(i) + \sum_{j=m+1}^{j=M} D_X^j(i)$$

$$\psi_{j,k}(t) = 2^{j/2} \psi\left(2^j \times t - k\right)$$

$$\begin{cases} A_X^m(i) = \sum_{k=-\infty}^{k=+\infty} \langle X, \varphi_{m,k} \rangle . \varphi_{m,k}(i) \\ D_X^m(i) = \sum_{k=-\infty}^{k=\infty} \langle X, \psi_{m,k} \rangle \psi_{m,k}(i) \end{cases}$$

9.3.4.4 Application of multi-resolution wavelet analysis

As mentioned above, multi-resolution wavelet can be used to make a filtering of the signal, and, more important, it can be used to study the detail of any dyadic scale "m" of the measured data. This makes possible to study the fluctuation characteristics of one component signal corresponding to time scale $2^m \times \Delta t$ such as the Fourier dominant period, the standard deviation, and so on. This also makes possible to obtain the correlation between the components with the same dyadic time scale of the two different signals.

The following is a simple example of the use of the multi-resolution wavelet to analyze a regular signal $X(t)$ to show the possible applications.

Example:

The signal: $X(t) = 1.5sin\left(\frac{2\pi t}{2^7 \Delta t}\right) + 3sin\left(\frac{2\pi t}{2^5 \Delta t}\right)$ (9-100)

where,

Δt is the time step and $\Delta t = 1s$;

t is the time, $t_{min} = 0s$ and $t_{max} = 1024s$.

In this example, the signal $X(t)$ (equation (9-100) and **Fig. 9-3**) is constructed by a Fourier bimodel with the 2 different wavelet dyadic time scales: $T_1 = 32s$ and $T_2 = 128s$ and 2 different corresponding amplitudes: $A_1 = 3$ and $A_2 = 1.5$. The main results are shown in the flowing figures from **Fig. 9-4** to **Fig. 9-8**.

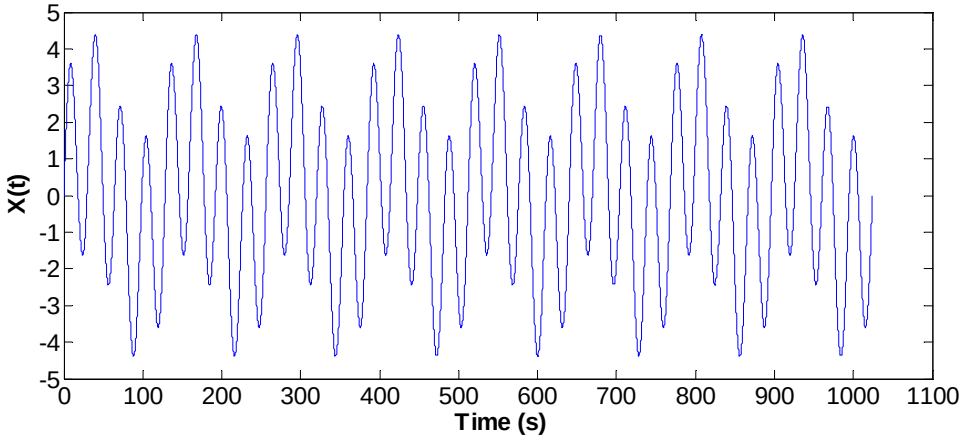

Fig. 9-3 Evolution of the regular signal $X(t) = 1.5sin\left(\frac{2\pi t}{2^7 \Delta t}\right) + 3sin\left(\frac{2\pi t}{2^5 \Delta t}\right)$

Fig. 9-4 shows the increasing approximations with the 10 increasing wavelet dyadic time scales. It can be seen that the top approximation A_{10} corresponding to the wavelet dyadic scale m=10 is the original signal $X(t)$. On contrast, in the figure of the residuals (**Fig. 9-5**),

the bottom residual corresponding to the wavelet dyadic scale m=1 is the original signal $X(t)$. In fact, the two figures show that the multi-resolution wave use two methods to construct a complete signal: (1) doing the sum of the components from the smallest wavelet dyadic time scale to the largest wavelet dyadic time scale (approximations); (2) doing the sum of the components from the lowest wavelet dyadic time scale to the largest wavelet dyadic time scale (residuals).

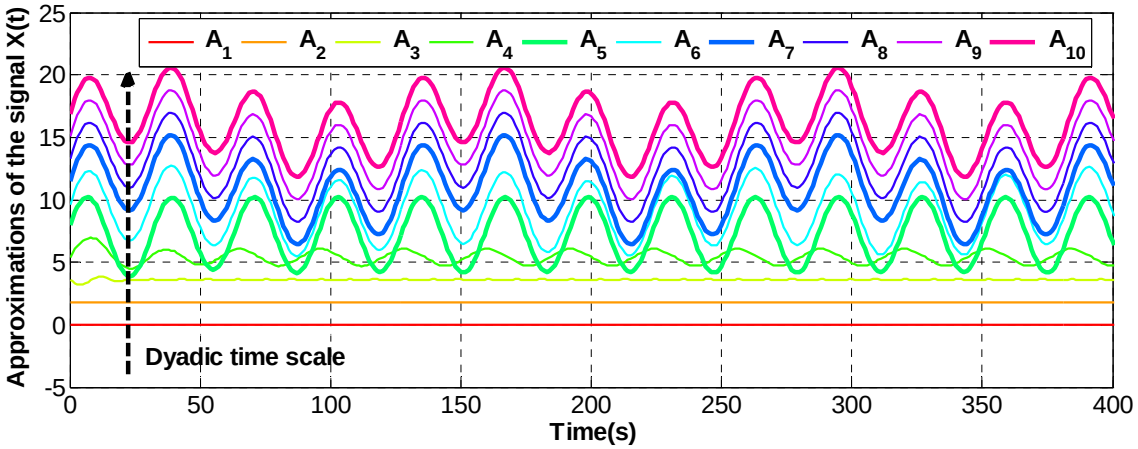

Fig. 9-4 Evolution of the approximations with the increasing dyadic time scale of the regular signal $X(t)$ by multi-resolution wavelet analysis

Note: in order to clearly show all the approximations, the absolute values of the residuals are added the changeable multiple of 1.8 from 0 to 9.

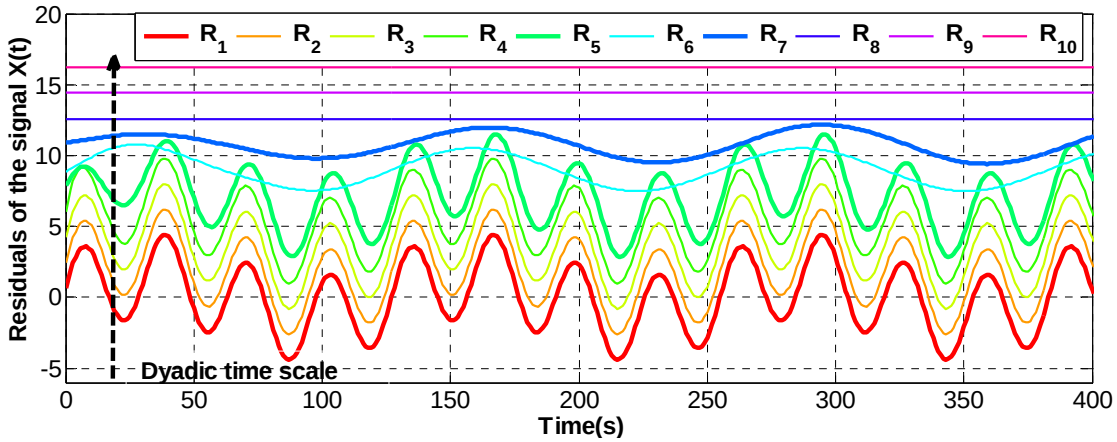

Fig. 9-5 Evolution of the residuals with the increasing dyadic time scale of the regular signal $X(t)$ with multi-resolution wavelet analysis

Note: in order to clearly show all the approximations, the absolute values of the residuals are added the changeable multiple of 1.8 from 0 to 9.

On the other hand, **Fig. 9-6** shows the principal details from C3 to C8 of the original signal $X(t)$. This figure clearly shows that the most dominant components are C5 and C7. Furthermore, the sum of the two components C5 and C7 can be done and compared it with the original signal (**Fig. 9-7**) to verify the selected dominant periods.

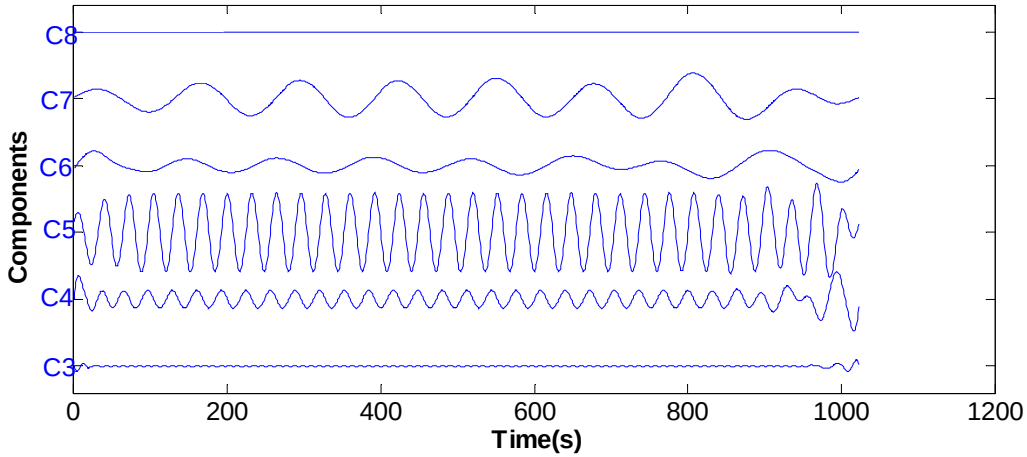

Fig. 9-6 Evolution of the principal dyadic components of the regular signal $X(t)$ by multi-resolution wavelet analysis with Daubechies20 filter

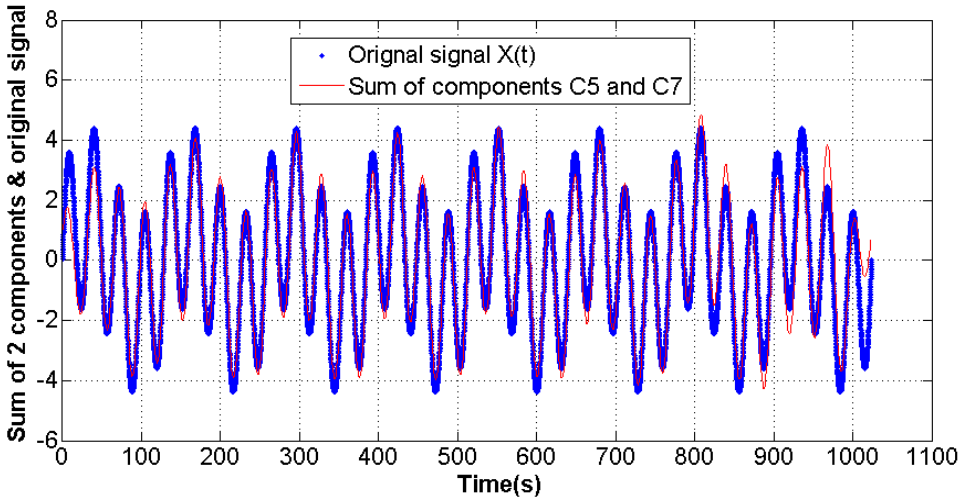

Fig. 9-7 Comparison of the evolution of the sum of the components C5 and C7, and the original signal $X(t)$ (multi-resolution wavelet analysis)

In addition, the dominant periods: $T_1 = 32s$ and $T_2 = 128s$ are re-obtained by analyzing the original signal $X(t)$ and the sum of the two components with Fourier single spectral analysis, as seen from **Fig. 9-8**. It is worthy noted that, in this example, for the regular signal or Fourier model signal, it is obtained that the wavelet dyadic time scale is identical with the corresponding Fourier dominant period. In fact, the wavelet dyadic time scale is just approximate to Fourier period, and this conclusion will be verified for the measured no-stationary water level fluctuations in Chapter 6.

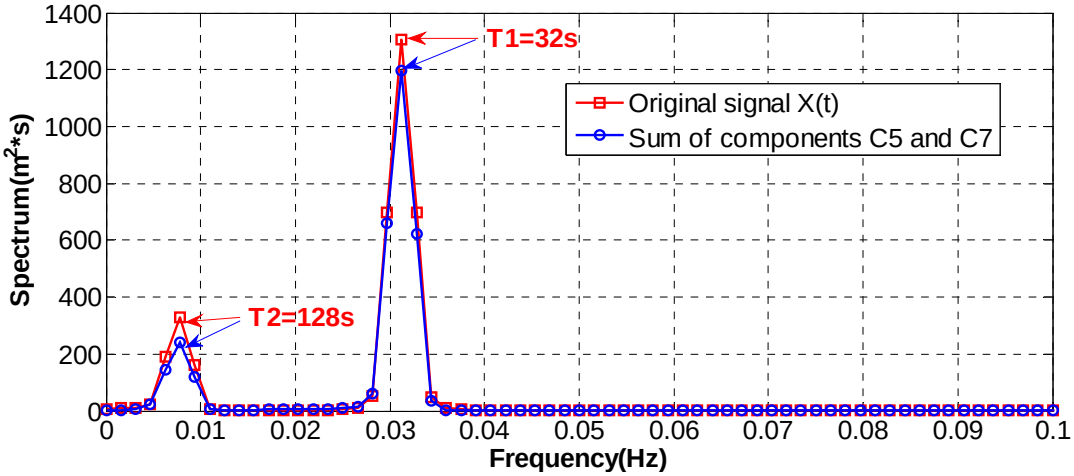

Fig. 9-8 Comparison of the Fourier spectral functions of the sum of the components C5 and C7, and the original signal $X(t)$ (Fourier spectral analysis, Tuckey filter, M=320<N/3=342, Δt =1s)
Note: wavelet dyadic time scale of C5: $T_5 = 2^5 \times \Delta t == 2^5 \times 1 = 32s$
wavelet dyadic time scale of C7: $T_7 = 2^2 \times \Delta t == 2^7 \times 1 = 128s$

Finally, the multi-resolution with the Daubechies20 filter is used in this example as well as in this thesis, because it is asymmetrical and it fits better with the measured signals which just are not symmetric. In fact, multi-resolution of the type Daubechies4 is also tested, and the results are not so much different from the ones obtained by the type Daubechies20 for the measured water level fluctuation.

9.4 Conclusion

The main theories of the signal processing methods and three signal filtering methods which are used together to analyzed the measured water level fluctuations in the slopping sandy beach in the Barcelona wave canal experiment are introduced in this chapter. The signal processing methods include the Fourier spectrum, multi-resolution wavelet and correlation analysis. There filtering methods are respectively the moving average, differential and multi-resolution wavelet filtering.

If the same filter time is chosen, the moving average and the multi-resolution wavelet filtering methods can obtain the same filtered and residual signals. However, compared with the moving average filtering, it is more complicated to determine the exact filter time for the multi-resolution wavelet filtering, because the wavelet dyadic time scale is just an approximate Fourier period for the general irregular signal.

Differential filtering is different from the moving average and the multi-resolution wavelet filtering. For the case of $\Delta t = costant$, the fluctuation characteristics of the difference of the original signal can be obtained by studying the filtered signal.

Considering that unbiased estimation of the correlation analysis (temporal analysis) can intuitively show the hidden periodicity of the two signals, while the 'biased' cannot show this characteristic, the biased estimation is used to calculate the Fourier spectrum, and at the same time, the unbiased estimation is used to do the direct single or cross analysis such as cross covariance function with respect to the lag to show the cross correlation of the signals between $Y(t)$ and $X(t)$.

Concerning the correlation analysis, considering that unbiased estimation can intuitively show the hidden periodicity of the two signals, while the 'biased' cannot show this characteristic, the biased estimation is used to calculate the Fourier spectrum, and at the same time, the unbiased estimation is used to do the direct single or cross analysis such as cross covariance function with respect to the lag to show the cross correlation of the signals between $Y(t)$ and $X(t)$.

The Fourier spectral analysis reflects the structure of the signal by decomposing a signal in periodic functions. Its advantage is to clearly manifest the distribution of the Fourier spectral functions with respect to the frequency (period). Accordingly, it can be used to study the fluctuation characteristics with respect to the frequency (period). For example, for a single analysis, it can be used to study the dominant periods of the measured water level fluctuations, and the propagation of the fluctuation energy of certain periods in the slopping sandy beach; for a cross analysis, it can be used to determine the coherency with the frequency between two water level fluctuations.

The wavelet transform makes the time-scale phenomena localized temporally or transient extend over a range of scales. The multi-resolution wavelet analysis makes a dyadic signal decomposed into a succession of approximations corresponding to increasing scales. It can especially be used to study the detail (one component) of any dyadic scale "m" of the measured data. This makes possible to study the fluctuation characteristics of one component signal corresponding to time scale $2^m \times \Delta t$ such as the Fourier dominant period, the standard deviation, and so on. This also makes possible to make the correlation between the components with the same dyadic time scale of the two different signals. Especially, for the non-stationary water level fluctuations, it gives more satisfactory results than the ones obtained with Fourier spectral analysis.

Finally, the three filtering methods will be compared and eventually will be combined with the three signal processing methods to filter and analyze the non-stationary water level fluctuations in the Barcelona wave canal experiment.

In addition, it can be noted that the weighting function $D(j)$ of Tuckey filter is a filter of $R_{XX}(j)$ in the dimensionless reduced Fourier spectral function, while the moving average, differential and multi-resolution wavelet filtering methods are used to directly filter the signal (data).

Chapter B10: Illustrations of the signal processing of the measured water level data $H_1(t)$ and $H_6(t)$ of the experiment in Barcelona

10.1 Introduction

As mentioned in **Chapter 5**, the sensor No.1 was placed near the still water / beach boundary to measure the water level fluctuations $\boldsymbol{H_1(t)}$ corresponding to the entry condition of the model.

As a result, the characteristics of $\boldsymbol{H_1(t)}$ play a dominant role in the 6 other sensors' water level fluctuations and in the whole sea/beach hydrodynamic partially saturated sloping sandy beach system. At the same time, from the measured results (**Fig. 5-8**) and according to the observation during the experiment, the water level fluctuations $\boldsymbol{H_2(t)}$, $\boldsymbol{H_3(t)}$, $\boldsymbol{H_4(t)}$ and $\boldsymbol{H_5(t)}$ are the mixed water levels composed of the surface water and the groundwater. From the point of view of the signal processing, they have many similar oscillatory characteristics with $\boldsymbol{H_1(t)}$, while $\boldsymbol{H_6(t)}$ and $\boldsymbol{H_7(t)}$ are pure groundwater levels, which are total different from $\boldsymbol{H_1(t)}$.

Therefore, practicing of the signal processing techniques for the $\boldsymbol{H_1(t)}$ and $\boldsymbol{H_6(t)}$ plays a very important role in eventually finding a good method for analyzing $\boldsymbol{H_2(t)}$, $\boldsymbol{H_3(t)}$, $\boldsymbol{H_4(t)}$ and $\boldsymbol{H_5(t)}$, and at the same time, in finding an another method for $\boldsymbol{H_7(t)}$.

In this chapter, three signal processing methods: Fourier spectrum, wavelet multi-resolution and temporal analysis methods together with three filtering methods have been practiced to analyze the measured water level fluctuations $H_1(t)$ and $H_6(t)$ in the sloping sandy beach , using signal analysis tools previously developed in the IMFT/GEMP group (*Fatmi 2009*) with concerned theories explained in detail in Appendix B: **Chapter 9**.

10.2 Preliminary note (Sub-sampling)

For the measured raw data in Barcelona, the time step is $\Delta t_0 = 0.01$ s $= 10^{-2}$ s. In order to reduce the degree of difficulty on the signal processing under the condition of unaffecting the

results of the raw original data, the time step of the sub-sampling for all results presented here is taken as $\Delta t_{SUB\text{-}SAMPLING} = 0.1\ s = 10\ \Delta t_0$.

The measured raw water levels for the 7 sensors in the sloping sandy beach (14 serial, measured 18 March 2008) are illustrated in **Fig. 10-1**. Especially, the raw $\boldsymbol{H_1(t)}$ and $\boldsymbol{H_6(t)}$ are shown in **Fig. 10-2**.

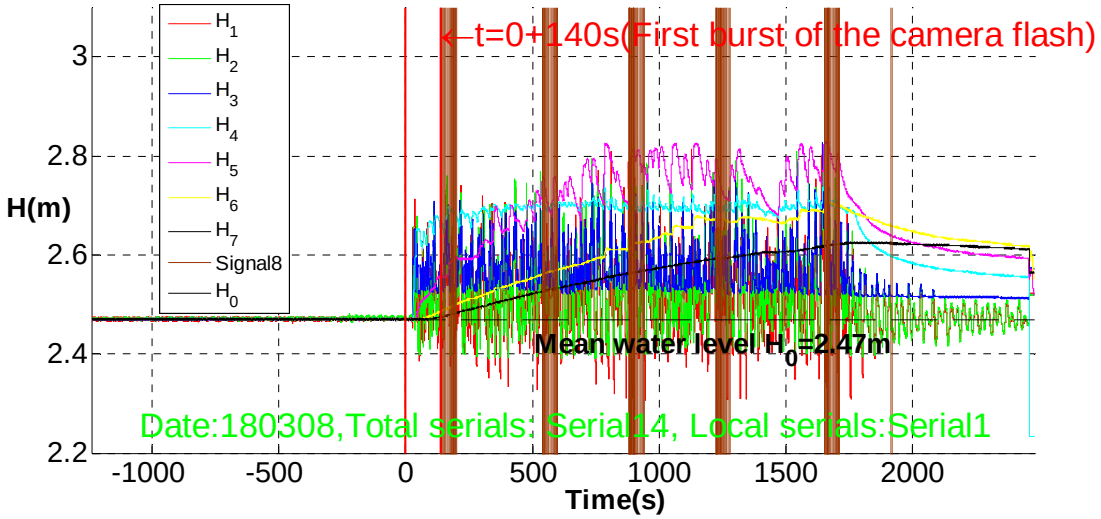

Fig. 10-1 Raw signal $H_i(t)(i=1,\ldots,7)$ measured in the sloping sands beach

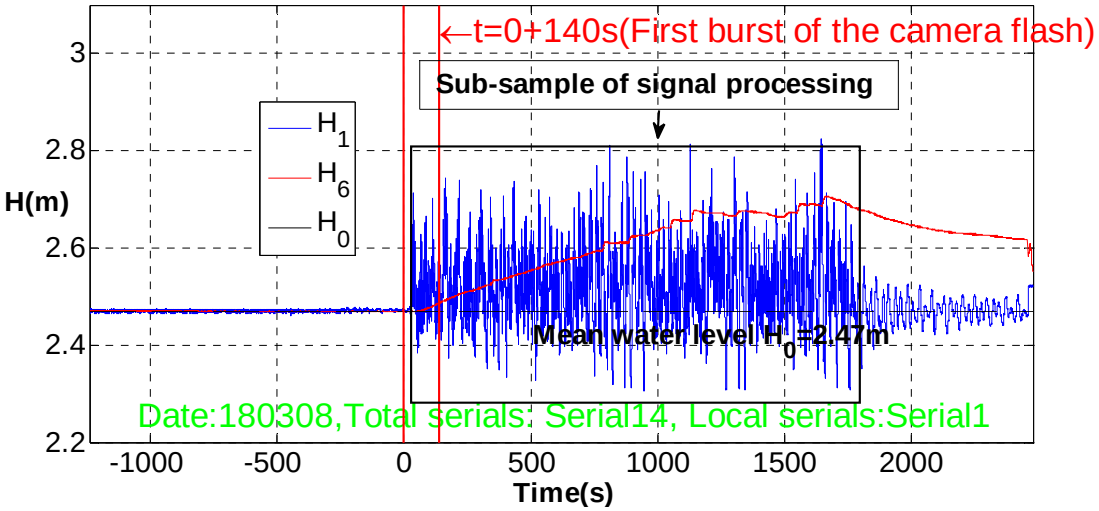

Fig. 10-2 Complete time series of $H_1(t)$ and $H_6(t)$

As a result, the data obtained by sub-sampling will be called original signal in this thesis.

10.3 Original signal of H_1 (t) and H_6 (t)

10.3.1 Introduction

In order to reduce the degree of difficulty of the signal processing, just the second step water level data (step (2) in **Fig. 5-8** and the part highlighted with the rectangular line in **Fig. 10-2**) are chosen to be analyzed here.

10.3.2 Original signal of $H_1(t)$

Sensor No.1 was placed near the still water / beach boundary to measure the water level fluctuations $\boldsymbol{H_1(t)}$. This sensor lied in the centre of the swash zone, and as result, the water level fluctuations $\boldsymbol{H_1(t)}$ are extremely random. The evolution of the original signal $\boldsymbol{H_1(t)}$ is shown in **Fig. 10-3**.

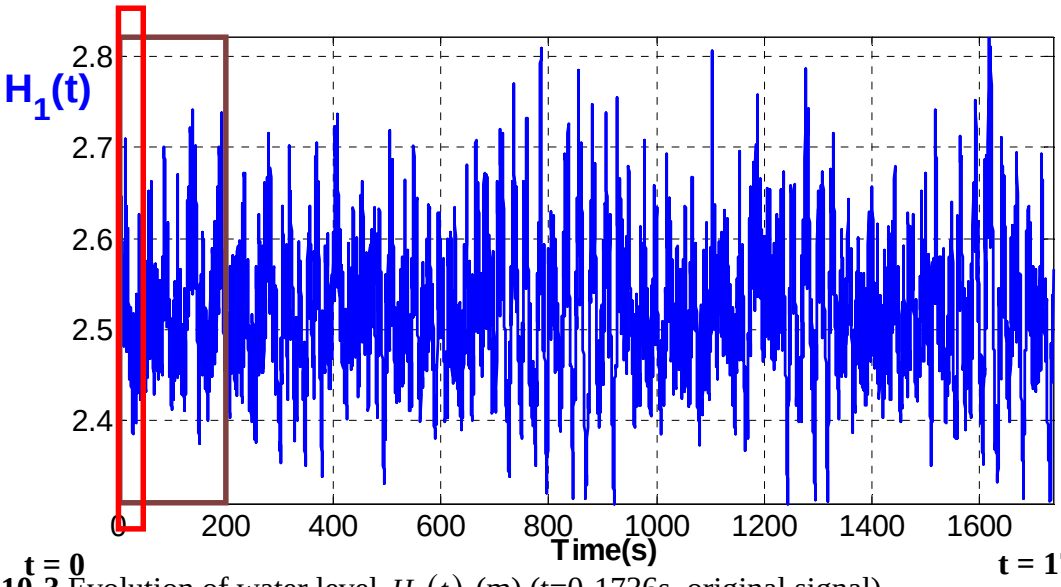

Fig. 10-3 Evolution of water level $H_1(t)$ (m) (t=0-1736s, original signal).

From the two zooms (the 2 part data respectively framed with the red rectangular line and the brown rectangular line, shown in **Fig. 10-4** and **Fig. 10-5**) of $\boldsymbol{H_1(t)}$, we can see that there are two series of period for $\boldsymbol{H_1(t)}$: small period serial from T=4.2s to 7.2s and big period serial from T=23.2s to 53.0s.

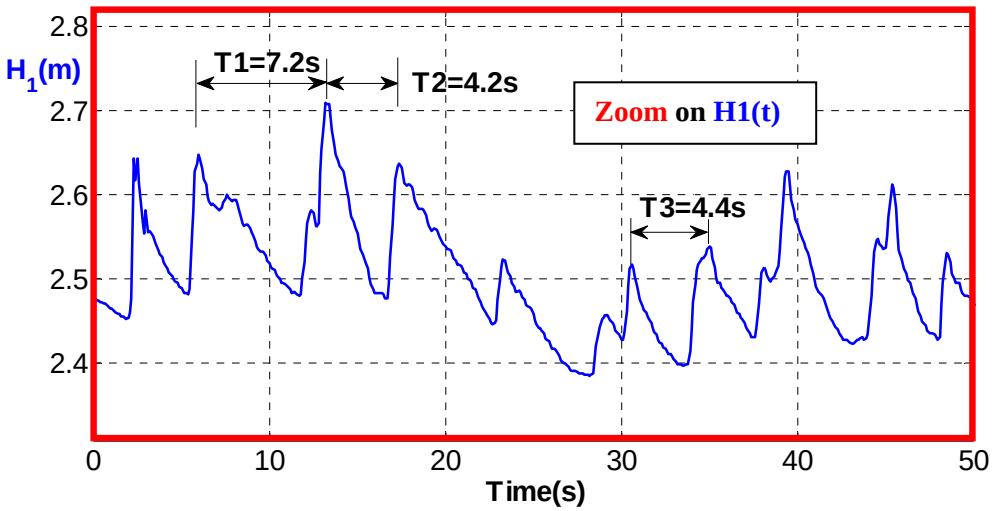

Fig. 10-4 Zoom of evolution of water level $H_1(t)$ (m) (t=0-50s, original signal).

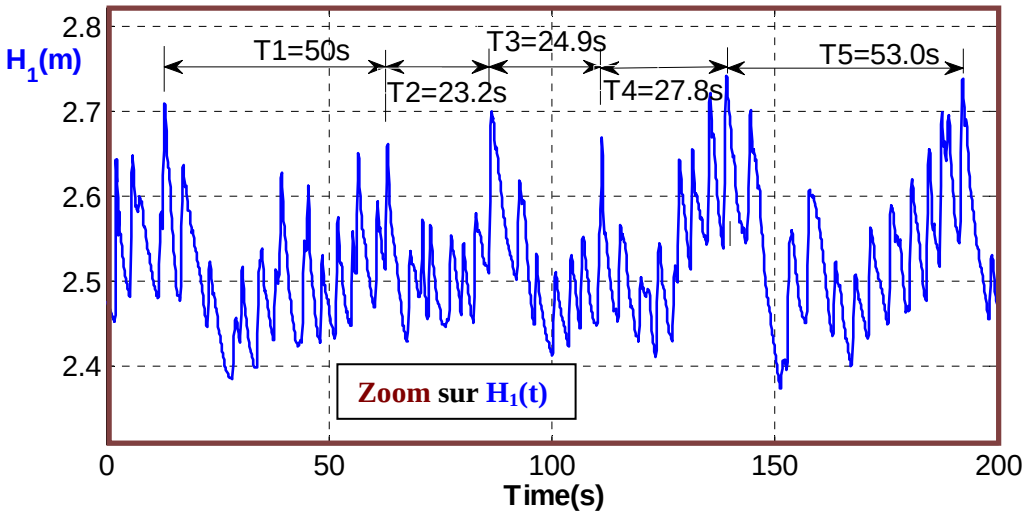

Fig. 10-5 Zoom of evolution of water level $H_1(t)$ (m) (t=0-200s, original signal).

10.3.3 Original signal of H_6 (t)

The sensor No.6 was placed about 2.5m horizontally to the right vertical wall of the canal. The evolution of the original signal $\boldsymbol{H_6(t)}$ is shown in **Fig. 10-6** . From this figure, we can see that the original signal $\boldsymbol{H_6(t)}$ is extremely irregular: the moving average increases linearly firstly with a steep slope and then with a flat slope; the fluctuations become more and more important with the time, and its periods vary from about T=48.3s to 228s.

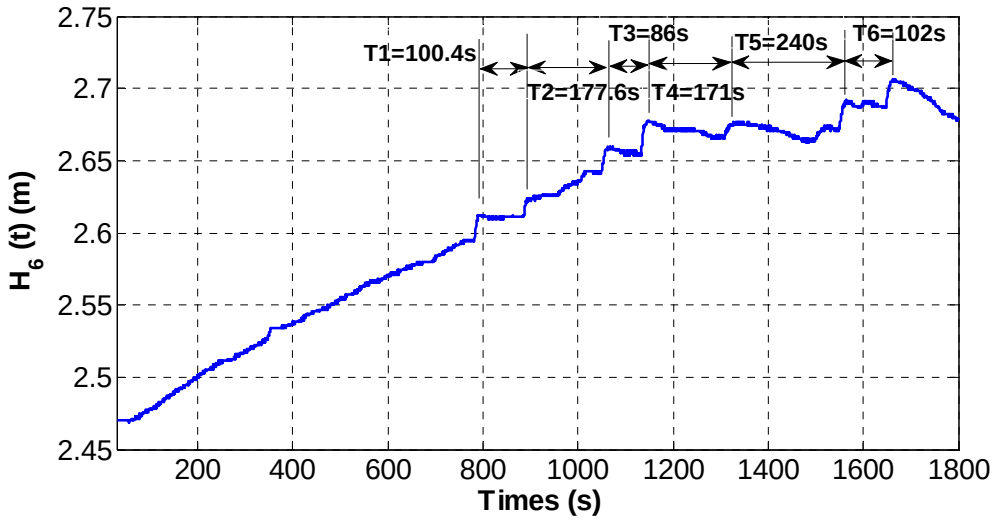

Fig. 10-6 Evolution of water level $H_6(t)$ (m) (t=0-1800s, original signal).

10.4 Signal processing of H_1 (t)

10.4.1 Introduction

The Fourier spectrum analysis, multi-resolution wavelet and temporal analysis methods are used to analyze the original signal $\boldsymbol{H_1(t)}$ and its residuals obtained respectively with moving average, differential, and multi-resolution filtering.

10.4.2 Signal processing of the original signal $H_1(t)$

The original signal $H_1(t)$ analyzed is shown in **Fig. 10-3.**

10.4.2.1 Analysis of the original signal $H_1(t)$ with Morlet wavelet analysis

Spectrum P(f) of $\boldsymbol{H_1(t)}$ with Morlet wavelet analysis, which is analyzed by A. SEVRAIN , is shown in **Fig. 10-7**. From this figure, it can be seen that the stronger spectrum density happens in two zones: f_1=0.02-0.08Hz (T_1=12.5-50s) and f_2=0.12-0.36 (T_2=2.76-8.33s); among them, the strongest spectrum density happens to the zone when f=0.04Hz (T=25s).

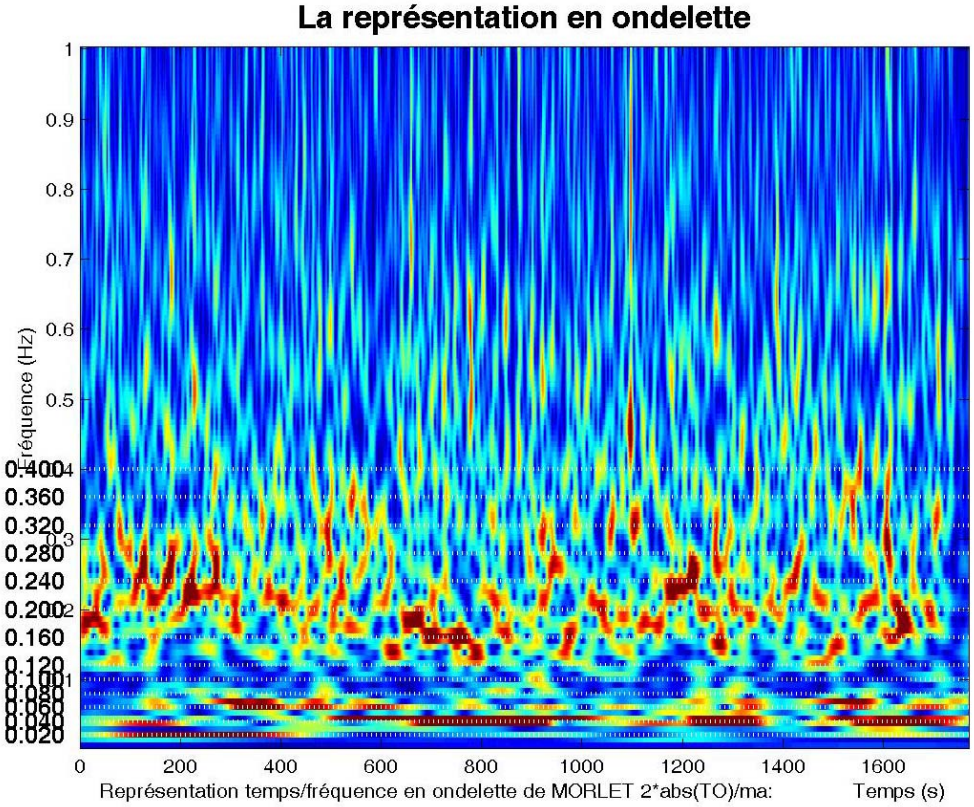

Fig. 10-7 Results of P(f) of the original signal $H_1(t)$ with Morlet wavelet analysis (A. SEVRAIN)

10.4.2.2 Analysis of the original signal $H_1(t)$ with Fourier spectrum analysis

The reduced Fourier spectrum with respect to the reduced frequency of the original signal $\boldsymbol{H_1(t)}$ is shown in **Fig. 10-8** and **Fig. 10-9** (in log-log axis).

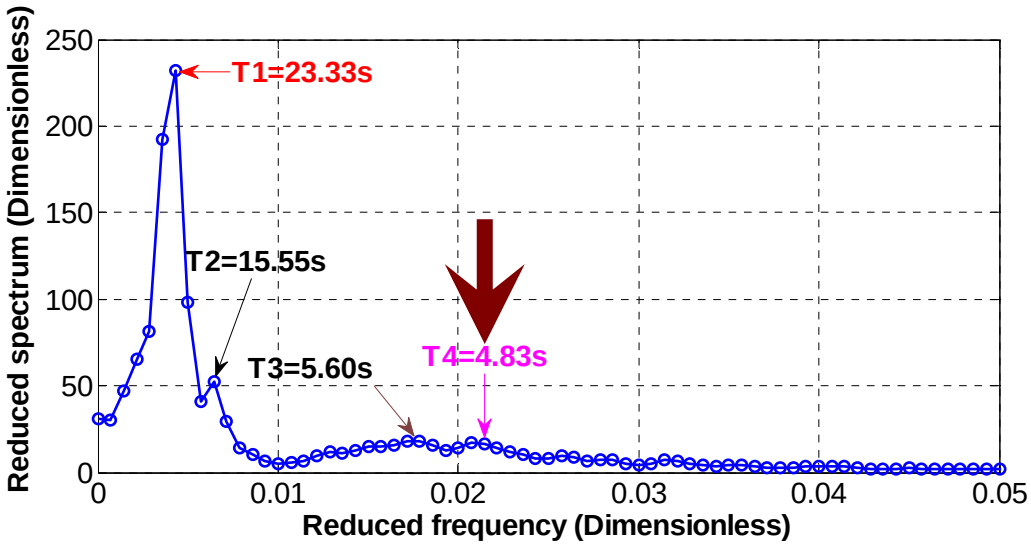

Fig. 10-8 Reduced Fourier spectrum with the respect to the reduced frequency (dimensionless, $H_1(t)$, original signal)

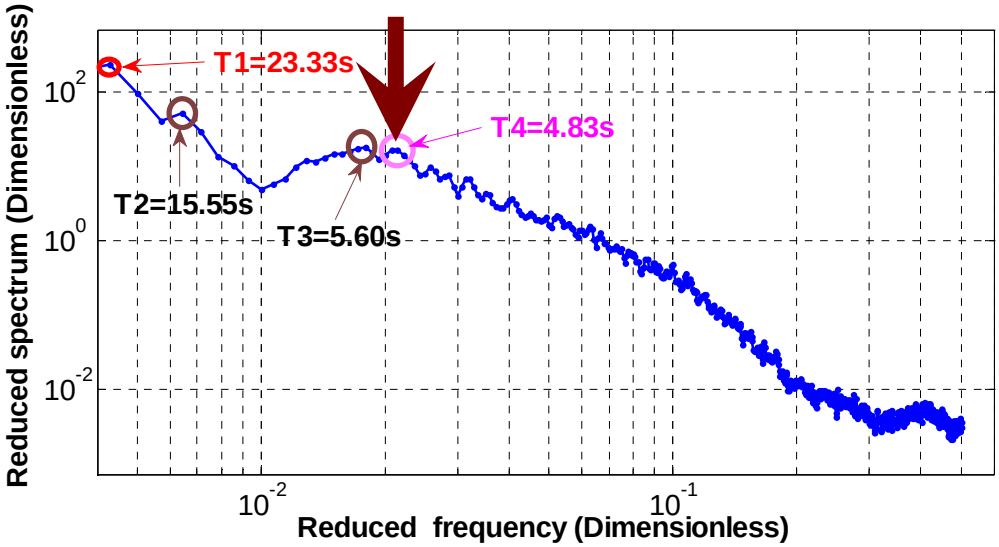

Fig. 10-9 Reduced Fourier spectrum with the respect to the reduced frequency in log-log axis (dimensionless, $H_1(t)$, original signal)

From these two figures, it can be seen that the period T_1=23.33s plays a dominant role in the signal, while the period T_4=4.83 which most approaches the period of the wave generator has very small influence on the signal fluctuation. What's more, the results of Fourier analysis coincide very well with those of Morelet wavelet spectrum analysis, seen in **Fig. 10-7**.

10.4.2.3 Analysis of the original signal $H_1(t)$ with multi-resolution wavelet

The evolution of the wavelet components of the original signal $\boldsymbol{H_1(t)}$ with multi-resolution wavelet is shown in **Fig. 10-10**.

Appendix B: Chapter B10 Illustrations of the signal processing of the measured water level data $\boldsymbol{H_1(t)}$ and $\boldsymbol{H_6(t)}$ of the experiment in Barcelona

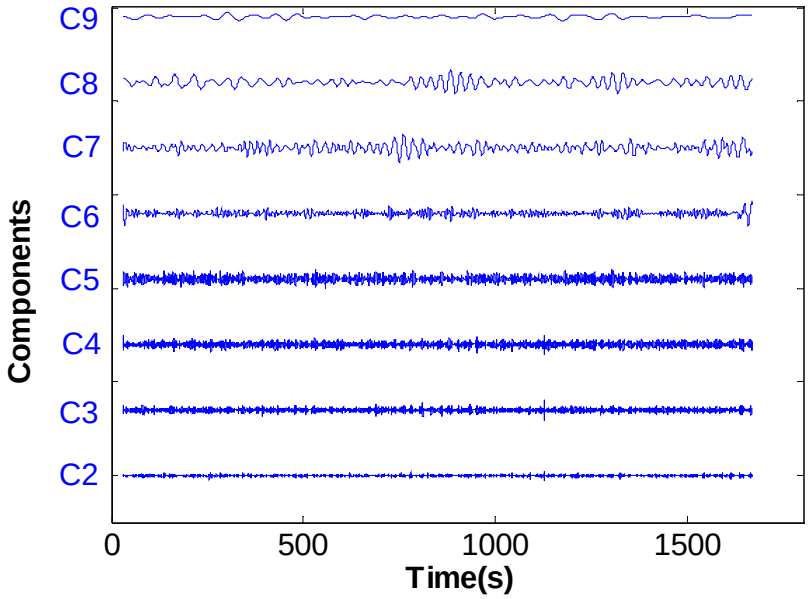

Fig. 10-10 Evolution of the dyadic wavelet components of the original signal $H_1(t)$ with multi-resolution wavelet

From this figure, it can be seen that the two components C_7 and C_8 play a dominant role in the signal. The evolution of the dyadic component C_7 and C_8 are respectively zoomed in **Fig. 10-11** and **Fig. 10-12**.

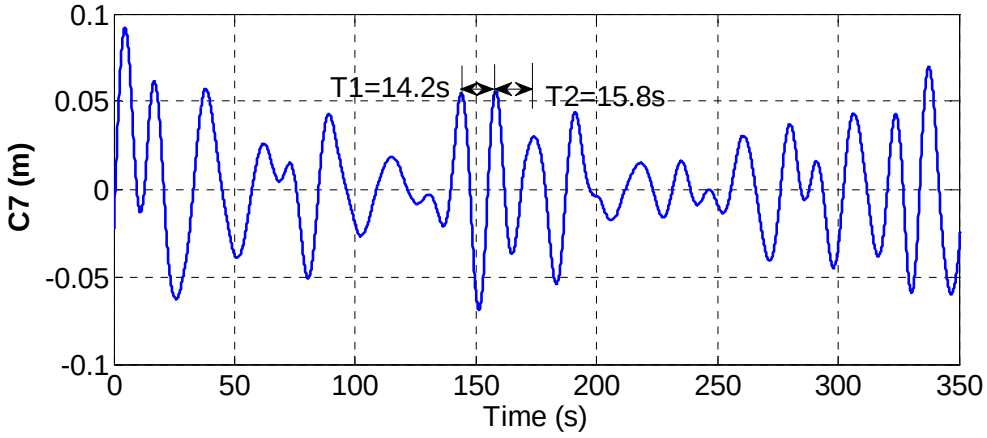

Fig. 10-11 Dyadic component C_7 of the original signal $H_1(t)$ obtained with multi-resolution wavelet (The time scale: $T_7 = 2^7.\Delta t = 12.8$ s)

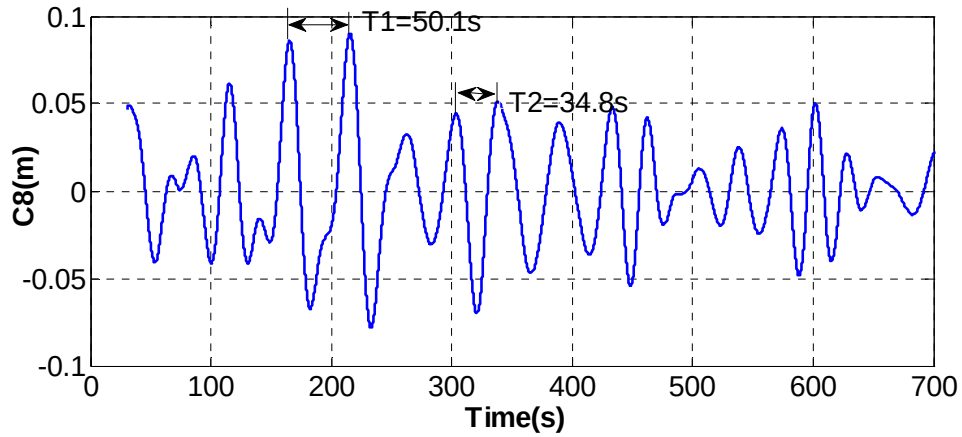

Fig. 10-12 Dyadic component C_8 of the original signal $H_1(t)$ obtained with multi-resolution wavelet (The time scale: $T_8 = 2^8.\Delta t = 25.6$ s)

At the same time, the evolution of the dyadic component C_5, which time scale ($T_5 = 2^5.\Delta t = 3.2$s) approaches the period of the wave generator of the Barcelona canal, is zoomed in **Fig. 10-13**.

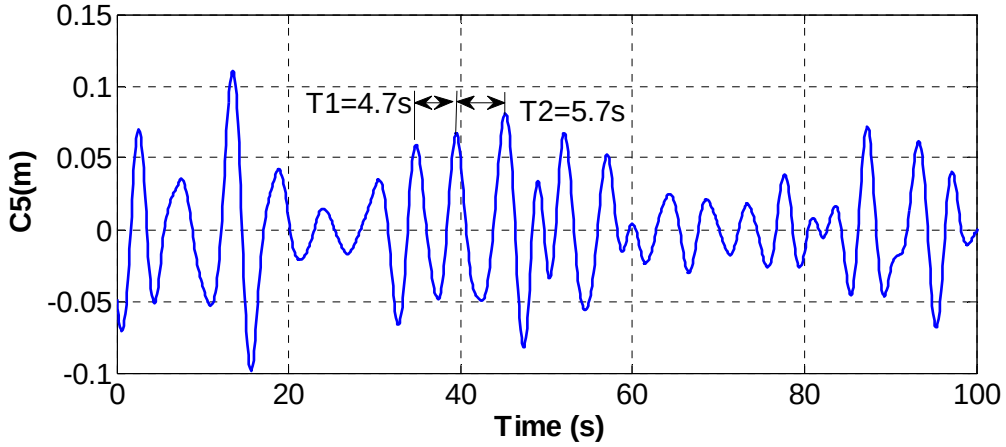

Fig. 10-13 Dyadic component C_5 of the original signal $H_1(t)$ obtained with multi-resolution wavelet (The time scale: $T_5 = 2^5.\Delta t = 3.2$ s)

From these three figures, it can be seen that the signal of the dyadic component with same time scale is still very irregular and the wavelet dyadic time scale is a little smaller than the one of the corresponding component.

10.4.2.4 Analysis of the original signal $H_1(t)$ with temporal analysis

The auto-correlation $\boldsymbol{R_{H_1H_1}(k)}$ of the original signal $\boldsymbol{H_1(t)}$ is shown in **Fig. 10-14**.

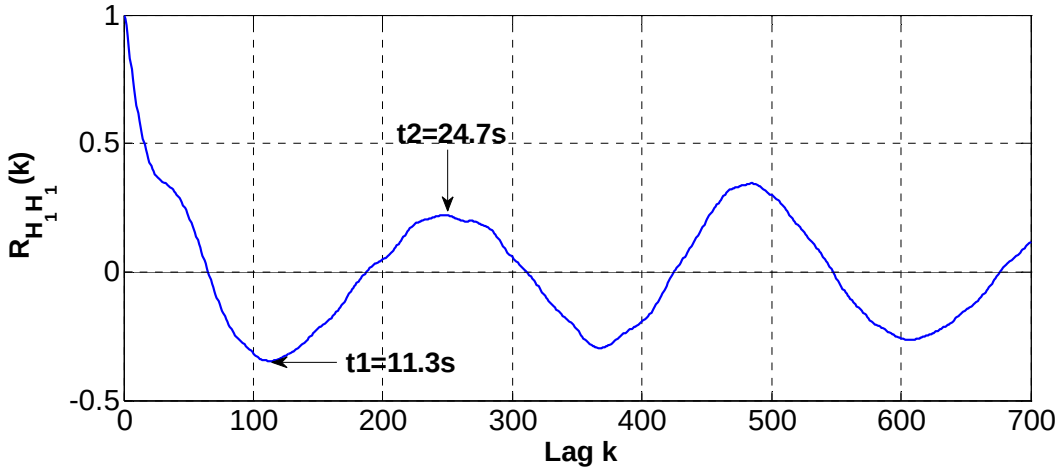

Fig. 10-14 Auto-correlation function $R_{H_1H_1}(k)$ of the original signal $H_1(t)$ (dt=0.1s)

It can be seen that the first period of the $\boldsymbol{R_{H_1H_1}(k)}$ t_2=24.7s is very approximate to the most dominant period of $\boldsymbol{H_1(t)}$ T_1=23.33s (**Fig. 10-8**)

10.4.3 Analysis of the residuals of $H_1(t)$

The residuals are respectively obtained with moving average, differential and multi-resolution filtering.

10.4.3.1 Residual of $H_1(t)$ with moving average filtering

The evolution of the original signal, its corresponding moving average and residual of $\boldsymbol{H_1(t)}$ are respectively shown in **Fig. 10-15**, **Fig. 10-16** and **Fig. 10-17**.

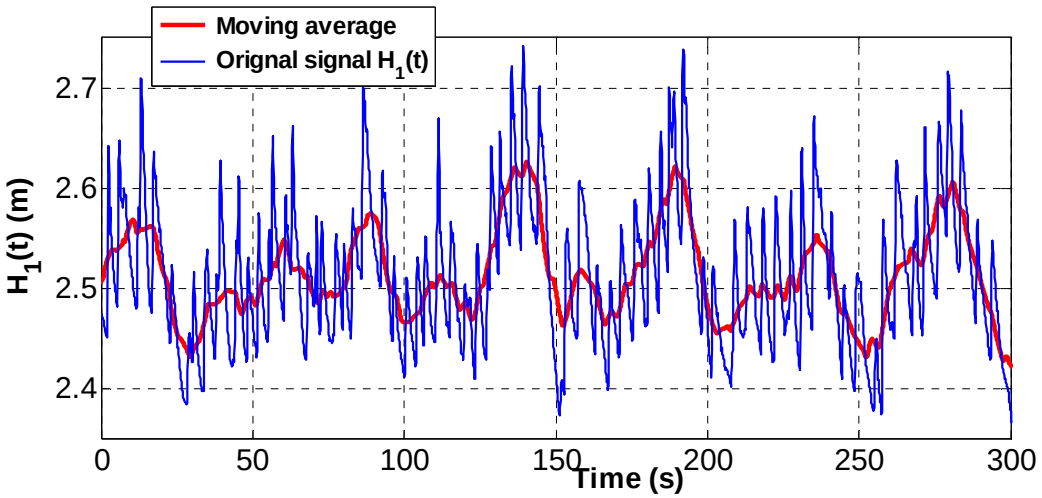

Fig. 10-15 Evolution of the original signal $H_1(t)$ and its corresponding moving average with moving average filtering (*window halfwidth* w_t=5s)**.**

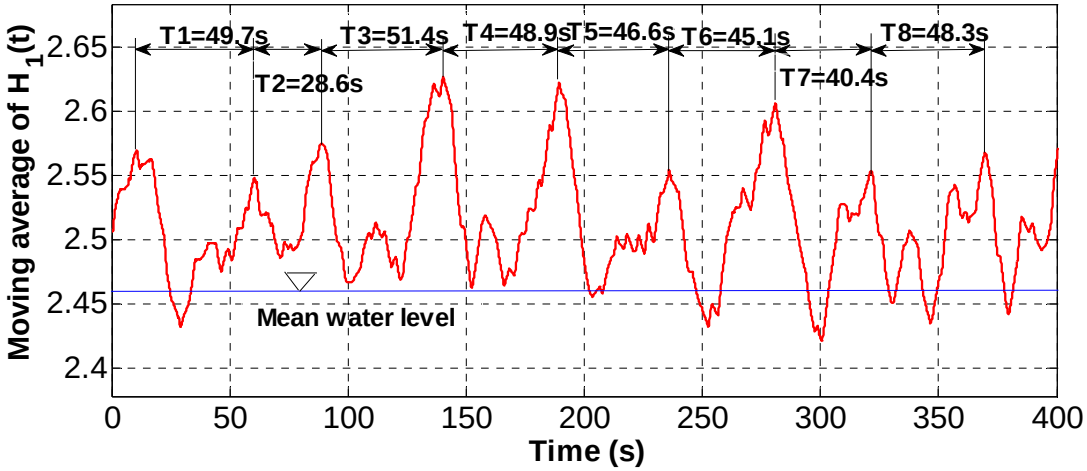

Fig. 10-16 Evolution of the moving average of the original signal $H_1(t)$ with moving average filtering (*window halfwidth* w_t=5s)**.**

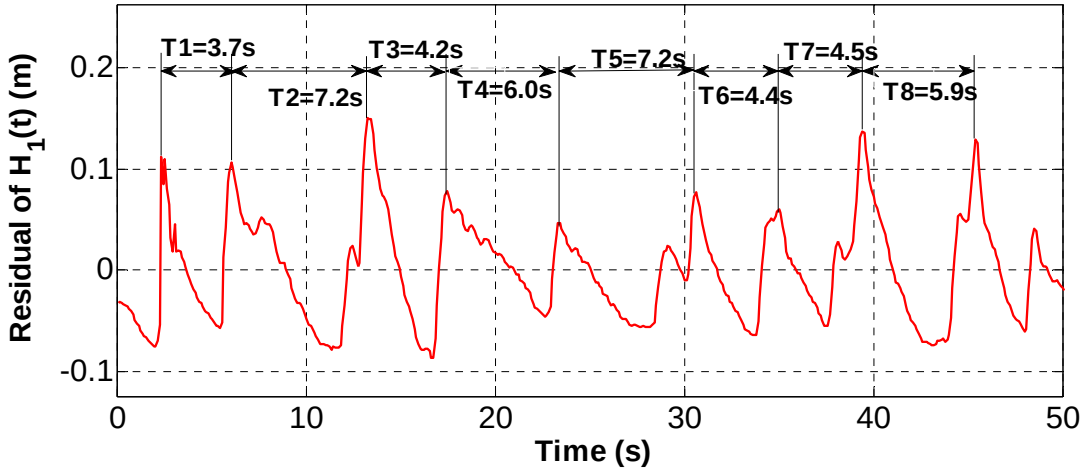

Fig. 10-17 Evolution of the residual of the original signal $H_1(t)$ with moving average filtering (*window halfwidth* w_t=5s)**.**

10.4.3.2 Analysis of the residual of $H_1(t)$ with moving average filtering and Fourier spectrum analysis

The Fourier spectrum function $\boldsymbol{S(f)}$ of the residual of $\boldsymbol{H_1(t)}$ with moving average filtering (*window halfwidth* w_t=5s) is shown in **Fig. 10-18** .

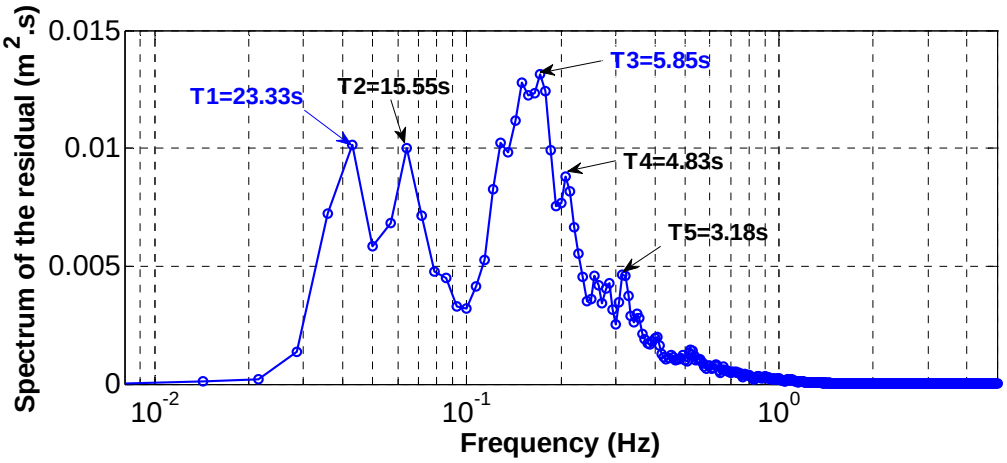

Fig. 10-18 Fourier spectrum function $S(f)$ of the residual of $H_1(t)$ with moving average filtering (*window halfwidth* wt=5s)

The most dominant period T_3=5.85s is in the middle of the periods shown in the evolution of the residual **Fig. 10-17**.

10.4.3.3 Analysis of the residual of $H_1(t)$ with moving average filtering and multi-resolution wavelet analysis

The evolution of the main wavelet dyadic components is shown in **Fig. 10-19**.

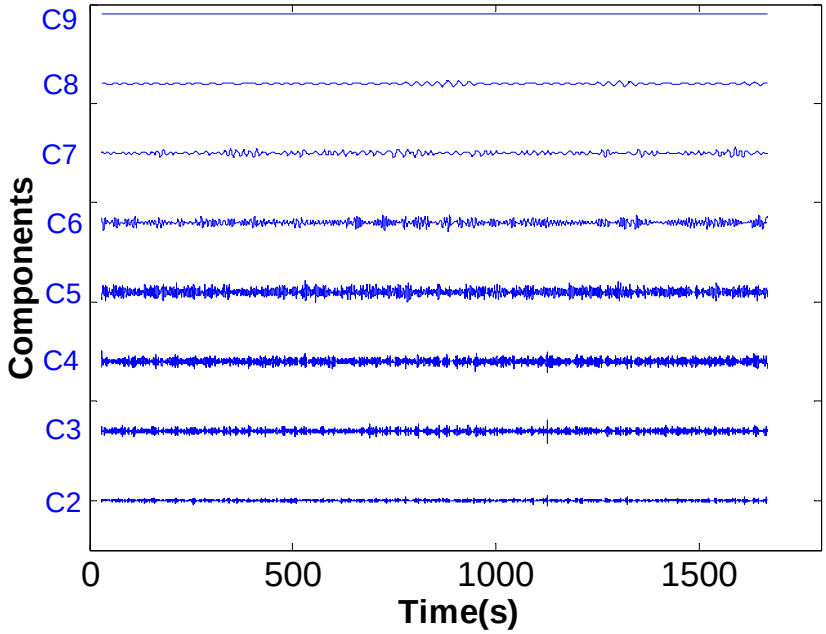

Fig. 10-19 Evolution of the wavelet dyadic components of residual of $H_1(t)$ with moving average filtering (*window halfwidth* w_t=5s)

It can be seen that the dominant component is C_5 (T_5=2^5*dt=3.2s), the Fourier period of which is 4.83s.

The sum of $C_5(t)$ and $C_7(t)$ (**Fig. 10-20**) agrees very well with the residual of $\boldsymbol{H_1(t)}$.

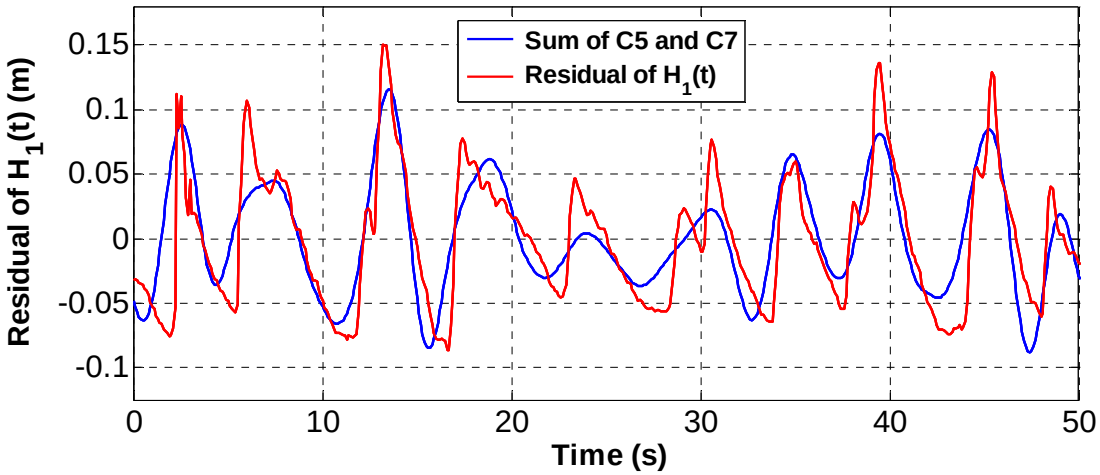

Fig. 10-20 Evolution of the sum of 2 wavelet dyadic components $C_5(t)$ and $C_7(t)$ of residual of $H_1(t)$ with moving average filtering (*window halfwidth* w_t=5s)

10.4.3.4 Analysis of the residual of $H_1(t)$ with moving average filtering and temporal analysis

The auto-correlation function $R_{H_{1\mathrm{Re}}H_{1\mathrm{Re}}}(k)$ of the residual of $\boldsymbol{H_1(t)}$ with moving average filtering is shown in **Fig. 10-21**.

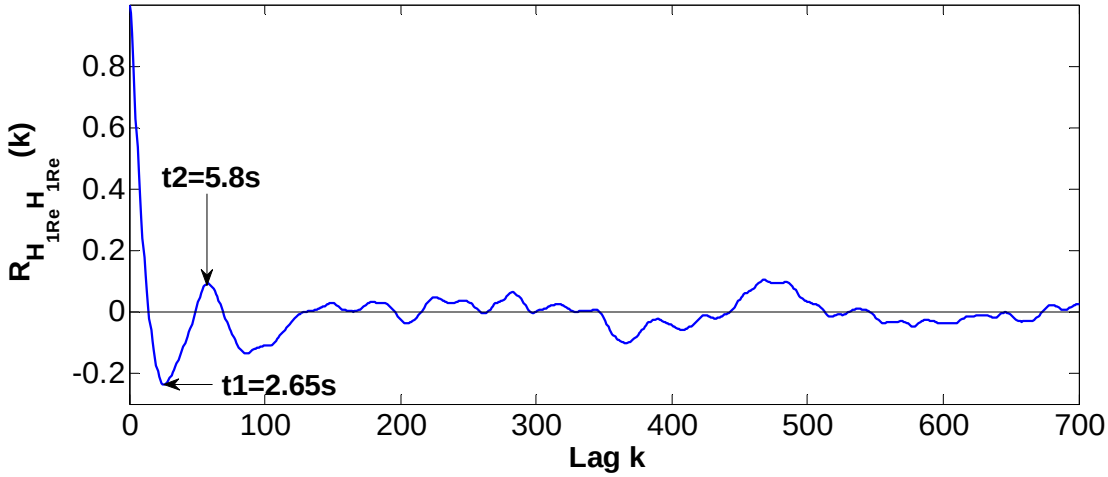

Fig. 10-21 Auto-correlation function $R_{H_{1\mathrm{Re}}H_{1\mathrm{Re}}}(k)$ of the residual of $H_1(t)$ with moving average filtering (*window halfwidth* w_t=5s) (dt=0.1s)

It can be seen that the first period t_2=5.8s approximate to the most dominant period of the corresponding residual T_3=5.85s (**Fig. 10-18**).

10.4.3.5 Residual of $H_1(t)$ with differential filtering

The evolution of the residual of $\boldsymbol{H_1(t)}$ with differential filtering is shown in **Fig. 10-22**.

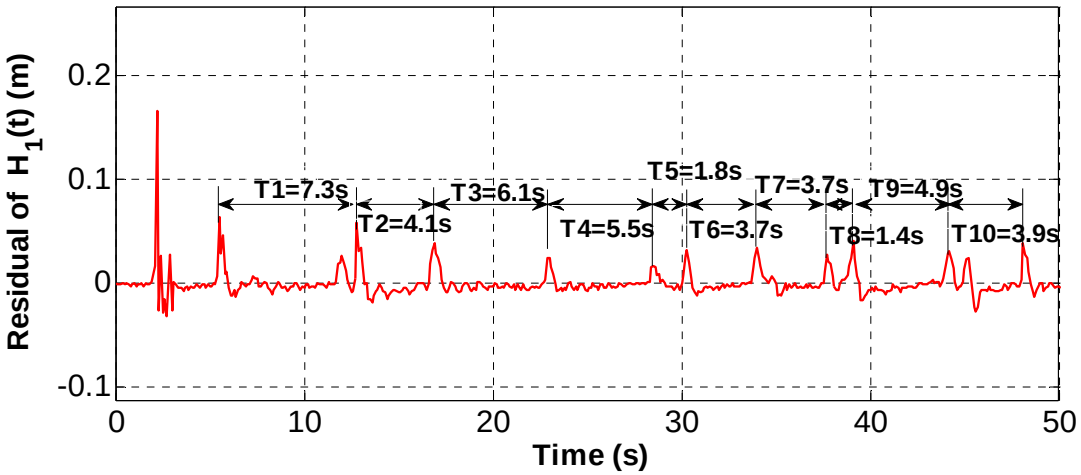

Fig. 10-22 Evolution of the residual of $H_1(t)$ with differential filtering

10.4.3.6 Analysis of the residual of $H_1(t)$ with differential filtering and Fourier spectrum analysis

The reduced Fourier spectrum function $\boldsymbol{S(f)}$ of the residual of $\boldsymbol{H_1(t)}$ with differential filtering is shown in **Fig. 10-23**.

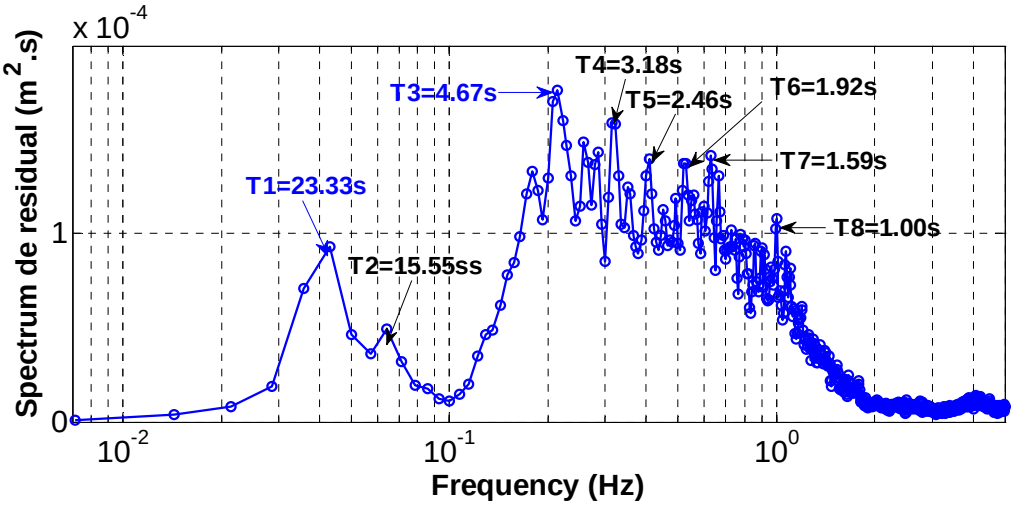

Fig. 10-23 Reduced Fourier spectrum function $S(f)$ of the residual of $H_1(t)$ with differential filtering (dimensional).

10.4.3.7 Analysis of the residual of $H_1(t)$ with differential filtering and multi-resolution wavelet

From the figure of the evolution of the main wavelet dyadic components (**Fig. 10-24**), it is not very easy to distinguish the dominant component, because there is to much noise in the components with low dyadic time scales. In spite of this, it seems that the fluctuation of C_3 is stronger that the other components. In addition, the evolution of the sum of 2 wavelet dyadic components $C_5(t)$ and $C_7(t)$ (**Fig. 10-25**) doesn't agree very well with the residual of $\boldsymbol{H_1(t)}$ with differential filtering.

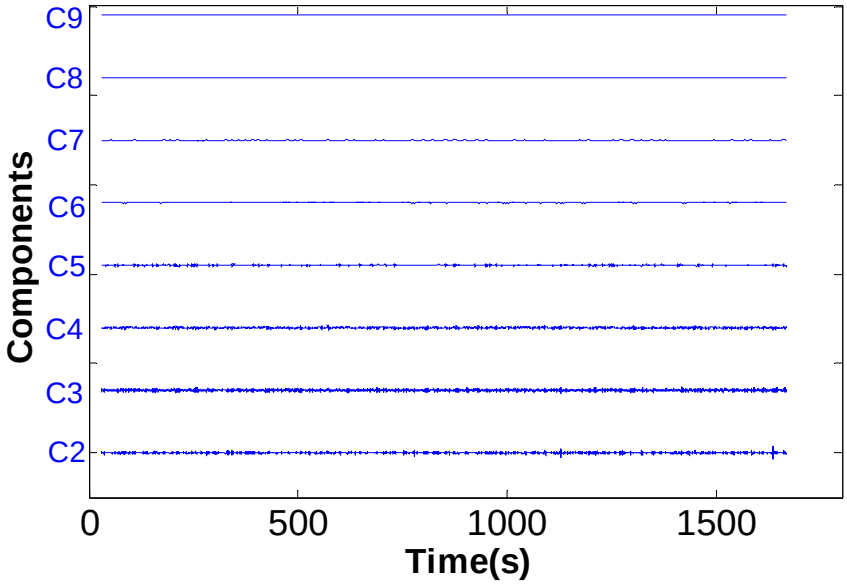

Fig. 10-24 Evolution of the wavelet dyadic components of residual of $H_1(t)$ with differential filtering

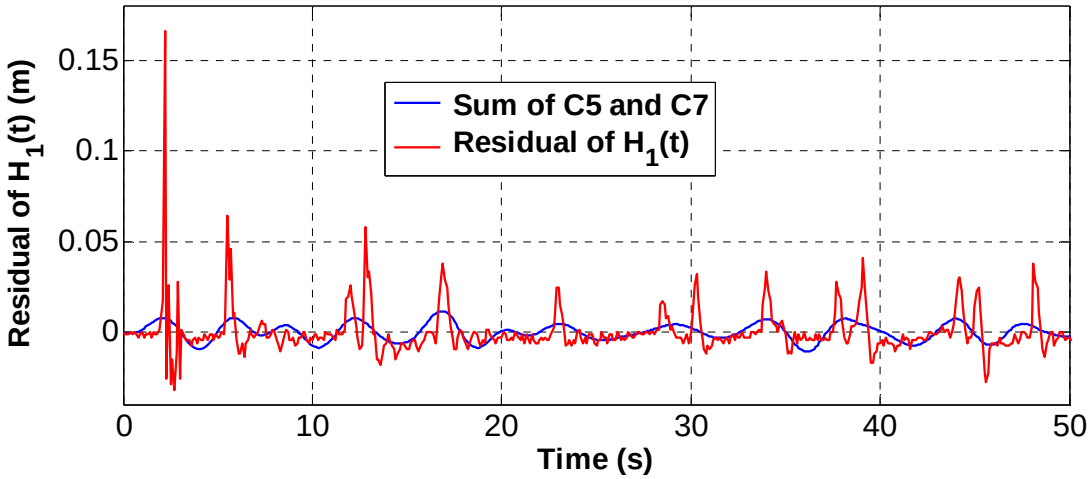

Fig. 10-25 Evolution of the sum of 2 wavelet dyadic components $C_5(t)$ and $C_7(t)$ of the residual of $H_1(t)$ (differential filtering) and the one of the original signal $H_1(t)$.

10.4.3.8 Analysis of the residual of $H_1(t)$ with differential filtering and temporal analysis

The auto-correlation function $R_{H_{1\mathrm{Re}}H_{1\mathrm{Re}}}(k)$ of the residual of $\boldsymbol{H_1(t)}$ with differential filtering is shown in **Fig. 10-26**.

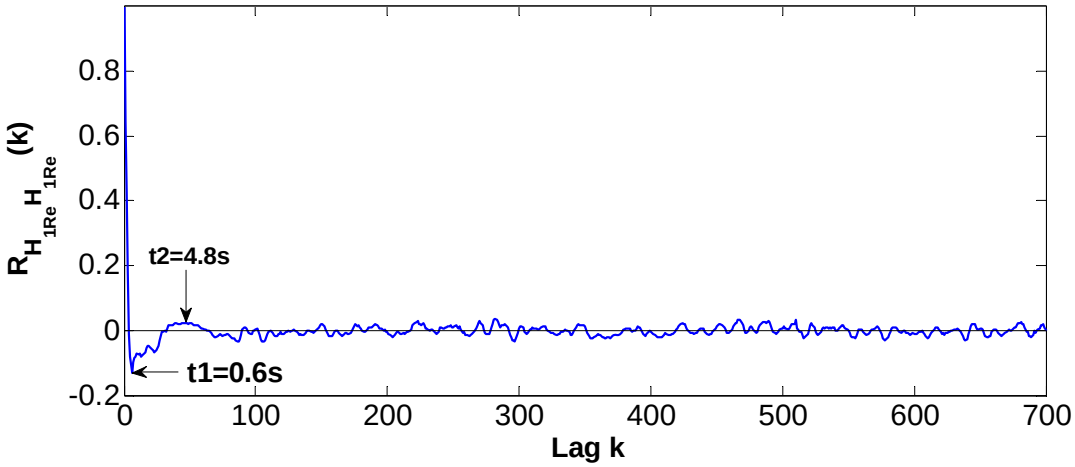

Fig. 10-26 Auto-correlation function $R_{H_{1\mathrm{Re}}H_{1\mathrm{Re}}}(k)$ of the residual of $H_1(t)$ with differential filtering (dt=0.1s)

It can be seen that the time t_2=4.8s is approximate to the most dominant period T_1=4.67s (**Fig. 10-23**) of the corresponding residual.

10.4.3.9 Residual of $H_1(t)$ with multi-resolution wavelet C_5

The evolution of the original signal $H_1(t)$, the approximation and the corresponding residual with multi-resolution wavelet are respectively shown in **Fig. 10-27**, **Fig. 10-28** and **Fig. 10-29**.

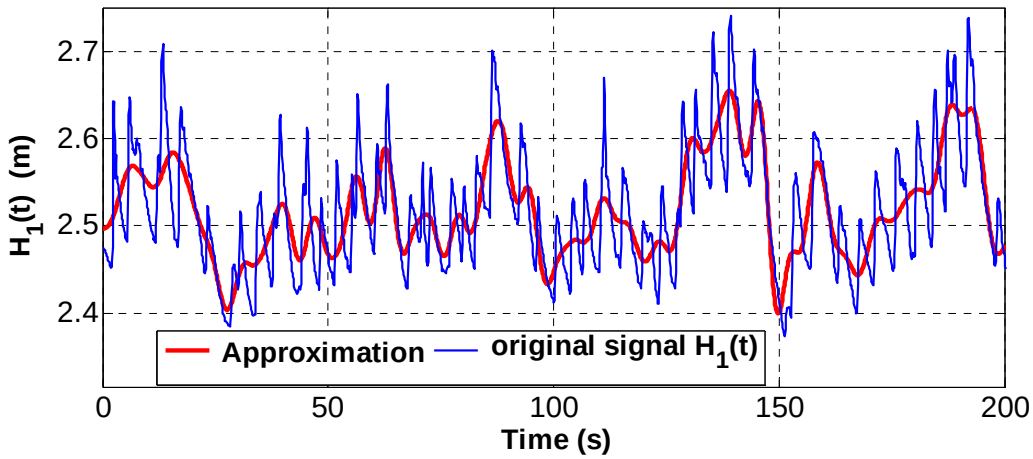

Fig. 10-27 Evolution of $H_1(t)$ and its approximation with multi-resolution wavelet (C_5)

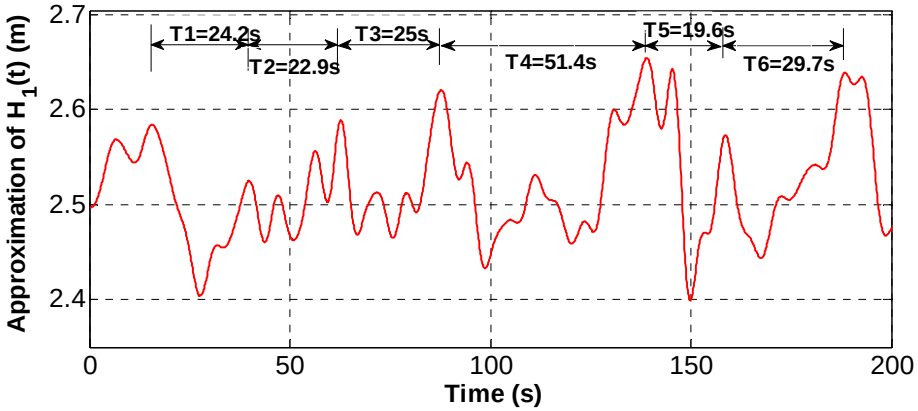

Fig. 10-28 Evolution of the approximation of $H_1(t)$ with multi-resolution wavelet (C_5)

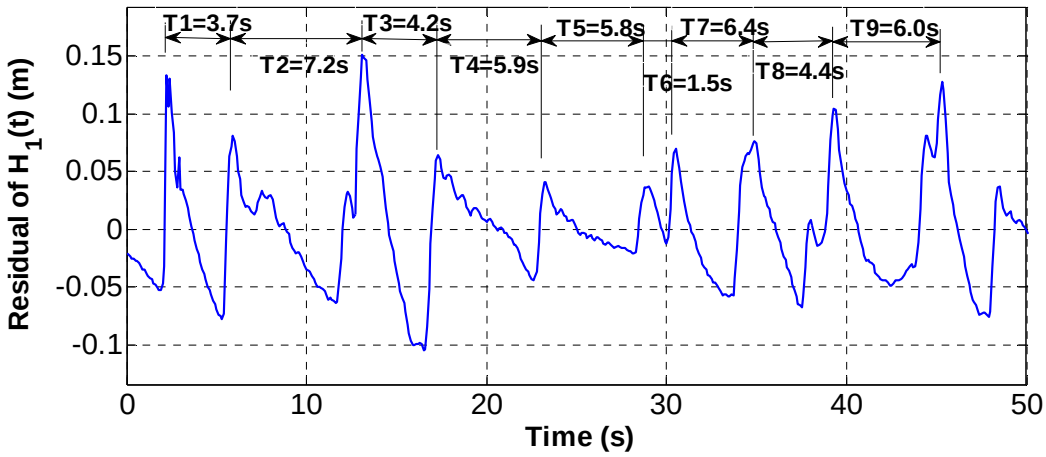

Fig. 10-29 Evolution of the residual of $H_1(t)$ with multi-resolution wavelet (C_5)

10.4.3.10 Analysis of the residual of $H_1(t)$ with multi-resolution wavelet and Fourier spectrum analysis

The Fourier spectrum function $\boldsymbol{S(f)}$ of the residual of $\boldsymbol{H_1(t)}$ with multi-resolution wavelet is shown in **Fig. 10-30**.

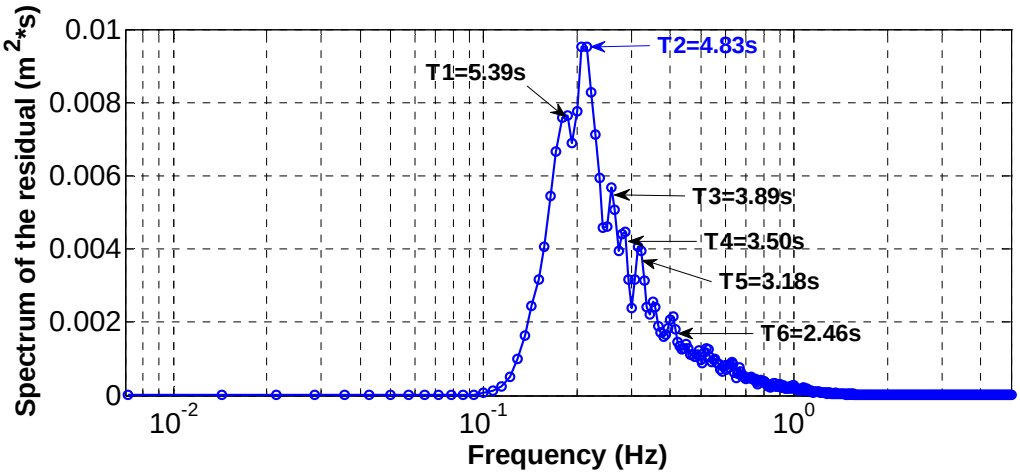

Fig. 10-30 Fourier spectrum with respect to the frequency $S(f)$ of the residual of $H_1(t)$ with multi-resolution wavelet.

10.4.3.11 Analysis of the residual of $H_1(t)$ with multi-resolution wavelet filtering and temporal analysis

The autocorrelation function $R_{H_{1\mathrm{Re}}H_{1\mathrm{Re}}}(k)$ of the residual of $\boldsymbol{H_1(t)}$ with temporal analysis and multi-resolution wavelet filtering is shown in **Fig. 10-31**.

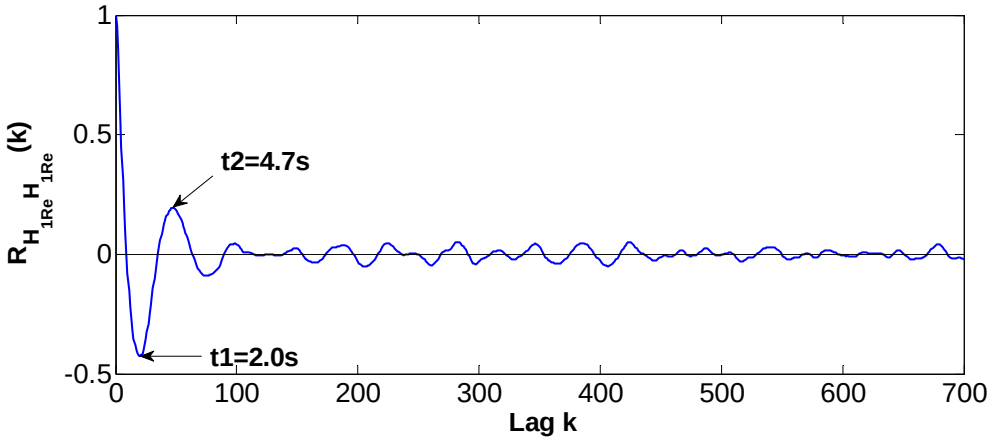

Fig. 10-31 Autocorrelation function $R_{H_{1\mathrm{Re}}H_{1\mathrm{Re}}}(k)$ of the residual of $H_1(t)$ with multi-resolution wavelet filtering.

10.4.3.12 Analysis of the residual of $H_1(t)$ with multi-resolution wavelet filtering and analysis

Although there is much noise in the components with low dyadic time scales, it can be still seen that the component C_5 play the most dominant role in the residual of $\boldsymbol{H_1(t)}$ with multi-resolution wavelet filtering (**Fig. 10-32**). What's more, the evolution of the sum of 2 wavelet dyadic components $C_5(t)$ and $C_7(t)$ of the residual coincides very well with the one of $\boldsymbol{H_1(t)}$ **(Fig. 10-33)**.

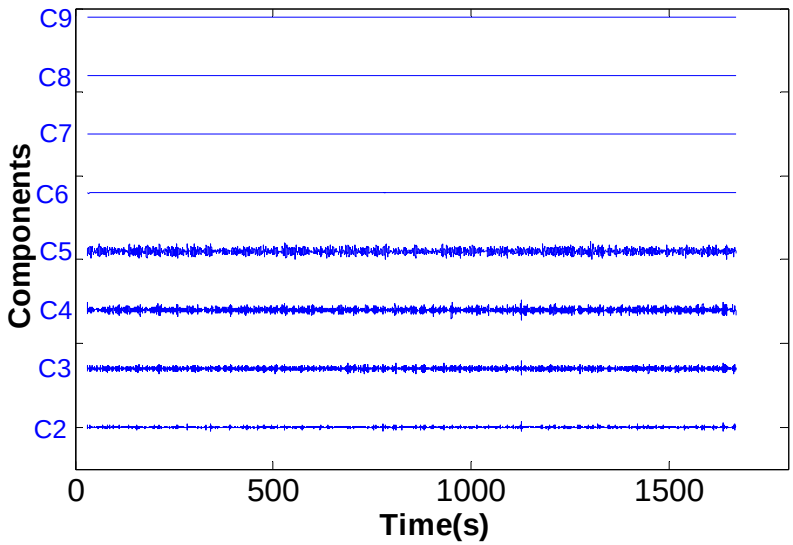

Fig. 10-32 Evolution of the wavelet dyadic components of residual of $H_1(t)$ with multi-resolution wavelet filtering (C_5)

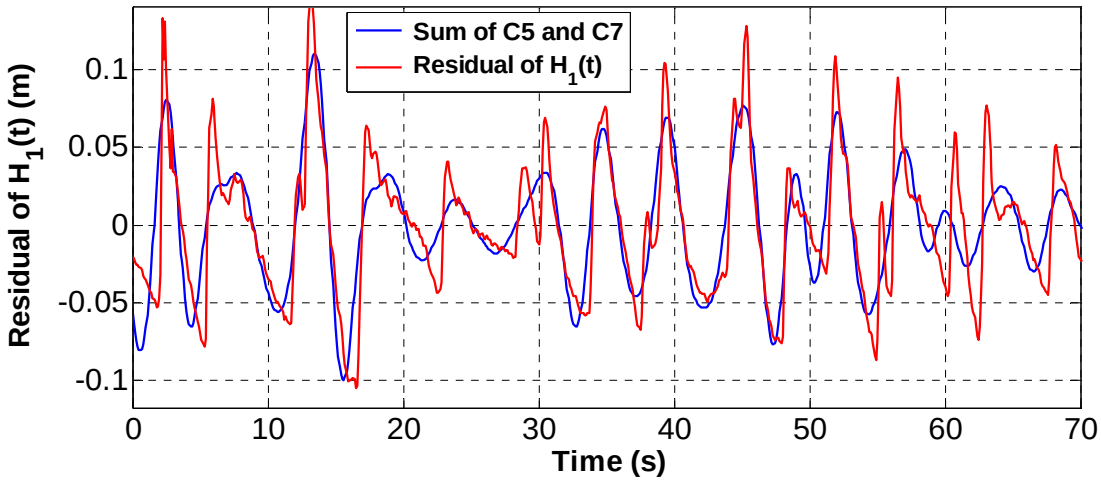

Fig. 10-33 Evolution of the sum of 2 wavelet dyadic components $C_5(t)$ and $C_7(t)$ of residual of $H_1(t)$ with multi-resolution wavelet filtering (C_5)

10.4.4 Comparison of the same wavelet dyadic component C_5

Fig. 10-34 shows the evolution of the wavelet dyadic component C_5 of the original signal $H_1(t)$ and its residuals obtained respectively with moving average filtering (*window halfwidth* w_t=5s), multi-resolution wavelet filtering (C_5) and differential filtering methods.

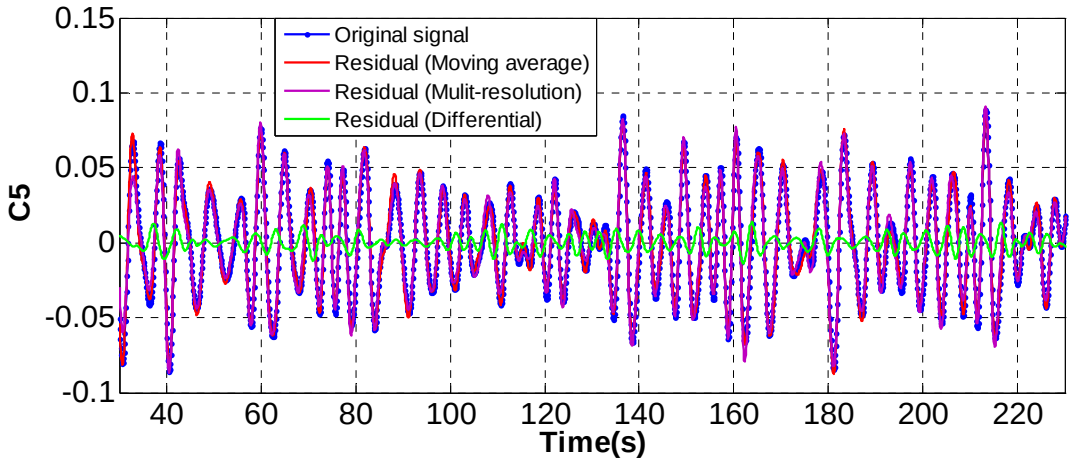

Fig. 10-34 Evolution of the wavelet dyadic component $C_5(t)$ of the residuals and the original signal of $H_1(t)$

The evolution of the component obtained with moving average filtering and multi-resolution wavelet filtering almost superpose together on the one of the original signal. However, the one obtained with differential filtering is much smaller than the 3 others.

As a result, the Fourier spectrum curves of the residuals obtained with moving average filtering and multi-resolution wavelet filtering methods superpose also with the one of the original signal. At the same time, the one of the residual obtained with differential filtering

has the same shape with them, and due to the lower amplitude, it has the lower spectrum energy (**Fig. 10-35**).

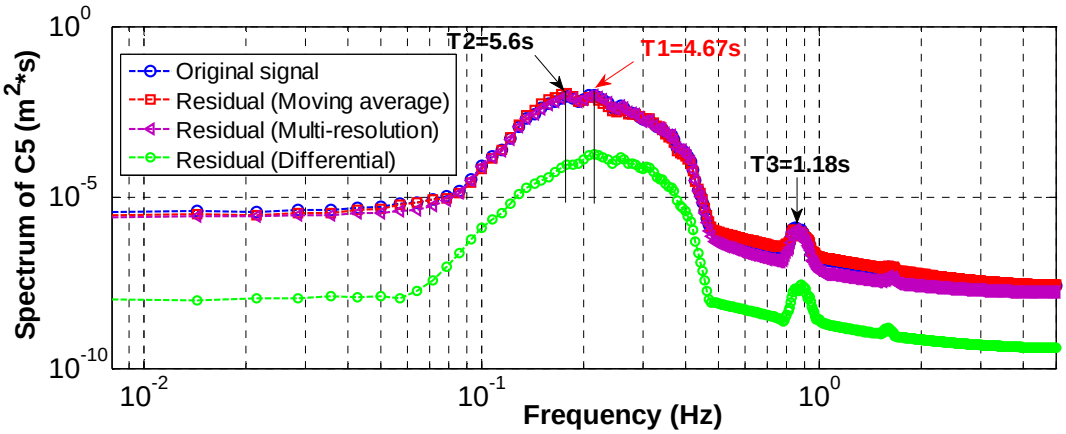

Fig. 10-35 Fourier spectra of the wavelet dyadic component C_5 of the residuals and the original signal of $H_1(t)$

10.5 Signal processing of $H_6(t)$

10.5.1 Introduction

The Fourier spectrum analysis, multi-resolution wavelet and temporal analysis methods are used to analysis the original signal $\boldsymbol{H_6(t)}$ and its residuals obtained respectively with moving average, differential, and multi-resolution filtering.

10.5.2 Analysis of the original signal $H_6(t)$

The original signal $H_6(t)$ analyzed is shown in **Fig. 10-6.**

10.5.2.1 Analysis of the original signal H_6 (t) with Fourier spectrum analysis

The Fourier spectrum of the original signal $\boldsymbol{H_6(t)}$ is shown in **Fig. 10-36** in log-log axis.

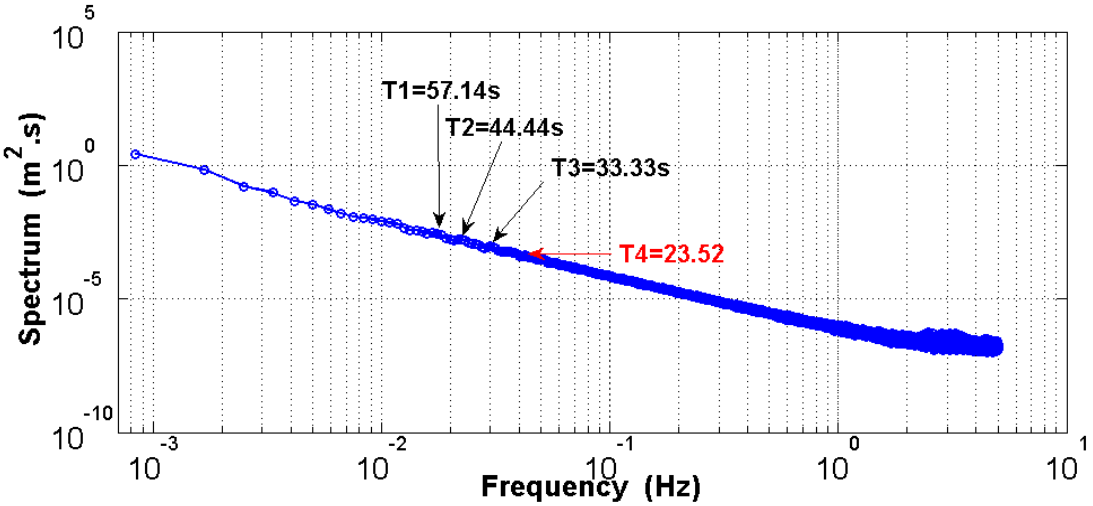

Fig. 10-36 Fourier spectrum of the original signal $H_6(t)$ in log-log axis (m=6000, dt=0.1s)

From this figure, the dominant period is not clear.

10.5.2.2 Analysis of the original signal $H_6(t)$ with multi-resolution wavelet

The evolution of the wavelet dyadic components of the original signal $\boldsymbol{H_6(t)}$ with multi-resolution wavelet is shown in **Fig. 10-37**.

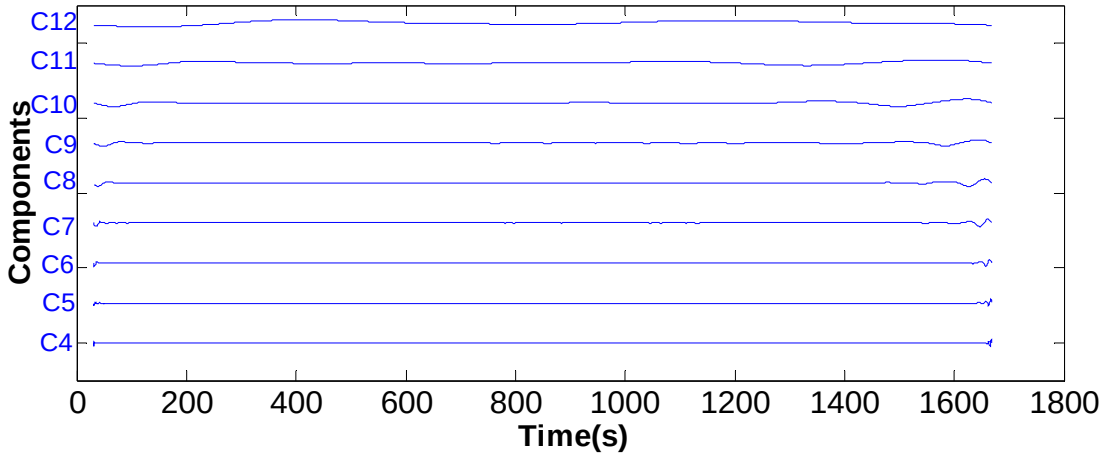

Fig. 10-37 Evolution of the wavelet components of the original signal $H_6(t)$ with multi-resolution wavelet

From this figure, from the component C_8 to C_{10}, although the fluctuations of the component become stronger and stronger in the beginning and in the end of the evolution of the signal, it is still very difficult to distinguish the most dominant period. The evolution of C_9 and C_{10} are shown alone respectively in **Fig. 10-38** and **Fig. 10-39**.

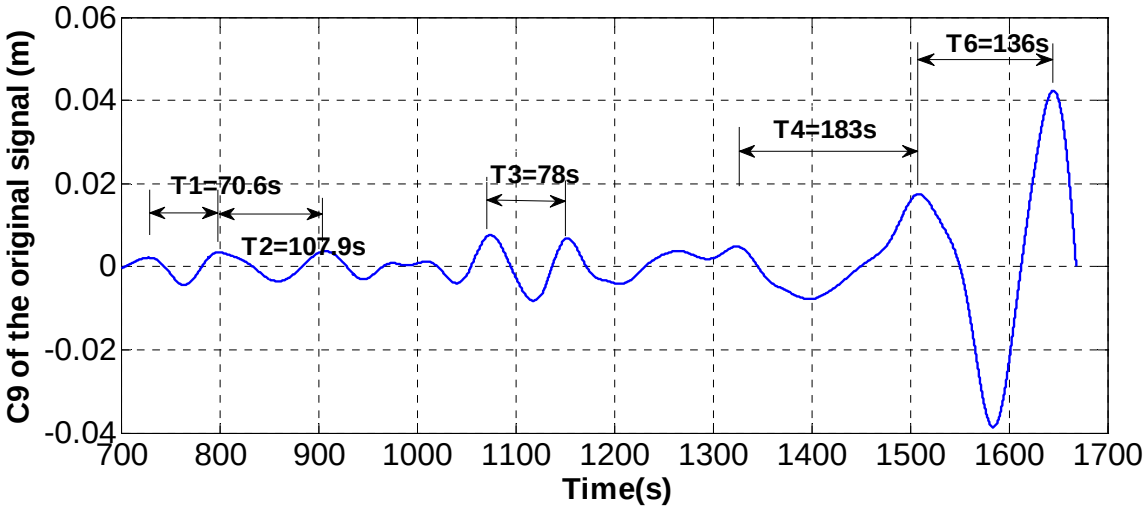

Fig. 10-38 Evolution of the wavelet dyadic component C_9 of the original signal $H_6(t)$ with multi-resolution wavelet

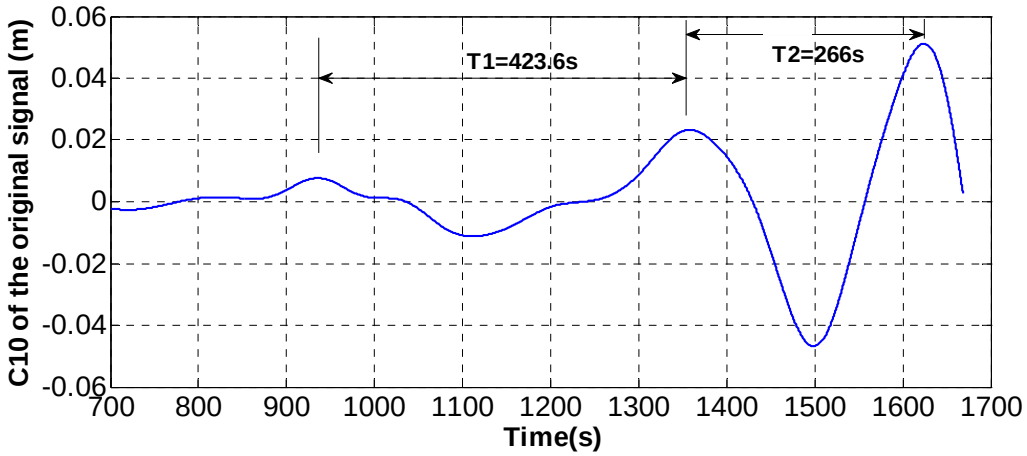

Fig. 10-39 Evolution of the wavelet dyadic component C_{10} of the original signal $H_6(t)$ with multi-resolution wavelet

10.5.2.3 Analysis of the original $H_6(t)$ with temporal analysis

The autocorrelation function of the original signal $\boldsymbol{H_6(t)}$ $\boldsymbol{R_{H_6H_6}(k)}$ with temporal analysis is shown in **Fig. 10-40**.

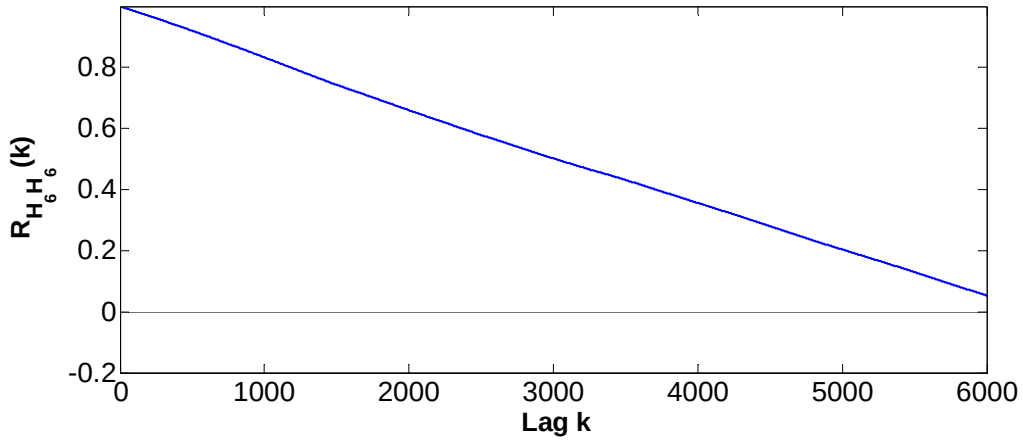

Fig. 10-40 Autocorrelation function of the original signal $H_6(t)$ $R_{H6H6}(k)$ (dt=0.1s)

From this figure, there is no visible fluctuation.

10.5.3 Analysis of the residual of $H_6(t)$

The residuals of $\boldsymbol{H_6(t)}$ are respectively obtained with moving average filtering, differential filtering and multi-resolution wavelet filtering.

10.5.3.1 Residual of $H_6(t)$ with moving average filtering

The evolution of the original signal $\boldsymbol{H_6(t)}$ and the corresponding moving average with moving average filtering (*window halfwidth* w_t=30s) is shown in **Fig. 10-41.**

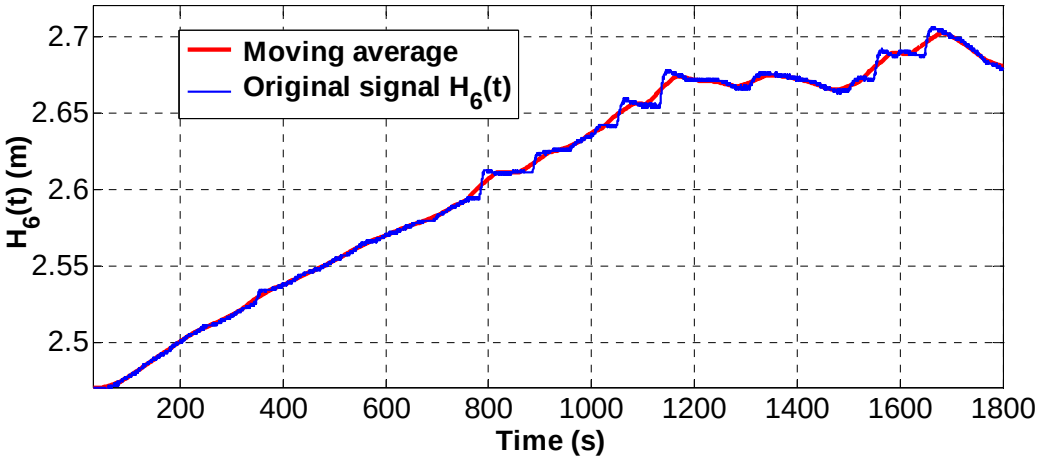

Fig. 10-41 Evolution of the original signal $H_6(t)$ and its corresponding moving average with moving average filtering (*window halfwidth* w_t=30s)

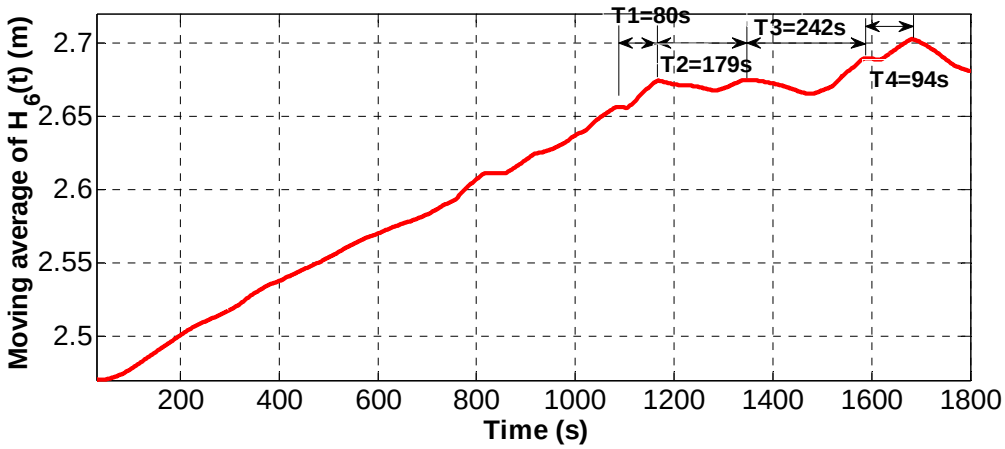

Fig. 10-42 Evolution of the moving average of $H_6(t)$ (*window halfwidth* w_t=30s)

The same moving average and the corresponding residual of $\boldsymbol{H_6(t)}$ are respectively alone shown in **Fig. 10-42** and **Fig. 10-43**.

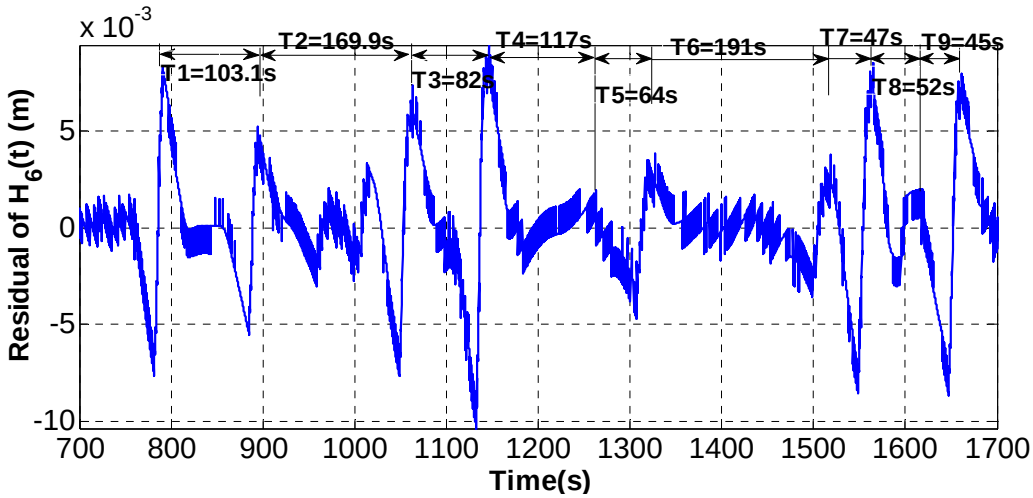

Fig. 10-43 Evolution of the residual of $H_6(t)$ with moving average filtering (*window halfwidth* w_t=30s)

10.5.3.2 Analysis of the residual of $H_6(t)$ with moving average filtering and Fourier spectrum analysis

The Fourier spectrum function $\boldsymbol{s(f)}$ of the residual of $\boldsymbol{H_6(t)}$ with moving average filtering (*window halfwidth* w_t=30s) is shown in **Fig. 10-44.**

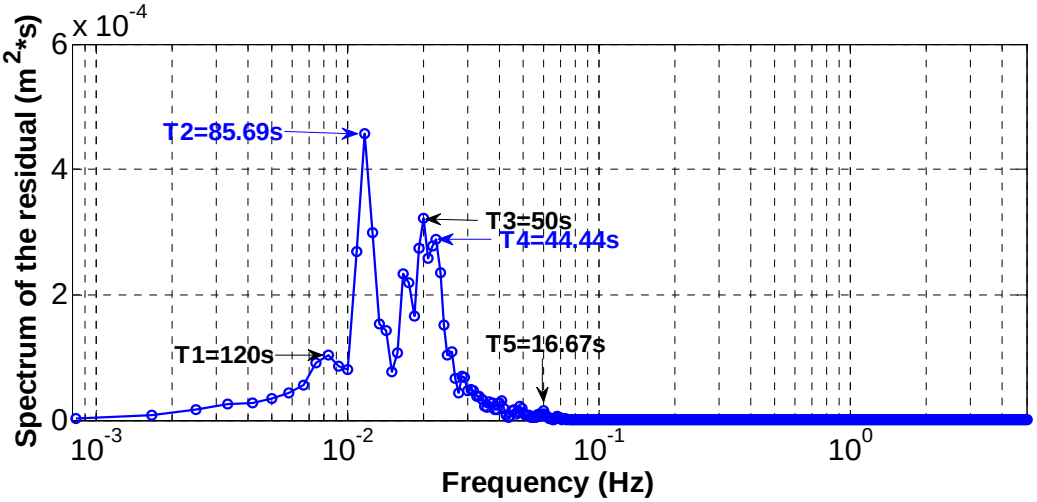

Fig. 10-44 Fourier spectrum function $S(f)$ of the residual of $H_6(t)$ with moving average filtering (*window halfwidth* w_t=30s)

From this figure, it can be seen that the period T_2=85.69 plays the most dominant role in the residuals, and at the same the period T_3=50s plays the second dominant role.

10.5.3.3 Analysis of the residual of $H_6(t)$ with moving average filtering and multi-resolution wavelet analysis

The evolution of the wavelet dyadic components is shown in **Fig. 10-45**. At the same time, the evolution of the components C_8 and C_9 are respectively shown in **Fig. 10-46** and **Fig. 10-47**.

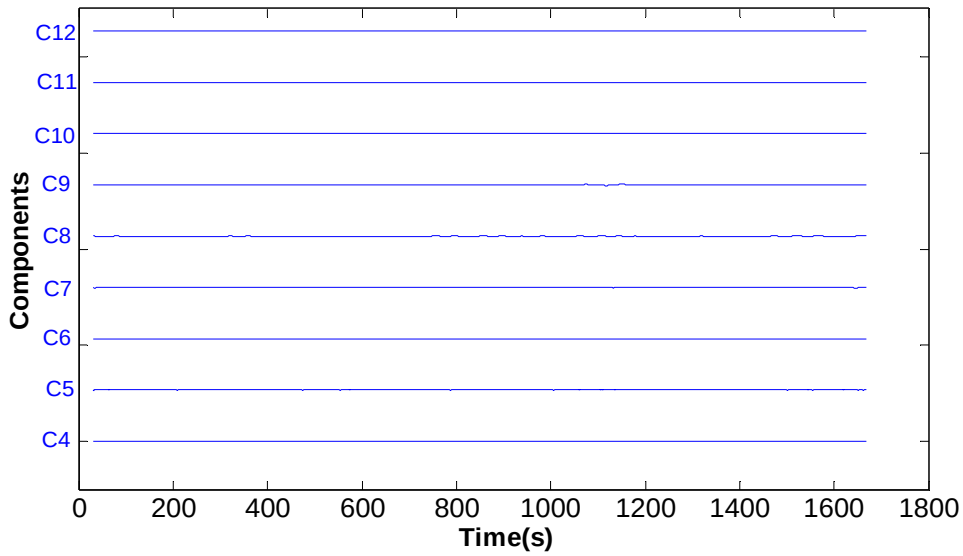

Fig. 10-45 Evolution of the wavelet components of the residual of $H_6(t)$ with moving average filtering and multi-resolution wavelet analysis

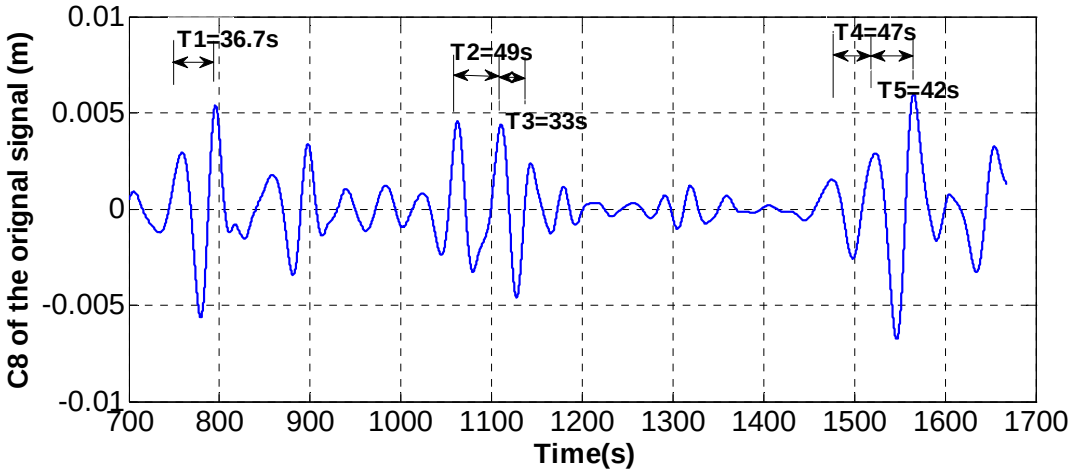

Fig. 10-46 Evolution of the wavelet dyadic component C_8 of the residual of $H_6(t)$ with moving average filtering and multi-resolution wavelet analysis

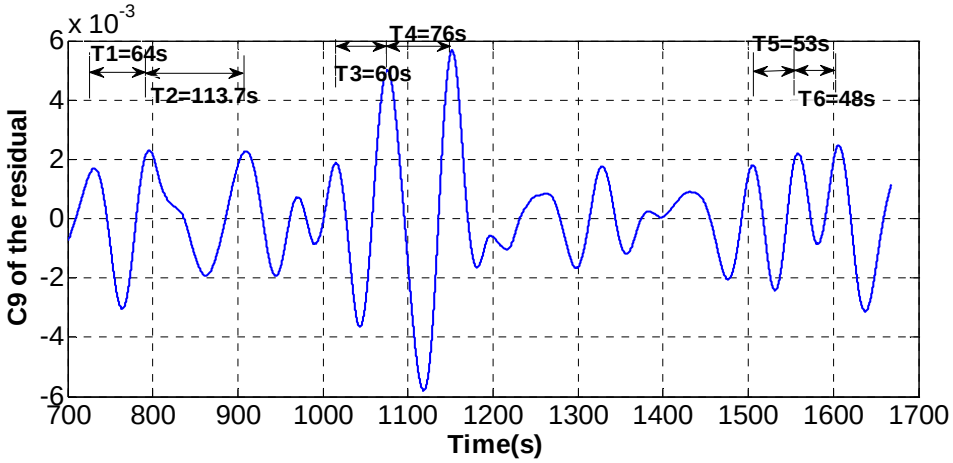

Fig. 10-47 Evolution of the wavelet dyadic component C_9 of the residual of $H_6(t)$ with moving average filtering and multi-resolution wavelet analysis

Although the fluctuation amplitudes of the component are very small, it can still be seen that C8 is the most dominant component in the residual.

10.5.3.4 Analysis of the residual of $H_6(t)$ with moving average filtering and temporal analysis

The autocorrelation function $R_{H_{6\mathrm{Re}}H_{6\mathrm{Re}}}(k)$ of the residual of $\boldsymbol{H_6(t)}$ with moving average filtering (*window halfwidth* w_t=30s) is shown in **Fig. 10-48**. In this figure, the time t_3=93.8s is approximate to the most dominant period T_2=85.69s obtained with Fourier spectrum analysis (**Fig. 10-44**).

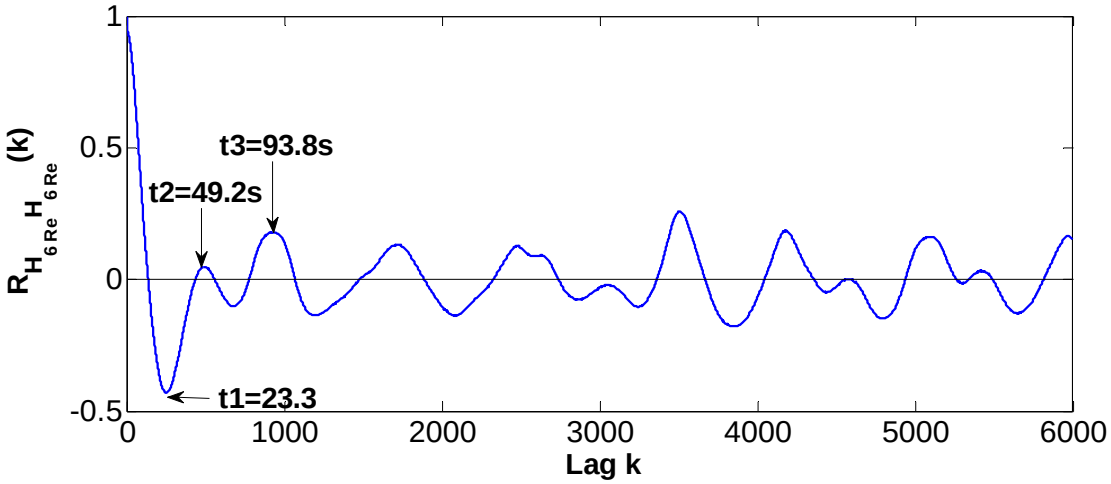

Fig. 10-48 Autocorrelation function $R_{H_{6\mathrm{Re}}H_{6\mathrm{Re}}}(k)$ (future)of the residual of $H_6(t)$ with moving average filtering (*window halfwidth* wt=30s)

10.5.3.5 Residual of $H_6(t)$ with differential filtering

The evolution of the residual of $\boldsymbol{H_6(t)}$ with differential filtering (t=1000-1050s) is shown in **Fig. 10-49**.

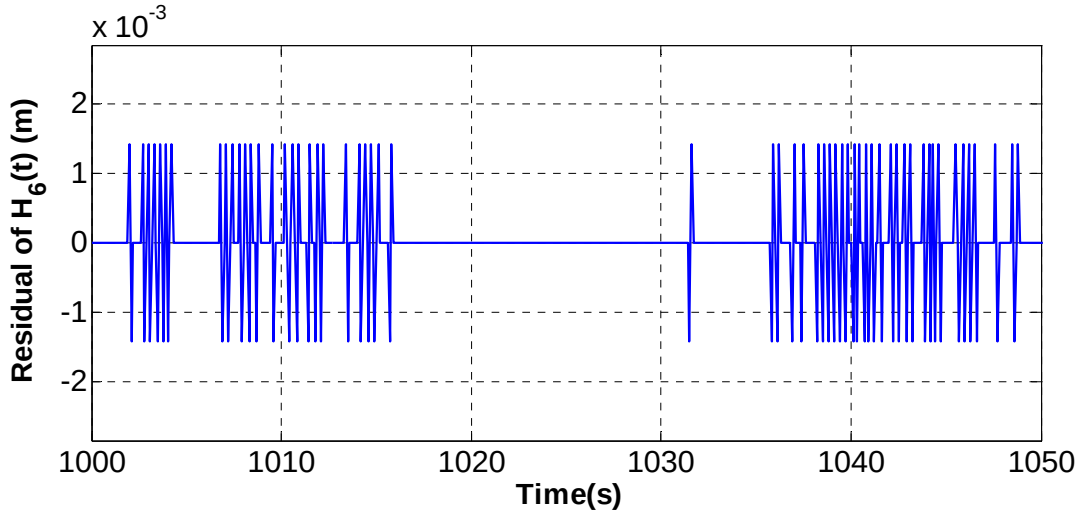

Fig. 10-49 Evolution of the residual of $H_6(t)$ with differential filtering (t=1000-1050s)

10.5.3.6 Analysis of the residual of $H_6(t)$ with differential filtering and Fourier spectrum analysis

The Fourier spectrum function with the respect to the frequency is shown in **Fig. 10-50**.

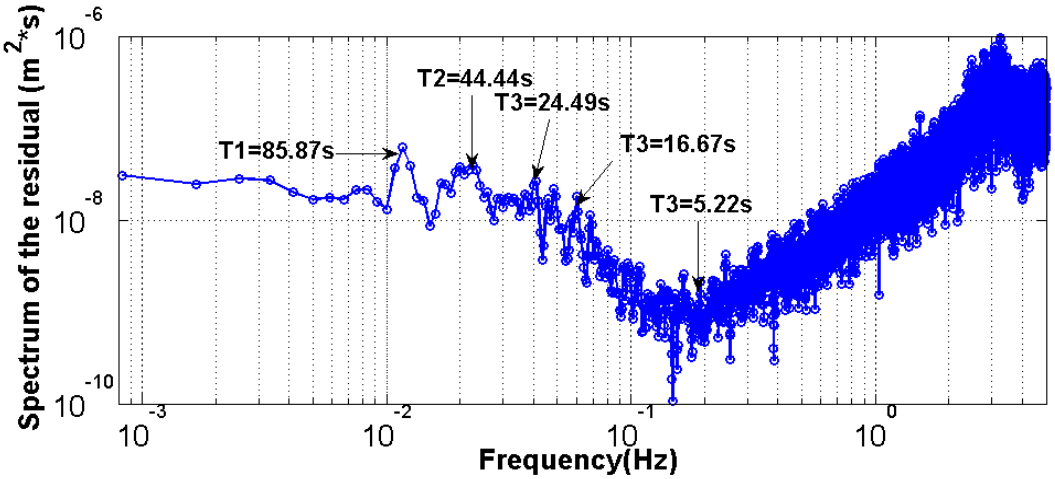

Fig. 10-50 Fourier spectrum function with the respect to the frequency of the residual of $H_6(t)$ with differential filtering

It shows almost the same dominant periods with the ones of the residual with moving average filtering (*window halfwidth* wt=30s), except the noise after T=5.22s.

10.5.3.7 Analysis of the residual of $H_6(t)$ with differential filtering and multi-resolution wavelet

In **Fig. 10-51** , the evolution of the components shows that the component C_9 plays dominant role in the residual signal of $\boldsymbol{H_6(t)}$ with differential filtering. In addition, the evolution of the C_9 is shown alone in **Fig. 10-52**.

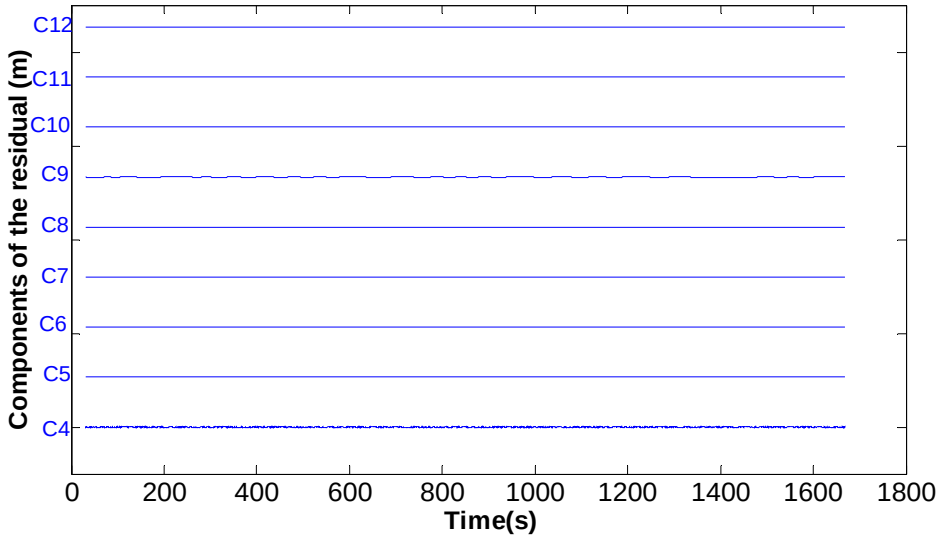

Fig. 10-51 Evolution of the wavelet dyadic components of the residual of $H_6(t)$ with differential filtering and multi-resolution wavelet

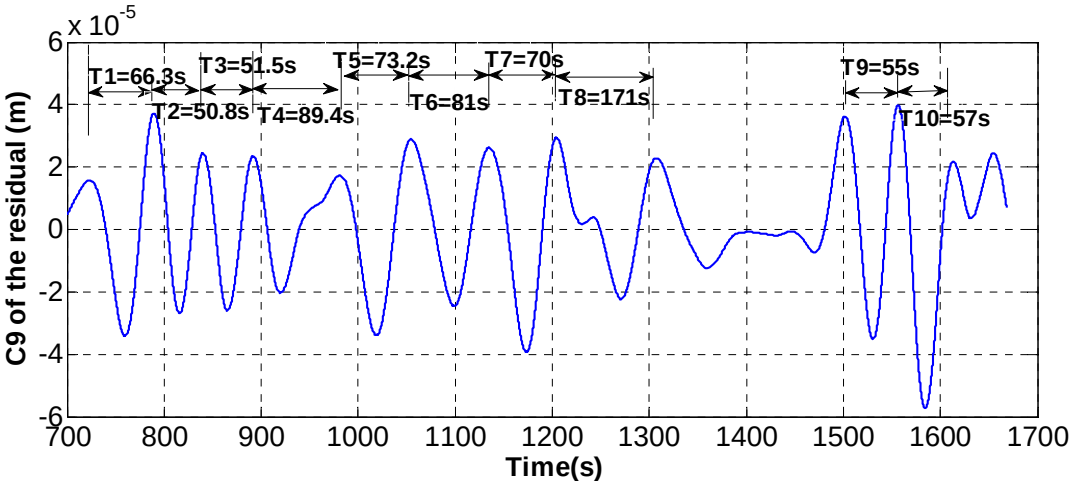

Fig. 10-52 Evolution of the wavelet dyadic component C_9 of the residual of $H_6(t)$ with differential filtering and multi-resolution wavelet

10.5.3.8 Analysis of the residual of $H_6(t)$ with differential filtering and temporal analysis

The autocorrelation function $R_{H_{6\mathrm{Re}}H_{6\mathrm{Re}}}(k)$ of the residual of $\boldsymbol{H_6(t)}$ with differential filtering is shown in **Fig. 10-53**. The time t_2=0.3 is not approximate to the dominant period T_2=85.87s.

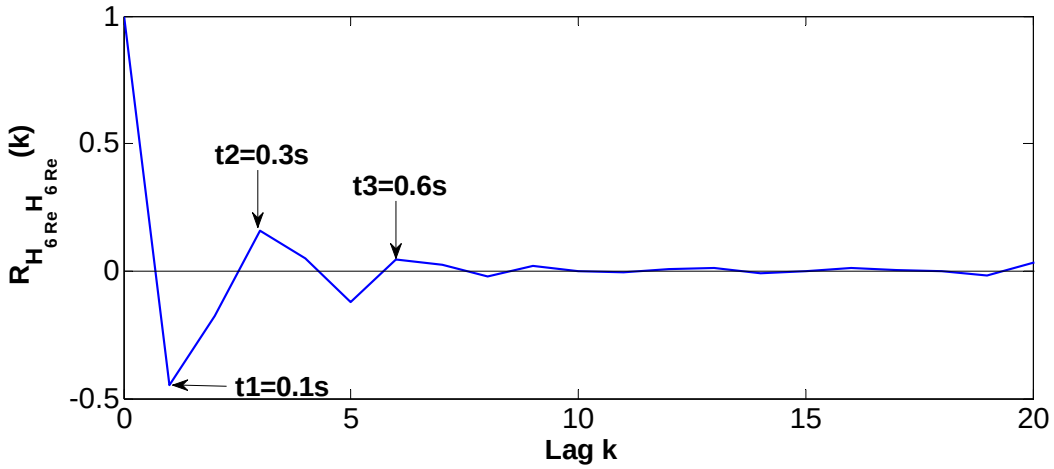

Fig. 10-53 Autocorrelation function $R_{H_{6\mathrm{Re}}H_{6\mathrm{Re}}}(k)$ of the residual of $H_6(t)$ with differential filtering

10.5.3.9 Residual of $H_6(t)$ with wavelet multi-resolution filtering

The evolution of $\boldsymbol{H_6(t)}$ and its approximation with multi-resolution wavelet filtering is shown in **Fig. 10-54**. The corresponding residual is shown in **Fig. 10-55**.

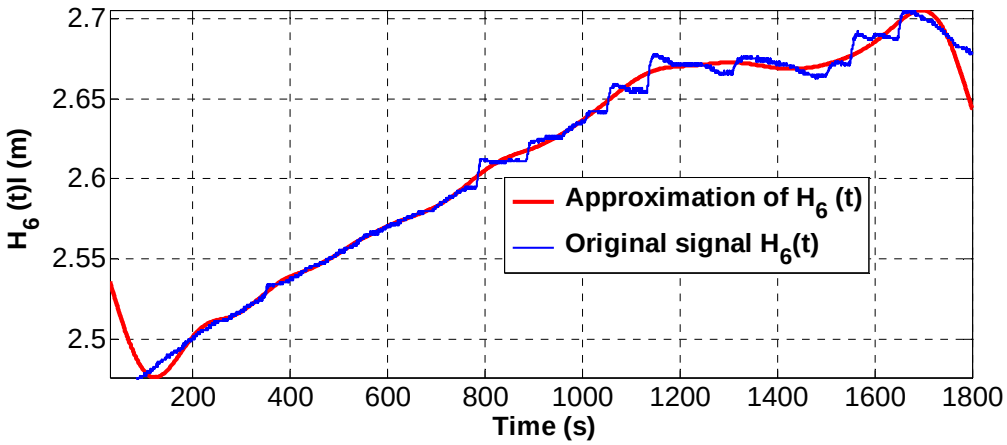

Fig. 10-54 Evolution of $H_6(t)$ and its approximation with multi-resolution wavelet filtering (C_{10})

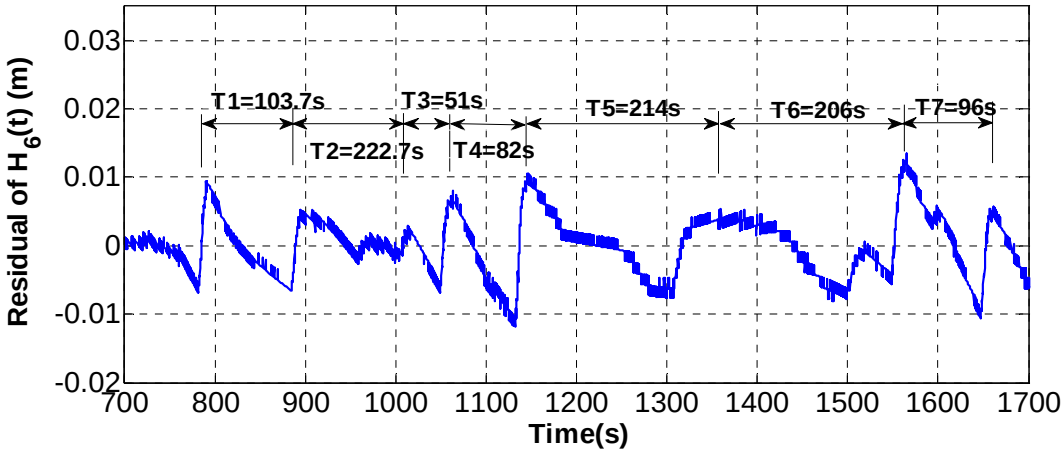

Fig. 10-55 Evolution of the residual of $H_6(t)$ with multi-resolution wavelet filtering (t=700-1700s)

10.5.3.10 Analysis of the residual of $H_6(t)$ with multi-resolution wavelet filtering and Fourier spectrum analysis

The Fourier spectrum function with respect to the frequency of the residual of $\boldsymbol{H_6(t)}$ is shown in **Fig. 10-56**.

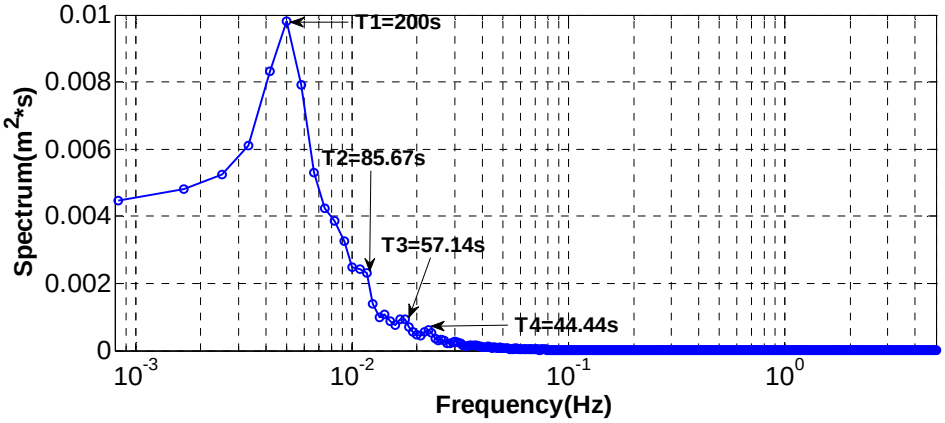

Fig. 10-56 Fourier spectrum function of the residual of $H_6(t)$ with multi-resolution wavelet filtering (m=6000, dt=0.1s) with respect to frequency

The most dominant period T_1=200s is longer than the one of the residual with moving average filtering and the one of the residual with differential filtering. However, the other dominant periods such as T_2=85.67s and T_4=44.44s are equal to the ones of the residual with the other two filtering methods, except that they have stronger Fourier spectrum density than those of the two other methods.

10.5.3.11 Analysis of the residual of $H_6(t)$ with multi-resolution wavelet filtering and its analysis

The evolution of the dyadic wavelet components is shown in **Fig. 10-57**.

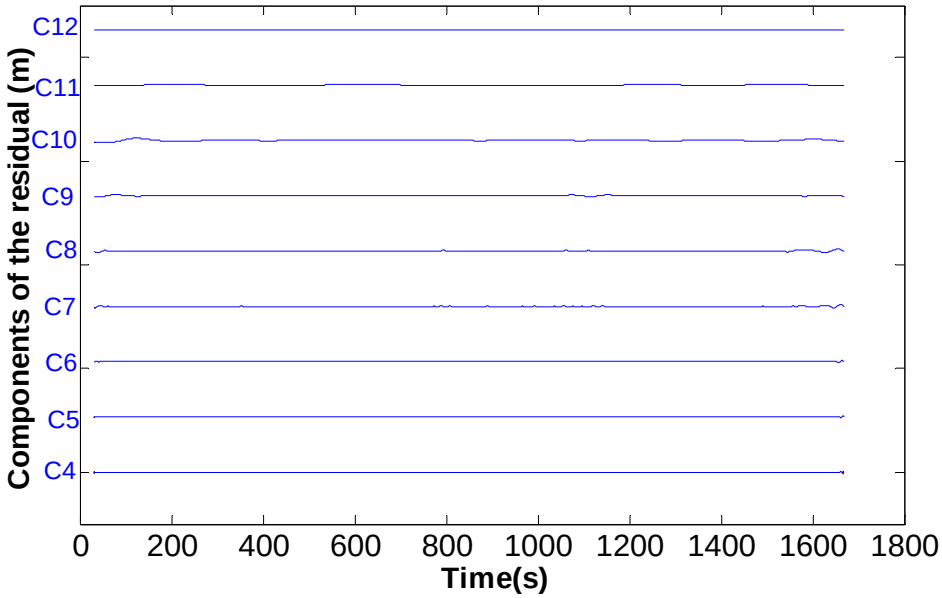

Fig. 10-57 Evolution of the wavelet dyadic components of the residual of $H_6(t)$ with multi-resolution wavelet filtering and analysis

The results in this figure show that the component C_9 is the dominant component in the residual of $\boldsymbol{H_6(t)}$ with multi-resolution (C_{10}). It is also shown alone in **Fig. 10-58**.

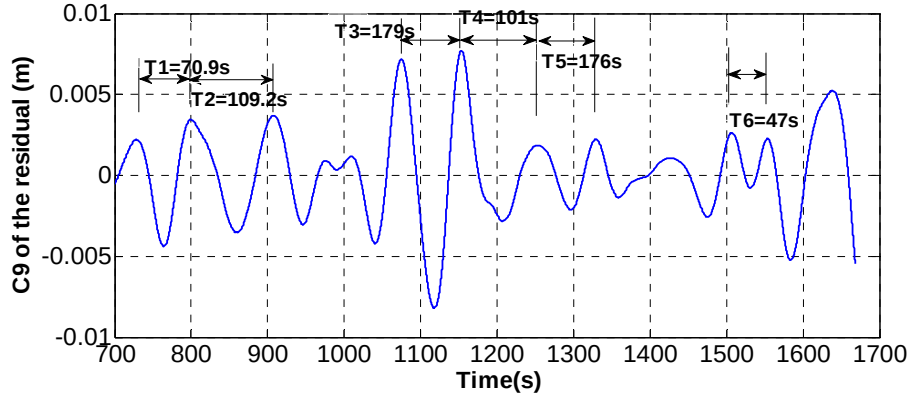

Fig. 10-58 Evolution of the wavelet dyadic component C_9 of the residual of $H_6(t)$ with multi-resolution wavelet filtering and analysis

10.5.3.12 Analysis of the residual of $H_6(t)$ with multi-resolution wavelet filtering and temporal analysis

The autocorrelation function $R_{H_{6\mathrm{Re}}H_{6\mathrm{Re}}}(k)$ with respect to the lag $\boldsymbol{k}$ is shown in **Fig. 10-59**.

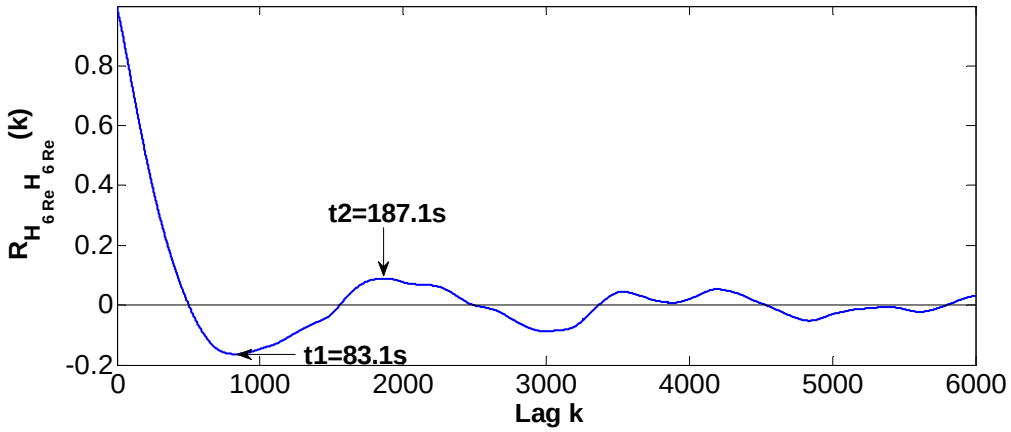

Fig. 10-59 Autocorrelation function $R_{H_{6\mathrm{Re}}H_{6\mathrm{Re}}}(k)$ of the residual of $H_6(t)$ with multi-resolution wavelet filtering

The time t_2=187.1s is approximate to the most dominant period T_1=200s.

10.5.4 Comparison of the same wavelet dyadic component C_9

Fig. 10-60 shows the evolution of the wavelet dyadic component C_9 of the original signal $H_6(t)$ and its residuals obtained respectively with moving average filtering (*window halfwidth* w_t=30s), multi-resolution wavelet filtering (C_{10}) and differential filtering methods.

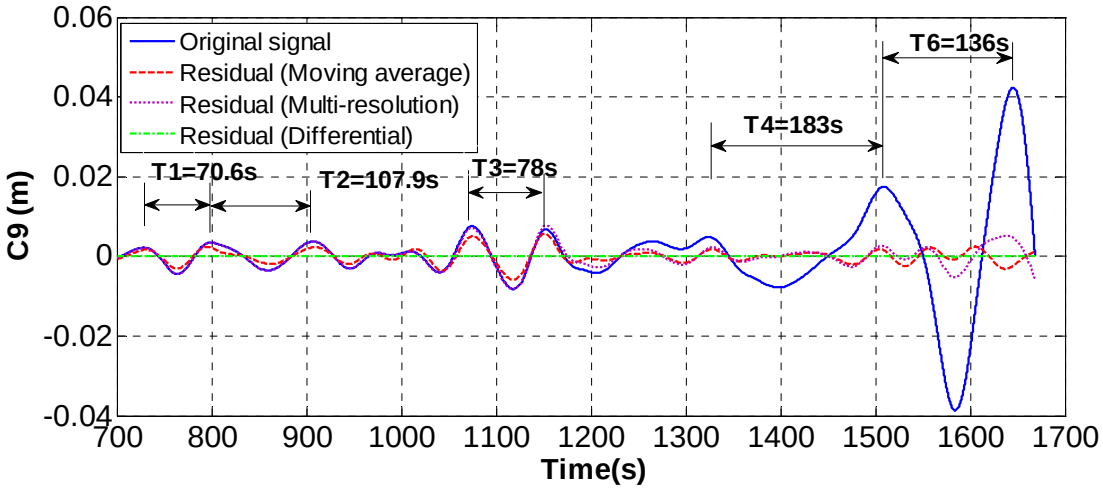

Fig. 10-60 Evolution of the wavelet dyadic component C_9(t) of $H_6(t)$

The evolution of the component obtained with moving average filtering and multi-resolution wavelet filtering approximates to the one of the original signal before t=1350s, and however, after this time, the fluctuation amplitudes and periods of the residuals all are smaller

than the ones of the original signal . In contrast, the fluctuation amplitudes of the residual obtained with differential filtering is smallest and they are very approximate to zero.

As a result, the most dominant period T_1=171.44s of the component C_9 of the original signal is bigger than the ones T_2=85.67s of the residuals obtained with 3 filtering methods (**Fig. 10-61**).

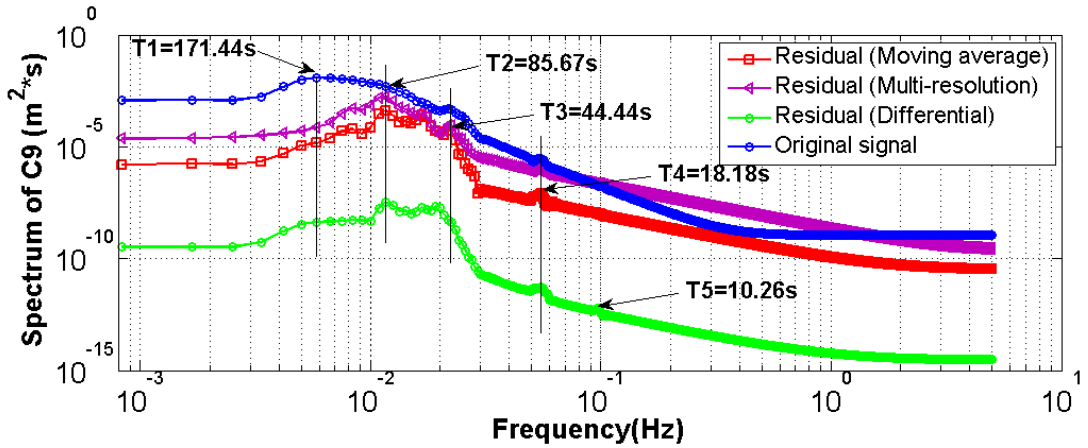

Fig. 10-61 Fourier spectrum of the wavelet dyadic component C_9 of $H_6(t)$ with respect to the frequency

10.6 Cross analysis between $H_1(t)$ and $H_6(t)$

10.6.1 Introduction

Cross analysis of the original signal and the residuals between $H_1(t)$ and $H_6(t)$ will be investigated with Fourier cross analysis, temporal cross analysis and multi-resolution wavelet. The residuals are obtained with moving average filtering, differential filtering and multi-resolution filtering analysis.

10.6.2 Cross analysis of the original signal between $H_1(t)$ and $H_6(t)$

The gain function (**Fig. 10-62**) shows that the Fourier spectrum energy decay very drastically for all the periods from $H_1(t)$ to $H_6(t)$.

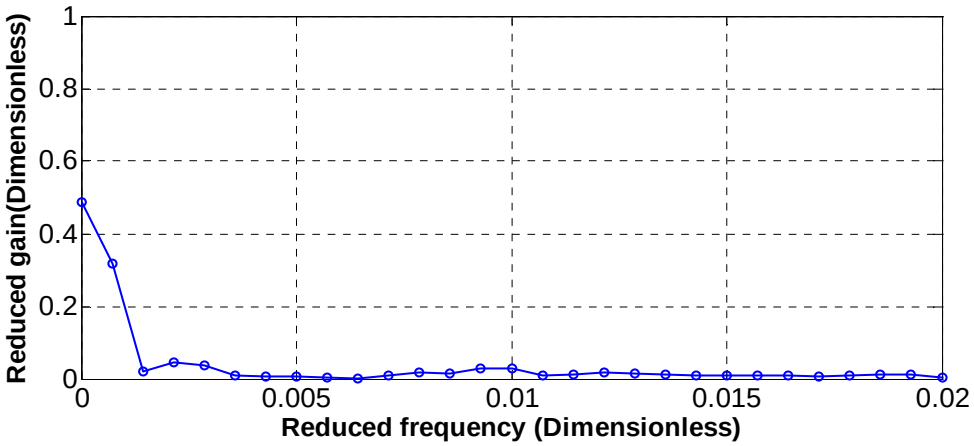

Fig. 10-62 Gain function with respect to the reduced frequency (m=700, dt=0.1s)

Appendix B: Chapter B10 Illustrations of the signal processing of the measured water level data $\boldsymbol{H_1(t)}$ and $\boldsymbol{H_6(t)}$ of the experiment in Barcelona

The coherency function (**Fig. 10-63**) indicates that there is very low coherency (coherency coefficients are smaller than 0.3) for all the periods between $H_1(t)$ and $H_6(t)$.

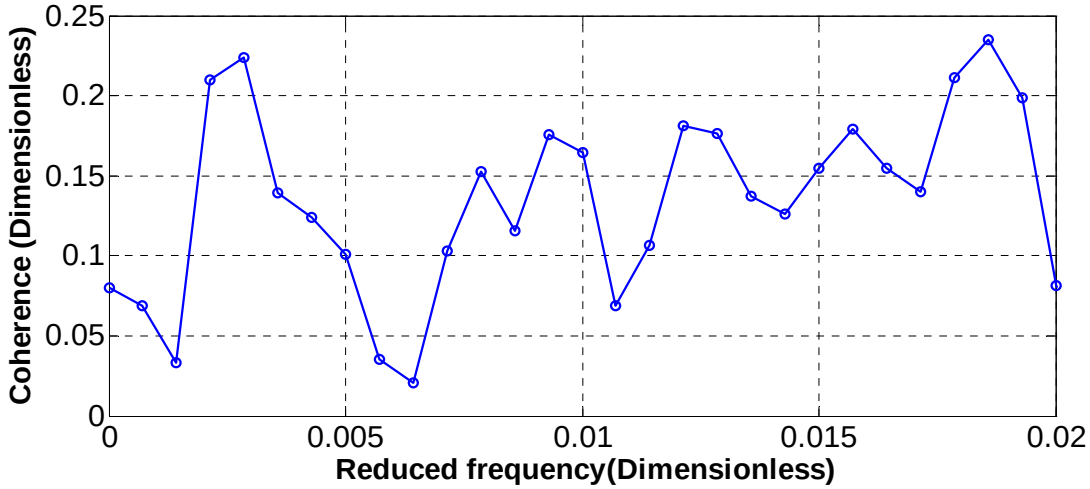

Fig. 10-63 Coherency function with respect to the reduced frequency (m=700, dt=0.1s)

The phase (**Fig. 10-64**) doesn't change with the period, and it fluctuations from $-\pi/2$ and $+\pi/2$.

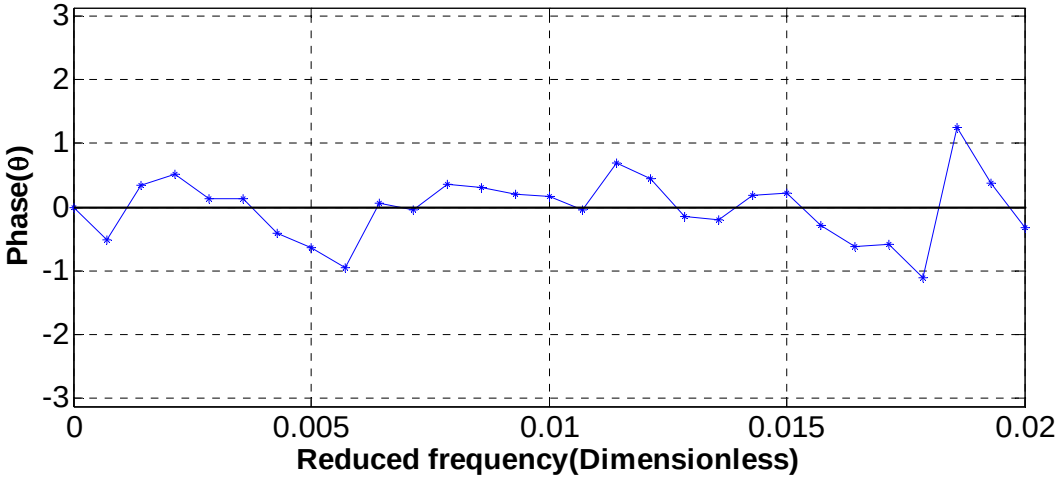

Fig. 10-64 Phase function with respect to the reduced frequency (m=700, dt=0.1s)

From the figure (**Fig. 10-65**) of the maximum inter-correlation of the components between $H_1(t)$ and $H_6(t)$ with respect to the wavelet dyadic time scale, it can be seen that there are two peaks for the components C_6 and C_{10}. Although the two components have better cross correlation than the other components, the correlation coefficients are less than 0.5.

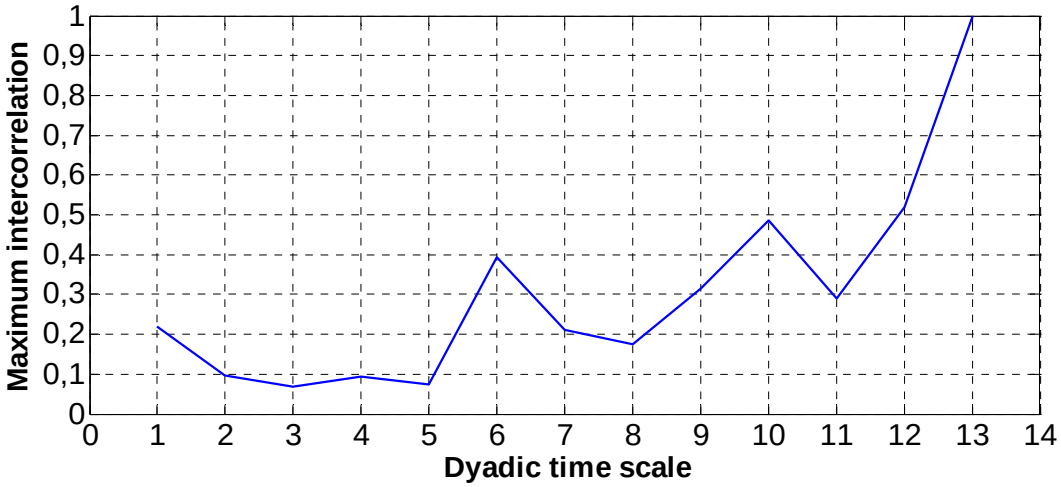

Fig. 10-65 Maximum inter-correlation with respect to the dyadic components

10.6.3 Cross analysis of the residuals between $H_1(t)$ and $H_6(t)$

10.6.3.1 Cross analysis of the residuals between $\boldsymbol{H_1(t)}$ and $\boldsymbol{H_6(t)}$ with moving average filtering

The residuals of $\boldsymbol{H_1(t)}$ and $\boldsymbol{H_6(t)}$ with moving average filtering (*wt_1=5s et wt_6=30s, t=0-1800s*) is shown in **Fig. 10-66**.

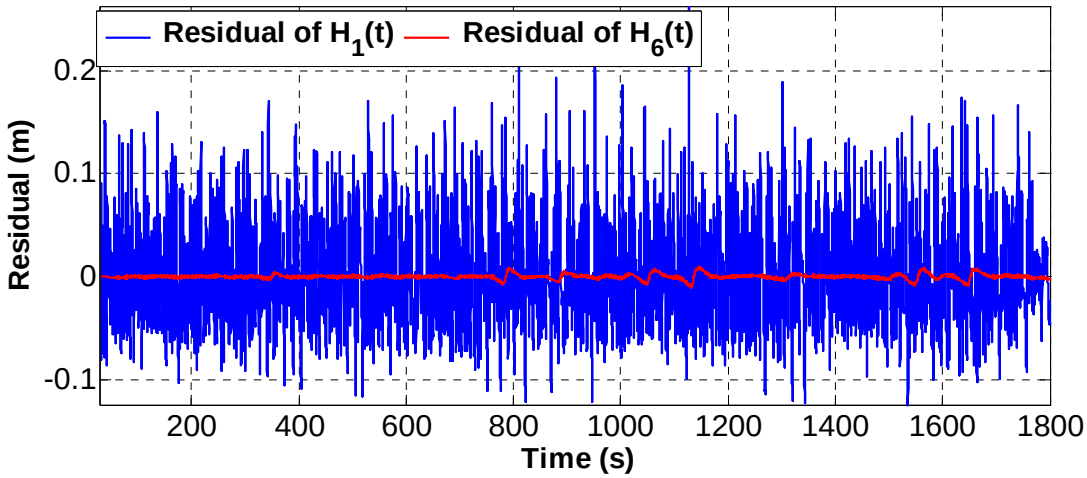

Fig. 10-66 Evolution of the residuals of $H_1(t)$ and $H_6(t)$ with moving average filtering (*wt_1=5s et wt_6=30s, t=0-1800s*)

It can be clearly seen that the fluctuation amplitudes of the residual of $\boldsymbol{H_1(t)}$ are much bigger than the ones of $\boldsymbol{H_6(t)}$.

The gain function (**Fig. 10-67**) shows that, besides the big Fourier energy decaying, there are much more noise in the residual of $H_6(t)$.

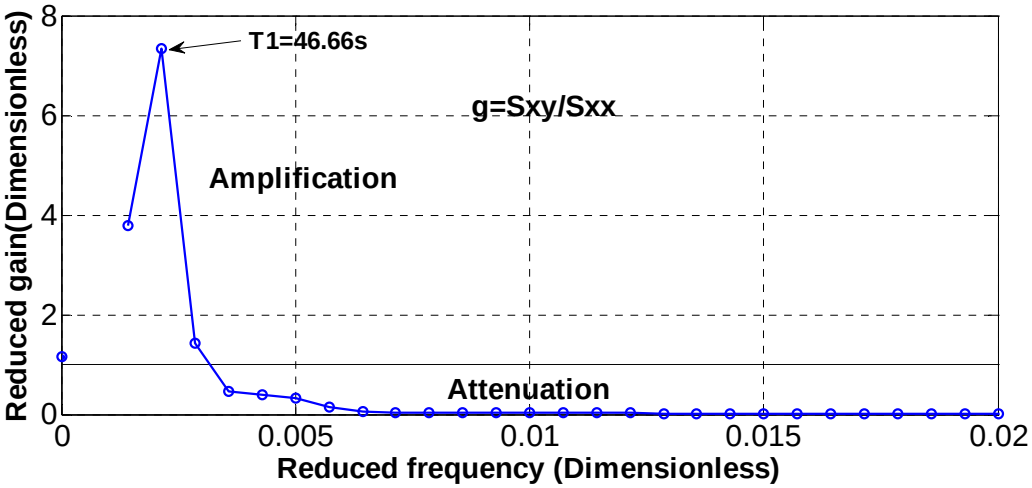

Fig. 10-67 Gain function of the residuals of $H_1(t)$ and $H_6(t)$ with moving average filtering (*wt_1=5s et wt_6=30s, t=0-1800s*) (m=700, dt=0.1s)

Compared with the coherency of the original signal, the coherency coefficients for the residuals between $H_1(t)$ and $H_6(t)$ (**Fig. 10-68**) have been improved. However, the biggest coefficient is still smaller than 0.5.

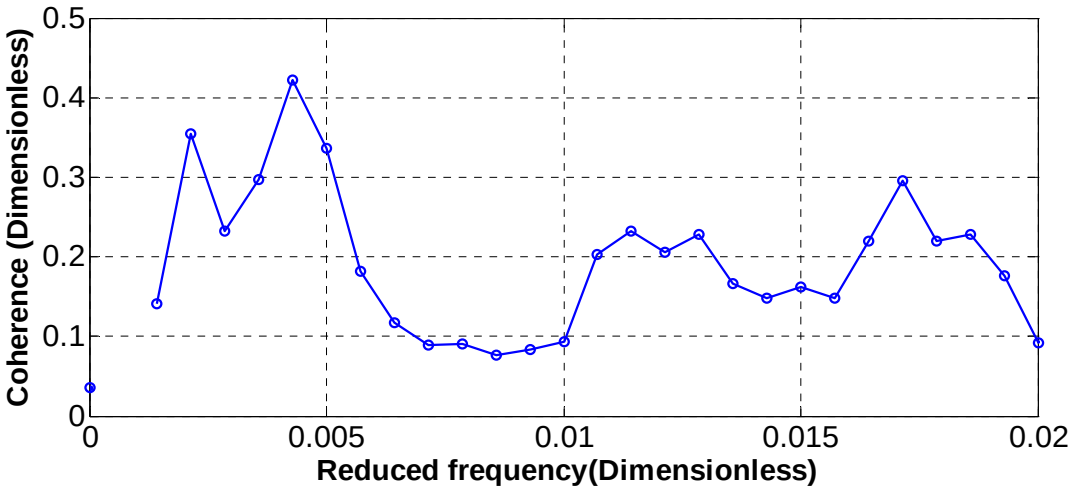

Fig. 10-68 Coherency function of the residuals of $H_1(t)$ and $H_6(t)$ with moving average filtering (*wt1=5s et wt6=30s, t=0-1800s*)(m=700, dt=0.1s)

Compared with the original signal, and phase function (**Fig. 10-69**) for the residual doesn't change very much.

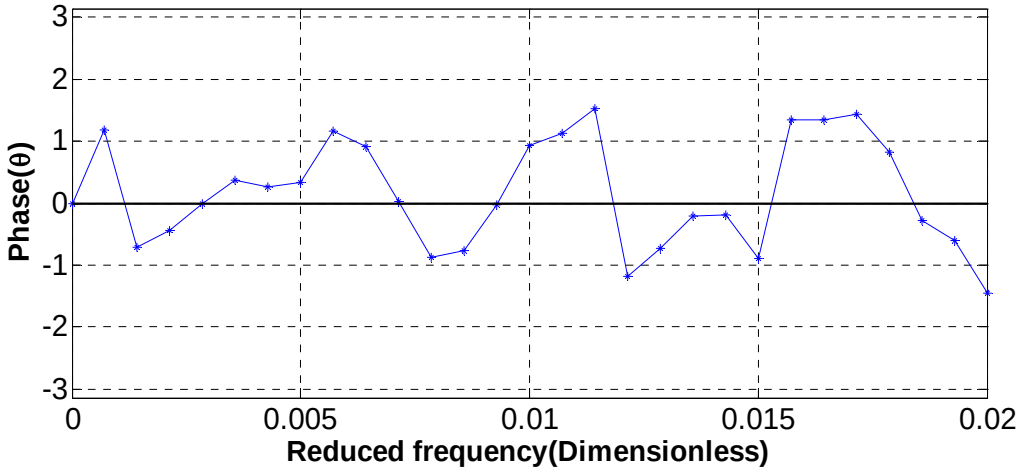

Fig. 10-69 Phase function of the residuals of $H_1(t)$ and $H_6(t)$ with moving average filtering (*wt1=5s et wt6=30s, t=0-1800s*) (m=700, dt=0.1s)

However, from **Fig. 10-70,** it can be seen that the positions and the values of the maximum inter-correlation of the components of the residual between $H_1(t)$ and $H_6(t)$ have changed. The peak C_6 has moved to C_7. The corresponding cross correlation coefficient has decreased to 0.22 from about 3.9. The cross correlation coefficient of C_7 has decreased to 0.42 from 0.48.

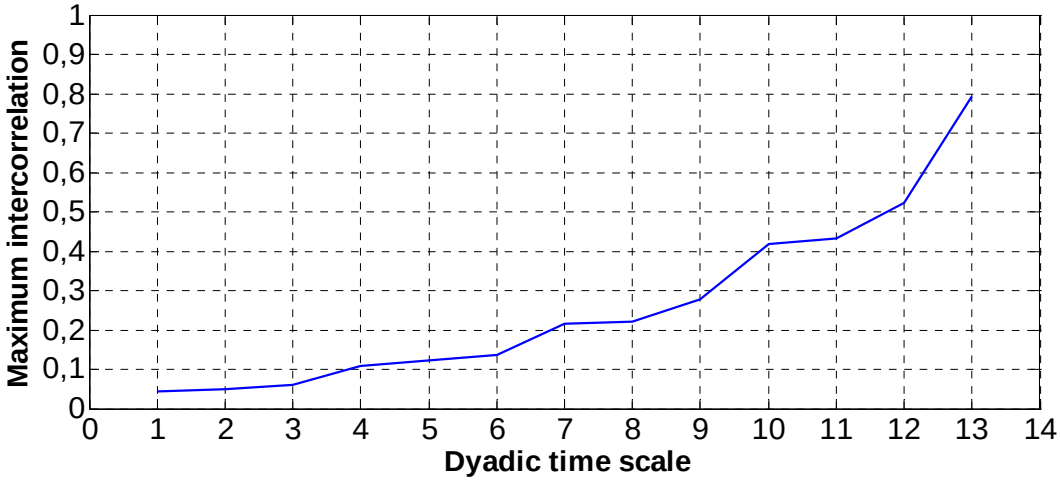

Fig. 10-70 Maximum inter-correlation between the residuals of $H_1(t)$ and $H_6(t)$ with moving average filtering (*wt_1=5s et wt_6=30s, t=0-1800s*) with respect to the dyadic components

10.6.3.2 Cross analysis of the residuals between $H_1(t)$ and $H_6(t)$ with differential filtering

The fluctuation amplitudes of the residuals of both signals are smaller than the ones of the residuals with moving average filtering, as seen in **Fig. 10-71**.

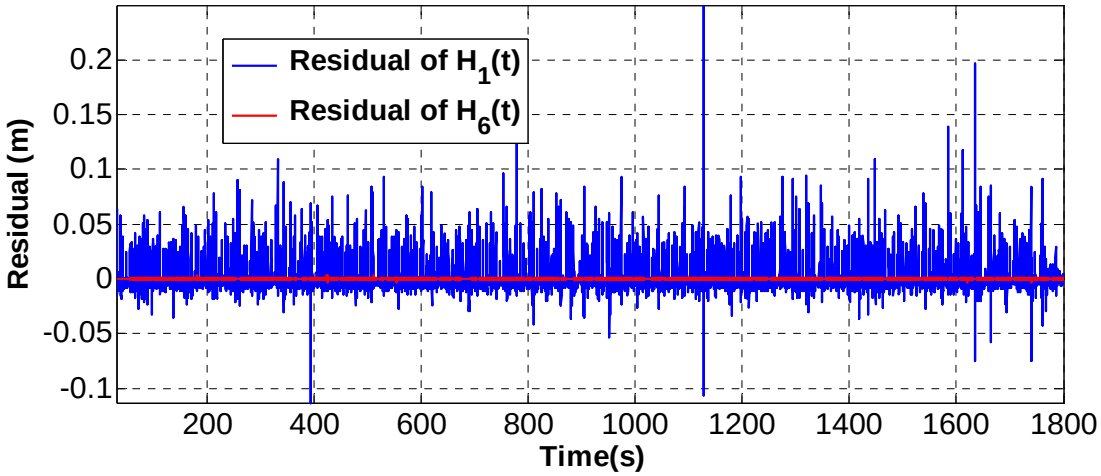

Fig. 10-71 Evolution of the residuals of $H_1(t)$ and $H_6(t)$ with differential filtering

The gain, coherency and phase functions (**Fig. 10-72, Fig. 10-73,** and **Fig. 10-74**), are still very similar to the ones of the residuals between $H_1(t)$ and $H_6(t)$ with moving average filtering. In contrast, the maximum cross correlation of the components between the residuals has been improved, as seen in **Fig. 10-75**. The maximum cross correlation of C_7 has been increased to 0.3, and especially the one of C_{10} has been increased to 0.62, which is also bigger than the one (0.48) of the original signal.

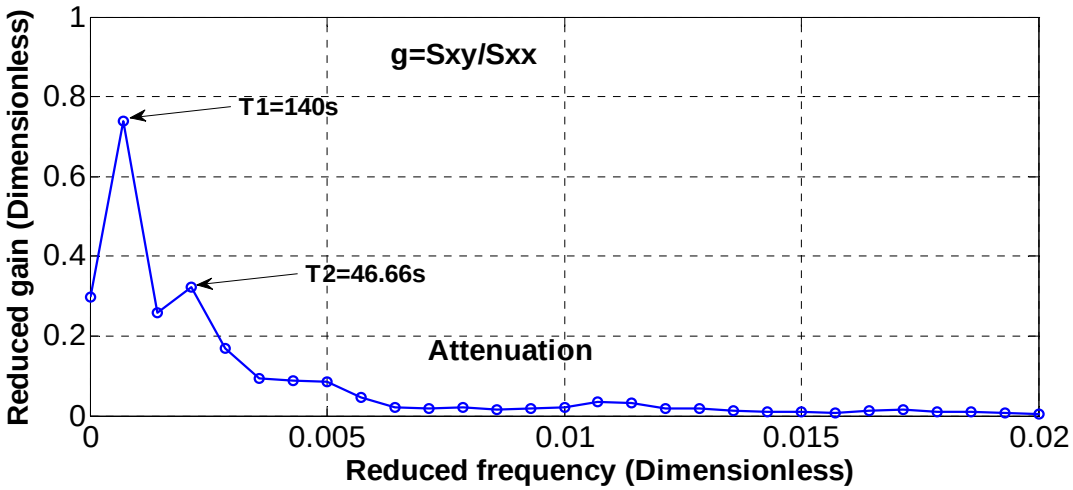

Fig. 10-72 Gain function of the residuals of $H_1(t)$ and $H_6(t)$ with differential filtering (m=700, dt=0.1s)

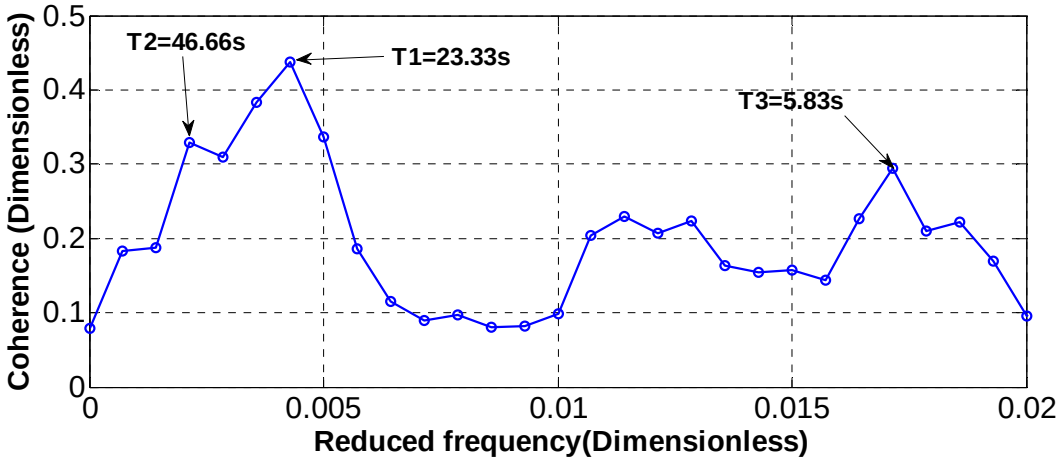

Fig. 10-73 Coherency function of the residuals of $H_1(t)$ and $H_6(t)$ with differential filtering (m=700, dt=0.1s)

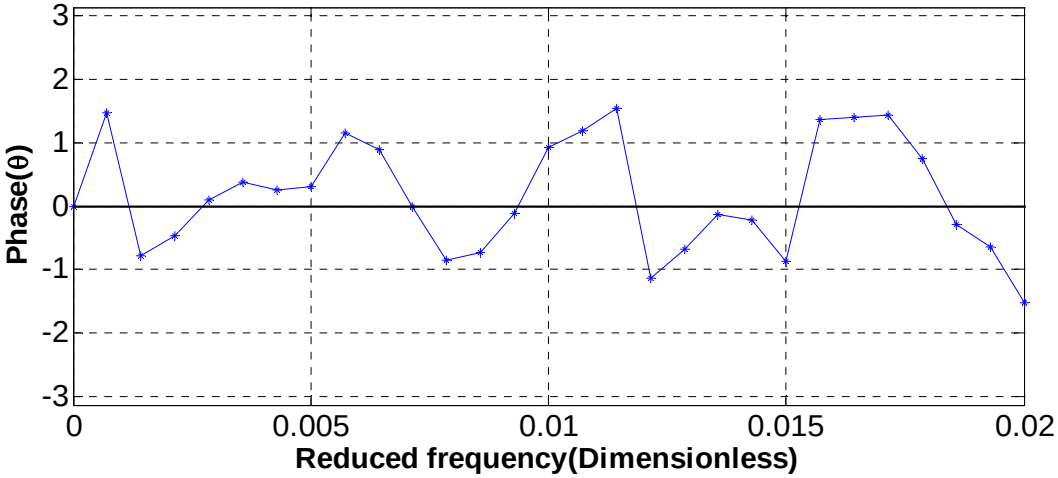

Fig. 10-74 Phase function of the residuals of $H_1(t)$ and $H_6(t)$ with differential filtering (m=700, dt=0.1s)

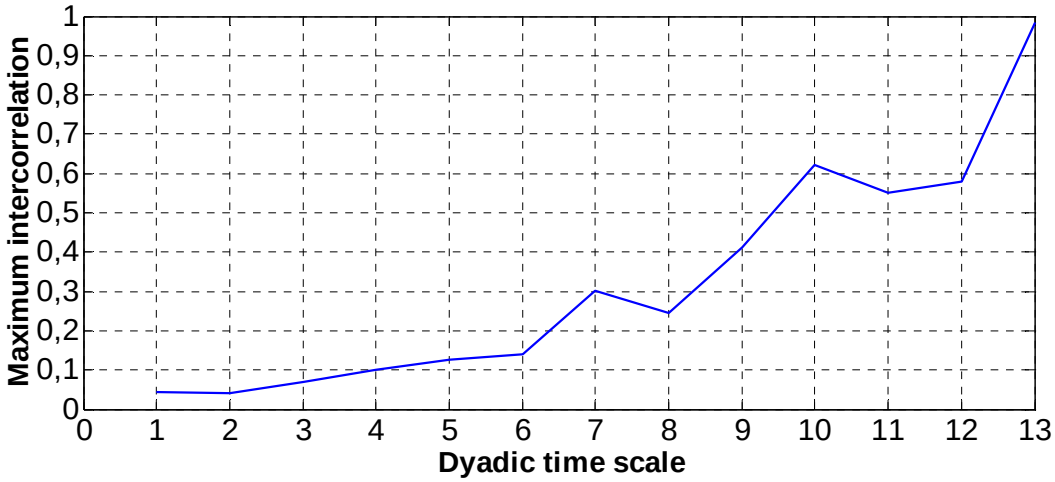

Fig. 10-75 Maximum inter-correlation between the residuals of $H_1(t)$ and $H_6(t)$ with differential filtering with respect to the dyadic time scale

10.6.3.3 Cross analysis of the residuals between $H_1(t)$ and $H_6(t)$ with multi-resolution wavelet filtering

The fluctuation amplitudes of the residual of $\boldsymbol{H_1(t)}$ obtained with multi-resolution wavelet filtering (C_5) are very approximate to the ones of the residual of $\boldsymbol{H_1(t)}$ obtained with moving average filtering (wt_1=5*s*), as seen in **Fig. 10-76**. In contrast, the residual of the $\boldsymbol{H_6(t)}$ obtained with multi-resolution wavelet filtering (C_{10}) is still very irregular.

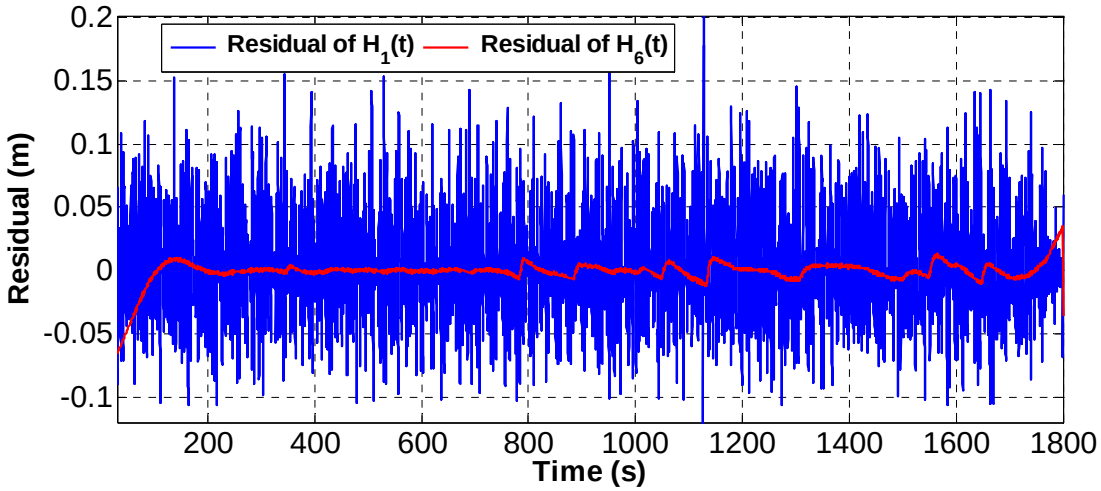

Fig. 10-76 Evolution of the residuals of $H_1(t)$ and $H_6(t)$ with multi-resolution wavelet filtering (C_5 *and* C_{10})

Compared with the residual obtained with the other methods, the gain function (**Fig. 10-77**) shows that there is still a great deal of Fourier spectrum energy decaying. At the same time, there is strong decreasing of the noise, which periods are shorter than 0.5s.

The coherency of the longer periods has obviously improved, as seen in **Fig. 10-78.** The biggest coherency coefficient is about 0.77 for the period T_2=12.73s. However, the coherency of the shorter periods has strongly decreased and most of them are smaller than 0.2.

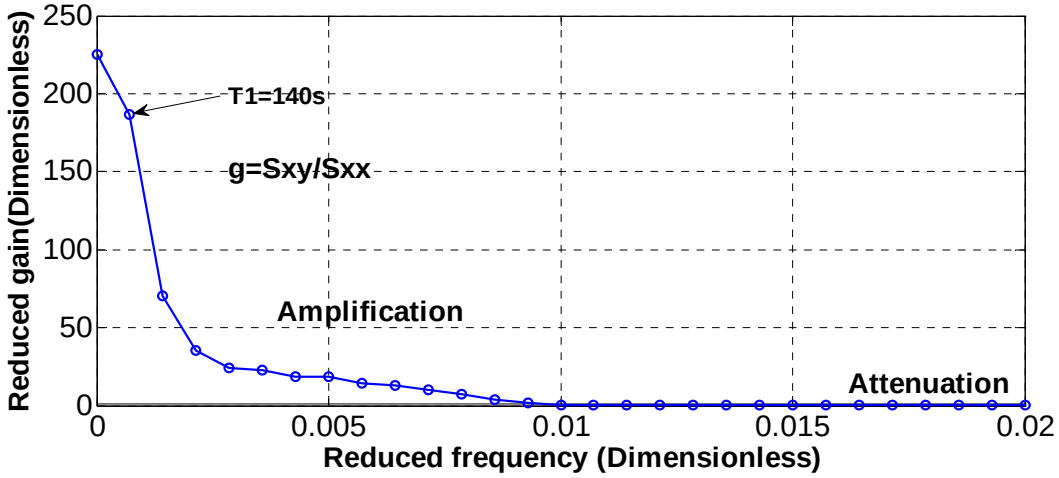

Fig. 10-77 Gain function of the residuals of $H_1(t)$ and $H_6(t)$ with multi-resolution wavelet filtering (C_5 *and* C_{10}) (m=700, dt=0.1s)

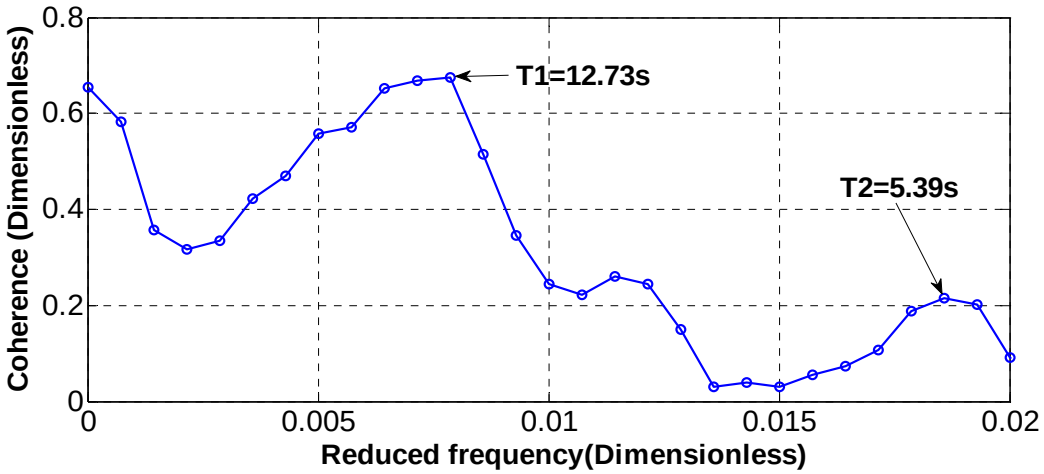

Fig. 10-78 Coherency function of the residuals of $H_1(t)$ and $H_6(t)$ with multi-resolution wavelet filtering (C_5 *and* C_{10}) (m=700, dt=0.1s)

As seen in **Fig. 10-79,** the fluctuations of the phase of the longer periods have decreased. However, the fluctuations of the phase of the shorter periods still vary between $-\pi/2$ and $+\pi/2$.

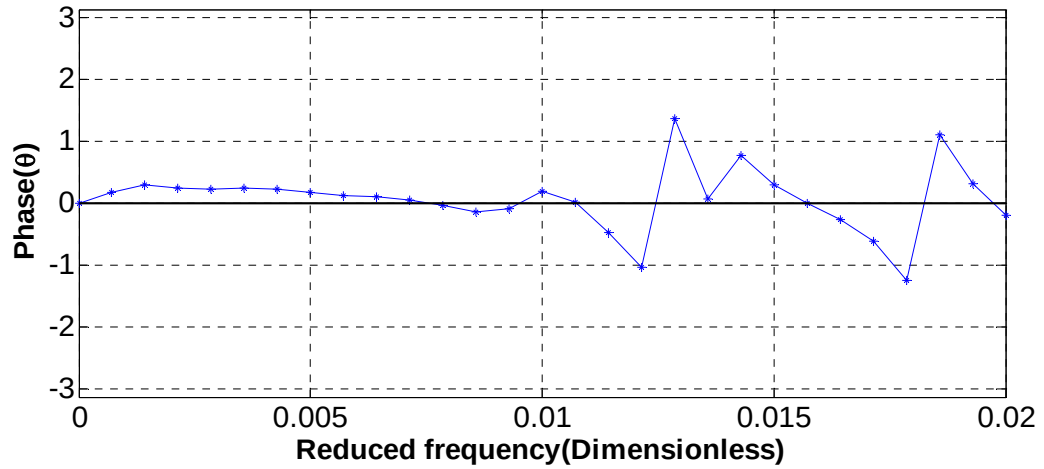

Fig. 10-79 Phase function of the residuals of $H_1(t)$ and $H_6(t)$ with multi-resolution wavelet filtering (C_5 *and* C_{10}) (m=700, dt=0.1s)

In addition, from **Fig. 10-80**, the positions of the two peaks of the maximum inter-correlation have changed, and the corresponding cross correlation coefficients have improved. The position of the first peak comes back to C_6 and the one of the second peak has moved to C_{11}. At the same time, the maximum cross correlation coefficient of the first peak has improved to about 0.52 and the one of the second peak has been improved to about 0.92.

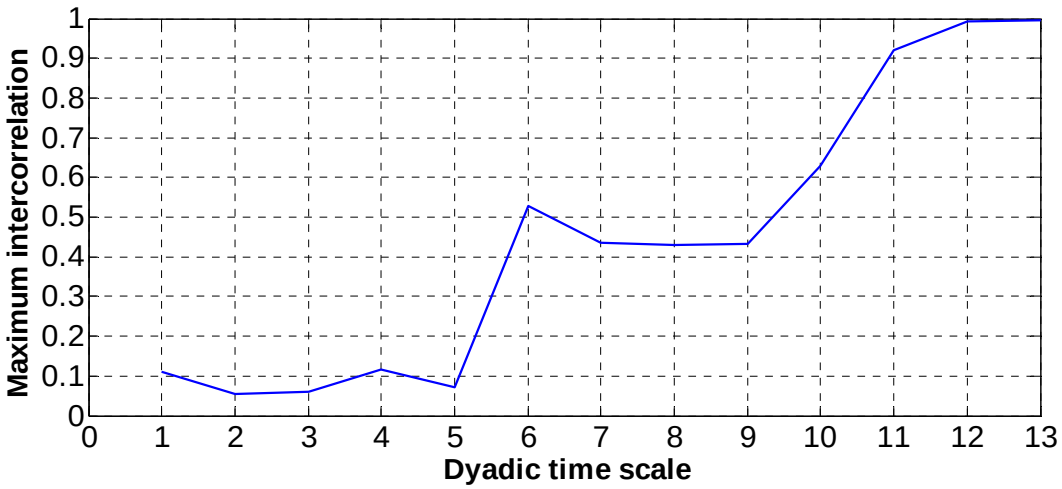

Fig. 10-80 Maximum inter-correlation between the residuals of $H_1(t)$ and $H_6(t)$ with multi-resolution wavelet filtering (C_5 *and* C_{10}) with respect to the dyadic time scale

10.7 Comparison of the wavelet dyadic component C_8 of $H_1(t)$ and $H_6(t)$

10.7.1 Wavelet dyadic component C_8 of the original signal of $H_1(t)$ and $H_6(t)$

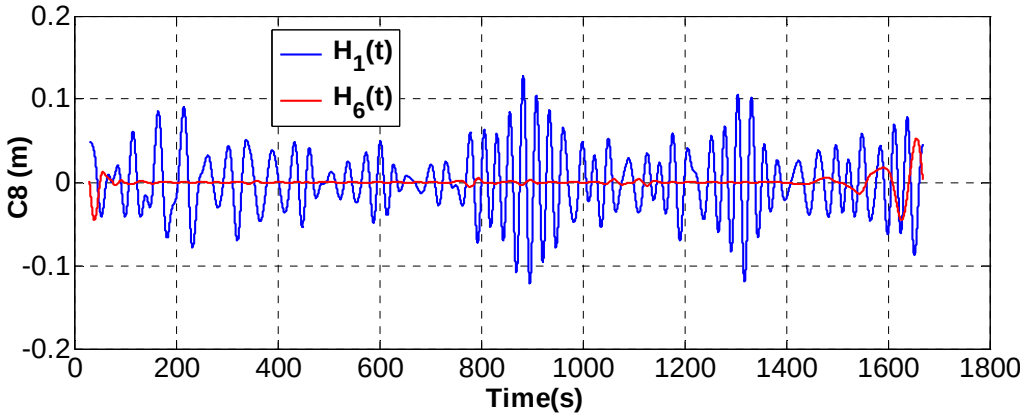

Fig. 10-81 Evolution of wavelet dyadic component $C_8(t)$ of the original signal $H_1(t)$ and $H_6(t)$

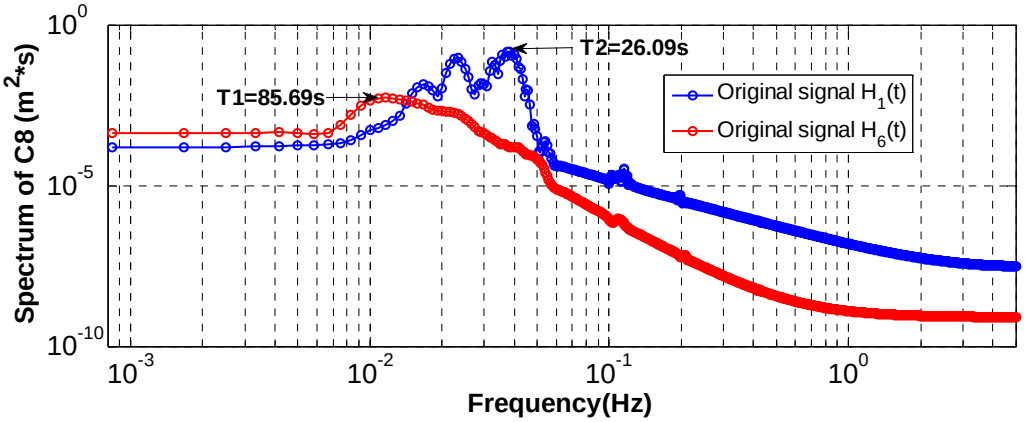

Fig. 10-82 Fourier spectrum of the wavelet dyadic component C8 of the original signal $H_1(t)$ and $H_6(t)$ with respect to the frequency

10.7.2 Wavelet dyadic component C_8 of the residuals of $H_1(t)$ and $H_6(t)$ with moving average filtering

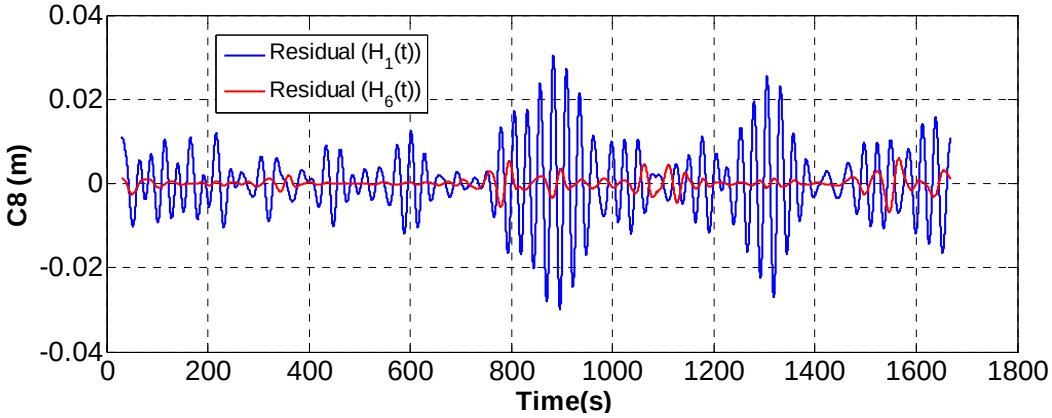

Fig. 10-83 Evolution of the dyadic wavelet component C_8 of the residuals of $H_1(t)$ and $H_6(t)$ with moving average filtering (*wt_1=5s et wt_6=30s, t=0-1800s*)

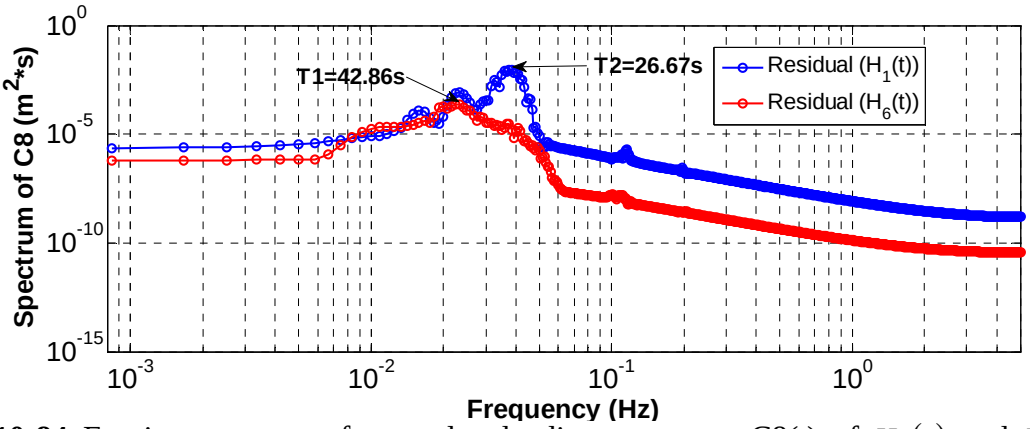

Fig. 10-84 Fourier spectrum of wavelet dyadic component C8(t) of $H_1(t)$ and $H_6(t)$ with moving average filtering (*wt_1=5s et wt_6=30s, t=0-1800s*) with respect to the frequency

10.7.3 Wavelet dyadic component C_8 of the residuals of $H_1(t)$ and $H_6(t)$ with differential filtering

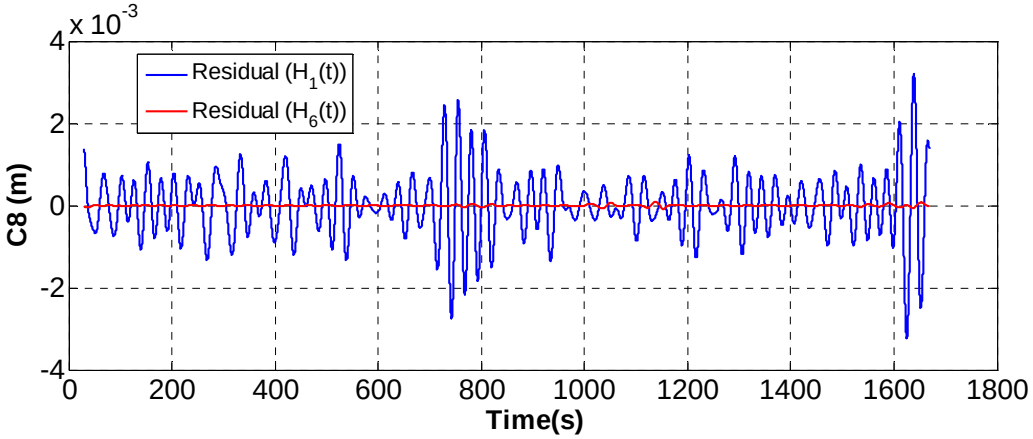

Fig. 10-85 Evolution of the dyadic wavelet component C_8 of the residual of $H_1(t)$ and $H_6(t)$ with differential filtering (*t=0-1800s*)

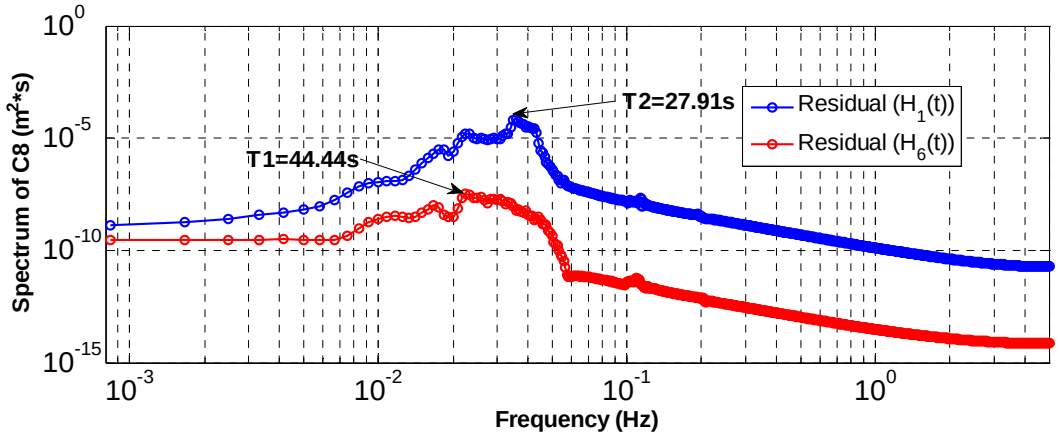

Fig. 10-86 Fourier spectrum with respect to the frequency of wavelet dyadic component $C_8(t)$ of $H_1(t)$ and $H_6(t)$ with differential filtering (*t=0-1800s*)

10.7.4 Wavelet dyadic component C_8 of the residuals of $H_1(t)$ and $H_6(t)$ with multi-resolution wavelet filtering

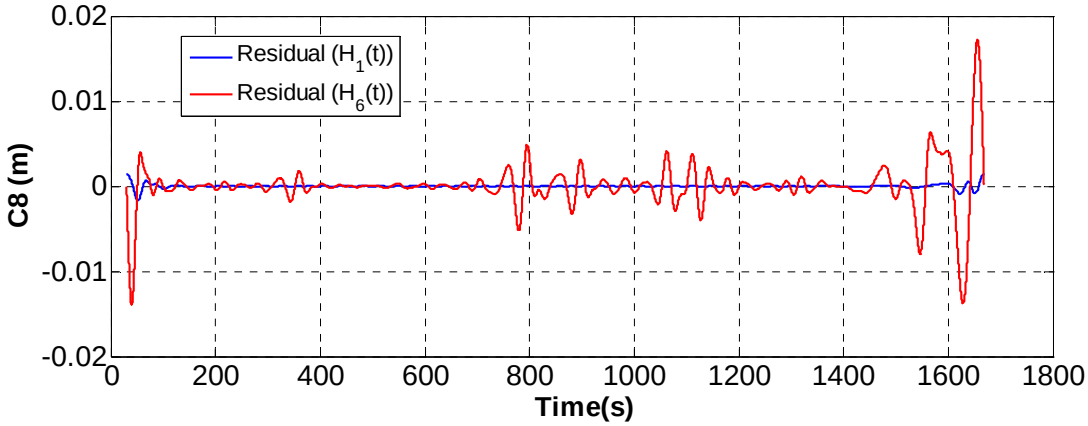

Fig. 10-87 Evolution of the dyadic wavelet component C_8 of the residuals o$H_1(t)$f and $H_6(t)$ with multi-resolution wavelet filtering (C_5 *and* C_{10}, *t=0-1800s*)

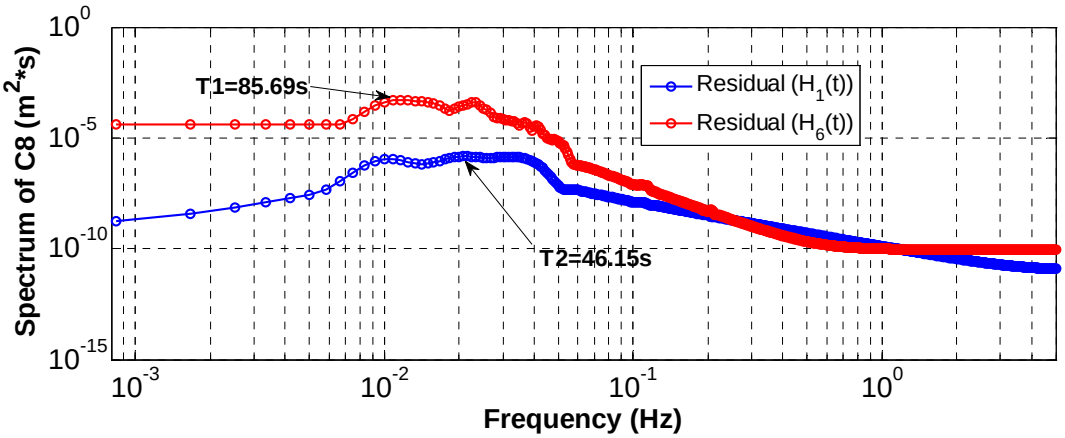

Fig. 10-88 Fourier spectrum of the wavelet dyadic component C8 of the residuals of $H_1(t)$ and $H_6(t)$ with multi-resolution wavelet filtering (C_5 *and* C_{10}, *t=0-1800s*) with respect to the frequency

From the above figures, corresponding to the comparison of the wavelet dyadic component C_8 of the original signal $H_1(t)$ and $H_6(t)$ (**Fig. 10-81),** the residuals with moving average filtering(**Fig. 10-83**), the residuals with differential filtering (**Fig. 10-85**), and the residuals with multi-resolution filtering (**Fig. 10-87**), it is clearly seen that the fluctuation amplitudes of C_8 of $H_1(t)$ are much bigger than the ones of the corresponding signal of $H_6(t)$, except for the residuals obtained with multi-resolution wavelet filtering.

At the same time, the dominant Fourier periods (**Fig. 10-82, Fig. 10-84, Fig. 10-86,** and **Fig. 10-88**) are almost between the two dyadic time scales of C_8 and C_9 for the original signal and the residuals of $H_1(t)$ obtained with three filtering methods. However, for the component C_8 of the original signal and the residuals obtained with multi-resolution, the corresponding Fourier periods are longer than the wavelet dyadic time scale of C_9.

10.8 Conclusion

In this section, the signal processing methods, such as Fourier spectrum analysis, multi-resolution wavelet and temporal analysis, and the three filtering methods (moving average filtering, differential filtering and multi-resolution wavelet) have been used to analyze the measured water fluctuation levels $\boldsymbol{H_1(t)}$and $\boldsymbol{H_6(t)}$. The summaries are flowing:

- **Analysis of $\boldsymbol{H_1(t)}$**

Morlet wavelet spectrum density P(f), the Fourier spectrum density S(f), the multi-resolution wavelet analysis, and temporal analysis of the original signal $\boldsymbol{H_1(t)}$ obtain the same results: the most dominant period of $\boldsymbol{H_1(t)}$ is T≈25s (wavelet dyadic wavelet C_7 and C_8).

In the different residuals of $\boldsymbol{H_1(t)}$, which are respectively obtained with moving average filtering (*window halfwidth* wt=5s), differential filtering, and multi-resolution wavelet filtering, the period T≈4.83s, which is approximate to the one of the wave maker 4s, plays the most dominant role. This result is also respectively obtained with Fourier spectrum analysis, multi-resolution, and temporal analysis.

In addition, the same wavelet dyadic component of the original signal and its residuals obtained with different filtering methods almost has the same Fourier period.

- **Analysis of $\boldsymbol{H_6(t)}$**

The dominant periods of the original signal $H_6(t)$ cannot be obtained with Fourier spectrum analysis and temporal analysis. In contrast, the ones of the residuals with moving average

filtering, differential analysis (k=1) and multi-resolution wavelet filtering can be obtained with Fourier spectrum analysis and temporal analysis (except the residuals with differential filtering). Concerning the multi-resolution wavelet analysis, it is capable to analyze the original signal and the filtered signal. Due to the very small fluctuation amplitudes of the components, it is very difficult to see immediately the dominant components in the figure of the evolution of all the wavelet dyadic components. However, the wavelet dyadic dominant components can be still obtained by watching the evolution of each component alone. Therefore the multi-resolution wavelet analysis is a good tool to analyze the very 'no-stationary' signal such as $H_6(t)$.

In addition, the wavelet dyadic component of the original signal $H_6(t)$ has longer most dominant period and the fluctuation amplitudes than the ones of the filtered signal.

- **Cross analysis between $\boldsymbol{H_1(t)}$ and $\boldsymbol{H_6(t)}$**

Since $H_6(t)$ is very 'no-stationary' and it has total different curve characteristic from $H_1(t)$, the results of the cross analysis of the original signal with Fourier cross analysis show that the two curves have very low cross correlation for the fluctuations of all the periods. At the same time, the component which has the best cross correlation between $H_1(t)$ and $H_6(t)$ can be found through the cross-analysis between the components of the two signals with temporal cross analysis.

The cross correlation of the results can be improved to some extent by doing the cross analysis between the residuals of the two signals. However, the parameters of the filtering methods play a very important role in the results. For instance, compared with the original signal, the coherency coefficients of the residuals obtained with moving average filtering have been improved a little, while the maximum cross correlation coefficients have been decreased; on contrast, the maximum coherency coefficient and the maximum cross-correlation coefficient have been improved for the residual obtained with multi-resolution wavelet.

For the original signal and the residuals of $H_1(t)$, the dominant Fourier period of the wavelet dyadic component is almost between the same dyadic time scale and the next dyadic time scale. In contrast, for the wavelet dyadic component of the original signal and the residuals of $H_6(t)$, its dominant period is longer than the next wavelet dyadic time scale.

Chapter B11: Single harmonic wave numerical experiment for the Barcelona canal (short run)

11.1 Introduction

In order to finally model the Barcelona experiment (**Chapter 7**): oscillations of the water level in a sloping sandy beach with very complex entry water level fluctuations, the first step is to model the oscillations of the water level in the same sloping sandy beach with entry water level fluctuations of one sinusoidal wave, the most single entry condition. In this chapter, we use VGM model to simulate the wave propagation in the sloping sandy beach with entry water level fluctuation of one single harmonic wave.

11.2 Simulation domain

Vertical 2D: L_x=10m; L_z=0.80m;

dx=0.02m ; dz=0.02m.

The sand beach slope is 1/15. The schema of the simulation geometry domain is shown in **Fig. 7-1**.

11.3 Boundary and initial conditions

- **Boundary condition**

Right boundary (all the other boundaries): flux=0.0. (Impermeable wall)

Left boundary: $H(0,t) = H_0 + A_0 \cdot sin\left(\frac{2\pi}{T}t\right)$ with $(H_0 = 0.40m,\ A_0 = 0.40m,\ A_0/H_0 = 1,\ T=30s)$, as shown in **Fig. 11-1**.

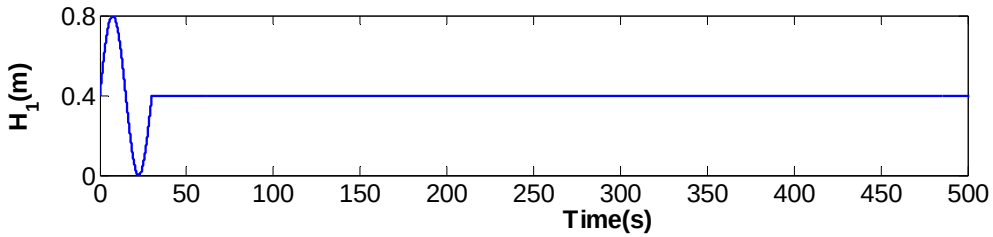

Fig. 11-1 Left regular entry water level fluctuations for one wave numerical test

- **Initial condition**

$H_0 = 0.40m$, $h_0 = H_0 - z$ (linear distribution)

11.3 Physical properties of the beach sands and the sea water

All the physical properties for the micro porous media and the macro media are listed in **Table 11-1.**

Table 11-1 Physical properties of the macro porous media and the micro porous media

Porous media	Physical properties								
	Hydraulic conductivity			Water content (m^3/m^3)		VGN model		Capillary length	Simulated time
	K_S (m/s)	$\frac{K_{s\_Macro}}{K_{s\_Micro\_}}$	K_r (m/s)	θ_s	θ_r	α (m^{-1})	n	λ_{cap} (cm)	
Micro porous media	0.05	1E+04	1.0E-7	0.38	0.0	5.0	1.5	20.00	t=500s
Macro porous media	500.0		1.0E-7	1	0.0	100.0	3.0	1.00	

The water content curve $\theta(h)$ in log-log and the hydraulic conductivity curve $K(h)$ in log-log of the two media are respectively shown in **Fig. 11-2** and **Fig. 11-3.**

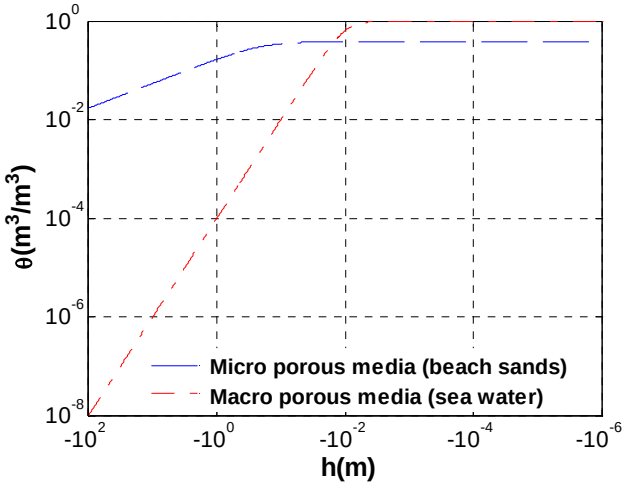

Fig. 11-2 Water content curve $\theta(h)$ in log-log of the micro porous media and the macro porous media

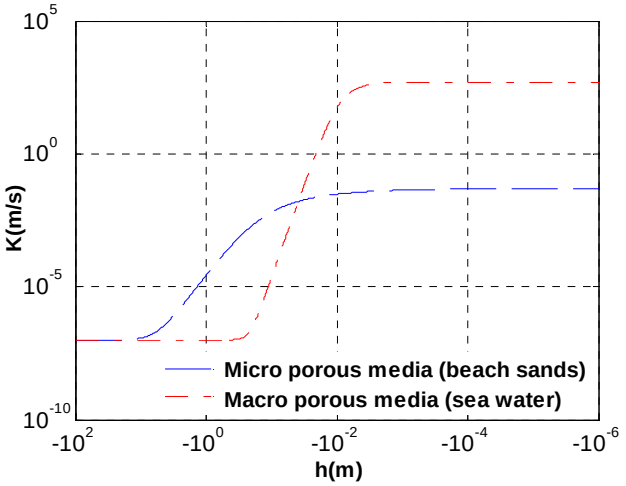

Fig. 11-3 Hydraulic conductivity curve $K(h)$ in log-log of the micro porous media and the macro porous media

From these two figures, it can be seen that the slopes of $\theta(h)$ and $K(h)$ of the macro porous medium (sea) are much more rapid than those of the micro porous medium (sloping sandy beach).

11.4 Duration of the simulation and numerical parameters

The simulated time is 500s.

The numerical caculation time parameters and the numerical criteria are listed in the **Table 7-3.**

11.5 Numerical behaviour of Bigflow during the simulation

The linear and nonlinear iteration process of the pressure head are respectively shown in **Fig. 11-4** and **Fig. 11-5**.

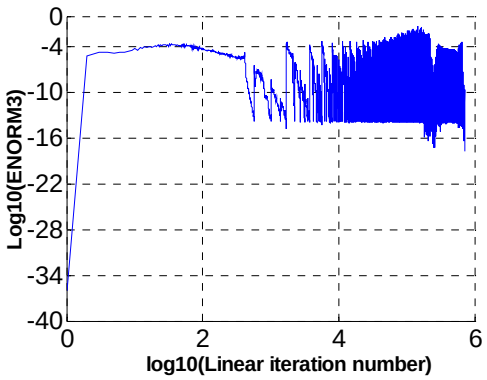

Fig. 11-4 Standarlized linear iteration process of the pressure head in log10

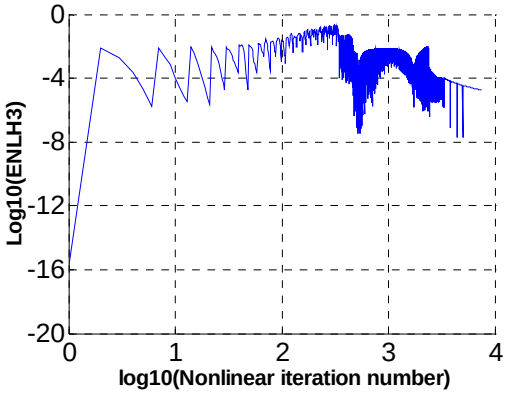

Fig. 11-5 Standarlized nolinear iteration process of the pressure head in log10

It can be seen that the minimum linear and nonlinear iteration errors are respectively about 1.0E-16 and 1.0E-8. Q_{Bound}, Q_{Mass}, V_{Bound} and V_{Mass} are obviously affected by the sine wave water levels on the left boudary. Their shapes are the same as the sinusoidal wave boudary water levels. These numerical behaviours are respectively shown in **Fig. 11-6,** and **Fig. 11-7.**

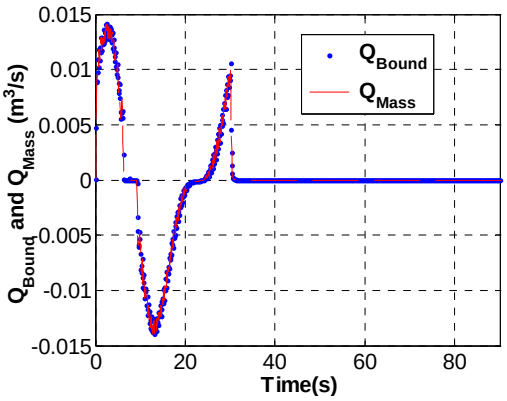

Fig. 11-6 Zoom of the evolution of Q_{Bound} and Q_{Mass} at t=0-90s

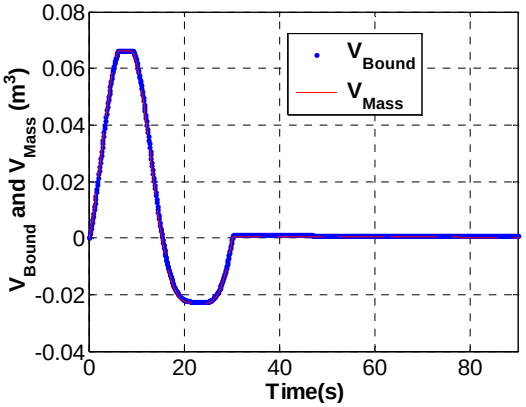

Fig. 11-7 Zoom of the evolution of V_{Bound} and V_{Mass} at t=0-90s

Note: The print time of the Head_Tx file has an influence on the evolution of Q_{Bound} and Q_{Mass}. This plot is the results of the simulation without the output file Head_Tx.

From the two figures, it can be seen that the curves of the evolution of Q_{Bound} and Q_{Mass}, completely superimpose together, and there exists the similar case for the curves of the evolution of V_{Bound} and V_{Mass}.

11.6 Result analysis of the one single harmonic wave test

11.6.1 Profiles of the pressure head contour and the flux velocity field

The profiles of the pressure head contour and the flux velocity field at t=T/8=3.75s, t=3T/8=11.25s, t=5T/8=18.75s and t=7T/8=26.25s are respectively shown in **Fig. 11-8**, **Fig. 11-9, Fig. 11-10** and **Fig. 11-11.**

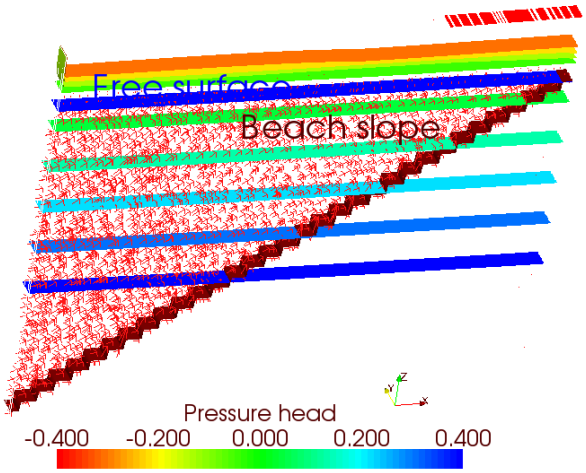

Fig. 11-8 Profile of the pressure head contours and flux velocity at t=T/8=3.75s (length scales in z and in y are respectively 10)

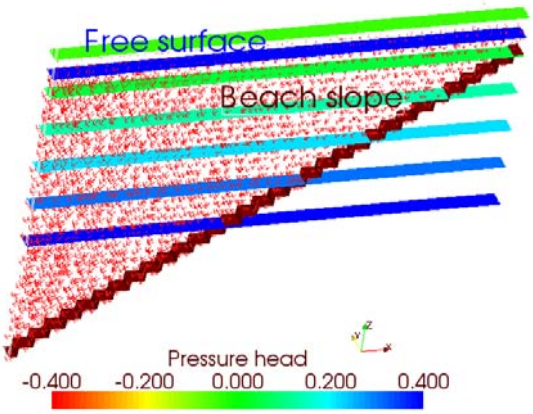

Fig. 11-9 Profile of the pressure head contours and flux velocity at t=3T/8=11.25s (length scales in z and in y are respectively 10)

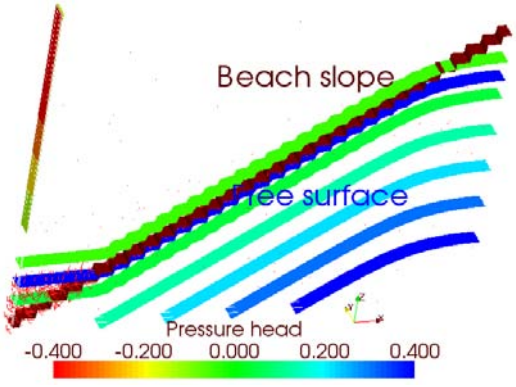

Fig. 11-10 Profile of the pressure head contours, and flux velocity at t=5T/8=18.75s (length scales in z and in y are respectively 10)

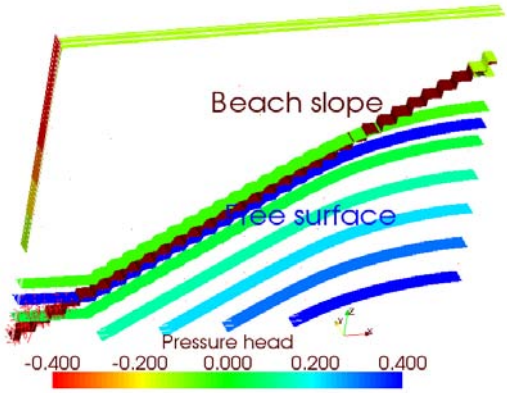

Fig. 11-11 Profile of the pressure head contours and flux velocity at t=7T/8=26.25s (length scales in z and in y are respectively 10)

When t=T/8=3.75s, the left boundary water level has just increased by 50% amplitude from the mean water level to the maximum (**Fig. 11-1**), at the same time, the water levels in the macro porous media rise with the same velocity of the boundary water level, while the ones in

the micro porous media increase much slower, and therefore, the flux flows upwards along the beach slope (as seen in **Fig. 11-8**).

When t=3T/8=11.25s, the left boundary water level has just descended by 50% amplitude from the maximum to the mean water level (**Fig. 11-1**), at the same time, the water levels in the macro porous media go down with the same velocity of the boundary water level, while the ones in the micro porous media go down much slower and as a result, the flux flows downwards along the beach slope (as seen in **Fig. 11-9**).

When t=5T/8=18.75s, the left boundary water level has continued to descend by 50% amplitude from the mean water level to the minimum (**Fig. 11-1**), at the same time, the water levels in the macro porous media go down with the same velocity of the boundary water level, while all the water levels in the macro porous media are higher than the ones in the macro porous media, and as a consequence, the flux flows downwards along the beach slope (seen in **Fig. 11-10**).

When t=7T/8=26.25s, the left boundary water level has gone up by 50% amplitude from the minimum to the mean water level (**Fig. 11-1**), at the same time, the water levels in the macro porous media go up with the same velocity of the boundary water level, although the part of the water levels in the micro porous media are still higher than the ones in the macro media , and as a consequence, the flux flows upwards along the beach slope (as seen in **Fig. 11-11**).

In addition, the sloping sandy beach, the flux is very small for all time.

11.6.2 Instantaneous water content distribution θ(h) in the vertical section

The instantaneous distributions of the water content $\theta(h)$ in the vertical section at t=T/8=3.75s, t=3T/8=11.25s, t=5T/8=18.75s and t=7T/8=26.25s are respectively shown in **Fig. 11-12**, **Fig. 11-13, Fig. 11-14** and **Fig. 11-15.**

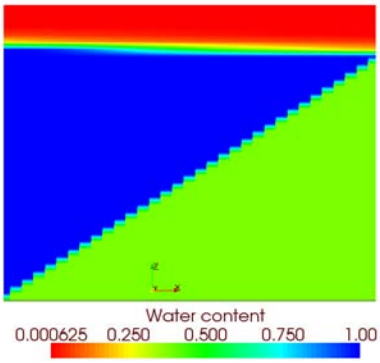

Fig. 11-12 Instantaneous profile of the water content $\theta(h)$ at t=T/8=3.75s in the vertical section (length scales in z and in y are respectively 10)

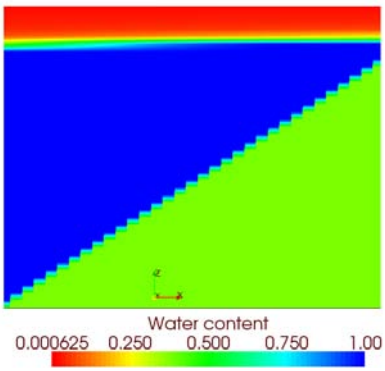

Fig. 11-13 Instantaneous profile of the water content $\theta(h)$ at t=3T/8=11.25s in the vertical section (length scales in z and in y are respectively 10)

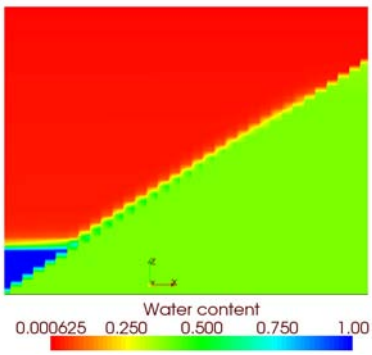

Fig. 11-14 Instantaneous profile of the water content $\theta(h)$ at t=5T/8=18.75s in the vertical section (length scales in z and in y are respectively 10)

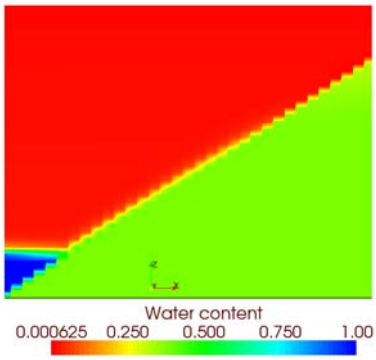

Fig. 11-15 Instantaneous profile of the water content $\theta(h)$ at t=7T/8=26.25s in the vertical section (length scales in z and in y are respectively 10)

They all correspond with the pressure head contour at the same time (**Fig. 11-8**, **Fig. 11-9**, **Fig. 11-10** and **Fig. 11-11**).

11.6.3 Water levels H(x,t) and pressure head h(x,z=0,t)

In this numerical simulation, the flow in the saturated zone is a quasi horizontal plane flow and therefore, the pressure head $h(x, z = 0, t)$ is approximate to the height of water table. This can be validated from two aspects: (1) if the pressure head $h(x = x_0, z, t)$ has a hydraulic linear distribution; (2) if $h(x, z = 0, t_0) = H(x, t_0)$. **Fig. 11-16** shows the profiles of the instantaneous pressure head $h(x = x_0, z, t)$ at $x_0 = 1.5$m and it indicates that, in the saturated zone or when $h(x = 1.5m, z, t) \geq 0$, $h(x = 1.5m, z, t) = z$ and it is hydraulic linear distribution. In addition, the pressure head profiles $h(x, z = 0, t_0)$ at $t_0 = T/4$ and $t_0 = 3T/4$ are illustrated in **Fig. 11-17**, and they respectively superpose on the instantaneous water level profile $H(x, t_0 = T/4)$ and $H(x, t_0 = 3T/4)$, as seen in **Fig. 11-18**.

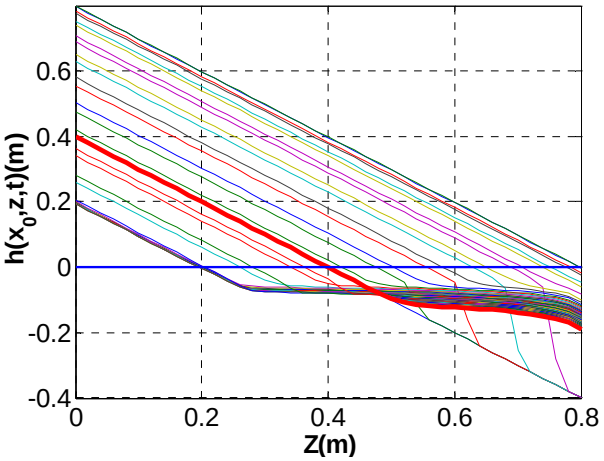

Fig. 11-16 Profiles of the pressure head evolution in the z direction at x=1.5m

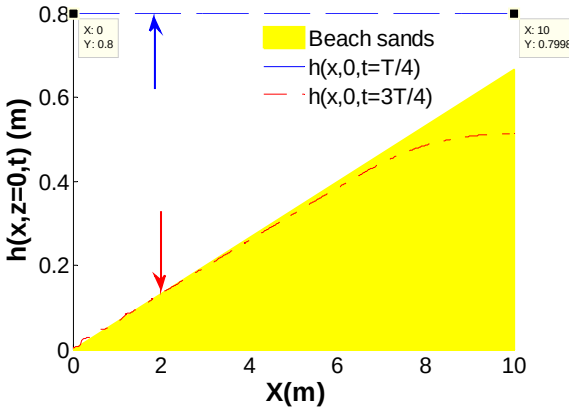

Fig. 11-17 Pressure head h(x,0,t) at t=T/4 and t=3T/4 obtained by the file OUTHPB

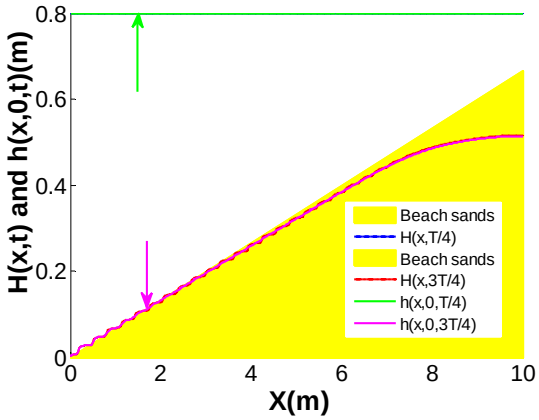

Fig. 11-18 Comparison of the pressure head h(x,0,t) and the free surface h(x,z,t)=0.0 at t=T/4 and t=3T/4

As a result, all the water levels $H(x,t)$ obtained in the numerical simulations for the modeling of the Barcelona experiment are obtained by probing the pressure head $h(x,z=0,t)$ in the file OUTHPB (a output file of BigFlow), except for the pressure head contours.

11.6.4 Evolution of the water level fluctuations in time and space

Profiles of the evolution of the horizontal line pressure head at z=0 or free surface (time interval=10dt=1.0s) are shown in **Fig. 11-19.**

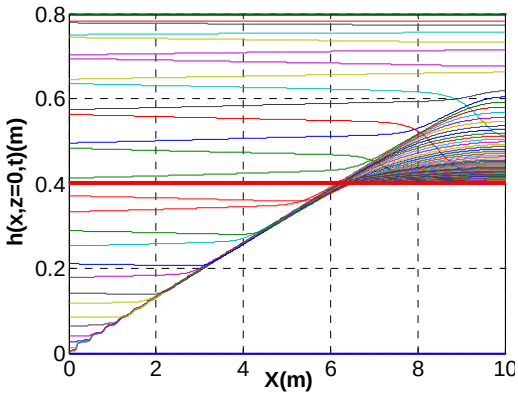

Fig. 11-19 Profile of the evolution of the horizontal line pressure head at z=0 $h(x,z=0,t)$ or the water level fluctuations $H(x,t)$ (time interval=10 dt=1.0s)

From this figure**,** it can be seen that all the movement area of the free surface in the two porous media during the simulation is the macro porous domain and the top part over the mean water level of the micro porous media domain. That is to say, even in the case when the left boundary water level goes down to the minimum water level H_0=0, the water level in the porous media is still higher than the mean water level in the simulation.

In order to observe the curve shape of the water level evolution at several different positions H(x0,t) in the porous media, 7 sensors are installed in the beach bottom, which have the same horizontal distances with the ones of the experiment in Barcelona. The evolution of the pressure head of the 7 sensors $h(x, z = 0, t)$ and its zooms, are respectively shown in **Fig. 11-20**, **Fig. 11-21** and **Fig. 11-22**.

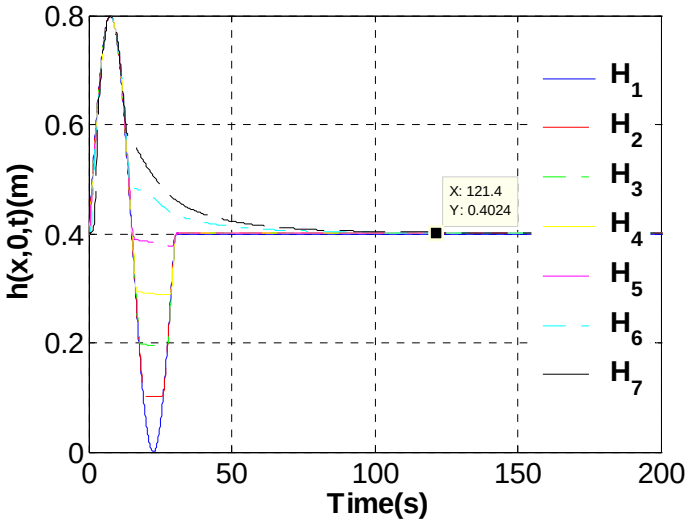

Fig. 11-20 Evolution of the approximate water levels of the 7 sensors at t=0-200s.

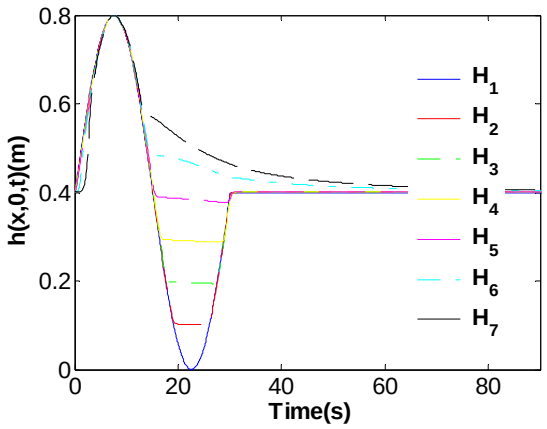

Fig. 11-21 Zoom of the evolution of the water levels of the 7 sensors at t=0-90s (t=0-3T).

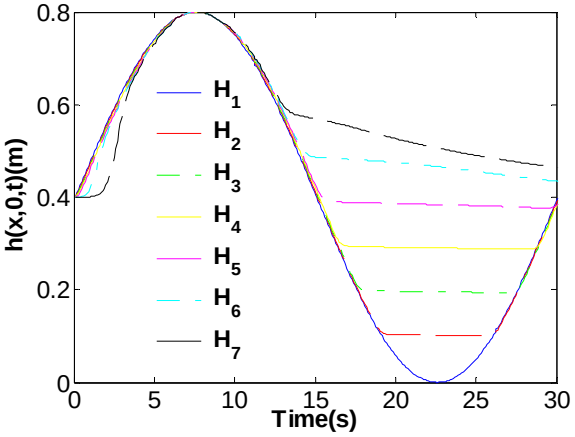

Fig. 11-22 Zoom of the evolution of the water levels of the 7 sensors at t=0-30s (t=0-T).

From these figures, it can be seen that all the front half-waves have the sine wave shape, except for a small delay of the propagation time for the sensor No.7; at the same time, the rear half-waves have different shapes according to the position in the porous media and they have an obvious amplitude decay. It means that the velocity of the water table going down is slower than the one going up in the porous media. In this numerical test, after the first half-wave, for the water levels of Sensors No.2, No.3, No.4 and No.5, the water table in the micro porous media has not descent to the minimum value, and due to the rising of the boundary

water level, it has to go up again; for the water levels of Sensors No.6 and No.7, just in the beginning of the descending, the water table is affected by the left oscillatory boundary water level, and then it goes down until the mean water level at t≈179s without the influence of the oscillatory water level.

In general, the water levels in the macro porous media rise and descend with the same velocity as the boundary water level, and the velocity of the water table when going down is slower than when going up in the porous media.

11.7 Analysis on the system energy balance during the numerical simulation

In order to analyze the energy changes of the system, the evolutions of Q_{Bound}, the left entry water level $H_1(t)$, and the inside water levels on the 7 sensors are plotted in the same figure in **Fig. 11-23**.

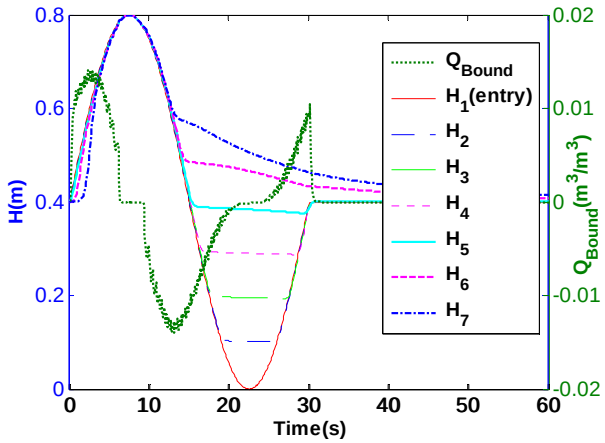

Fig. 11-23 Evolution of the entry water level, Q_{Bound} and the inside water levels in the porous media

From this figure, it can be seen that before the entry water level increases to the maximum, the water flow in the left side enters into the simulated domain. And especially when entry water level rises to about 150% of the mean water level, the Q_{Bound} reaches the maximum, and then decreases gradually to zero when the entry water level rises to the maximum water level. After the maximum entry water level, there is a zero ladder for Q_{Bound} because of the influence of the top wall, on which the boundary flux is 0. Then with the descending of the entry water level, the flow on the left side begins to flow out of the simulated domain until the entry water level descends to the minimum. The same case produces when the entry water level descends to the height of 50% H_0, the velocity for the flow going out reaches the maximum. And when entry water level descends to the minimum, there is another zero ladder

for Q_{Bound}, because of the bottom wall, on which the flux is zero. Then with the increasing of the entry water level, the flow begins to flow into the simulated domain again. When the entry water level rises the mean water level and then keeps this level, the Q_{Bound} quickly descends to zero.

The inside water levels are mainly influenced by the entry water level and its positions in the micro porous media. From **Fig. 11-23,** it can be seen that during the first increasing of the entry water level, there is a different delay for the water levels on the sensor No.7 and the sensor No.6 (when their water levels are less than the height of the porous media, and there is no delay for the other sensors whose water levels are always higher than the height of the micro porous media); during the descending of the entry water level, each water level decreases obviously more slower than the entry water level when it reaches the height of the micro porous media; then with the increasing again of the entry water level, each water level of the inside 5 sensors, whose water level are lower than the mean water level, rises with the entry water level until the mean water level; for the sensor No.6 and No.7, their water levels are higher than the mean water level and this increasing of the entry water level has no influence on them, and they descend slowly until the mean water level.

The mean entry water level gradient $\overline{\frac{\partial H_1(t)}{\partial x}}$ can be obtained from the $Q_{Bound}(t)(m^3/s)$ calculation and $q_{Bound}(t)(m/s)$ and its deduction is as follows:

$$Q_{Bound}(t)(m^3/s) = -L_Y \int_{z=0}^{z=L_z} K\big(h(0,z,t)\big) \times \frac{\partial h(0,z,t)}{\partial x} dz \tag{11-1}$$

$$q_{Bound}(t)(m/s) = \frac{Q_{BOUND}}{A_{Face1}} = -\frac{1}{L_Z} \int_{z=0}^{z=L_z} K\big(h(0,z,t)\big) \times \frac{\partial h(0,z,t)}{\partial x} dz \approx -\frac{1}{L_Z} K_S \times$$

$$H_1(t) \times \overline{\frac{\partial H_1(t)}{\partial x}} \tag{11-2}$$

$$\overline{\frac{\partial H_1(t)}{\partial x}} \approx -\frac{q_{BOUND}(t)}{\frac{1}{L_Z} \times K_S \times H_1(t)} \tag{11-3}$$

where, L_Z—the height of the simulated domain in z direction;

L_Y—the width of the simulated domain in y direction;

h—pressure head;

H—water level;

K—hydraulic conductivity;

$Q_{Bound}(t)$—boundary discharge(m^3/s);

q_{Bound}—boundary flux (m/s)or boundary unity discharge;

A_{Face1}—area of the entry water level boundary face;

$\overline{\frac{\partial H_1(t)}{\partial x}}$—water level gradient on the left boundary with respect to x.

The mean entry water level gradient $\overline{\frac{\partial H_1(t)}{\partial x}}$ (equation (11-3)) is plotted in **Fig. 11-24.**

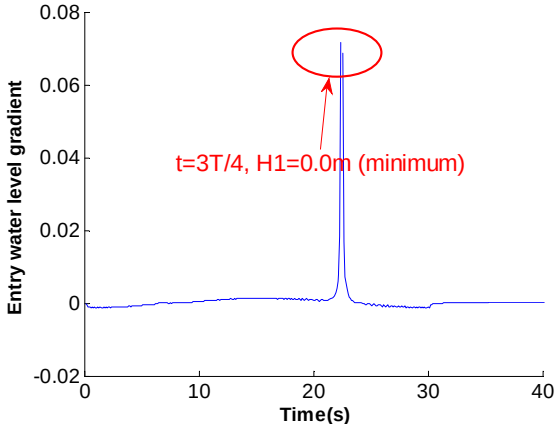

Fig. 11-24 Evolution of the mean entry water level gradient $\overline{\frac{\partial H_1(t)}{\partial x}}$

From this figure, it can be seen that, the mean entry water level gradient fluctuates with the entry water level and generally they have the small values, except when the entry water level arrived at the minimum value zero, it is positively infinite.

11.8 Conclusion on one single harmonic wave test

When the ratio of the saturated hydraulic conductivity is equal to 10000, Bigflow code is able to model the coupling between the micro porous media and macro porous media. It means that the entry oscillatory water levels can be directly put on the beach slope without the water level loss.

The one sinusoidal wave numerical test with VGM model works very well. Its results very clearly show the response process of a beach system under the oscillatory water level condition at the left boundary.

When the left boundary water level rises or descends, the ones in the sea (macro porous media) correspondingly rise or descend with the same velocity, while the water levels in the beach responds much more slowly, depending on the parameters of the sands.

The maximum water level in the porous media depends very much on the position of the right boundary. The shorter the horizontal distance of the beach is, the higher water level will be obtained in the beach. The increasing process of the water level in the beach is clearly shown in the animation obtained with the numerical results.

It is worth noted that, in this numerical simulation, the flow in the saturated zone is a quasi horizontal plane flow, which is validated and therefore the pressure head $h(x, z = 0, t)$ is approximate to the height of the water table. As a result, all the water levels $H(x, t)$ obtained by the numerical simulations for the modeling of the Barcelona experiment can be obtained by probing the pressure head $h(x, z = 0, t)$ in the file OUTHPB, except for the pressure head contours.

In addition, the left entry water level has the lag time of about T/4 to the left entry discharge $Q_{Bound}(t)$. At the same time, the entry water level gradient with respect to x is equal to infinite when $H_1(3T/4)$ =0.

Chapter B12: Single harmonic wave numerical experiment for the Barcelona experiment (long run)

12.1 Introduction

In order to finally model the Barcelona experiment (**Chapter 7**): oscillations of the water level in a sloping sandy beach with very complex entry water level fluctuations, the second step is to model the oscillations of the water level in the same sloping sandy beach with an entry water level fluctuations made of the several continuous sinusoidal waves. In this chapter, we use the VGM model to simulate the wave propagation in the sloping sandy beach with an entry water level fluctuation of several single harmonic waves.

12.2 Simulation domain

Vertical 2D: L_x=10m; L_z=0.80m;

dx=0.02m ; dz=0.02m.

The schema of the simulation geometry domain is same as one single harmonic numerical experiment with one period (short run) (**Fig. 7-1)..**

12.3 Boundary and initial condition

- **Boundary condition**

Left boundary: $H(0,t) = H_0 + A_0 \cdot sin\left(\frac{2\pi}{T}t\right)$ witrh ($H_0 = 0.20m$, $A_0 = 0.10m$, $A_0/H_0 = 0.5$, T=30s), as shown in **Fig. 12-1.**

Right boundary (all the other boundaries): flux=0. (Impermeable wall).

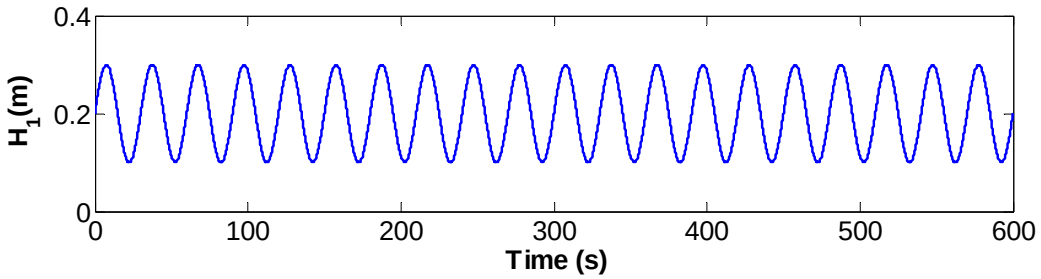

Fig. 12-1 Left regular entry water level fluctuations with several continuous waves

- **Initial condition**

$H_0 = 0.20m$, $h_0 = H_0 - z$ (linear distribution)

12.3 Physical properties of the sand beach and the sea water

All the physical properties of the micro porous media and the macro media are the same as one single harmonic numerical experiment with one period (short run, Appendix B: **Chapter 11**), which are listed in **Table 11-1.** The water content curve $\theta(h)$ in log-log and the hydraulic conductivity curve $K(h)$ in log-log for the two media are respectively shown in **Fig. 11-2** and **Fig. 11-3** in the previous chapter**.**

12.4 Duration of the simulation and numerical parameters

The simulated time is 600s which corresponds to 20T.

The numerical caculation time parameters and the numerical criteria are also same as short run wave test in the prevous chapter, which are listed in **Table 7-3.**

12.5 Numerical behaviour of Bigflow during the simulation

The evolutions of the linear iteration, nonlinear iteration criteria of the pressure head, Q_{Bound}, Q_{Mass}, V_{Bound} and V_{Mass} are obviously affected by the sine wave water levels on the left boudary. Their shapes are the same as the sine wave boudary water levels. These numerical behaviours are respectively shown in **Fig. 12-2, Fig. 12-3, Fig. 12-4,** and **Fig. 12-5.**

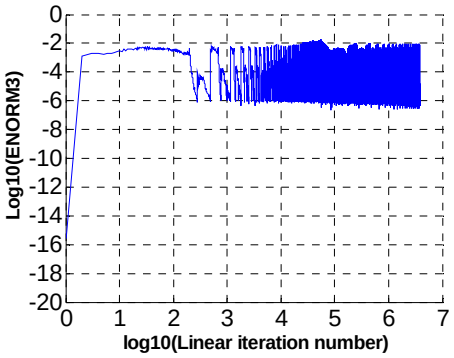

Fig. 12-2 Standarlized linear iteration process of the pressure head in log10

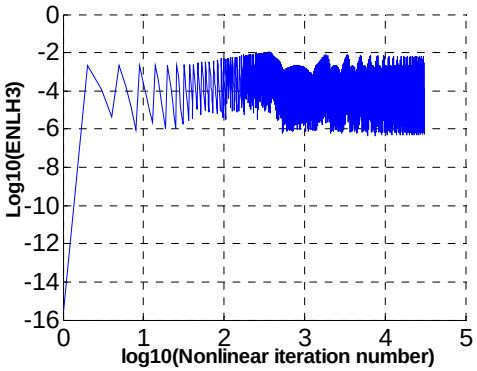

Fig. 12-3 Standarlized nolinear iteration process of the pressure head in log10

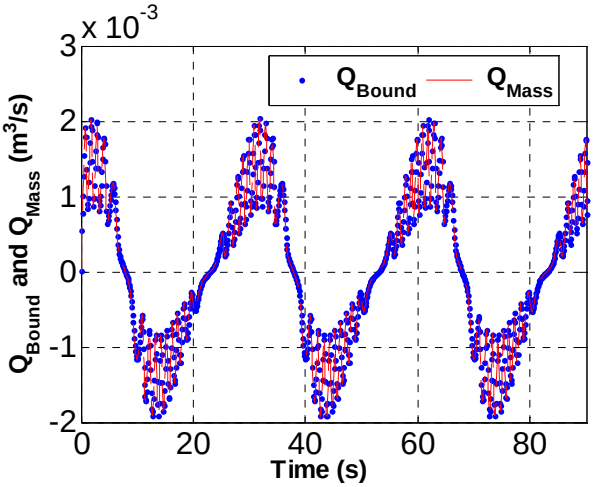

Fig. 12-4 Zoom of the evolution of Q_{Bound} and Q_{Mass} at t=0-90s

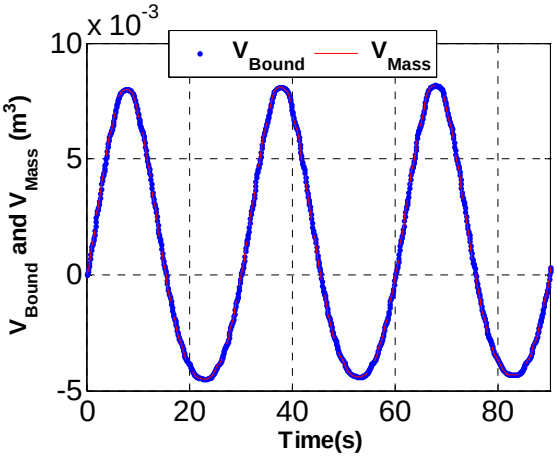

Fig. 12-5 Zoom of the evolution of V_{Bound} and V_{Mass} at t=0-90s

Note: The print time of the Head_Tx file has the influence on the evolution of Q_{Bound} and Q_{Mass}. This plot is the results of the simulation without the output file Head_Tx.

The minimum linear and nonlinear iteration errors for the pressure head are less than 1.0E-6. The curves of the evolution of Q_{Bound} and Q_{Mass} completely superimpose together, and there exists the similar case for the curves of the evolution of V_{Bound} and V_{Mass}.

From the curves of Q_{Mass} and Q_{Bound}, it can be seen when entry water levels are the maximum and the minimum, the iterations are therefore difficult.

12.6 Result analysis of continuous wave test

12.6.1 Profiles of the pressure head contour and the flux velocity field

The profiles of the pressure head contours and the flux velocity at t=33.75s (T+T/8), t=303.75s (10T+T/8), t= 41.25s (T+3T/8) and t=311.25s (10T+3T/8) are respectively shown in **Fig. 12-6, Fig. 12-7, Fig. 12-8** and **Fig. 12-9.**

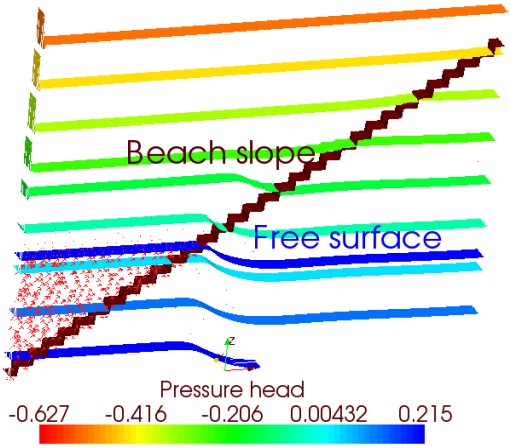

Fig. 12-6 Profile of the pressure head contours, the flux velocity and the beach slope at t=T+T/8=33.75s (length scale in z and in y are 10)

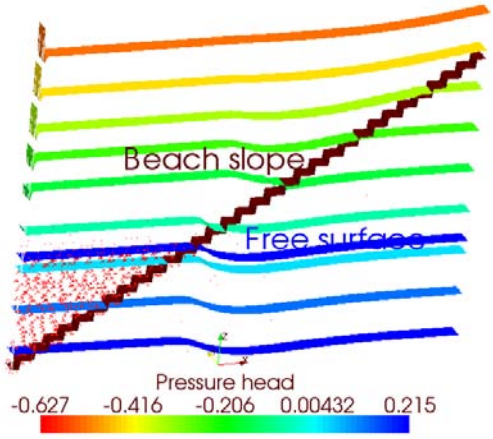

Fig. 12-7 Profile of the pressure head contours, the flux velocity and the beach slope at t=10T+T/4=303.75s (length scale in z and in y are 10)

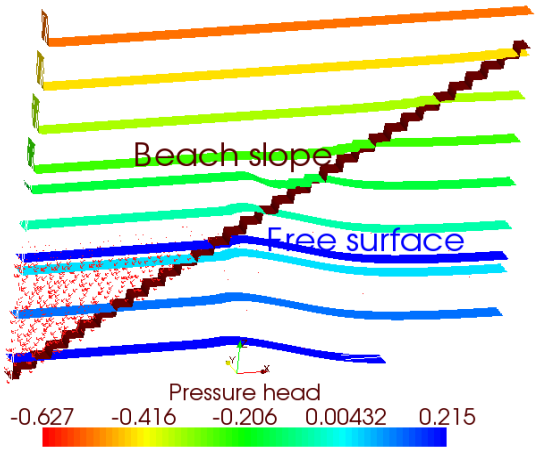

Fig. 12-8 Profile of the pressure head contours, the flux velocity and the beach slope at t=T+3T/8=41.5s (length scale in z and in y are 10)

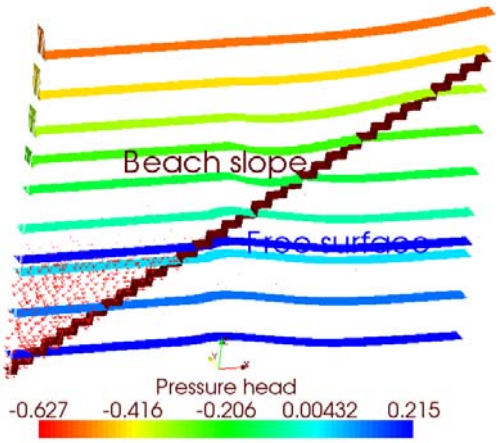

Fig. 12-9 Profile of the pressure head contours ,the flux velocity and the beach slope at t=10T+3T/8=311.25s (length scale in z and in y are 10)

When t=T+T/8=33.75s, the left boundary water level has rosed amost 50% amplitude (H_1=0.3m) from the mean water level to the maximum (**Fig. 12-1**), at the same time, the water levels in the macro porous media rise with the same velocity of the boundary water level, while the ones in the micro porous media increase much slower and therefore, the flux flows upwards along the beach and flows towards the beach, the micro porous media (seen in **Fig. 12-6**).

When t=10T+T/8=303.75s, due to the same boundary condition of the periodic water level as t=T+T/8=33.75s, the pressure head contours and the flux field are almost same as the ones when t=T+T/8=33.75s (seen in **Fig. 12-7**).

When t=T+3T/8=41.25s, the left boundary water level has decreased by 50% amplitude (H_1=0.3m) from the maximum to the mean water level (**Fig. 12-1**), at the same time, the water levels in the macro porous media go down with the same velocity of the boundary water level, while the ones in the micro porous media go down much slower and they are higher than the ones in the macro media and as a result, the flux flows downwards along the beach slope (seen in **Fig. 12-8**).

When t=10T+3T/8=311.75s, due to the same boundary condition of the periodic water level as t=T+3T/8=41.25s, the pressure head contours and the flux field are almost the same as the ones when t=T+3T/8=41.75s (seen in **Fig. 12-9**).

12.6.2 Instantaneous water content distribution θ(h) in the vertical section

The instantaneous distributions of the water content $\theta(h)$ in the vertical section at t=T+T/8=33.75s, t=10T+T/8=303.75s, t=T+3T/8=41.25s and t=10T+3T/8=311.25s are respectively shown in **Fig. 12-10, Fig. 12-11, Fig. 12-12** and **Fig. 12-13**.

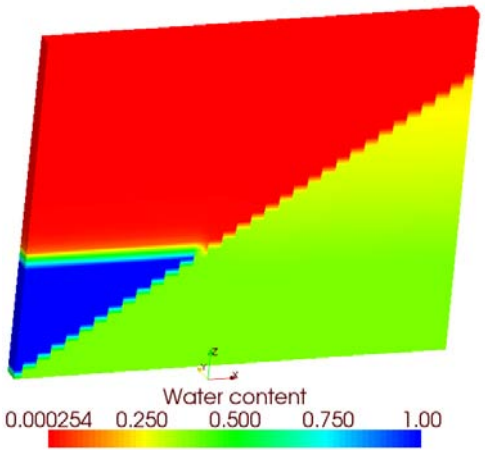

Fig. 12-10 Profile of the water content $\theta(h)$ at t=T+T/8=33.75s in the vertical section (length scale in z and in y are 10)

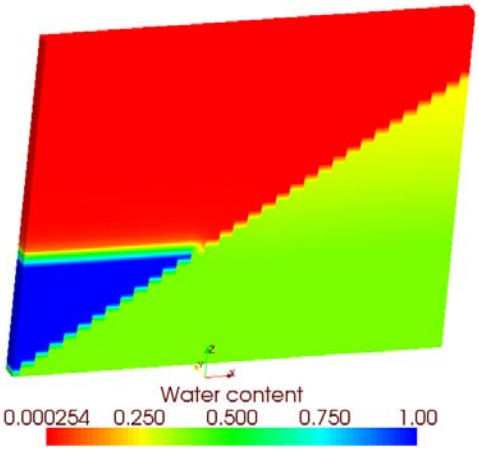

Fig. 12-11 Profile of the water content $\theta(h)$ at t=10T+T/8=303.75s in the vertical section (length scale in z and in y are 10)

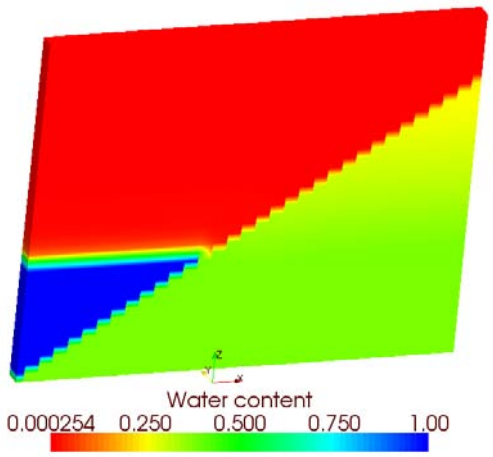

Fig. 12-12 Profile of the water content $\theta(h)$ at t=T+3T/8=41.5s in the vertical section (length scale in z and in y are 10)

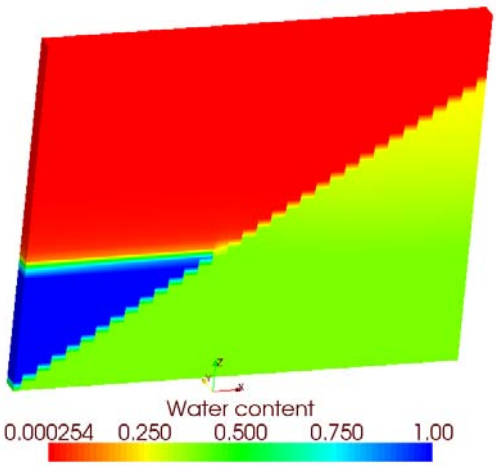

Fig. 12-13 Profile of the water content $\theta(h)$ at t=10T+3T/8=311.5s in the vertical section (length scale in z and in y are 10)

They all are consistent with the pressure head contour at the corresponding time (**Fig. 12-6, Fig. 12-7, Fig. 12-8** and **Fig. 12-9.**).

12.6.3 Evolution of the water level fluctuations in time and space

Profiles of the evolution of the horizontal line pressure head at z=0 (time interval=10 dt=1.0s) are shown in **Fig. 12-14**.

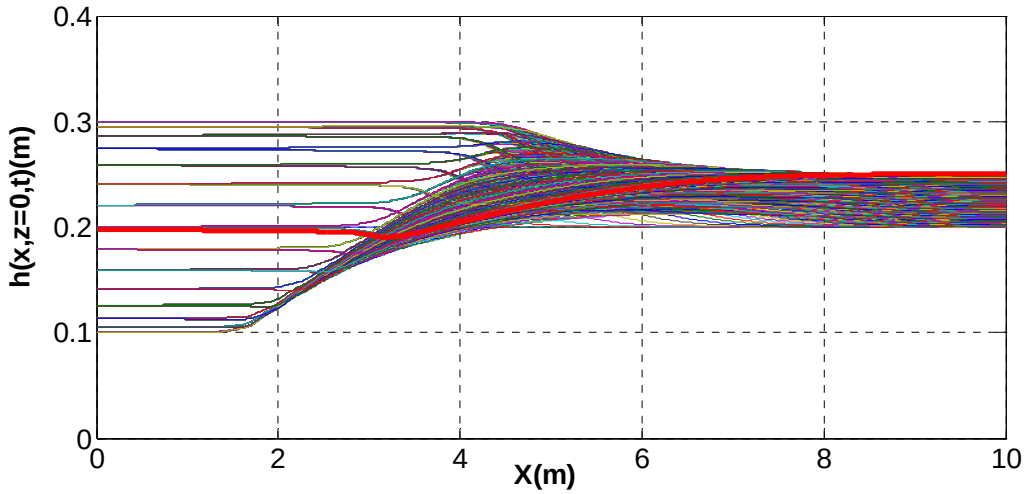

Fig. 12-14 Profile of the pressure head evolution on the bottom z=0 (per each 10 time steps).

From this figure, it can be seen that all the movement area of the free surface in the porous media during the simulation are equal or lower than the maximum boundary water level 0.3m. From x=0 to x=4.5m, it is the mixture zone of the surface water and the ground water; from x=4.5 to x=10 m, it corresponds to the pure groundwater zone and in this zone, the movement area of the free surface gradually decrease and finally tends to a steady state. In an another

words in this zone, the maximum groundwater table become constant and the minimum water table is equal to the initial mean water level H_0.

In order to observe the curve shape of the water level evolution at several different positions $H(x_0, t)$in the porous media, 7 sensors are installed in the beach bottom, which have the same horizontal distances as the ones of the experiment in Barcelona. The evolution of the pressure head of the 7 sensors $h(x, z = 0, t)$ and its zooms, are respectively shown in **Fig. 12-15,** and **Fig. 12-16**.

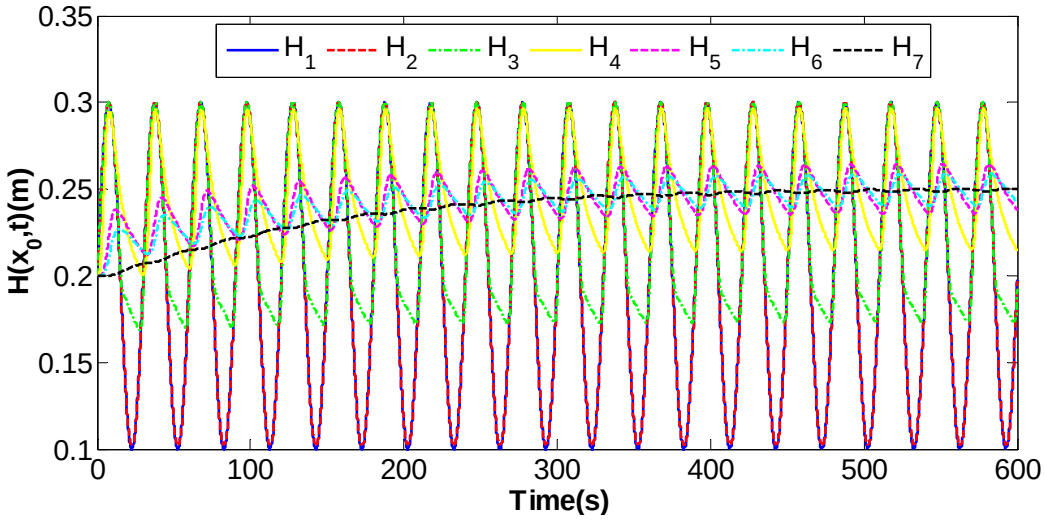

Fig. 12-15 Evolution of the water levels at the 7 sensors at t=0-600s.

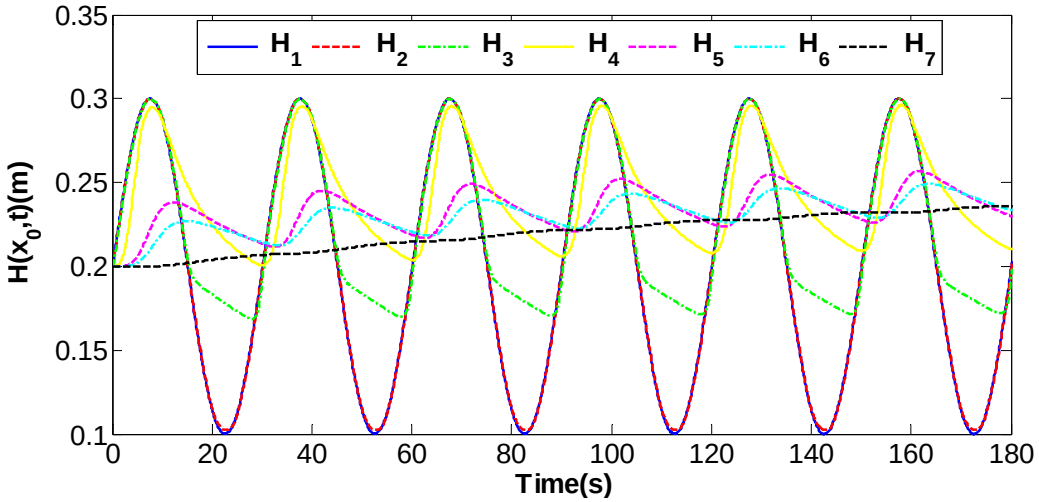

Fig. 12-16 Zoom of the evolution of the water levels at the 7 sensors at t=0-180s (t=0-6T).

From these two figures, it can be seen that there are obvious amplitude decays for all the ground water level fluctuations as well as a phase delay for the pure groundwater levels of the sensors No.4, No.5, No.6 and No.7. The velocity of the water table going down is still slower than the one going up in the micro porous media. After the first half-waves, for the Sensors

No.2 and No.3, the water table in the micro porous media has not descended (reach regularly) to the minimum value, and due to the rising of the boundary water level, it has to rise again.

In addition, the evolution of the water levels (probed the pressure head $h(x, z = 0, t)$ from the file OUTHPB) of the 6 sensors are also separately shown in **Fig. 12-17**.

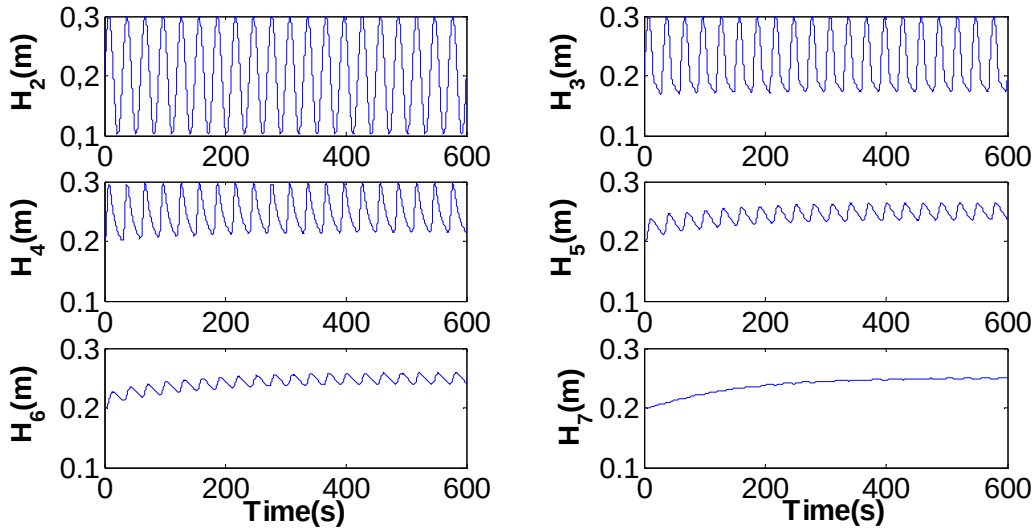

Fig. 12-17 Evolution of the water levels of 6 sensors (t=0-600s)

From this figure, it can be seen that:

- all the mean water levels of the 6 sensors first increase and then tend to a different constant level according to the sensor positions;
- the maximum water levels are equal to (in the mixed zone) or less than (in the pure groundwater zone) the maximum boundary water levels;
- in the mixture zone of the surface zone and groundwater ($x \leq 4.5m$,where the height of the beach sands is equal to $H_0 + A_0$=0.3m), the mean water levels of the sensors (sensors No.2 and No.3) gradually increase with the increasing of distance from the left boundary;
- at the same time, in the pure groundwater zone ($x \geq 4.5m$), the mean water levels of the sensors (sensors No.4, No.5, No.6 and No.7) gradually decrease and finally tend to a constant with the increasing of distance from the left boundary and they are always bigger than the initial water level H_0.

The original signals of $H_i(t)(i = 2, \dots, 7)$ all have a very good agreement with $H_1(t)$ and the cross-correlation coefficients are greater than 0.9, as shown in **Fig. 12-18**

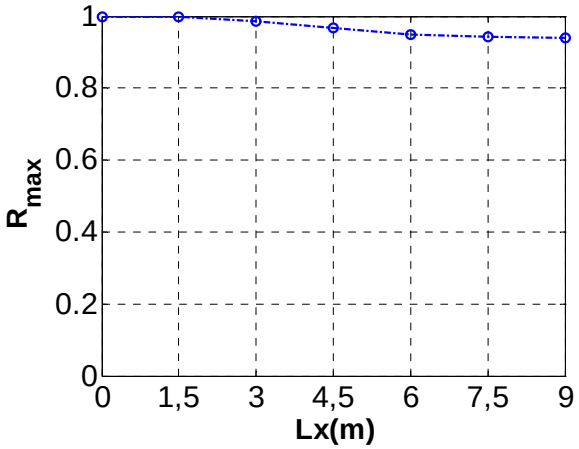

Fig. 12-18 Maximum cross-correlation between $H_1(t)$ and $H_i(t)(i=2,\ldots,7)$ $R_{max}(Lx)$ with respect to the horizontal distance of the sensor position from the sensor No.1 *(Original signal)*

At the same time, the lag time from $H_1(t)$ to $H_2(t)$ and from $H_1(t)$ to $H_3(t)$ is zero, and the ones from $H_1(t)$ to $H_4(t)$, $H_1(t)$ to $H_5(t)$, $H_1(t)$ to $H_6(t)$, and $H_1(t)$ to $H_7(t)$ are longer and longer and they are respectively 2.2s, 5.4s,5.7s and 17.3s, as seen in **Fig. 12-19**.

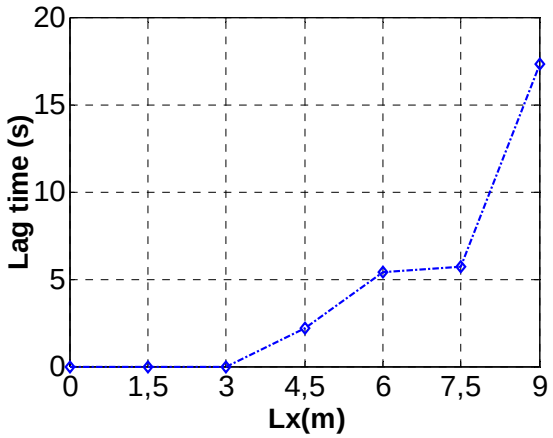

Fig. 12-19 Lag time corresponding to the maximum cross-correlation between $H_1(t)$ and $H_i(t)(i=2,\ldots,7)$ with respect to the horizontal distance of the sensor position from the sensor No.1 *(Original signal)*

In fact, the lag time t=17.3s from $H_1(t)$ to $H_7(t)$ obtained by analyzing the cross-correlation between the original signal $H_1(t)$ and the residual of $H_7(t)$ with moving average filtering (*window halfwidth =30s*) is more reasonable than the one t=0 obtained by analyzing the cross-correlation between the original signals of $H_1(t)$ and $H_7(t)$.

12.7 Analysis on the system energy balance during the numerical simulation

In order to analyze the energy change of the system, the evolutions of Q_{Bound}, the left entry water level $H_1(t)$, and the inside water levels of the 7 sensors are plotted in the same figure as seen in **Fig. 12-20**.

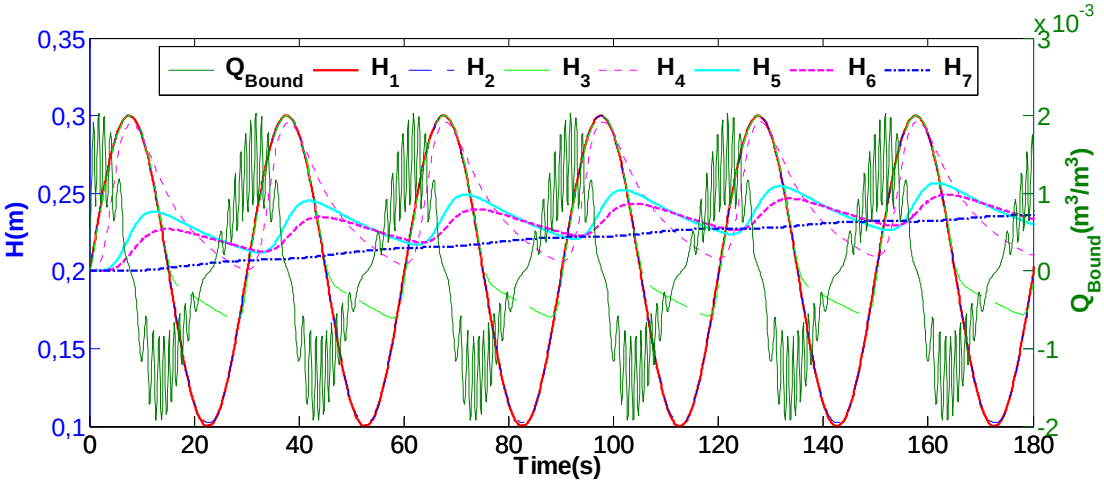

Fig. 12-20 Evolution of the entry water level $H_1(t)$, Q_{Bound} and the inside water levels of the 6 sensors in the porous media

From this figure**,** it can be seen that before the entry water increase to the maximum water level, the water flow in the left side enters into the simulated domain. Especially when the entry water level rises to the height of about 150% of the mean water H_0, Q_{Bound} reaches the maximum, and then decreases gradually to zero when the entry water level rises to the maximum water level. Then, with the decreasing of the entry water level, the flow on the left side begins to flow out of the simulated domain until the entry water level descends to the minimum, and when the entry water level descends to the height of 50% H_0, the Q_{Bound} arrives at the minimum. With the increasing of the entry water level, the flow begins to flow into the simulated domain again. This behaviour is periodically repeated. This result can also be obtained from the figure of the cross correlation $R_{H_1 Q_{BOUND}}(tau)$ (**Fig. 12-21**).

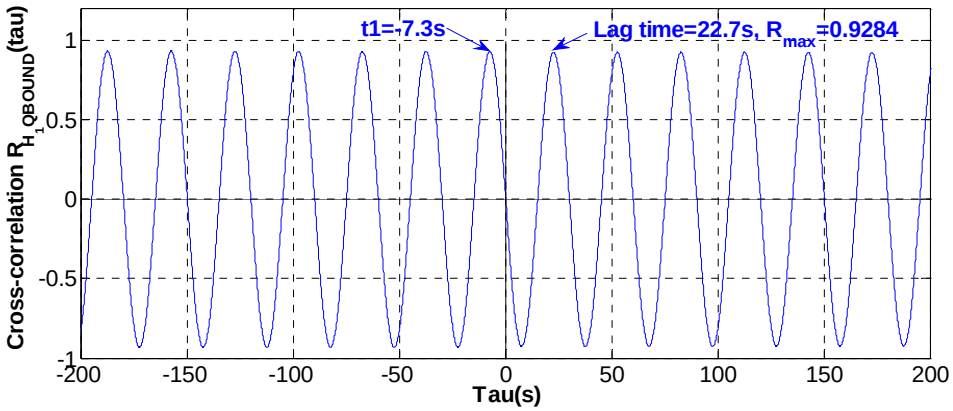

Fig. 12-21 Cross correlation of entry water level $H_1(t)$ and entry water discharge Q_{Bound} $R_{H_1Q_{Bound}}$ at tau (lag time)=-200s-+200s with XCOV(Q_{Bound} , H_1) (unbiased)

From this figure, it can be seen Q_{Bound} has the same oscillatory period T=30s as $H_1(t)$, Q_{Bound} has a lag time of 22.7s (about 3T/4) to $H_1(t)$, and the two signals are in a good agreement (the maximum cross correlation coeffient $R_{H_1Q_{BOUND}}$=0.9284).

The mean entry water level gradient $\overline{\frac{\partial H_1(t)}{\partial x}}$ and $H_1(t)$ have a similar good relationship ($R_{max} > 0.9$) as the one between Q_{Bound} and $H_1(t)$ and have the same period T=30s, as seen in **Fig. 12-22** and **Fig. 12-23**. The difference is that $\overline{\frac{\partial H_1(t)}{\partial x}}$ has a lag time of 7.7s (about T/4) to $H_1(t)$. That is to say, the maximum values of Q_{Bound} are obtained during the increasing of the entry water level, while the ones of $\overline{\frac{\partial H_1(t)}{\partial x}}$ are obtained during the decreasing of $H_1(t)$. Inversely, the minimum values of Q_{Bound} are obtained during the decreasing of the entry water level and the ones of $\overline{\frac{\partial H_1(t)}{\partial x}}$ are obtained during the increasing of $H_1(t)$. In addition, from **Fig. 12-20** and **Fig. 12-22**, it can be seen that $-0.5 \times 10^{-3} < \overline{\frac{\partial H_1(t)}{\partial x}} < 0.5 \times 10^{-3}$ and $-2 \times 10^{-3}\, m^3/s < Q_{Bound} < 2 \times 10^{-3}\, m^3/s$.

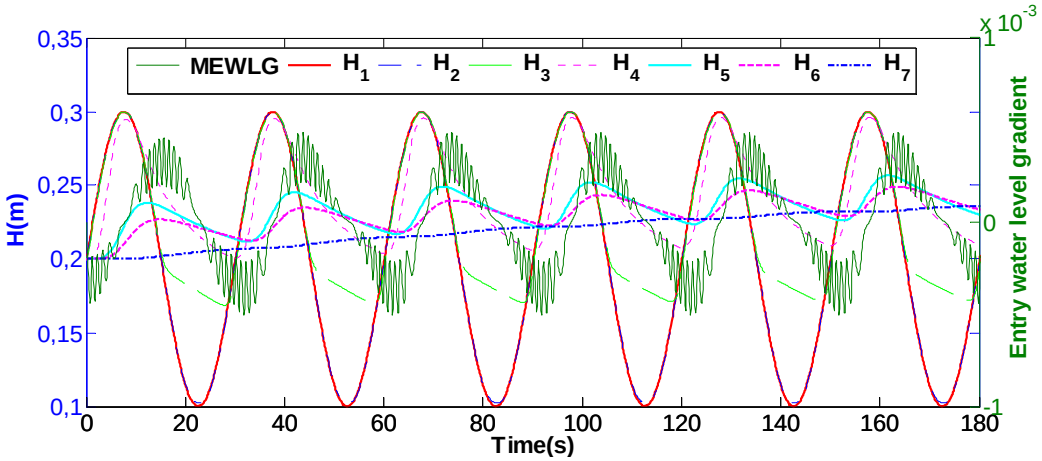

Fig. 12-22 Evolution of the mean entry water level gradient $\frac{\partial \overline{H_1(t)}}{\partial x}$, entry water level $H_1(t)$ and the inside water levels of the 6 sensors in the porous media

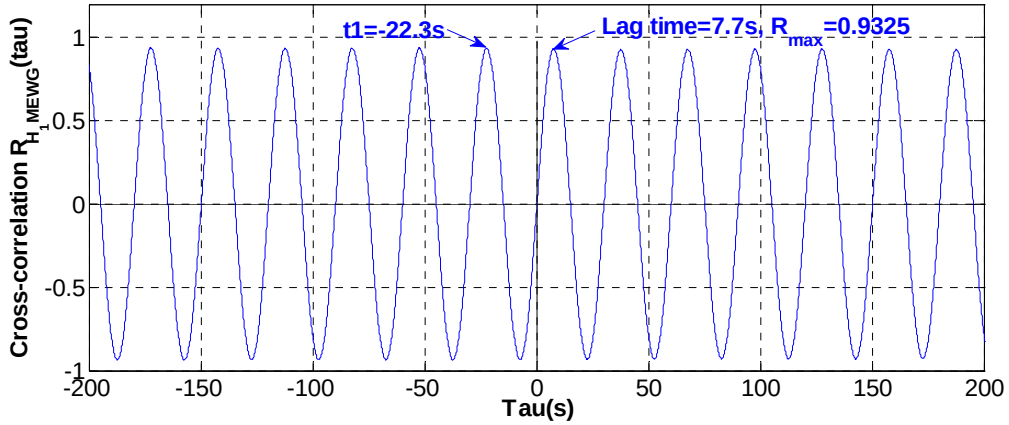

Fig. 12-23 Cross correlation of $H_1(t)$ and mean entry water level gradient $\frac{\partial \overline{H_1(t)}}{\partial x}$ $R_{H_1 MEWLG}$ at tau (lag time)=-200s-+200s with XCOV($\frac{\partial \overline{H_1(t)}}{\partial x}$, H_1) (unbiased)

12.8 Sensitivity analysis of the VGM parameters, soil physical properties, mean free water levels and beach slopes on the groundwater level fluctuations

The objective of the sensitivity analysis is to investigate the influence of all the possible parameters on the water level fluctuation characteristic parameters with respect to space: the approximate stable mean water level $H_{Os}(x)$ and the corresponding amplitude (downword) $A_{Os}(x)$ $(downward)$. All the results have been obtained in numerical cases with the entry oscillatory water level boundary condition made of a single continuous harmonic wave.

Eventually, the dominant parameters will be helpful to realize the numerical simulation for the Barcelona experiment.

From the analytical solutions of the Boussinesq equation for a plane flow with oscillatory entry water level (**Chaper 4**) and simplified solution of phreatic saturation line under the actions of rainfall and reservoir water level fluctuation (Feng. 2006), the beach sand physical properties: saturated hydraulic conductivity K_s and saturated water content θ_s, the entry water level fluctuations: the amplitude A_0, the period T_0 and the mean free water level H_0 which is considered same as the initial water level in the sand beach, the beach slope i, and the unsaturated parameters: α and n (VGM model).

All the results of the sensitivity analysis are illustrated in **Fig. 12-24, Fig. 12-25, Fig. 12-26** and **Fig. 12-27.**

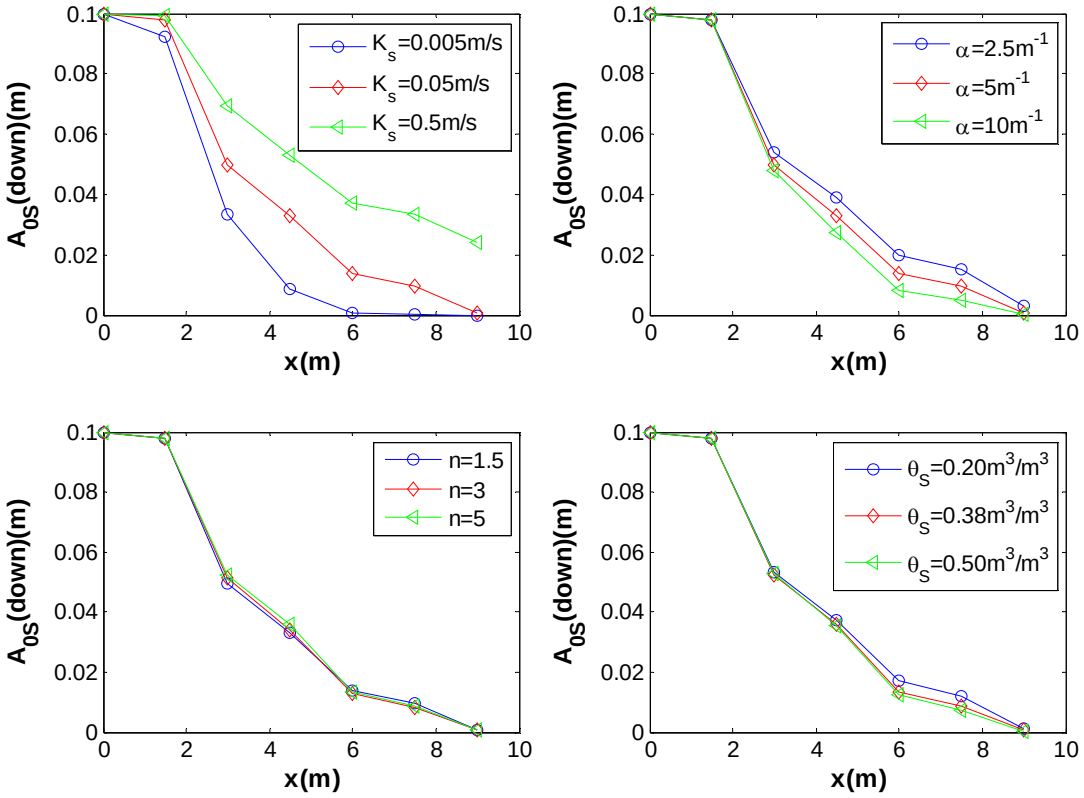

Fig. 12-24 Sensibility analysis of the saturated hydraulic conductivity K_S, VGM parameters (α,n), saturated water content θ_S on the amplitudes of the groundwater level fluctuations.

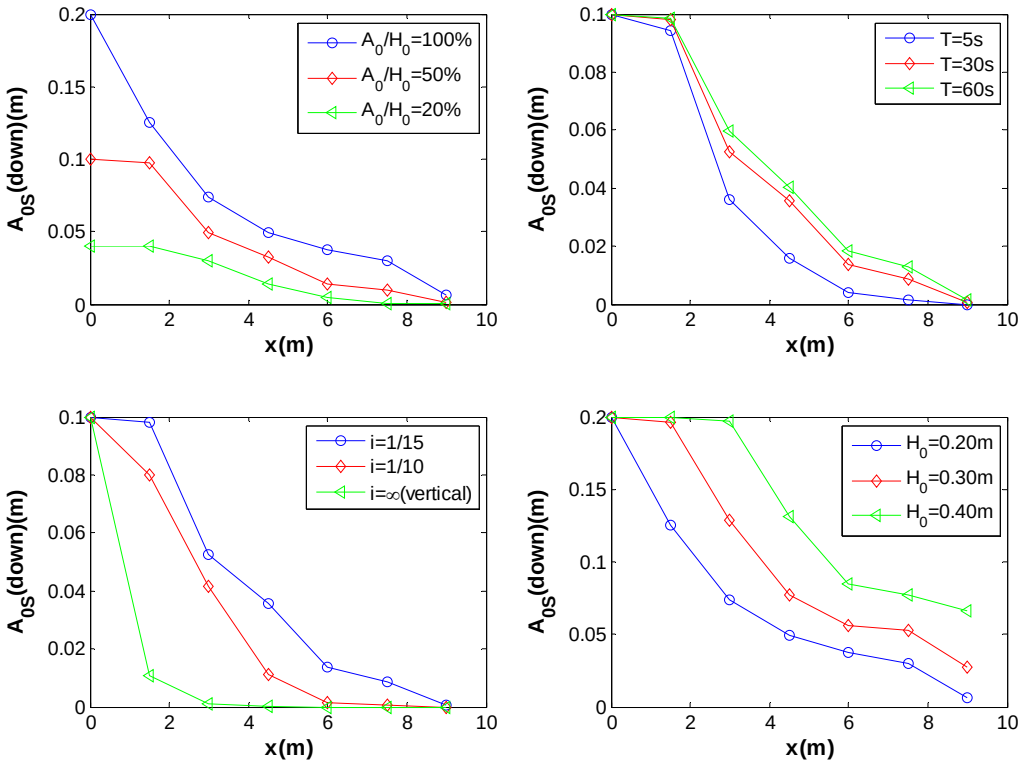

Fig. 12-25 Sensibility analysis of the entry amplitude A_0, entry period T, and beach slope on the amplitudes of the groundwater level fluctuations.

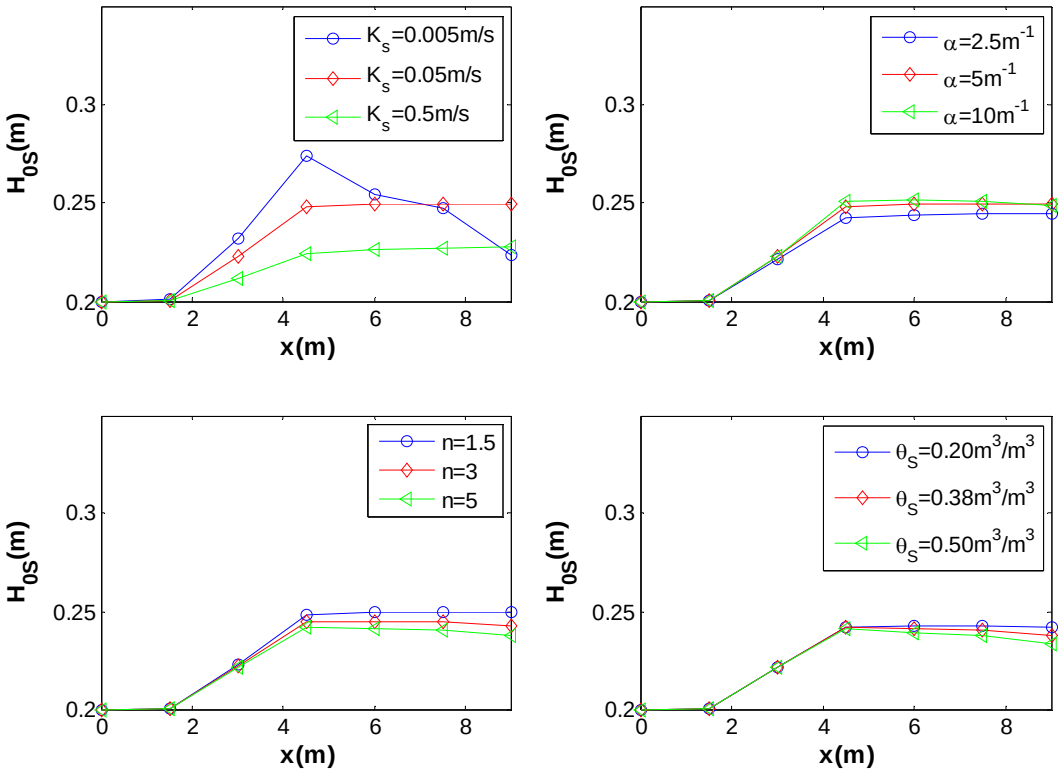

Fig. 12-26 Sensibility analysis of the saturated hydraulic conductivity K_S, VGM parameters (α,n), saturated water content θ_S on the steady mean groundwater levels.

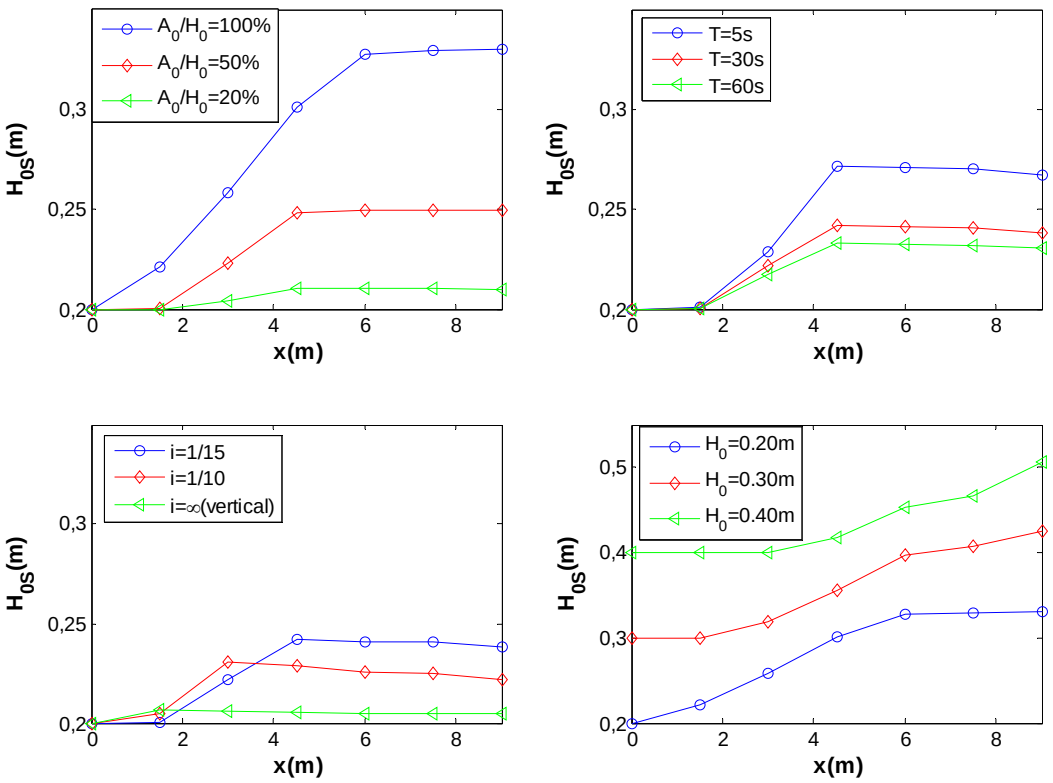

Fig. 12-27 Sensibility analysis of the entry amplitude A_0, entry period T, and beach slope on the steady mean groundwater levels.

The saturated hydraulic conductivity K_s has a dominant influence on the water level fluctuations in the porous media among the four parameters: K_s, θ_s, α and n. The parameter α has the bigger influence on it. On the opposite, θ_s and n has a very small influence on the water level fluctuations. By contrast, the entry amplitude A_0, period T_0, and mean water level H_0 all have dominant influence on the water level fluctuations in the porous media as K_s.

There is almost the same kind of influence with the up and down amplitudes which happens to the approximate stable mean water level. The entry amplitude A_0, period T_0, mean water level H_0 and the saturated hydraulic conductivity K_s have great influence on the water level fluctuations in the porous media.

12.9 Conclusions and outlook

From the results of the sensitivity analysis, we obtain that:

- For the water level oscillations: the saturated hydraulic conductivity K_s has dominant influence on the water level fluctuations in the porous media among the four parameters: K_s, θ_s, α and n; α has bigger influence on it; θ_s and n has a very small influence on the water level fluctuations; and at the same time, the entry amplitude A_0,

period T_0, and mean water level H_0 all have dominant influence on the water level fluctuations in the porous media as K_s.

- For the approximate stable mean water level: the entry amplitude A_0, period T_0, mean water level H_0 and the saturated hydraulic conductivity K_s have great influence on the stable mean water level in the porous media.

Althrough the results obtained from the single harmonic wave numerical experiments with several continuous periods (long run) are qualitative, they will be very helpful to succeed in similating the Barcelona experiment.

In fact, in the Barcelona experiment, the entry water level periods, the entry amplitudes, the beach slope are fixed. The saturated water content θ_s, and VGM parameters α and n has smaller influences on the water level fluctuations in the porous media. Thereofore, the most important parameter is still the saturated hydraulic conductivity K_s. This parameter will be validated with the Barcelona experimental results by Boussinesq model and Richards model. In addition, the entry mean water level H_0 is another important parameter which could be properly adjusted in the numerical simulation.

12.10 Key questions and discussion

From this numerical simulation, we know that there is a key point which divides the whole simulated domain into two zones: mixture zone of the groundwater and the surface water and the pure groundwater zone. At this key point, the height of the beach H_{kp} is equal to the maximum entry water level H_{1max}, and the distance from the left boundary condition $L_{kp} = \frac{H_{kp}}{I} = \frac{H_1(t)_{max}}{1/15}$ =4.5m. All the evolution of the mean water levels of the 7 sensors first increases and then tends to a different constant water level. However, in the mixture zone, the mean water levels of the sensors (sensors No.2 and No.3) gradually increase with the increasing distance from the left boundary; at the same time, in the pure groundwater zone, the mean water levels of the sensors (sensors No.4, No.5, No.6 and No.7) gradually decrease to tend to a constant with the increasing distance from the left boundary and they are always bigger than the initial water level H_0. It means that the variation of the mean water levels with the distance $DH(x)$ is different in the two zones.

REFERENCES

References

[1] Polubarinova-Kochina P. YA. (1962). *Theory of Ground Water Movement*. Princeton University Press, Princeton, New Jersey, 1962.

[2] Bear J. (1972). *Dynamics of Fluids in Porous Media*. Dover Books on Physics and Chemistry, 1972.

[3] Yevjevich V. (1972). Stochastic processes in hydrology. *Water Resources Publications*, Fort Collins, Colorado, U.S.A., (8 Chapters, 276 pp.).

[4] Mualem Y. (1976). A new model for predicting the hydraulic conductivity of unsaturated porous media. *Water Resources Research*, 12(3), pp. 513- 522, 1976.

[5] Waddell E. (1976). Swash-groundwater-beach profile interactions. *In: R.A. Davis and R.L. Etherington, Editors, Beach and nearshore sedimentation*, Society of Economic and Paleontological Mineralogists Special Publication 24 (1976), pp. 115–125.

[6] Waddell E. (1980). Wave forcing of beach groundwater. *Proceedings of the 17th International Conference on Coastal Engineering*, pp. 1436–1452, 1980.

[7] Mangin A. (1984). Pour une meilleure connaissance des systèmes hydrologiques à partir des analyses corrélatoires et spectrales. *Journal of Hydrology*, 67:25–43, 1984.

[8] Mallat S. (1989). A theory for multiresolution signal decomposition : The wavelet representation. *IEEE Trans. on Pattern Anal. and Mach. Int.*, 11 (7), pp. 674-693, 1989.

[9] Nielsen P. (1990). Tidal dynamics of the water table in beaches. *Water Resources Research*, 26(9), pp. 2127–2134, 1990.

[10] Ababou R. (1991): *Approaches to Large Scale Unsaturated Flow in Heterogeneous, Stratified, and Fractured Geologic Media*. Report NUREG/CR-5743, U.S. Nuclear Regulatory Commission, Government Printing Office, Washington DC, 150 pp., 1991.

[11] Gourlay M.R. (1992). Wave set-up, wave run-up and beach water table: interaction between surf zone hydraulics and groundwater hydraulics. *Coastal Engineering*, 17:93–144, 1992.

[12] Turner I.L. (1993). Water table outcropping on macro-tidal beaches: a simulation model. *Marine Geology*, 115, pp. 227–238, 1993.

[13] Nielsen P. (1997). Coastal groundwater dynamics. *In: E.B. Thornton, Editor, Coastal Dynamics 97*, American Society of Civil Engineers, New York (1997), pp. 546–555.

[14] Turner I.L. (1998). Monitoring groundwater dynamics in the littoral zone at seasonal, storm, tide and swash frequencies. *Coastal Engineering*, 35:1–16, 1998.

[15] Mallat S. (1999). *A wavelet tour of signal processing*. Academic Press, 2nd ed., 637 pp.

[16] Nielsen P. (1999). Groundwater dynamics and salinity in coastal barriers. *Journal of Coastal Research*, 15(3), pp. 732–740, 1999.

[17] Trégarot G. (2000). *Modélisation couplée des écoulements à saturation variable avec hétérogénéités, forçage et interface hydrologique*. Thèse de doctorat. IMFT, Institut National Polytechnique de Toulouse, 2000.

[18] Horn D.P. (2002). Beach groundwater dynamics. *Geomorphology*, 48:121–146, 2002.

[19] Horn D. (2006). Measurements and modelling of beach groundwater flow in the swash-zone: a review. *Continental Shelf Research*, 26:622–652, 2006.

[20] Ababou R. (2007). *Eléments d'Hydrologie Souterraine*. Document polycopié, 103 pp., 2007.

[21] Fatmi H. (2009). *Méthodologie d'analyse des signaux et caractérisation hydrogéologique : application aux chroniques de données obtenues aux laboratoires souterrains du Mont Terri, Tournemire et Meuse/Haute-Marne*. Thèse de doctorat. IMFT, Institut National polytechnique de Toulouse, 2009.

[22] Lewandowski A. and Zeidler R.B.(1978). Beach ground-water oscillations. *Proceedings of the 16th Conference on Coastal Engineering*, pp. 2051-2065.

[23] Papoulis A. and S. Unnikrishna Pillai (2002). *Probality, Random Variables and Stochastic Processes*. Tata McGraw-Hill Publishing Company Limited, the 4th edition, pp. 412, 2002.

[24] Werner A.D. and D.A. Lockington (2003). Influence of hysteresis on tidal capillary fringe dynamics in a well-sorted sand. *Advances in Water Resources*, 26(11), pp. 1199–1204.

[25] Baird A.J. and D.P. Horn (1996). Monitoring and modelling ground water behaviour in sandy beaches. *Journal of Coastal Research*, 12(3):630–640, 1996.

[26] Baird A.J., T.E. Mason, and D.P. Horn (1998). Validation of a Boussinesq model of beach ground water behaviour. *Marine Geology*, 148, pp. 55–69, 1998.

[27] Chan A.T. and S.W.C. Lee (2001). Wave characteristics past a fexible fishnet. *Ocean Engineering*, 28: 1517–1529, 2001.

[28] Brossard J. Azhar S., C. Dardab and M. Chagdali (2008). Etude analytique de l'interaction houle - digue poreuse. *Xèmes Journées Nationales Génie Côtier – Génie Civil*, 14-16 octobre 2008, Sophia Antipolis.

[29] Raubenheimer B., R.T. Guza, and S. Elgar(1999). Tidal watertable fluctuations in a sandy ocean beach. *Water Resources Research*, 35(8), pp. 2313–2320. ISSN: 0043-1397, 1999.

[30] Hegge B.J. and G. Masselink (1991). Groundwater-table responses to wave run-up: an experimental study from western australia. *Journal of Coastal Research*, 7(3), pp. 623–634.

[31] Blewett J. C., P. Holmes, and D. P. Horn(2001). Field measurements of swash on gravel beaches. *Proceedings of the Fourth Conference, Coastal Dynamics '01, ASCE*, pp. 828-837. doi 10.1061/40566(260)85.

[32] Robinson C., T.E. Baldock, D.P. Horn, B. Gibbes, M.G. Hughes, P. Nielsen, and L.(2005) Li. Measurement of groundwater and swash interactions on a sandy beach. *Coastal Dynamics 2005 — State of the Practice Proceedings of 5th International Conference , ASCE*, http://dx.doi.org/10.1061/40855(214)104, 2006.

[33] Labat D., R. Ababou, and A. Mangin (2000a). Rainfall-runoff relations for karstic springs – part i : Convolution and spectral analyses. *Journal of Hydrology*, 238, Issues 3-4, 5 Dec.2000, pp.123-148.

[34] Labat D., R. Ababou, and A. Mangin (2000b). Rainfall-runoff relations for karstic springs part ii : Continuous wavelet and discrete orthogonal multiresolution analyses. *Journal of Hydrology*, 238, Issues 3-4, 5 Dec.2000, pp.149-178.

[35] M. A. Losada Dalrymple R. A. and P. A. Martin (1991). Reflection and transmission from porous structures under oblique wave attack. *Journal of Fluid Mechanics*, 224:pp. 625–644, 1991.

[36] Braja M. Das. *Advanced Soil Mechanics*. Taylor and Francis, 3 edition, 2008.

[37] Horn D.P., T.E. Baldock, A.J. Baird, and T. Mason (1998). Field measurements of swash induced pressure gradients within a sandy beach. *In: Proceedings of the 26th*

International Conference on Coastal Engineering, American Society of Civil Engineers, New York, pp. 2812–2825.

[38] Waddell E.(1973). Dynamics of swash and implications to beach response. *Technical Report 139, Coastal Studies Institute*, Louisiana State University, Baton Rouge (1973) (49pp).

[39] Childs E.C. and N. Collis-George (1950). The permeability of porous materals. *Proceedings of Royal Society of London, Series A: Mathematical and Physical Sciences*, 201, pp. 392-405.

[40] Dominick F.T., B. Wilkins Jr., and Roberts H. (1971). Mathematical model for beach groundwater fluctuations. *Water Resources Research*, 7(6), pp. 1626-1635. doi:10.1029/WR007i006p01626, 1971.

[41] Dean R. G. and R. A. Dalrymple. *Water wave mechanics for engineers and scientists*. World Scientific, 2000.

[42] Strang G. and T. Nguyen (1996). Wavelets and filter banks. *Wellesley-Cambridge Press*, 490 pp., 1996.

[43] Fatmi H., R. Ababou, and J.-M. Matray (2008). Statistical pre-processing and analyses of hydrogeo-meteorological time series in a geologic clay site (methodology and first results for Mont Terri's PP experiment). *Physics and Chemistry of the Earth: Special Issue on «Clays in Natural & Engineered Barriers for Radioactive Waste Confinement»* (Internat. Conf. CLAY'2007, Lille, France) 33:14–23, 2008.

[44] Kang H-Y. and P. Nielsen (1996). Water table dynamics in coastal areas. *Proceedings of the 25th International Conference on Coastal Engineering*, American Society of Civil Engineers, New York , pp. 4601–4612.

[45] White I. and M.J. Sully (1987). Macroscopic and microscopic capillary length and time scales from field infiltration. *Water Resources. Research*, 23(8): 1514-1522, 1987.

[46] White I. and M.J. Sully (1988). Field characteristics of the macroscopic capillary length or alpha parameter. *Conference Proceedings. Validation of Flow and Transport Models for the Unsaturated Zone*, P.J. Wierenga and D. Bachelet, eds.

[47] Turner I.L. and P. Nielsen (1997). Rapid water table fluctuations within the beach face: Implications for swash zone sediment mobility? *Coastal Engineering*, 32(1):45–59, 1997.

[48] Turner I.L. and G. Masselink (1998). Swash infiltration-exfiltration and sediment transport. *Journal of Geophysical Research*, 103(C13), pp. 30, 813-30, 824. doi:10.1029/98JC02606, 1998.

[49] Parlange J.-Y. and W. Brutsaert (1987). A capillary correction for free surface flow of groundwater. *Water Resources Research*, 23 (5), pp. 805–808, doi:10.1029/WR023i005p00805., 1987.

[50] Alastal K., R. Ababou, and D. Astruc (2010). Partially saturated oscillatory flow in a sandy beach (numerical modeling). *CMWR'2010, 21-24 June 2010, XVIIIth International Conf. on Computational Methods in Water Resources (Barcelona, Spain)*, J. Carrera (Ed.), CIMNE, Barcelona 2010 (10 p.).

[51] Sollitt C. K. and R. H. Cross (1972). Wave transmission through permeable breakwaters. *Proc. 13th ASCE Conf. Coastal Eng.*, 1827–46.

[52] Kang H.Y., A.M Aseervatham, and P. Nielsen (1994). Field measurements of wave runup and the beach water table. *Research Report no. CE148, Department of Civil Engineering, University of Queensland*, 44 pp.

[53] Li L. and D.A. Barry (2000). Wave-induced beach groundwater flow. *Advances in Water Resources*, 23, pp. 325–337, 2000.

[54] Li L., Barry D. A., and Pattiaratchi C. B. (1996). Modeling coastal ground-water response to beach dewatering. *J. Waterway., Port, Coast., and Oc. Engrg, ASCE*, 122 (6), pp. 273-280 (November/December 1996).

[55] Li L., D.A. Barry, J.-Y. Parlange, and C.B. Pattiaratchi (1999). Reply (to Nielsen 1999), *Water Resources Research*, 35, pp. 1325–1327.

[56] Li L., Barry D.A., and Pattiaratchi C.B. (1997b). Numerical modelling of tide-induced beach water table fluctuations. *Coastal Engineering*, 30(1/2), pp. 105–123, 1997.

[57] Li L., Barry D.A., Stagnitti F., and Parlange J.-Y. (2000a). Groundwater waves in a coastal aquifer: A new governing equation including vertical effects and capillarity. *Water Resources Research*, 36(2), pp. 411–420. doi:10.1029/1999WR900307, 2000.

[58] Li L., Barry D.A., Parlange J.-Y., and Pattiaratchi C. B. (1997a). Beach water table fluctuations due to wave run-up: Capillarity effects. *Water Resources Research*, 33(5), pp. 935–945. doi:10.1029/96WR03946, 1997.

[59] Turner I. L., B. P. Coates, and R. I. Acworth (1997). Tides, waves and the super-elevation of groundwater at the coast. *Journal of Coastal Research*, 13:46–60 (36 ref.), 1997.

[60] Priestley M.B.(1981). Spectral analysis and time series. *Acad. Press*, 890 pp.

[61] Cartwright N., T.E. Baldock, P. Nielsen, D.-S. Jeng, and L. Tao (2005). Swash–aquifer interaction in sandy beaches. *Coasts and Ports, 17th Australasian Coastal and Ocean Engineering Conference, Adelaide, Australia*, September 2005.

[62] Cartwright N., L. Li, and P. Nielsen (2004a). Response of the salt–freshwater interface in a coastal aquifer to a wave-induced groundwater pulse: field observations and modelling. *Advances in Water Resources*, 27, pp. 297–303.

[63] Cartwright N., P. Nielsen, and O. Z. Jessen (2002). Swash zone and near-shore watertable dynamics. *COASTAL ENGINEERING*, Proceedings of the 28th International Conference on Coastal Engineering. World Scientific, New York, pp. 1006–1015., 2002.

[64] Cartwright N., P. Nielsen, and L. Li (2004b). Experimental observations of watertable waves in an unconfined aquifer with a sloping boundary. *Advances in Water Resources*, 27:991–1004. doi:10.1016/j.advwatres.2004.08.006, 2004.

[65] Cartwright N., P. Nielsen, and L. Li (2004c). The influence of offshore storm waves on groundwater dynamics and salinity in a sandy beach. *In: Proceedings of the 29th International Conference on Coastal Engineering*, World Scientific, Singapore, pp. 1841–1850.

[66] Conway P. and D. Frame (2000). A spectral analysis of new zealand output gaps using fourier and wavelet techniques. *Reserve bank of New Zealand*, DP2000/06.

[67] Nielsen P. and H.Y. Kang (1995). Ground water dynamics in beaches and coastal barriers. *In: W.R. Dally and R.B. Zeidler, Editors, Coastal Dynamics '95*, American Society of Civil Engineers, New York, pp. 521–532.

[68] Nielsen P. and I.L. Turner (2000). Groundwater waves and water exchange in beaches. *Proceedings of the 27th International Conference on Coastal Engineering*, American Society of Civil Engineers, New York:2356–2363, 2000.

[69] Nielsen P. and P. Perrochet (2000a). Watertable dynamics under capillary fringes: experiments and modelling. *Advances in Water Resources*, 23, pp. 503-515, 2000.

[70] Nielsen P. and P. Perrochet (2000b). Errata: Watertable dynamics under capillary fringes: experiments and modelling. *Advances in Water Resources*, 23, pp. 907-908, 2000.

[71] Nielsen P., R. Aseervatham, J. D. Fenton, and P. Perrochet (1997). Groundwater waves in aquifers of intermediate depths. *Advances in Water Resources, Vol. 20, No. 1, pp. 37-43, 1997*, 20 (1), pp. 37-43, 1997.

[72] Nielsen P., G.A. Davis, J.M. Winterbourne, and G. Elias (1988). Wave setup and the water table in sandy beaches. *Technical Memorandum T.M. 88/1, New South Wales Public Works Department, Coastal Branch*, page 132, 1988.

[73] Ababou R. (2008) : *Quantitative Stochastic Hydrogeology : the Heterogeneous Environment.* Chap 8 in Part III of "Overexploitation & Contamination of Shared Groundwater Resources : Management, (Bio)Technological, & Political Approaches to Avoid Conflicts." NATO-ASI: Advanced Studies Institute Series, C.J.G. Darnault (ed.), Springer Science & Business Media BV, January 2008 (pp. 119-182).

[74] Ababou R. and A. C. Bagtzoglou (1993). Bigflow: A numerical code for simulating flow in variably saturated, heterogeneous geologic media (theory and user's manual, version 1.1). *Report NUREG/CR-6028, US Nuclear Regulatory Commission, Government Printing Office, Washington DC, USA*, 139pp.

[75] Ababou R. and A. Al-Bitar, (2008): *Coupled Surface / Subsurface Flow Systems : Numerical Modeling.* Chap. 7 in "Overexploitation & Contamination of Shared Groundwater Resources". NATO-ASI: Advanced Studies Institute Series, C.J.G. Darnault (ed.), Springer Science & Business Media BV, January 2008 (pp. 105-117).

[76] Bras R. and I. Rodriguez-Iturbe (1985). *Random functions in hydrology*. Dover, New York, 1985 (re-edited in 1993).

[77] Vichnevetsky R. and J. B. Bowles(1982). *Fourier Analysis of Numerical Approximations of Hyperbolic Equations*. The Society for Industrial and Applied Mathematics (SIAM), 1982.

[78] Blackman R.B. and J.W. Tuckey (1958). *The measurement of power spectra*. Dover Publications, New York, 1958.

[79] Atherton R.J., A.J. Baird, and G.F.S. Wiggs (2001). Inter-tidal dynamics of surface moisture content on a meso-tidal beach. *Journal of Coastal Research*, 17(2): pp. 482–489, 2001.

[80] Silliman S.E., B. Berkowitz, J. Simunek, and M.T. van Genuchten (2002). Fluid flow and solute migration within the capillary fringe. *Ground Water*, 40, pp. 76–84, 2002.

[81] Butt T., P. Russell, and I. Turner (2001). The influence of swash infiltration–exfiltration on beach face sediment transport: onshore or offshore ? *Coastal Engineering*, 42(1), pp. 35-42. DOI: 10.1016/S0378-3839(00)00046-6, 2001.

[82] Chwang A. T. and A. T. Chan (1998). Interaction between porous media and wave motion. *Annu. Rev. Fluid Mech.*, 30:53–84, 1998.

[83] Baldock T.E., A.J. Baird, D.P. Horn, and T. Mason (2001). Measurements and modelling of swash-induced pressure gradients in the surface layers of a sand beach. *Journal of Geophysical Research*, 106(C2), pp. 2653–2666, 2001.

[84] Van Genuchten M. Th. (1980). A closed-form equation for predicting the hydraulic conductivity of unsaturated soils. *Soil Sci. Soc. Am. J.*, 44:892-898.

[85] Menke W., A. L. Lerner-Lam, and R. Mithal (1991). Spatial coherence of 5-25 Hz seismic wavefields at a hard rock site. *Structural Safety, Special Issue*, 10:145–162, 1991.

[86] Green W.H. and Ampt G.A. (1911). Studies on soil physics I : the flow of air and water through soils. *Journal of Agricultural Science*, IV(I), pp. 1–24., 1911.

[87] Feng W.K., Y.Ch. Shi, H.J. Chai, H.Ch. Liu, and J. Feng (2006). The simplified solution of phreatic saturation line under the actions of rainfall and reservoir water level fluctuation. *Journal of Chengdu University of Technology (Science& Technology Edition)*, 33(1), pp. 90-94, 2006.

[88] Mo W.W., P. Xu, and X.L. Ding (2006). Research advances on the influence of reservoir water level fluctuation on slope stability. *Chinese Journal of Underground Space and Engineering*, 2(6), pp. 997-1002, 2006.

[89] Yu X. and A. T. Chwang (1994). Wave motion through porous structures. *Journal of Engineering Mechanics*, 120: 989-1008, doi 10.1061/(ASCE)0733-9399(1994)120:5(989), 1994.

[90] Wang Y., R. Ababou, and M. Marcoux (2008). Etude expérimentale et numérique des oscillations hydrodynamiques en milieux poreux partiellement saturés. Communication poster aux 33emes journées du GFHN (Groupement Francophone d'Humidimétrie et Transferts en Milieux Poreux): « Impact de l'usage du sol sur les ressources en eau souterraine ». Avignon, France, 19-20 Novembre 2008 (UmmaH – INRA & Université d'Avignon). Abstract étendu (2 pp.) Publié dans le *Bulletin du GFHN* (Avignon, 2008).

[91] Cao Y.Z., M. Gunzburger, F. Hua ., and X.M. Wang (2010). Coupled stokes-darcy model with beavers-joseph interface boundary condition. *Communications in Mathematical Sciences*, 8(1), pp. 1-25, 2010.

[92] Song Z-Y., L. Li, J. Kong, and H-G Zhang (2007). A new analytical solution of tidal water table fluctuations in a coastal unconfined aquifer. *Journal of Hydrology*, 340:256–260, 2007.

[93] Wang Y., R. Ababou, M. Marcoux, 2008: "Oscillatory Flows and Wave Propagation in Porous Media : Partially Saturated Free Surface Hydraulics". *Proceedings, International Symposium IAHR-GW 2008 (Flow and Transport in Heterogeneous Subsurface Formations : theory, modelling and application).* Internat. Assoc. of Hydraulics Research - Ground Water, Istanbul, Turkey, 18-20 June 2008 (9 pp.).

[94] Wang Y., R. Ababou, M. Marcoux (2010): "Signal Processing of Water Level Fluctuations in a Laboratory Experiment: Sloping Sandy Beach in a Wave Canal (Hydralab Project Barcelona)". GeoShanghaï 2010 Internat. Conf. (Shanghaï 3-5 June 2010), GeoShanghaï Paper#553, *American Society of Civil Engineers: ASCE Geotechnical Special Publication (GSP).* (6 pp.).

List of Figures

Figure 0-1. Three Gorges Dam Reservoir filled to 135 meters (international PROBE, Mu Lan, June 2003). 1

Figure 0-2. Sea beach of Rincon, Puerto Rico taken from the Red Door. 1

Fig. 1-1 Effective water content model $\theta_e(h)$ of the macro porous media 25

Fig. 1-2 Hydraulic conductivity model $K(h)$ of the macro porous media 25

Fig. 2-1 Schematic of the numerical iterations in the Bigflow code27

Fig. 2-2 Schematic of the time-varying water level $H(x_0, y, t)$ boundary condition in time and space for the Boussinesq model 28

Fig. 2-3 Schematic of the time-varying pressure head $h(x_0, z, t)$ boundary condition in time and space for the Richards model 28

Fig. 2-4 Simplified schema of the permeameter made up of the macro/micro porous media 31

Fig. 2-5 Schema of the variable head permeameter 32

Fig. 2-6 Standardized linear iteration process curve of the pressure head in log10 35

Fig. 2-7 Standardized nonlinear iteration process curve of the pressure head in log10 35

Fig. 2-8 Evolution of Q_{Bound} and Q_{Mass} (local mass balance)..... 35

Fig. 2-9 Evolution of V_{Bound} and V_{Mass} (global volume balance) 35

Fig. 2-10 Standarlized linear iteration process curve of the pressure head in log10 36

Fig. 2-11 Standarlized nonlinear iteration process curve of the pressure head in log10 36

Fig. 2-12 Evolution of Q_{Bound} and Q_{Mass} (local mass balance)..... 36

Fig. 2-13 Evolution of V_{Bound} and V_{Mass} (global volume balance) 36

Fig. 2-14 Vertical profiles of the calculated pressure head for different time (t=0s, 90s, 180s, 280s, 500s, 1000s, and 2000s) with Exponential model 37

Fig. 2-15 Evolution of the pressure head h(t) at the boundary (z=0.5m) between the macro (water) and micro (sand) porous media at t=0-2000s 38

Fig. 2-16 Ln(h) (t, z=0.5m) and the corresponding linear fitting curve at t=0-180s..... 38

Fig. 2-17 Vertical profiles of the calculated pressure head for different time (t=0s, 90s, 180s, 260s, 500s, 1000s, and 2000s) with VGM model 39

Fig. 2-18 Evolution of the pressure head h(t) at the boundary (z=0.5m) between the macro (water) and micro (sand) porous media at t=0-2000s 40

Fig. 2-19 Ln(h) (t, z=0.5m) and the corresponding linear fitting curve at t=0-180s..... 40

Fig. 3-1 Sand size distribution curve 42

Fig. 3-2 Sand box-imbibition in a dry river bank: imbibition profile at t=14minutes 43

Fig. 3-3 Water content curve $\theta(h)$ of the sand with $\alpha = 4.6m^{-1}$ and n=5. 47

Fig. 3-4 Hydraulic conductivity curve K(h) of the sand with $\alpha = 4.6m^{-1}$ and n=5. 47

Fig. 3-5 Capillary diffusion $D(h)$ of the sand with $\alpha = 4.6m^{-1}$ and n=5..... 47

Fig. 3-6 Capillary capacity $C(h)$ of the sand with $\alpha = 4.6m^{-1}$ and n=5..... 47

Fig. 3-7 Standarlized linear iteration process curve of the pressure head in log10 48

Fig. 3-8 Standarlized nonlinear iteration process curve of the pressure head in log10 48

Fig. 3-9 Evolution of Q_{Bound} and Q_{Mass} (local mass balance) 49

Fig. 3-10 Evolution of V_{Bound} and V_{Mass} (global volume balance)..... 49

Fig. 3-11 The flux field at t=6 minutes. The green curve (h=-0.20m) corresponds to S=0.62, and it also corresponds to the isovalue $h = h_{cap} = -\alpha^{-1}m^{1/n}$ (chapter.4, R. Ababou, 1991 [10]). 49

Fig. 3-12 The flux field at t=15 minutes. The green curve (h=-0.20m) corresponds to S=0.62, and it also corresponds to the isovalue $h = h_{cap} = -\alpha^{-1}m^{1/n}$ (chapter.4, R. Aababou, 1991 [10])..... 50

Fig. 3-13 Sensitivity analysis: evolution of the saturation front toe $X_F(\sqrt{t})$ for the 3 group of parameters: 51

Fig. 3-14 Sensitivity analysis: inflow discharge at bank-river interface with respect to the time $Q_{\inf low}(t)$ in log-log for the 3 group of parameters: 51

Fig. 3-15 (a) (b) Evolution of the saturation front toe. Comparison between the analytical solution of Polubarinova (without any capillary effect) and the numerical Richards model (Num.1) which includes capillary effects in the unsaturated zone. 52

Fig. 3-16 Inflow discharge at bank-river interface with respect to the time $Q_{\inf low}(t)$ in log-log. Comparison between the analytical solution of Polubarinova without any capillary effect and the numerical Richards model (Num.1). 53

Fig. 3-17 Evolution of the saturation front toe $X_F(\sqrt{t})$: simulation "Num.4". Comparison between the analytical solution of Polubarinova without any capillary effects and the numerical Richards model (Num.4)**.** 53

Fig. 3-18 Inflow discharge $Q_{inflow}(t)$ at the bank-river interface in log-log (simulation "Num.4"). Comparison between Polubarinova's solution and the numerical Richards model (Num.4). 53

Fig. 3-19 The schema of the discharge problem 56

Fig. 3-20 Profile of the initial surface in the river bank 58

Fig. 3-21 The discharge process of the free surface in the river bank (aquifer) 59

Fig. 3-22 Standarlized linear iteration process curve of the pressure head in log10 60

Fig. 3-23 Standarlized nonlinear iteration process curve of the pressure head in log10 60

Fig. 3-24 Evolution of Q_{Bound} and Q_{Mass} (local mass balance) 61

Fig. 3-25 Evolution of V_{Bound} and V_{Mass} (global volume balance) 61

Fig. 3-26 Comparison: instantaneous profile of the free surface in the river bank ($h(x,z,t_0)=0.0$) at t=3 hours 61

Fig. 3-27 Comparison: instantaneous profile of the free surface in the river bank ($h(x,z,t_0)=0.0$) at t=10 hours 61

Fig. 3-28 Evolution of the outflow discharge $Q(0,t)$ at the left boundary (river/bank inter face) in semi-log scale, and comparison with the linearized analytical solution. 62

Fig. 3-29 Water content curve $\theta(h)$ of the river bank soil. 63

Fig. 3-30 Hydraulic conductivity curve $K(h)$ of the river bank soil 63

Fig. 3-31 Capillary diffusion $D(h)$ of the river bank soil. 63

Fig. 3-32 Capillary capacity $C(h)$ of the river bank soil. 63

Fig. 3-33 Standarlized linear iteration process curve of the pressure head in log10 for the case: α=20 $m^{(-1)}$, n=3 (VGM) 64

Fig. 3-34 Standarlized nonlinear iteration process curve of the pressure head in log10 for the case: α=20 $m^{(-1)}$, n=3 (VGM) 64

Fig. 3-35 Evolution of Q_{Bound} and Q_{Mass} (local mass balance) for the case: α=20 $m^{(-1)}$, n=3 (VGM) 64

Fig. 3-36 Evolution of V_{Bound} and V_{Mass} (global volume balance) for the case: α=20 $m^{(-1)}$, n=3 (VGM) 64

Fig. 3-37 Water content curve $\theta(h)$ of the river bank soil (Exp.). 65

Fig. 3-38 Hydraulic conductivity curve $K(h)$ of the river bank soil (Exp.). 65

Fig. 3-39 Capillary diffusion $D(h)$ of the river bank soil (Exp.). 65

Fig. 3-40 Capillary capacity $C(h)$ of the river bank soil (Exp.). 65

Fig. 3-41 Standarlized linear iteration process curve of the pressure head in log10 for the case: α=20m^{-1}, β =6.667m^{-1}, Hb=0.0 (Exp.)..... 65

Fig. 3-42 Standarlized nonlinear iteration process curve of the pressure head in log10 for the case: α=20m^{-1}, β =6.667m^{-1}, Hb=0.0 (Exp.)..... 65

Fig. 3-43 Evolution of Q_{Bound} and Q_{Mass} (local mass balance) for the case: α=20m^{-1}, β =6.667m^{-1}, Hb=0.0 (Exp.) 66

Fig. 3-44 Evolution of V_{Bound} and V_{Mass} (global volume balance) for the case: α=20m^{-1}, β =6.667m^{-1}, Hb=0.0 (Exp.) 66

Fig. 3-45 Comparison of the vertical profile of the instantaneous static curve and the VGM dynamic curve of the degree of saturation at t=10 hours at X_0=50m with partially saturated Richards model in the case of VGM parameters: (a) α=6m^{-1}, n=3, m=1-1/n; (b) α=20m^{-1}, n=3, m=1-1/n. 66

Fig. 3-46 Comparison of the instantaneous static curve and the computed dynamic curve of the degree of saturation at t=10 hours at X_0=50m with partially saturated Richards model in the case of the exponential model parameters: (a) α=6m^{-1}, β =2m^{-1}, Hb=0.0; (b) α=20m^{-1}, β =6.667m^{-1}, Hb=0.0. 67

Fig. 3-47 Vertical profile of the instantaneous distributions of the pressure head $h(x,z,t_0)$ and the degree of saturation $S(x,z,t_0)$ at t=10 hours with partial saturated Richards model in the case of VGM parameters: (a) α=6m^{-1}, n=3, m=1-1/n; (b) α=20m^{-1}, n=3, m=1-1/n 67

Fig. 3-48 Vertical profile of the instantaneous distributions of the pressure head $h(x,z,t_0)$ and the degree of saturation $S(x,z,t_0)$ at t=10 hours with 3D Richards unsaturated model in the case of the exponential model parameters: (a) α=6m^{-1}, β=2m^{-1}, Hb=0.0; (b) α=20m^{-1}, β=6.667m^{-1}, Hb=0.0**.** Note: 1. in the figure (a), the red curve (h=-0.17m) corresponds to S=0.72 and the yellow curve (h=-0.05m) corresponds to S=0.9; **2.** in the figure (a), the red curve (h=-0.05m) corresponds to S=0.72 and the yellow curve (h=-0.02m) corresponds to S=0.9. 68

Fig. 3-49 Vertical profile of the instantaneous flux field $q(x,z,t_0)$ and pressure head $h(x,z,t_0)$ contours at t=10 hours with partial saturated Richards model in the case of VGM parameters: (a) α=6m^{-1}, n=3, m=1-1/n; (b) α=20m^{-1}, n=3, m=1-1/n. Note: Scale$_{flux}$=0.7. 69

Fig. 3-50 Vertical profile of the instantaneous flux field $q(x,z,t_0)$ and pressure head $h(x,z,t_0)$ contours at t=10 hours with partial saturated Richards model in the case of exponential

model parameters: (a) α=6m^{-1}, β=2m^{-1}, Hb=0.0; (b) α=20m^{-1}, β=6.667m^{-1}, Hb=0.0. Note: $\beta = \alpha / 3$ and Scale$_{flux}$=0.7. 70

Fig. 3-51 Comparison of the instantaneous free surfaces ($h(x,z,t_0)$ =0) at t=10 hours in the river bank of the linearized analytical solution of the plane flow Boussinesq equation and the numerical simulations with 2 partially saturated Richards models in the case of the parameters of VGM model (Num.2): α=6m^{-1}, n=3, m=1-1/n and parameters of exponential model (Num.4): α=6m^{-1}, β=2m^{-1}, Hb=0.0..... 71

Fig. 3-52 Comparison of the instantaneous free surfaces ($h(x,z,t_0)$=0) t=10 hours in the river bank of the linearized analytical solution of the plane flow Boussinesq equation and the numerical simulations with 2 partially saturated Richards models in the case of the parameters of VGM model (Num.3): α=20m^{-1}, n=3, m=1-1/n, and the parameters of exponential model (Num.5): α=20m^{-1}, β=6.667m^{-1}, Hb=0.0..... 71

Fig. 3-53 Comparison of the outflow discharge $Q(0,z,t)$ at the bank/river interface: (1) linearized analytical solution of Boussinesq equation; (2) numerical simulation of the Boussinesq equation (Num.1); (3) simulation with Richards model for 2 sets of parameters: 72

Fig. 4-1 "Darcy-scale" experiment in a small wave canal at IMFT laboratory. 76

Fig. 4-2 Tested sensors: CP5230 transmitter and Mini-Diver 77

Fig. 4-3 Tested sensors: capacitve sensor used to measure the water level fluctuations in the sandbox..... 78

Fig. 4-4 Instrumentation of the sandbox experiment in a small wave canal of IMFT laboratory: (a) capacitive sensor; (b) voltage transformation box and the computer..... 80

Fig. 4-5 Time evolution of measured water levels H(x,t) (symbols) and the corresponding theoretical values (solid curves) at different locations in the sandbox: x_0=0.0, x_1=3.0, x_2=6.0cm, x_3=8.2cm (period T=0.6896s, amplitude A_0 = 0.2521 cm)..... 81

Fig. 4-6 Plot of ln(A(x)/Ao) versus distance x from the right boundary of the sandbox (inlet): measured values (symbols) and straight line fit, in the case: T = 0.6896 s, A_0 = 0.2521 cm... 82

Fig. 4-7 Evolution of Q_{Bound} and Q_{Mass} 90

Fig. 4-8 Evolution of V_{Bound} and V_{Mass} 90

Fig. 4-9 Transient profiles of water height $H(x,t)$ at time t = T/4, T/2, 3T/4 and T, where T (0.2s) is the period of the water level imposed at the left boundary. Note: the amplitude of boundary oscillations is 50% of the mean water depth H_0 and H_0=0.2m. 91

Fig. 4-10 Water level profile $H(x,t_0)$ at t_0=T/4, T, 3T/4 and T: response to oscillations at left in the case: H_0=0.2m, A_0 / H_0=0.5, K_s=1.0E-3m/s, θ_s =0.2m^3/m^3 and $T = 0.2s$. 91

Fig. 4-11 Evolution of water level $H(x_0,t)$: response to oscillations at $x_0 = \delta/2$=0.004m, where δ is the wave decay length. 92

Fig. 4-12 Profile of the distribution of the maximum relative error $\varepsilon_{Max}(A_0/H_0, x)$ and the relationship curve of the ε_{Max} with respect to dimensionless parameter A_0/H_0 with the formula 1 for the numerical case 1:..... 95

Fig. 4-13 Profile of the distribution of the maximum relative error $\varepsilon_{Max}(A_0/H_0, x)$ and the relationship curve of the ε_{Max} with respect to dimensionless parameter A_0/H_0 with the formula **2** for the numerical case 1:..... 96

Fig. 5-1 Schema of the infrastructure of the wave canal 101

Fig. 5-2 Sand size distribution of the sediments..... 101

Fig. 5-3 Calibration of the capacitive sensors of the groundwater level for the Barcelona experiment..... 102

Fig. 5-4 Schematic of the layout of the capacitive sensors in the swash zone (vertical axial section). Sensor N°1 is closest to the free water. 104

Fig. 5-5 Sand beach with capacitive sensors / micro-piezometers at the HYDRALAB-SANDS wave canal (CIEM flume) in Barcelona. Incoming water waves are visible in the rear..... 104

Fig. 5-6 (a) (b) Evolution of the free water level fluctuation *WG0(t)* (15m right from the wave maker front)..... 105

Fig. 5-7 Fourier spectrum of *WG0(t)* (t = 0-1800 s, $\tau_{Tuckey} = 600s$)..... 106

Fig. 5-8 Water levels $H_i(t)$ versus time at the 7 sensors (Test 1: 18 March 2008)..... 108

Fig. 6-1 Zoom of the evolution of water level H_1(m) (Original signals, t=30-230s) 112

Fig. 6-2 Zoom of the evolution of water level H_1(m) (Original signals, t=30-80s)..... 112

Fig. 6-3 Fourier frequency spectrum of the water level fluctuations $H_1(t)$ (t=30-2459s).... 113

Fig. 6-4 Fourier frequency spectrum of the water level fluctuations $H_1(t)$ for two different time windows (during and after wave generation)..... 113

Fig. 6-5 Evolution of the main components C_4, C_5, C_6, C_7, C_8 , C_9 , C_{10} and C_{11} of the completed signal $H_1(t)$ by adding the mean water level (t = 30- 3306.8s, the number of the data is $N=2^L+1$, and L=15 is the dyadic scale)..... 115

Fig. 6-6 Fourier frequency spectrum S(f) of the component C_5 and C_7 of $H_1(t)$ with τ_{Tuckey} =600s.. 115

Fig. 6-7 Fourier frequency spectrum S(f) of the component C_5 of $H_1(t)$ (τ_{Tuckey} =70s)..... 116

Fig. 6-8 Wavelet analysis of signal H_1(t): comparison of original signal, bimodal Fourier signal, and 2-component wavelet..... 118

Fig. 6-9 Wavelet analysis of signal H_1(t): the dyadic components C_7 & C_5..... 118

Fig. 6-10 Original signals $H_7(t)$ (t=30-2459s) and its moving average with window halfwidth w_t=70s. 120

Fig. 6-11 Fourier frequency spectrum of the residual of H_7(t) with moving average filtering (w_t=70s and τ_{Tuckey}=600s) 120

Fig. 6-12 Original signals and the moving averages of $H_i(t)$ (i=1, …, 3) with moving average filtering 122

Fig. 6-13 Original signals and moving averages of $H_i(t)$ (i=4, …, 7) with moving average filtering 123

Fig. 6-14 Residuals of $H_i(t)$ (i=1, …, 7) with moving average filtering 123

Fig. 6-15 Fourier frequency spectrum of the residuals of $H_i(t)$ (i=1,…,7) and of WG_0(t), the "free water level" measured in the vicinity of the wave maker (free water level). 124

Fig. 6-16 Fourier spectrum function with respect to the frequency of the residuals of $H_i(t)$ (i=4,6,7). 125

Fig. 6-17 Fourier spectrum function with respect to the frequency of the residual of $H_7(t)$. 125

Fig. 6-18 Fourier frequency spectrum (energy spectrum) of water levels in the canal as a function of position (x), for different selected frequencies f_i fi or periods $T_i = 1/f_i$ $Ti = 1/fi$. 127

Fig. 6-19 Maximum cross correlation coefficient, lag time and wave propagation velocity of the residuals between $H_i(t)$ and $H_{i+1}(t)$ $(i = 1,...,6)$ (spatial distribution). 129

Fig. 6-20 The maximum cross-correlation coefficient of the future first wave and the corresponding lag time of the components of the original signal between $H_1(t)$ and $H_i(t)$ (i=2,…,7) with respect to the dyadic time scale 131

Fig. 6-21 The maximum cross-correlation coefficient of the future first wave and the corresponding lag time of the components C_7, C_8, C_9 and C_{10} of the original signal between $H_1(t)$ and $H_i(t)$ (i=2,…,7) with respect to the horizontal distance. 132

Fig. 6-22 Fourier cross analysis: spectral coherency between the residuals of $H_1(t)$ and $H_i(t)(i = 2,3,4)$ at t=400-1700s for a frequency range f = 0-0.2 Hz (or $T \geq 5s$). Spectral estimation with τ_{Tuckey}=300s. 133

Fig. 6-23 Fourier cross analysis: spectral coherency between the residuals of $H_1(t)$ and $H_i(t)(i = 4,\ldots,7)$ for a frequency range f = 0-0.2 Hz (or $T \geq 5s$). Spectral estimation with τ_{Tuckey}=300s. 133

Fig. 6-24 Fourier cross analysis: spectral coherency between the residuals of $H_1(t)$ and $H_i(t)(i=2,\ldots,7)$ for a frequency range f = 0-0.2 Hz (or $T \geq 5s$). Spectral estimation with τ_{Tuckey} =30s instead of 300s..... 134

Fig. 6-25 Coherencies of the residuals, plotted with respect to horizontal distance, for several particular harmonics (periods T_j). Note: τ_{Tuckey} =30s (strong spectral smoothing). 137

Fig. 6-26 Coherency function versus normalized frequency (frequency × lag time increment $\Delta\tau$, as explained in the text). 137

Fig. 6-27 Evolution of $H_1(t)$ and $H_3(t)$ at t=0-200s..... 138

Fig. 6-28 Evolution of $H_1(t)$ and $H_3(t)$ at t=1700-1900s..... 139

Fig. 6-29 Coherency between the residuals of $H_1(t)$ and $H_3(t)$ with respect to dimensional frequency..... 140

Fig. 6-30 Reduced gain between the residuals of $H_1(t)$ and $H_3(t)$ with respect to dimensional frequency..... 140

Fig. 6-31 Phase between the residuals of $H_1(t)$ and $H_3(t)$ with respect to dimensional frequency..... 141

Fig. 6-32 Cross-correlation function of the residuals of $H_1(t)$ and $H_3(t)$ (t=400s-1700s) with respect to lag time (Matlab function xcov, *unbiased* estimate) 142

Fig. 6-33 The maximum positive cross-correlation coefficient of the positive lag time, and the corresponding lag time of the components of the original signal between $H_1(t)$ and $H_3(t)$ 142

Fig. 6-34 Cross correlation function of the wavelet dyadic components C_5, C_7 and C_8 between $H_1(t)$ and $H_3(t)$. 143

Fig. 6-35 Evolution of $H1t$ and $H7t$ & the corresponding moving average..... 144

Fig. 6-36 Evolution of the residual of $H_1(t)$ and $H_7(t)$ 145

Fig. 6-37 Coherency functions of the residuals of $H_1(t)$ and $H_7(t)$ with respect to the frequency at $\tau_{\mathbf{Tuckey}}$ =30s and $\tau_{\mathbf{Tuckey}}$ =300s..... 145

Fig. 6-38 Reduced gain function of the residuals of $H_1(t)$ and $H_7(t)$ with respect to the frequency at $\tau_{\mathbf{Tuckey}}$ =30s and $\tau_{\mathbf{Tuckey}}$ =300s..... 146

Fig. 6-39 Phase function of the residuals of $H_1(t)$ and $H_7(t)$ with respect to the frequency at $\tau_{\mathbf{Tuckey}}$ =30s and $\tau_{\mathbf{Tuckey}}$ =300s..... 146

Fig. 6-40 Cross-correlation function of the residuals of $H_1(t)$ and $H_7(t)$ with respect to the past and the future lag time (Matlab function xcov, *unbiased estimate*) 147

Fig. 6-41 The maximum cross-correlation coefficient of the first wave in the positive lag time and the corresponding lag time of the components of the original signals between $H_1(t)$ and $H_7(t)$ 147

Fig. 6-42 Cross correlation function of the wavelet dyadic components C_5, C_7 and C_8 between $H_1(t)$ and $H_7(t)$ 148

Fig. 6-43 Wave phase velocity between water level sensors $H_i(t)$ and H_{i+1} (groundwater micro-piezometers) and the one between WG_i and WG_{i+1} (open water pressure sensor) with respect to the horizontal x(i+1), in the Barcelona wave canal. 149

Fig. 6-44 Wave phase velocity in the sandy beach from the Dupuit-Boussinesq model, plotted with respect to the period T (range T=0-40s)..... 151

Fig. 7-1 vertical cross section of the numerical simulations of Richards model 156

Fig. 7-2 Boundary water level condition $H_1(t)$ (experimental results) 156

Fig. 7-3 Evolution of Q_{Bound} and Q_{Mass} 159

Fig. 7-4 Evolution of V_{Bound} and V_{Mass} 159

Fig. 7-5 (a) Comparisons of the measured water levels and the numerical results for the Boussinesq flow model with Ks=2.8E-2m/s: evolution of the water level at different positions : Sensors No.2, No.3, No.4, No.5, No.6 and No.7.(t=0-2450s) 159

Fig. 7-6 (a) Sensitivity analysis of simulated water level evolution at different positions : Sensors No.2, No.3, No.4, No.5, No.6 and No.7.(t=0-2450s) in the cases: Ks=2.8E-1, 2.8E-2, and 2.8E-3m/s..... 161

Fig. 7-7 Water content curve $\theta(h)$ in log-log of the micro porous media and the macro porous media 166

Fig. 7-8 Hydraulic conductivity curve $K(h)$ in log-log of the micro porous media and the macro porous media 166

Fig. 7-9 Capillary diffusion $D(h)$ in log-log of the micro porous media and the macro porous media 166

Fig. 7-10 Capillary capacity $C(h)$ in log-log of the micro porous media and the macro porous media 166

Fig. 7-11 Standardized linear iteration process of the pressure head in log10 167

Fig. 7-12 Standardized nolinear iteration process of the pressure head in log10 167

Fig. 7-13 Evolution of Q_{Bound} and Q_{Mass} 168

Fig. 7-14 Evolution of the difference of the entry water level fluctuations..... 168

Fig. 7-15 Experimental profile of the instantaneous water level fluctuations in the vertical section (7 sensors) per 1s. Note the red course line is the free surface of the last time. 169

Fig. 7-16 Numerical profile of the instantaneous water level fluctuations in the vertical section (7 sensors) per 1s. Note the red course line is the free surface of the last time. 169

Fig. 7-17 Profiles of the instantaneous water level fluctuations in the vertical section: comparison between the numerical results (Richards model) and the experimental results.. 170

Fig. 7-18 Evolution of the water levels of 6 sensors (comparison with the experimental results) 171

Fig. 7-19 Zoom of evolution of the water levels of 3 sensors at t=0-200s (comparison with the experimental results) 171

Fig. 7-20 Fourier spectrum function with respect to the frequency (m=700, dt=0.1s)..... 172

Fig. 7-21 Evolution of the residual of $H_6(t)$ (window halfwidth=300s, k=1,dt=0.1s) 172

Fig. 7-22 Fourier spectrum function with respect to the frequency (m=6000, dt=0.1s)..... 172

Fig. 7-23 Auto-correlation function $R_{H_3H_3}(\tau)$ of $H_3(t)$ with respect to the lag time..... 173

Fig. 7-24 Auto-correlation function of the residual of $H_6(t)$ $R_{H_{6\,Re}H_{6\,Re}}(\tau)$ with respect to the lag time 173

Fig. 7-25 Coherency function with respect to the reduced frequency 173

Fig. 7-26 Reduced gain function ($H_1(t)\&H_3(t)$) with respect to the reduced frequency (Fourier analysis: m=700, dt=0.1s) 174

Fig. 7-27 Phase function ($H_1(t)\&H_3(t)$) with respect to the reduced frequency (Fourier analysis: m=700, dt=0.1s) 174

Fig. 7-28 Cross-correlation ($H_1(t)\&H_3(t)$) with respect to the lag time..... 175

Fig. 7-29 Relationship of the maximum inter-correlation and the dyadic time scale between $H_1(t)$ and $H_3(t)$ with multi-resolution wavelet and temporal analysis methods. 175

Fig. 7-30 Evolution of the wavelet dyadic component C8 of $H_3(t)$ 176

Fig. 7-31 Sensitivity analysis: evolution of the water levels of sensor No.7 $H_7(t)$ (comparison with the experimental results) 177

Fig. 7-32 Sensitivity analysis: Profiles of the instantaneous water level fluctuations in the vertical section (comparison with the experimental results)..... 178

Fig. 7-33 Water content curve $\theta(h)$ in semi-log x axis of the micro porous media and the macro porous media (*Exp. model*)..... 180

Fig. 7-34 Hydraulic conductivity curve $K(h)$ in log-log of the micro porous media and the macro porous media (*Exp. model*)..... 180

Fig. 7-35 Capillary diffusion $D(S_e)$ in semi-log y axis of the micro porous media and the macro porous media 180

Fig. 7-36 capillary capacity $C(S_e)$ in semi-log y axis of the micro porous media and the macro porous media 180

Fig. 7-37 Standarlized linear iteration process of the pressure head in log10 (*Exp. model*). 180

Fig. 7-38 Standarlized nolinear iteration process of the pressure head in log10 (*Exp. model*) 180

Fig. 7-39 Evolution of Q_{Bound} and Q_{Mass} (*Exp. model*) 181

Fig. 7-40 Evolution of the water levels of 6 sensors (comparison with the experimental results) (*Exp. model*) 181

Fig. 7-41 Profile of the pressure head contours, the flux velocity and the beach slope at t=735s (length scale in z and in y are 10) (*Exp. model*)..... 183

Fig. 7-42 Profile of the pressure head contours, the flux velocity and the beach slope at t=735s (length scale in z and in y are 10) (*VGM model*) 183

Fig. 7-43 Profile of the water content $\theta(h)$ at t=735s in the xz plane (length scale in z and in y are respectively 10) (*Exp. model*)..... 183

Fig. 7-44 Profile of the water content $\theta(h)$ at t=735s in the xz plane (length scale in z and in y are respectively 10) (*VGM model*) 183

Fig. 7-45 Profile of the instantaneous pressure head contours, the flux velocity and the beach slope at t=980s (length scales in z and in y are respectively 10) (*Exp. model*)..... 183

Fig. 7-46 Profile of the instantaneous pressure head contours ,the flux velocity and the beach slope at t=980s (length scales in z and in y are respectively 10) (*VGM model*) 183

Fig. 7-47 Profile of the instantaneous water content $\theta(h)$ at t=980s in the xz plane (length scales in z and in y are respectively 10) (*Exp. model*) 184

Fig. 7-48 Profile of the instantaneous water content $\theta(h)$ at t=980s in the xz plane (length scales in z and in y are respectively 10) (*VGM model*)..... 184

Fig. 7-49 Zoom of the evolution of $H_1(t)$ at t=700s-1000s..... 185

Fig. 9-1 Calculation of the moving average for a random time serial of the atmospheric pressure with time Δt (i) 219

Fig. 9-2 Schema of the sampling of a discrete-time signal on a temporal observation window with the finite size. 231

Fig. 9-3 Evolution of the regular signal $X(t) = 1.5sin\left(\frac{2\pi t}{2^7 \Delta t}\right) + 3sin\left(\frac{2\pi t}{2^5 \Delta t}\right)$ 238

Fig. 9-4 Evolution of the approximations with the increasing dyadic time scale of the regular signal $X(t)$ by multi-resolution wavelet analysis 239

Fig. 9-5 Evolution of the residuals with the increasing dyadic time scale of the regular signal $X(t)$ with multi-resolution wavelet analysis 239

Fig. 9-6 Evolution of the principal dyadic components of the regular signal $X(t)$ by multi-resolution wavelet analysis with Daubechies20 filter 240

Fig. 9-7 Comparison of the evolution of the sum of the components C5 and C7, and the original signal $X(t)$ (multi-resolution wavelet analysis) 240

Fig. 9-8 Comparison of the Fourier spectral functions of the sum of the components C5 and C7, and the original signal $X(t)$ (Fourier spectral analysis, Tuckey filter, M=320<N/3=342, Δt =1s) 241

Fig. 10-1 Raw signal $H_i(t)$(i=1,…,7) measured in the sloping sands beach245

Fig. 10-2 Complete time series of $H_1(t)$ and $H_6(t)$ 245

Fig. 10-3 Evolution of water level $H_1(t)$ (m) (t=0-1736s, original signal). 246

Fig. 10-4 Zoom of evolution of water level $H_1(t)$ (m) (t=0-50s, original signal). 246

Fig. 10-5 Zoom of evolution of water level $H_1(t)$ (m) (t=0-200s, original signal). 247

Fig. 10-6 Evolution of water level $H_6(t)$ (m) (t=0-1800s, original signal). 247

Fig. 10-7 Results of P(f) of the original signal $H_1(t)$ with Morlet wavelet analysis (A. SEVRAIN) 248

Fig. 10-8 Reduced Fourier spectrum with the respect to the reduced frequency (dimensionless, $H_1(t)$, original signal) 249

Fig. 10-9 Reduced Fourier spectrum with the respect to the reduced frequency in log-log axis (dimensionless, $H_1(t)$, original signal) 249

Fig. 10-10 Evolution of the dyadic wavelet components of the original signal $H_1(t)$ with multi-resolution wavelet 250

Fig. 10-11 Dyadic component C_7 of the original signal $H_1(t)$ obtained with multi-resolution wavelet (The time scale: $T_7 = 2^7.\Delta t = 12.8$ s) 250

Fig. 10-12 Dyadic component C_8 of the original signal $H_1(t)$ obtained with multi-resolution wavelet (The time scale: $T_8 = 2^8.\Delta t = 25.6$ s) 251

Fig. 10-13 Dyadic component C_5 of the original signal $H_1(t)$ obtained with multi-resolution wavelet (The time scale: $T_5 = 2^5.\Delta t = 3.2$ s) 251

Fig. 10-14 Auto-correlation function $R_{H_1H_1}(k)$ of the original signal $H_1(t)$ (dt=0.1s) 252

Fig. 10-15 Evolution of the original signal $H_1(t)$ and its corresponding moving average with moving average filtering (*window halfwidth* w_t=5s) 252

Fig. 10-16 Evolution of the moving average of the original signal $H_1(t)$ with moving average filtering (*window halfwidth* w_t=5s). 253

Fig. 10-17 Evolution of the residual of the original signal $H_1(t)$ with moving average filtering (*window halfwidth* w_t=5s). 253

Fig. 10-18 Fourier spectrum function $S(f)$ of the residual of $H_1(t)$ with moving average filtering (*window halfwidth* wt=5s) 254

Fig. 10-19 Evolution of the wavelet dyadic components of residual of $H_1(t)$ with moving average filtering (*window halfwidth* w_t=5s) 254

Fig. 10-20 Evolution of the sum of 2 wavelet dyadic components C_5(t) and C_7(t) of residual of $H_1(t)$ with moving average filtering (*window halfwidth* w_t=5s) 255

Fig. 10-21 Auto-correlation function $R_{H_{1\mathrm{Re}}H_{1\mathrm{Re}}}(k)$ of the residual of $H_1(t)$ with moving average filtering (*window halfwidth* w_t=5s) (dt=0.1s) 255

Fig. 10-22 Evolution of the residual of $H_1(t)$ with differential filtering 256

Fig. 10-23 Reduced Fourier spectrum function $S(f)$ of the residual of $H_1(t)$ with differential filtering (dimensional). 256

Fig. 10-24 Evolution of the wavelet dyadic components of residual of $H_1(t)$ with differential filtering 257

Fig. 10-25 Evolution of the sum of 2 wavelet dyadic components C_5(t) and C_7(t) of the residual of $H_1(t)$ (differential filtering) and the one of the original signal $H_1(t)$. 257

Fig. 10-26 Auto-correlation function $R_{H_{1\mathrm{Re}}H_{1\mathrm{Re}}}(k)$ of the residual of $H_1(t)$ with differential filtering (dt=0.1s) 258

Fig. 10-27 Evolution of $H_1(t)$ and its approximation with multi-resolution wavelet (C_5) ... 258

Fig. 10-28 Evolution of the approximation of $H_1(t)$ with multi-resolution wavelet (C_5) .. 259

Fig. 10-29 Evolution of the residual of $H_1(t)$ with multi-resolution wavelet (C_5) 259

Fig. 10-30 Fourier spectrum with respect to the frequency $S(f)$ of the residual of $H_1(t)$ with multi-resolution wavelet..... 259

Fig. 10-31 Autocorrelation function $R_{H_{1\mathrm{Re}}H_{1\mathrm{Re}}}(k)$ of the residual of $H_1(t)$ with multi-resolution wavelet filtering..... 260

Fig. 10-32 Evolution of the wavelet dyadic components of residual of $H_1(t)$ with multi-resolution wavelet filtering (C_5)..... 260

Fig. 10-33 Evolution of the sum of 2 wavelet dyadic components C_5(t) and C_7(t) of residual of $H_1(t)$ with multi-resolution wavelet filtering (C_5) 261

Fig. 10-34 Evolution of the wavelet dyadic component C_5(t) of the residuals and the original signal of $H_1(t)$ 261

Fig. 10-35 Fourier spectra of the wavelet dyadic component C_5 of the residuals and the original signal of $H_1(t)$ 262

Fig. 10-36 Fourier spectrum of the original signal $H_6(t)$ in log-log axis (m=6000, dt=0.1s) 262

Fig. 10-37 Evolution of the wavelet components of the original signal $H_6(t)$ with multi-resolution wavelet 263

Fig. 10-38 Evolution of the wavelet dyadic component C_9 of the original signal $H_6(t)$ with multi-resolution wavelet..... 263

Fig. 10-39 Evolution of the wavelet dyadic component C_{10} of the original signal $H_6(t)$ with multi-resolution wavelet..... 264

Fig. 10-40 Autocorrelation function of the original signal $H_6(t)$ $R_{H6H6}(k)$ (dt=0.1s) 264

Fig. 10-41 Evolution of the original signal $H_6(t)$ and its corresponding moving average with moving average filtering (*window halfwidth* w_t=30s)..... 265

Fig. 10-42 Evolution of the moving average of $H_6(t)$ (*window halfwidth* w_t=30s) 265

Fig. 10-43 Evolution of the residual of $H_6(t)$ with moving average filtering (*window halfwidth* w_t=30s) 265

Fig. 10-44 Fourier spectrum function $S(f)$ of the residual of $H_6(t)$ with moving average filtering (*window halfwidth* w_t=30s) 266

Fig. 10-45 Evolution of the wavelet components of the residual of $H_6(t)$ with moving average filtering and multi-resolution wavelet analysis..... 266

Fig. 10-46 Evolution of the wavelet dyadic component C_8 of the residual of $H_6(t)$ with moving average filtering and multi-resolution wavelet analysis 267

Fig. 10-47 Evolution of the wavelet dyadic component C_9 of the residual of $H_6(t)$ with moving average filtering and multi-resolution wavelet analysis 267

Fig. 10-48 Autocorrelation function $R_{H_{6\mathrm{Re}}H_{6\mathrm{Re}}}(k)$ (future)of the residual of $H_6(t)$ with moving average filtering (*window halfwidth* wt=30s) 268

Fig. 10-49 Evolution of the residual of $H_6(t)$ with differential filtering (t=1000-1050s) 268

Fig. 10-50 Fourier spectrum function with the respect to the frequency of the residual of $H_6(t)$ with differential filtering..... 269

Fig. 10-51 Evolution of the wavelet dyadic components of the residual of $H_6(t)$ with differential filtering and multi-resolution wavelet 269

Fig. 10-52 Evolution of the wavelet dyadic component C_9 of the residual of $H_6(t)$ with differential filtering and multi-resolution wavelet 270

Fig. 10-53 Autocorrelation function $R_{H_{6\mathrm{Re}}H_{6\mathrm{Re}}}(k)$ of the residual of $H_6(t)$ with differential filtering..... 270

Fig. 10-54 Evolution of $H_6(t)$ and its approximation with multi-resolution wavelet filtering (C_{10})..... 271

Fig. 10-55 Evolution of the residual of $H_6(t)$ with multi-resolution wavelet filtering (t=700-1700s)... 271

Fig. 10-56 Fourier spectrum function of the residual of $H_6(t)$ with multi-resolution wavelet filtering (m=6000, dt=0.1s) with respect to frequency 271

Fig. 10-57 Evolution of the wavelet dyadic components of the residual of $H_6(t)$ with multi-resolution wavelet filtering and analysis..... 272

Fig. 10-58 Evolution of the wavelet dyadic component C_9 of the residual of $H_6(t)$ with multi-resolution wavelet filtering and analysis 272

Fig. 10-59 Autocorrelation function $R_{H_{6\mathrm{Re}}H_{6\mathrm{Re}}}(k)$ of the residual of $H_6(t)$ with multi-resolution wavelet filtering..... 273

Fig. 10-60 Evolution of the wavelet dyadic component $C_9(t)$ of $H_6(t)$ 273

Fig. 10-61 Fourier spectrum of the wavelet dyadic component C_9 of $H_6(t)$ with respect to the frequency..... 274

Fig. 10-62 Gain function with respect to the reduced frequency (m=700, dt=0.1s) 274

Fig. 10-63 Coherency function with respect to the reduced frequency (m=700, dt=0.1s).... 275

Fig. 10-64 Phase function with respect to the reduced frequency (m=700, dt=0.1s) 275

Fig. 10-65 Maximum inter-correlation with respect to the dyadic components 276

Fig. 10-66 Evolution of the residuals of $H_1(t)$ and $H_6(t)$ with moving average filtering (*wt_1=5s et wt_6=30s, t=0-1800s*) 276

Fig. 10-67 Gain function of the residuals of $H_1(t)$ and $H_6(t)$ with moving average filtering (*wt_1=5s et wt_6=30s, t=0-1800s*) (m=700, dt=0.1s) 277

Fig. 10-68 Coherency function of the residuals of $H_1(t)$ and $H_6(t)$ with moving average filtering (*wt1=5s et wt6=30s, t=0-1800s*)(m=700, dt=0.1s) 277

Fig. 10-69 Phase function of the residuals of $H_1(t)$ and $H_6(t)$ with moving average filtering (*wt1=5s et wt6=30s, t=0-1800s*) (m=700, dt=0.1s) 278

Fig. 10-70 Maximum inter-correlation between the residuals of $H_1(t)$ and $H_6(t)$ with moving average filtering (*wt_1=5s et wt_6=30s, t=0-1800s*) with respect to the dyadic components 278

Fig. 10-71 Evolution of the residuals of $H_1(t)$ and $H_6(t)$ with differential filtering 279

Fig. 10-72 Gain function of the residuals of $H_1(t)$ and $H_6(t)$ with differential filtering (m=700, dt=0.1s) 279

Fig. 10-73 Coherency function of the residuals of $H_1(t)$ and $H_6(t)$ with differential filtering (m=700, dt=0.1s) 280

Fig. 10-74 Phase function of the residuals of $H_1(t)$ and $H_6(t)$ with differential filtering (m=700, dt=0.1s) 280

Fig. 10-75 Maximum inter-correlation between the residuals of $H_1(t)$ and $H_6(t)$ with differential filtering with respect to the dyadic time scale 280

Fig. 10-76 Evolution of the residuals of $H_1(t)$ and $H_6(t)$ with multi-resolution wavelet filtering (*C_5 and C_{10}*) 281

Fig. 10-77 Gain function of the residuals of $H_1(t)$ and $H_6(t)$ with multi-resolution wavelet filtering (*C_5 and C_{10}*) (m=700, dt=0.1s) 281

Fig. 10-78 Coherency function of the residuals of $H_1(t)$ and $H_6(t)$ with multi-resolution wavelet filtering (*C_5 and C_{10}*) (m=700, dt=0.1s) 282

Fig. 10-79 Phase function of the residuals of $H_1(t)$ and $H_6(t)$ with multi-resolution wavelet filtering (*C_5 and C_{10}*) (m=700, dt=0.1s) 282

Fig. 10-80 Maximum inter-correlation between the residuals of $H_1(t)$ and $H_6(t)$ with multi-resolution wavelet filtering (*C_5 and C_{10}*) with respect to the dyadic time scale 283

Fig. 10-81 Evolution of wavelet dyadic component $C_8(t)$ of the original signal $H_1(t)$ and $H_6(t)$ 283

Fig. 10-82 Fourier spectrum of the wavelet dyadic component C8 of the original signal $H_1(t)$ and $H_6(t)$ with respect to the frequency 283

Fig. 10-83 Evolution of the dyadic wavelet component C_8 of the residuals of $H_1(t)$ and $H_6(t)$ with moving average filtering (*wt_1=5s et wt_6=30s, t=0-1800s*)..... 284

Fig. 10-84 Fourier spectrum of wavelet dyadic component C8(t) of $H_1(t)$ and $H_6(t)$ with moving average filtering (*wt_1=5s et wt_6=30s, t=0-1800s*) with respect to the frequency..... 284

Fig. 10-85 Evolution of the dyadic wavelet component C_8 of the residual of $H_1(t)$ and $H_6(t)$ with differential filtering (*t=0-1800s*)..... 284

Fig. 10-86 Fourier spectrum with respect to the frequency of wavelet dyadic component C_8(t) of $H_1(t)$ and $H_6(t)$ with differential filtering (*t=0-1800s*)..... 285

Fig. 10-87 Evolution of the dyadic wavelet component C_8 of the residuals o $H_1(t)$ f and $H_6(t)$ with multi-resolution wavelet filtering (*C_5 and C_{10}, t=0-1800s*) 285

Fig. 10-88 Fourier spectrum of the wavelet dyadic component C8 of the residuals of $H_1(t)$ and $H_6(t)$ with multi-resolution wavelet filtering (*C_5 and C_{10}, t=0-1800s*) with respect to the frequency..... 285

Fig. 11-1 Left regular entry water level fluctuations for one wave numerical test 288

Fig. 11-2 Water content curve $\theta(h)$ in log-log of the micro porous media and the macro porous media 289

Fig. 11-3 Hydraulic conductivity curve $K(h)$ in log-log of the micro porous media and the macro porous media 289

Fig. 11-4 Standarlized linear iteration process of the pressure head in log10 290

Fig. 11-5 Standarlized nolinear iteration process of the pressure head in log10 290

Fig. 11-6 Zoom of the evolution of Q_{Bound} and Q_{Mass} at t=0-90s..... 290

Fig. 11-7 Zoom of the evolution of V_{Bound} and V_{Mass} at t=0-90s..... 290

Fig. 11-8 Profile of the pressure head contours and flux velocity at t=T/8=3.75s (length scales in z and in y are respectively 10)..... 291

Fig. 11-9 Profile of the pressure head contours and flux velocity at t=3T/8=11.25s (length scales in z and in y are respectively 10)..... 291

Fig. 11-10 Profile of the pressure head contours, and flux velocity at t=5T/8=18.75s (length scales in z and in y are respectively 10)..... 291

Fig. 11-11 Profile of the pressure head contours and flux velocity at t=7T/8=26.25s (length scales in z and in y are respectively 10)..... 291

Fig. 11-12 Instantaneous profile of the water content $\theta(h)$ at t=T/8=3.75s in the vertical section (length scales in z and in y are respectively 10) 292

Fig. 11-13 Instantaneous profile of the water content $\theta(h)$ at t=3T/8=11.25s in the vertical section (length scales in z and in y are respectively 10) 292

Fig. 11-14 Instantaneous profile of the water content $\theta(h)$ at t=5T/8=18.75s in the vertical section (length scales in z and in y are respectively 10) 293

Fig. 11-15 Instantaneous profile of the water content $\theta(h)$ at t=7T/8=26.25s in the vertical section (length scales in z and in y are respectively 10) 293

Fig. 11-16 Profiles of the pressure head evolution in the z direction at x=1.5m 293

Fig. 11-17 Pressure head h(x,0,t) at t=T/4 and t=3T/4 obtained by the file OUTHPB..... 294

Fig. 11-18 Comparison of the pressure head h(x,0,t) and the free surface h(x,z,t)=0.0 at t=T/4 and t=3T/4 294

Fig. 11-19 Profile of the evolution of the horizontal line pressure head at z=0 $h(x, z=0, t)$ or the water level fluctuations $H(x,t)$ (time interval=10 dt=1.0s)..... 294

Fig. 11-20 Evolution of the approximate water levels of the 7 sensors at t=0-200s..... 295

Fig. 11-21 Zoom of the evolution of the water levels of the 7 sensors at t=0-90s (t=0-3T).295

Fig. 11-22 Zoom of the evolution of the water levels of the 7 sensors at t=0-30s (t=0-T)... 295

Fig. 11-23 Evolution of the entry water level, Q_{Bound} and the inside water levels in the porous media 296

Fig. 11-24 Evolution of the mean entry water level gradient $\frac{\partial \overline{H_1(t)}}{\partial x}$ 298

Fig. 12-1 Left regular entry water level fluctuations with several continuous waves 301

Fig. 12-2 Standarlized linear iteration process of the pressure head in log10 302

Fig. 12-3 Standarlized nolinear iteration process of the pressure head in log10 302

Fig. 12-4 Zoom of the evolution of Q_{Bound} and Q_{Mass} at t=0-90s..... 302

Fig. 12-5 Zoom of the evolution of V_{Bound} and V_{Mass} at t=0-90s..... 302

Fig. 12-6 Profile of the pressure head contours, the flux velocity and the beach slope at t=T+T/8=33.75s (length scale in z and in y are 10) 303

Fig. 12-7 Profile of the pressure head contours, the flux velocity and the beach slope at t=10T+T/4=303.75s (length scale in z and in y are 10) 303

Fig. 12-8 Profile of the pressure head contours, the flux velocity and the beach slope at t=T+3T/8=41.5s (length scale in z and in y are 10) 303

Fig. 12-9 Profile of the pressure head contours ,the flux velocity and the beach slope at t=10T+3T/8=311.25s (length scale in z and in y are 10) 303

Fig. 12-10 Profile of the water content $\theta(h)$ at t=T+T/8=33.75s in the vertical section..... 304

Fig. 12-11 Profile of the water content $\theta(h)$ at t=10T+T/8=303.75s in the vertical section (length scale in z and in y are 10)..... 304

Fig. 12-12 Profile of the water content $\theta(h)$ at t=T+3T/8=41.5s in the vertical section (length scale in z and in y are 10)..... 305

Fig. 12-13 Profile of the water content $\theta(h)$ at t=10T+3T/8=311.5s in the vertical section (length scale in z and in y are 10)..... 305

Fig. 12-14 Profile of the pressure head evolution on the bottom z=0 (per each 10 time steps). 305

Fig. 12-15 Evolution of the water levels at the 7 sensors at t=0-600s. 306

Fig. 12-16 Zoom of the evolution of the water levels at the 7 sensors at t=0-180s (t=0-6T). 306

Fig. 12-17 Evolution of the water levels of 6 sensors (t=0-600s)..... 307

Fig. 12-18 Maximum cross-correlation between $H_1(t)$ and $H_i(t)(i=2,\ldots,7)$ $R_{max}(Lx)$ with respect to the horizontal distance of the sensor position from the sensor No.1 *(Original signal)*..... 308

Fig. 12-19 Lag time corresponding to the maximum cross-correlation between $H_1(t)$ and $H_i(t)(i=2,\ldots,7)$ with respect to the horizontal distance of the sensor position from the sensor No.1 *(Original signal)*..... 308

Fig. 12-20 Evolution of the entry water level $H_1(t)$, Q_{Bound} and the inside water levels of the 6 sensors in the porous media 309

Fig. 12-21 Cross correlation of entry water level $H_1(t)$ and entry water discharge Q_{Bound} $R_{H_1Q_{Bound}}$ at tau (lag time)=-200s-+200s with XCOV(Q_{Bound} , H_1) (unbiased) 310

Fig. 12-22 Evolution of the mean entry water level gradient $\frac{\partial\overline{H_1(t)}}{\partial x}$, entry water level $H_1(t)$ and the inside water levels of the 6 sensors in the porous media..... 311

Fig. 12-23 Cross correlation of $H_1(t)$ and mean entry water level gradient $\frac{\partial\overline{H_1(t)}}{\partial x}$ R_{H_1MEWLG} at tau (lag time)=-200s-+200s with XCOV($\frac{\partial\overline{H_1(t)}}{\partial x}$, H_1) (unbiased) 311

Fig. 12-24 Sensibility analysis of the saturated hydraulic conductivity K_S, VGM parameters (α ,n), saturated water content θ_S on the amplitudes of the groundwater level fluctuations. 312

Fig. 12-25 Sensibility analysis of the entry amplitude A_0, entry period T, and beach slope on the amplitudes of the groundwater level fluctuations. 313

Fig. 12-26 Sensibility analysis of the saturated hydraulic conductivity K_S, VGM parameters (α,n), saturated water content θ_S on the steady mean groundwater levels..... 313

Fig. 12-27 Sensibility analysis of the entry amplitude A_0, entry period T, and beach slope on the steady mean groundwater levels..... 314

List of Tables

Table 2-1 Time-varying boundary condition in the INPUT1 of Bigflow 29

Table 2-2 Model types and corresponding source files for the executable files of Bigflow .. 30

Table 2-3 Boundary conditions on six faces of the calculated column 33

Table 2-4 Hydraulic properties and numerical parameters of the micro and macro porous media..... 34

Table 2-5 Numerical parameters (INPUT1) for the calculation of time step, non-linear/outer (Picard) and linear/inner iterations 34

Table 3-1 Numerical parameters (INPUT1) for the calculation of time step, non-linear/outer (Picard) and linear/inner iterations 48

Table 3-2 Numerical parameters (INPUT1) for the calculation of time step, non-linear/outer (Picard) and linear/inner iterations 60

Table 4-1 Estimated saturated hydraulic conductivity 83

Table 4-2 Numerical parameters (INPUT1) for the calculation of time step, non-linear/outer (Picard) and linear/inner iterations 89

Table 4-3 Main parameters for the cases of the numerical simulations 94

Table 5-1 Grain size distribution 102

Table 5-2 Sample statistics 102

Table 5-3 Coefficient values of the linear relationship between the voltage output signal and the measured water level in the static clear water for seven capacitive sensors 103

Table 5-4 Coefficient values of the linear relationship between the voltage output signal and the measured water level in Barcelona wave canal for seven capacitive sensors 104

Table 5-5 Position of the 14 sensors for the free water level fluctuations from the wave generator front to the swash zone..... 105

Table 5-6 All the carried tests in the Barcelona wave canal 107

Table 6-1 Wavelet component dyadic time scale and corresponding Fourier period of $H_1(t)$ 116

Table 6-2 Coefficients of the 'analytical' bimodal approximation 118

Table 6-3 The wave propagation velocity between Sensor No.1 and Sensor No.3 139

Table 7-1 Horizontal distance of the sensors from the left boundary 156

List of Tables

Table 7-2 Calculated saturated hydraulic conductivity by Kozeny-Carman formula 1 157

Table 7-3 Numerical parameters (INPUT1) for the calculation of time step, non-linear/outer (Picard) and linear/inner iterations 158

Table 7-4 Physical properties of the micro and macro porous media 166

Table 7-5 Pamameter values for the sensitivity analysis on the numerical results 176

Table 7-6 Physical properties of the beach and the sea of the numerical simulation with exponential model 179

Table 9- 1 Main equations of the orthogonal multi-resolution wavelet analysis 237

Table 11-1 Physical properties of the macro porous media and the micro porous media 289